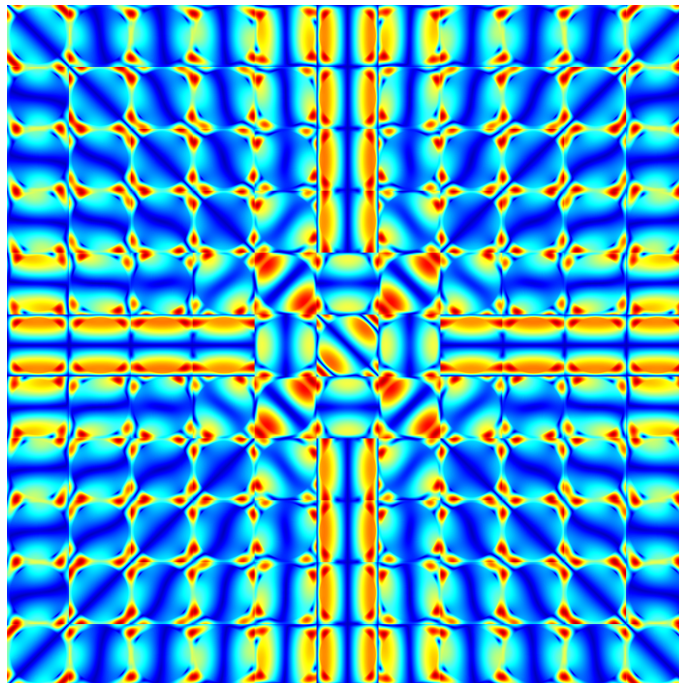


2D H-polarized Auxiliary Basis Functions for the Extension of the Photonic Wannier Function Expansion for Photonic Crystal Circuitry



PhD Thesis
by
Dipl. Phys. Patrick Mack

11.02.2011

Instructor: Prof. Dr. Kurt Busch
2nd Instructor: Prof. Dr. Peter Wölfle

2D H-polarized Auxiliary Basis Functions for the
Extension of the Photonic Wannier Function Expansion for
Photonic Crystal Circuitry

Zur Erlangung des akademischen Grades eines

DOKTORS DER NATURWISSENSCHAFTEN

von der Fakultät für Physik des Karlsruher Instituts für Technologie (KIT)

genehmigte

DISSERTATION

von

Dipl. Phys. Patrick Mack
aus Frankenthal (Pfalz)

Tag der mündlichen Prüfung: 11.02.2011

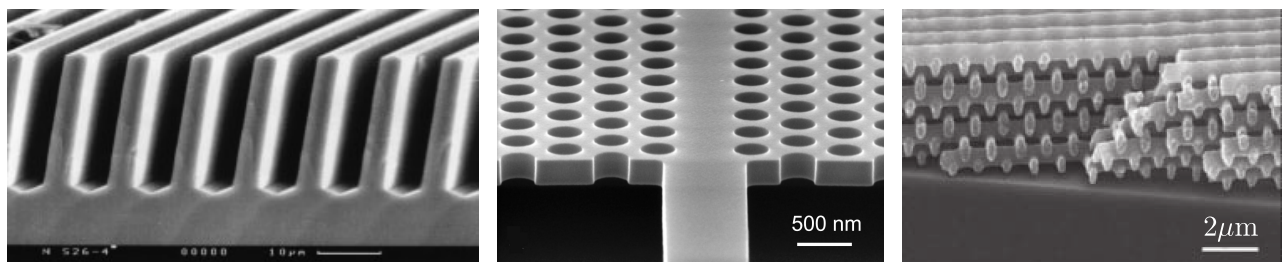
Referent: Prof. Dr. K. Busch
Korreferent: Prof. Dr. P. Wölffe

*Dedicated to Christina and Marco
Thank You
for the summer of my life*

Introduction

Light was among the very first things created by God in Christian mythology, followed by mankind and the assignment to ‘subdue the earth’,¹ and scientists have made vast progress since then to ‘subdue’ light: The discovery of Maxwell’s equations [1] provided the basis for a full understanding of classical electromagnetic wave propagation, the introduction of the photon by Einstein [2] lay ground to the development of the quantum theory of light which in turn made the invention of the laser possible. These tools and the advancements in creating structures on the micrometer and nanometer scale in a controlled fashion paved the way for the emerging field of photonics: scientists no longer depend merely on utilizing the optical properties of natural materials, but actively create and tailor artificial materials with novel and unprecedented effects on light propagation.

One notable milestone in this respect was the introduction of the concept of photonic crystals (PC) by John [3] and Yablonovitch [4]. These are periodic arrangements of dielectric materials, where the basic building blocks—the unit cells of the crystals—are repeated periodically in one, two or three dimensions. Examples of real structures are shown in Fig. 0.1. The combination of light scattering at the single constituents and Bragg scattering due to the underlying lattice gives rise to a band structure in the multi-branch dispersion relation for light propagating through these crystals. This, in turn, offers the possibility to open stop bands which are frequency ranges that prohibit light propagation along certain directions. By carefully adjusting the fabrication parameters (refractive index of constituent materials, lattice symmetry, geometry of one unit cell), one can get these stop bands to overlap, thus forming complete photonic band gaps (PBG). In those frequency ranges, wave propagation is forbidden regardless of the propagation direction. Thus, PBG materials can act as insulators for light.



(a) Bragg stack. Copyright Wiley-VCH Verlag GmbH & Co. KGaA. Reproduced with kind permission from [5].

(b) PC slab. Courtesy of The Optical Society. Reproduced with kind permission from [6].

(c) Woodpile structure. Reprinted by kind permission from Macmillan Publishers Ltd: Nature Materials [7], copyright (2004).

Figure 0.1: *Micrographs of photonic crystals with periodicities in (a) 1D, (b) 2D, and (c) 3D.*

Purposely designed defect structures in PCs break the translational symmetry and introduce strongly localized light modes in the band gaps. Their mode profiles penetrate the surrounding PC only a few

¹Genesis 1, 28, The Bible (King James Version).

lattice constants. This offers a new guiding mechanism for light besides index guiding in fibres,² enabling the construction of low loss sharp-bend waveguides, resonators with high Q-factors and complex photonic circuitry. These functional elements rely on the existence of the band gap which in turn derives from the Bragg scattering of light on the periodic structures. Since the lowest Bragg order corresponds to a lattice constant of roughly half the wavelength, photonic devices that manipulate light with wavelengths of about $1\ \mu\text{m}$ in this way (exploiting the band gap) must feature lattice constants and unit cell dimensions of the order of $0.5\ \mu\text{m}$.³ This length scale is realized in the structures of Fig. 0.1 and it is also the order of telecommunication wavelengths, where a wavelength of $1.5\ \mu\text{m}$ is currently employed in fibre networks [8]. Such fibre networks are in broad use today for data transmission over long distances (e.g., Internet data transmission) as well as short distances (e.g., local area networks). Optical fibres offer much higher data rates than electric signals can carry.⁴ However, for signal routing the optical signals still have to be converted to electrical signals, processed by electronic devices, and converted back to optical signals. This constitutes a bottle-neck, effectively reducing the high data rates. Therefore, the vision of all-optical signal processing emerged, eliminating the detour via electronic devices. Photonic crystals may provide the basis for photonic devices realizing this vision. Examples for the desired functionality photonic devices should provide are shown in Fig. 0.2. The ability to fabricate such integrated photonic circuitry would have the same revolutionary impact on the modern information society as the invention of transistors and integrated electronic circuits had, which finally made the development of computers and the world wide web possible.

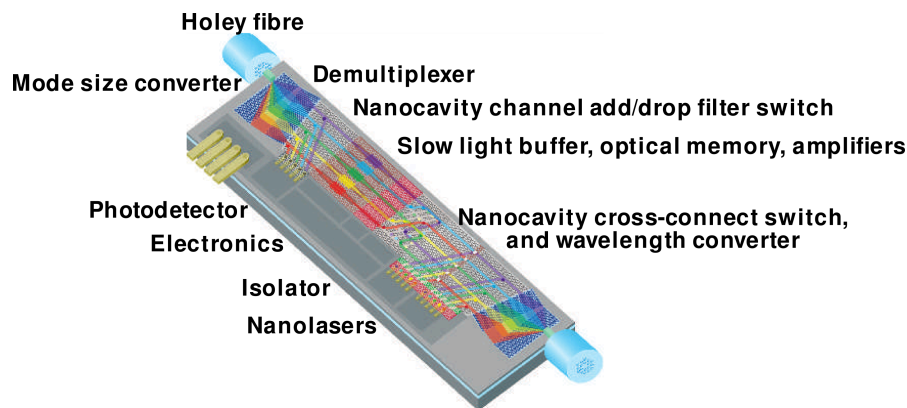


Figure 0.2: *Examples for signal processing components needed in integrated photonic circuitry for all-optical data processing and connection to electronic circuits. Reprinted by kind permission from Macmillan Publishers Ltd: Nature Photonics [10], copyright (2007).*

The potential usefulness of PCs in optical signal processing relies on the complete PBG. Since natural materials do not show a magnetic response for optical frequencies (i. e. visible light and the near infrared), we may set the magnetic permeability μ to one throughout this thesis. The effects of photonic crystals

²Light confinement in optical glass fibres is achieved by total internal reflection which relies on layers of different refractive indices.

³This is in contrast to metamaterials which are also periodic nanostructures. However, the lattice constant employed in that case is much smaller than the wavelength of light. For this reason, the dominant optical effects of metamaterials are described by effective constant values for the permittivity and permeability instead of a band structure for light. These effective parameters can be tailored to take on unusual values, e.g., an effective permeability not equal to one and even negative values are possible.

⁴In 2009, Alcatel-Lucent Bell Labs reported a data rate of 100 Petabit per second and kilometer which is 'equivalent to sending 400 DVDs per second over transoceanic cable' [9].

are then fully described by their position dependent, periodic electric permittivity distribution $\varepsilon(\mathbf{r})$. The experimental challenge consists in fabricating structures with a particular desired permittivity distribution that has complete photonic band gaps. However, only three-dimensional PCs localize light for all spatial directions by this effect. Great effort is put today to fabricate three-dimensional structures, but research also focused on simpler two-dimensional structures, the PC slabs. These are sheets of dielectrics that are periodically structured in one plane which provides the band gap. In the third dimension, localization of light is provided by index guiding. For technical applications as mentioned above, defect structures have to be designed and incorporated into these slabs. This in turn has not only desired effects, since the stop band in the third dimension is missing, allowing light scattered on defects to couple to leaky modes of the surrounding vacuum and get lost. Thus, the functionality of defect structures is also accompanied by a new loss mechanism. However, these are experimental and fabrication problems. The idealization of PC slabs to actual two-dimensional PCs yields model systems that are easier to study (neglecting out-of-plane loss mechanisms). In particular, the vectorial wave equations decouple in this case and wave propagation is governed by two simpler, scalar equations. These equations describe two distinct polarization states, the H-polarized and the E-polarized waves. They are completely determined by specifying the z -component H_z of the magnetic field—called H-polarized, also transverse electric (TE) polarization—or the z -component E_z of the electric field—called E-polarized, also transverse magnetic (TM) polarization.

These model systems provide insight to the principal working mechanisms and the functionality of optical devices, but exact analytical solutions to Maxwell's equations are rare in these systems. Due to the many possibilities to design PCs and the countless defect configurations, a numerical analysis of light propagation in PCs is vital to rate and also optimize the desired functionality. The focus of this thesis lies in the study of these two-dimensional PCs and the numerical analysis of the localized defect states therein. The model systems employed in this thesis consist of two-dimensional square and triangular lattices of cylindrical air holes in silicon, respectively, which are widely studied in the photonics community. Inspired by experimental advances in local pore infiltration [11–13], the defect types treated in this thesis are restricted to holes infiltrated with isotropic and anisotropic dielectrics, changing the permittivity locally and preserving the hole geometry [14]. This allows the design of actively tunable defect structures and to control the optical properties of the defects, instead of relying only on passively tuned designs by adjusting fabrication parameters.

The Wannier Function Approach: For finding numerical solutions to Maxwell's equations, a number of all-purpose as well as specially adapted methods are available [15]. One of the most popular methods is the finite-difference time-domain method which computes the time evolution of electromagnetic fields directly from specified sources or initial field distributions [16]. However, the analysis of circuits in PCs requires to model rather large systems with low group velocities of the waves, resulting in long simulation times. Additionally, suppressing reflections at the boundaries of the computational domains is not easy in PCs. For obtaining stationary states of a definite frequency, the plane-wave expansion and plane-wave based supercell method are widely used [17, 18], but they are also not feasible to describe systems larger than 10 lattice constants in each direction. This is because the localized defect modes in the band gap are expanded in a basis of spatially extended functions. For special systems containing highly symmetric scatterers, particularly adapted and highly accurate methods such as the multiple multipole method based on cylindrical [19] or vector spherical harmonics [20] are available. Further methods employed are the finite-element [21] and related discontinuous Galerkin [22, 23] methods. However, these methods either neglect the periodicity of the underlying PC, the localized nature of the defect modes one is interested in, or unit cell geometries other than cylinders and spheres.

So the idea came up to expand the wave equations into a set of basis functions that share as many properties as possible with the desired defect states in order to obtain a fast and memory efficient numerical scheme. This is similar to perturbative approaches, where states for weak perturbations resemble the eigenstates of the unperturbed systems which then constitute good expansion bases. However, in the case of defect structures in PCs, the exponentially localized defect modes hardly resemble the eigenmodes of the unperturbed PCs, which are infinitely extended Bloch modes (the same reason also limits the applicability of the supercell approach). With this observation in mind, localized Hermite-Gaussian functions are quite successful in the description of PC fibres [24, 25]. Even more adapted to the periodicity of the PC and the localized nature of defect modes in the band gap are the Wannier functions (WF). They have been introduced by Wannier [26] in 1937 and used in the description of localized electronic states in solid state theory. They are defined via a lattice Fourier transform of the Bloch modes of the unperturbed periodic system and can, in principle, be chosen to be exponentially localized [27]. However, they have seen little use in numerical calculations because they are not uniquely determined and constitute rather a class of functions than a particular set of functions. Nevertheless, in 1993, Leung [28] suggested a numerical scheme that employed photonic WFs also in the computation of localized defect states in PCs. The interest in developing numerical methods based on WFs rose again with the publications of two ground breaking papers by Marzari and Vanderbilt [29] and Souza et al. [30]. They proposed an iteration method to compute maximally localized electronic WFs from the Bloch modes of a crystal. Their method was quickly adapted to also compute photonic WFs for one- and two-dimensional PCs [31–34].

Generation of Photonic Wannier Functions: In the Photonics Group of Prof. Busch, the Souza-Marzari-Vanderbilt algorithm was extended to the bottom-up approach to generate arbitrarily many photonic WFs mainly by Schillinger [35]. His implementation of this algorithm treats two-dimensional photonic WFs and requires a couple of input parameters from a user. These parameters were mostly determined by a trial-and-error process, substantially slowing down the generation time for a particular set of WFs. In order to determine these parameters in a more systematic fashion, he stated a set of selection rules⁵ based on empirical observations in the generation of the first 38 WFs of one of the triangular model systems employed in the present thesis. These rules related the symmetry of some of the Bloch modes with the anticipated symmetry of the resulting WFs, rediscovering results from Cloizeaux [36] and Krüger [37, 38]. In the course of the present thesis, it became clear that more WFs were needed for obtaining accurate results in defect computations. Therefore, the connection between Bloch mode symmetries and WFs symmetries was studied in more depth, resulting in the complete set of symmetry selection rules for the model systems in Tabs. 2.1 and 2.2. These tables and subsequent examples for their application to the construction of WFs are one of the major results of this thesis.

Auxiliary Basis Functions: The anticipated numerical efficiency of the WFs was confirmed in the TM case, where only a few electric field WFs were sufficient to obtain accurate results for many defect configurations [32]. Subsequently, many methods for the computation of localized cavity defect modes, waveguide dispersions and transmission characteristics of functional elements have been adapted for the photonic WF method. However, obtaining the same level of accuracy for TE modes remained problematic [34]. The reason for this different behavior of the two polarizations derives from the fact that the magnetic field WFs fail to describe one property of the anticipated magnetic field defect modes. As Takeda et al. [39] pointed out, the discontinuous jumps in the permittivity distribution of PCs causes discontinuities in general electric fields and, hence, the derivatives of general magnetic fields (visible as

⁵Rules aiding in the selection of WF construction parameters.

kinks in field profiles). However, in the special case of TM polarization, the electric fields are indeed smooth (i. e., continuously differentiable), whereas the kinks in the magnetic fields for TE polarization persist. For the magnetic field in PCs, the ratio of the derivatives on both sides of a dielectric boundary depends on the ratio of permittivities involved. Thus, the WFs inherit this ratio from the Bloch modes they were constructed from and pass it on to any linear combination approximating the defect modes, whose kinks may have a different shape. For low-index defects, the accuracy is still sufficient to model complex defect designs [40]. For high-index defects, such as non-etched holes (that are the most widely studied among experimentalists), the accuracy of WF based computations deteriorates quickly.

In [39], it was proposed to modify the electric field WFs based on the particular defect structures they should be able to describe. However, the aim of this thesis is to describe a whole class of defect structures comprising holes infiltrated with low-index and high-index isotropic materials, as well as anisotropic materials. Therefore, a new suggestion is presented here. The properties of the WF basis should be preserved, i. e. localization, orthonormality and, in prospect of future vectorial computations, the divergenceless of the magnetic field WFs, which is a necessary restriction of the wave equations. The basis is thereby augmented by additional auxiliary basis functions that are capable of modelling the proper continuity conditions of the magnetic field defect modes across dielectric boundaries. Several sets of these auxiliary basis functions are proposed and their wide applicability is shown by computing eigenstates of complex cavity defect setups and waveguides incorporating both isotropic and anisotropic materials with varying parameters. Furthermore, this approach increases the numerical effort only slightly and is easily extendable to three-dimensional vectorial computations as well. These sets of auxiliary basis functions as well as the quantification of their usefulness to overcome the problems of the pure WF basis is the second major result presented in this work.

Numerical Considerations: Physical equations are usually stated as differential equations, relating continuous quantities with each other: instances of time, positions in space, field values and permittivity distributions. However, a computer can only process discrete values of these quantities, described by sequences consisting of the basic discrete states 0 and 1. In order to model continuous operations like differentiation and integration suitable for a computer to apply in a numerical solution scheme, all continuous quantities have to be expressed by discrete ones. This process is called 'discretization' and there is no unique way to achieve this. Therefore, different discretization methods (or schemes) exist, that facilitate this transition, usually depending on additional parameters. Each method has inherent advantages and drawbacks, e. g., the accuracy with which the exact continuous quantities are modeled or the time consumption of applying a differentiation/integration. The particular properties of various discretization schemes have to be kept in mind when comparing the efficiency and accuracy of numerical methods among each other. Therefore, great care has been taken to obtain accurate reference solutions to compare the WF and auxiliary function based solutions with. The influence of the discretization parameters on the construction of WFs and their accuracy in subsequent defect computations has been investigated and documented. That way, errors due to discretization schemes and parameters were kept to a minimum and the dominant source of errors was shown to be the lack of auxiliary basis functions in the pure Wannier function computations.

Most of all, the discretization method for the permittivity distribution has great influence on the accuracy of numerical electrodynamics [41, 42]. Therefore, the influence of the permittivity discretization on the errors in the Wannier approach is also investigated in this work. Finally, the results justify the usage of a simpler discretization scheme than what is usually proposed for high-accuracy computations.

Outline: The thesis starts with a derivation of the basic wave equations in Chap. 1 that have to be solved. In particular, symmetry arguments are used to justify the Bloch theorem and the allowed form of a tensorial permittivity that allows to treat two-dimensional PCs in TE and TM polarization. That chapter summarizes the basic physical properties of PCs and defect modes. Furthermore, it reviews the localization properties of WFs and defines the model systems.

In Chap. 2, the group representation theory of symmorphic plane groups is reviewed. It provides the theoretical foundation for the site symmetry analysis which determines the WF symmetries from the underlying Bloch mode symmetries. It is accompanied by App. F, where many additional tables for the actual application of the results to the WF generation are assembled.

Chap. 3 briefly summarizes the WF generation algorithms and features many examples of the application of the site symmetry analysis. The influence of the various construction parameters is documented and interpreted. Based on these observations, several suggestions to improve the Wannier generation in the future are given.

In Chap. 4, a detailed derivation of the numerical methods based on the WF expansion used in this thesis is provided. This comprises the computation of localized cavity defect modes, supercell and on-shell waveguide dispersions. The detailed derivation of scattering matrix computations for transmission calculations of photonic circuits has been omitted and is found elsewhere [43].

Chap. 5 investigates the influence of various construction parameters on the accuracy of the discretized WFs which are a numerical approximation to the exact WFs. Some statistics on the operator matrices occurring in the Wannier approach are also documented.

In Chap. 6, the sets of auxiliary basis functions are introduced and their improvements of the accuracy of defect computations are documented thoroughly.

Chap. 7 analyzes the possibilities to reduce the number of basis functions used in computations and the accuracies that can be expected then.

Chap. 8 investigates the improvements due to the usage of highly symmetric WFs in defect computations.

Finally, the thesis is concluded with a summary of the main results in Chap. 9.

The appendices feature more information on various topics and document the numerical parameters used in the computations. App. A features properties of Fourier transforms and WFs, as well as definitions regarding the error plots presented in this work.

App. B summarizes the discretization schemes that are employed and compared in this thesis.

App. C documents the parameters used to obtain accurate reference modes by the MIT photonic bands (MPB) package.

App. D lists all relevant numerical parameters that were used for particular computations, like the construction of WFs and defect computations, for reference and reproducibility.

App. E shows more defect computations involving auxiliary basis functions. These results are summarized in Chap. 6.

In App. F, additional data and tables are assembled that accompany the site symmetry approach of Chaps. 2 and 3.

Acknowledgements

A doctoral thesis is never the product of one single person's effort, and certainly this one is not different. It would never have become reality without the help and suggestions of many supportive friends and colleagues.

In particular, I like to thank Prof. Dr. Kurt Busch for entrusting me with the Wannier function project. He always took great care of my financial support and offered me many possibilities to attend interesting scientific conferences abroad. His constant optimism and endorsement kept me going on through all the years of this thesis.

My thanks also go to Prof. Dr. Peter Wölfle who accepted to co-referee my work.

I am greatly indebted to Dr. Jens Niegemann for many suggestions and for being a trustful climbing partner.

No less thanks go to Christian Wolff who provided the Wannier generation code I used. I thank him for many fruitful discussions and sparking many ideas that are worked out in this thesis, as well for a sheer never-ending supply of sweets and cakes.

Additionally to the contribution of Christian Wolff, I was happy to build upon the scientific contribution of former works on photonic Wannier functions from Dr. Matthias Schillinger, Dr. Daniel Hermann, Dr. Sergei Mingaleev, Christopher Kölper, Christian Blum and Alexandra Graham.

I thank Prof. Dr. Wondratschek for taking his time to discuss some aspects of group theory with me.

I am also grateful to our secretaries Edith Herzog and Evmarie Schwartz for their support in administrative tasks.

Furthermore, for the tedious task of proof reading the thesis, my thanks go to Christian Wolff, Jens Niegemann, Michael König, Richard Diehl, Jens Küchenmeister, Thomas Zebrowski, Michael Walz, Martin Köhl, Timo Köllner, Paolo Longo, Benjamin Lutz, Alexander Wlotzka, and Christoph Martens.

Additionally to the serious aspects of everyday scientific work, I am happy to thank all current and former members of the Photonics Group for countless barbecues (regardless of the weather conditions), even more cake, funny Christmas parties, funny movie nights, thrilling poker games, LAN parties, pizza seminars, action-packed outings, some more barbecues, and many conferences. It was a delightful time with You!

Last but not least, my greatest thanks go to the most important persons in my life: my parents Helga and Heinz as well as my sister Sandra. You were with me in my darkest hours, in joy and sorrow. With all my heart, I thank You and Sophie S. for helping me through a rough time of severe injury.

Contents

Introduction	vii
Acknowledgements	xiii
1 Classical Electromagnetism in Photonic Crystals	1
1.1 Dielectrics in the Optical Regime	1
1.2 Photonic Crystals	4
1.2.1 Lattice and Reciprocal Lattice	5
1.2.2 Bloch Theorem	6
1.2.3 Scale Invariance and Dimensionless Units	7
1.2.4 Scalar Wave Equations in 2D	7
1.2.5 Birefringence of Liquid Crystals	10
1.2.6 Gyrotropy	12
1.2.7 Model Systems	13
1.2.8 Bloch Modes and Band Structure	13
1.2.9 Bloch Mode Orthonormality and Scalar Products	15
1.2.10 Defect Structures in Photonic Crystals	16
1.2.11 Functional Elements	20
1.2.12 The Wannier Function Approach	20
1.3 Summary	23
2 Group Representation Theory	25
2.1 Groups	25
2.2 Transform Operators	27
2.3 Plane Groups	28
2.4 Representations	29
2.4.1 Characters	30
2.4.2 Bases of Representations	30
2.4.3 Reducible Representations	30
2.4.4 Projection Operators	33
2.4.5 The Group of an Operator	33
2.4.6 Subduced Representations	33
2.4.7 Induced Representations	35
2.4.8 The Frobenius Reciprocity Theorem	35
2.5 Representations of Plane groups	35
2.5.1 Translation Groups	36
2.5.2 Point Groups	37
2.5.3 Full Plane Groups	38
2.5.4 Site Symmetry Groups	39
2.5.5 Generalized Wannier Functions	40

2.5.6	Wannier Function Symmetries and Localization	41
2.6	Summary	44
3	Wannier Function Generation	47
3.1	Definition and Properties of Wannier Functions	47
3.2	Localization Properties Of Wannier Basis	48
3.3	Review Of Spread Minimization Procedure	52
3.3.1	Marzari-Vanderbilt Spread Minimization	52
3.3.2	Choice Of Initial Transform Matrices	53
3.3.3	Souza Subspace Optimization	54
3.3.4	Frequency Windows	56
3.3.5	Choice of Initial Subspaces	56
3.3.6	Bottom-Up Approach	57
3.4	Discussion of Spread Minimization Procedure: Square Lattice	58
3.4.1	Single Bands 1 and 2	58
3.4.2	Closed Set of Bands 3–7	63
3.4.3	Closed Set of Bands 2–7	66
3.5	Entangled Bands	69
3.5.1	Bands 12–15	69
3.6	Discussion of Spread Minimization Procedure: Triangular Lattice	82
3.7	Instabilities of Souza Subspace Optimization	82
3.8	Enforcing Symmetry	91
3.8.1	Choosing Appropriate Trial Functions	91
3.8.2	Symmetry Adapted Construction	93
3.8.3	A Posteriori Symmetrization	93
3.9	Final Wannier Functions	94
3.9.1	Fully Hybridized Wannier Functions 1–38 (WF38-MV)	95
3.9.2	Souza-Marzari-Vanderbilt Wannier Functions 1–101 (WF101-SMV)	95
3.9.3	Symmetrized Souza-Marzari-Vanderbilt Wannier Functions 1–38 (WF38-sym)	97
3.10	Summary	97
4	Wannier Function Expansion	101
4.1	Wannier Matrix Elements	101
4.1.1	Wave Equations	101
4.1.2	Complex Defect Structures in Photonic Crystals	104
4.2	Truncated Index Domains	110
4.3	Cavity Modes	111
4.4	Dispersion Relations $\omega(\mathbf{k})$	112
4.5	On-shell Waveguide Dispersion $k(\omega)$	114
4.5.1	Wave Equation	114
4.5.2	Transfer Matrix For Waveguide Dispersions	115
4.5.3	Properties of the System Matrix	118
4.6	Scattering Matrix Formalism	118
4.7	Summary	119
5	Wannier Function Parameters	121
5.1	Choice of Resolutions	121

5.1.1	Wannier Functions	121
5.1.2	Real Space Decay Behavior of Wannier Functions	121
5.1.3	Convergence of Operator Matrix Elements	122
5.1.4	Decay and Sparsity of Operator Matrix Elements	122
5.1.5	Band Structure Accuracy	122
5.2	Operator Matrices of Final Wannier Functions	127
5.2.1	Statistics of Operator Matrices	127
5.2.2	Band Structure Reconstruction	129
5.3	Summary	129
6	Auxiliary Basis Functions	131
6.1	Boundary Conditions	131
6.1.1	2D TM Modes	133
6.1.2	2D TE Modes	136
6.2	Sets of Auxiliary Basis Functions	138
6.2.1	More Wannier Functions	138
6.2.2	Supercell Defect Modes	138
6.2.3	Fourier-Bessel Functions	139
6.2.4	Inverse System Wannier Functions	140
6.3	Cavity Defect Modes Convergence	142
6.3.1	Cavity Setup A_i	144
6.4	Comparison of all Auxiliary Basis Functions	149
6.5	Complex Isotropic Defect Clusters	152
6.6	Anisotropic Defects	154
6.7	Isotropic Waveguide Dispersion, $W1-1$	155
6.8	Complex Isotropic Waveguides	156
6.9	Anisotropic Waveguides	159
6.10	Summary	159
7	Defect Mode Convergence	163
7.1	Cavity Defect Clusters	163
7.1.1	Computational Domain Size	163
7.1.2	Sparsity	165
7.1.3	Relevant Basis Functions	165
7.2	Waveguide Dispersions	168
7.2.1	Supercell Computations	169
7.2.2	On-Shell Computations	169
7.3	Summary	169
8	Symmetric Wannier Functions	173
8.1	Degeneracy of Cavity Defect Modes	173
8.2	Symmetry of Waveguide Modes	173
8.3	Summary	174
9	Summary and Outlook	177
9.1	Summary	177
9.2	Outlook	179

A	Definitions and Proofs	181
A.1	Fourier Transforms	181
A.1.1	Lattice Periodic Functions in Direct Space	181
A.1.2	Lattice Periodic Functions in Reciprocal Space	181
A.1.3	Fourier Sum Identities	182
A.2	Wannier Function Properties	182
A.2.1	Translational Properties	183
A.2.2	Orthonormality	183
A.2.3	Integration by Parts	184
A.3	Operator Matrix Properties	184
A.3.1	Hermiticity	184
A.3.2	Translational Invariance	185
A.4	Relative Errors	185
A.4.1	Relative Errors	185
A.4.2	Comparing Matrices	186
A.4.3	Orders Of Convergence	186
A.5	Scalar Product for Electrical Fields	186
B	Discretizations	189
B.1	Fields	189
B.2	Integration	190
B.3	Derivatives	191
B.3.1	Finite Differences	191
B.3.2	Spectral Derivatives	193
B.3.3	Problems of Discretized Derivatives	193
B.4	Dielectric Function	193
B.5	Brillouin Zone	195
C	Reference Modes	199
C.1	Numerical Parameters	199
C.1.1	Tolerance	199
C.1.2	Sub-Pixel Smoothing Mesh Size $N_{\text{SPS},i}$	199
C.1.3	Real Space Resolution $N_{\text{res},i}$	199
C.1.4	Supercell Size $N_{\text{cells},i}$	199
C.2	Reference Frequencies and Parameters	201
C.2.1	Band Structure in Triangular Model System	201
C.2.2	Non-Etched Hole in Triangular Model System	203
C.2.3	Ring of Six Non-Etched Holes in Triangular Model System	205
C.2.4	W1-1 Waveguide of Non-Etched Holes in Triangular Model System	206
D	Numerical Parameters	207
E	Auxiliary Basis Functions	211
E.1	Comparison of Various Auxiliary Basis Function Sets	211
E.2	Waveguides W1-1	211
F	Group Representation Theory	219

F.1 Index Ordering of (2.21)	219
F.2 Cell Diagram Notation	220
F.3 Square Lattice: P4mm (C_{4v})	220
F.3.1 Possible Site Symmetry Group Representations $D^{(\mathbf{q}\beta)}$	230
F.4 Triangular Lattice: P6mm (C_{6v})	232
F.4.1 Possible Site Symmetry Group Representations $D^{(\mathbf{q}\beta)}$	239
List of Acronyms	243
Bibliography	245

1

Chapter 1

Classical Electromagnetism in Photonic Crystals

In this chapter, we define the model photonic crystals investigated in this work. Starting from Maxwell's equations, we derive the wave equations governing light propagation (i. e., electromagnetic waves at optical frequencies) in these systems. For two-dimensional structures, the vectorial wave equations can be separated into two simpler, independent scalar wave equations. The form of an anisotropic permittivity tensor that allows this decoupling is derived based on symmetry considerations.

We discuss the consequences of the translational symmetry of photonic crystals, leading to a band structure for light and possible band gaps. Defects breaking the symmetry of photonic crystals can introduce strongly localized defect modes with frequencies in the band gap. We introduce the defect class of infiltrated holes, allowing to build resonators, waveguides and complex functional elements in the model systems.

Finally, the possibility of calculating the localized defect modes numerically by an expansion into localized photonic Wannier function is discussed. Therefore, a brief review on Wannier function localization is provided.

Some symmetry related terminology is already used in this chapter which will be introduced in greater detail in Chap. 2.

A basic introduction to classical electromagnetism can be found in Griffiths [44], a comprehensive standard reference is the text book by Jackson [45]. A thorough theoretical survey on optical phenomena in media is provided by Römer [46]. Nice introductions to the physics of photonic crystals are the text books by Joannopoulos et al. [47] and Sakoda [48]. A comprehensive survey on photonic crystals and their technical applications is given by Inoue [49].

1.1 Dielectrics in the Optical Regime

The time evolution of classical electromagnetic fields in arbitrary media is generally given by Maxwell's equations in matter in International System (SI) units:

$$\nabla \cdot \mathbf{D}(\mathbf{r}, t) = \rho_{\text{free}}(\mathbf{r}, t), \quad (1.1a)$$

$$\nabla \times \mathbf{E}(\mathbf{r}, t) = -\partial_t \mathbf{B}(\mathbf{r}, t), \quad (1.1b)$$

$$\nabla \cdot \mathbf{B}(\mathbf{r}, t) = 0, \quad (1.1c)$$

$$\nabla \times \mathbf{H}(\mathbf{r}, t) = \mathbf{j}_{\text{free}}(\mathbf{r}, t) + \partial_t \mathbf{D}(\mathbf{r}, t). \quad (1.1d)$$

They feature the electric field \mathbf{E} , the electric displacement \mathbf{D} , the magnetic induction \mathbf{B} and the magnetic field \mathbf{H} which are all vectorial functions of space and time. The free charge density ρ_{free} as well as the free current density \mathbf{j}_{free} are responsible for the creation of these fields. In this form, Maxwell's equations describe the macroscopically averaged fields, where field fluctuations and molecular/atomic distributions of matter on the microscopic scale are neglected (Fig. 1.1). In dielectric (non-conducting) media, the

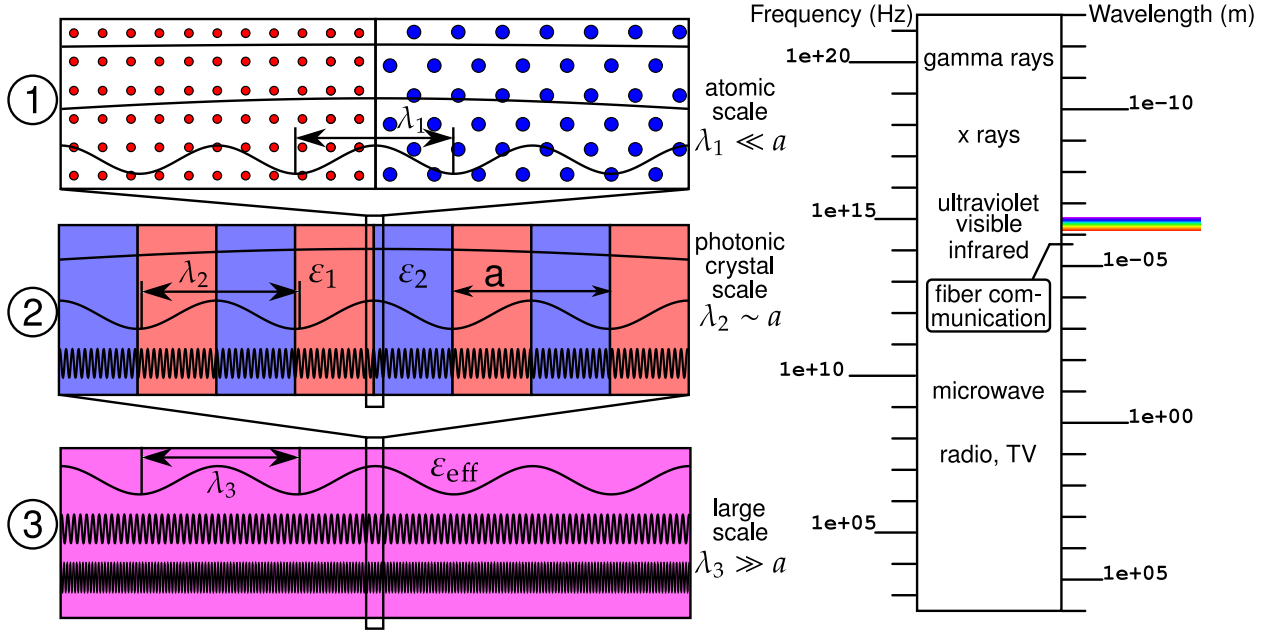


Figure 1.1: Left: Various wavelength regimes and description of dielectric media. Wavelengths are not to scale. (1) Short wavelengths of the order of atomic extents lead to atomic scattering. (2) For longer wavelengths, one oscillation cycle comprises many atoms. This case can be treated by position dependent macroscopic material parameters, like the permittivity ϵ . (3) For wavelengths much larger than the variation length of the material parameters, the medium looks homogeneous with an effective constant permittivity ϵ_{eff} . Right: Orders of magnitude for various types of electromagnetic radiation after [44]. Optical frequencies are those in the visible regime and its vicinity, the near-infrared. Current fiber communication networks employ wavelengths around $1.5 \mu\text{m}$.

fields \mathbf{E} and \mathbf{B} exert forces on the charge carriers making up the matter (negatively charged electrons and positively charged nuclei), leading to complicated rearrangements and induction of electric and magnetic dipole moments.¹ These polarization effects can be rather complicated in general which is expressed in a functional relation between the fields \mathbf{E} , \mathbf{B} and \mathbf{D} , \mathbf{H} , the constitutive relations

$$\mathbf{D} \equiv \mathbf{D}[\mathbf{E}, \mathbf{B}], \quad (1.2)$$

$$\mathbf{H} \equiv \mathbf{H}[\mathbf{E}, \mathbf{B}]. \quad (1.3)$$

Potential effects include [46]

non-locality: The spatial derivatives of the fields become relevant (e. g. natural optical activity),

¹Higher order multipole moments are usually negligibly small and do not contribute significantly to the macroscopic physics [45, 46].

non-Markovian effects (non-locality in time): The field values of all earlier instances of time become relevant (e. g. dispersion),

non-linearity: Not only linear terms $|\mathbf{E}|$ contribute, but also higher orders $|\mathbf{E}|^2$, $|\mathbf{E}|^3$ (e. g. frequency conversion effects),

anisotropy: The vectorial character of \mathbf{E} and \mathbf{B} becomes relevant (e. g. birefringence),

bi-(an)isotropy: \mathbf{B} influences \mathbf{D} , \mathbf{E} influences \mathbf{H} .

We restrict ourselves to optical frequencies, for which the magnetic response is practically absent in bulk dielectrics, since the microscopic magnetic dipoles just cannot respond to the rapidly oscillating fields [45].²

Furthermore, we are mainly concerned with air and silicon as dielectrics, for which we may also neglect dispersion and losses for optical frequencies.

Finally, we are interested in linear effects only which all leads to

$$\boxed{\mathbf{D}(\mathbf{E}) = \varepsilon_0 \underline{\underline{\varepsilon}} \mathbf{E}, \quad \mathbf{H}(\mathbf{B}) = \frac{1}{\mu_0} \mathbf{B},} \quad (1.4)$$

where ε_0 and μ_0 are the permittivity and permeability of free space, respectively. This form of constitutive relations that will be used throughout this thesis. However, we allow the relative tensor permittivity $\underline{\underline{\varepsilon}}$ to be a function of position \mathbf{r} and further parameters that can be governed by external static electric and magnetic fields \mathbf{E}_{ext} and \mathbf{B}_{ext} , respectively. This way, we can model tunable birefringence of liquid crystals and tunable magneto-optical activity. We also work exclusively with relative permittivities and drop the term 'relative' from now on to shorten the notation.

We are concerned with the propagation of waves only which is why we set $\rho_{\text{free}} = 0$ and $\mathbf{j}_{\text{free}} = 0$ in (1.1). Now that we have stated our final constitutive relations, we can substitute the \mathbf{D} and \mathbf{B} fields in (1.1) by (1.4) and write down the source-free Maxwell's equations for linear dielectrics:

$$\nabla \cdot (\underline{\underline{\varepsilon}} \mathbf{E}) = 0, \quad (1.5a)$$

$$\nabla \times \mathbf{E} = -\mu_0 \partial_t \mathbf{H}, \quad (1.5b)$$

$$\nabla \cdot \mathbf{H} = 0, \quad (1.5c)$$

$$\nabla \times \mathbf{H} = \varepsilon_0 \underline{\underline{\varepsilon}} \partial_t \mathbf{E}. \quad (1.5d)$$

We could have expressed these equations in terms of \mathbf{E} and \mathbf{B} as well, but we stick to this convention with \mathbf{E} and \mathbf{H} . We can derive wave equations by substituting Maxwell's equations among each other. Multiplying (1.5d) from the left with $\underline{\underline{\varepsilon}}^{-1}$, taking the curl again, and plugging in (1.5b), yields time-domain wave equation

$$\nabla \times (\underline{\underline{\varepsilon}}^{-1} \cdot \nabla \times \mathbf{H}) + \frac{1}{c_0^2} \partial_t^2 \mathbf{H} = 0 \quad (1.6)$$

for the magnetic field. Here, we introduced the vacuum speed of light c_0 which obeys $\varepsilon_0 \mu_0 = 1/c_0^2$. On the other hand, curling (1.5b) and inserting (1.5d) yields the electric field wave equation

$$\nabla \times (\nabla \times \mathbf{E}) + \frac{1}{c_0^2} \underline{\underline{\varepsilon}} \partial_t^2 \mathbf{E} = 0, \quad (1.7)$$

²However, great effort has been put recently into constructing artificial metamaterials with a magnetic response at optical frequencies. This allows to achieve a negative refractive index [50, 51], making it possible to construct perfect lenses [52] and cloaking devices [53, 54].

in time-domain.

These equations have to be solved for the geometries and materials making up a particular system which enter the equations in the form of a spatially varying $\underline{\underline{\epsilon}}(\mathbf{r})$. The two wave equations are redundant, as either of them describes the full electromagnetic response of a system. However, it is sometimes preferable to solve the magnetic wave equations, since they feature a Hermitian differential operator. Furthermore, the divergence constraint (1.5c) can be fulfilled regardless of the particular permittivity distribution $\underline{\underline{\epsilon}}$ which is favorable for some numerical methods and also for the Wannier function approach.

In this work, we examine linear material responses only. This enables us to examine the wave equations in frequency-domain which is convenient for characterizing the optical properties of linear systems in stationary states, i.e., light states with a definite frequency ω [55]. The frequency representation is obtained by assuming a harmonic time dependence of the electromagnetic fields, generally written as

$$\mathbf{E}(\mathbf{r}, t) = e^{-i\omega t} \mathbf{E}(\mathbf{r}, \omega), \quad \mathbf{H}(\mathbf{r}, t) = e^{-i\omega t} \mathbf{H}(\mathbf{r}, \omega). \quad (1.8)$$

This is basically a Fourier transform in time. Expressing the time-domain wave equations with this ansatz yields

3D Vectorial Wave Equations in Frequency Domain

$$\nabla \times (\nabla \times \mathbf{E}) - \frac{\omega^2}{c_0^2} \underline{\underline{\epsilon}} \cdot \mathbf{E} = 0, \quad \nabla \cdot (\underline{\underline{\epsilon}} \cdot \mathbf{E}) = 0, \quad (1.9a)$$

$$\nabla \times (\underline{\underline{\eta}} \cdot \nabla \times \mathbf{H}) - \frac{\omega^2}{c_0^2} \mathbf{H} = 0, \quad \nabla \cdot \mathbf{H} = 0. \quad (1.9b)$$

These wave equations constitute a generalized eigenvalue problem (1.9a) and a regular eigenvalue problem (1.9b), respectively. Note that the equations are only complete with their corresponding divergence conditions which the physical solutions have to obey. Here we have also introduced the commonly used inverse permittivity

$$\underline{\underline{\eta}}(\mathbf{r}) := \underline{\underline{\epsilon}}^{-1}(\mathbf{r}) \quad (1.10)$$

for the matrix inverse of the tensor permittivity. We will refer to both these functions generally as the dielectric function.

For various choices of the dielectric function distributions $\underline{\underline{\epsilon}}(\mathbf{r})$, we will solve these partial differential eigenvalue equations numerically for the fields $\mathbf{E}(\mathbf{r}, \omega)$ or $\mathbf{H}(\mathbf{r}, \omega)$ and the corresponding eigenfrequencies ω . The combination of such a spatial field distribution and the corresponding eigenfrequency is called an eigenmode or just mode for short.

From now on, we work exclusively in the frequency domain and therefore drop the frequency dependence in the notation for the fields.

1.2 Photonic Crystals

A PC is a spatially periodic dielectric heterostructure. The periodicity justifies the physical term ‘crystal’, while ‘photonic’ denotes that we investigate light propagation in this periodic structure. This distinguishes the photonic crystal from electronic crystals made of periodic arrangements of atoms that are traditionally investigated in solid state physics. Additionally, ‘photonic’ also refers to the wavelength regime, for which the typical optical effects in PCs can be observed. By wavelength we mean the corresponding wavelength of a plane wave in vacuum of the same frequency as the light mode under consideration (cf. Fig. 1.1, 2).

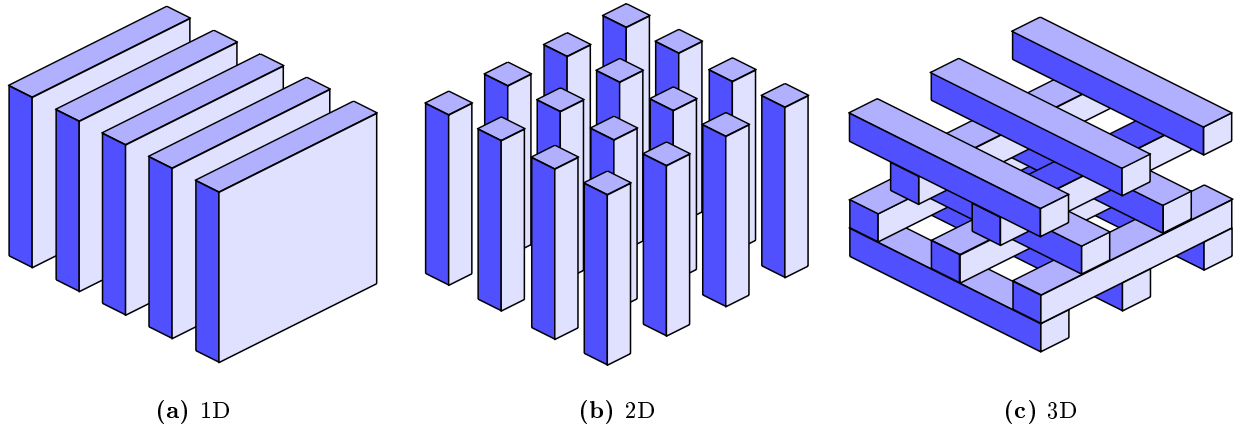


Figure 1.2: Schematic illustrations of photonic crystals with periodicities in various dimensions.

The dielectric function $\underline{\underline{\epsilon}}_{\text{PC}}(\mathbf{r})$ of a d -dimensional PC is periodic with respect to translations \mathbf{R} from a discrete and infinite set of spatial vectors $\mathbb{L}_{\text{PC}} \subset \mathbb{R}^d$ which is called the lattice:

$$\underline{\underline{\epsilon}}_{\text{PC}}(\mathbf{r} + \mathbf{R}) = \underline{\underline{\epsilon}}_{\text{PC}}(\mathbf{r}), \quad \forall \mathbf{R} \in \mathbb{L}_{\text{PC}}, \quad (1.11)$$

$$\mathbb{L}_{\text{PC}} := \left\{ \sum_{i=1}^d z_i \mathbf{a}_i : z_i \in \mathbb{Z} \right\}. \quad (1.12)$$

Here, we have introduced the primitive lattice translations $\mathbf{a}_i \in \mathbb{R}^d$ whose integral linear combinations build up the whole lattice. Examples are shown in Fig. 1.2. The position vectors \mathbf{R} of the set \mathbb{L}_{PC} are also called the lattice sites.

1.2.1 Lattice and Reciprocal Lattice

The whole PC can be built from $\underline{\underline{\epsilon}}_{\text{PC}}(\mathbf{r})$ given on one unit cell and shifted periodically in space by lattice vectors $\mathbf{R} \in \mathbb{L}_{\text{PC}}$ (see Fig. 1.3a). A primitive unit cell is the spatial domain defined by the parallelepiped with sides \mathbf{a}_i . More convenient for theoretical considerations is the Wigner-Seitz cell (WSC), which comprises all points around a particular lattice site closer to that site than to any other. Its volume V_{WSC} is the same as that of the primitive unit cell. A supercell is a unit cell that is larger than a primitive unit cell and that can also build the whole crystal when shifted by lattice vectors \mathbf{S} from a periodic superlattice $\mathbb{L}_{\text{per}} \subset \mathbb{L}_{\text{PC}}$.

The reciprocal lattice \mathbb{L}_{PC}^* also plays a crucial role for the understanding of wave propagation in periodic media. Its primitive lattice translations \mathbf{b}_i are built from the primitive lattice translations \mathbf{a}_i of the direct lattice \mathbb{L}_{PC} as follows:

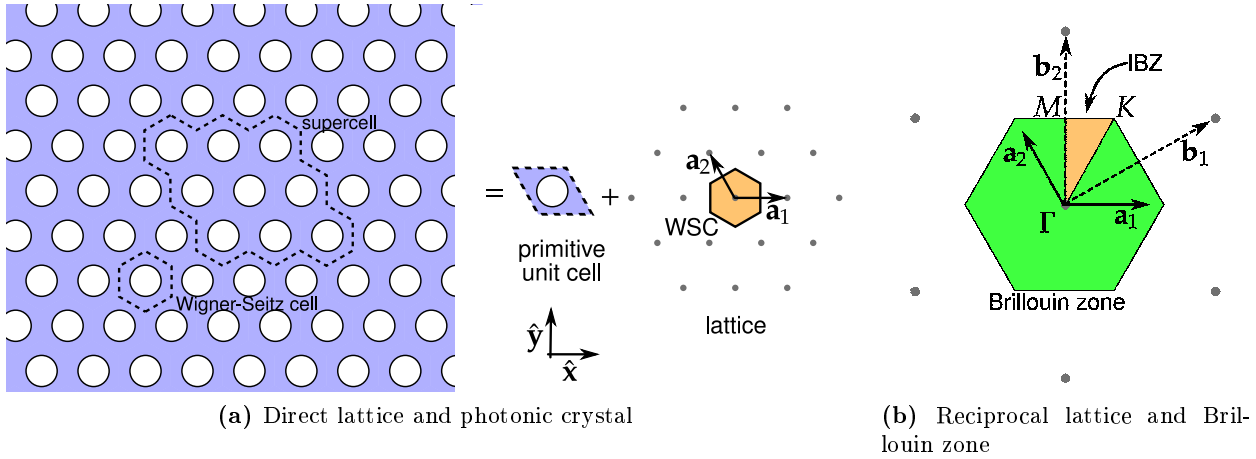
$$V_{\text{WSC}} = |(\mathbf{a}_1 \times \mathbf{a}_2) \cdot \mathbf{a}_3|, \quad (1.13)$$

$$\mathbf{b}_i := \frac{2\pi}{V_{\text{WSC}}} \mathbf{a}_j \times \mathbf{a}_k \quad (ijk \text{ is an even permutation of } 123), \quad (1.14)$$

$$\mathbb{L}_{\text{PC}}^* := \left\{ \sum_{i=1}^d z_i \mathbf{b}_i : z_i \in \mathbb{Z} \right\}. \quad (1.15)$$

The primitive lattice translations have the important orthogonality property

$$\mathbf{a}_i \cdot \mathbf{b}_j = 2\pi \delta_{ij}. \quad (1.16)$$



(a) Direct lattice and photonic crystal

(b) Reciprocal lattice and Brillouin zone

Figure 1.3: (a) Example for a two dimensional (2D) PC defined on a triangular lattice \mathbb{L}_{PC} of cylindrical air holes. The Wigner-Seitz cell (WSC) along with other cells is also shown. (b) The reciprocal lattice \mathbb{L}_{PC}^* with the Brillouin zone (BZ) and the irreducible wedge of the Brillouin zone (IBZ), as well as the high symmetry points.

Here, δ_{ij} is the Kronecker delta.

The WSC of the reciprocal lattice is called the Brillouin zone (see Fig. 1.3b).³ The corners and lines of the irreducible wedge of the Brillouin zone (IBZ) lying on the boundary of the Brillouin zone (BZ) are labeled by capital Latin letters, whereas the point and lines in the interior of the BZ are labeled by capital Greek letters (see also Figs. 1.8b and 1.8d). These are the so-called high symmetry points and lines, respectively.

1.2.2 Bloch Theorem

The Bloch theorem determines some analytic properties of the eigenmodes $\psi(\mathbf{r})$ of position dependent differential operators $\hat{H}(\mathbf{r})$ which are periodic under translations \mathbf{R} on a given lattice \mathbb{L}_{per} . It is ubiquitous and well known in those areas of solid state theory which deal with periodic structures such as crystals. Proofs can be found in [47, 56]. Another justification based on group theory is given in Sec. 2.5.1.

The periodicity stated above for a differential operator $\hat{H}(\mathbf{r})$ means

$$\hat{H}(\mathbf{r} + \mathbf{R}) = \hat{H}(\mathbf{r}) \quad \forall \mathbf{R} \in \mathbb{L}_{\text{per}}. \quad (1.17)$$

This operator shall have the eigenmodes $\psi(\mathbf{r})$ with eigenvalues Λ :

$$\hat{H}(\mathbf{r})\psi(\mathbf{r}) = \Lambda\psi(\mathbf{r}). \quad (1.18)$$

The Bloch theorem states that in this case the eigenfunctions $\psi(\mathbf{r})$ can in fact be written as

$$\psi(\mathbf{r}) \equiv \psi_{n\mathbf{k}}(\mathbf{r}), \quad (1.19a)$$

$$\psi_{n\mathbf{k}}(\mathbf{r}) = e^{i\mathbf{k}\mathbf{r}} \mathbf{u}_{n\mathbf{k}}(\mathbf{r}), \quad (1.19b)$$

$$\mathbf{u}_{n\mathbf{k}}(\mathbf{r} + \mathbf{R}) = \mathbf{u}_{n\mathbf{k}}(\mathbf{r}) \quad \forall \mathbf{R} \in \mathbb{L}_{\text{per}}. \quad (1.19c)$$

³In fact, it is the *first* Brillouin zone, but higher zones are rarely used, hence we use the short name.

Here, $\mathbf{u}_{n\mathbf{k}}(\mathbf{r})$ is the lattice periodic part of the eigenmode, \mathbf{k} is a vector from the BZ of the reciprocal lattice $\mathbb{L}_{\text{per}}^*$, and $n \in \mathbb{N}$ is the band index⁴ distinguishing the infinitely many eigenmodes for any given \mathbf{k} . We refer to the $\psi_{n\mathbf{k}}$ also as Bloch modes because they are eigenmodes of an operator with the Bloch property

$$\psi_{n\mathbf{k}}(\mathbf{r} - \mathbf{R}) = e^{-i\mathbf{k}\mathbf{R}}\psi_{n\mathbf{k}}(\mathbf{r}) \quad (1.20)$$

under translations.

The set of all eigenvalues $\Lambda_{n\mathbf{k}}$ of an operator form continuous intervals, the bands. The set of these intervals is called band structure, but we also use that name for the set of eigenvalues $\Lambda_{n\mathbf{k}}$. We also refer to the set of Bloch modes $\psi_{n\mathbf{k}}$ for a given n as a band.⁵ Summing up, this terminology is often used in a sloppy way.

1.2.3 Scale Invariance and Dimensionless Units

Maxwell's equations (1.1) and the wave equations derived thereof do not depend on a particular length or energy scale. This enables us to actually compute whole solution classes for a particular choice of the dielectric function $\underline{\underline{\varepsilon}}(\mathbf{r})$ at once.

Suppose for a dielectric function $\underline{\underline{\varepsilon}}(\mathbf{r})$ we are given the eigenmodes $\psi(\mathbf{r})$ with eigenfrequencies ω . Then the corresponding solutions $\psi'(\mathbf{r})$ with frequencies ω' for the system enlarged by a factor α can be obtained via

$$\underline{\underline{\varepsilon}}'(\mathbf{r}) := \underline{\underline{\varepsilon}}(\mathbf{r}/\alpha), \quad \psi'(\mathbf{r}) := \psi(\mathbf{r}/\alpha), \quad \omega' := \omega/\alpha. \quad (1.21)$$

These relations are easily checked by inserting them into the wave equations (1.9).

The spatial scaling law (1.21) suggests to present all frequencies and wave vectors in plots and results for photonic crystals as dimensionless quantities ω' and \mathbf{k}' that are independent of the actual lattice constant a . The corresponding quantities in SI units can then be obtained by

$$\omega = \frac{2\pi c_0}{a} \omega', \quad \lambda = \frac{a}{\omega'}, \quad \mathbf{k} = \frac{2\pi}{a} \mathbf{k}'. \quad (1.22)$$

Again, λ is the wave length of a plane wave in vacuum with the same frequency ω as the eigenmode ψ .

1.2.4 Scalar Wave Equations in 2D

As pointed out in [47], wave propagation in two dimensional (2D) PC for *scalar* $\varepsilon(\mathbf{r})$ can be described by two independent scalar equations if we have:

Homogeneity of the dielectric function along the z -direction: Then the PC structure is symmetric with respect to a reflection $\sigma_z : z \mapsto -z$ for all planes parallel to the xy -plane.

In-plane propagation: This means, we are only concerned with waves having wave vectors $\mathbf{k}_{\parallel} = (k_x, k_y)$ in the xy -plane.

Both conditions together imply that the wave equations are invariant under mirror reflections σ_z for all planes parallel to the xy -plane. In-plane propagation and existence of *only one* such reflection plane means that the modes are either even or odd under this particular reflection (i.e., they have eigenvalues ± 1 as eigenmodes of the reflection operator). This situation occurs in photonic crystal slabs (see Fig. 1.4a). In the notation of Sec. 2.4.5 this means that each mode in a PC slab belongs to

⁴More precisely, it should be called band function index or band branch index.

⁵In some publications, the term band function is also used.

an irreducible representation with the character (coincides with the eigenvalue under mirror reflections σ_z) $\chi(\sigma_z)$ being either $+1$ or -1 . In the -1 case, from the transformation law for rank-1-functions (2.11) follows that the z -component $\psi_z(\mathbf{r})$ of the mode is necessarily 0 in the xy -plane. Applying this observation to the electric field \mathbf{E} for eigenvalue -1 means that $E_z(\mathbf{r}) = 0$ in the xy -plane. In the $+1$ case, the *magnetic* field component $H_z(\mathbf{r})$ is necessarily 0 in the xy -plane. Using these cases as restrictions to the solutions, it is then possible to solve the wave equation either just for the one or just for the other type of eigenmodes.

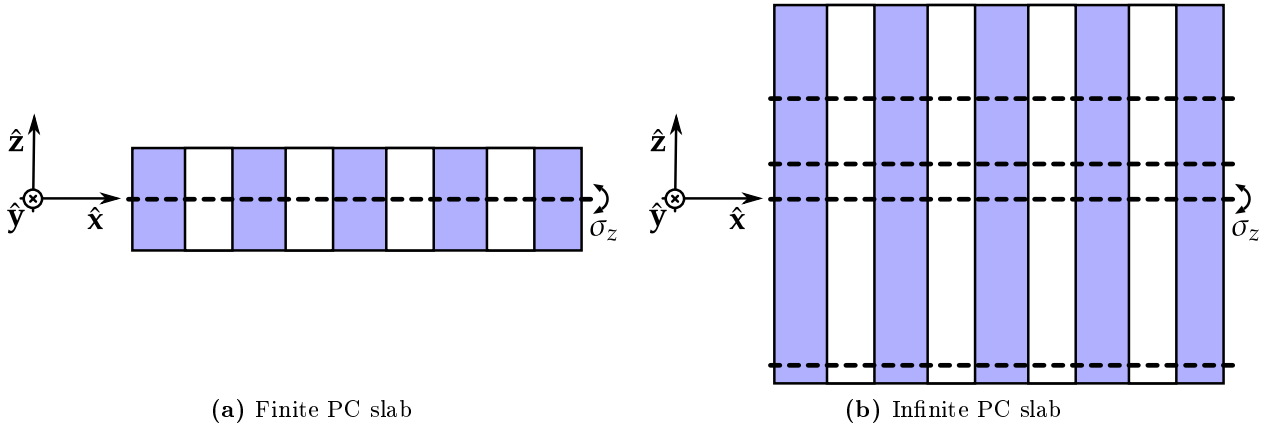


Figure 1.4: (a) PC slab of finite thickness with one σ_z mirror plane (dashed line). (b) Infinite PC slab with infinitely many σ_z mirror planes.

Then again if infinitely many of these reflection planes parallel to each other exist, the same argument is true for *each single one* of these planes, not only the xy -plane at $z = 0$. Then follows that the electric field eigenmodes must either have $E_z \equiv \text{const}$ (for eigenvalue $+1$) or $E_z \equiv 0$ (for eigenvalue -1) *everywhere*, not just one single plane. In either case we have

$$\partial_z \mathbf{E}_{n\mathbf{k}_n} = 0, \quad (1.23)$$

i. e., z -derivatives do not occur at all in the wave equations. Inserting this property and $\partial_z \varepsilon_{\text{PC}} = 0$ into the vectorial wave equations, one obtains two independent scalar wave equations for two different polarization states similar to the two irreducible representation states in the PC slab (shown in Eq. (1.29) and Fig. 1.5). This concludes the discussion for scalar permittivities ε .

Now we want to find the allowed form of the *tensorial* dielectric function $\underline{\underline{\varepsilon}}_{\text{PC}}(\mathbf{r})$ that still leads to this scalar decoupling. By the same argument as in the scalar case, the tensor $\underline{\underline{\varepsilon}}_{\text{PC}}$ has to be symmetric under mirror reflections of all possible planes parallel to the xy -plane. We will assume a 2D PC which is homogeneous in z -direction and infinitely extended in z -direction (see Fig. 1.4b), i. e.,

$$\partial_z \underline{\underline{\varepsilon}}_{\text{PC}}(\mathbf{r}) = 0, \quad (1.24)$$

such that the first requirement mentioned above is still fulfilled in the special case of an isotropic permittivity $\underline{\underline{\varepsilon}} \equiv \varepsilon \mathbf{1}$. The transform matrix $R(\sigma_z)$ of the reflection in Cartesian coordinates is given by

$$R(\sigma_z) = \begin{pmatrix} 1 & 0 & 0 \\ 0 & 1 & 0 \\ 0 & 0 & -1 \end{pmatrix} = R^{-1}(\sigma_z), \quad (1.25)$$

and the dielectric function transforms like a rank-2-tensor (2.12), i. e., the tensor $\underline{\underline{\epsilon}}'_{\text{PC}}(\mathbf{r})$ of the reflected structure is given by

$$\epsilon'_{ij}(\mathbf{r}) = \sum_{i'j'} R_{ii'} R_{jj'} \epsilon_{i'j'}(R^{-1}\mathbf{r}). \quad (1.26)$$

By (1.24) the entries $\epsilon_{i'j'}$ are constant along the z -direction, so

$$\epsilon_{i'j'}(x, y, -z) \stackrel{(1.24)}{=} \epsilon_{i'j'}(x, y, z). \quad (1.27)$$

Thus the entries are essentially a function of x and y only. By carrying out the transformation (1.26)

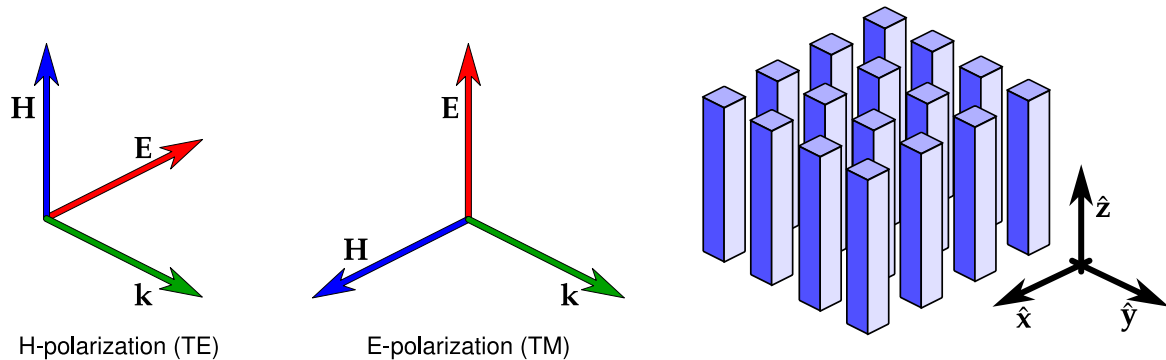


Figure 1.5: Orientation of field vectors for H-polarized and E-polarized waves propagating with $\mathbf{k} \perp \hat{\mathbf{z}}$ in 2DPC. The field components lie either in the xy -plane or are oriented along the z -direction.

and enforcing the invariance of $\underline{\underline{\epsilon}}_{\text{PC}}$ we obtain the necessary condition

$$\begin{pmatrix} \epsilon_{xx} & \epsilon_{xy} & \epsilon_{xz} \\ \epsilon_{yx} & \epsilon_{yy} & \epsilon_{yz} \\ \epsilon_{xz} & \epsilon_{yz} & \epsilon_{zz} \end{pmatrix} \stackrel{!}{=} \begin{pmatrix} \epsilon_{xx} & \epsilon_{xy} & -\epsilon_{xz} \\ \epsilon_{yx} & \epsilon_{yy} & -\epsilon_{yz} \\ -\epsilon_{xz} & -\epsilon_{yz} & \epsilon_{zz} \end{pmatrix} \implies \underline{\underline{\epsilon}}_{\text{PC}}(\mathbf{r}_{\parallel}) = \begin{pmatrix} \epsilon_{xx}(\mathbf{r}_{\parallel}) & \epsilon_{xy}(\mathbf{r}_{\parallel}) & 0 \\ \epsilon_{yx}(\mathbf{r}_{\parallel}) & \epsilon_{yy}(\mathbf{r}_{\parallel}) & 0 \\ 0 & 0 & \epsilon_{zz}(\mathbf{r}_{\parallel}) \end{pmatrix}, \quad (1.28)$$

where we used the notation $\mathbf{r}_{\parallel} = (x, y)$ for a position vector in the xy -plane. This reflection property holds for any z which is the necessary property for the desired decoupling as explained above. That means, for dielectric tensors of the form (1.28) (as long as an eventual anisotropy contains no z -component other than ϵ_{zz}), a wave with electric field $\mathbf{E}(\mathbf{r})$ and magnetic field $\mathbf{H}(\mathbf{r})$ propagating with $\mathbf{k} \perp \hat{\mathbf{z}}$ can be decomposed as (Fig. 1.5)

$$\mathbf{E} = \underbrace{E_z \hat{\mathbf{z}}}_{\text{E-pol.}} + \underbrace{\mathbf{E}_{\text{TE}}}_{\text{H-pol.}}, \quad \mathbf{H} = \underbrace{\mathbf{H}_{\text{TM}}}_{\text{E-pol.}} + \underbrace{H_z \hat{\mathbf{z}}}_{\text{H-pol.}}. \quad (1.29)$$

$\mathbf{E}_{\text{TE}} \perp \hat{\mathbf{z}}$ can be calculated from H_z and $\mathbf{H}_{\text{TM}} \perp \hat{\mathbf{z}}$ can be calculated from E_z . These two scalar components evolve independently and the partial waves are said to be E-polarized or H-polarized. The terms TM waves for E-polarization and TE waves for H-polarization are also common.⁶ After inserting these polarizations by choosing $\mathbf{H}(\mathbf{r}) = H_z(\mathbf{r}_{\parallel})\hat{\mathbf{z}}$ and $\mathbf{E}(\mathbf{r}) = E_z(\mathbf{r}_{\parallel})\hat{\mathbf{z}}$ into the vectorial wave equations

⁶However, sometimes they are defined just the other way round, like in [57]

(1.9) for the tensor (1.28) and considering (1.23), we get

2D Scalar Wave Equations in Frequency Domain

$$\left[\partial_x^2 + \partial_y^2 \right] E_z + \frac{\omega^2}{c_0^2} \varepsilon_{zz} E_z = 0, \quad (1.30a)$$

$$\begin{pmatrix} \partial_y \\ -\partial_x \end{pmatrix} \cdot \left[\underline{\underline{\eta}}_{\parallel} \cdot \begin{pmatrix} \partial_y \\ -\partial_x \end{pmatrix} \cdot H_z \right] + \frac{\omega^2}{c_0^2} H_z = 0, \quad (1.30b)$$

$$\underline{\underline{\eta}}_{\parallel}(\mathbf{r}_{\parallel}) := \begin{pmatrix} \eta_{xx}(\mathbf{r}_{\parallel}) & \eta_{xy}(\mathbf{r}_{\parallel}) \\ \eta_{yx}(\mathbf{r}_{\parallel}) & \eta_{yy}(\mathbf{r}_{\parallel}) \end{pmatrix}. \quad (1.30c)$$

1.2.5 Birefringence of Liquid Crystals

A liquid crystal (LC) is a substance sharing liquid and crystalline properties. Usually it exhibits an anisotropic dielectric tensor $\underline{\underline{\varepsilon}}$. Most LCs consist of long molecules which can move around freely like in a liquid, but show long range orientational and/or positional order in equilibrium like in an ordinary crystal. In fact, of all the various types of LCs we want to consider only *nematic* LCs here. The structure of this particular type of LC is schematically shown in Fig. 1.6. The molecule axes are not perfectly aligned, but in average they all point along a direction $\hat{\mathbf{n}}$ called the (nematic) director of the LC. In a nematic LC the molecules do not have special equilibrium positions in space.

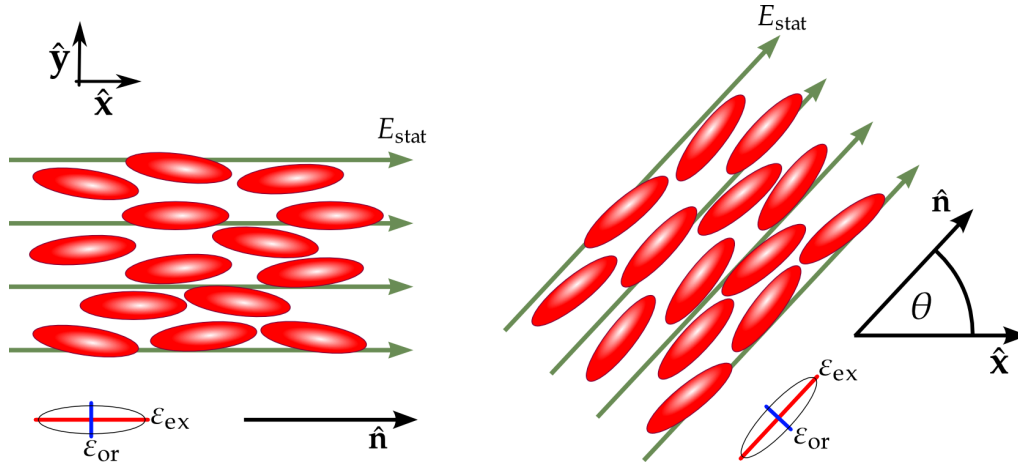


Figure 1.6: LCs aligned along static homogeneous electric fields \mathbf{E}_{stat} . The individual molecules are on average aligned along the nematic director $\hat{\mathbf{n}}$, the director angle θ describes the tilt of $\hat{\mathbf{n}}$ against the x -axis. The birefringence property of each individual molecule then averages to the macroscopic values of the ordinary and extraordinary dielectric constant ε_{or} and ε_{ex} , respectively.

The advantage in utilizing LCs for optical devices consists in the great variety of ways to alter the optical properties of these crystals, most important among those is the field induced reorientation of the molecules. Static electric fields can force the molecules to align themselves along new axes as shown in Fig. 1.6. Thus it is possible to actively tune direction-dependent optical properties of systems containing LCs.

In a coordinate system whose axes coincide with the molecule axes, the dielectric tensor of such a

crystal becomes diagonal:

$$\underline{\underline{\epsilon}}_{\text{diag}}^{\text{lc}} = \begin{pmatrix} \epsilon_{\text{ex}} & 0 & 0 \\ 0 & \epsilon_{\text{or}} & 0 \\ 0 & 0 & \epsilon_{\text{or}} \end{pmatrix}. \quad (1.31)$$

Usually there are only two different dielectric constants, depending on the polarization of the light mode. The extraordinary axis with extraordinary dielectric constant ϵ_{ex} coincides with the director $\hat{\mathbf{n}}$. Electromagnetic waves whose electric components are polarized in the plane perpendicular to $\hat{\mathbf{n}}$ are influenced by the ordinary dielectric constant ϵ_{or} . The electric component parallel to $\hat{\mathbf{n}}$ then ‘sees’ the dielectric constant ϵ_{ex} .

We want to restrict ourselves to anisotropies in the xy -plane of a 2D PC, i. e., we only consider directors $\hat{\mathbf{n}}$ lying in the xy -plane of wave propagation. Then we can fully describe the anisotropic effects in TE polarization and we may discard the irrelevant dielectric constant along the z -axis (this was discussed in Sec. 1.2.4). The diagonal dielectric tensor for such a 2D system is then given by

$$\underline{\underline{\epsilon}}_{\text{diag}}^{\text{lc}} = \begin{pmatrix} \epsilon_{\text{ex}} & 0 \\ 0 & \epsilon_{\text{or}} \end{pmatrix}. \quad (1.32)$$

When working in TE polarization, we will also be in need of the inverse $\underline{\underline{\eta}}$ of the dielectric tensor which is given as

$$\underline{\underline{\eta}}_{\text{diag}}^{\text{lc}} := \left[\underline{\underline{\epsilon}}_{\text{diag}}^{\text{lc}} \right]^{-1} = \begin{pmatrix} \frac{1}{\epsilon_{\text{ex}}} & 0 \\ 0 & \frac{1}{\epsilon_{\text{or}}} \end{pmatrix}. \quad (1.33)$$

The orientation of the molecules can now be described by the director angle θ between the director $\hat{\mathbf{n}}$ and the x -axis (see Fig. 1.6). An arbitrarily oriented crystal then has the dielectric tensor

$$\underline{\underline{\epsilon}}^{\text{lc}}(\theta) = R(\theta) \cdot \underline{\underline{\epsilon}}_{\text{diag}}^{\text{lc}} \cdot R^T(\theta), \quad (1.34)$$

where $R(\theta)$ denotes the rotation matrix around the z -axis:

$$R(\theta) = \begin{pmatrix} \cos \theta & -\sin \theta \\ \sin \theta & \cos \theta \end{pmatrix}, \quad R^T(\theta) = \begin{pmatrix} \cos \theta & \sin \theta \\ -\sin \theta & \cos \theta \end{pmatrix}. \quad (1.35)$$

The inverse $\underline{\underline{\eta}}^{\text{lc}}$ of the general dielectric tensor becomes

$$\underline{\underline{\eta}}^{\text{lc}}(\theta) := \left[\underline{\underline{\epsilon}}^{\text{lc}}(\theta) \right]^{-1} \quad (1.36)$$

$$\stackrel{(1.34)}{=} \left[R^T(\theta) \right]^{-1} \cdot \left[\underline{\underline{\epsilon}}_{\text{diag}}^{\text{lc}} \right]^{-1} \cdot \left[R(\theta) \right]^{-1} \quad (1.37)$$

$$\stackrel{(1.33)}{=} R(\theta) \cdot \begin{pmatrix} \frac{1}{\epsilon_{\text{ex}}} & 0 \\ 0 & \frac{1}{\epsilon_{\text{or}}} \end{pmatrix} \cdot R^T(\theta) \quad (1.38)$$

$$\stackrel{(1.33)}{=} R(\theta) \cdot \underline{\underline{\eta}}_{\text{diag}}^{\text{lc}} \cdot R^T(\theta). \quad (1.39)$$

Here we exploited the orthogonality property $R^{-1} = R^T$ of rotation matrices.

Real LCs have a microscopic structure that is in general more complicated than the one we have assumed above. Nematic liquid crystal director fields $\hat{\mathbf{n}}(\mathbf{r})$ usually are neither homogeneous nor constrained to the xy -plane in general [58]. An orientation model coming closest to our assumptions would

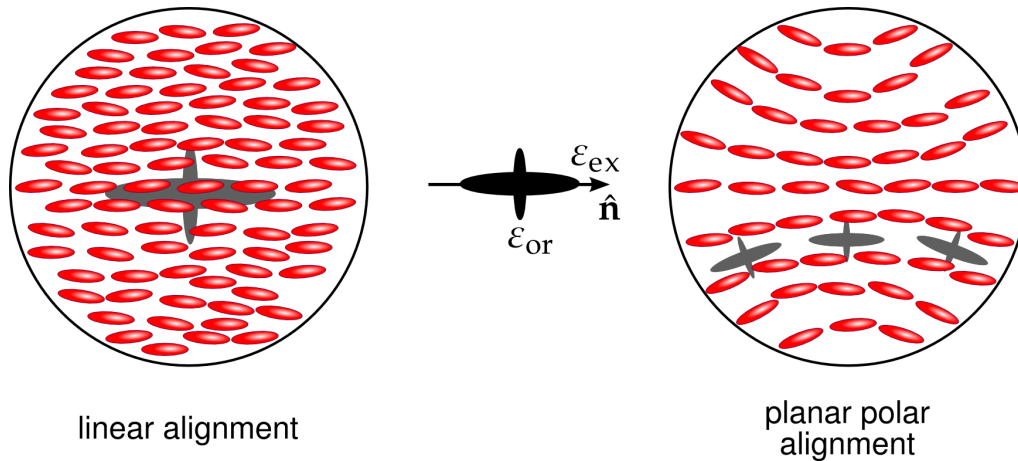


Figure 1.7: *LC alignments.* The linear alignment is unphysical but can be regarded as an approximation of the physical planar polar alignment in cylindrical holes. The principal axes ε_{ex} and ε_{or} of the tensor dielectric function are shown schematically as mutually perpendicular ellipsoids. These axes are oriented homogeneously over the cylinder for linear alignment, but vary in space for planar polar alignment. The values of $\hat{\mathbf{n}}$, ε_{ex} and ε_{or} used when working with the linear alignment model have to be understood to be macroscopically averaged values for the LC from the planar polar case.

be the planar polar model as shown in Fig. 1.7. Applying static electric fields can still force the molecules to point into a new direction in the xy -plane. By approximating the total LC by effective mean values of (a homogeneous and isotropic) $\hat{\mathbf{n}}$, ε_{ex} , and ε_{or} , we may nevertheless get accurate results, even if we do not take the full microscopic details into account [59, 60]. This approximation is frequently used for the sake of numerical simplicity [61]. The Wannier function approach to numerically investigate the optical properties of such defects is in principle also capable of taking these details into account (but that has not been implemented so far).

1.2.6 Gyrotropy

In materials with magneto-optic response, a static magnetic field \mathbf{H}_{stat} can also alter the dielectric permittivity tensor. Note that this is not a contradiction to setting $\mu(\omega) \equiv 0$ for optical frequencies because we treat the effects of *static* magnetic fields now.

The physical origin of this effect lies in the fact that the bound charges in a dielectric cannot only oscillate/be displaced by electric fields, but also rotate under the influence of a magnetic field. This breaks the reciprocity in the wave equations, where reciprocity means the following [62]:

A source at point A creates the same field (amplitude and phase) at a point B , as that source placed at B would create at point A .

We already restricted ourselves to source-free wave propagation. The breaking of reciprocity then manifests as itself as waves that do not return to their origin when the propagation direction of these waves is reversed. This allows the construction of optical isolators that can guide back-scattered waves into another direction than the one the waves originally came from [63].

According to [46], the magneto-optic permittivity tensor $\underline{\underline{\varepsilon}}^{\text{mo}}$ in first order of \mathbf{H}_{stat} has the form

$$\underline{\underline{\varepsilon}}^{\text{mo}}(\mathbf{H}_{\text{stat}}) = \underline{\underline{\varepsilon}}_{\text{diag}}^{\text{mo}} + i\underline{\underline{\varepsilon}}_{\text{off-diag}}^{\text{mo}}(\mathbf{H}_{\text{stat}}), \quad (1.40)$$

where $\underline{\underline{\epsilon}}_{\text{diag}}^{\text{mo}}$ is symmetric and $\underline{\underline{\epsilon}}_{\text{off-diag}}^{\text{mo}}$ is anti-symmetric, making $\underline{\underline{\epsilon}}^{\text{mo}}$ a Hermitian tensor. The electric displacement \mathbf{D} after (1.4) can then be written in the form

$$\mathbf{D} = \epsilon_0 \underline{\underline{\epsilon}}_{\text{diag}}^{\text{mo}} \mathbf{E} + \mathbf{iE} \times \mathbf{g}, \quad (1.41)$$

where the gyration vector \mathbf{g} up to first order in \mathbf{H}_{stat} is given by

$$\mathbf{g} = \epsilon_0 \underline{\underline{\chi}}_{\text{mag}} \mathbf{H}_{\text{stat}}. \quad (1.42)$$

Here, $\underline{\underline{\chi}}_{\text{mag}}$ is the magnetic susceptibility tensor which in turn reduces to a scalar χ_{mag} in the isotropic case.⁷ If we still want to treat our 2D systems in TE and TM polarization with the scalar wave equations (1.30), then the only allowed gyrotropy may be created by a static external magnetic field in the z -direction leading to

$$\underline{\underline{\epsilon}}^{\text{mo}} = \begin{pmatrix} \epsilon_{\text{diag}} & +ig_z & 0 \\ -ig_z & \epsilon_{\text{diag}} & 0 \\ 0 & 0 & \epsilon_{\text{diag}} \end{pmatrix}. \quad (1.43)$$

The vector \mathbf{g} (and, hence, the component g_z) is usually much smaller than ϵ_{diag} . Comparing the form (1.43) with (1.30c) we see that incorporating magneto-optic effects in the 2D scalar treatment is only possible in TE polarization.

1.2.7 Model Systems

The 2D model systems investigated in this work are cylindrical air holes in silicon arranged in a triangular lattice and a square lattice, respectively (see Fig. 1.8). The square lattice of silicon rods arranged in air is reviewed briefly for comparison in Sec. 6. The radii of these cylinders are denoted by r . The TE polarized case is most interesting because of the large band gaps that are possible then (cf. Fig. 1.10). We use the values $\epsilon_{\text{air}} = 1$ and $\epsilon_{\text{Si}} = 12$.

The scalar dielectric functions $\epsilon_{\text{PC}}(\mathbf{r})$ for these PCs are given as piecewise continuous step functions, defined in closed form as

$$\epsilon_{\text{PC}}(\mathbf{r}) = \epsilon_{\text{back}} + (\epsilon_{\text{cyl}} - \epsilon_{\text{back}}) \sum_{\mathbf{R} \in \mathbb{L}_{\text{PC}}} \Theta_{\text{cyl}}(\mathbf{r} - \mathbf{R}). \quad (1.44)$$

Here, the scalar background and cylinder permittivities ϵ_{back} and ϵ_{cyl} are used. The indicator function⁸ Θ_{cyl} takes on the value 1 inside a cylinder of radius r and 0 otherwise.⁹ It can be expressed in terms of the Heaviside step function $\Theta(\mathbf{r})$ as

$$\Theta_{\text{cyl}}(\mathbf{r} - \mathbf{R}) := \Theta(r - |\mathbf{r} - \mathbf{R}|). \quad (1.45)$$

1.2.8 Bloch Modes and Band Structure

We summarize the consequences of the Bloch theorem for a perfect PC with periodic dielectric function (1.11) for the model systems. The wave equations (1.9) can be cast in the common form

$$\hat{H}(\mathbf{r})\psi(\mathbf{r}) = \frac{\omega^2}{c_0^2}\psi(\mathbf{r}). \quad (1.46)$$

⁷Isotropic in the magnetic response, the dielectric permittivity is still a non-trivial tensor.

⁸Indicates whether the position \mathbf{r} is inside a cylinder.

⁹Other hole geometries are possible [64], but not investigated here.

Here, $\boldsymbol{\psi}$ stands for either the magnetic or electric field with the position dependent differential operators \hat{H} acting on the fields $\boldsymbol{\psi}$ as

$$\hat{H}^{\text{el}}(\mathbf{r})\boldsymbol{\psi}(\mathbf{r}) := \underline{\underline{\epsilon}}_{\text{PC}}^{-1}(\mathbf{r}) \cdot \nabla \times (\nabla \times \boldsymbol{\psi}(\mathbf{r})), \quad (1.47)$$

$$\hat{H}^{\text{mag}}(\mathbf{r})\boldsymbol{\psi}(\mathbf{r}) := \nabla \times (\underline{\underline{\epsilon}}_{\text{PC}}^{-1}(\mathbf{r}) \cdot \nabla \times \boldsymbol{\psi}(\mathbf{r})), \quad (1.48)$$

These differential operators are invariant under lattice translations

$$\mathbf{r} \mapsto \mathbf{r}' := \mathbf{r} + \mathbf{R} \text{ for } \mathbf{R} \in \mathbb{L}_{\text{PC}} \quad (1.49)$$

because of the periodicity of the dielectric function and spatial derivatives:

$$\underline{\underline{\epsilon}}_{\text{PC}}(\mathbf{r}') = \underline{\underline{\epsilon}}_{\text{PC}}(\mathbf{r} + \mathbf{R}) \stackrel{(1.11)}{=} \underline{\underline{\epsilon}}_{\text{PC}}(\mathbf{r}), \quad (1.50)$$

$$dr'_i = dr_i \Rightarrow \nabla' \times = \nabla \times. \quad (1.51)$$

Therefore, $\hat{H}(\mathbf{r}') = \hat{H}(\mathbf{r})$, in which case the solutions $\boldsymbol{\psi}$ take on the particular form of the Bloch theorem stated in (1.19).

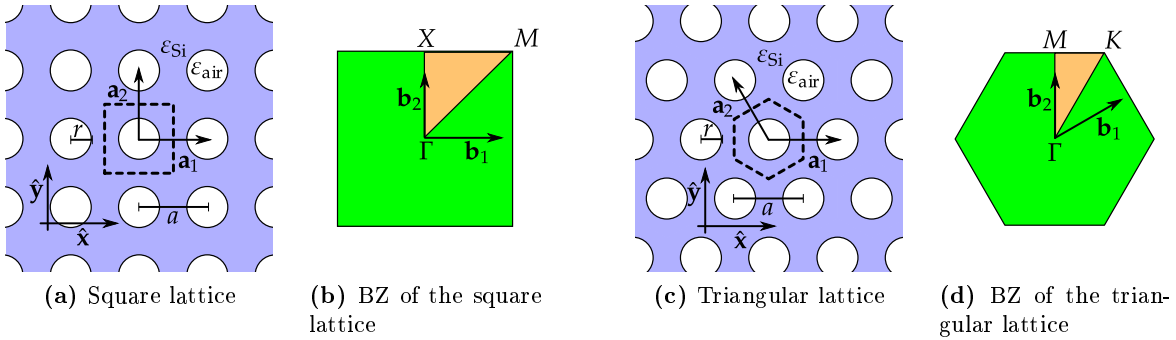


Figure 1.8: Cylindrical air holes in silicon arranged in a square and triangular lattice. The WSC, primitive lattice translations \mathbf{a}_i , the lattice constant $a = |\mathbf{a}_i|$, and hole radius r are shown.

Some typical band structures for the 2DPC model systems of Sec. 1.2.7 with scalar permittivity are shown in Fig. 1.9. Low frequencies correspond to long wavelengths, where the PC looks effectively homogeneous and features a linear dispersion relation (this corresponds to case 3 of Fig. 1.1). With higher frequencies, the band structure becomes non-trivial with possible band gaps opening. In these regions, for given ω no real-valued solutions for \mathbf{k} can be found. Thus, these modes do not propagate but decay exponentially in space. At a PC surface, light with these frequencies is perfectly reflected, inside the PC it is trapped.

Fig. 1.10 displays gap maps for the two TE model systems. They reveal which radii r yield the largest band gaps for the H- and E-polarized modes. Only the triangular system (for cylindrically shaped air holes) shows a large gap overlap for both polarizations which is of great technical importance in order to control the light flow in these PCs. The radius $r = 0.45a$ is the best compromise between experimental accessibility and large band gaps for both polarizations. This is why the triangular system with that particular radius is preferred for the investigation of functional elements, whereas the square lattice modes are easier to plot and comprehend and are therefore used to illustrate the theory.

The wave vector \mathbf{k} also labels the irreducible representation of the translation group which the Bloch mode belong to. This is explained and discussed in Sec. 2.5.1. Additionally, the Bloch modes can

also be labeled by the irreducible representations of the point groups of the symmetry group of the PC (cf. Sec. 2.5.2) which has been shown in Figs. F.6 and F.7. These labels become important in the construction of exponentially localized Wannier functions later on which is explained in greater detail in Chap. 2.

1.2.9 Bloch Mode Orthonormality and Scalar Products

For the Bloch modes $\psi_{n\mathbf{k}}$, we now introduce the compact Dirac notation $|n\mathbf{k}\rangle$. Then we may write the standard scalar product in d dimensions as we know it from quantum mechanics as

$$\langle \psi_{n'\mathbf{k}'} | \psi_{n\mathbf{k}} \rangle := \int d^d r \psi_{n'\mathbf{k}'}^*(\mathbf{r}) \cdot \psi_{n\mathbf{k}}(\mathbf{r}), \quad (1.52)$$

$$\langle \psi_{n'\mathbf{k}'} | \hat{O} | \psi_{n\mathbf{k}} \rangle := \int d^d r \psi_{n'\mathbf{k}'}^*(\mathbf{r}) \cdot (\hat{O} \psi_{n\mathbf{k}}(\mathbf{r})). \quad (1.53)$$

where \hat{O} stands for an arbitrary operator acting on the fields.

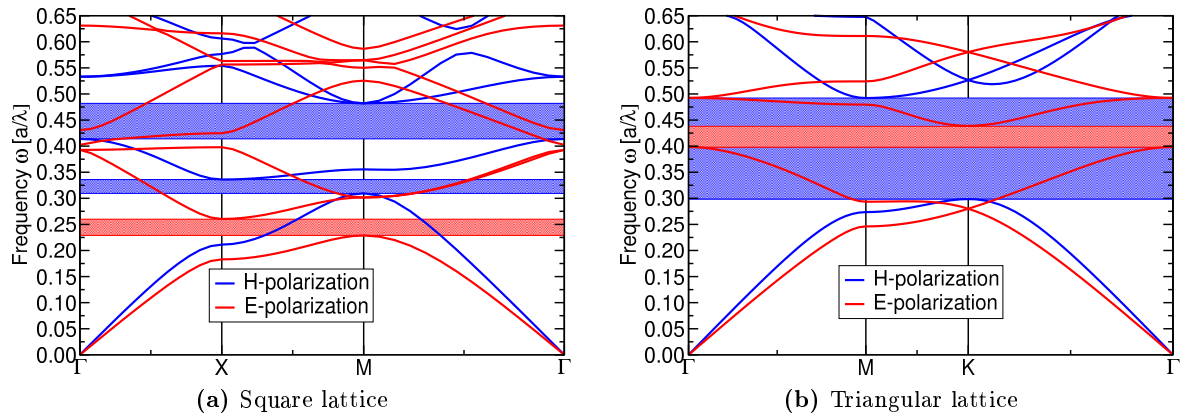


Figure 1.9: Exemplary band structures for the 2DPC made of cylindrical air holes in silicon ($\varepsilon_{\text{air}} = 1$, $\varepsilon_{\text{Si}} = 12$) from Fig. 1.8 for a radius ratio $r/a = 0.45$. Shaded regions denote band gaps.

In the magnetic field case, \hat{H}^{mag} is a Hermitian operator with respect to the standard scalar product and its Bloch modes can therefore be chosen to be orthogonalized. This is not true for the electric field case, but the electric field Bloch modes are orthogonal for a modified scalar product that features the permittivity tensor as integration kernel (see App. A.5). Many algorithms introduced in this work rely on the orthonormality of the fields. In order to treat electric field and magnetic field equations in the same fashion, we introduce a polarization independent scalar product $\langle\langle \cdot | \cdot \rangle\rangle$ by

$$\langle\langle \psi_{n'\mathbf{k}'} | \psi_{n\mathbf{k}} \rangle\rangle := \begin{cases} \langle \psi_{n'\mathbf{k}'} | \psi_{n\mathbf{k}} \rangle & : \text{magnetic field,} \\ \langle \psi_{n'\mathbf{k}'} | \underline{\underline{\varepsilon}}_{\text{PC}} | \psi_{n\mathbf{k}} \rangle & : \text{electric field,} \end{cases} \quad (1.54)$$

$$\stackrel{(1.52)(1.53)}{=} \begin{cases} \int d^d r \psi_{n'\mathbf{k}'}^*(\mathbf{r}) \cdot \psi_{n\mathbf{k}}(\mathbf{r}) & : \text{magnetic field,} \\ \int d^d r \psi_{n'\mathbf{k}'}^*(\mathbf{r}) \cdot \underline{\underline{\varepsilon}}_{\text{PC}}(\mathbf{r}) \cdot \psi_{n\mathbf{k}}(\mathbf{r}) & : \text{electric field,} \end{cases} \quad (1.55)$$

$$= \delta_{n'n} \delta^{(d)}(\mathbf{k}' - \mathbf{k}). \quad (1.56)$$

Here, $\delta_{n'n}$ denotes the Kronecker delta and $\delta^{(d)}(\mathbf{k}' - \mathbf{k})$ the Dirac delta function in d dimensions. Matrix elements for E-polarization are meant to be computed as

$$\langle\langle \mathbf{E} \| \hat{O} \| \mathbf{E}' \rangle\rangle := \int d^d r \mathbf{E}^* \cdot \underline{\underline{\epsilon}} \cdot (\hat{O} \mathbf{E}). \quad (1.57)$$

Furthermore, this also defines a norm in the magnetic and electric function spaces by

$$\|\psi\|_2 := \sqrt{\langle\langle \psi \| \psi \rangle\rangle}. \quad (1.58)$$

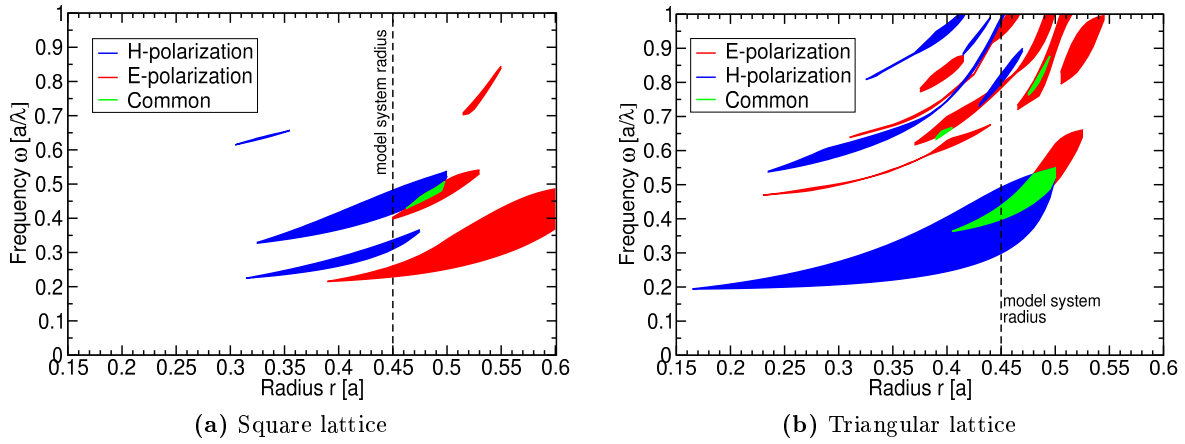


Figure 1.10: The band gaps for the systems defined by Fig. 1.8 for various radii r/a . The band gaps for TE (H -polarization) and TM (E -polarization) modes have large overlap in the triangular lattice.

1.2.10 Defect Structures in Photonic Crystals

The existence of a band structure and, hence, the band gaps, is a direct consequence of the Bloch theorem which itself derives from the periodicity of the perfect PC. When this periodicity is broken on purpose, we may expect new behavior for optical modes, in particular for those newly introduced in the band gap. Examples for point defect structures are shown in Fig. 1.11. Due to the etching processes used for the realization of this type of PC, most of such structures were restricted to changes in the geometry, like resizing [65, 66] or relocating the air holes [67, 68]. Recent advances in single pore infiltration techniques [11–13] and tuning of the dielectric constant of defects [69, 70] open way more possibilities to influence the optical behavior of defects.

Arising from the broken symmetry, there may now be eigenmodes with frequencies ω in the band gap (Fig. 1.12). In the vicinity of such point defects, the light field is subject to the periodic part of the PC, forcing the mode profile to decay exponentially as explained in section Sec. 1.2.8. This decay behavior is shown for a single non-etched hole in Fig. 1.13. Such structures can act as resonators and optical filters [49], whose operating frequencies can be tuned by adjusting the geometry or infiltrating materials with various permittivities ϵ and, e.g., can be used to enhance light matter interaction in quantum electrodynamical processes [71]. By using actively tunable materials like liquid crystals or magneto-optic materials, one could actively tune the resonator frequencies by applying static electric or

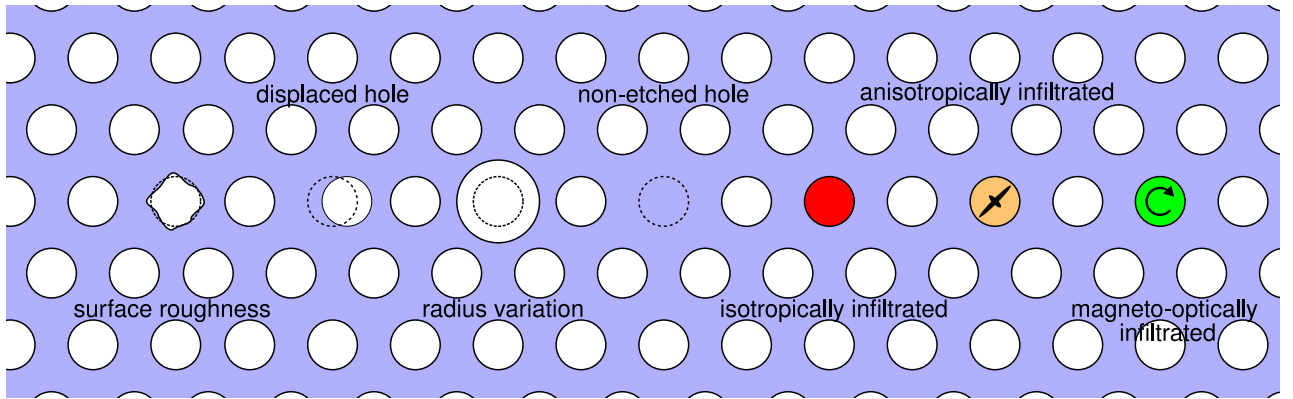


Figure 1.11: Selected types of point defects. While surface roughness is due to imperfections in the production process and should be avoided, the other defects shown here are introduced on purpose and used to deliberately alter and tune the optical response of the system.

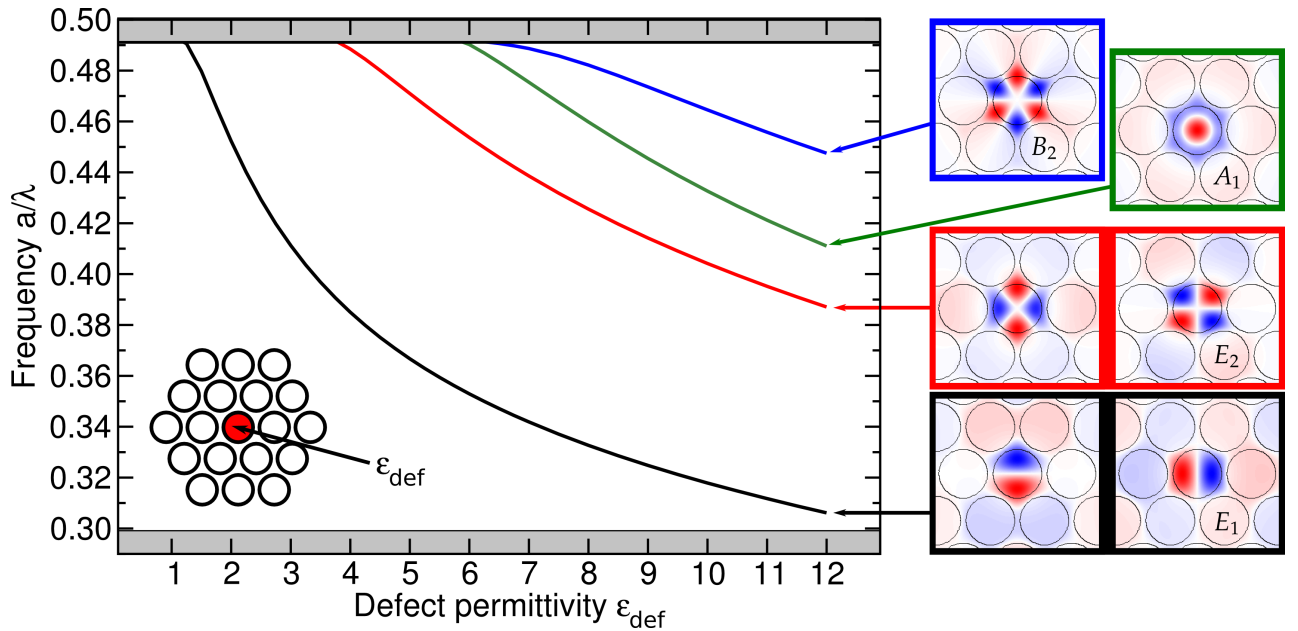


Figure 1.12: H -field defect mode frequencies in the band gap of the triangular TE model system for a single infiltrated hole. Bulk PC band frequency regions are denoted by grey shaded areas. The mode profiles are shown for the case of a non-etched hole, including the irreducible representations of the point group C_{6v} they form (cf. Tab. F.8). The numerical data was obtained by an MPB supercell calculation for 11×11 unit cells.

magnetic fields, respectively. This is in contrast to passively tuned cavities, whose resonance frequencies remain fixed after production.

If just a single hole is infiltrated, the structure loses its lattice periodicity but retains the rotational symmetries of the former PC around the center of the infiltrated hole. Thus, by Sec. 2.4.5, the eigenmodes shown can be classified as the irreducible representations of the point group C_{6v} (see Tab. F.8).

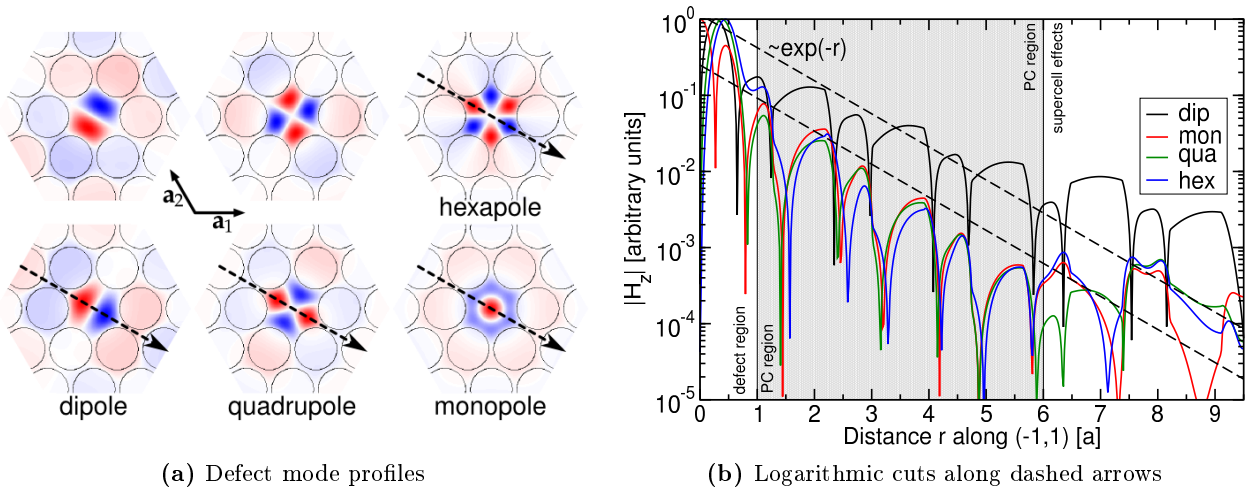


Figure 1.13: Cuts along localized defect mode profiles in the band gap of the model system for a non-etched hole. The numerical data was obtained by an MPB supercell calculation for 11×11 unit cells.

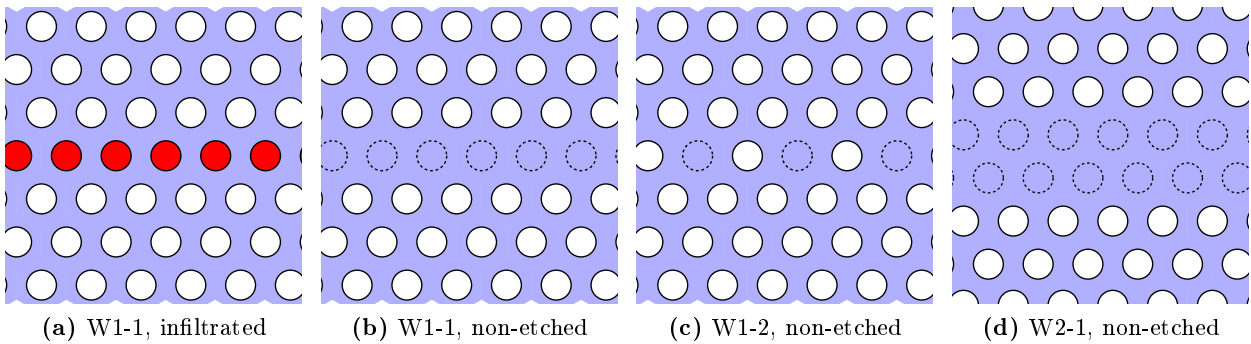


Figure 1.14: Schematic illustrations of waveguides in photonic crystals.

One can as well design defect structures that still retain some translational symmetry such as line defects (Fig. 1.14). In this case, extended propagating modes in the direction of periodicity are allowed due to the Bloch-Floquet theorem (Fig. 1.15), whereas in perpendicular directions the mode profiles again decay exponentially (Fig. 1.16). Thus, the modes are confined to and propagate along the defect line which forms a waveguide then. Such a waveguide can be regarded as a 1D PC, whose band structure is one-dimensional as well and is referred to as the waveguide dispersion (Fig. 1.15a). Its eigenmodes form irreducible representations of the point group C_{1h} with $\sigma = \sigma_y$ (cf. Tab. F.8), thus the eigenmodes can be classified as being even under a mirror reflection in the xz -plane (A, eigenvalue $\chi(\sigma_y) = +1$) or odd (B, eigenvalue $\chi(\sigma_y) = -1$). Since the two branches shown in Fig. 1.15a belong to different representations, they may cross each other.

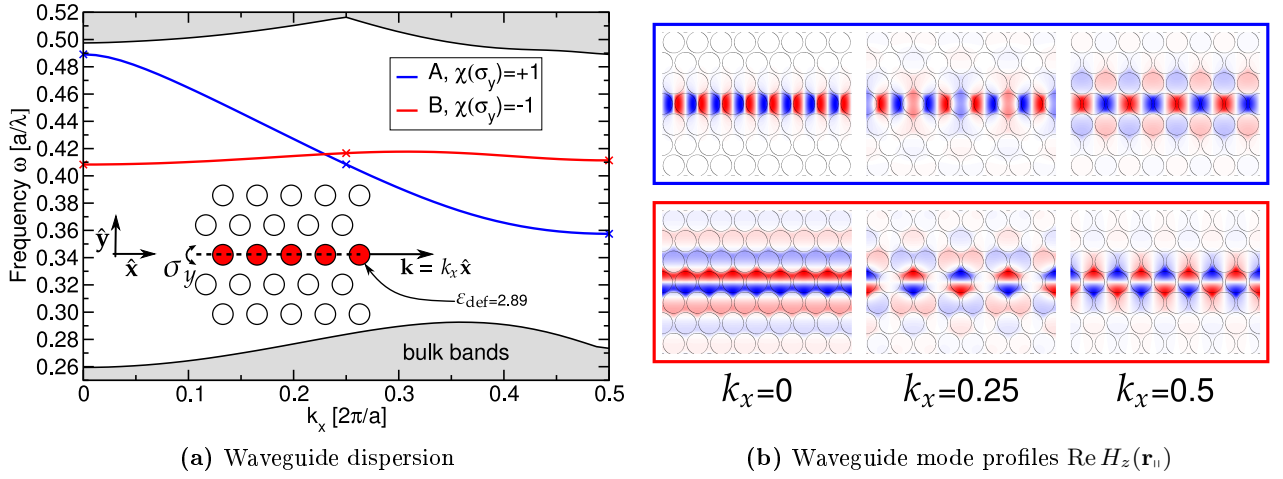


Figure 1.15: Waveguide dispersion $\omega(k_x)$ and corresponding magnetic field TE mode profiles for a W1-1 waveguide of infiltrated pores with $\varepsilon_{\text{def}} = 2.89$. The wave number k_x , for which the mode profiles are shown, are denoted by crosses. The modes are either even or odd under σ_y mirror reflections.

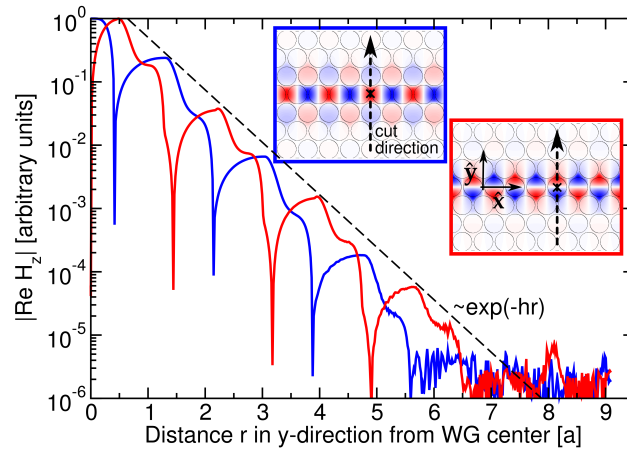


Figure 1.16: Analogous to localized defect modes, the guided modes in a waveguide decay exponentially into the PC-region ($h > 0$).

1.2.11 Functional Elements

Defect clusters connected via waveguides form circuits out of functional elements. Some examples for such functional elements based on infiltrated pores are shown in Fig. 1.17. As the name suggests, they serve a special function in optical signal processing. A waveguide bend couples modes from one incoming waveguide to another outgoing waveguide, hereby changing the direction of the modes. A Y-splitter distributes incoming waves from one arm to all three arms, since some part of the waves is always reflected back. The naive design for an add-drop filter employs a tunable LC resonator between two waveguides, allowing waves at the resonance frequency to be switched between the waveguides.

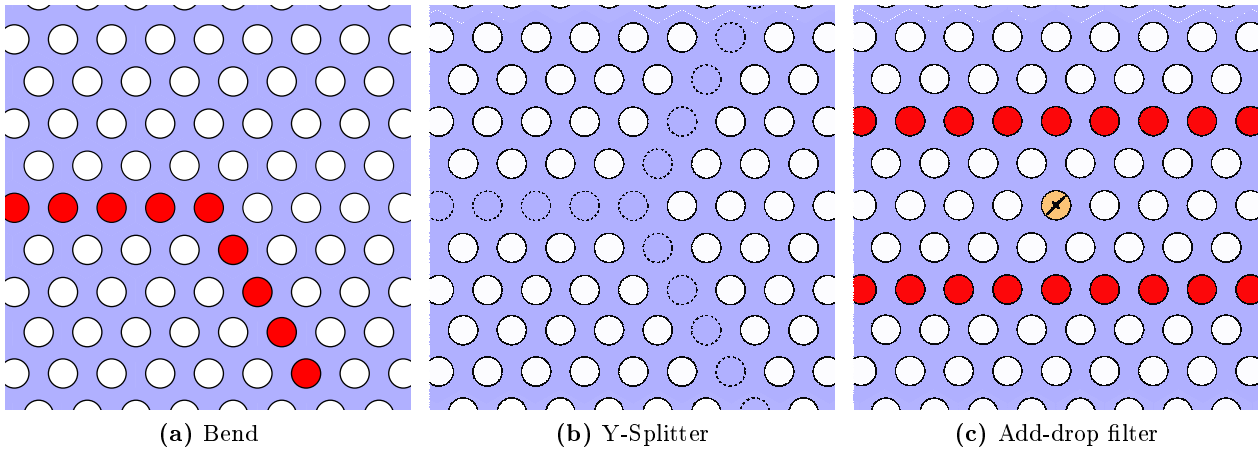


Figure 1.17: *Schematic illustrations of devices in photonic crystals based on single pore infiltration.*

Further examples for functional elements designed by single pore infiltration are found in [14, 40, 72]. In order to be useful in actual photonic devices, such designs have to be optimized, e. g., to reduce reflections or tune the working frequencies at which they are supposed to operate. For this task, an accurate and efficient numerical method is needed. The scattering matrix approach based on the localized basis expansion is such a method. It will be reviewed briefly in Sec. 4.6.

1.2.12 The Wannier Function Approach

In order to describe the localized defect mode profiles numerically, one can expand the wave equations in a localized orthonormal set of basis functions and solve the equations within that basis. For this task, the photonic WFs are a natural choice. The aim of this thesis is to analyze and increase the accuracy of this Wannier expansion. Therefore, a brief summary of Wannier function properties is given here.

The WFs $W_{n\mathbf{R}}(\mathbf{r})$ have been introduced by Wannier [26] as a lattice Fourier transform of the Bloch modes $\psi_{n\mathbf{k}}(\mathbf{r})$ of a crystal for the electronic case:

$$W_{n\mathbf{R}}(\mathbf{r}) = \frac{1}{N_{\mathbf{k}\text{-res}}} \sum_{\mathbf{k} \in \text{BZ}} e^{-i\mathbf{k}\mathbf{R}} \psi_{n\mathbf{k}}(\mathbf{r}). \quad (1.59)$$

Here, $N_{\mathbf{k}\text{-res}}$ is the total number of \mathbf{k} -vectors in the BZ. The WFs were assumed to be localized at the crystal unit cell at lattice site \mathbf{R} and used for the description of localized (electronic) states. However, the explicit construction of these functions from Bloch modes was not trivial, since the Bloch modes are only defined up to a complex phase factor $\exp(i\phi_n(\mathbf{k}))$. The phase angle $\phi_n(\mathbf{k})$ can be chosen differently

at each \mathbf{k} -point for each band n , leading to different sets of WFs with different localization properties and function profiles.

Nonetheless did the WFs' success in electronic crystal theory spark the interest to also describe localized light modes, as they occur in PC functional devices (cf. Figs. 1.13, 1.16), in a localized basis of vectorial photonic WFs $\mathbf{W}_{n\mathbf{R}}(\mathbf{r})$ [28, 32, 73]. This method to solve for localized defect states of the wave equations (1.9) in PCs is based on an expansion of the unknown fields $\boldsymbol{\psi}(\mathbf{r})$ into WFs $\mathbf{W}_{n\mathbf{R}}(\mathbf{r})$ obtained from the vectorial electromagnetic Bloch modes $\boldsymbol{\psi}_{n\mathbf{k}}(\mathbf{r})$,

$$\boldsymbol{\psi}(\mathbf{r}) = \sum_{n\mathbf{R}} c_{n\mathbf{R}} \mathbf{W}_{n\mathbf{R}}(\mathbf{r}), \quad (1.60)$$

where the expansion coefficients $c_{n\mathbf{R}} \in \mathbb{C}$ are the new unknowns to solve for. We apply this ansatz only in the scalar 2D case and work with scalar photonic WFs $W_{n\mathbf{R}}(\mathbf{r})$. By this expansion, the differential operators in the wave equations are expressed in the Wannier basis as matrices (analogous to quantum mechanical computations). These matrices can be diagonalized by a computer, yielding numerical approximations of the $c_{n\mathbf{R}}$ as eigenvectors and the frequencies as approximations to the eigenvalues. This procedure as well as the computation of transmission/reflection characteristics of functional elements in the Wannier function approach is explained in detail in Chap. 4. The resulting matrix elements decay fast with increasing separation distance between the WFs which is a direct consequence of their high degree of localization.

Hence, in order for numerical methods based on an expansion into localized WFs to work efficiently, the WFs actually have to be available and to be as localized as possible. Therefore, a brief review about the localization properties of WFs is given here.

Kohn [74] showed for a one dimensional (1D) crystal that the Bloch mode phases $\phi_n(k)$ can be adjusted to yield exponentially localized WFs $W_n(x)$. These are purely real functions and their localization center lies within the WSC at the origin, either in the center or the edge of that cell. They are either symmetric or antisymmetric with respect to point reflections. These symmetry properties of WFs are generalized to two dimensions in Chap. 2. These localized WFs decay like $\exp(-|x|h_n)$, actually meaning that

$$\lim_{x \rightarrow \infty} W_n(x) \exp(-|x|q) = \begin{cases} 0 & : q < h_n, \\ \infty & : q > h_n, \end{cases} \quad (1.61)$$

where $h_n > 0$ is a real constant characteristic for each WF band n . This parameter h_n is determined by the analytic continuation of the band structure ω_{nk} for complex values of $k \in \mathbb{C}$ (which is easier to study for 1D crystals). It denotes the size of the smallest strip around the real k -axis, where the band structure ω_{nk} is an analytic function until branch points appear. An example band structure illustrating the location of these branch points for a 1D PC is shown in Fig. 1.18. Examples for complex 2D band structures are found in [75, 76].

The authors He and Vanderbilt [27] studied this decay property and proved the more precise decay law in 1D to be

$$W_n(x) \approx |x|^{-3/4} \exp(-|x|h_n). \quad (1.62)$$

They also confirmed this decay law empirically by actually constructing 2D and three dimensional (3D) WFs. In order to judge the decay behavior of the WFs presented in this work, we either show a pure exponential function $\exp(-|x|)$ or $|x|^{-3/4} \exp(-|x|h)$ as a guide to the eye in the WF plots, similar to Fig. 1.13.

The sizes h_n can be estimated by the size of the band gaps between the bands on the real k -axis. Thus, the closer two bands are, the less localized their WFs become. Consequently, when the bands

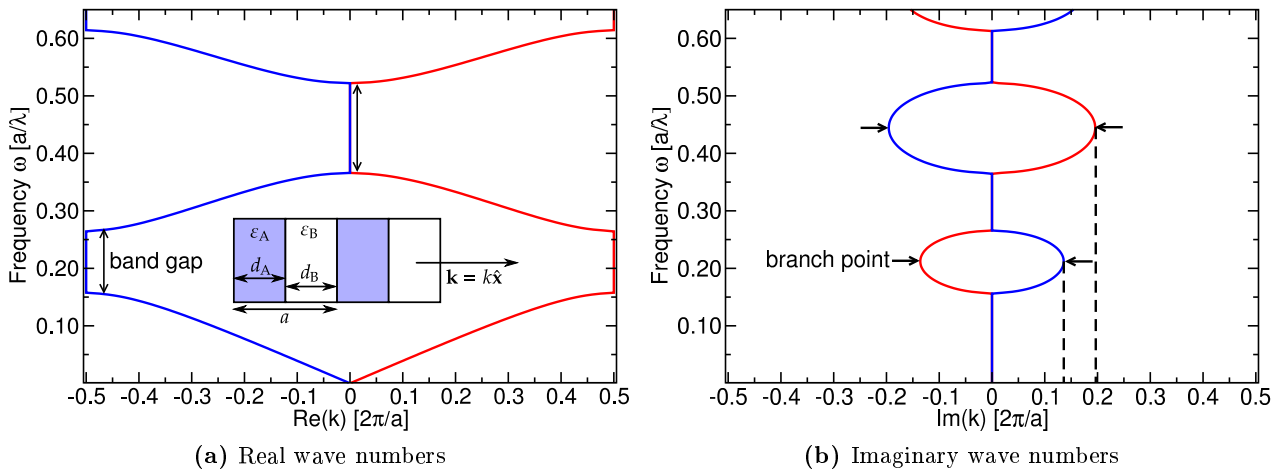


Figure 1.18: Photonic band structure for a silicon Bragg stack in air (Fig. 1.2a) with parameters $d_A = d_B = a/2$ and $\varepsilon_A = 12$, $\varepsilon_B = 1$. The band structure was obtained by solving the corresponding exact transcendental equations numerically [77]. Imaginary parts $\text{Im}(k)$ only occur for $\text{Re}(k) = 0$ or $\text{Re}(k) = \pm\pi/a$. The branch points where the band structure $\omega(k)$ becomes a double-valued function for complex k are denoted by black arrows. The corresponding values for k determine the decay parameters h_n in (1.61) and (1.62) and can be estimated by the size of the band gaps [78].

intersect each other, the WFs can become totally delocalized, which requires a modified definition, the generalized WFs

$$W_{n\mathbf{R}}(\mathbf{r}) = \frac{1}{N_{\mathbf{k}\text{-res}}} \sum_{\mathbf{k} \in \text{BZ}} e^{-i\mathbf{k}\mathbf{R}} \sum_m \psi_{m\mathbf{k}}(\mathbf{r}) U_{mn}(\mathbf{k}). \quad (1.63)$$

They are no longer constructed from a single band of Bloch modes, but by a unitary transform $U(\mathbf{k})$ among the Bloch modes for each \mathbf{k} . Cloizeaux [36] and Krüger [37, 38] extensively studied the localization properties of WFs for this case. They stated the restrictions for the unitary transforms $U(\mathbf{k})$ based on the symmetries of the Bloch modes that finally yield localized WFs. Their investigations are based on group representation theory of crystals with 2D plane groups and 3D space groups. In order to understand and apply their results, the necessary group theory is summarized in Chap. 2 and applied to the numerical construction of WFs in Chap. 3.

A method for the numerical construction of maximally localized WFs, that does not yet take the symmetry considerations into account was published by Marzari and Vanderbilt [29] and Souza et al. [30]. Their algorithms construct maximally localized WFs that are found by minimizing the real space extent of the WFs. Their method does not need the WFs explicitly to judge the degree of localization and works with the Bloch modes only. It was extended to the bottom-up approach by Schillinger [35] (for the scalar 2D case) which theoretically allows to construct arbitrarily many WFs bands n . That work and the improved and optimized implementation of the bottom-up method by Wolff [79] is the basis of the present thesis.

The magnetic field WFs are anticipated to be a good expansion basis for defect modes in 3D, since they already fulfill the divergence constraint of (1.9b) which avoids unphysical zero-frequency solutions.¹⁰ However, as is going to be discussed in Chap. 6, they are unable to model the continuity conditions of defect modes across dielectric boundaries properly. That is why the WF basis must be augmented

¹⁰A problem that every method based on function expansions has to face, e. g. the finite element method [21].

by additional localized auxiliary basis functions for accurate defect mode frequency solutions. This approach is discussed thoroughly in Chap. 6.

1.3 Summary

We derived the wave equations for electromagnetic wave propagation in dielectric media at optical frequencies. The only material parameter entering the equations is a position dependent (possibly anisotropic) dielectric permittivity distribution $\underline{\underline{\epsilon}}(\mathbf{r})$. Photonic crystals have been introduced as periodic arrangements of dielectric materials. For in-plane propagation in two-dimensional photonic crystals, the vectorial wave equations may be separated into two independent scalar equations describing just the scalar z -component of the E-field and the H-field, respectively. The form of the anisotropic permittivity tensor allowing this decoupling was derived based on symmetry considerations. Such a permittivity tensor is found in nematic liquid crystals and some magneto-optic materials. Their optical properties can be tuned by external static electric and magnetic fields, respectively. Two-dimensional photonic crystals provide test systems, for which many effects also occurring in real photonic crystal slabs can be studied.

The periodicity of photonic crystals can be described in terms of lattices and light wave propagation is described with the help of the Brillouin zone. It provides the allowed wave vectors, playing the same role as for the propagation of electron waves in the solid state theory of electronic crystals. The well known Bloch theorem is applicable to light waves in photonic crystals as well, explaining the formation of a band structure. The band structures of the two-dimensional model systems were discussed, documenting the design parameters that lead to band gaps in these band structures.

The effect of defect structures breaking the translational symmetry of the photonic crystal was reviewed. Point defects introduce eigenmodes with frequencies in the band gaps, whose mode profiles decay exponentially in space. Line defects form waveguides, whose guided modes are spatially confined to the waveguide region. Perpendicular to the waveguide, the mode profiles also decay exponentially in space. The light confinement is rather strong, and mode profiles decay to 1% of their maximum value usually after three to six lattice constants a . Their possibility to confine light to small volumes and the wide range of fabrication parameters for tuning the optical response qualifies photonic crystals as building blocks for novel integrated devices in optical signal processing.

The wave equations can be solved by an expansion into a complete orthonormal function system. This yields an efficient numerical method if as many properties of the desired solutions are already present in the expansion basis. Due to the strong localization of the defect modes, an expansion of the wave equations into localized photonic Wannier functions was suggested by some authors for an efficient numerical scheme to analyze optical circuitry in photonic crystals. This idea, known in electronic solid state physics for decades, requires the numerical construction of localized Wannier functions $W_{n\mathbf{R}}(\mathbf{r})$ from the Bloch modes of the perfectly periodic crystal. Therefore, the constraints leading to localized Wannier functions were reviewed. In the best case, these functions decay like $|\mathbf{r}|^{-3/4} \exp(-h|\mathbf{r}|)$, in the worst case like $1/|\mathbf{r}|$. The decay behavior and symmetries of the Wannier functions are directly connected to the symmetries of the Bloch modes from which they were constructed. This connection is studied in more detail in the next chapter.

2

Chapter 2

Group Representation Theory

In this chapter, the consequences of rotational, translational and mirror symmetries of PCs are discussed. The main result consists in the observation that the eigenstates of a differential operator form irreducible representations of all the groups of symmetry transforms which commute with that differential operator. The consequences of this fundamental theorem include the Bloch-Floquet theorem, the definition of the Brillouin zone, the classification of spatial symmetries of eigenmodes (for Bloch modes and defect states), and the possibility to treat two separate scalar wave equations in 2D, one for TE and one for TM polarization, respectively. Last but not least, a justification for the definition of Wannier functions as a lattice Fourier transform of Bloch modes is given and the connection of Bloch mode symmetries with Wannier function symmetries and their localization properties is established. Unfortunately, in order to reproduce the results based on this chapter, extensive definitions, tables and notational overhead are necessary, many of which have been moved to App. F.

The theory presented here is simplified for the case of symmorphic plane groups in $d = 2$ dimensions. A full introduction comprising also non-symmorphic plane (2D) and space (3D) groups with all mathematical rigor would go way beyond the scope of this work. Therefore, the interested reader may resort to the following text books.

General introductions to the theory of plane groups in solid state physics and group representation theory can be found in Cornwell [80] and Lax [81]. A thorough and well readable treatment is found in Dresselhaus et al. [82]. The connection between the symmetry of Bloch modes and Wannier functions via the site symmetry approach is explained in detail in Evarestov [83].

A less mathematical introduction with examples on the symmetries of photonic crystals can be found in Joannopoulos et al. [47]. Many examples for the application of group theory to photonic crystals are also compiled in Sakoda [48].

A basic introduction to crystallography as needed for this chapter is found in Borchardt-Ott [84], whereas the standard reference on that subject are the International Tables of Crystallography [85].

2.1 Groups

A set G together with a multiplication between its elements for $g_1, g_2 \in G$ is called a group if

(closure condition) $g_1 g_2$ is an element of G for every $g_1, g_2 \in G$,

(existence of identity element) there is one unique $e \in G$ such that for every $g \in G$ the relation $ge = eg = g$ holds,

(**existence of inverse element**) every $g \in G$ has one unique $g^{-1} \in G$ with $gg^{-1} = g^{-1}g = e$,

(**associative law**) $(g_1g_2)g_3 = g_1(g_2g_3)$.

A group is called Abelian,¹ if the commutative law also holds: $g_1g_2 = g_2g_1$.

The order n_G of a group is the number of its distinct elements. A finite group is one of finite order. We only deal with finite groups here. A minimal set is one with the smallest order (least number of elements) possible, such that a particular condition holds.

The generators of a group G are a minimal subset g_i of elements of G such that any arbitrary element g can be expressed as a multiplication of finitely many g_i and their inverses in arbitrary combinations. Thus, the g_i generate any element of G by means of the group multiplication.

A cyclic group is generated by the powers g^n of a single element g . Cyclic groups are necessarily Abelian. The generator g of a finite cyclic group necessarily produces the identity e for $n = n_G$, the order of the finite cyclic group.

A subgroup $H \subset G$ is a subset of elements $g \in G$ such that any of its products are still contained in H (the closure relation is fulfilled).

A group homomorphism² Φ is a mapping $\Phi : G \rightarrow G'$ between two groups G and G' that preserves the multiplicative group structure, meaning that

$$\Phi(g_1g_2) = \Phi(g_1)\Phi(g_2) \quad \forall g_1, g_2 \in G. \quad (2.1)$$

A group homomorphism maps the identity and inverse elements of G to those of G' . The simplest group homomorphism is $\Phi(g) \equiv e \in G' \quad \forall g \in G$. A bijective homomorphism is called a group isomorphism.³ If there exists any isomorphism between two groups G and G' , the groups are said to be isomorphic: $G \cong G'$. Since a group G is readily defined by its abstract multiplication rules, an isomorphic group G' whose elements can be attributed a particular meaning (e. g., geometric transformations) is also called a realization of G . For instance, we are going to encounter various different realizations of one and the same point group as the site symmetry groups of spatial positions in a crystal later on.

Two elements $g_1, g_2 \in G$ are said to be conjugate if there is a $g \in G$ such that the relation $gg_1g^{-1} = g_2$ holds.⁴ The subsets of conjugate elements in G are called (conjugacy) classes. The conjugacy relation is mathematically an equivalence relation, thus any element $g \in G$ belongs to exactly one class and G is partitioned into disjoint conjugacy (equivalence) classes, or just classes for short. Any member of a class is its representative, as it defines the whole class unambiguously. In an Abelian group, each element forms its own conjugacy class. A function $f : G \rightarrow S$ (S being an arbitrary destination set) which has the same values for all members of the same class, is called a class function.

Remark: Another possibility of partitioning a group G into subsets is the construction of cosets for one of its subgroups H . This definition is important for the mathematical theory, but the results stated in the chapter abstract above can be understood without it. Therefore, to shorten the presentation here, it has been omitted.

¹In honor of the Norwegian mathematician Niels Abel.

²Greek, 'of similar shape'

³Greek, 'of equal shape'

⁴In linear algebra, this is the same as the similarity of matrices. The elements g depend on the various g_i and are not unique for a class.

2.2 Transform Operators

We define the geometric operations to transform functions (such as fields and permittivity distributions) in space by translations, rotations, reflections, and combinations thereof. These operations g are elements of a group acting on position vectors \mathbf{r} . These actions are used to define transform operators $\hat{D}(g)$ on a function space mapping functions onto their geometrically transformed functions.

The Euclidean space \mathbb{R}^2 has the Euclidean metric

$$\|\mathbf{r} - \mathbf{r}'\|_2 = \left[\sum_{i=1}^2 (r_i - r'_i)^2 \right]^{\frac{1}{2}} \quad (2.2)$$

in Cartesian coordinates. It defines the distance between two points $\mathbf{r}, \mathbf{r}' \in \mathbb{R}^2$. An isometry⁵ on \mathbb{R}^2 is a mapping $\Phi : \mathbb{R}^2 \rightarrow \mathbb{R}^2$ that leaves the Euclidean metric invariant:

$$\|\Phi(\mathbf{r}) - \Phi(\mathbf{r}')\| = \|\mathbf{r} - \mathbf{r}'\|. \quad (2.3)$$

The Euclidean group $E(2)$ of all possible isometries is the symmetry group of the Euclidean space. This group has infinite order, since it is a continuous group (its elements are parametrized by continuous parameters, like real rotation angles and real shifting distances).

Its elements can be written as $\{R|\mathbf{t}\}$, where R is an orthogonal matrix⁶ and \mathbf{t} is a vector of \mathbb{R}^2 , defining a translation. The action of such an isometry on a vector $\mathbf{r} \in \mathbb{R}^2$ is

$$\{R|\mathbf{t}\}\mathbf{r} := R\mathbf{r} + \mathbf{t}. \quad (2.4)$$

The identity element is $\{E|\mathbf{0}\}$ with E being the two-dimensional unit matrix. The composition of two isometries is

$$\{R_1|\mathbf{t}_1\}\{R_2|\mathbf{t}_2\}\mathbf{r} = \{R_1|\mathbf{t}_1\}(R_2\mathbf{r} + \mathbf{t}_2) \quad (2.5)$$

$$= R_1R_2\mathbf{r} + R_1\mathbf{t}_2 + \mathbf{t}_1. \quad (2.6)$$

The inverse of an isometry is

$$\{R|\mathbf{t}\}^{-1} = \{R^{-1} | -R^{-1}\mathbf{t}\}. \quad (2.7)$$

A pure translation is described by $\{E|\mathbf{t}\}$, a pure generalized rotation (rotations and reflections) keeping the the origin fixed is described by $\{R|\mathbf{0}\}$. Combinations of these elements describe rotations around arbitrary origins and angles, reflections along arbitrary lines and pure translations.⁷

A rank-0-tensor-valued⁸ function $f : \mathbb{R}^2 \rightarrow \mathbb{C}$ can also be shifted and rotated by means of an isometry $\{R|\mathbf{t}\} \in E(2)$. The transformed function $f'(\mathbf{r})$ under $\{R|\mathbf{t}\}$ is obtained via a linear operator $\hat{D}(\{R|\mathbf{t}\})$ acting on the space of these functions (cf. Fig. 2.1) by

$$f'(\mathbf{r}) = [\hat{D}(\{R|\mathbf{t}\})f](\mathbf{r}) \quad (2.8)$$

$$:= f(\{R|\mathbf{t}\}^{-1}\mathbf{r}) \quad (2.9)$$

$$\stackrel{(2.7)}{=} f(R^{-1}(\mathbf{r} - \mathbf{t})). \quad (2.10)$$

⁵Greek, 'of equal measure'

⁶That means $R \in O(2)$, where $O(2)$ is the group of all matrices with determinants $\det(R) = \pm 1$.

⁷In three dimensions, screw-axes, roto-reflections and space-inversions are added.

⁸Commonly referred to as a scalar. I deliberately chose this term because physicists immediately tend to think of pseudo-scalars as well, but this notion is introduced later on when treating representations and bases thereof. The transformation law introduced here knows nothing about being 'true' or 'pseudo' in the sense used in physics.

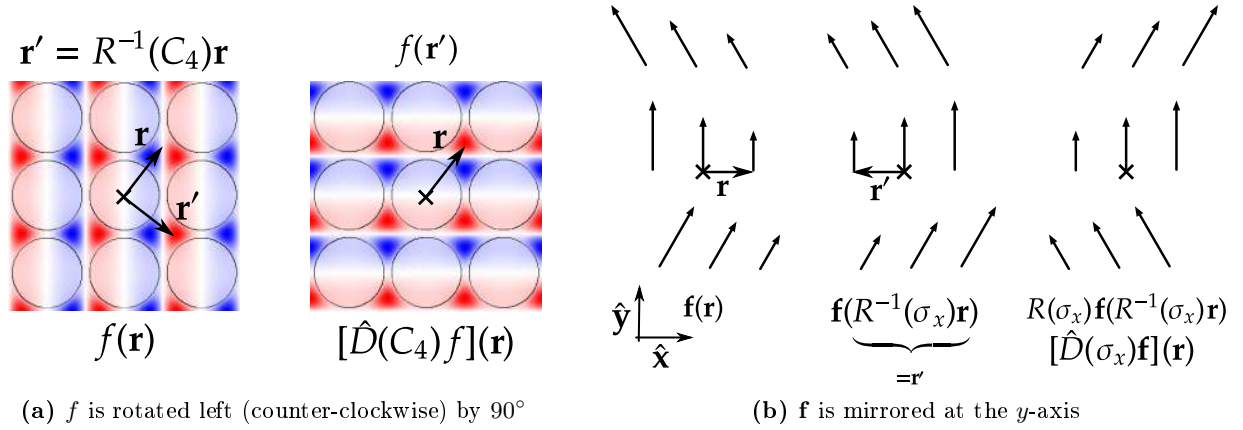


Figure 2.1: Action of the transformation operator $\hat{D}(g)$ on (a) a rank-0-valued function $f(\mathbf{r})$ ($g = C_4$) and a (b) rank-1-valued function $\mathbf{f}(\mathbf{r})$ ($g = \sigma_x$). Note how the full transformation law of (2.11) is needed for rotating the function \mathbf{f} properly. For symmetry notation, see Tab. F.2.

The mapping \hat{D} from the group of isometries $g = \{R|\mathbf{t}\} \in E(2)$ to the group of operators $\hat{D}(g)$ is a group homomorphism. Rank-1-tensor-valued and rank-2-tensor-valued functions $f_i(\mathbf{r})$ and $f_{ij}(\mathbf{r})$ are transformed as

$$f'_i(\mathbf{r}) = \sum_{i'} R_{ii'} f_{i'}(R^{-1}(\mathbf{r} - \mathbf{t})), \quad (2.11)$$

$$f'_{ij}(\mathbf{r}) = \sum_{i'j'} R_{ii'} R_{jj'} f_{i'j'}(R^{-1}(\mathbf{r} - \mathbf{t})). \quad (2.12)$$

As an example, the electric field $\mathbf{E}(\mathbf{r})$ and the magnetic field $\mathbf{H}(\mathbf{r})$ are to be transformed by (2.11).

2.3 Plane Groups

We introduce the group of all geometric transformations (translations, rotations, reflections and combinations thereof) that leave a photonic crystal invariant. This group is the space group (in 3D) or the plane group (in 2D) of that crystal. We consider two-dimensional photonic crystals only and say that the crystal is symmetric under the operations of its plane group. These statements are formulated more rigorously in the following.

A two-dimensional photonic crystal is invariant under operations of some discrete subgroup $G \subset E(2)$. Being invariant means that the permittivity distribution $\varepsilon_{\text{PC}}(\mathbf{r})$ does not change under applications of the isometries $\{R|\mathbf{t}\} \in G$, extending the relation (1.11) to

$$[\hat{D}(\{R|\mathbf{t}\})\varepsilon_{\text{PC}}](\mathbf{r}) = \varepsilon_{\text{PC}}(R^{-1}(\mathbf{r} - \mathbf{t})) \quad (2.13)$$

$$= \varepsilon_{\text{PC}}(\mathbf{r}). \quad (2.14)$$

The invariance condition is analogous for tensorial permittivities $\underline{\underline{\varepsilon}}_{\text{PC}}$ which have to be transformed by (2.12) and are investigated in Sec. 1.2.4. This group G is called the plane group of the PC. The term wallpaper group is also used. In 3D, we speak of space groups.

For any plane group G with elements $\{R|\mathbf{t}\}$ we define the point group G_0 of the plane group as the set of all orthogonal transforms R that occur at all in G (regardless of the translation \mathbf{t}):

$$G_0 := \left\{ \{R|\mathbf{0}\} : \exists \{R|\mathbf{t}\} \in G \right\}. \quad (2.15)$$

This point group G_0 need not be a subgroup of G , but for symmorphic plane groups it always is. The plane group G is said to be symmorphic if all the translation vectors \mathbf{t} are restricted to lattice vectors \mathbf{R} of the underlying crystal lattice $\mathbb{L} = \mathbb{L}_{\text{PC}}$ of (1.12) only. If also fractional lattice translations $\mathbf{t} \notin \mathbb{L}$ occur, it is called non-symmorphic. The group $T(\mathbb{L})$ of pure lattice translations is defined by

$$T(\mathbb{L}) := \left\{ \{E|\mathbf{R}\} : \mathbf{R} \in \mathbb{L} \right\}. \quad (2.16)$$

The group theory presented here is particularly well-behaved for symmorphic plane groups G because the full plane group is the semi-direct product of the point group G_0 and the translational group $T(\mathbb{L})$. In particular, this means that *any* arbitrary element $\{R|\mathbf{R}\} \in G$ of a symmorphic plane group G can be written as the product of a pure translation and a pure rotation, i. e.

$$\{R|\mathbf{R}\} = \{E|\mathbf{R}\} \cdot \{R|\mathbf{0}\}, \quad \{E|\mathbf{R}\} \in T(\mathbb{L}), \{R|\mathbf{0}\} \in G_0. \quad (2.17)$$

We only deal with symmorphic plane groups because we are going to apply the results of this chapter only to the two symmorphic model systems introduced in Sec. 1.2.7.⁹

For the numerical construction of Wannier functions we have to discretize an integral over the Brillouin zone by a sum over finitely many \mathbf{k} -points. This implicitly establishes the connection to the finite model of crystals,¹⁰ which we are going to introduce now.

We consider a finite parallelogram supercell of the crystal extending N_i unit cells in each lattice direction \mathbf{a}_i . This is called the main region and comprises the finite set of lattice sites

$$\mathbb{L}_{\text{main}} := \left\{ \sum_{i=1}^2 z_i \mathbf{a}_i : z_i = 0, 1, \dots, N_i - 1 \right\}. \quad (2.18)$$

In this picture, the infinite crystal is approximated by an infinite periodic tiling of these main regions that are *physically identical*. Shifting this crystal by N_i primitive lattice translations \mathbf{a}_i not only keeps the crystal invariant, but also reproduces it identically which is represented by the finite set of lattice translations $T(\mathbb{L}_{\text{main}})$ generated by the generators $\{E|\mathbf{a}_i\}$ with the property

$$\left(\{E|\mathbf{a}_i\} \right)^{N_i} = \{E|\mathbf{0}\}. \quad (2.19)$$

Thus, the finite $T(\mathbb{L}_{\text{main}})$ is a cyclical group in contrast to the infinite translation group $T(\mathbb{L})$.

2.4 Representations

A representation D of a group G is the special case of a matrix-valued group homomorphism, with non-singular square matrices.¹¹ These matrices $D(g) \in \mathbb{C}^{\mu \times \mu} \quad \forall g \in G$ are the images of the μ -dimensional representation $D : G \rightarrow \mathbb{C}^{\mu \times \mu}$ and form themselves a group with the usual matrix-matrix multiplication. We follow the suggestion of [83] and write *rep* as a shorthand notation for representation. If $\mu = 1$, we also say the rep is non-degenerate. In the case $\mu \geq 2$, we say the rep is degenerate.

⁹And because the theory presented here is much easier then.

¹⁰in solid state physics, this model is usually invoked when the Bloch modes $\psi_{n\mathbf{k}}(\mathbf{r})$ are subject to Born-von Kármán boundary conditions.

¹¹The matrices have to be square and non-singular such that the inverses of each element exist.

2.4.1 Characters

In order to characterize the properties of a rep D independently from the particular matrix elements $D_{ij}(g)$, one can define the character $\chi \in \mathbb{C}$ of a rep matrix $D(g)$ as the trace of this matrix:

$$\chi(g) := \text{Tr } D(g) = \sum_{ii} D_{ii}(g). \quad (2.20)$$

The trace is invariant under matrix similarity transforms. This implies that the character $\chi(g)$ is the same for all g in the same conjugacy class. It is thus a class function as defined above. The character $\chi(e)$ of the identity element is always equal to the dimension μ of the rep, since $D(e)$ is always the identity matrix of dimension μ . This follows from D being a group homomorphism, where the identity element of the group $\mathbb{C}^{\mu \times \mu}$ is the $\mu \times \mu$ unit matrix. The set of characters $\chi(g)$ characterizes the homomorphism D without the need to specify the particular matrix elements $D_{ij}(g)$.

2.4.2 Bases of Representations

We restrict ourselves to rank-0-tensor-valued functions here. A basis of a rep D of dimension μ is a set of μ linearly independent functions $f_i(\mathbf{r})$ for $i = 1, \dots, \mu$, that are transformed via (2.10) into linear combinations of each other. The coefficients of this linear combination are the rep matrix elements $D_{ij}(g)$ for $g = \{R|\mathbf{t}\}$ (note the ordering of indices):

$$\hat{D}(g)f_j(\mathbf{r}) = \sum_i f_i(\mathbf{r})D_{ij}(g). \quad (2.21)$$

Thus, the operator $\hat{D}(g)$ on the function space is represented by the complex numbers D_{ij} . The functions are said to transform like this rep for short.¹² This simply means that the new rotated/reflected functions $f_i(g^{-1}\mathbf{r})$ can be expressed as linear combinations of the former functions $f_j(\mathbf{r})$ (see Fig. 2.2). Several distinct orthogonal sets of functions can transform like the same rep D which is covered in the next section. The definition (2.21) may seem strange due to the unusual index ordering, however this is sensible since it ensures that the mapping from operator \hat{D} defined via (2.10) onto reps D is a group homomorphism with respect to the standard matrix-matrix multiplication¹³.

If the basis functions f_i are orthonormal with respect to each other, the representation matrices $D(g)$ in (2.21) can be obtained by computing the matrix elements of the transformation operators $\hat{D}(g)$ via

$$D_{ij}(g) = \langle f_i | \hat{D}(g) | f_j \rangle. \quad (2.22)$$

2.4.3 Reducible Representations

A rep D is said to be unitary if all the matrices $D(g)$ are unitary. Given a rep D for a group G , the similarity transformed matrices $D'(g) := A \cdot D(g) \cdot A^{-1}$ for any non-singular square matrix A form a so called equivalent rep of G (see Fig. 2.3). Any rep of a finite group is equivalent to a unitary one [80], and by Sec. 2.4.1 all equivalent reps have the same set of characters $\chi(g)$. The characters thus summarize the essential properties of equivalent reps which can all be studied for the simple case of unitary reps. Thus, we are only concerned with unitary reps and from now on, all reps are assumed to be unitary ones.

¹²Combining these functions to a row vector, this would read $(f_1, \dots, f_d) \cdot D(g)$ with the usual matrix-matrix multiplication.

¹³This statement is proven in App. F.1

$$\begin{aligned}
\hat{D}(C_4) \left(\underbrace{\begin{pmatrix} \text{[Pattern 1]} \\ \text{[Pattern 2]} \\ \text{[Pattern 3]} \\ \text{[Pattern 4]} \end{pmatrix}}_{f_1} \quad \underbrace{\begin{pmatrix} \text{[Pattern 5]} \\ \text{[Pattern 6]} \\ \text{[Pattern 7]} \\ \text{[Pattern 8]} \end{pmatrix}}_{f_2} \right) &= \left(\underbrace{\begin{pmatrix} \text{[Pattern 5]} \\ \text{[Pattern 6]} \\ \text{[Pattern 7]} \\ \text{[Pattern 8]} \end{pmatrix}}_{f_2} \quad \underbrace{\begin{pmatrix} \text{[Pattern 1]} \\ \text{[Pattern 2]} \\ \text{[Pattern 3]} \\ \text{[Pattern 4]} \end{pmatrix}}_{-f_1} \right) \\
&= \left(\underbrace{\begin{pmatrix} \text{[Pattern 1]} \\ \text{[Pattern 2]} \\ \text{[Pattern 3]} \\ \text{[Pattern 4]} \end{pmatrix}}_{f_1} \quad \underbrace{\begin{pmatrix} \text{[Pattern 5]} \\ \text{[Pattern 6]} \\ \text{[Pattern 7]} \\ \text{[Pattern 8]} \end{pmatrix}}_{f_2} \right) \cdot \underbrace{\begin{pmatrix} 0 & -1 \\ 1 & 0 \end{pmatrix}}_{=D(C_4)}.
\end{aligned}$$

Figure 2.2: Example for basis functions f_1 and f_2 of a degenerate representation of dimension $\mu = 2$ according to (2.21).

$$\left(\begin{pmatrix} \text{[Pattern 1]} \\ \text{[Pattern 2]} \\ \text{[Pattern 3]} \\ \text{[Pattern 4]} \end{pmatrix} \quad \begin{pmatrix} \text{[Pattern 5]} \\ \text{[Pattern 6]} \\ \text{[Pattern 7]} \\ \text{[Pattern 8]} \end{pmatrix} \right) = \left(\begin{pmatrix} \text{[Pattern 5]} \\ \text{[Pattern 6]} \\ \text{[Pattern 7]} \\ \text{[Pattern 8]} \end{pmatrix} \quad \begin{pmatrix} \text{[Pattern 1]} \\ \text{[Pattern 2]} \\ \text{[Pattern 3]} \\ \text{[Pattern 4]} \end{pmatrix} \right) \cdot \underbrace{\begin{pmatrix} \frac{\sqrt{3}}{2} & -\frac{1}{2} \\ \frac{1}{2} & \frac{\sqrt{3}}{2} \end{pmatrix}}_{=U^\dagger}$$

Figure 2.3: Example for two sets of basis functions f_1 and f_2 of a degenerate representation of dimension $\mu = 2$ that are related by a unitary transform U . If the right hand side functions are bases for a rep D , then the left hand side functions are bases for the equivalent rep with matrices $D'(g) = UD(g)U^\dagger$. Note that the right hand side functions look more symmetric because the rep matrices $D(g)$ are either diagonal or have a simple off-diagonal structure for the (arbitrarily chosen) generators C_4 and σ_x .

If the linear space¹⁴ \mathbb{C}^μ on which the matrices $D(g)$ act contains any invariant subspaces (i. e., invariant for all g), the rep D is said to be reducible. This means D is equivalent to a rep D' , whose matrices $D'(g)$ all share the same block-diagonal structure, where the submatrix of each block operates within the invariant subspaces. That means, there exists one single unitary matrix U such that all the matrices $D(g)$ can be transformed via

$$D'(g) = UD(g)U^\dagger = \begin{pmatrix} D^{(1)}(g) & 0 & 0 \\ 0 & D^{(2)}(g) & 0 \\ 0 & 0 & \ddots \end{pmatrix}. \quad (2.23)$$

The matrices $D^{(\alpha)}(g)$ form reps of dimension $\mu^{(\alpha)} < \mu$. The space \mathbb{C}^μ is then the direct sum of the invariant subspaces and the reduced rep D' is the direct sum of the reps $D^{(\alpha)}$:

$$D' = \bigoplus_{\alpha} D^{(\alpha)}. \quad (2.24)$$

¹⁴In German, this is called a *Vektorraum*.

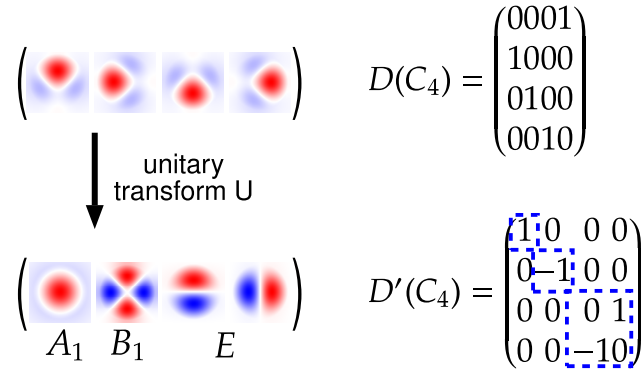


Figure 2.4: Example for a reduction procedure by (2.23). The reduced rep matrices D' all have the same block diagonal structure for all point transforms of C_{4v} . Here, the rep D is reduced to the irreps A_1, B_1, E of C_{4v} , i. e., D is equivalent to $D' = A_1 + B_1 + E$.

Eq. (2.23) can be considered to be the definition of the notation (2.24). However, regular plus signs + and a multiplicative notation are also common (see Fig. 2.4). The examples later on will clarify this notation. If no invariant subspaces and hence no such matrix U exist, the rep D is called an irreducible representation. We write irrep for short. Naturally, the following question arises:

What matrices (up to equivalence) form the set of all possible irreducible representations of a given group G and which dimensions μ do they have?

Burnside's Theorem states that there are exactly as many non-equivalent irreps of a group as it has conjugacy classes. These irreps can be characterized by their character sets

$$\{(g, \chi(g)) : g \text{ is an arbitrary representative of each conjugacy class}\}. \quad (2.25)$$

A list of characters for the conjugacy classes and each possible irrep is called a character table and is an important tool in the analysis of reps and the study of symmetries in crystals (see Tabs. F.3 and F.8).

There is a simple test to decide whether a rep D is reducible or not. One can compute

$$\frac{1}{n_G} \sum_{g \in G} |\chi(g)|^2 = \begin{cases} 1 & : D \text{ is irreducible,} \\ \neq 1 & : D \text{ is reducible.} \end{cases} \quad (2.26)$$

If the dimension μ of a rep D is larger than the largest possible dimension of the irreps of G , it is certainly reducible. In other cases it might be either reducible or be a degenerate irrep of G . In order to decide which irreps $D^{(\alpha)}$ are contained in the reduction (2.23) of a rep D , one can compute the multiplicity¹⁵ $\lambda^{(\alpha)}$ by

$$\lambda^{(\alpha)} := \frac{1}{n_G} \sum_{g \in G} \chi^*(g) \chi^{(\alpha)}(g), \quad (2.27)$$

where * means complex conjugation, $\chi(g)$ is the character of $D(g)$ and $\chi^{(\alpha)}(g)$ the character of the irrep matrix $D^{(\alpha)}(g)$. The reduced form D' of D in (2.27) contains then $\lambda^{(\alpha)}$ submatrices for the irreducible representation $D^{(\alpha)}$.

¹⁵Also called frequencies, defining how frequent a rep occurs.

2.4.4 Projection Operators

An arbitrary function f can be decomposed into sets of functions transforming like the different irreps $D^{(\alpha)}$ of a plane group G . Thus, one can disassemble the function f according to different symmetries. The projection operator

$$\hat{P}^{(\alpha)} := \frac{\mu^{(\alpha)}}{n_G} \sum_{g \in G} \chi^{(\alpha)*}(g) \hat{D}(g) \quad (2.28)$$

projects out that part of a function f that transforms like the rep $D^{(\alpha)}$ of G . Here, n_G is the order of the group G , $\mu^{(\alpha)}$ is the dimension of the irrep, $\chi^{(\alpha)}(g)$ its characters and $\hat{D}(g)$ the transformation operator (2.10) and $*$ denotes the complex conjugate. For a given function f , one can obtain one basis function $\hat{P}^{(\alpha)}f$ for each rep $D^{(\alpha)}$ contained in f . A full orthonormalized basis set can then be obtained by applying the transformations g and the Gram-Schmidt orthogonalization procedure (see Fig. 2.5). The rep matrices $D^{(\alpha)}$, in turn, can then be obtained by (2.22). Thus, a single function f can generate several irreps (i. e., the actual matrix elements $D_{ij}^{(\alpha)}$) of a group G from their set of characters.

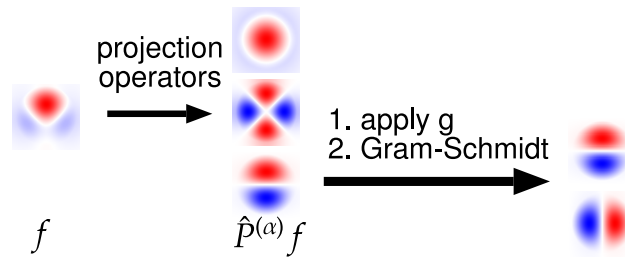


Figure 2.5: Generation of basis functions of irreps $D^{(\alpha)}$ by applying the projection operators $\hat{P}^{(\alpha)}$ of (2.28). In this example, the irreps of group C_{4v} (cf. Tab. F.3) are generated. Note that the projection operator only creates one basis function for each rep.

2.4.5 The Group of an Operator

If an operator \hat{H} commutes with the transformation operators $\hat{D}(g)$ of some group G , i. e. ($[\cdot, \cdot]$ being the commutator)

$$[\hat{H}, \hat{D}(g)] = 0 \quad \forall g \in G, \quad (2.29)$$

then the eigenstates of \hat{H} form bases of the irreps of G [82]. The full set of all those operations that commute with \hat{H} is called the group of \hat{H} . The consequences of this fundamental theorem are ubiquitous in physics (cf. the text-books mentioned in the chapter abstract): conservation of linear and angular momentum, selection rules in radiative atomic transitions, vibrational spectra of molecules, compatibility relations in band structure theory, spin-orbit coupling, with applications in particle physics and possible field theories, just to name a few.

We need this theorem to classify the Bloch modes and defect modes in a PC by their symmetry properties, i. e., we label the modes (additionally to their band index n) by those irreps $D^{(\alpha)}$ which they are basis functions of.

2.4.6 Subduced Representations

There are two basic mechanisms, how irreps of one group can create new (generally reducible) reps in another group:

by subduction: A group G passes its irreps down to one of its smaller subgroups $H \subset G$,

by induction: A subgroup $H \subset G$ passes its irreps up to the larger supergroup G .

The reps obtained by these procedures are in general reducible in the new group. For generating localized and symmetric Wannier functions, the relation between the characters and the explicit reduction and induction procedures involved are of relevance.

The subduction procedure is the simpler one and shall be discussed first. Given a rep D of G with matrices $D(g)$ for $g \in G$, one can simply define the subduced rep D' on H by reusing the matrices for the elements $g \in H$:

$$D'(g) := D(g) \quad \forall g \in H. \quad (2.30)$$

This is possible because H is a subgroup of G and all symmetry operations of H are also contained in G . The characters are unchanged (the traces of the matrices are still the same), there are just less characters than before because H has less conjugacy classes. A common notation for subduced reps is $D' = D \downarrow H$. When the particular supergroup G used shall be stressed, we also write¹⁶ $D' = D(G) \downarrow H$. If D was irreducible in G , the subduced D' may be in general reducible, e. g. if a degenerate irrep is subduced to a subgroup containing only non-degenerate irreps.

The reducibility of the subduced reps can be easily checked with (2.26) with the help of the characters of the irreps of both groups, i. e., the actual rep matrices D are not needed at all.

The reduction of a subduced representation results in a unitary transform which brings the former rep matrices $D(g)$ for $g \in H$ into block-diagonal form. The transformed basis functions f_i for that equivalent rep are then also basis functions for the irreps occurring in the reduction (see Fig. 2.6).

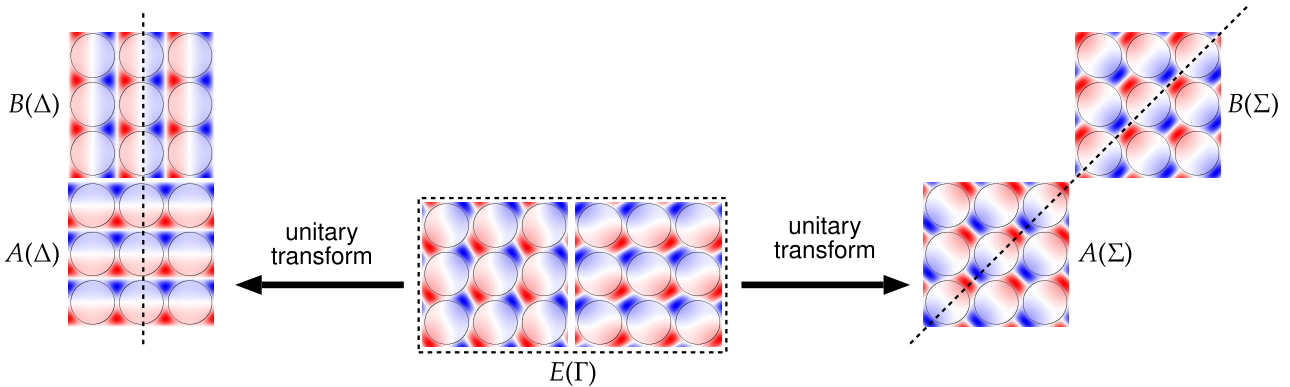


Figure 2.6: Basis functions of a degenerate rep E of the point group C_{4v} that can be unitarily transformed to basis functions of irreps A and B of subgroups C_{1h} of C_{4v} . Thus, the subduced two-dimensional rep $E(C_{4v}) \downarrow C_{1h}$ is reducible as $A(C_{1h}) + B(C_{1h})$. In this example, degenerate Bloch modes at the Γ -point are reduced with respect to the little co-groups of the Σ and Δ lines in a square lattice. Note that the particular realization of C_{1h} as $G_{0\Delta}$ or $G_{0\Sigma}$ determines the actual profiles of the new basis functions. See also App. F for a list of high symmetry points and little co-groups.

As was discussed in the previous section, the symmetries of the basis functions under transformations g determine the rep unambiguously. Thus, a set of basis functions f_i for irreps of G defines the subduced reps in H equally well.

¹⁶This is admittedly a sloppy notation, since $D(G)$ is technically the whole set of rep matrices $D(g)$.

2.4.7 Induced Representations

We now take the basis functions for an irrep D of a subgroup H and construct a larger set of basis functions transforming according to all $g \in G$ and forming a new representation D' for the supergroup $G \supset H$. The key to this construction is the fact that for the μ basis functions f_i of the μ -dimensional rep D for H the transformed $\hat{D}(g)f_i$ transform like (and define) some D' of G with dimension $\mu' > \mu$. This is the induced rep $D' = D \uparrow G$ (see Fig. 2.7). However, the new functions form in general *not* an orthogonal set and are therefore not a basis of the induced rep. The proper construction of the induced reps makes use of characters and cosets only. This involves some clumsy definitions which are not repeated here and the interested reader is referred to the literature cited in the chapter abstract.

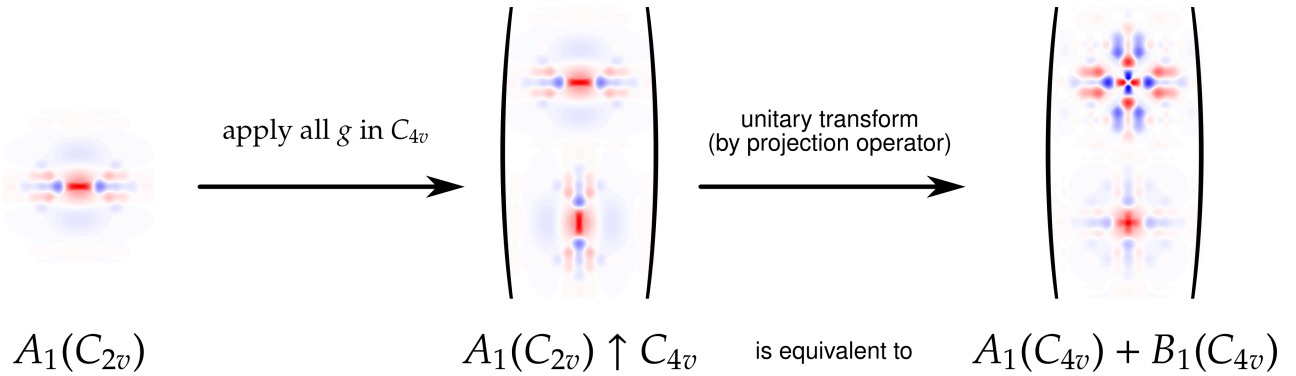


Figure 2.7: Example for a basis function of the non-degenerate rep $A_1(C_{2v})$ that is used to construct the basis functions of the degenerate induced rep $A_1(C_{2v}) \uparrow C_{4v}$. This induced rep is reducible in C_{2v} , thus there is a unitary transform generating basis functions for the irreps $A_1(C_{4v})$ and $B_1(C_{4v})$.

Fortunately, since we deal with Wannier functions in the end, all new functions $\hat{D}(g)f_i$ that we encounter in the following *indeed are* orthonormal (and are therefore bases of the induced rep) which is why we are allowed to introduce this simpler definition of the induced rep D' . By (2.22) the rep matrices $D'(g) \forall g \in G$ can be obtained by using an arbitrary orthonormal subset of the new functions $\hat{D}(g)f_i$, since some functions appear more than once with phase factors (± 1 in our cases).

2.4.8 The Frobenius Reciprocity Theorem

For the groups $H \subset G$, the following relation holds for the irreps $D^{(\alpha)}(G)$ and $D^{(\beta)}(H)$: The number of times that $D^{(\alpha)}(G)$ is contained in $D^{(\beta)}(H) \uparrow G$ is equal to the number of times that $D^{(\beta)}(H)$ is contained in $D^{(\alpha)}(G) \downarrow H$.

This theorem relates the complicated induction procedure with the simpler subduction procedure. It is implicitly used for the construction of the Tabs. 2.1 and 2.2.

2.5 Representations of Plane groups

We review the possible reps of plane groups here. This part is simplified for symmorphic plane groups. For non-symmorphic plane groups, some definitions and theorems become more complicated and should therefore be looked up in the literature cited in the chapter abstract for maximal rigor.

General remark on the notation used: We introduce some subgroups of the plane group G in the following that are distinguished by subscript vectors: $G_{\mathbf{k}}, G_{\mathbf{q}} \subset G$. These groups are understood to consist of elements $\{R|\mathbf{R}\}$ with non-trivial lattice vectors \mathbf{R} . Secondly we deal with subgroups $G_{0\mathbf{k}}, G_{0\mathbf{q}} \subset G_0$ of the point group (2.15) that always comprise only elements $\{R|\mathbf{0}\}$ which is denoted by the subscript number 0.

2.5.1 Translation Groups

In the following, we need to define shifts by lattice vectors $\mathbf{R} \in \mathbb{L}_{\text{main}}$ more precisely by their lattice coordinates n_i as

$$\{E|\mathbf{a}_{\mathbf{n}}\} := \{E|n_1\mathbf{a}_1 + n_2\mathbf{a}_2\}, \quad n_i \in \mathbb{Z}. \quad (2.31)$$

The subgroup $T(\mathbb{L}_{\text{main}})$ of pure translations in the cyclic model of a photonic crystal is an Abelian group and therefore has N_1N_2 irreps distinguished by integers p_1 and p_2 with possible values $p_i = 0, \dots, N_i - 1$. The characters of these irreps are

$$\chi^{(p_1, p_2)}(\{E|n_1\mathbf{a}_1 + n_2\mathbf{a}_2\}) = \exp\left(-2\pi i(p_1n_1/N_1 + p_2n_2/N_2)\right), \quad n_i \in \mathbb{Z}. \quad (2.32)$$

For the finite lattice \mathbb{L}_{main} one defines a set of allowed wave vectors

$$\mathbf{k}_{\mathbf{p}} = \frac{p_1}{N_1}\mathbf{b}_1 + \frac{p_2}{N_2}\mathbf{b}_2, \quad (2.33)$$

which can be used to label the various irreps of $T(\mathbb{L}_{\text{main}})$ and the characters can then be expressed as

$$\chi^{(\mathbf{k})}(\{E|\mathbf{a}_{\mathbf{n}}\}) = \exp(-i\mathbf{k} \cdot \mathbf{a}_{\mathbf{n}}), \quad (2.34)$$

for any allowed wave vector \mathbf{k} of which there are infinitely many up to this point. Any reciprocal lattice vector $\mathbf{K} \in \mathbb{L}_{\text{PC}}^*$ can be added to \mathbf{k} without affecting the characters $\chi^{(\mathbf{k})} = \chi^{(\mathbf{k}+\mathbf{K})}$, hence $\mathbf{k} + \mathbf{K}$ labels *the very same rep* and $\mathbf{k} + \mathbf{K}$ is called an equivalent wave vector. Therefore, the allowed wave vectors \mathbf{k} from the parallelepiped shaped unit cell (2.33) of the reciprocal lattice label all possible different irreps of the translation group. In physics, it is customary to choose the wave vectors from the more symmetric Brillouin zone (which is constructed like the WSC, only in the reciprocal lattice) to label the translation group irreps (cf. Sec. 1.2.1). However, in the numerical construction of WFs we resort to parallelogram shaped domains again (cf. Fig. B.7) which are *not identical* to (2.33).

The basis functions transforming like the irrep \mathbf{k} of the translation group $T(\mathbb{L}_{\text{main}})$ are called Bloch functions.¹⁷ By Sec. 2.4.5, the eigenstates of the wave equation for a perfect PC can be labeled by the particular wave vector as $|n\mathbf{k}\rangle$ which characterizes their transformation behavior under translations. The band index n distinguishes different basis functions transforming like the same irrep \mathbf{k} . Moreover, when also applying an orthogonal transformation R , we get a new Bloch function transforming according to the irrep $R\mathbf{k}$. The full transformation law is found in [37, 83]. Thus, the Bloch-Floquet theorem of Sec. 1.2.2 is the direct consequence of the wave equation being invariant under translations $T(\mathbb{L})$ and the transformation behavior (2.21) with characters (and one-dimensional rep matrices) $\exp(-i\mathbf{k}\mathbf{R})$ of its group irreps \mathbf{k} .

¹⁷Note that we reserved the word mode for eigenstates of the wave equation. Therefore, the eigenmodes are Bloch functions, the so called Bloch modes.

2.5.2 Point Groups

In 2D, the point group (2.15) comprises rotations and reflections only.¹⁸ It is in general not Abelian, hence there are usually only a few different irreps. The irreps of the point groups for square and triangular lattices are labeled by Latin letters A and B for non-degenerate irreps and E for degenerate irreps by convention (cf. Tab. F.3 and Tab. F.8). The characters for these cases are always real and in the non-degenerate case, they can be understood to be the eigenvalues of the operators $\hat{D}(g)$ for the particular eigenmodes of the wave equation.¹⁹

In symmorphic plane groups, the reciprocal lattice is invariant under the pure orthogonal transformations $\{R|\mathbf{0}\} \in G_0$. It is used to construct the whole BZ from the IBZ by²⁰ (cf. Fig. 1.8)

$$\text{BZ} = \bigcup_{g \in G_0} g \cdot \text{IBZ}, \quad (2.35)$$

where the action of $g = \{R|\mathbf{0}\}$ on a vector \mathbf{k} from reciprocal space is meant to be

$$g\mathbf{k} = \{R|\mathbf{0}\}\mathbf{k} = R \cdot \mathbf{k}. \quad (2.36)$$

Given a wave vector \mathbf{k} from the BZ one can construct the subgroup $G_{0\mathbf{k}} \subset G_0$ which transforms \mathbf{k} into itself or an equivalent vector $\mathbf{k} + \mathbf{G}$. This is the so called little co-group of \mathbf{k} (whereas little point group of \mathbf{k} would be a more sensible nomenclature).

In the BZ the points of symmetry and highest symmetry are of special interest. In the infinite model of a crystal ($N_i \rightarrow \infty$), the BZ is a dense set with boundary. A high symmetry point²¹ \mathbf{k}_{HS} has higher symmetry than any other \mathbf{k} in a small domain around \mathbf{k}_{HS} . That means, $G_{0\mathbf{k}} \subset G_{0\mathbf{k}_{\text{HS}}}$ is always a proper subgroup with less elements $n_{G_{0\mathbf{k}}}$ than the order of $G_{0\mathbf{k}_{\text{HS}}}$. Such points typically lie on the boundary and in the center of the BZ, (like Γ, X, M in the square lattice and Γ, M, K in the triangular lattice). Lines of symmetry are defined by points on lines with the same group $G_{0\mathbf{k}}$. Examples in the square lattice are $\overline{\Gamma X}$, \overline{XM} and \overline{MT} . However if $G_{0\mathbf{k}}$ consists of the identity element only, then \mathbf{k} is called a general point in the BZ.

Given a Bloch mode $|n\mathbf{k}\rangle$ of wave vector \mathbf{k} which is invariant under some point group $G_{0\mathbf{k}}$, the Bloch mode can be classified by the irreps of that point group, additionally to the irrep \mathbf{k} of the translational group. Examples are shown in Figs. F.6 and F.7. This is necessary to define the full irreps of the full plane group.

Looking at the high symmetry points of the Brillouin zones of Figs. F.4 and F.13, we see that some high symmetry points also lie on high symmetry lines, e. g. the Γ -point in the square lattice is also a Δ -point as well as a Σ -point. That means, Bloch modes at Γ with $\mathbf{k} = (0, 0)$ can therefore be unitarily transformed to be basis functions for the little co-groups of these high-symmetry lines with lower symmetry (not at the same time, of course) and then continuously connected with Bloch modes of these neighboring \mathbf{k} -vectors. The irreps that are possible to connect to are given by the subduction of the irreps for the higher symmetry \mathbf{k} -point to the irreps to the \mathbf{k} -point of lower symmetry. The multiplicities of irreps in the subduced reps are known as compatibility relations. Examples can be found in Figs. 2.6, F.6, and F.7.

¹⁸A full inversion in 2D is just a rotation by 180° .

¹⁹Compare, e. g., Tab. F.3 with the basis functions of Figs. F.8 and F.9 for the square lattice.

²⁰This statement does not hold for the general case of non-symmorphic plane groups.

²¹In the notation of Krüger [37, 38], they are labeled \mathbf{k}_Σ (not to confuse with the Σ -point of the BZ). In [83], these are just called points of symmetry. The lines and planes of symmetry of [83] are the ordinary points of symmetry in Krüger [37, 38].

2.5.3 Full Plane Groups

The irreps of a symmorphic plane group G are constructed in a straightforward fashion from the irreps of its underlying translation group $T(\mathbb{L})$ and point group G_0 . This simplicity is a direct consequence of the multiplicative property (2.17).

The subgroup $G_{\mathbf{k}} \subset G$ is called the little group of \mathbf{k} , and contains all possible plane group elements that involve the point transforms of the little co-group $G_{0\mathbf{k}}$.²²

$$G_{\mathbf{k}} := \left\{ \{R|\mathbf{R}\} : \{R|\mathbf{0}\} \in G_{0\mathbf{k}}, \{E|\mathbf{R}\} \in T(\mathbb{L}_{\text{main}}) \right\}. \quad (2.37)$$

The star of \mathbf{k} is the set $*\mathbf{k}$ of $t = n_G/n_{G_{\mathbf{k}}}$ non-equivalent wave vectors \mathbf{k} that can be generated by means of the little-co group, i. e.

$$*\mathbf{k} := \{g\mathbf{k} : g \in G_{0\mathbf{k}}\}. \quad (2.38)$$

Examples are shown in Figs. F.4 and F.13.

We summarize now the construction of possible irreps of a little group $G_{\mathbf{k}}$ for symmorphic plane groups. The full construction for non-symmorphic plane groups is described in [83]. Given an irrep²³ $D^{(\alpha)}$ of the point group $G_{0\mathbf{k}}$, with matrices $D^{(\alpha)}(R)$ for the discrete orthogonal transformations R , one can build the full irreps $D^{(\mathbf{k}\alpha)}$ of the plane group $G_{\mathbf{k}}$ via²⁴

$$D^{(\mathbf{k}\alpha)}(\{R|\mathbf{R}\}) := \exp(-i\mathbf{k} \cdot \mathbf{R})D^{(\alpha)}(R). \quad (2.39)$$

The eigenmodes $|n\mathbf{k}\rangle$ of the wave equation for a fixed \mathbf{k} form sets of bases for these irreps $D^{(\mathbf{k}\alpha)}$. Their translational behavior is determined by \mathbf{k} and their rotational behavior by the particular α . If there are $\mu^{(\alpha)}$ Bloch modes and t inequivalent elements in the star $*\mathbf{k}$, one can use the $t\mu^{(\alpha)}$ basis functions to induce the full irrep $D^{(*\mathbf{k}\alpha)}$ for the full plane group G .²⁵

$$D^{(*\mathbf{k}\alpha)} = D^{(\mathbf{k}\alpha)}(G_{\mathbf{k}}) \uparrow G. \quad (2.40)$$

By the induction procedure discussed above, this simply means applying all possible rotations to the given Bloch basis functions of $D^{(\mathbf{k}\alpha)}$, see Fig. 2.8.

Any element $\{R|\mathbf{R}\} = g \in G$ transforms a basis function of $D^{(*\mathbf{k}\alpha)}$ of wave vector \mathbf{k} either

1. into one with non-equivalent wave vector $R\mathbf{k}$, either with an additional phase factor or being the unitary transform of other basis functions with wave vector $R\mathbf{k}$ (if $\mu^{(\alpha)} > 1$), or
2. into one with equivalent wave vector $\mathbf{k} + \mathbf{K}$ (that is essentially \mathbf{k}), either with an additional phase factor or being the unitary transform of other basis functions of the rep $D^{(\mathbf{k}\alpha)}$ (if $\mu^{(\alpha)} > 1$).

If $D^{(\alpha)}$ is one-dimensional, then there is always only a phase factor involved in the transformation rather than a whole matrix.

²²For non-symmorphic plane groups, one has to consider also the fractional translations.

²³For our cases later on, these are mostly one-dimensional reps. Some two-dimensional also occur.

²⁴According to [83] and [37], this is always true for symmorphic but not for non-symmorphic groups.

²⁵This simple statement is only valid in symmorphic plane groups.

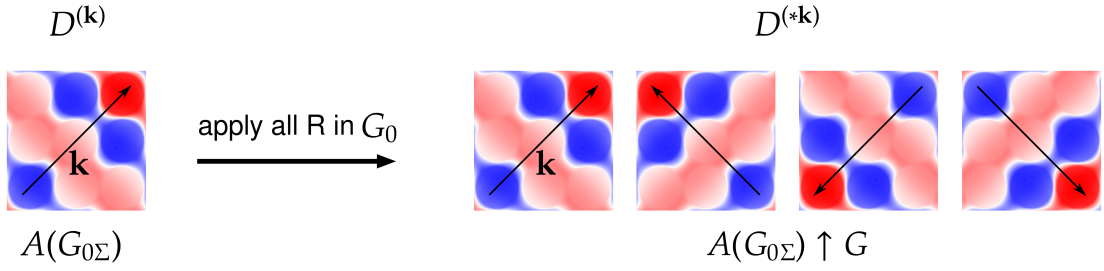


Figure 2.8: Construction of an irrep $D^{(*k\alpha)}$ of a full plane group G by induction of an irrep $D^{(k\alpha)}$ of a little co-group G_{0k} . In this example, basis functions for the Σ point in the square lattice are used.

2.5.4 Site Symmetry Groups

In this section, a review of the site symmetry analysis procedure is given. It was introduced in [36] and determines the “natural” symmetries the exponentially localized generalized Wannier functions may have according to the symmetries of the Bloch modes from which they were constructed. We follow the description of [83].

Site symmetry groups $G_{\mathbf{q}}$ and their point groups $G_{0\mathbf{q}}$ for direct space are similar (but not identical) to the notions of $G_{\mathbf{k}}$ and $G_{0\mathbf{k}}$ for reciprocal space. Given an arbitrary position \mathbf{q} in the main region of the cyclic crystal, all possible points $g\mathbf{q}$ for $g \in G$ form the crystallographic orbit²⁶ of \mathbf{q} . In analogy to (2.38) we denote the crystallographic orbit by the set

$$G\mathbf{q} := \{g\mathbf{q} : g \in G\}. \quad (2.41)$$

There are at most n_G different points in the crystallographic orbit, one for each possible g , but there may be less if \mathbf{q} is invariant under some operations g . The set of all $g \in G$ leaving the point \mathbf{q} invariant in space is denoted by $G_{\mathbf{q}}$ and called the site symmetry group:

$$g \in G_{\mathbf{q}} \Leftrightarrow g\mathbf{q} = \mathbf{q}. \quad (2.42)$$

In that case, the crystallographic orbit contains only $n_G/n_{G_{\mathbf{q}}}$ different points in total. The site symmetry group $G_{\mathbf{q}}$ is isomorphic to the point group $G_{0\mathbf{q}}$ which consists of the pure generalized rotations of $G_{\mathbf{q}}$ by removing the translational parts:

$$G_{0\mathbf{q}} := \left\{ \{R|\mathbf{0}\} : \exists \{R|\mathbf{R}\} \in G_{\mathbf{q}} \right\}. \quad (2.43)$$

Due to the isomorphy $G_{\mathbf{q}} \cong G_{0\mathbf{q}}$, we can use the irrep labels of the point groups of Tabs. F.3 and F.8 to classify the basis function of irreps of $G_{\mathbf{q}}$ (see Fig. 2.9).

If $g \in G$ transforms \mathbf{q} to a point \mathbf{q}' in the orbit, then their site symmetry groups are related by

$$G_{\mathbf{q}'} = gG_{\mathbf{q}}g^{-1}. \quad (2.44)$$

Then $G_{\mathbf{q}'}$ is also isomorphic to $G_{0\mathbf{q}}$ and great care has to be taken not to confuse the irrep labels for actual computations. This is one of the reasons for the elaborate App. F.

²⁶In [36] the generating point \mathbf{q} was denoted by M_0 and the crystallographic orbit was called general lattice \mathcal{L} .

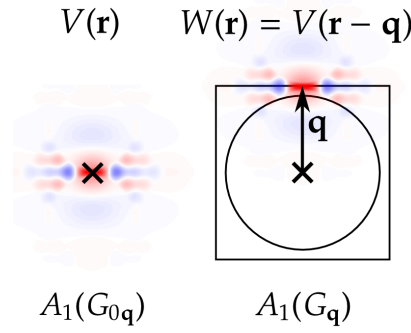


Figure 2.9: Basis functions for an irrep of a point group and a site symmetry group. The cross denotes the center of rotations for orthogonal transforms. In this example, the site symmetry group $G_{0\mathbf{q}}$ is chosen for the Wyckoff position c . This demonstrates, how the irreps of $G_{0\mathbf{q}}$ are connected with the ones of $G_{\mathbf{q}}$.

On the other hand, all those points \mathbf{q} and \mathbf{q}' belong to the same Wyckoff position if their site symmetry group (that leave these points invariant, respectively) are conjugate to each other, i. e., they obey (2.44). The Wyckoff positions are labeled by small roman letters. They are shown in Figs. F.3 and F.12. The term 'position' is a bit misleading here, since some positions of the coordinates of these positions contain one or more free parameters, defining in fact lines and planes of points with conjugate site symmetry groups.

The irreps of site symmetry groups can be used to classify Wannier functions and localized defect modes. If a defect (like an infiltrated hole in Fig. 1.12) breaks the translational symmetry of the crystal, then the crystal with defect is invariant under the smaller site symmetry group of the defect (i. e., operations g of the full crystal plane group G leaving the defect invariant). Since the site symmetry group is isomorphous to a point group, defect states are classified by the irrep labels of that point group (see Fig. 2.9).

2.5.5 Generalized Wannier Functions

In the previous section we have seen how the irreps $D^{(\mathbf{k}\alpha)}$ of little groups $G_{\mathbf{k}}$ induced the irreps $D^{(*\mathbf{k}\alpha)}$ of the full space group G :

$$D^{(*\mathbf{k}\alpha)} = D^{(\mathbf{k}\alpha)}(G_{\mathbf{k}}) \uparrow G. \quad (2.45)$$

Now we will investigate which reps are induced by irreps $D^{(\mathbf{q}\beta)} = D^{(\beta)}(G_{\mathbf{q}})$ of the site symmetry groups $G_{\mathbf{q}}$, i. e., we consider $D^{(\mathbf{q}\beta)} \uparrow G$ and its reductions into irreps $D^{(*\mathbf{k}\alpha)}$ of G . This is finally going to lead to the lattice Fourier transform of Bloch modes defining the Wannier functions.

We consider a position \mathbf{q} and a basis function $W(\mathbf{r}) := V(\mathbf{r} - \mathbf{q})$ for an irrep $D^{(\mathbf{q}\beta)}$ of the site symmetry group $G_{\mathbf{q}}$. $V(\mathbf{r})$ shall be a basis function for the corresponding irrep of the point group $G_{0\mathbf{q}}$, localized at the origin. Hence, $W(\mathbf{r})$ is localized at \mathbf{q} (see Fig. 2.9).

Performing the induction procedure according to Sec. 2.4.7 by applying all possible $g \in G$ (translations and rotations), we obtain the set of functions $\{\hat{D}(g)W : g \in G\}$. Each of these functions is now localized at one point in the crystallographic orbit $G\mathbf{q}$ of \mathbf{q} . We assume now that these functions form an

orthonormal set.²⁷ Thus, they are a basis of the induced rep

$$D^{(G\mathbf{q}\beta)} = D^{(\mathbf{q}\beta)} \uparrow G. \quad (2.46)$$

The Bloch modes (eigenstates of the PC wave equation) of the perfect PC are basis functions of the irreps $D^{(*\mathbf{k}\alpha)}$ of G , thus the induced rep $D^{(G\mathbf{q}\beta)}$ can be reduced in terms of the irreps of the Bloch modes. However, we obtain Bloch *functions* $\tilde{\psi}_{\mathbf{k}}$ (irreps of the translation group) first which can be further reduced to Bloch modes $\psi_{n\mathbf{k}}$ (eigenmodes of the wave equation) by taking also the rotational symmetries into account.

In order to determine which Bloch functions and plane group irreps $D^{(*\mathbf{k}\alpha)}$ are contained in $D^{(G\mathbf{q}\beta)}$, one can apply the projection operators (2.28) to the $W(\mathbf{r})$. We do this in the two steps alluded to above for didactic purposes and start with the translational part:

$$\tilde{\psi}_{\mathbf{k}}(\mathbf{r}) \stackrel{(2.28)}{=} \hat{P}^{\mathbf{k}} W(\mathbf{r}) \quad (2.47)$$

$$\stackrel{(2.28)}{=} \frac{1}{N_1 N_2} \sum_{\{E|\mathbf{R}\} \in T(\mathbb{L}_{\text{main}})} \left[\chi^{(\mathbf{k})}(\{E|\mathbf{R}\}) \right]^* \hat{D}(\{E|\mathbf{R}\}) W(\mathbf{r}) \quad (2.48)$$

$$\stackrel{(2.34)(2.10)}{=} \frac{1}{N_1 N_2} \sum_{\mathbf{R} \in \mathbb{L}_{\text{main}}} \exp(i\mathbf{k} \cdot \mathbf{R}) W(\mathbf{r} - \mathbf{R}). \quad (2.49)$$

By the inverse relation (A.8), this means that

$$W(\mathbf{r}) = \sum_{\mathbf{k} \in \text{BZ}} \exp(-i\mathbf{k} \cdot \mathbf{r}) \tilde{\psi}_{\mathbf{k}}, \quad (2.50)$$

which is the discretized version of the definition of generalized WFs because $\tilde{\psi}_{\mathbf{k}}(\mathbf{r})$ so far is just a Bloch function, that is some basis function for the rep \mathbf{k} of the translational group $T(\mathbb{L}_{\text{main}})$. There is no connection yet to the eigenmodes of the wave equation. This can be established by projecting the Bloch functions²⁸ $\tilde{\psi}_{\mathbf{k}}$ onto the eigenmodes $\psi_{n\mathbf{k}}$ of the PC and defining coefficients U as

$$U_m(\mathbf{k}) := \langle \langle \psi_{m\mathbf{k}} | \tilde{\psi}_{\mathbf{k}} \rangle \rangle. \quad (2.51)$$

Now we justify a posteriori the assumption of $\hat{D}(g)W$ being all orthonormal to each other. When we use orthonormalized eigenmodes $\psi_{n\mathbf{k}}$ of the wave equation of the perfectly periodic PC as Bloch functions *and require* the transformation matrices U_{mn} that build new generalized Bloch modes to be unitary,

$$\tilde{\psi}_{n\mathbf{k}} := \sum_m \psi_{m\mathbf{k}} U_{mn}, \quad (2.52)$$

then the generalized Wannier functions constructed from Eqs. (2.52) and (2.50) will be orthogonal (cf. Sec. A.2.2). Thus we are allowed to define the induced representations above the way we did.

2.5.6 Wannier Function Symmetries and Localization

We want to use the WFs as a localized basis for an expansion of the wave equations because the defect mode solutions in the band gap (which we are interested in) are exponentially localized (cf. Figs. 1.13

²⁷Arbitrary localized functions do not have this property, but WFs W are orthonormalized. We justify this a posteriori below.

²⁸In the Wannier related literature of solid state physics, they are often referred to as generalized Bloch modes.

and 1.16). We review briefly the connection between Bloch mode symmetries and WFs symmetries and localization properties that have been investigated by Des Cloizeaux [36, 86, 87] and Krüger [37, 38].

When evaluating (2.50) numerically for Bloch modes from standard band structure codes, one does in general not obtain well localized, exponentially decreasing WFs, but functions that show a rather erratic behavior and decay like $1/|\mathbf{r}|$ at best which is too slow for efficient calculations (cf. Figs. 3.7, 3.9 and 3.10). This is illustrated and discussed in more detail in Chap. 3. One source of this behavior is an inconsistent phase choice in the Bloch modes. As eigenmodes of the wave equation, they are defined up to an arbitrary complex phase factor $\exp(i\phi(\mathbf{k}))$ that can change drastically between \mathbf{k} -points.

To summarize the findings of the papers cited above, one has to ensure the following properties for constructing localized and symmetric WFs:

- When constructing single band WFs by (2.50), the phase choices of the Bloch modes in the BZ have to be such that they are continuous functions in \mathbf{k} within the BZ *and* over the boundary of the BZ (cf. Figs. 3.9, 3.10 and 3.14).
- When constructing multiband WFs after (2.52), the continuity condition implies certain restrictions on the unitary transforms $U(\mathbf{k})$ that take into account the information about the plane group irreps of the Bloch modes. This implies certain symmetries and localization centers for the corresponding exponentially localized WFs, i. e., the possible Wyckoff positions and irreps of the site symmetry group for that position are restricted to few choices.²⁹ This is illustrated in the examples below.

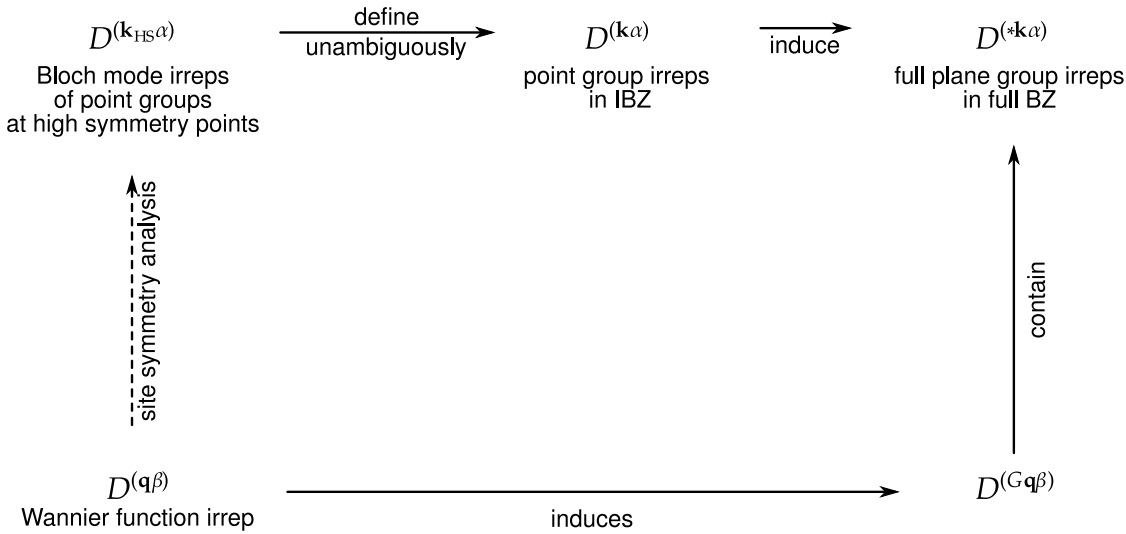


Figure 2.10: Schematic of the site symmetry analysis for the construction of localized Wannier functions with particular symmetries (i. e., forming a particular irrep of the site symmetry group for Wyckoff position \mathbf{q}). The labels α and β for the representations $D^{(\mathbf{q}\alpha)}$ and $D^{(\mathbf{k}_{\text{HS}}\beta)}$ are given in Tabs. 2.1 and 2.2. Examples for the $D^{(\mathbf{k}_{\text{HS}}\beta)}$ for a whole band are given in Figs. F.6 and F.7.

Construction of exponentially localized WFs that are basis functions for a particular site symmetry irrep $D^{(\mathbf{q}\beta)}$ is only possible if the available Bloch modes are bases of those irreps $D^{(*\mathbf{k}\alpha)}$ of the plane group

²⁹Mostly, but not always, they are uniquely determined.

G which occur in the reduction of the full plane group rep $D^{(G\mathbf{q}\beta)}$ induced by $D^{(\mathbf{q}\beta)}$ [36]. Fortunately, all the information needed to determine these irreps $D^{(*\mathbf{k}\alpha)}$ is already contained in the point group irreps $D^{(\mathbf{k}\alpha)}$ that induced $D^{(*\mathbf{k}\alpha)}$ for the Bloch modes at the high symmetry points $\mathbf{k} = \mathbf{k}_{\text{HS}}$ of the BZ. That means, knowing the point group irreps $D^{(\mathbf{k}_{\text{HS}}\beta)}$ of Bloch modes at Γ, X, M for the square lattice or Γ, M, K for the triangular lattice enables one to predict the possible allowed symmetries of exponentially localized WFs built from the corresponding Bloch mode bands. The reduction procedure can be carried out with the help of the Frobenius reciprocity theorem (Sec. 2.4.8), and the multiplicities of the reps involved can be computed by (2.27). Fortunately, there exists the freely usable program SITESYM [88] provided online by the Bilbao Crystallographic Server [89, 90] that accomplishes this. It uses crystallographic notation which is why we have to explicitly and thoroughly define all particular choices for Wyckoff-positions, irrep labels and high symmetry points in the BZ in crystallographic and our notation. The necessary tables and figures are listed in App. F.

Carrying out the reduction procedure by [88], one obtains the reduction tables Tab. 2.1 for the square lattice and Tab. 2.2 for the triangular lattice. They show the reduction procedure denoted by the dashed arrow in Fig. 2.10. The tables are rather complicated and densely packed with information. In the first column, the possible site symmetry representation $D^{(\mathbf{q}\beta)}$ for the exponentially localized WFs at the Wyckoff position \mathbf{q} of the second row are shown. The particular Wyckoff position used (from the crystallographic orbit $G\mathbf{q}$) to obtain the data is given in ITA and PLT coordinates (cf. App. F). The particular choice for definite coordinates of a Wyckoff position affects the labeling of the irreps (see also Fig. F.8). Therefore, extensive care has to be taken in the assembly of these tables. Columns 3–5 list the Bloch mode irreps $D^{(*\mathbf{k}_{\text{HS}}\alpha)}$ of the little co-groups $G_{0\mathbf{k}_{\text{HS}}}$. The particular choice of coordinates for the high symmetry point \mathbf{k}_{HS} from the star $*\mathbf{k}_{\text{HS}}$ is also given in ITA and PLT coordinates. It affects the labeling of irreps in the same fashion as the Wyckoff positions.

The tables are used as follows. Given a set of Bloch modes (single band or multiband), one determines the set of irreps they form at the high symmetry points \mathbf{k}_{HS} of the BZ.³⁰ Then one can read off the site symmetry group irreps of the corresponding exponentially localized WFs in the first column from the allowed combinations of Bloch mode irreps.

Example 1: Consider the second band of the square lattice model system (Sec. 3.4.1). The Bloch modes at the high symmetry points \mathbf{k}_{HS} belong to irreps $A_1(\Gamma)$, $B_2(X)$ and $B_2(M)$ (Tab. 3.1 and Fig. 3.6). By Tab. 2.1, the exponentially localized WFs for this band have the symmetry $A_1(b)$ (see Fig. 3.7b). Note that one can indeed use different phase choices for the Bloch modes, leading to WFs transforming like other site symmetry group irreps. However, these WFs decay like $1/|\mathbf{r}|$ in some directions, since the continuity condition mentioned above is not met then (see Figs. 3.7b and 3.10).

Example 2: Bands 2–7 of the square lattice model system have the band rep shown in Tab. 3.3. By Tab. 2.1, this leads to allowed WF site symmetry group irreps $E(a)$, $A_1(b)$, $B_1(b)$, $E(b)$, but also to $E(a)$, $A(f)$ (Fig. 3.15). The four-fold degenerate $A(f)$ irrep is obtained, when the four basis functions $A_1(b)$, $B_1(b)$, $E(b)$ hybridize (i. e., transform unitarily to basis functions of the new rep). This means, the site symmetry analysis need not yield unique combinations of WF symmetries, but usually restricts them to a few. The WFs obtained still differ in their degree of localization. In that case, the more localized versions are usually better suited for expansion method introduced in Chap. 4.

The entries of these tables are not independent from each other which helps in finding typos. The site symmetry groups of Wyckoff positions \mathbf{Q} can have subgroups of site symmetry groups for other Wyckoff

³⁰This set is sometimes referred to as the band rep in the literature.

positions \mathbf{q} . This is the case, e. g. if the choice of general coordinates x lead to coordinates of another Wyckoff position in the tables. This is exactly same principle responsible for the compatibility relations in the classification of Bloch modes symmetries in the band structure.

Example: In Tab. 2.1, all positions in the WSC with primitive lattice translation (PLT) coordinates $(0, x)$ belong to Wyckoff position e . Choosing $x = 0$ yields Wyckoff position a . This means, the irreps of e can be reduced to irreps of a , e. g. $A(e) = A_1(a) + B_1(a) + E(a)$. Then the reduction of $A(e)$ into the irreps of $D(\mathbf{k}_{\text{HS}}\alpha)$ must equal the sum of those reductions for $A_1(a)$, $B_1(a)$, $E(a)$ for each high symmetry point \mathbf{k}_{HS} .

2.6 Summary

We introduced the concepts of irreducible representations (irreps) of groups. The eigenmodes of the wave equations form basis functions of the plane group irreps of the system under investigation. For perfectly periodic crystals, the eigenmodes have Bloch form: Their translational properties are determined by the wave vector \mathbf{k} from the Brillouin zone (label for the irrep of the translation subgroup) and their rotational properties by the particular irrep of the point group (the little co-group of \mathbf{k}) they belong to.

The construction of Wannier functions as lattice Fourier transforms of generalized Bloch modes is justified by group theoretical considerations. Hereby, the lattice Fourier transform arises naturally from the characters of the translation irreps of the Bloch modes. The symmetries of Wannier functions are classified by the irreps of the site symmetry group of their localization centers. This group is the maximal set of plane group operations which leave the localization center invariant. The possible localization centers are labeled by the Wyckoff letters.

The main result of this chapter consists in the tables 2.1 and 2.2. They contain those combinations of Bloch mode symmetries that lead to the allowed site symmetry group irreps and localization centers of the corresponding Wannier functions that can be exponentially localized. These tables help to determine the best starting points for the minimization algorithms used to generate these exponentially localized Wannier functions, and they aid in choosing the band sets that have to be grouped together for this task. The following chapter contains many examples for the application of these tables.

The generalization of this approach to 3D PC is not easy, since the systems most promising for 3D applications are non-symmorphic crystals, e. g., the silicon woodpile structure [91]. In that case, the site symmetry analysis becomes more complicated.

$D^{(\mathbf{q}\beta)}$	\mathbf{q}	$D^{(\mathbf{k}_{\text{HS}}\alpha)}$		
		$\mathbf{k}_{\text{HS}} = \Gamma$ 0, 0 (ITA) 0, 0 (PLT)	$\mathbf{k}_{\text{HS}} = X$ -1/2, 0 (ITA) 0, 1/2 (PLT)	$\mathbf{k}_{\text{HS}} = M$ -1/2, 1/2 (ITA) 1/2, 1/2 (PLT)
A_1	a	A_1	A_1	A_1
A_2	0, 0 (ITA)	A_2	A_2	A_2
B_1	0, 0 (PLT)	B_1	A_1	B_1
B_2		B_2	A_2	B_2
E		E	$B_1 + B_2$	E
A_1	b	A_1	B_2	B_2
A_2	1/2, 1/2 (ITA)	A_2	B_1	B_1
B_1	1/2, 1/2 (PLT)	B_1	B_2	A_2
B_2		B_2	B_1	A_1
E		E	$A_1 + A_2$	E
A_1	$2c$	$A_1 + B_1$	$A_1 + B_2$	E
A_2	1/2, 0 (ITA)	$A_2 + B_2$	$A_2 + B_1$	E
B_1	0, 1/2 (PLT)	E	$A_2 + B_2$	$A_2 + B_2$
B_2		E	$A_1 + B_1$	$A_1 + B_1$
A	$4d$	$A_1 + B_2 + E$	$A_1 + B_1 + A_2 + B_2$	$A_1 + B_2 + E$
B	$-x, x$ (ITA) x, x (PLT)	$A_2 + B_1 + E$	$A_1 + B_1 + A_2 + B_2$	$A_2 + B_1 + E$
A	$4e$	$A_1 + B_1 + E$	$2A_1 + B_1 + B_2$	$A_1 + B_1 + E$
B	$-x, 0$ (ITA) $0, x$ (PLT)	$A_2 + B_2 + E$	$2A_2 + B_1 + B_2$	$A_2 + B_2 + E$
A	$4f$	$A_1 + B_1 + E$	$A_1 + A_2 + 2B_2$	$A_2 + B_2 + E$
B	1/2, x (ITA) $x, 1/2$ (PLT)	$A_2 + B_2 + E$	$A_1 + A_2 + 2B_1$	$A_1 + B_1 + E$
A	$8g$	$A_1 + A_2 + B_1$	$2A_1 + 2A_2$	$A_1 + A_2 + B_1$
	$-x, y$ (ITA) x, y (PLT)	$+B_2 + 2E$	$+2B_1 + 2B_2$	$+B_2 + 2E$

Table 2.1: Reduction multiplicities of induced reps $D^{(G\mathbf{q}\beta)} \downarrow G$ into irreps $D^{(*\mathbf{k}\alpha)}$ of the plane group G for the square lattice. $D^{(G\mathbf{q}\beta)}$ is fully determined and labeled by the irreps of $D^{(\mathbf{q}\beta)}$, $D^{(*\mathbf{k}\alpha)}$ is fully determined and labeled by the irreps $D^{(\mathbf{k}_{\text{HS}}\alpha)}$. The Wyckoff positions from Tab. F.4 and high symmetry points in the BZ from Fig. F.6 were used and given with their multiplicities in a WSC. The “dictionary” Tab. F.5 was used in the interpretation of the SITESYM output and compilation of this table.

$D(\mathbf{q}\beta)$	\mathbf{q}	$D(\mathbf{k}_{\text{HS}\alpha})$		
		$\mathbf{k}_{\text{HS}} = \Gamma$ 0, 0 (ITA) 0, 0 (PLT)	$\mathbf{k}_{\text{HS}} = M$ -1/2, 0 (ITA) 0, 1/2 (PLT)	$\mathbf{k}_{\text{HS}} = K$ -2/3, 1/3 (ITA) 1/3, 1/3 (PLT)
A_1	a	A_1	A_1	A_1
A_2	0, 0 (ITA)	A_2	A_2	A_2
B_1	0, 0 (PLT)	B_1	B_1	A_1
B_2		B_2	B_2	A_2
E_1		E_1	$B_1 + B_2$	E
E_2		E_2	$A_1 + A_2$	E
A_1	$2b$	$A_1 + B_2$	$A_1 + B_2$	E
A_2	1/3, 2/3 (ITA)	$A_2 + B_1$	$A_2 + B_1$	E
E	1/3, 2/3 (PLT)	$E_1 + E_2$	$A_1 + A_2 + B_1 + B_2$	$A_1 + A_2 + E$
A_1	$3c$	$A_1 + E_2$	$A_1 + B_1 + B_2$	$A_1 + E$
A_2	0, 1/2 (ITA)	$A_2 + E_2$	$A_2 + B_1 + B_2$	$A_2 + E$
B_1	1/2, 0 (PLT)	$B_1 + E_1$	$A_1 + A_2 + B_1$	$A_1 + E$
B_2		$B_2 + E_1$	$A_1 + A_2 + B_2$	$A_2 + E$
A	$6d$	$A_1 + B_1 + E_1 + E_2$	$2A_1 + A_2 + 2B_1 + B_2$	$2A_1 + 2E$
B	0, x (ITA) $x, 0$ (PLT)	$A_2 + B_2 + E_1 + E_2$	$A_1 + 2A_2 + B_1 + 2B_2$	$2A_2 + 2E$
A	$6e$	$A_1 + B_2 + E_1 + E_2$	$2A_1 + A_2 + B_1 + 2B_2$	$A_1 + A_2 + 2E$
B	-2 $x, -x$ (ITA) $x, 2x$ (PLT)	$A_2 + B_1 + E_1 + E_2$	$A_1 + 2A_2 + 2B_1 + B_2$	$A_1 + A_2 + 2E$
A	$12f$	$A_1 + A_2 + B_1$ $+B_2 + 2E_1 + 2E_2$	$3A_1 + 3A_2 + 3B_1 + 3B_2$	$2A_1 + 2A_2 + 4E$

Table 2.2: Reduction multiplicities of induced reps $D^{(G\mathbf{q}\beta)} \downarrow G$ into irreps $D^{(*\mathbf{k}\alpha)}$ of the plane group G for the triangular lattice. $D^{(G\mathbf{q}\beta)}$ is fully determined and labeled by the irreps of $D(\mathbf{q}\beta)$, $D^{(*\mathbf{k}\alpha)}$ is fully determined and labeled by the irreps $D(\mathbf{k}_{\text{HS}\alpha})$. The Wyckoff positions from Tab. F.10 and high symmetry points in the BZ from Fig. F.11 were used and given with their multiplicities in a WSC. The “dictionary” Tab. F.9 was used in the interpretation of the SITESYM output and compilation of this table.

3

Chapter 3

Wannier Function Generation

The generation of maximally localized Wannier functions described here follows the publications of Marzari and Vanderbilt [29] and Souza et al. [30] and their adaption to the photonic case after Schillinger [35] and Wolff [79]. These algorithms are reviewed here, along with a discussion of their shortcomings. In order to generate maximally localized generalized Wannier functions from Bloch modes, the unitary transform matrices $U(\mathbf{k})$ creating the generalized Bloch modes, which in turn build the Wannier functions, must be determined. Therefore, a measure for the real space extent of the Wannier functions is defined. It depends on the number of bands in a set that are allowed to transform to new generalized Bloch modes by the unitary transform matrices $U(\mathbf{k})$, and on these transform matrices themselves. The sum of the extents of all Wannier functions constructed from a given set of Bloch modes is the spread functional Ω . The maximally localized WFs are found by searching for the smallest spread by a combined steepest descent and conjugate-gradient minimization procedure which yields the final transform matrices $U(\mathbf{k})$ as solutions. The Wannier functions are not required explicitly for the minimization procedures. They are only constructed at the end once a suitable set of unitary matrices $U(\mathbf{k})$ has been found. Instead, all quantities needed for that minimization can be expressed by the scalar products between the periodic parts of the Bloch modes.

The generation procedure is discussed and illustrated by many examples. The behavior of the minimization procedures is interpreted taking the results of the site symmetry analysis of Chap. 2 into account. This will explain which symmetries are present in the final Wannier functions and why they cannot be constructed symmetric and localized at all in some cases, thus solving a long standing mystery. We investigate the improvements that can be expected if the theoretical results of Chap. 2 are also incorporated into the generation procedure. Therefore, some improvements for these algorithms are proposed, that can be formulated based on a few precomputed matrices that avoid carrying out time consuming scalar products between fields over and over again.

Finally, some possible sets of Wannier functions obtained with this approach are documented. The Wannier functions are not uniquely determined and the performance of different sets in subsequent computations is investigated in Chaps. 5 and 6. This will help to determine if one choice of construction parameters should be favored over others.

The natural number d is used for the spatial dimension in this chapter.

3.1 Definition and Properties of Wannier Functions

The Wannier functions originally introduced by Wannier [26] were defined for the proper Bloch modes $\psi_{n\mathbf{k}}$, i. e., the eigenmodes of a lattice periodic wave operator. As we have seen in seen in Sec. 2.5.6,

exponentially localized Wannier functions are only obtained by defining them via generalized Bloch modes, i. e., unitary transforms among the proper Bloch modes. These definitions then read¹

$$|W_{n\mathbf{R}}\rangle := \frac{1}{V_{\text{BZ}}} \int_{\text{BZ}} d^d k e^{-i\mathbf{k}\mathbf{R}} |\tilde{\psi}_{n\mathbf{k}}\rangle, \quad (3.1)$$

with generalized Bloch modes

$$|\tilde{\psi}_{n\mathbf{k}}\rangle := \sum_m |\psi_{m\mathbf{k}}\rangle U_{mn}(\mathbf{k}), \quad (3.2)$$

where at each \mathbf{k} a different unitary transformation matrix $U_{mn}(\mathbf{k})$ is used. In the single band case (when the summation index m comprises only one single band) this matrix reduces to the simplest unitary transform possible, a multiplication with a \mathbf{k} -dependent phase factor $\exp(i\phi_n(\mathbf{k}))$. The band index n is inherited from the Bloch bands, from which the corresponding WF was constructed.

The sum over m does not have to run over all infinitely many bands, but can be a subset thereof. The procedures described in the following for constructing maximally localized WFs determine the lower and upper bounds for the summation index m (i. e., the set of bands used to construct a set of WFs) and the matrices $U_{mn}(\mathbf{k})$ that lead to maximally localized WFs. The index n is then an arbitrary numbering to distinguish the different WFs. The ordering of the matrix indices m and n is kept in compliance with [29, 35].

The most notable properties of the WFs are their behavior under translations

$$\hat{D}(\{E|\mathbf{R}'\})|W_{n\mathbf{R}}\rangle = |W_{n\mathbf{R}-\mathbf{R}'}\rangle, \quad (3.3)$$

$$\Rightarrow \mathbf{W}_{n\mathbf{R}}(\mathbf{r}) = \mathbf{W}_{n\mathbf{0}}(\mathbf{r} - \mathbf{R}), \quad (3.4)$$

and their orthogonality

$$\langle\langle \mathbf{W}_{n'\mathbf{R}'} | \mathbf{W}_{n\mathbf{R}} \rangle\rangle = \frac{1}{V_{\text{BZ}}} \delta_{n'n} \delta_{\mathbf{R}'\mathbf{R}}. \quad (3.5)$$

The discretized WFs are normalized after their construction such that they indeed orthonormalized in the end. Both relations are proven Sec. A.2.

3.2 Localization Properties Of Wannier Basis

In order to judge the degree of localization in space of the WFs, we look at the spread $(\Delta\mathbf{r})^2$ of one WF with band index n . For the definition we need the first and second moment of the position operator \mathbf{r} , defined as expectation values of \mathbf{r} and r^2 :

$$\langle\mathbf{r}\rangle_n = \langle\langle W_{n\mathbf{0}} | \mathbf{r} | W_{n\mathbf{0}} \rangle\rangle, \quad (3.6)$$

$$\langle r^2 \rangle_n = \langle\langle W_{n\mathbf{0}} | r^2 | W_{n\mathbf{0}} \rangle\rangle. \quad (3.7)$$

The mean value of \mathbf{r} is hereby defined componentwise as

$$\langle\mathbf{r}\rangle_n := \sum_i \hat{\mathbf{e}}_i \langle r_i \rangle_n. \quad (3.8)$$

We can restrict ourselves to the expectation values of WFs belonging to the origin cell $\mathbf{R} = \mathbf{0}$ here because the final expression (3.9) for the real space extent is independent of the particular cell. This is obvious, since the spatial extent of a function is invariant under translations of that function.

¹Note that the WFs are orthogonal, but not normalized by this definition. See Sec. A.2.2 for details.

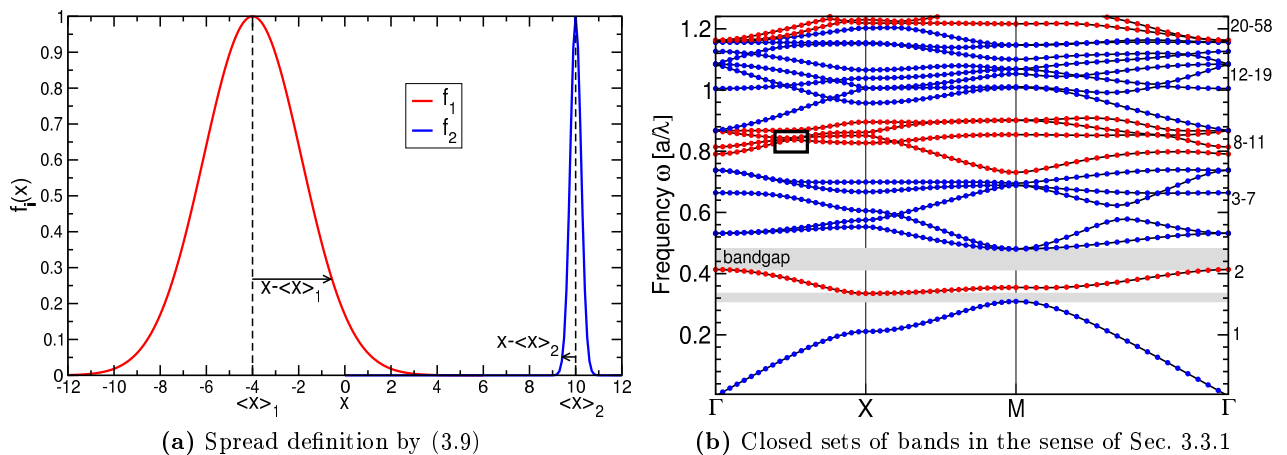


Figure 3.1: (a) Example for the spread definition of (3.9). The broad function f_1 has a spread $\Omega_1 = 24$, whereas the narrow function f_2 has $\Omega_2 = 0.033$. (b) Examples for closed sets of bands in the sense of Sec. 3.3.1. The bands of each set cross each other, but none of the bands of other closed sets. The respective band ranges are shown on the right side margin. The inset is shown close-up in Fig. 3.2.

With these values at hand, we can define a measure for the real space extent of a WF by

$$(\Delta \mathbf{r}_n)^2 := \langle (\mathbf{r} - \langle \mathbf{r} \rangle_n)^2 \rangle_n \quad (3.9)$$

$$= \langle r^2 \rangle_n - \langle \mathbf{r} \rangle_n^2. \quad (3.10)$$

As alluded to above, the spread $(\Delta \mathbf{r}_n)^2$ is independent of the lattice site index \mathbf{R} . For notational consistency, we also write

$$\Omega_n := (\Delta \mathbf{r}_n)^2 \quad (3.11)$$

for the individual spread of a WF with band label n .

In the magnetic field case, the interpretation of the spread as the real space extent of the function is straightforward and illustrated in Fig. 3.1a. In the electric field case, the scalar product (1.56) also contains the periodic permittivity distribution which pronounces field values in the high index region of the PC. Then the spread (3.9) is no longer a direct measure for spatial localization, but still takes on small values for highly localized functions. That means, minimizing this value still leads to very well localized functions that tend to be more localized in the low index regions due to the permittivity function in the scalar product. Using the proper scalar product is important, since the algorithms reviewed in the following rely on the use of orthogonal Bloch modes.

For the numerical construction of the Wannier functions, the continuous definition (3.1) has to be discretized by (A.8), where we only have to construct a WF for $\mathbf{R} = \mathbf{0}$ for each band and construct the WFs for all other lattice vectors by exploiting their translational behavior (3.4). Then we arrive at an expression similar to (2.50),

$$|W_{n\mathbf{0}}\rangle = \frac{1}{N_{\mathbf{k}\text{-res}}} \sum_{\mathbf{k}} |\tilde{\psi}_{n\mathbf{k}}\rangle, \quad (3.12)$$

which is easily interpreted. The WF for the generalized Bloch mode band n is just the averaged Bloch mode profile over all $N_{\mathbf{k}\text{-res}}$ available wave vectors \mathbf{k} (depending on the particular discretization). The WF $|W_{n\mathbf{0}}\rangle$ will be localized if

1. the field values of $|\tilde{\psi}_{n\mathbf{k}}\rangle$ sum up to their maximum at one position in space (the localization center),
2. cancel out at positions far off the localization center, facilitating the rapid decay.

As an example, Fig. 3.2 shows the absolute values of the profiles of proper Bloch modes along the high symmetry lines of the BZ. The green and blue bands continuously exchange their mode profiles, whereas the red band passes unchanged through the former. This means, simply rearranging the frequency ordered labeling for n ,

$$\omega_n \leq \omega_{n+1}, \quad (3.13)$$

and adjusting the phases $\exp(i\phi_n(\mathbf{k}))$ is not enough to meet the two conditions above for highly localized WFs. The green and blue bands are called entangled and only a non-trivial unitary transform $U(\mathbf{k})$ among the two bands can separate the mode information into generalized Bloch bands in a way that yields highly localized WFs. Finding these transforms is the purpose of the Souza-Marzari-Vanderbilt algorithm.

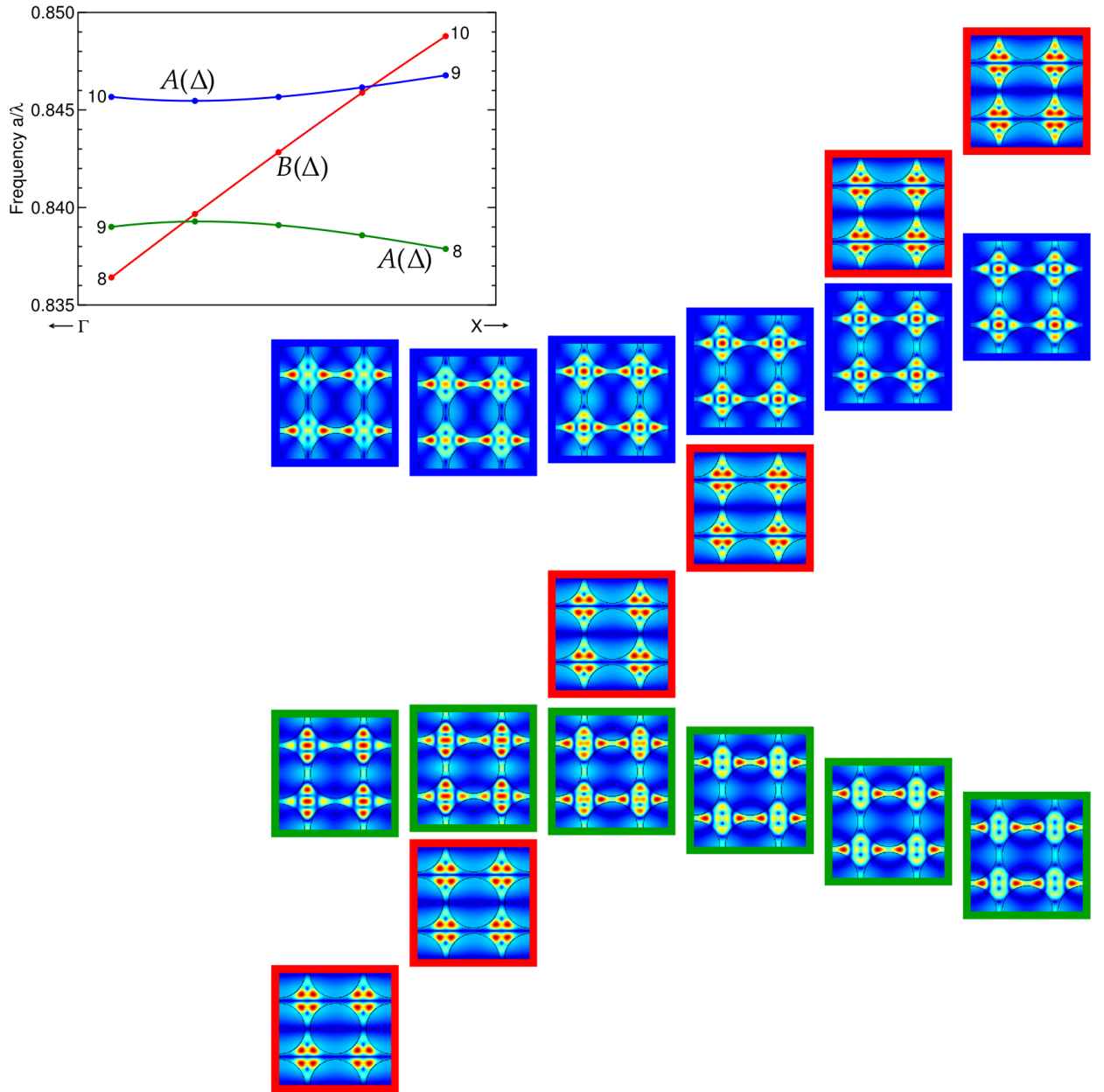


Figure 3.2: *Avoided crossing and crossings of bands with equal and different spatial symmetries, respectively. The band structure inset of Fig. 3.1b is shown along with the little co-group irreps of the Bloch modes. The absolute values $|H_{n\mathbf{k}}(\mathbf{r})|$ of proper Bloch modes for the TE square model system are arranged according to their frequency and wave vector. While the red band passes unaltered through the other two, the blue and green bands exchange their mode profiles continuously along the \mathbf{k} -space path $\overline{\Gamma X}$. Thus, one single value n of the frequency ordered numbering scheme (shown in the band structure inset) labels bands with different mode profiles.*

3.3 Review Of Spread Minimization Procedure

The choice of (3.9) for measuring the real space extent of WFs allows to derive a minimization scheme for the combined spread Ω of several WFs which is by (3.2) a function of the particular choices of transformation matrices $U(\mathbf{k})$ used to construct the generalized Bloch modes:

$$\Omega[U] := \sum_n \Omega_n[U]. \quad (3.14)$$

The sum runs over those contiguous band indices that generate the N_{WF} WFs in the end.

The task is now to find those sets of transformation matrices that minimize the spread functional Ω and yield highly localized WFs then. We will briefly summarize the main ideas of these algorithms here.

Note that the knowledge of Chap. 2 is not incorporated in the algorithms presented here, but some results can be understood and explained by a symmetry analysis.

3.3.1 Marzari-Vanderbilt Spread Minimization

In the case of a closed set of bands, the spread minimization algorithm proposed by [29] can be used to determine the desired $U_{mn}(\mathbf{k})$. It is an iterative procedure that starts from initial transforms $U_{mn}^{(0)}(\mathbf{k})$ and in each step i constructs new $U_{mn}^{(i)}(\mathbf{k})$ leading to a smaller combined spread $\Omega[U]$, until the smallest spread value is obtained. Sets of bands are called closed if the bands belonging to the set are possibly degenerate among each other, but not with bands of higher or lower lying sets. Examples for such closed sets of bands are depicted in Fig. 3.1b. Unions of closed sets are also closed.

Since at some point the integration (3.1) in reciprocal space has to be carried out, we discretize the BZ by a mesh of uniformly spaced nodes \mathbf{k} assembled in a Monkhorst-Pack mesh (cf. Sec. B.5) which is known to ease \mathbf{k} -space integration [92]. Examples are shown in Figs. 3.8 and B.7.

Now one starts with initial guesses $U_{mn}^{(0)}(\mathbf{k})$ for each \mathbf{k} in the Monkhorst-Pack (MP) mesh which yield WFs with combined spread $\Omega^{(0)}$. The crucial point here is that one does not need to compute the spread functional (3.14) by evaluating Eqs. (3.1), (3.2) and (3.9) explicitly which would be a time consuming task and an unfeasible procedure for each iteration step. The discretized generalized WFs according to (3.12) are then given in terms of the proper Bloch modes $|\psi_{m\mathbf{k}}\rangle$ by

$$|W_{n\mathbf{0}}\rangle = \frac{1}{N_{\mathbf{k}\text{-res}}} \sum_{m,\mathbf{k}} U_{mn}(\mathbf{k}) |\psi_{m\mathbf{k}}\rangle. \quad (3.15)$$

This sum has to be evaluated only after the final unitary transforms U have been found.

The main idea is to express the position operator in reciprocal space as $\mathbf{r} = i\nabla_{\mathbf{k}}$. It turns out that one can express all relevant quantities by the overlap matrices of the periodic parts of the *initial proper Bloch modes* as

$$M_{mn}^{(0)}(\mathbf{k}, \mathbf{b}) := \langle\langle u_{m\mathbf{k}} | u_{n\mathbf{k}+\mathbf{b}} \rangle\rangle, \quad (3.16)$$

where the vectors \mathbf{b} point to the neighbors of \mathbf{k} in the chosen mesh and facilitate a finite difference discretization of the reciprocal space gradient $\nabla_{\mathbf{k}}$ by:

$$\nabla_{\mathbf{k}} f(\mathbf{k}) \approx \sum_{\mathbf{b}} w_{\mathbf{b}} \mathbf{b} [f(\mathbf{k} + \mathbf{b}) - f(\mathbf{k})]. \quad (3.17)$$

The weight factors $w_{\mathbf{b}}$ are directly linked yet not identical with the ones given in Sec. B.3.1. The spread (3.9) can be expressed in terms of $\nabla_{\mathbf{k}}$ which in turn introduces the overlap matrices (3.16).

Noting that the unitary transform matrices $U(\mathbf{k})$ can be expressed by anti-Hermitian matrices $W(\mathbf{k}) = -W^\dagger(\mathbf{k})$ as $U(\mathbf{k}) = \exp(W(\mathbf{k}))$, an iterative update scheme for the matrices can be established via

$$U^{(i+1)}(\mathbf{k}) = U^{(i)}(\mathbf{k}) \exp(\Delta W^{(i)}(\mathbf{k})), \quad (3.18)$$

$$M^{(i+1)}(\mathbf{k}, \mathbf{b}) = U^{(i+1)\dagger}(\mathbf{k}) M^{(0)} U^{(i+1)}(\mathbf{k}, \mathbf{b}). \quad (3.19)$$

The discretized expectation values of the moments of the position operator (3.6) for the WFs are given for each iteration step i in terms of the Bloch modes as

$$\langle \mathbf{r} \rangle_n^{(i)} = \frac{i}{N_{\mathbf{k}\text{-res}}} \sum_{\mathbf{k}, \mathbf{b}} w_{\mathbf{b}} \mathbf{b} [M_{nn}^{(i)}(\mathbf{k}, \mathbf{b}) - 1], \quad (3.20)$$

$$\langle r^2 \rangle_n^{(i)} = \frac{1}{N_{\mathbf{k}\text{-res}}} \sum_{\mathbf{k}, \mathbf{b}} w_{\mathbf{b}} [2 - 2 \operatorname{Re} M_{nn}^{(i)}(\mathbf{k}, \mathbf{b})]. \quad (3.21)$$

With these values at hand, the localization centers $\langle \mathbf{r} \rangle_n^{(i)}$ of the WFs, the individual spreads $\Omega_n^{(i)}$ and also the combined spread $\Omega^{(i)}$ are known at each step i .

In [29, 35], the anti-unitary update matrices $\Delta W^{(i)}(\mathbf{k})$ in the i th iteration step are obtained by a steepest descent step in the direction of smaller values for the spread functional Ω , however the implementation by Christian Wolff [79] using a conjugate gradient (CG) minimization drastically improved the convergence speed and made the construction of the final 101 WFs possible in the first place.

The gradient matrices $\partial \Omega^{(i)} / \partial W_{mn}(\mathbf{k})$ required at each node \mathbf{k} can be expressed solely in terms of the matrix elements $M_{mn}^{(i)}(\mathbf{k}, \mathbf{b})$ given by the previous iteration step. We only aim at a principal understanding of the algorithm, so the full expressions have been omitted here.

3.3.2 Choice Of Initial Transform Matrices

The minimization being an iteration procedure, its convergence rate and sometimes also the minimum found depend on the initial choice of transforms $U^{(0)}(\mathbf{k})$. By (3.1) and (3.2), this corresponds to a particular choice of initial WFs $|W_{n\mathbf{R}}^{(0)}\rangle$.

One could simply start with a unit matrix, but a choice that yields initial functions which already resemble the anticipated final WFs can yield better starting points. The trial function based initialization is a procedure to construct initial transforms $U^{(0)}(\mathbf{k})$ from a set of such trial functions $|T_n\rangle$. The basic idea is to construct initial generalized Bloch modes $|\tilde{\psi}_{n\mathbf{k}}^{(0)}\rangle$ such that the initial WFs $|W_{n\mathbf{R}}^{(0)}\rangle$ are the best approximation to the trial functions $|T_n\rangle$ in a least squares sense. Hence that part of the trial functions that can be represented in terms of a lattice Fourier transform of the chosen bands has to be determined by a projection into the space of given Bloch modes. This procedure leads to the definition of possibly non-unitarian initial transforms $A(\mathbf{k})$ by applying the projection operator $|\psi_{m\mathbf{k}}\rangle\langle\psi_{m\mathbf{k}}|$:

$$|\phi_{n\mathbf{k}}\rangle = \sum_m |\psi_{m\mathbf{k}}\rangle \underbrace{\langle\langle\psi_{m\mathbf{k}}||T_n\rangle\rangle}_{=: A_{mn}(\mathbf{k})}. \quad (3.22)$$

If we allow non-orthogonal trial functions, then the $A(\mathbf{k})$ will not be unitary and the $|\phi_{n\mathbf{k}}\rangle$ are also not orthogonal and not a valid initial guess for generalized Bloch modes. We have to apply an orthogonalization procedure to those functions then. The Gram-Schmidt procedure would be ill-suited in this case because it can change the functions drastically and they may differ strongly from their initial shape $|\phi_{n\mathbf{k}}\rangle$. In our case, we want the orthogonalized $|\tilde{\psi}_{n\mathbf{k}}^{(0)}\rangle$ to deviate as little as possible from their previous

shape $|\phi_{n\mathbf{k}}\rangle$, so that the initial WFs deviate as little as possible from the chosen trial functions $|T_n\rangle$. Therefore, Löwdin's symmetric orthogonalization procedure is used. It constructs new orthogonalized functions $|\tilde{\psi}_{n\mathbf{k}}^{(0)}\rangle$, whose combined mean square deviation from the original functions $|\phi_{n\mathbf{k}}\rangle$ is minimal [93]. Performing this procedure leads to the definitions

$$U^{(0)}(\mathbf{k}) := A(\mathbf{k})S^{-\frac{1}{2}}(\mathbf{k}), \quad (3.23)$$

where $S(\mathbf{k}) := A^\dagger(\mathbf{k})A(\mathbf{k})$ are the overlap matrices of the non-orthogonal $|\phi_{n\mathbf{k}}\rangle$:

$$S_{mn}(\mathbf{k}) := \langle\langle \phi_{m\mathbf{k}} | \phi_{n\mathbf{k}} \rangle\rangle. \quad (3.24)$$

Their inverse square roots are computed by diagonalizing them, taking the inverse square roots of the diagonal elements and transforming them back. If the functions were orthogonal right from the start, the $S(\mathbf{k})$ would just be unit matrices.

If only one band is involved, then by choosing appropriate trial functions (under consideration of the symmetry relations of Sec. 2.5.6) the construction of initial WFs can already yield the maximally localized WFs without any further minimization step [87]. This is rarely the case but can be used to construct WFs with desired symmetry properties, as will be investigated in Sec. 3.4. For sets containing more than one band, the choice of trial functions with the proper symmetry after the tables of Sec. 2.5.6 can reduce the minimization time and even avoid false minima, i. e., terminated iterations that yield asymmetric or delocalized WFs.

Judging from (3.12) again, one can deduce that the Bloch modes at the Γ -point of the BZ are well suited as trial functions [35]. This can be seen as follows. If WFs for the lowest possible resolution $N_{\mathbf{k}\text{-res},i} = 1$ are constructed, the corresponding MP mesh contains just $\mathbf{k} = \mathbf{0}$ and the numerical WF for that case is just the Bloch mode at the Γ -point. Successively increasing the resolution $N_{\mathbf{k}\text{-res},i}$ will continuously generate better approximations to the proper WF. In practice, we use Γ -point Bloch modes and unitary transforms thereof that are cropped to one WSC-shape domain which is located at one of the Wyckoff positions of the center cell. The transforms and positions to use are governed by the site symmetry analysis Sec. 2.5.6. Before any knowledge about symmetries was available, randomly positioned Gaussian functions were also used. Their performance is investigated in the examples starting with Sec. 3.4.

3.3.3 Souza Subspace Optimization

If no closed sets of bands are available or the closed set available has so many bands that the Marzari-Vanderbilt spread minimization is no longer feasible, an artificially closed set of generalized bands has to be constructed. This is accomplished by the Souza subspace optimization which is designed to create such an artificial set of the periodic parts $|\tilde{u}_{n\mathbf{k}}\rangle$ of generalized band functions, for which the Marzari-Vanderbilt algorithm can be applied later on. Additionally it can also be used to increase the localization WFs by relieving the delocalization effects of avoided crossings between closed sets of bands.

Mathematically speaking, in order to construct N_{WF} WFs, the Marzari-Vanderbilt algorithm expects a linear space $\mathcal{S}(\mathbf{k})$ at each node \mathbf{k} in the MP mesh, spanned by N_{WF} functions $|\tilde{u}_{n\mathbf{k}}\rangle$. For closed sets of bands, the periodic parts $|u_{n\mathbf{k}}\rangle$ of proper Bloch modes could readily be used as those $|\tilde{u}_{n\mathbf{k}}\rangle$. The key idea for the treatment of entangled bands lies in the fact that by the entanglement some mode information is carried away out of these spaces $\mathcal{S}(\mathbf{k})$. This information has to be put back somehow into the desired spaces $\mathcal{S}(\mathbf{k})$ while removing unwanted Bloch mode profiles that destroy the localization of the WFs. This idea leads to a procedure creating subspaces $\mathcal{S}(\mathbf{k})$ which are as similar as possible in a sense to be defined in the following. This is schematically illustrated in Fig. 3.3.

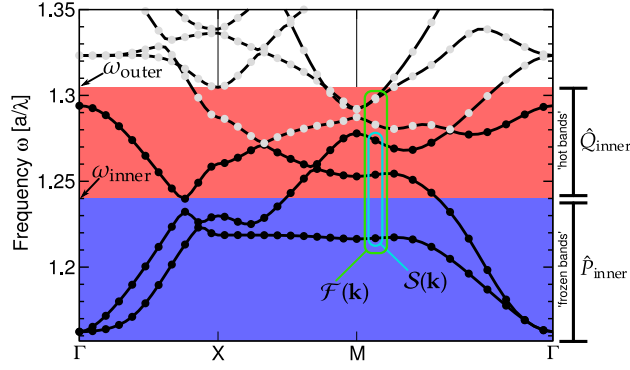


Figure 3.3: Schematic for the Souza subspace optimization with frequency windows. In this example, $N_{\text{WF}} = 3$ WFs shall be constructed from the Bloch modes belonging to the black dotted bands. They form N_{WF} -dimensional subspaces $\mathcal{S}(\mathbf{k})$, which may interchange Bloch modes with the grey dotted bands lying within the outer window defined by ω_{outer} . This defines the larger spaces $\mathcal{F}(\mathbf{k})$, with $N_{\mathcal{F}(\mathbf{k})} = 5$ in this example. The bands within the inner frequency window ω_{inner} may not leave the subspaces $\mathcal{S}(\mathbf{k})$. Figuratively speaking, one can think of frozen bands that may not change, and hot bands, whose mode information is liquefied such that the wanted information settles down (into $\mathcal{S}(\mathbf{k})$) and the unwanted profiles float up like slag in a blast-furnace.

Therefore, at each \mathbf{k} node in the MP mesh, one looks at linear spaces $\mathcal{F}(\mathbf{k})$ spanned by *more* proper periodic parts $|u_{n\mathbf{k}}\rangle$ than are needed to construct just N_{WF} WFs. From these spaces $\mathcal{F}(\mathbf{k})$, one picks a basis of exactly N_{WF} generalized periodic parts $|\tilde{u}_{n\mathbf{k}}\rangle$ that form the artificial generalized bands spanning $\mathcal{S}(\mathbf{k})$. The subspace optimization procedure now picks those N_{WF} basis functions (forming the optimized subspaces $\mathcal{S}(\mathbf{k})$) that lead to optimal localization of the WFs constructed from the unitary transforms $U(\mathbf{k})$ found by the Marzari-Vanderbilt algorithm afterwards.

The basis for this procedure is the fact that the spread functional Ω is actually the sum

$$\Omega = \Omega_{\text{I}} + \Omega_{\text{D}} + \Omega_{\text{OD}}, \quad (3.25)$$

where Ω_{D} and Ω_{OD} depend on the diagonal and off-diagonal elements of the overlap matrices $M(\mathbf{k}, \mathbf{b})$, respectively, and Ω_{I} is invariant under unitary transforms $U(\mathbf{k})$ *within* the subspaces $\mathcal{S}(\mathbf{k})$. Thus, the choice of subspaces $\mathcal{S}(\mathbf{k})$ affects the lower boundary $\Omega_{\text{I}} \leq \Omega$, which has to be minimized now.

It turns out that Ω_{I} becomes smaller if all the neighboring subspaces $\mathcal{S}(\mathbf{k} + \mathbf{b})$ differ as little as possible from each $\mathcal{S}(\mathbf{k})$. Thus Ω_{I} measures the 'global smoothness of connection' between the spaces $\mathcal{S}(\mathbf{k})$ in the whole BZ, vanishing when they all become identical. By this procedure, a prerequisite for meeting the continuity condition of Sec. 2.5.6 is facilitated in this step. The task of finding the optimal spaces is expressed as a self-consistent iteration scheme, where the mismatch between each new subspace $\mathcal{S}^{(i+1)}(\mathbf{k})$ and its neighboring spaces $\mathcal{S}^{(i)}(\mathbf{k}, \mathbf{b})$ from the previous iteration step is minimized.

This ansatz leads to the definition of projection operators

$$\hat{P}^{(i)}(\mathbf{k}) := \sum_n |\tilde{u}_{n\mathbf{k}}^{(i)}\rangle \langle \tilde{u}_{n\mathbf{k}}^{(i)}|, \quad (3.26)$$

that project onto the space spanned by the $N_{\mathcal{F}(\mathbf{k})}$ periodic parts of the generalized Bloch modes from

the i th iteration step. Then the eigenvalue problem for each of the operators

$$\hat{Z}^{(i)}(\mathbf{k}) := \sum_{\mathbf{b}} w_{\mathbf{b}} \hat{P}^{(i)}(\mathbf{k} + \mathbf{b}), \quad (3.27)$$

$$\hat{Z}^{(i)}(\mathbf{k})|\tilde{u}_{n\mathbf{k}}^{(i+1)}\rangle = \lambda_{n\mathbf{k}}|\tilde{u}_{n\mathbf{k}}^{(i+1)}\rangle \quad (3.28)$$

has to be solved at each \mathbf{k} , where the N_{WF} eigenvectors with largest eigenvalues $\lambda_{n\mathbf{k}}$ form the new optimal subspace $\mathcal{S}^{(i+1)}(\mathbf{k})$ because spaces spanned by these functions have largest overlap and are therefore most similar. In the implementation of the algorithm, the operators $\hat{Z}^{(i)}(\mathbf{k})$ can be expressed by the overlap matrices $M^{(i)}(\mathbf{k}, \mathbf{b})$, for which the explicit update scheme has been omitted here.

3.3.4 Frequency Windows

In order to have some rudimentary control over which mode information is allowed to leave and enter the spaces $\mathcal{S}(\mathbf{k})$, one could explicitly define which periodic parts $|u_{n\mathbf{k}}\rangle$ must stay in $\mathcal{S}(\mathbf{k})$ which ones are allowed to leave $\mathcal{S}(\mathbf{k})$ and which ones are allowed to enter from the larger spaces $\mathcal{F}(\mathbf{k})$. For the sake of simplicity, this is done by defining contiguous frequency intervals (frequency windows) of cold/frozen and hot/molten functions $|u_{n\mathbf{k}}\rangle$ that are prohibited or allowed to take part in the subspace optimization procedure, respectively. These figures of speech mean that frozen bands do not change at all, while the mode information in molten bands is allowed to leave the spaces $\mathcal{S}(\mathbf{k})$ and can be switched with other bands defined in $\mathcal{F}(\mathbf{k})$. All Bloch modes $|u_{n\mathbf{k}}\rangle$ with frequencies $\omega_{n\mathbf{k}}$ below the inner frequency ω_{inner} are frozen, while those with frequencies between ω_{inner} and the outer frequency window ω_{outer} take part in the optimization and exchange mode information with each other.

The actual choices of these frequencies can alter the final WFs drastically, up to the point where the algorithm gets unstable and cannot find the proper maximally localized WFs any more. The symmetry considerations of Sec. 2.5.6 however can guide the choice, as will be investigated in the examples.

3.3.5 Choice of Initial Subspaces

One has to construct the initial subspaces $\mathcal{S}^{(0)}(\mathbf{k})$ under the frequency window constraints: all Bloch modes $|\psi_{n\mathbf{k}}\rangle$ with frequencies below ω_{inner} *must* be included, while the other Bloch modes are allowed to form new basis states of the rest of the space $\mathcal{F}(\mathbf{k})$. This is again done by specifying N_{WF} trial functions $|T_n\rangle$ and constructing that many generalized Bloch $|\tilde{\psi}_{n\mathbf{k}}\rangle$ modes by (3.23). Then one defines the projection operators $\hat{P}_{\mathcal{F}(\mathbf{k})}$ onto the full $\mathcal{F}(\mathbf{k})$ and \hat{P}_{inner} that projects on the space of fixed Bloch modes in the inner frequency window:

$$\hat{P}_{\mathcal{F}(\mathbf{k})} := \sum_n |\tilde{\psi}_{n\mathbf{k}}\rangle\langle\tilde{\psi}_{n\mathbf{k}}|, \quad (3.29)$$

$$\hat{P}_{\text{inner}}(\mathbf{k}) := \sum_{n:\omega_{n\mathbf{k}} < \omega_{\text{inner}}} |\psi_{n\mathbf{k}}\rangle\langle\psi_{n\mathbf{k}}|. \quad (3.30)$$

For $\hat{P}_{\mathcal{F}(\mathbf{k})}$, the generalized WFs $|\tilde{\psi}_{n\mathbf{k}}\rangle$ for the exceeding bands n that have no trials specified are just taken to be the proper Bloch function $|\psi_{n\mathbf{k}}\rangle$. The operator

$$\hat{Q}_{\text{inner}}(\mathbf{k}) := \hat{\mathbb{1}} - \hat{P}_{\text{inner}}(\mathbf{k}) \quad (3.31)$$

projects onto that subspace of $\mathcal{F}(\mathbf{k})$, where the basis functions are allowed to change and finally one solves the eigenvalue equation

$$\hat{Q}_{\text{inner}}(\mathbf{k})\hat{P}_{\mathcal{F}(\mathbf{k})}(\mathbf{k})\hat{Q}_{\text{inner}}(\mathbf{k})|\lambda_{n\mathbf{k}}\rangle = \lambda_{n\mathbf{k}}|\lambda_{n\mathbf{k}}\rangle. \quad (3.32)$$

The eigenfunctions $|\lambda_{n\mathbf{k}}\rangle$ with largest eigenvalues are used to extend the fixed basis to N_{WF} basis functions of $\mathcal{S}^{(0)}(\mathbf{k})$. These basis functions have the largest overlap with the chosen trial functions, approximating them best within the subspaces $\mathcal{S}^{(0)}(\mathbf{k})$.

A schematic illustration of the full Souza-Marzari-Vanderbilt spread minimization procedure with initialization of the subspaces and basis functions is shown in Fig. 3.4.

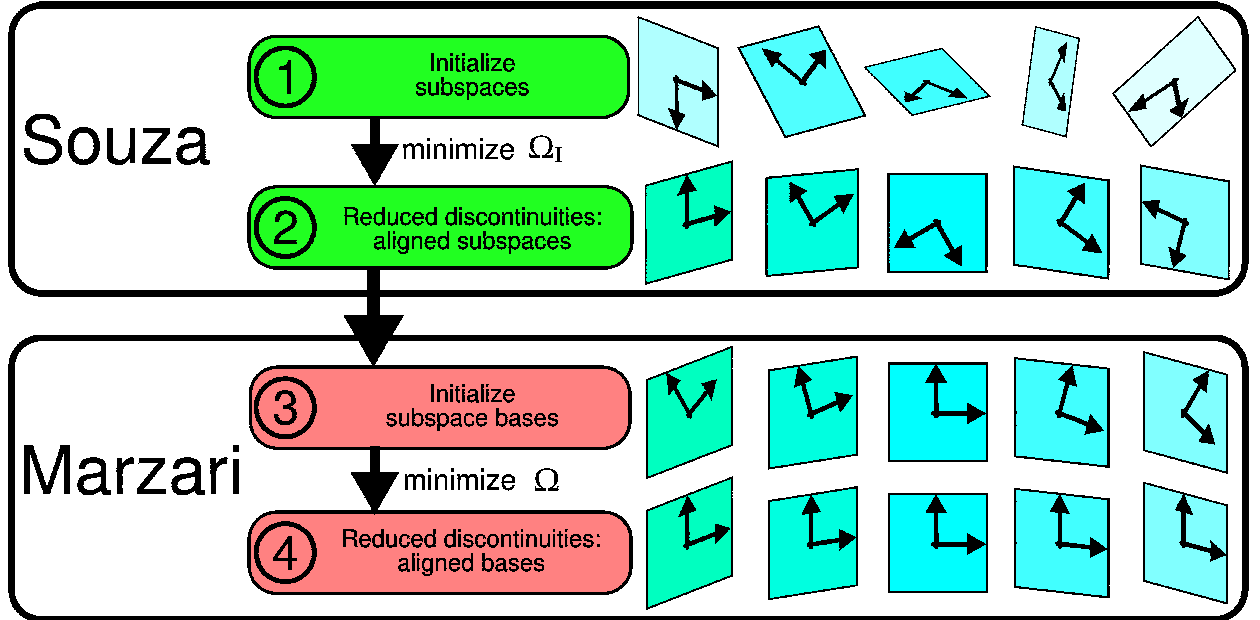


Figure 3.4: Schematic illustration of the full Souza-Marzari algorithm. Subspaces $\mathcal{S}(\mathbf{k})$ for adjacent nodes \mathbf{k} are shown as planes (two-dimensional linear spaces) embedded in three-dimensional spaces $\mathcal{F}(\mathbf{k})$. The generalized Bloch functions $|\tilde{\psi}_{n\mathbf{k}}\rangle$ are depicted as orthogonal basis vectors spanning the planes. After choosing initial subspaces (1), the Souza algorithm minimizes the invariant part Ω_I by aligning the spaces as well as possible (2). The particular choice of basis functions is not relevant. After the spaces $\mathcal{S}(\mathbf{k})$ have been fixed, the trial functions provide a rough guess for aligning the basis functions (3). Their alignment is further optimized by minimizing the spread functional Ω , yielding generalized Bloch modes $|\tilde{\psi}_{n\mathbf{k}}\rangle$ that are as smooth in \mathbf{k} as is possible, yielding localized WFs (4).

3.3.6 Bottom-Up Approach

So far, eventual Bloch mode profiles have been moved to higher generalized Bloch bands by the Souza subspace optimization. These generalized Bloch modes outside the subspaces $\mathcal{S}(\mathbf{k})$ have to be used for the construction of WFs for higher bands by repeating the steps of the full Souza-Marzari-Vanderbilt (SMV) algorithm of Fig. 3.4. This iterated procedure is referred to as the bottom-up approach and allows to produce an unlimited number of WFs in theory, starting from the first band of the band structure. Thus, a large unitary transform matrix $U(\mathbf{k})$ in (3.2) is successively built from smaller transform matrices obtained for each chose band set and frequency windows. Some examples for final WFs are shown in Fig. 3.44 with corresponding parameters listed in Tab. D.1b.

3.4 Discussion of Spread Minimization Procedure: Square Lattice

We discuss the various steps of the spread minimization procedures and the parameter choices for the TE square model system because the modes are easier to visualize than in the triangular case.

3.4.1 Single Bands 1 and 2

The first two bands of Fig. 3.1b are separated by band gaps and thus form two closed sets of bands. Hence, one can construct one WF for each band. The site symmetry analysis by Tab. 2.1 is shown in Tab. 3.1 and yields two unique solutions for symmetric WFs: $A_1(a)$ for band 1 and $A_1(b)$ for band 2. As mentioned in Sec. 3.3.2, the choice of proper trial functions (i. e., having the spatial symmetry and

Γ	X	M	WF irrep	Γ	X	M	WF irrep
A_1	A_1	A_1	$A_1(a)$	A_1	B_2	B_2	$A_1(b)$
(a) Band 1				(b) Band 2			

Table 3.1: Symmetry of Bloch modes for the closed bands 1 and 2. They yield unique representations for the WFs.

localization center of the anticipated WF), will make the initial WF also the final maximally localized WFs. No further minimization step is necessary then.

Various choices of truncated Γ -point Bloch modes as trial functions and the resulting initial WFs along with their spread $(\Delta\mathbf{r})^2$ are shown in Figs. 3.5 and 3.6. The trial functions are cropped around the Wyckoff positions a, b, c . These positions suffice, since further possible site symmetry representations for WFs can be constructed from them (see Sec. 3.8.1).

The WF profiles have been plotted along the dashed cut directions in Fig. 3.7. As mentioned in [37], only the proper choice of symmetries after Sec. 2.5.6 ensures exponential decay of the WFs, otherwise they decay like $1/r$ in some directions.

To illustrate the meaning of the proper phase choices $\exp(i\phi_n(\mathbf{k}))$ in the single band case, the phase distribution for the two bands has been plotted in Figs. 3.9 and 3.10. In particular, Fig. 3.10 shows that one has some direct control over the localization of the WF within the center cell by adjusting the global phase factors of the Bloch modes [37].

In Fig. 3.11, the Marzari-Vanderbilt spread minimization has been carried out for the various choices of trial functions from Figs. 3.5 and 3.6. The number of iteration steps before termination are shown in the legends. One can see that choosing the trial functions according to the symmetry considerations of Sec. 2.5.6, no further improvement in the localization can be achieved. Moreover, the trial choice for band 2 strongly affects the final WF obtained. For all three choices other than the one predicted by symmetry analysis, the minimization algorithm got stuck in local minima and yielded unsymmetric WFs, that are worse localized. Even in this simple case, the outcome of the Marzari-Vanderbilt procedure strongly depends on the choice of initial parameters provided by the user.

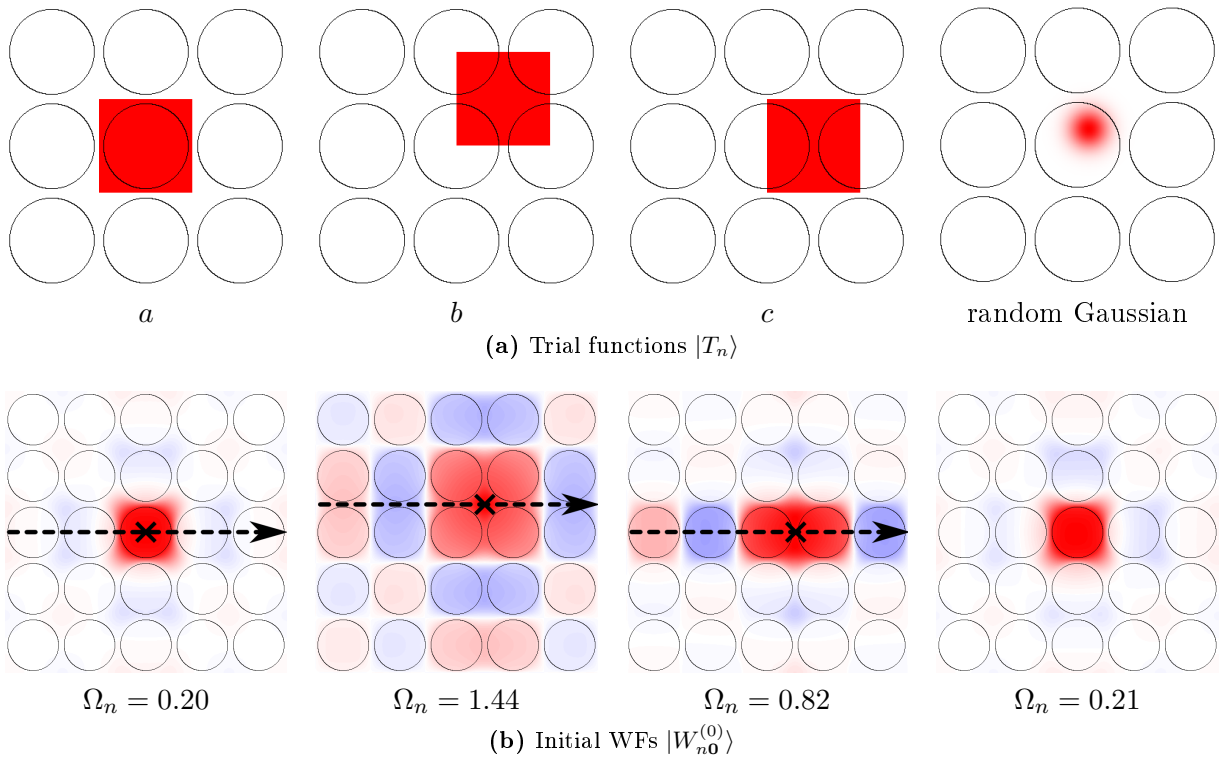


Figure 3.5: Trial functions and corresponding initial (non-minimized) WFs with individual spreads Ω_n for band $n = 1$. The first three trial functions are the Γ -point ($\mathbf{k} = \mathbf{0}$) Bloch modes $|n\mathbf{k}\rangle$ of the first band, truncated on a WSC centered around the annotated Wyckoff positions.

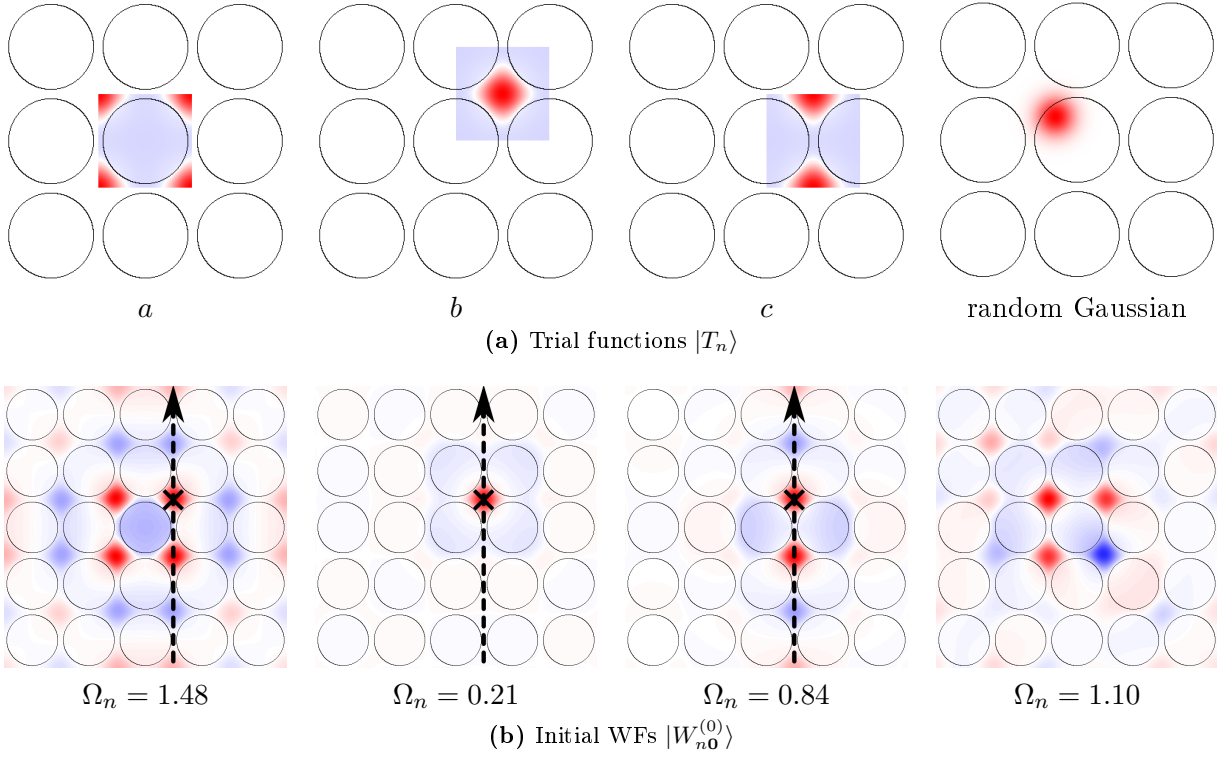


Figure 3.6: Trial functions and corresponding initial (non-minimized) WFs with spreads Ω_n for band $n = 2$. See also caption of Fig. 3.5.

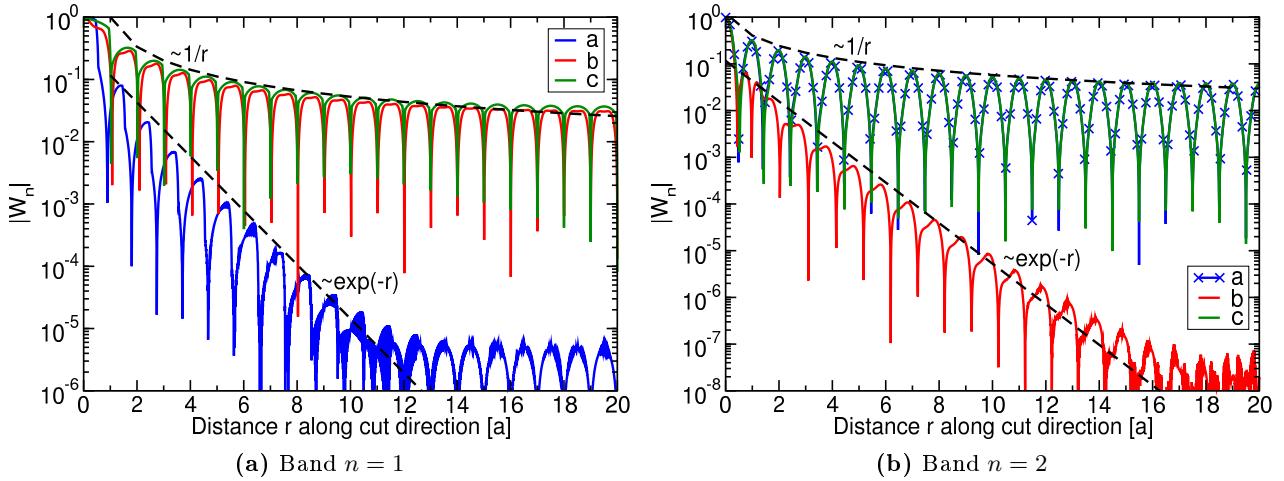


Figure 3.7: Wannier function profiles along the dashed cut directions of Figs. 3.5 and 3.6.

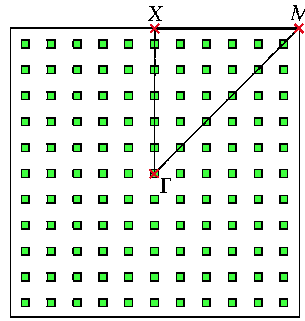


Figure 3.8: The MP mesh discretization of the BZ with resolution $N_{\mathbf{k}\text{-res},i} = 11$ used to construct the WFs in this chapter after (3.12).

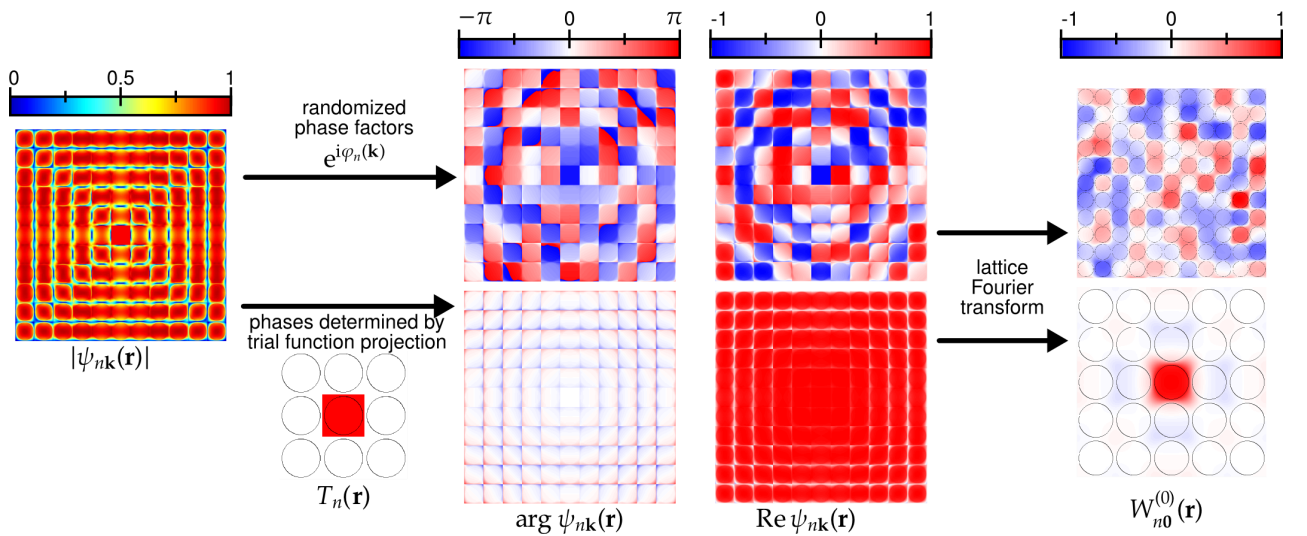


Figure 3.9: Absolute values, phase distributions and real parts of the Bloch modes on a WSC before and after the trial function projection, plotted at each \mathbf{k} of the MP mesh shown in Fig. 3.8. On the right, the resulting WFs for these choices of Bloch modes are shown. This illustrates the necessary continuity in \mathbf{k} of the Bloch modes, in order to produce localized WFs. Note also the symmetric phase distribution and the resulting symmetry of the WF.

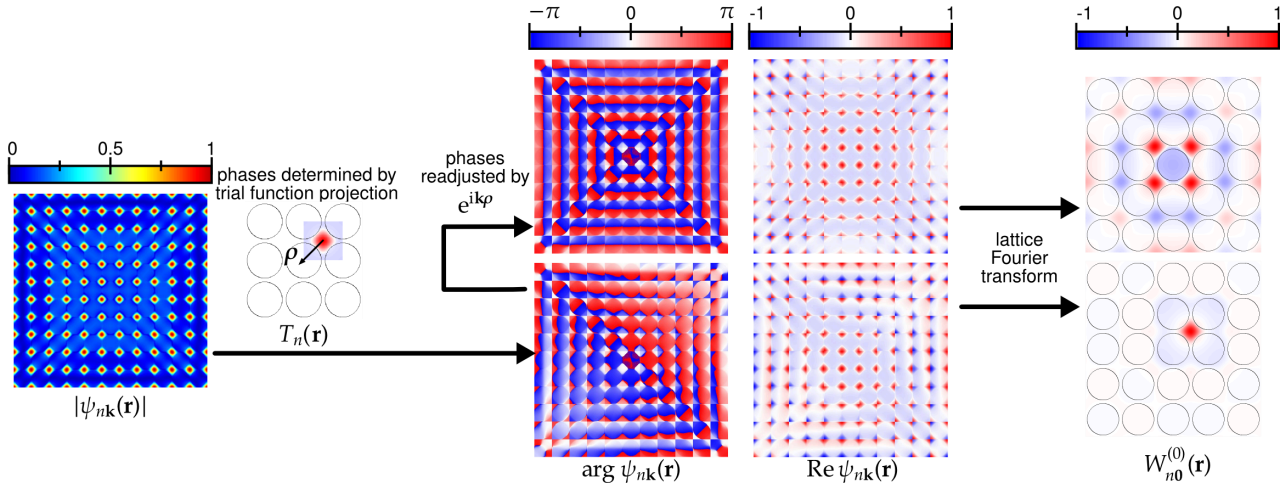


Figure 3.10: For explanation, see caption of Fig. 3.9. The localization center within the WSC can be shifted by $\boldsymbol{\rho} \in \mathbb{R}^d$, when multiplying the phase distribution by the \mathbf{k} -dependent phase factor $\exp(i\mathbf{k}\boldsymbol{\rho})$.

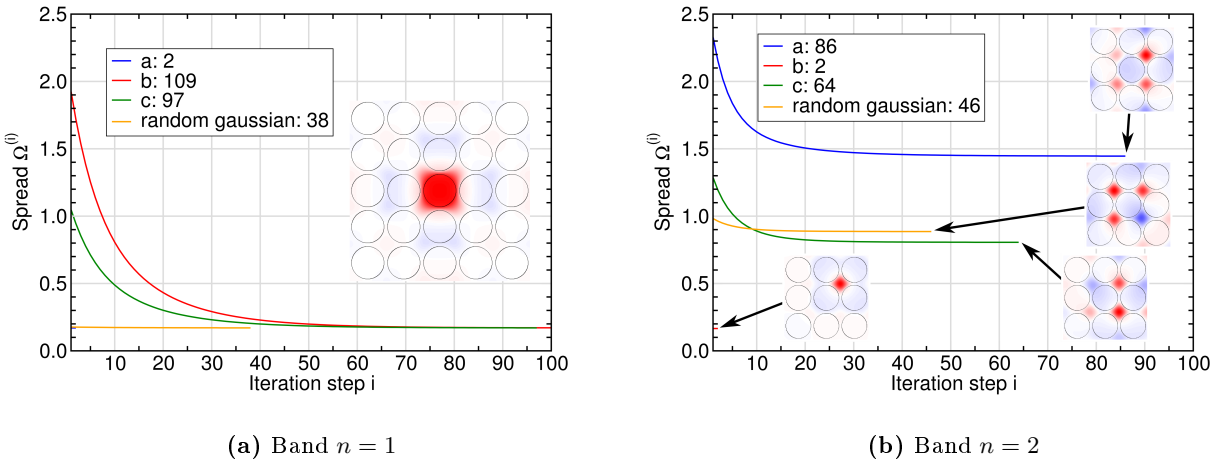


Figure 3.11: Spreads in the Marzari-Vanderbilt minimization procedure and the final WFs obtained for the various choices of trial functions of Figs. 3.5 and 3.6. Legend also shows number of iteration steps before the minimization terminated. Note that the trial function choice by the anticipated symmetry and localization already yielded the maximally localized WFs, while arbitrary choices led to false minima and unsymmetric and worse localized WFs.

3.4.2 Closed Set of Bands 3–7

Bands 3–7 of Fig. 3.1b form a closed set and the site symmetry analysis predicts the unique site symmetry irreps $E(a)$, $E(b)$ and $B_1(b)$ for the WFs, shown in Tab. 3.2.

Γ	B_1	E		E	
X	B_2	A_1	A_2	B_1	B_2
M	A_2	E		E	
WF irreps	$B_1(b)$	$E(b)$		$E(a)$	

Table 3.2: Symmetry of Bloch modes for the closed set of bands 3–7. They yield unique site symmetry irreps for the WFs after Tab. 2.1.

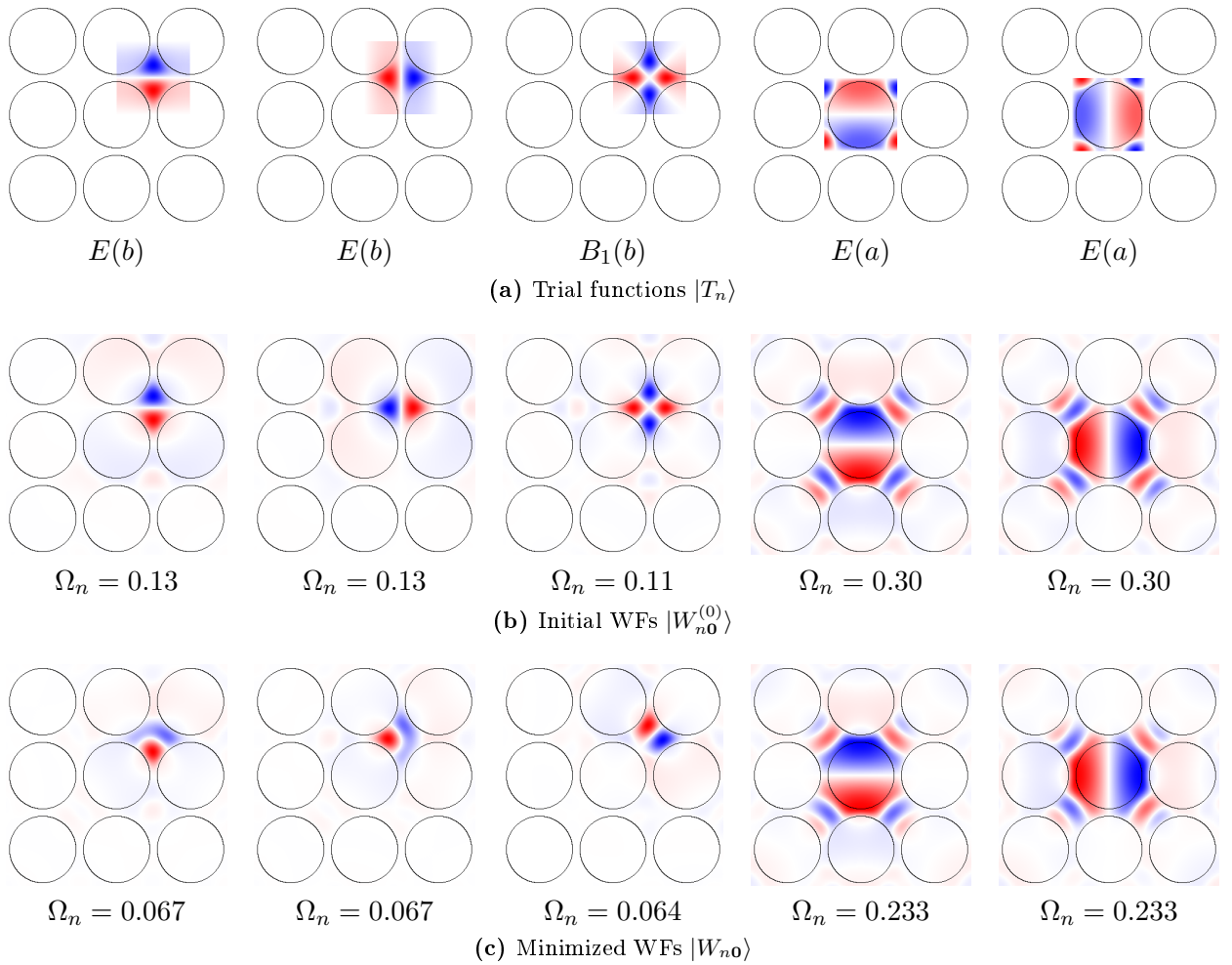


Figure 3.12: Trial functions, corresponding initial (non-minimized) and final (spread minimized) WFs with individual spreads Ω_n for bands 3–7.

The cropped Γ -point trials and initial as well as final (spread minimized) WFs are shown in Fig. 3.12. Though the individual spreads are reduced by the Marzari-Vanderbilt minimization procedure, the WFs

obtained are strangely distorted and do not resemble the anticipated symmetry. However, this result can still be understood with Tab. 2.1. The first three functions localized in the vicinity of Wyckoff position b look quite similar to basis functions of the site symmetry irrep $A(f)$ in Fig. F.9. Apparently the spread minimization tries to hybridize three functions to this four-dimensional irrep $A(f)$ which produces better localized but unsymmetric WFs, since the fourth function is missing. There are three possible solutions:

1. One could work with the already well localized initial WFs.
2. One could enforce the desired irreps by forcing some constraints on the unitary transforms $U(\mathbf{k})$ [37, 38]. This would require a substantial adaption of the Marzari-Vanderbilt algorithm.
3. One could use a larger closed set of bands, in the hope that the new bands introduce the symmetries needed to establish the $A(f)$ representation.

Item 1 would require the least work, item 2 is possible and a systematic approach to obtain the best localization possible. Item 3 depends on the particular band structure and whether a band with the desired symmetries exists in the vicinity of the band set 3–7. Fortunately, this rare situation is the case here and investigated in Sec. 3.4.3.

Let us briefly review the continuity condition for the generalized Bloch modes in this example. Fig. 3.14 shows the absolute values of the complex Bloch modes before and after the trial function projection and the WFs they produce. One can see, how the band structure is disentangled by the trial function projection which puts similar mode profiles into the same generalized Bloch mode bands $|\tilde{\psi}_{n\mathbf{k}}\rangle$.

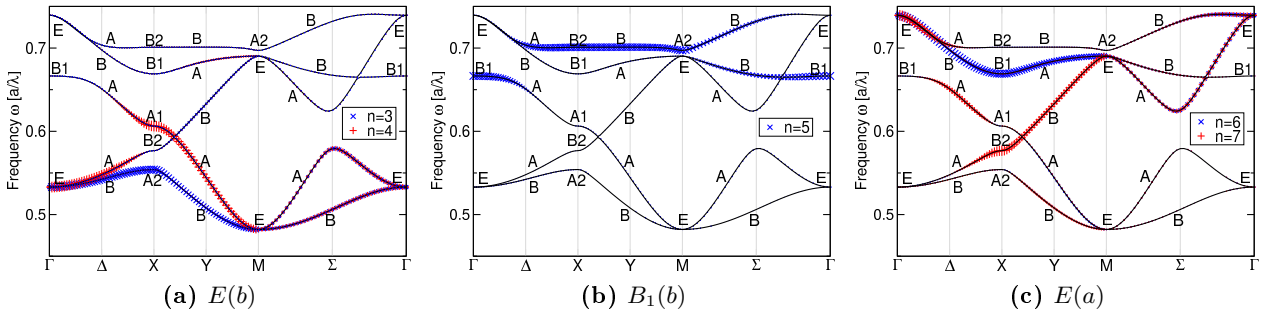


Figure 3.13: Overlaps $|\langle\langle\psi_{m\mathbf{k}}|W_{n\mathbf{0}}^{(0)}\rangle\rangle|^2$ (as symbol size) along the high symmetry lines of the BZ, illustrating the distribution of the generalized Bloch mode profiles that yield maximally localized WFs among the entangled bands. $m = 3, \dots, 7$ labels the bands in black. For explanation, see text.

As a further illustration for the wild distribution of the generalized Bloch mode information which leads to exponentially localized WFs, the contributions $|\langle\langle\psi_{m\mathbf{k}}|W_{n\mathbf{0}}^{(0)}\rangle\rangle|^2$ of the Bloch modes to the particular WFs is plotted in Fig. 3.13. The Bloch mode irrep labels according to the little co-group $G_{0\mathbf{k}}$ are also shown. The $B_1(b)$ WF (Fig. 3.13b), e. g., needs $B_1(\Gamma)$, $B_2(X)$ and $A_2(M)$ Bloch modes according to Tab. 2.1. Fig. 3.13b illustrates this nicely, as the highest contributions for this WF come from the Bloch mode band 5 at Γ . Then the contribution is continuously transferred along the $\overline{\Gamma X}$ -direction between bands 5 and 7 as an anticrossing (because these bands transform like the same irreps A). Afterwards it passes through the X -point, where the Bloch modes form the irrep $B_2(X)$, stays in band 7 until the M -point, where the mode information again is transferred continuously into band 5. The degenerate WF irreps can be visualized in the same fashion (Figs. 3.13a and 3.13c), but all WFs of the irrep have to be considered. The WF information is split up among several Bloch bands here.

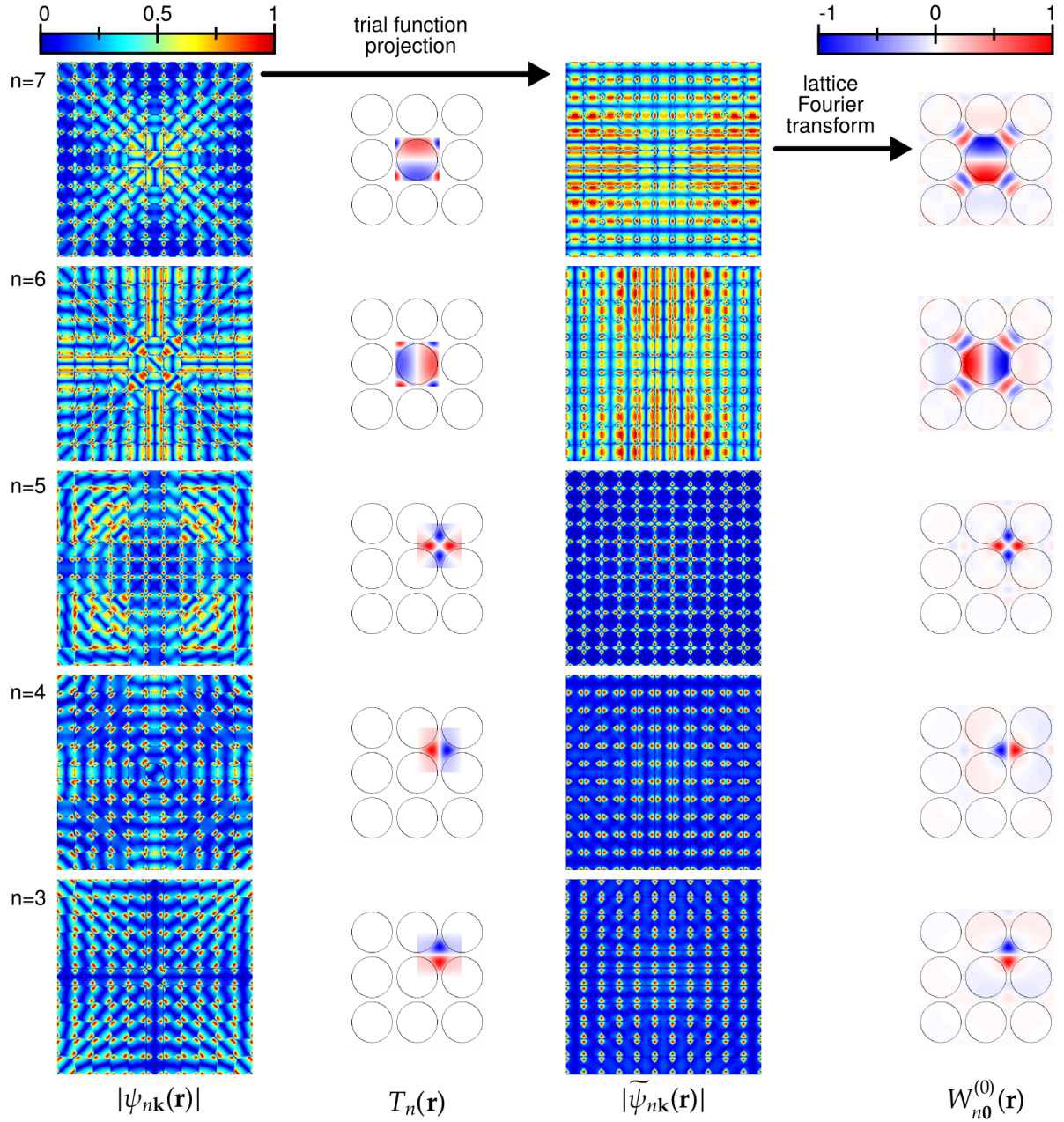


Figure 3.14: Absolute values of the Bloch modes before and generalized Bloch bands after the trial function projection, plotted at each \mathbf{k} -point of the MP mesh of Fig. 3.8. The disentanglement achieved for $|\psi_{nk}\rangle$, whose profiles are continuous in \mathbf{k} now, is clearly visible.

3.4.3 Closed Set of Bands 2–7

As hinted to in Sec. 3.4.2, an alternative closed set of bands can be considered for the Marzari-Vanderbilt spread minimization. The Bloch mode irreps of Bands 2–7 are shown in Tab. 3.3, yielding two possible sets of WFs site symmetry irreps after Tab. 2.1. One possible choice is $A_1(b)$, $E(b)$, $B_1(b)$ and $E(a)$, another choice is $A(f)$ and $E(a)$, where the four functions for $A_1(b)$, $E(b)$, $B_1(b)$ hybridized to four functions of $A(f)$. As it turns out, the hybridized versions have lower spread Ω and are therefore favored by the Marzari-Vanderbilt spread minimization. This is illustrated in Fig. 3.15.

Γ	A_1	B_1	E		E	
X	B_2	B_2	A_1	A_2	B_1	B_2
M	B_2	A_2	E		E	
WF irreps	$A_1(b)$	$B_1(b)$	$E(b)$		$E(a)$	
	$A(f)$				$E(a)$	

Table 3.3: *Symmetry of Bloch modes for the closed set of bands 2–7. Two sets of WF site symmetry irreps are allowed now (see text).*

In this case (as opposed to using bands 3–7), the Marzari-Vanderbilt spread minimization yielded the predicted site symmetry irreps for the WFs. But what if band 2 had not given the desired combination of Bloch mode symmetries? Then we would really have to resort to the initial WFs $|W_{n\mathbf{0}}^{(0)}\rangle$ that may not be as well localized as would be possible after a symmetry enforced spread minimization.

Choosing the proper trial functions for this band set is again crucial for the shape of the final spread minimized WFs as well as for the number of iteration steps. In Fig. 3.16 the spread $\Omega^{(i)}$ in the i th iteration step is shown for various choices of trial functions. The legend labels the following choices of trial functions:

- The Wyckoff letters a , b , c stand for the WSC-cropped Γ -point Bloch modes for bands 3–7,
- ‘ant center’ means Γ -point Bloch modes cropped to a WSC that is centered around the anticipated Wyckoff positions a and b according to the predicted site symmetry irreps (b was chosen to model the irrep $A(f)$),
- ‘ant rep’ stands for the trial functions shown in Fig. 3.15a that have also been unitarily transformed such that they are already basis functions for the predicted site symmetry irreps,
- random Gaussians as trial functions have also been investigated for comparison.

Both sets of trial functions were used in two procedures:

- A steepest descent minimization which terminated for a relative spread change of 10^{-4} and was followed by a CG minimization (Fig. 3.16a), and
- a pure CG minimization (Fig. 3.16b).

The legend shows the *total* number of iteration steps i performed until the iteration terminated.

Both plots show that the influence of the trial functions on the outcome is tremendous. In Fig. 3.16a, the combined use of both minimization techniques yielded the final WFs of Fig. 3.15c in any case, but the number of iteration steps needed varies between 185 and 1055. Apparently, the trial functions that

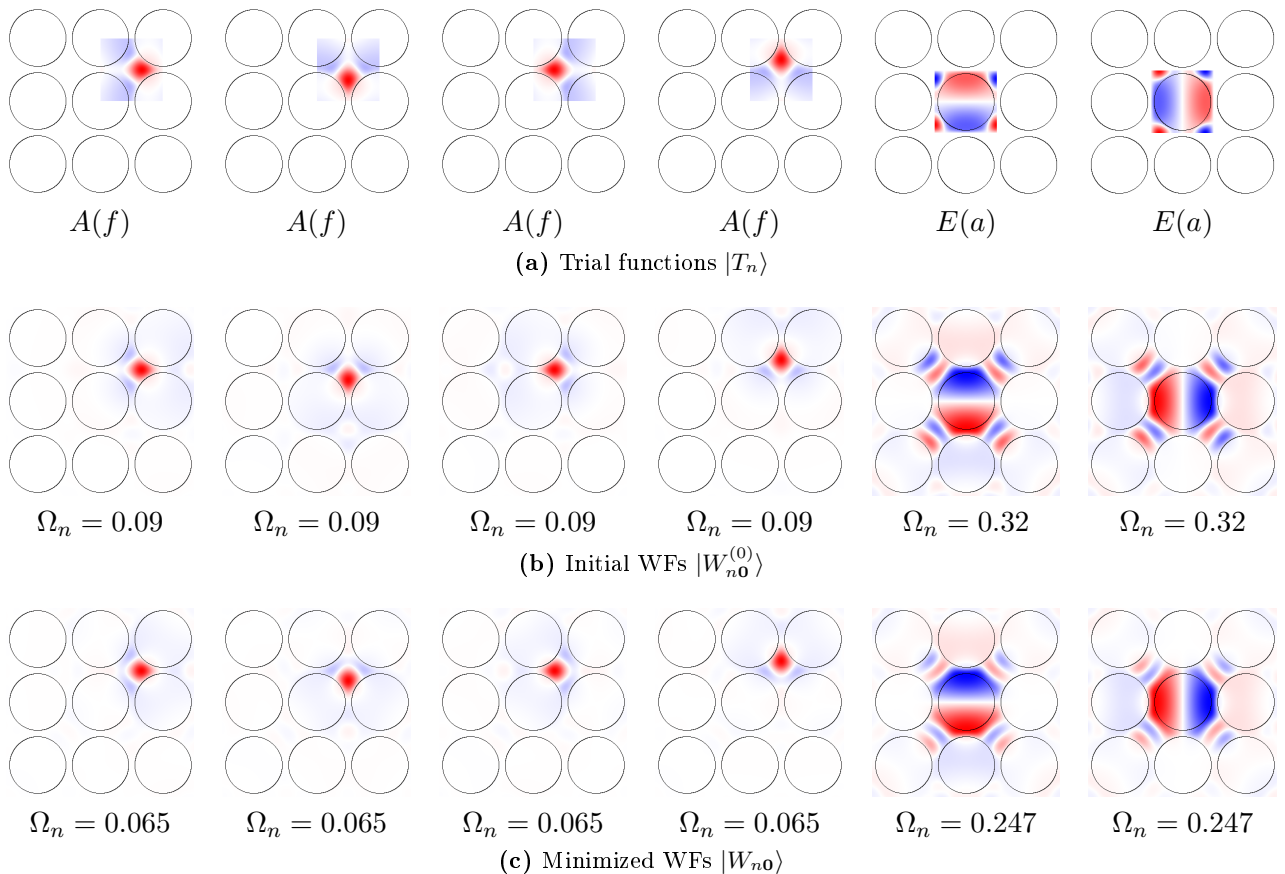


Figure 3.15: Trial functions, corresponding initial (non-minimized) and final (spread minimized) WFs with spreads Ω_n for bands 2–7. The Γ -point trials have been unitarily transformed to the anticipated site symmetry irreps predicted by Tab. 3.3. Note the striking similarity of the Γ -point trials and the initial WFs.

already form bases of the anticipated site symmetry irreps resemble the final WFs the most and yielded the fastest spread minimization procedure. In Fig. 3.16b, only three choices (ant rep, ant center, c) of trial functions led to the WFs of Fig. 3.15c at all. The other choices caused the minimization to get stuck in false local spread minima. Again, the ant rep versions performed best, yielding the spread minimized WFs with the fewest number of iteration steps. This outcome is as expected, since the CG minimization algorithm only works well for good starting points near a local minimum, but then it converges very fast.

In order to decide, whether the WFs obtained are symmetric or not, one usually has to assemble the WFs in real space by evaluating (3.12). Then the symmetry of the resulting WFs can be investigated. Depending on the total number of \mathbf{k} points $N_{\mathbf{k}\text{-res}}$ and the real space resolution $N_{\text{res},i}$ of the Bloch modes, this consumes a lot of time and can easily dominate the whole minimization process. However, the localization centers $\langle \mathbf{r} \rangle_n$ after (3.6) are a byproduct of the spread minimization and available even before the WFs are assembled. In order that the WFs form site symmetry irreps, a necessary condition is that their localization centers should add up to integer multiples of half a lattice vector (accounting

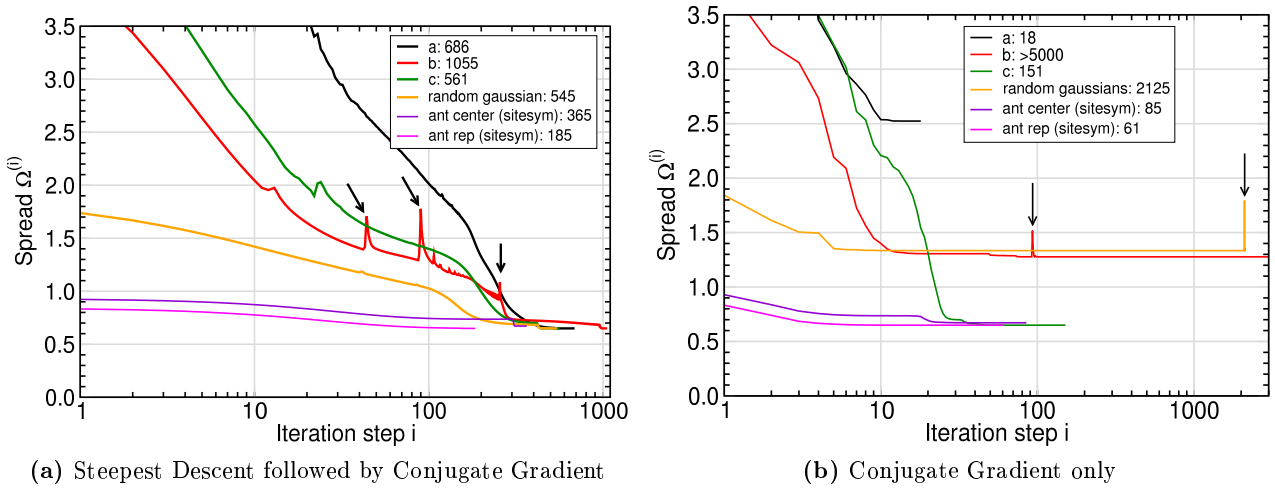


Figure 3.16: Spreads $\Omega^{(i)}$ after i iteration steps for the Marzari-Vanderbilt minimization using various choices of trial functions (i. e., initial WFs $|W_{n\mathbf{0}}^{(0)}\rangle$). For explanation, see text. Black arrows denote instabilities in the minimization algorithm, where the spread suddenly grows instead of becoming smaller.

for the allowed Wyckoff positions b and c), otherwise their centers would be distorted. That means

$$\sum_n \langle \mathbf{r} \rangle_n \stackrel{!}{=} s_1 \mathbf{a}_1 + s_2 \mathbf{a}_2, \quad s_i \in \{0, \pm 0.5, \pm 1, \dots\}. \quad (3.33)$$

If this condition is violated, the WFs are surely unsymmetric and need not be plotted. This also holds for the electric field case, even if $\langle \mathbf{r} \rangle_n$ is not exactly the localization center. Due to the full symmetry of $\varepsilon_{\text{PC}}(\mathbf{r})$, the sum $\sum_n \langle \mathbf{r} \rangle_n$ still has to fulfill condition (3.33). An example for this quantity is found in Tab. 3.5.

3.5 Entangled Bands

In this section, the Souza subspace optimization is demonstrated by an example.

3.5.1 Bands 12–15

As seen in the previous sections, the proper choice of trial functions is vital for the rate and success of convergence of the Marzari algorithm. Therefore, we usually want to include as much knowledge about the final WFs as possible into the trial functions. For entangled bands (i.e., a subset of bands from a closed set of bands), the symmetry analysis according to Sec. 2.5.6 cannot be applied. Furthermore, the artificially closed set of bands generated by the Souza subspace optimization cannot be analyzed in terms of irreps of little co-groups $G_{0\mathbf{k}}$, since the generalized Bloch modes are some linear combination of the proper Bloch modes and, hence, do no longer form definite irreps with definite symmetries.

However, we may still take a look at the available proper Bloch mode symmetries and assemble a list of the most probable anticipated WFs symmetries and localization centers. This will help us in constructing the trial functions from the Γ -point Bloch modes.

We consider bands 12–15 of the closed set 12–19 for didactical purposes, since 12–19 is still small enough to be processed with the Marzari-Vanderbilt spread minimization algorithm.

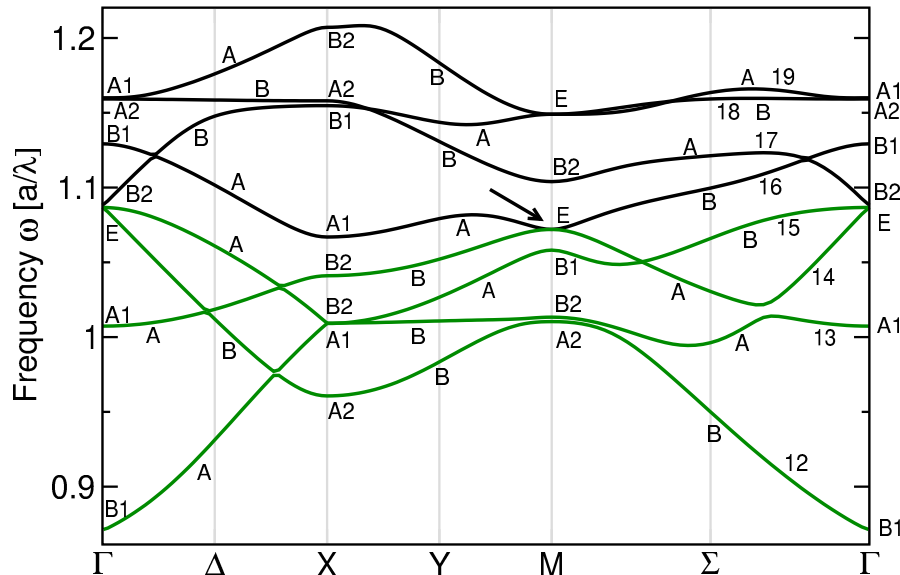


Figure 3.17: Bands 12–19 of the TE square model system with little co-group irrep labels. We want to construct four WFs. However, the lowest four bands (12–15, green) do not form a closed set, since they are degenerate with a higher band at the M -point (denoted by the arrow).

Marzari-Vanderbilt Spread Minimization

The Bloch mode symmetries from Fig. 3.17 for the bands 12–15 are shown in Tab. 3.4. The bands do not form a closed set now, with the consequence that only one of two degenerate E irrep Bloch modes is available at the M -point. However, this band 15 belongs to irreps $B(Z)$ along \overline{XM} and $A(\Sigma)$ along $\overline{M\Gamma}$. By the compatibility relations, these modes could as well end in a B_2 irrep at the M -point (as band 17 does). In the MP mesh of Fig. 3.8 that is used for constructing the WFs of this chapters, the

M -point is not included. That means, judging by symmetry alone, the numerical WFs do not “know” if there is an E or B_2 mode at the M -point. In the latter case, the site symmetry analysis by Tab. 2.1 allows the WFs irreps $B_1(a)$, $A_1(b)$ and $B_1(c)$. Indeed, these WFs symmetries are obtained from the Marzari-Vanderbilt spread minimization regardless of the particular trial functions used. Furthermore, as Fig. 3.19c shows, the contributions to the $B_1(c)$ WFs also come from the Bloch modes belonging to band 15 around the M -point, supporting the interpretation of the single $E(M)$ Bloch modes as $B_2(M)$.

Γ	B_1	A_1	E	
X	A_1	B_2	A_2	B_2
M	B_1	B_2	A_2	(E, B_2)
WF irreps	$B_1(a)$	$A_1(b)$	$B_1(c)$	

Table 3.4: *Symmetry of Bloch modes for the set of bands 12–15. At M only one of two degenerate E modes is available for this band set. However, by the compatibility relations, this mode may also appear as having B_2 symmetry. For explanation, see text.*

The connection between Bloch mode symmetries and final WFs can also be seen from the overlap data of Fig. 3.19. The overlaps $|\langle\langle\psi_{m\mathbf{k}}|W_{n\mathbf{0}}^{(0)}\rangle\rangle|^2$ illustrate which Bloch modes m in the band structure contribute to the final spread minimized WFs n at each \mathbf{k} . One can clearly see that the bands with the proper symmetry predicted by the site symmetry analysis of Tab. 2.1 contribute the most to a WF forming a particular site symmetry irrep. This observation corresponds well to the plot of the overlaps $|\langle\langle\psi_{m\mathbf{k}}|T_n\rangle\rangle|^2$ of Bloch modes m with the trial functions n chosen in Fig. 3.18a. The similarity between the plots shows that the overlap of the Γ -point Bloch modes used as trial functions yields a very good estimate for the expected contributions of Bloch modes to the final WFs. Additionally, as Fig. 3.18b shows, using these trials already gives initial WFs $W_{n\mathbf{0}}^{(0)}$ that are very close to the spread minimized final WFs. The degenerate individual spread Ω_n indicates that the initial WFs are more symmetric than the final spread minimized ones. Thus, the minimization procedure tends to distort the WFs. All in all, these results illustrate nicely the ability of properly chosen symmetry adapted Γ -point trials to give a very good estimate of the final maximally localized symmetric WFs.

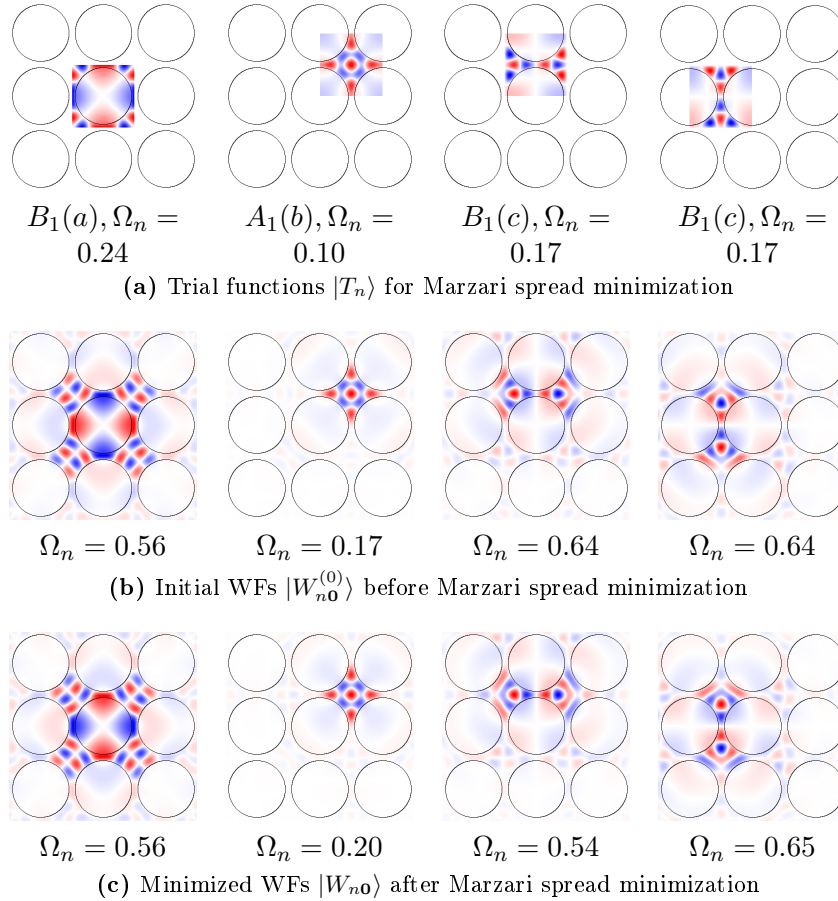


Figure 3.18: Trial functions, corresponding initial WFs and final WFs after Marzari spread minimization (no Souza subspace optimization was carried out) for the bands 12–15 of Fig. 3.17. The anticipated site symmetry irreps constructed from the Γ -point Bloch modes were used as trials. Judging from the non-degenerate individual spread Ω_n , the degenerate $B_1(c)$ modes are still a bit distorted, though they look perfectly symmetric. The initial WFs are again very similar to the Γ -point trial functions used.

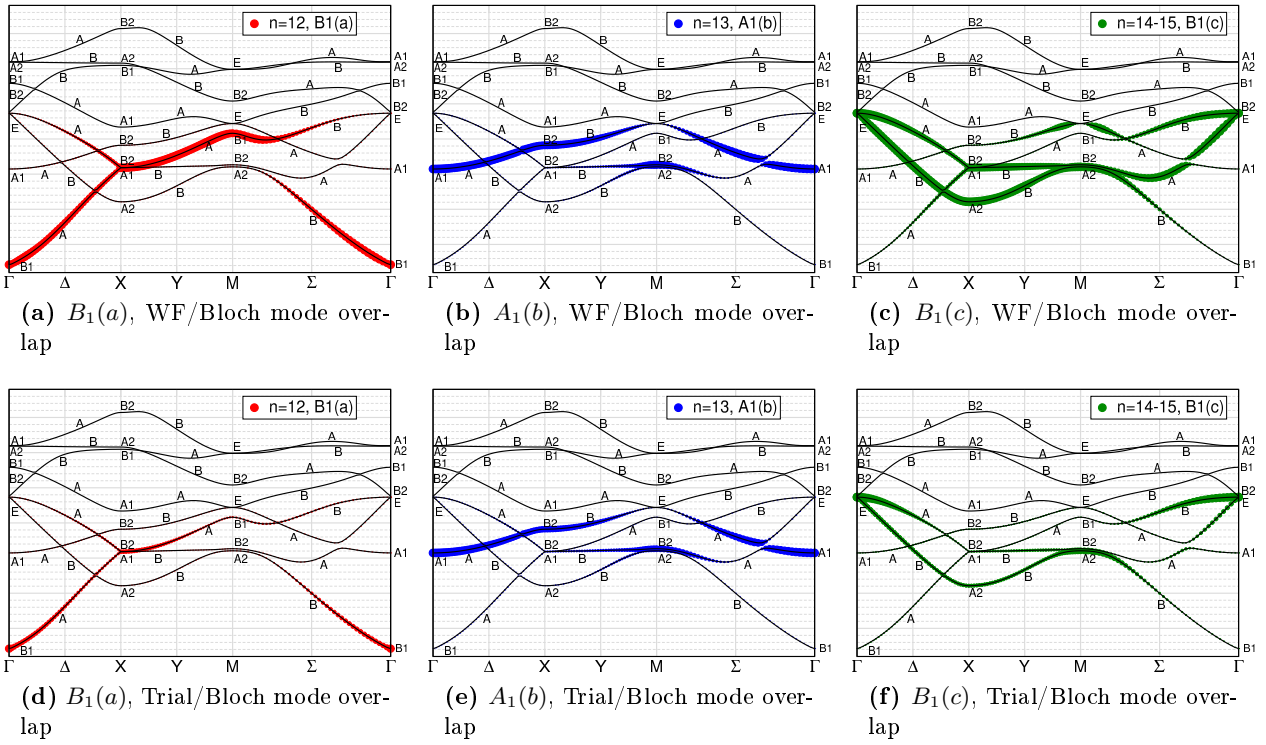


Figure 3.19: Bloch mode overlaps (as symbol size) (a)–(c) $|\langle \psi_{m\mathbf{k}} | W_{n\mathbf{0}}^{(0)} \rangle|^2$ with final WFs (Fig. 3.18c) and (d)–(f) $|\langle \psi_{m\mathbf{k}} | T_n \rangle|^2$ with trial functions (Fig. 3.18a) along the high symmetry lines of the BZ, illustrating the entanglement of the Bloch mode information that yield maximally localized WFs. $m = 12, \dots, 19$ labels the bands in black. For explanation, see text.

Souza Subspace Optimization

Now we want to see which WFs can be created from the Souza subspace optimization using the chosen band set. To this end, we vary the frequency windows and trial functions and investigate the symmetries and spreads of the resulting final WFs. For the sake of simplicity, we use the same sets of trials for both the Souza and Marzari-Vanderbilt initialization.

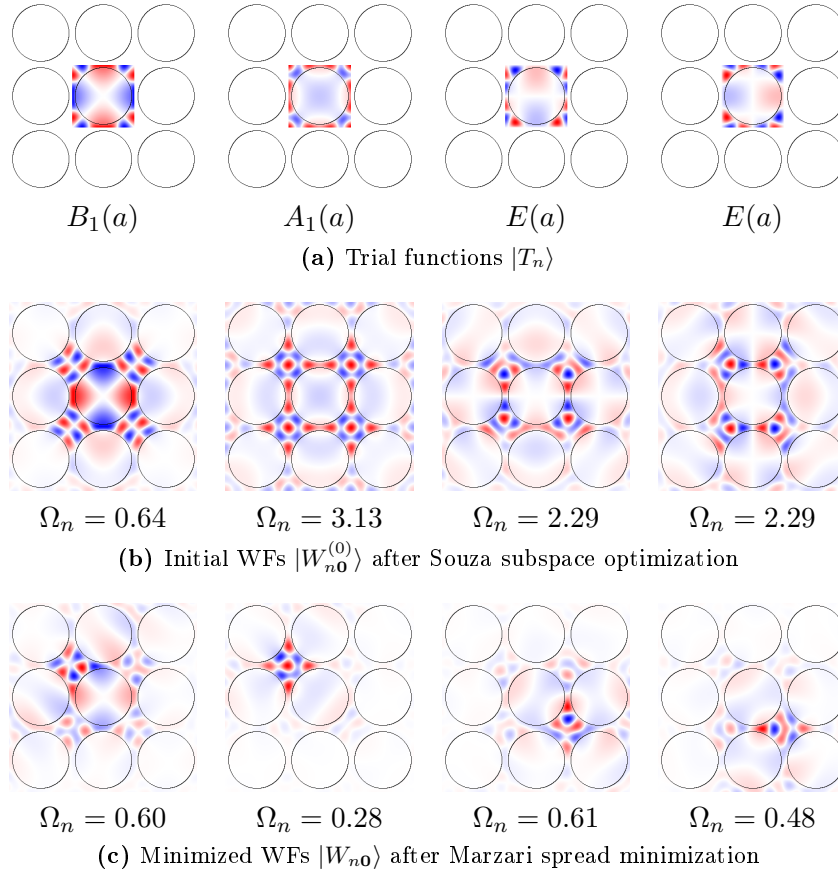


Figure 3.20: Trial functions (Γ -point trials cropped around Wyckoff position a) and corresponding initial WFs after Souza subspace optimization ($\omega_{\text{inner}} = 0.0$, $\omega_{\text{outer}} = 1.1$) and after Marzari spread minimization.

First of all, we keep the outer frequency $\omega_{\text{outer}} = 1.1$ fixed and do not use an inner frequency, effectively setting $\omega_{\text{inner}} = 0.0$. This allows the mode information of band 16 (first black band in Fig. 3.17) to be incorporated into the WFs. The Γ -point trials cropped to a WSC around Wyckoff position a were used in Fig. 3.20 and yielded strongly distorted WFs. Random Gaussians (Fig. 3.22) gave similar results. The use of trials cropped around Wyckoff position b , however, gave four symmetric and highly localized $A(f)$ WFs with degenerate individual spreads (Fig. 3.21). There are two possible unitary transforms to create trial functions transforming like the irrep $A(f)$ from Γ -point Bloch modes. Both choices lead to the same final WFs with the combined Souza-Marzari-Vanderbilt algorithm. They are shown in Figs. 3.23 and 3.24, where the similarity between the trials and the final spread minimized WFs is striking. Comparing the spreads of initial and final WFs, it seems that the trial function combination with lower initial spread determines the shape of the final WFs, but this conjecture is based merely on the investigation of this single case. However, the information about the initial WF spread is readily available before any

iteration procedure and can be used to aid in the choice of appropriate trials before any time consuming minimization or WF assembly step has been carried out.

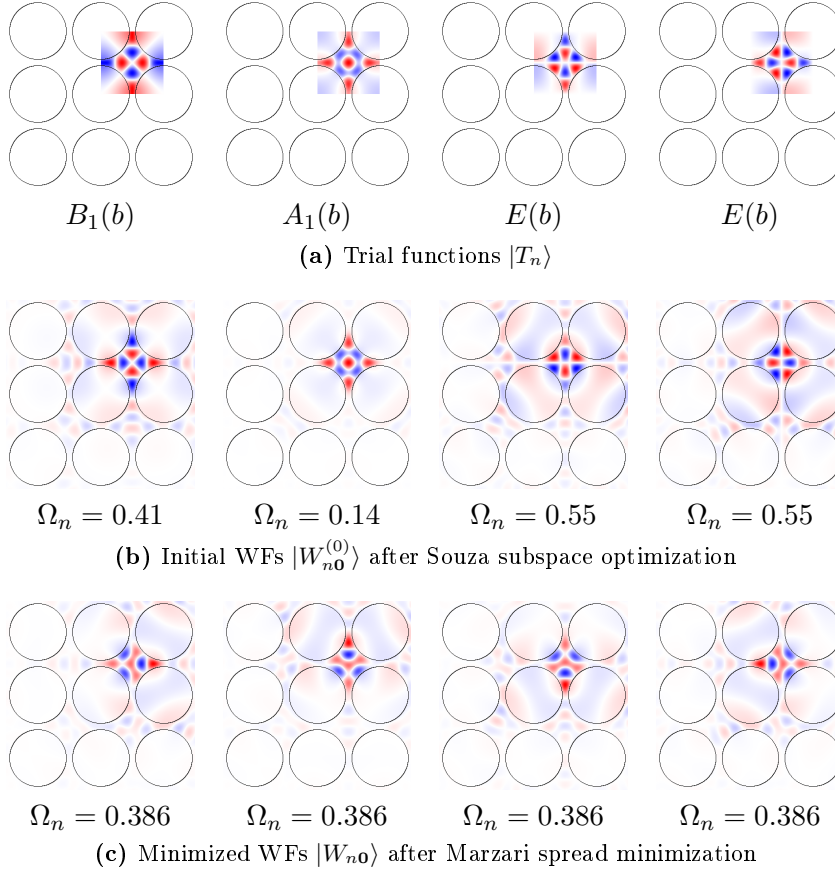


Figure 3.21: Trial functions (Γ -point Bloch modes cropped around Wyckoff position b) and corresponding initial WFs after Souza subspace optimization and after Marzari spread minimization.

The importance of choosing proper trial function combinations can be seen from Fig. 3.25, most of all Fig. 3.25a. There we see that the trial choices of a , c and random Gaussians yield a *smaller* invariant spread Ω_I as the choices c , $A(f)$ variant 1 and $A(f)$ variant 2 do. However, only the latter three give symmetric and localized WFs with smallest final spread Ω . Additionally, the anticipated $A(f)$ irrep trials of variant 1 yield the final WFs after the smallest number of iteration steps. Thus, it is not the global minimum of Ω_I that leads to maximally localized final WFs, but the local minimum which is determined by the proper choice of trial functions.

The degree of distortion of the WFs from the anticipated irreps can be estimated before carrying out the time consuming assembly procedure (3.15) and then plotting the WFs. By (3.33), we can determine the deviation from symmetric versions of the WFs in each iteration step by evaluating the sum of their localization centers according to (3.20). Tab. 3.5 lists the sum of centers for the final WFs of this section. Note how centers sum up according to (3.33) for the symmetric WFs in the plots.

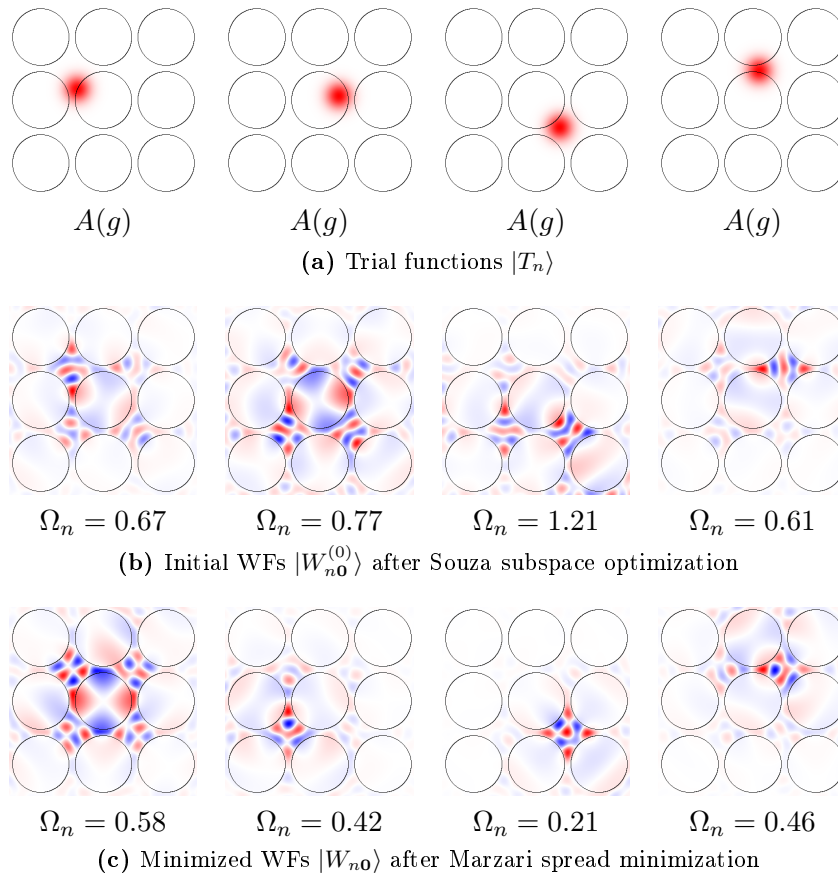


Figure 3.22: Trial functions (random Gaussians) and corresponding initial WFs after Souza subspace optimization and after Marzari spread minimization.

Trial function set $ T_n\rangle$	$\left 2 \sum_n \langle \mathbf{r} \rangle_n - \mathbf{R}_{\text{nearest}}\right ^2$
WSC a (Fig. 3.20)	1.05×10^{-1}
WSC b (Fig. 3.21)	2.90×10^{-16}
WSC c (no plots)	7.70×10^{-4}
Rnd. Gaussians (Fig. 3.22)	4.02×10^{-1}
ant. rep 1 (Fig. 3.24)	1.30×10^{-15}
ant. rep 2 (Fig. 3.23)	5.50×10^{-17}

Table 3.5: Deviation of (twice the) sum of centers (3.20) from the nearest lattice vector $\mathbf{R}_{\text{nearest}}$ for the spread minimized WFs obtained with the combined SMV spread minimization for bands 12–15, depending on the chosen trial functions. Note how the small deviations from (3.33) are correlated with the symmetric WFs.

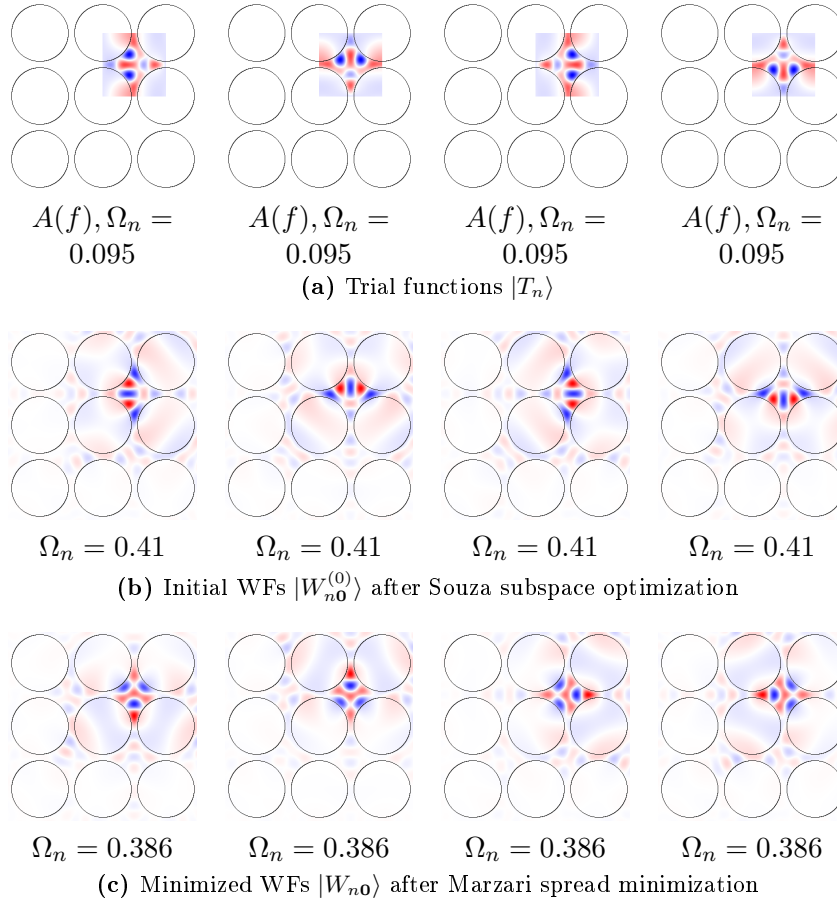


Figure 3.23: Trial functions and corresponding initial WFs after Souza subspace optimization and after Marzari spread minimization. These trial functions are referred to as anticipated $A(f)$ irrep 2.

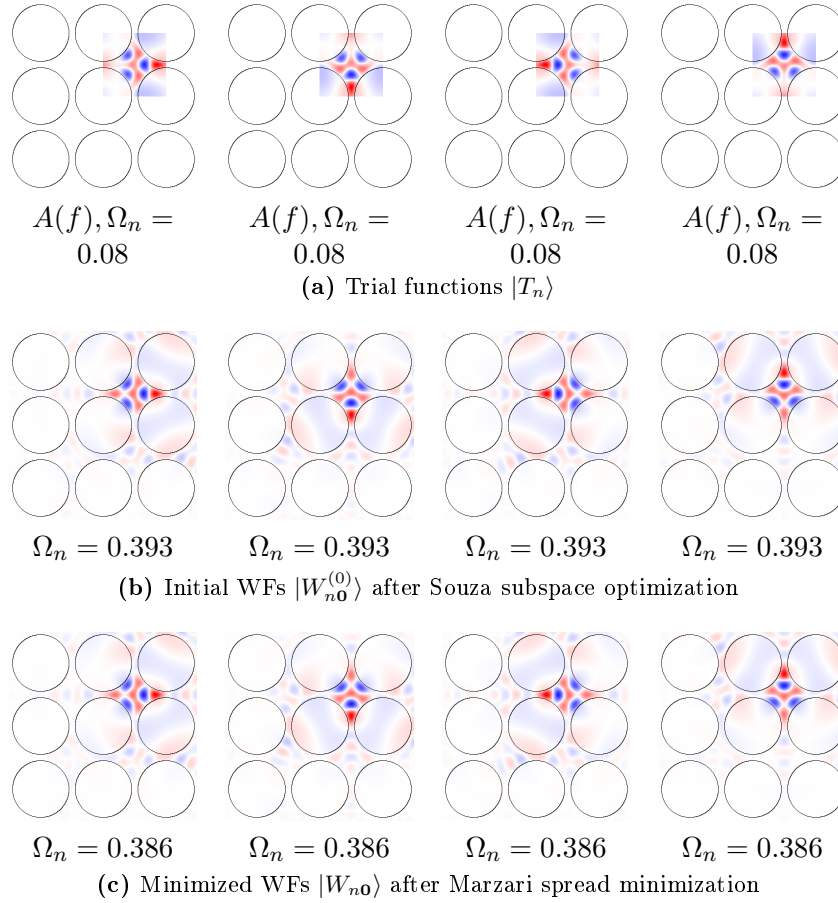


Figure 3.24: Trial functions and corresponding initial WFs after Souza subspace optimization and after Marzari spread minimization. These trial functions are referred to as anticipated $A(f)$ irrep 1.

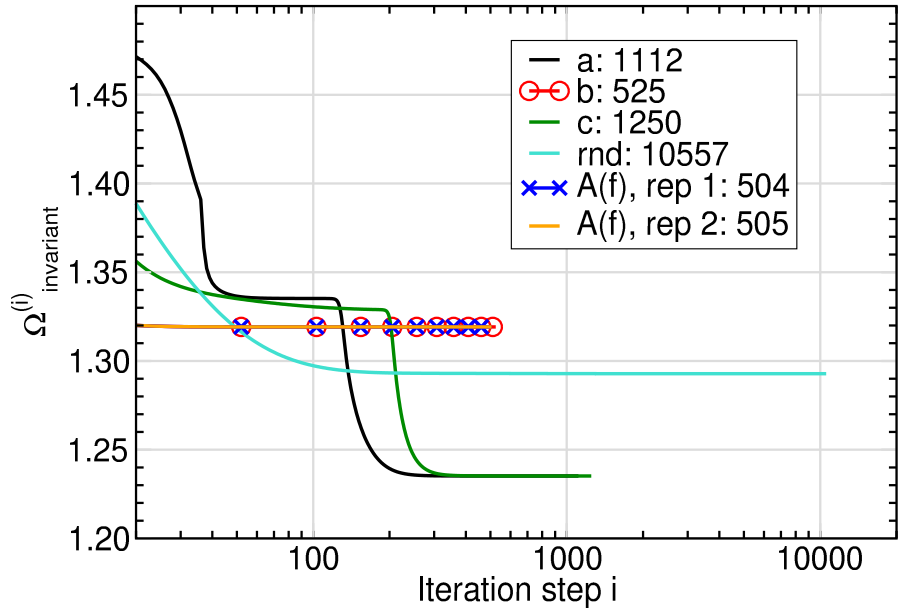
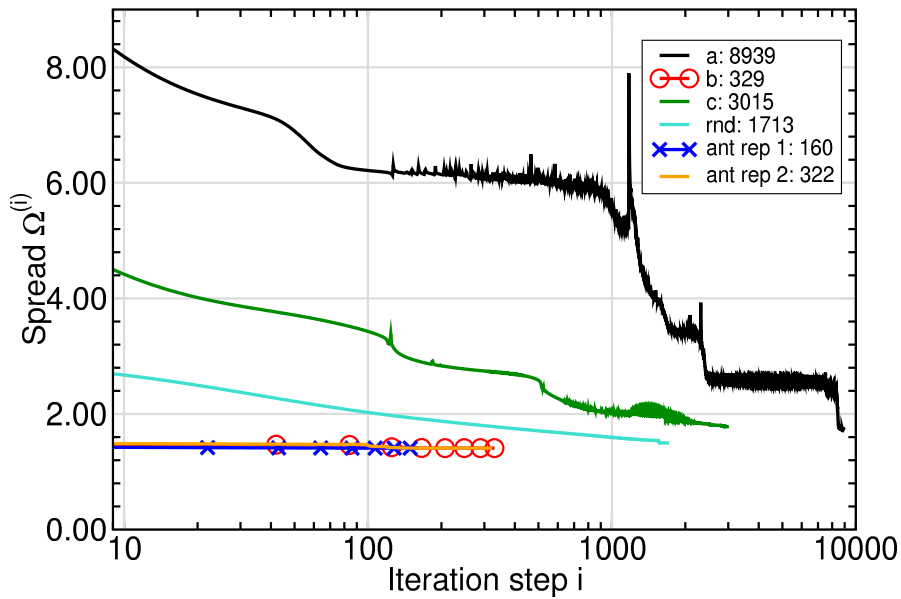
(a) Ω_I convergence for various trial functions(b) Ω convergence for various trial functions

Figure 3.25: Convergence of Ω_I for the Souza subspace optimization and the final combined spread Ω for the subsequent Marzari-Vanderbilt spread minimization for various choices of trial functions shown in Figs. 3.20 to 3.24. Trials used were Γ -point Bloch modes cropped to a WSC around Wyckoff position *a* (Fig. 3.20), *b* (Fig. 3.21), *c* (functions not plotted), random Gaussians (Fig. 3.22), and the anticipated $A(f)$ irreps by the site symmetry analysis, in variant 1 of Fig. 3.24 and variant 2 of Fig. 3.23. Note the fast convergence and lack of instabilities (increasing spread causing peaks) when using *b*, irrep variant 1 and irrep variant 2.

Outer Frequency Window ω_{outer} and Wannier Function Localization

Now we want to investigate the influence of the frequency windows on the localization of the final WFs. We use the $A(f)$ trial functions of Fig. 3.24 for both the Souza and Marzari-Vanderbilt initialization. Therefore, the trial function overlap $|\langle\psi_{m\mathbf{k}}|T_n\rangle|^2$ is plotted along with the final spread achieved in Fig. 3.26. The trial function overlap gives a rough estimate which Bloch bands will contribute signifi-

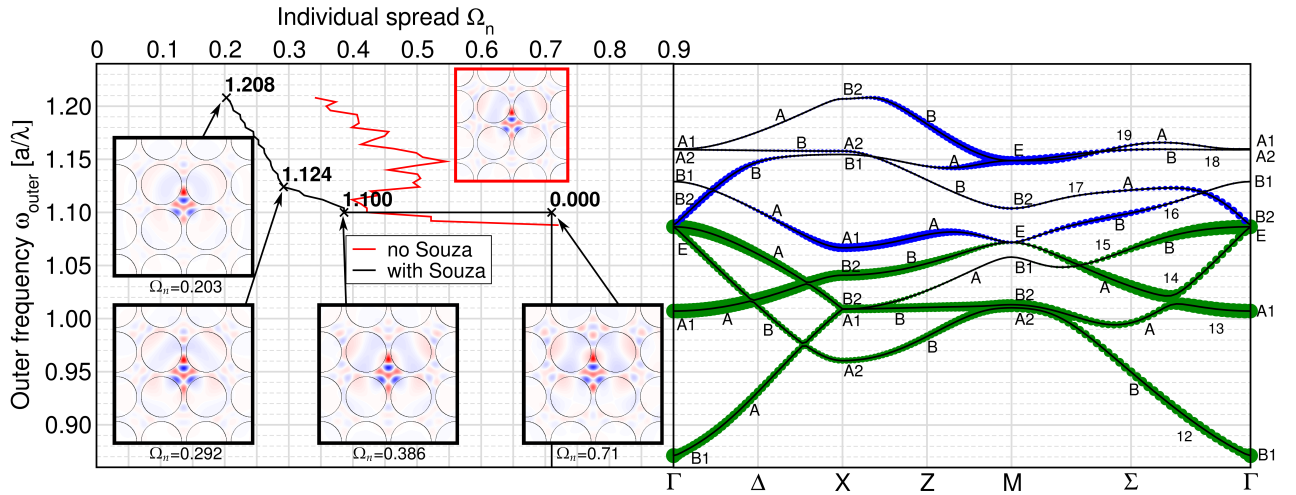


Figure 3.26: Left: Individual spreads Ω_n of final WF band $n = 12$ for various upper frequency values ω_{outer} (no Souza means, only the subspace initialization but no Souza iteration step was carried out). The inset pictures are annotated with the particular values for spread and ω_{outer} . Right: Overlaps $\sum_n |\langle\psi_{m\mathbf{k}}|T_n\rangle|^2$ for the anticipated site symmetry irreps $A(f)$ trial functions of Fig. 3.24a for each Bloch band $m = 12, \dots, 19$. For explanation, see text.

cantly to the final WFs. In the spread plot (Ω achieved for outer frequency ω_{outer}), the inset WFs shown were obtained with and without running the Souza subspace optimization, but with initializing the subspaces using varying upper frequencies ω_{outer} after Sec. 3.3.5. The WF for $\omega_{\text{outer}} = 0.0$ was obtained by using the pure Marzari-Vanderbilt minimization only, the results of which are shown in Fig. 3.27. This gives an impression on the effect of the Souza subspace optimization procedure and its influence on the spread of the final WFs.

As soon as the Souza optimization is used ($\omega_{\text{outer}} = 1.1$), the individual spread Ω_n drops to less than half the previous value. This corresponds with the trial function overlap of band 16, in particular along \overline{XM} and the missing overlap of band 14. The unnecessary mode information of band 14 may leave the subspace while the mode information of band 16 now enters the subspace forming the final WFs (cf. Fig. 3.3). With increasing ω_{outer} the individual spread Ω_n drops continuously with a knee at $\omega_{\text{outer}} = 1.124$. The reason for this behavior is not fully clear.

The read curve in Fig. 3.26 shows the spreads obtained for just carrying out the subspace initialization procedure without any further Souza iteration step optimization. These WFs show no unified behavior. Their spread rises and falls, showing that one cannot neglect the subspace optimization if one is interested in obtaining localized WFs.

The correspondence between trial function overlap and localization of WFs again nicely illustrates the power of the site symmetry analysis. The final $A(f)$ WFs are almost supported by bands 12–15 alone (green bands in Fig. 3.17): instead of the B_1 Bloch mode irrep at M , this would require the two E modes at M . But this information is only available when the frequency windows mentioned above are

used and the unwanted B_1 Bloch modes around M may leave the subspace.

We compare the final WFs and final spreads obtained by the Souza subspace optimization with the ones obtained by using the Marzari-Vanderbilt minimization only, as in the previous section. This time, however, we use the $A(f)$ version 1 trial functions which is shown in Fig. 3.27.

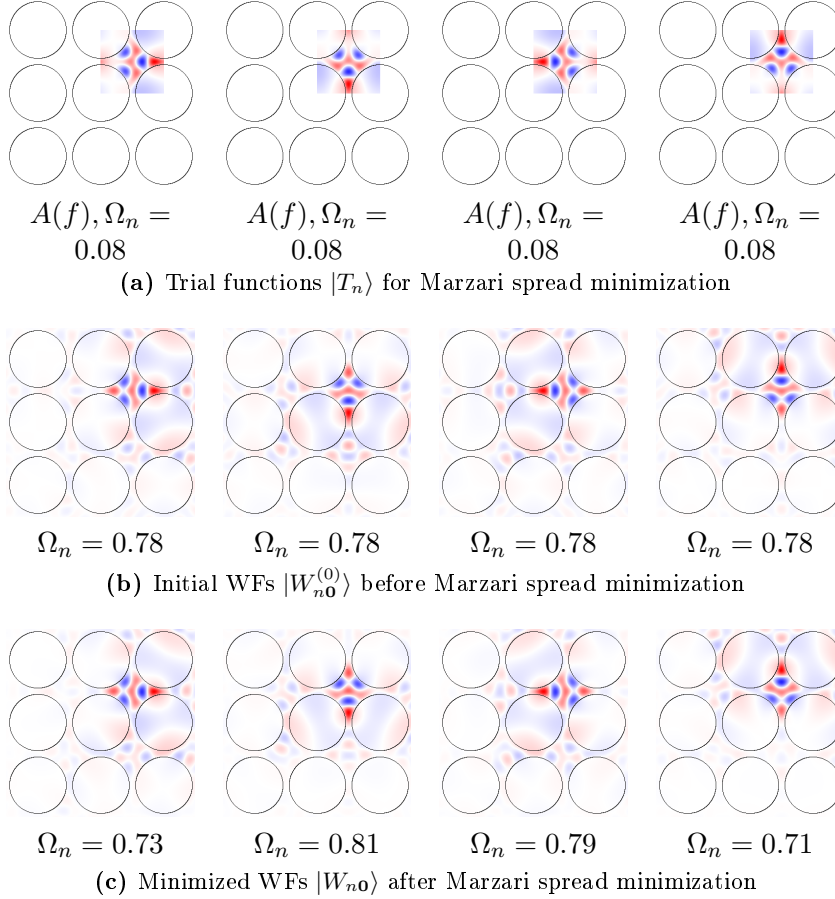


Figure 3.27: Trial functions, corresponding initial WFs and final WFs after Marzari spread minimization (no Souza subspace optimization was carried out) for the bands 12–15 of Fig. 3.17. The anticipated site symmetry irreps constructed from the Γ -point Bloch modes were used as trials. However, the final WFs are slightly distorted which can also be seen from their non-degenerate individual spreads.

Though it is possible, to construct initial WFs with the desired symmetry (which was also possible for the bands 1 and 2, cf. Figs. 3.5 and 3.6), the individual spread of $\Omega_n = 0.78$ is still large, and in fact, larger than the combined spread of the WFs obtained in the previous section considering the proper site symmetry analysis of the set of bands 12–15. The Marzari-Vanderbilt spread minimization does not improve the spread significantly here, but it distorts the symmetric initial WFs.

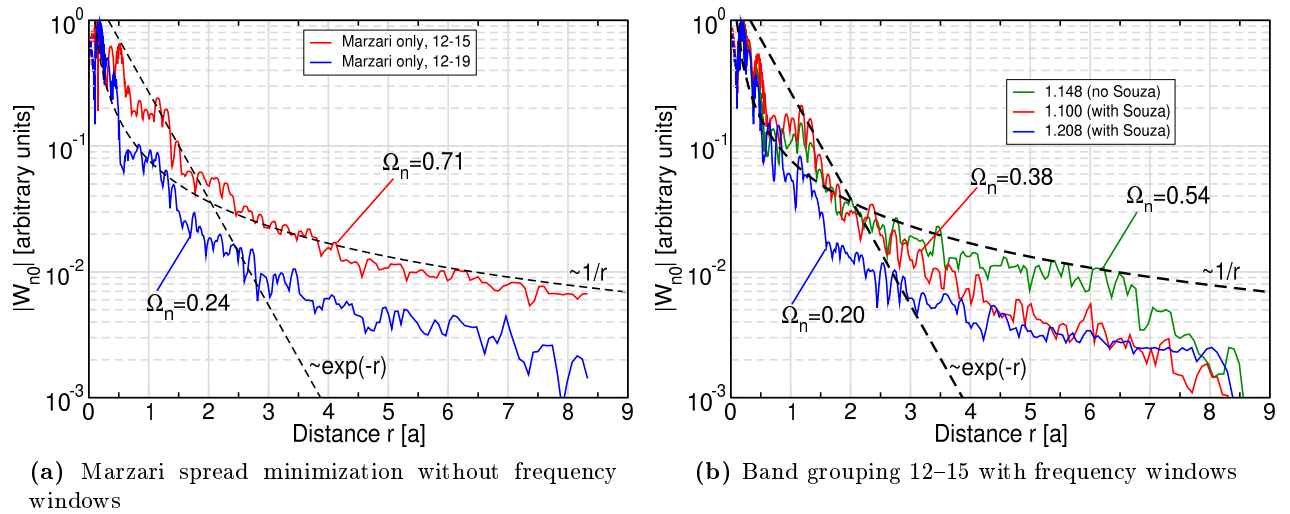


Figure 3.28: Real space decay behavior of WF band $n = 12$ obtained with the various methods discussed in this section (no Souza means, only the subspace initialization but no Souza iteration step was carried out). For distance r from the center $\langle \mathbf{r} \rangle$ of the WF the value $\max_{\mathbf{r}:|\mathbf{r}-\langle \mathbf{r} \rangle|=r} |W_{n0}(\mathbf{r}-\langle \mathbf{r} \rangle)|$ has been plotted (maximal WF value on circles around the localization center $\langle \mathbf{r} \rangle$, but still retain rather high values between 10^{-2} and 10^{-3} of the maximal function value for larger distances).

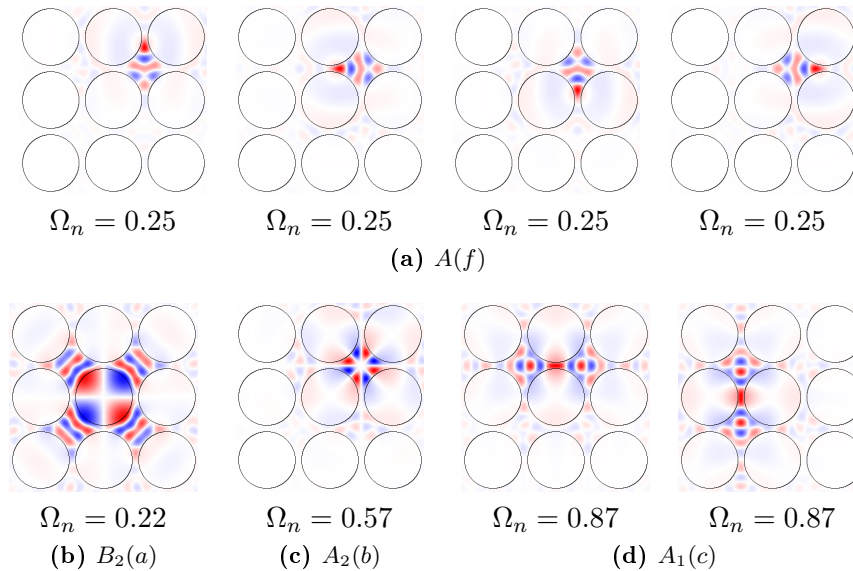


Figure 3.29: Final WFs for closed set 12-19 obtained with Marzari-Spread minimization. The WF irreps obtained agree with the available Bloch mode irreps Fig. 3.17 and the allowed irreps of Tab. 2.1.

3.6 Discussion of Spread Minimization Procedure: Triangular Lattice

The band structure for the lowest 9 bands of the triangular model system is shown in Fig. 3.30. The

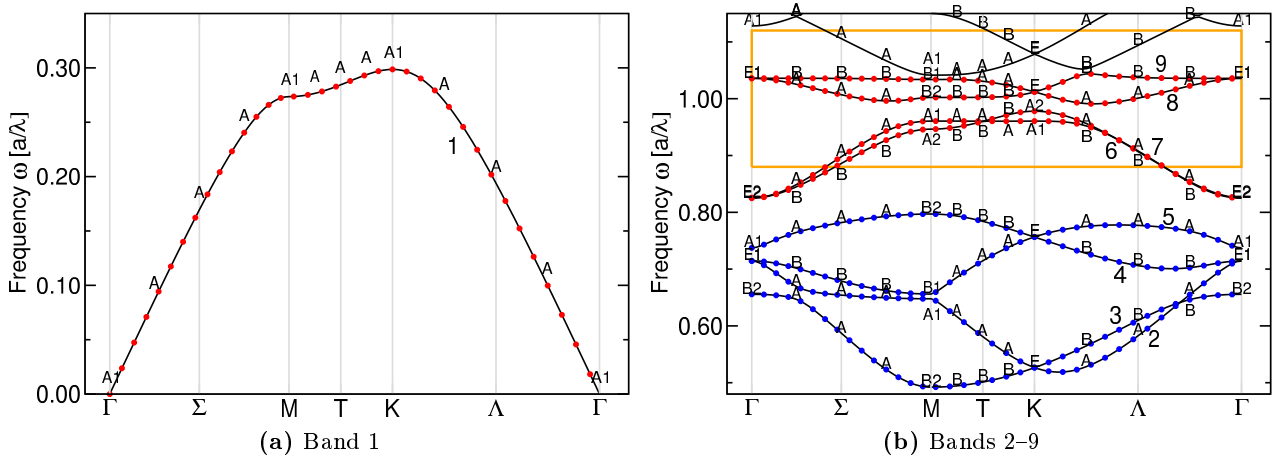


Figure 3.30: Band structure with irreps of Bloch modes along the high symmetry lines of the triangular model system. The frequency range 0.88–1.12 is shown as the orange rectangle.

resulting possible combinations of WF irreps for the closed sets of bands according to Tab. 2.2 are shown in Tab. 3.6. Some WFs of the combinations suggested in Tab. 3.6 are shown in Fig. 3.31. Bands 2–5 form a closed set with definite irreps (Fig. 3.31b), and so do bands 8–9, though they are rather extended with large spread Ω (Fig. 3.31d). For the set 6–7, no irrep is predicted at all. Therefore, it is more promising to look at the band set 2–9.

For the closed set of bands 2–9, the Marzari-Vanderbilt spread minimization yields distorted functions, even though Tab. 3.6 predicted definite site symmetry irreps for this set. This case is similar to Fig. 3.12, where the predicted irreps were not obtained because unsymmetric combinations yielded an even smaller combined spread Ω . The reason here is that the band gap between bands 9 and 10 is quite small which allows those bands to swap mode information of bands 8 and 9 with higher bands.²

A symmetry enforcing variant of the Marzari-Vanderbilt algorithm could help here, but is not yet available. However, using the Souza subspace optimization with the parameters of Fig. 3.31f gathers the WF contributions from the higher bands and creates symmetric WFs.

Though the dipoles $E_1(a)$ from the set 2–5 and 2–9 (symmetric SMV versions) look quite similar, they differ drastically in their decay behavior (Fig. 3.32). While the closed set versions decay exponentially, the SMV versions decay like $1/|\mathbf{r}|$ after about three lattice sites distance from the localization center. Thus, the Souza subspace optimization destroys the theoretically expected exponential localization of the WFs, and it is desirable to use the Marzari-Vanderbilt (MV) spread minimization for closed sets whenever possible. We will address this problem again later.

3.7 Instabilities of Souza Subspace Optimization

Unfortunately, the Souza subspace optimization is quite sensitive to changes in the MP mesh resolution $N_{\mathbf{k}\text{-res},i}$. Here is an example from the triangular lattice for the bands 10–17 of the triangular model

²The smaller the gap between closed sets of bands, the less localized the resulting WFs are. This is discussed by Kohn [74] and He and Vanderbilt [27].

Γ	A_1					Γ	E_1	A_1	B_2			Γ	E_2				
M	A_1	E_1	B_1	B_2	A_1	B_2	A_1	B_2	M	A_1	A_2	K	A_1	A_2			
K	A_1	E			E			K	A_1	A_2		WF irrep	n.a.	n.a.			
(a) Band 1		(b) Bands 2–5						(c) Bands 6–7 (no definite WF irreps available)									
Γ	E_1					Γ	E_1					Γ	E_1				
M	A_1					M	B_1					M	B_1	B_2			
K	A_1					K	E					K	E				
WF irrep		$E_1(a)$				WF irrep		$E_1(a)$				WF irreps		$E_1(a)$		$A(e)$	
(e) Bands 6–9				(f) Bands 2–9													

Table 3.6: Symmetry of Bloch modes for the closed sets of Fig. 3.30 and WF site symmetry irreps they allow. Not all combinations yield definite WF irreps. Some site symmetry irreps are not unique; only one possible combination is shown then.

system.

For a MP mesh resolution of $N_{\mathbf{k}\text{-res},i} = 11$ and the parameters $\omega_{\text{inner}} = 1.3$ and $\omega_{\text{outer}} = 1.49$ the WFs of Fig. 3.35a were obtained. By the symmetries of the Bloch modes in Tab. 3.7, the WFs irreps $E_2(a)$ and $A(e)$ would be allowed if at K one A_1 irrep were switched with the missing E basis function in the higher bands (arrow in Fig. 3.33). This is the task of the Souza subspace optimization: allowing the contaminating contributions of the A_1 Bloch modes to diffuse to higher bands and letting the wanted contributions from the full E irrep enter the subspace that builds the WFs.

Γ	E_2	A_1	B_2	E_1	E_2				
M	A_1	A_2	A_1	A_1	A_2	B_1	B_2	B_2	
K	E			A_1	A_2	E	(E)		A_1
WF irreps		$E_2(a)$		“ $A(e)$ ”					

Table 3.7: Symmetry of Bloch modes for the bands 10–17 of Fig. 3.33. The E irrep at the M -point in parentheses means that only one of the two basis functions is included in this band set choice. The $A(e)$ irrep is not complete and therefore put in quotation marks.

This works well for $N_{\mathbf{k}\text{-res}} = 11$, but constructing the same WFs with the same frequency windows

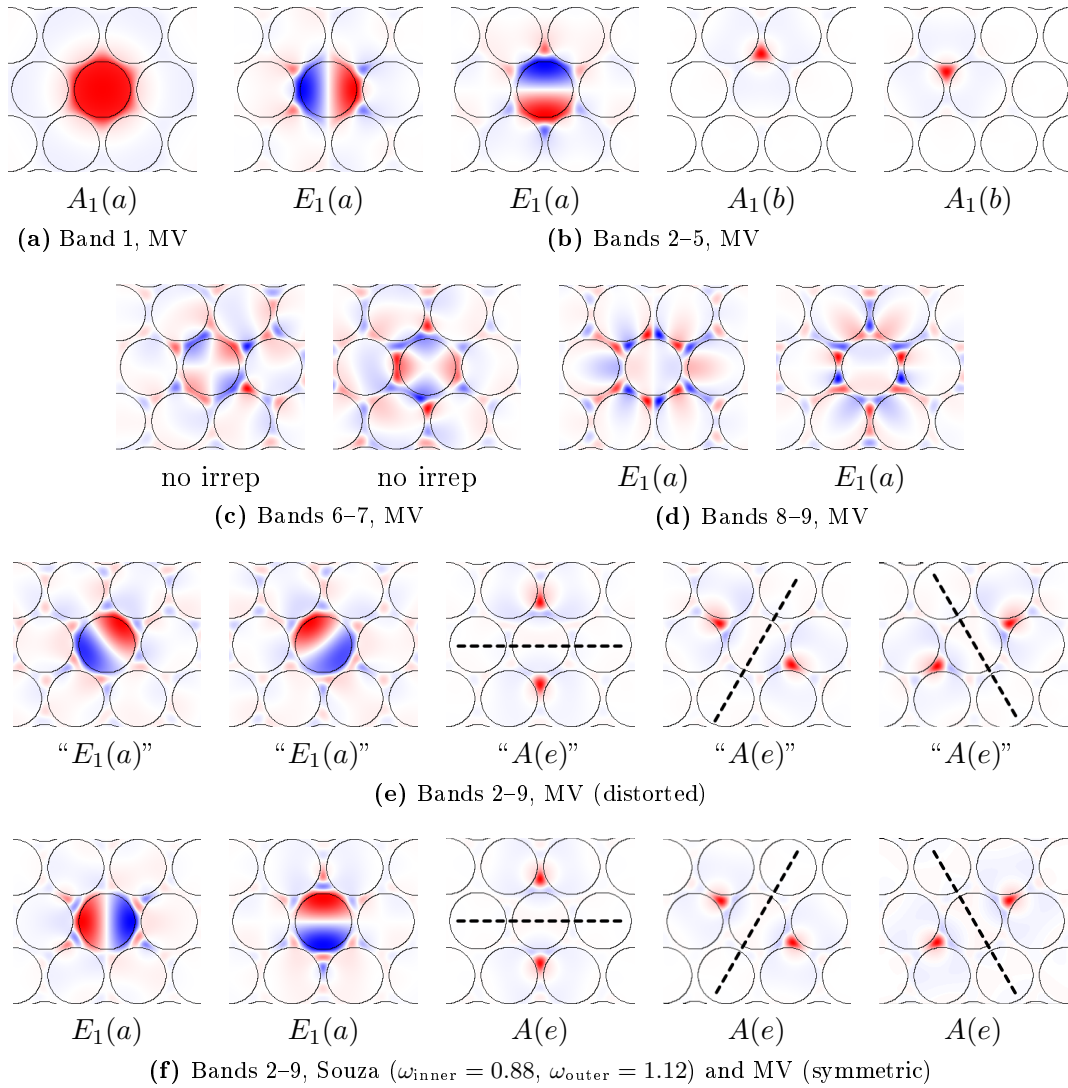


Figure 3.31: WFs for some of the combinations of Tab. 3.6 obtained by (a)–(e) the Marzari-Vanderbilt spread minimization and (f) the full Souza-Marzari-Vanderbilt algorithm (with the frequency windows shown in Fig. 3.30). The WFs shown in (a), (c), (d) and (b) have the predicted symmetries of Tab. 3.6. The WFs in (e) show slight deviations from these symmetries similar to Fig. 3.12c. Instead of choosing a larger band set (as in Fig. 3.15c), the Souza algorithm has been used here to create the more symmetric WFs of (f).

fails for the higher MP mesh resolution $N_{\mathbf{k}\text{-res},i} = 25$ and yields distorted WFs (Fig. 3.35b), even though the WFs obtained from the lower resolution were used as trials (and as such, the best possible starting configuration for the spread minimization procedure).

One can ask now, what if the frequency windows have been chosen too large such that the Souza subspace optimizer gets confused and creates undesired subspaces (that yield distorted functions)? In order to choose different, specially adapted frequency windows, we have a look at the overlaps $|\langle\langle\psi_{m\mathbf{k}}|W_{n\mathbf{0}}\rangle\rangle|^2$ for the WFs obtained with the lower MP mesh resolution ($N_{\mathbf{k}\text{-res},i} = 11$) along the high symmetry lines of the PC again in Fig. 3.34. The upper orange rectangle denotes the frequency window used for con-

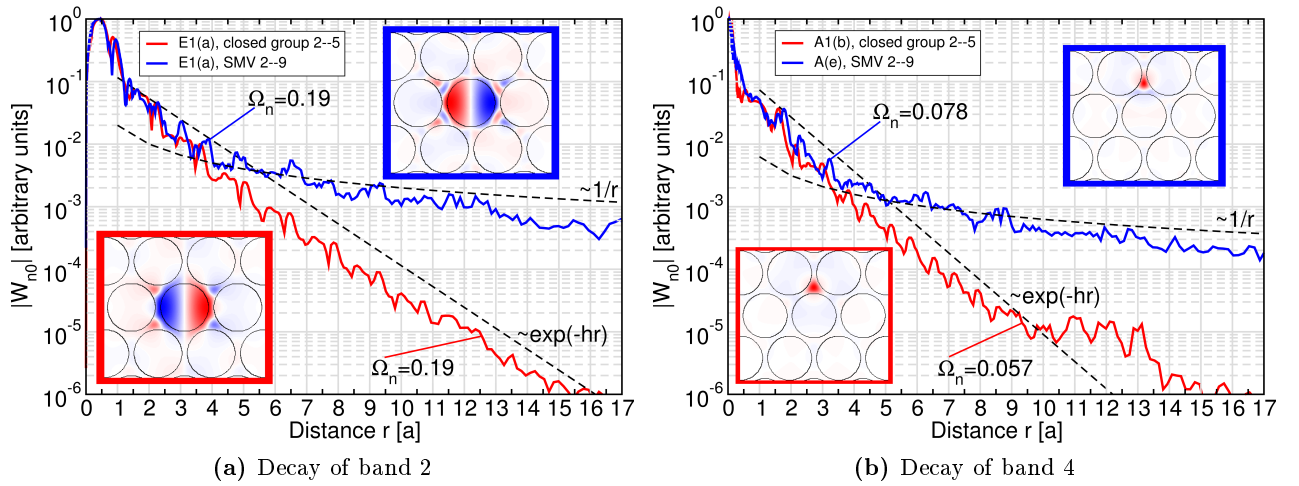


Figure 3.32: Real space decay behavior of WF from Figs. 3.31b and 3.31f. For distance r from the center $\langle \mathbf{r} \rangle$ of the WF the value $\max_{\mathbf{r}:|\mathbf{r}-\langle \mathbf{r} \rangle|=r} |W_{n0}(\mathbf{r} - \langle \mathbf{r} \rangle)|$ has been plotted (maximal WF value on circles around the localization center). The Marzari-Vanderbilt spread minimized WFs for closed band sets (Fig. 3.31b) are exponentially localized, whereas the Souza subspace optimization (Fig. 3.31f) destroys the exponential localization. Note the equal individual spreads Ω_n in (a).

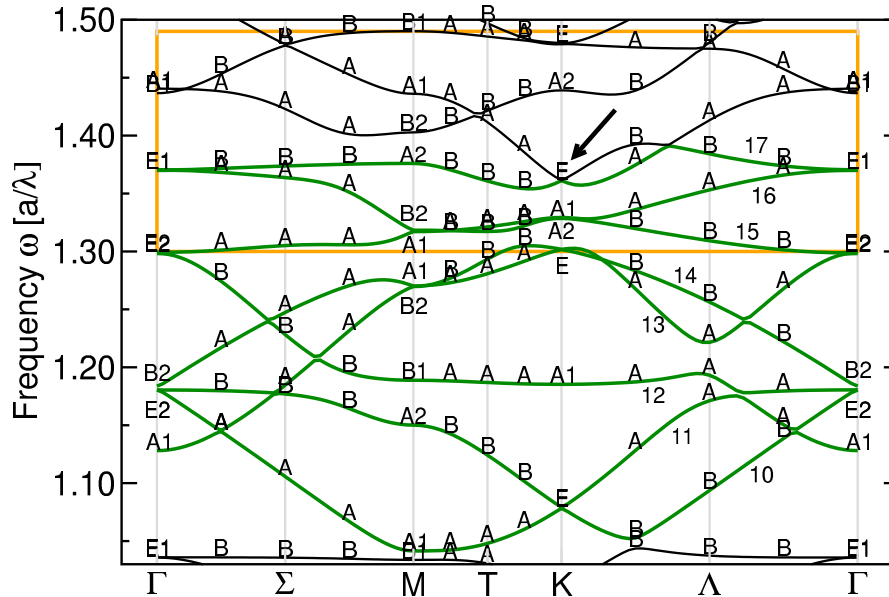


Figure 3.33: Bands 10–17 (green) with little co-group irrep labels. Note that only one of the two E irrep basis functions at the M -point (arrow) is included in this choice of band set 10–17.

structuring the WFs of Fig. 3.35. First of all, the overlaps of WFs and Bloch modes become small very fast for higher frequencies, indicating that the higher bands below $\omega_{\text{outer}} = 1.49$ do not contribute at all to the WFs. Therefore, two new, lower frequencies $\omega_{\text{outer}} = 1.395$ and $\omega_{\text{outer}} = 1.44$ are tried with the same new inner frequency $\omega_{\text{inner}} = 1.31$ (cyan rectangles). This new inner frequency freezes a larger portion of band 15 with large overlaps for the $E_2(a)$ WFs. These Bloch modes are not altered by the

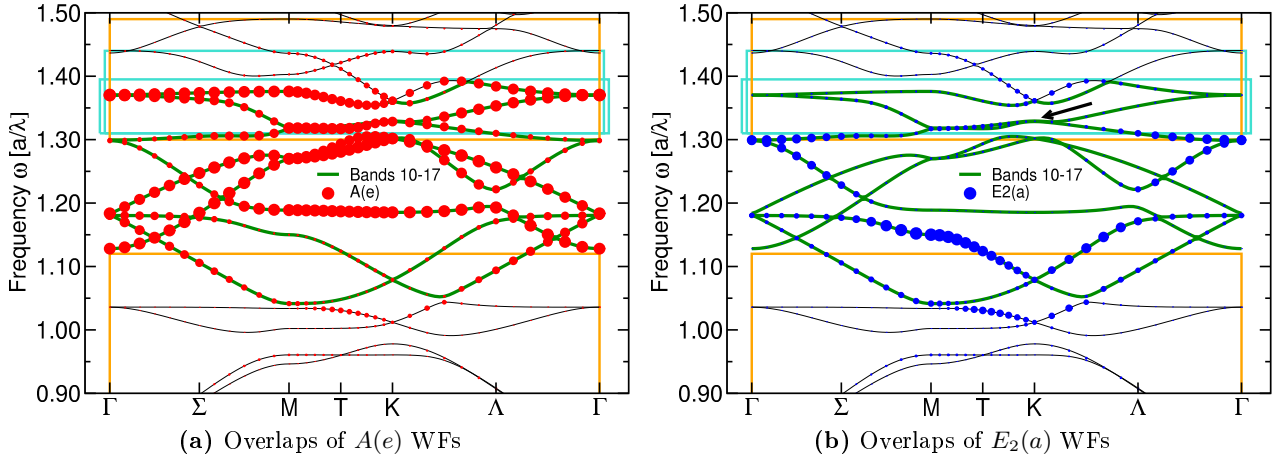


Figure 3.34: Overlaps $|\langle \psi_{m\mathbf{k}} | W_{n\mathbf{0}} \rangle|^2$ (as symbol size) for the final WF bands $n = 10, \dots, 17$ (Fig. 3.35a) obtained with the full Souza-Marzari-Vanderbilt spread minimization with frequencies $\omega_{\text{inner}} = 1.3$ and $\omega_{\text{outer}} = 1.44$ (upper orange rectangle) and MP mesh resolution $N_{\mathbf{k}\text{-res},i} = 11$ (cf. Fig. B.7b). The Bloch bands $m = 10, \dots, 17$ are shown as fat green lines. The lower orange rectangle denotes the frequency window $\omega_{\text{inner}} = 0.88$ and $\omega_{\text{outer}} = 1.12$ for the computation of the preceding WF set of Fig. 3.31f. The turquoise rectangles denote the frequency windows with $\omega_{\text{inner}} = 1.31$ and $\omega_{\text{outer}} = 1.395$ and $\omega_{\text{outer}} = 1.44$, respectively. The black arrow denotes the region around the M-point, where the mismatching A_1 Bloch modes should be switched with the E-modes of the higher bands by the Souza subspace optimization. For further explanation, see text.

Souza subspace optimization. For comparison, also a much lower inner window $\omega_{\text{inner}} = 1.28$ is used. However, no resulting WFs are satisfyingly symmetric (Fig. 3.36).

A possible explanation is given in Fig. 3.37 by further defining the type of entanglement between bands. This definition was formed by the author based on the observations presented in this chapter. Bands are trivially entangled³ if they are actually simple overlays of closed groups of bands (Fig. 3.37a), for which the site symmetry analysis of Sec. 2.5.6 was applicable. In that case, the Souza subspace optimization may in principle be able to separate the Bloch mode information and symmetry to artificially separate the sets such that they support WFs for the predicted irreps.

If the entanglement is not such a simple overlay (Fig. 3.37b), the site symmetry analysis is not applicable and it may not be possible at all to separate the mode information in a way as to create symmetric WFs.

Note how in both examples band combinations with the same degeneracy points occur, but in Fig. 3.37a the branches at K along $\overline{K\Gamma}$ continuously meet again at Γ , whereas they drift apart in Fig. 3.37b. The latter situation also occurs for bands 10–17 in Fig. 3.33 (denoted by black arrow).

However, this is a mere empirical observation, since a general theory concerning entangled bands is lacking. Most of all, a thorough analysis should provide rigorous definitions, whether one is talking about frequency ordered, symmetry ordered or continuously ordered (i. e., continuous in \mathbf{k}) band branches.

To back up this hypothesis about trivially and non-trivially entangled bands, we can ask if the predicted WFs irreps are at least obtained if we treat a larger closed band set with the MV spread minimization only. Luckily, the band set 10–26 is closed. Therefore, we have a look at the WFs for $N_{\mathbf{k}\text{-res},i} = 25$

³Coincidentally, there is also a rigorous mathematical term, the trivial vector bundle, connected with the localization of generalized WFs [94, 95]. Thanks to Christian Wolff for bringing my attention to this.

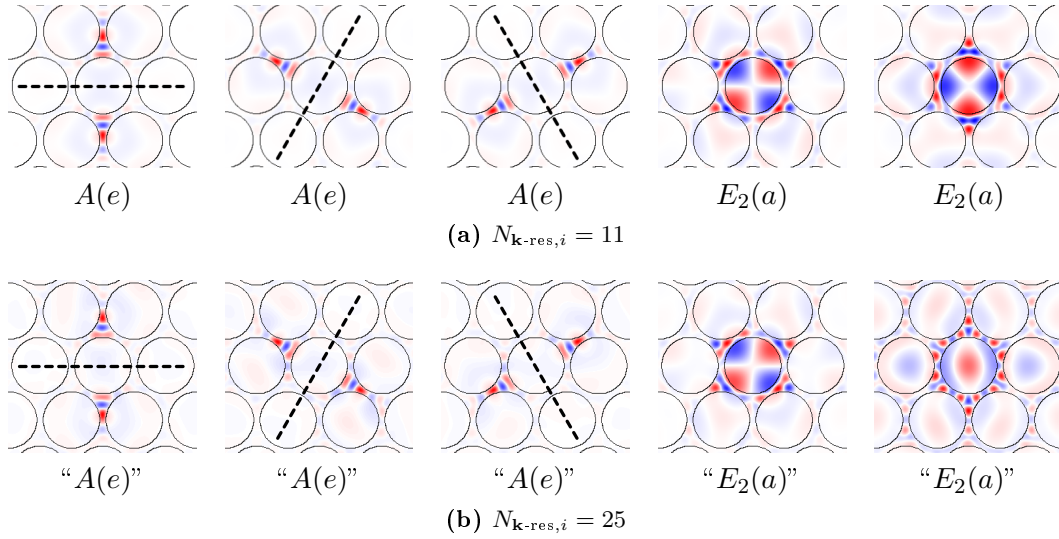


Figure 3.35: The WFs obtained for Bands 10–17, with Souza ($\omega_{\text{inner}} = 1.3$, $\omega_{\text{outer}} = 1.49$) and MV spread minimization for two different MP mesh resolution $N_{\mathbf{k}\text{-res},i}$. The higher $N_{\text{res},i}$ yielded distorted WFs which is why the irrep labels have been put in quotation marks.

obtained in this way by using the WFs for $N_{\mathbf{k}\text{-res},i} = 11$ (shown in Fig. 3.44) as trial functions.

Fig. 3.38 shows these MV WFs for the closed set 10–26. Some WFs form clearly identifiable irreps, while four functions seem distorted. However, these are hybridized versions of the former $E_2(a)$, $B_1(a)$, and $B_2(a)$ irreps obtained for $N_{\mathbf{k}\text{-res},i} = 11$. Basis functions for these irreps can be retrieved by applying the projection operator $\hat{P}^{(\alpha)}$ (2.28) on the hybridized WFs. In order to see which irreps are contained in these hybridized functions, $\|\hat{P}^{(\alpha)}W_{n\mathbf{0}}\|_2^2$ is shown in Fig. 3.39 for the site symmetry irreps of Wyckoff position a . This quantity is a measure of the contribution of a particular irrep to the distorted hybridized WFs of Fig. 3.38.

The irrep contribution plot reveals that the former irreps are contained in these hybridized functions, along with some contamination from $A_1(a)$, $A_2(a)$ and $E_1(a)$ irreps. In order to get rid of these contamination we can project out the $E_2(a)$, $B_1(a)$, and $B_2(a)$ irreps and use these symmetric functions, forming the anticipated irreps, as new trial functions $|T_n\rangle$. A second run of the spread minimization would again lead to the hybridized WFs. Therefore, we only construct the initial WFs by (3.22) and (3.23) using the spread minimized (Fig. 3.38) and projected WFs from the former minimization run. This yields the WFs of Fig. 3.40 which have larger individual spreads Ω_n than the prior hybridized versions. The initial WFs are shown here because the MV spread minimization would tend to produce the hybridized WFs with lower spread again. The contamination of the $E_1(a)$ irreps is still present in Fig. 3.39b, which may still be due to avoided crossings between the upper bands of the closed set with higher bands. This contamination may also stem from the other trials of the closed set which have not been symmetrized. Due to the symmetrization procedure (3.23), slight distortions in one subset of the trials may affect the initial WFs for other subsets. Another possible source of asymmetry could be asymmetries in the Bloch modes themselves as they are output by MPB which has a hard time separating mode information (and their respective symmetries) for near degenerate bands.

Finally, this discussion gave an overview over the problems of the Souza subspace optimization and how the results can be interpreted with the help of the site symmetry analysis.

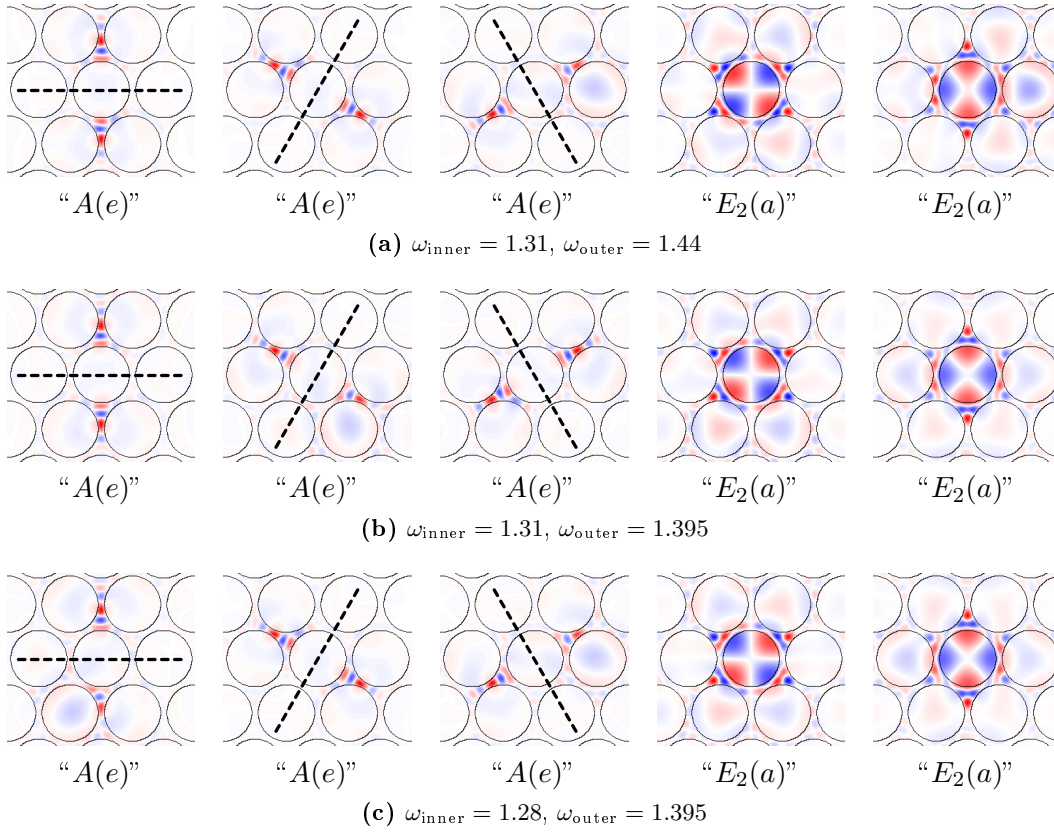


Figure 3.36: The WFs obtained for Bands 10–17 for $N_{\mathbf{k}\text{-res},i} = 25$, with Souza and MV spread minimization. The Souza frequency windows based on the overlap analysis of Fig. 3.34 are used here. Some WFs become more symmetric than Fig. 3.35b, but are still not yet satisfying.

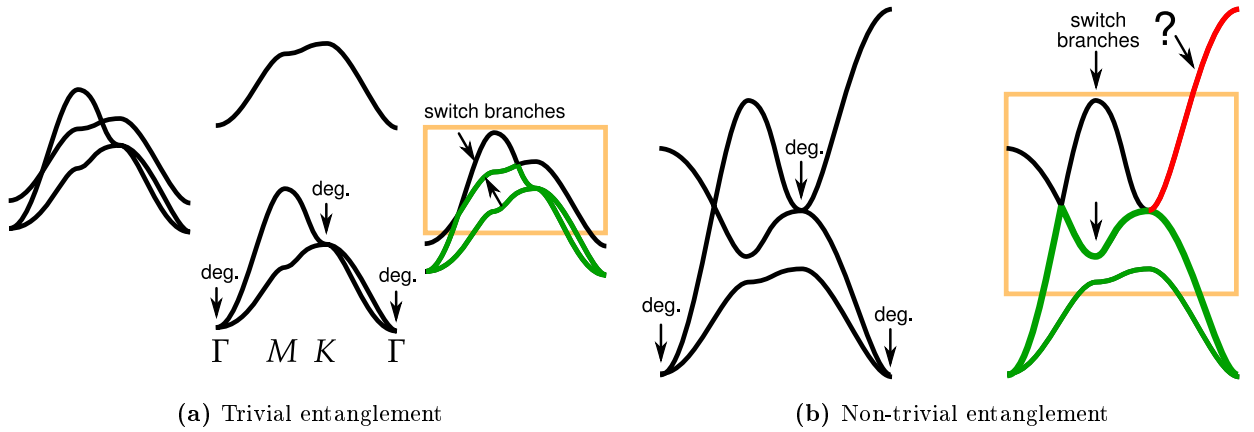


Figure 3.37: Types of band entanglement. Orange rectangles show suggested frequency windows for the Souza subspace optimization. Green highlighted parts show the lowest two frequency ordered bands. This example deals with two cases of two bands which are degenerate at Γ and K . (a) Trivial entanglement which is basically the overlay of closed sets of bands. Left: The example band structure. Middle: The two closed sets of bands making up this sample band structure, arrows denote degeneracies (deg.). Right: Suggested Souza frequency window that should allow for the mode information in the branches marked with arrows to switch such that WFs for the single and the double set can be created separately. The degenerate parts leave K and meet again at Γ along $\overline{K\Gamma}$. (b) Nontrivial entanglement, where Souza algorithm cannot artificially separate closed sets because the entanglement is not a result of a simple set overlay. Left: arrows denote degeneracies as in (a). However, this band structure is not the result of a simple overlay. Right: Suggested Souza frequency window allows the left peak (arrow) to enter the Wannier subspace, but the other branch (red, denoted with question mark), is neither fully incorporated nor fully excluded: the degenerate parts leave K and split up, not joining again in the same degenerate band at Γ along $\overline{K\Gamma}$.

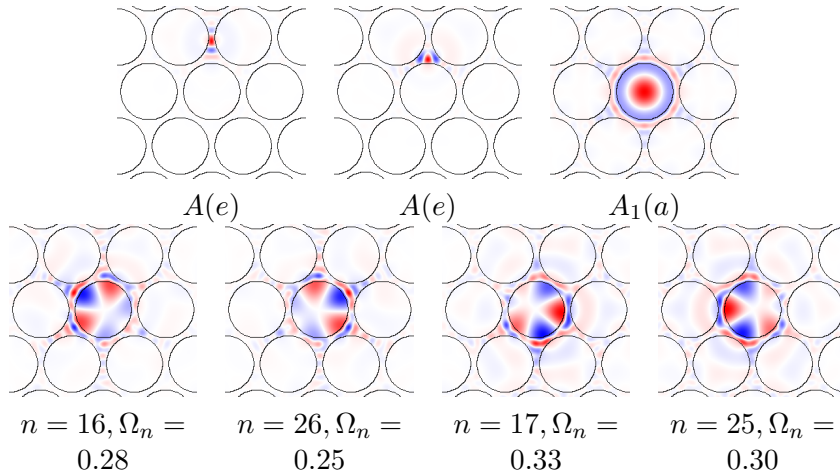


Figure 3.38: The WFs obtained from the MV spread minimization for the closed set of bands 10–26 with $N_{\mathbf{k}\text{-res},i} = 25$, using the SMV WFs for 10–26 from Fig. 3.44 (with $N_{\mathbf{k}\text{-res},i} = 11$) as trials. The upper WFs form definite site symmetry irreps (the $A(e)$ functions are six-fold degenerate, respectively; only one function for each set is shown here), while the lower WFs hybridized.

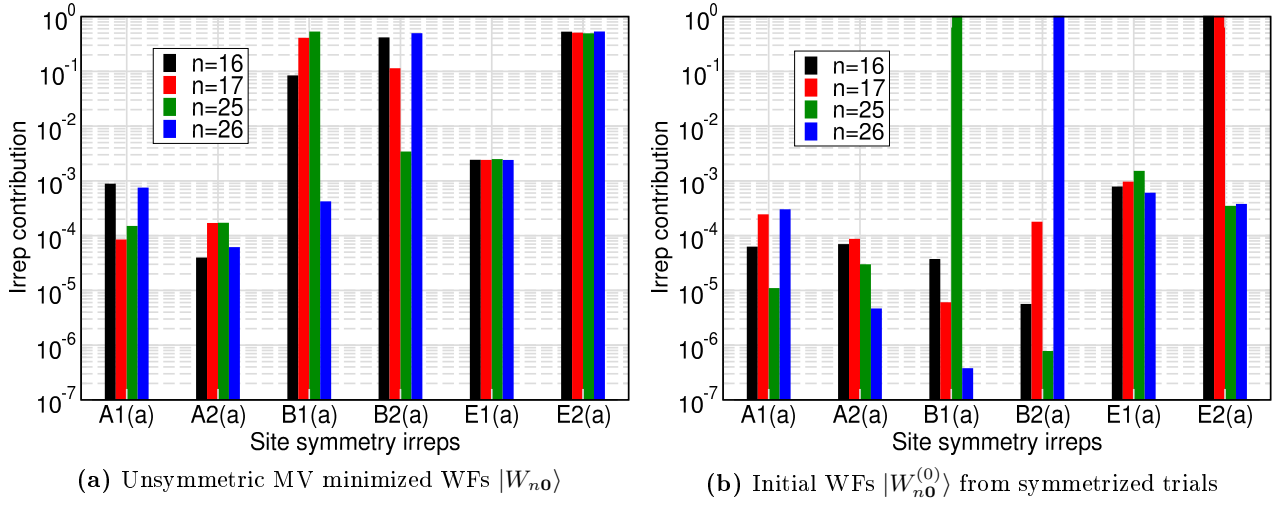


Figure 3.39: Irrep contribution $\|\hat{P}^{(\alpha)}W_{n\mathbf{0}}\|_2^2$ for the (a) hybridized WFs of Fig. 3.38 and (b) initial WFs constructed from the symmetrized versions of Fig. 3.38.

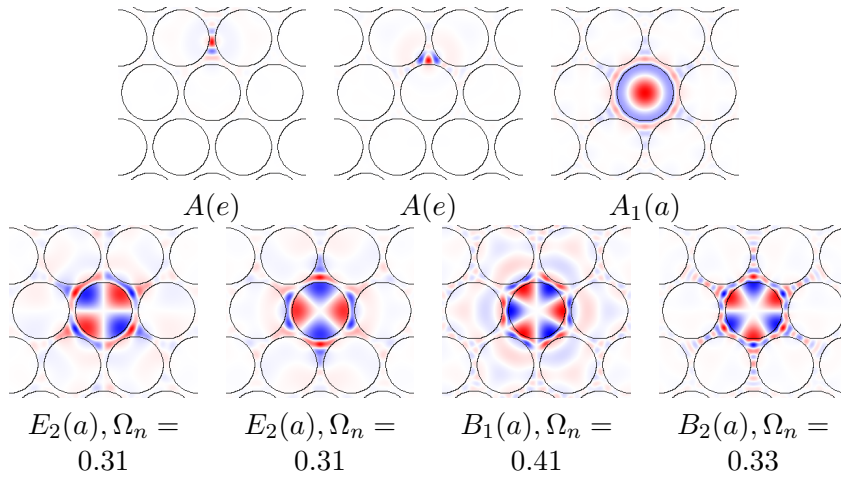


Figure 3.40: The initial WFs $|W_{n\mathbf{0}}^{(0)}\rangle$ for $N_{\mathbf{k}\text{-res},i} = 25$ obtained when using the irrep projections of the distorted WFs Fig. 3.38 as trial functions. The individual spreads are larger than those of the hybridized functions.

3.8 Enforcing Symmetry

The discussion so far showed that the choice of trial functions affects the symmetries and shapes of the final WFs. Furthermore, even if the best possible trial functions (e. g., WFs from a former minimization procedure) are used, the spread minimized WFs can still be distorted and may not form their anticipated irreps predicted by the site symmetry analysis. Therefore, suggestions for enforcing these symmetries in the WFs in the construction process are given in this section.

3.8.1 Choosing Appropriate Trial Functions

We have seen that the proper choice of trial functions $|T_n\rangle$ has a tremendous impact on the final WFs in both the Marzari-Vanderbilt and Souza algorithm. It was shown that Γ -point Bloch modes which have been cropped to one WSC around the Wyckoff positions of a unit cell, yield the spread minimized WFs with the fewest iteration steps. If the anticipated WFs were higher dimensional site symmetry irreps, the transformed and cropped Γ -point Bloch modes forming bases of those anticipated irreps yielded the best initial WFs for both iteration procedures.

However, computing the trial function matrices A in (3.22) (used for initializing both the Marzari-Vanderbilt and Souza minimization) requires time consuming evaluations of the overlap integrals of trials with Bloch modes. Usually one computes one full matrix $A(\mathbf{k})$ for all available Bloch bands and \mathbf{k} -points for one set of trial functions. However, the anticipated symmetries are not always known in full detail right from the start (before any WFs have been generated at all) because the choice for band sets that are used for the minimization procedures, evolves in the course of the generation process. One uses a band combination (with frequency windows) that yielded a set of localized WFs, and afterwards the next possible band set is investigated. Therefore, it would be helpful to change and try out different choices for irreps of the trial functions with as little effort as possible. This can be accomplished as follows.

For each lattice, one constructs the WSC-cropped Γ -point trials $|T_n^{(\mathbf{Q})}\rangle$ at the relevant Wyckoff positions \mathbf{Q} . The relevant Wyckoff positions in this respect are a, b, c_1, c_2 for the square lattice and $a, b_2, b_2, c_1, c_2, c_3$ for the triangular lattice. Basis functions of site symmetry irreps for the other Wyckoff positions \mathbf{q} can be generated from these relevant \mathbf{Q} , because the site symmetry groups for \mathbf{q} are subgroups of those for \mathbf{Q} (cf. Figs. F.3 and F.12).

The trials can be transformed by a unitary matrix $V^{(\mathbf{q}\alpha)}$ to form bases $|T_n^{(\mathbf{q}\alpha)}\rangle$ for the anticipated WF site symmetry irreps $D^{(\mathbf{q}\alpha)}$ (as has been done in Figs. 3.23 and 3.24). Since the necessary trials $|T_n^{(\mathbf{Q})}\rangle$ forming bases of irreps $D^{(\mathbf{q}\alpha)}$ are usually not consecutively ordered, one sums over the finite set $\mathcal{N}^{(\mathbf{q}\alpha)} \subset \mathbb{N}$ of the needed trial function band indices of a given set of bands to create WFs from:

$$|T_n^{(\mathbf{q}\alpha)}\rangle = \sum_{n' \in \mathcal{N}^{(\mathbf{q}\alpha)}} |T_{n'}^{(\mathbf{Q}(\mathbf{q}))}\rangle V_{n'n}^{(\mathbf{q}\alpha)}, \quad (3.34)$$

where α labels the irrep of the site symmetry group of the Wyckoff position \mathbf{q} and $\mathbf{Q}(\mathbf{q})$ is the necessary Wyckoff position of the smaller set of relevant positions. The matrix elements of $A^{(\mathbf{q}\alpha)}(\mathbf{k})$ for a chosen site symmetry irrep are then simply given by

$$A_{mn}^{(\mathbf{q}\alpha)}(\mathbf{k}) \stackrel{(3.22)}{=} \langle\langle \psi_{m\mathbf{k}} | T_n^{(\mathbf{Q}(\mathbf{q}\alpha))} \rangle\rangle \quad (3.35)$$

$$\stackrel{(3.34)}{=} \sum_{n' \in \mathcal{N}^{(\mathbf{q}\alpha)}} \underbrace{\langle\langle \psi_{m\mathbf{k}} | T_{n'}^{(\mathbf{Q}(\mathbf{q}))} \rangle\rangle}_{=: A_{mn}^{(\mathbf{Q}(\mathbf{q}))}(\mathbf{k})} V_{n'n}^{(\mathbf{q}\alpha)} \quad (3.36)$$

The combinations of trials cropped around the relevant \mathbf{Q} yielding all possible irreps at any Wyckoff position \mathbf{Q} are listed in Tab. 3.8.

$\mathbf{q}(\mathbf{Q})$	\mathbf{Q}	$\mathbf{q}(\mathbf{Q})$	\mathbf{Q}
a	a	a	a
b	b	$2b$	b_1, b_2
$2c$	c_1, c_2	$3c$	c_1, c_2, c_3
$4d$	$4a$ or $4b$	$6d$	$6a$ or $2c_1, 2c_2, 2c_3$
$4e$	$4a$ or $2c_1, 2c_2$	$6e$	$6a$ or $3b_1, 3b_2$
$4f$	$4b$ or $2c_1, 2c_2$		
(a) Square lattice		(b) Triangular lattice	

Table 3.8: Relevant Wyckoff positions, from whose irreps all other site symmetry irreps can be generated. The positions are listed in Figs. F.3 and F.12. This shows that the possible mappings from \mathbf{Q} to \mathbf{q} are not unique. However, one usually just needs one combination for obtaining good initial WFs $|W_{n0}^{(0)}\rangle$ for the iteration procedures.

Example: In the square lattice, Tab. 3.8a tells us that all four basis functions for any irrep of the site symmetry group of Wyckoff position f can be obtained by unitarily transforming either four basis functions of b irreps or two c_1 irreps together with two c_2 irreps. Fig. 3.41 shows one example for $A(f)$ basis functions obtained from b basis functions.

$$\begin{aligned}
 & \overbrace{\left(\begin{array}{cccc} \text{[Lattice with 4 basis functions]} \\ \text{[Lattice with 4 basis functions]} \\ \text{[Lattice with 4 basis functions]} \\ \text{[Lattice with 4 basis functions]} \end{array} \right)}^{A(f)} \\
 &= \left(\begin{array}{ccc} \text{[Lattice with 1 basis function]} & \text{[Lattice with 2 basis functions]} & \text{[Lattice with 1 basis function]} \\ \text{[Lattice with 1 basis function]} & \text{[Lattice with 2 basis functions]} & \text{[Lattice with 1 basis function]} \\ \text{[Lattice with 1 basis function]} & \text{[Lattice with 2 basis functions]} & \text{[Lattice with 1 basis function]} \\ \text{[Lattice with 1 basis function]} & \text{[Lattice with 2 basis functions]} & \text{[Lattice with 1 basis function]} \end{array} \right) \cdot \underbrace{\begin{pmatrix} \frac{1}{2} & \frac{1}{2} & \frac{1}{\sqrt{2}} & \frac{1}{2} \\ -\frac{1}{\sqrt{2}} & 0 & \frac{1}{\sqrt{2}} & 0 \\ 0 & \frac{1}{\sqrt{2}} & 0 & -\frac{1}{\sqrt{2}} \\ \frac{1}{2} & -\frac{1}{2} & \frac{1}{2} & -\frac{1}{2} \end{pmatrix}}_{=V(\mathbf{q})}
 \end{aligned}$$

Figure 3.41: Example of (3.34) for constructing four $A(f)$ basis functions $|T_n^{(\mathbf{q})}\rangle$ (left hand side) from trials $|T_n^{(\mathbf{Q})}\rangle$ for Wyckoff position $\mathbf{Q} \equiv b$ (right hand side) by a unitary transform matrix $V(\mathbf{q})$.

Thus, from a small set of precomputed matrices $A^{(\mathbf{Q})}(\mathbf{k})$ one can construct a huge variety of different trial matrices $A^{(\mathbf{q}\alpha)}$ by fast linear operations. The best initial guesses are those combinations that yield the smallest combined spread Ω which can be computed very quickly from the matrices without performing any minimization steps.

This first guess of WFs can still be made better. Instead of cropping the fields on a WSC, one can as well multiply the periodically extended Γ -point Bloch modes by a Gaussian function centered around the respective Wyckoff position. This would resemble the final, exponentially localized WFs even more

and the procedure for creating the matrices $A^{(\mathbf{q}\alpha)}$ outlined above is still applicable.

3.8.2 Symmetry Adapted Construction

As Krüger [37, 38] showed, the anticipated irreps of the WFs can also be taken into account when constructing the transform matrices $U(\mathbf{k})$ under special constraints. He specified these constraints explicitly using the representation matrices of the little co-group irreps of the Bloch modes in the IBZ. Incorporating his suggestions would require substantial modifications of the present code that was used to obtain all the WFs of this chapter. However, since the transform matrices $U(\mathbf{k})$ are fully determined for \mathbf{k} from the IBZ already, the spread minimization procedure could be carried out on 1/8 of the \mathbf{k} -points for the square lattice and 1/12 of the \mathbf{k} -points of the triangular lattice. Hybridizations as were encountered in Fig. 3.12 could also be avoided then. In 2D computations, however, the spread minimization procedure is already quite fast and the assembly procedure (3.15) is the most time consuming part. Furthermore, for this ansatz to work, all the Bloch modes used in this case should also transform perfectly like their respective little co-group irreps. Otherwise, any numerical deviation would then also be found in the overlap matrices $M_{mn}(\mathbf{k}, \mathbf{b})$ which would violate the conditions to apply Krüger's method.

3.8.3 A Posteriori Symmetrization

If the WFs are just slightly distorted, one can apply the projection operators $\hat{P}^{(\mathbf{q}\alpha)}$ of (2.47) for the site symmetry irreps $D^{(\mathbf{q}\alpha)}$ which discards any contributions in the WFs that do not transform as the irrep they are supposed to be basis functions of. Afterwards the projected WFs are extended periodically on a larger supercell and cropped to a super WSC of the same volume as the support domain of the former WFs given on a parallelogram. This procedure ensures that the discretized WFs and the matrix operator elements computed thereof are as symmetric as possible. The discretized curls of the WFs are taken before the fields are cropped to a super WSC in order to avoid sharp field discontinuities which in turn would introduce errors as described in Sec. B.3. Of course, since some small amount of WFs field information is discarded by the projection, one has to make sure that the benefits from symmetrization outweigh this newly introduced error. The symmetrized WFs should still be able to describe the band structure of the PC within reasonable accuracy. This is investigated in Sec. 5.2.2.

The actual symmetrization procedure is carried out as follows. For one-dimensional irreps, just the corresponding projection operator has to be applied and the WF has to be cropped to a super WSC afterwards. For degenerate irreps, symmetrization requires more effort. If the WFs can be rotated such that they are aligned in one direction (as in Fig. 3.42a), one has to adjust the phases and add up all the WFs. This is because one does not know, how the WFs are distorted that is why taking the averaged of the WF profiles treats all available WFs equally. This sum of WFs can now be projected, normalized and rotated back, forming a perfect set of basis functions for the respective rep.

If the WFs are degenerate but cannot be aligned by rotations (Fig. 3.42b), then we pick just one single basis function and discard the others. This single WF is now projected onto its respective irrep (which discards any distorting contributions) and is used to generate the remaining basis functions of the respective irrep as follows. We apply a rotation, that generates a linearly independent new function which is orthonormalized by the Gram-Schmidt procedure. The resulting WFs are now basis functions of the respective irrep.

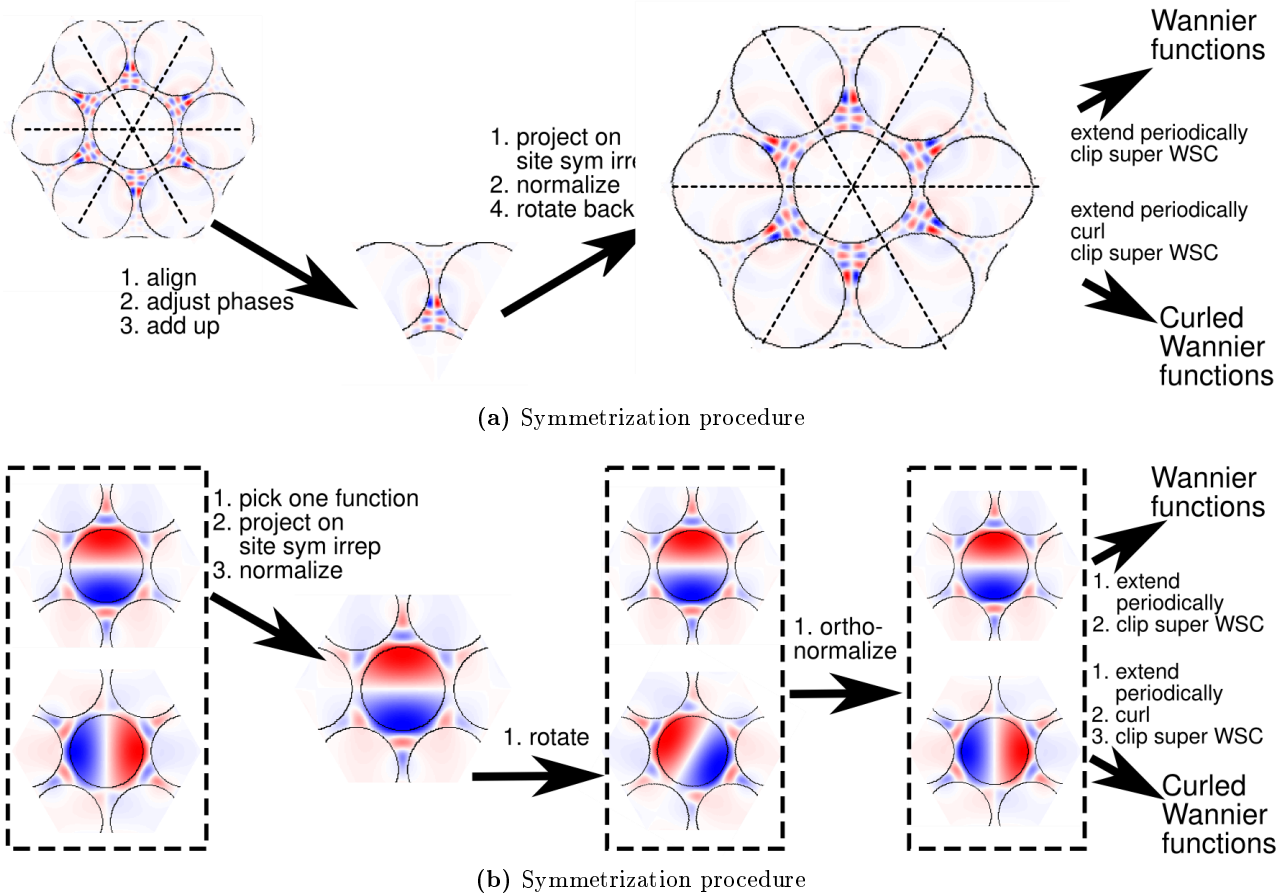


Figure 3.42: Schematic of the symmetrization procedures for WFs. If the WFs can be averaged after adjusting their phases as in (a), one projects the averaged part and creates the remaining basis functions by applying the proper rotations. In the other case (b), one picks one single function and applies the projection operator for the respective irrep. Afterwards one creates a linearly independent set by applying a rotation. Orthonormalization by the Gram-Schmidt procedure yields the symmetrized basis functions. Finally, the pure functions and their curls are cropped to a super WSC (square shaped domain for the square lattice, hexagonal shaped domain for the triangular lattice).

3.9 Final Wannier Functions

As we have seen in the previous sections, one can create many different sets of WFs from a set of given Bloch modes. Some WFs are more symmetric than others, some are more localized. Some of these sets could be generated quickly, others needed substantial tuning of the minimization input parameters. In order to judge the performance of different sets of WFs in subsequent computations, three choices of parameters are finally presented here. Their ability to reproduce the band structure of the PC and model localized defect states is investigated in the following chapters. For historical reasons, the WFs set 1–38 is investigated and compared to the set 1–101 because the former set was the one available from the previous work of Schillinger [35] and Hermann [43]. Therefore, documenting the improvements by using more WFs is essential to decide, whether the effort of generating a particular set of or just more WFs is justified.

3.9.1 Fully Hybridized Wannier Functions 1–38 (WF38-MV)

As we have seen, applying the MV spread minimization to closed sets of bands yields the best localized WFs. The natural consequence would be to choose the closed set as large as possible and obtain WFs that are as highly localized as possible. This has been done for the closed set of bands 1–38 in Fig. 3.43. Some sets form complete site symmetry irreps (13–38), others are symmetric but provide only half of the necessary basis functions to be a site symmetry irrep of their localization center (1–12). The superior localization is shown and compared to a more symmetric choice of WFs in Fig. 3.45. However, these WFs are nevertheless not suited to describe the defect states in PC properly (cf. Fig. 6.13).

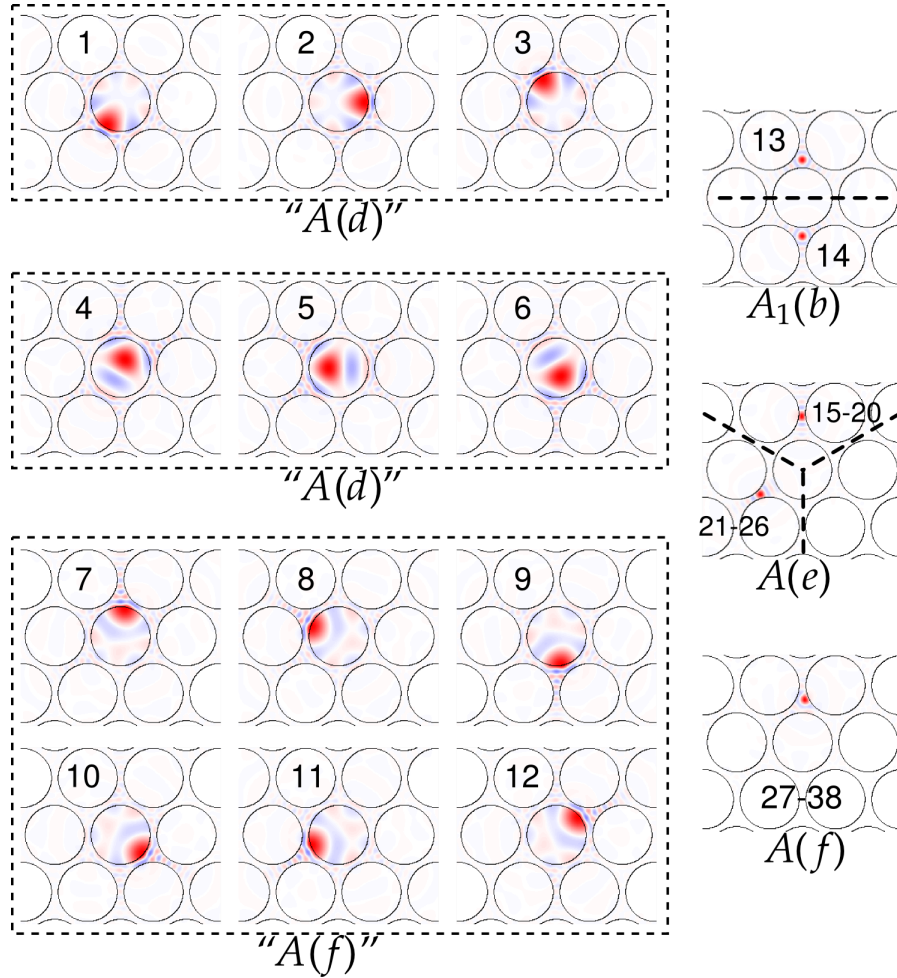


Figure 3.43: WFs obtained by the Marzari-Vanderbilt spread minimization for the closed set 1–38. They are referred to as WF38-MV. Note that the $A(e)$ irreps 15–20 may look similar to 21–26, but they are orthogonal sets. The incomplete irreps are given in quotation marks. The construction parameters are the same as in Tab. D.1a.

3.9.2 Souza-Marzari-Vanderbilt Wannier Functions 1–101 (WF101-SMV)

These WFs have been computed with the full SMV algorithm with the parameters of Tab. D.2. Their real space decay behavior is shown in Fig. 3.45. Though some of them decay like $1/|\mathbf{r}|$ a few lattice sites

away from their localization center, they all form bases for irreps of the respective site symmetry groups. Their ability to model defect states in PC is investigated in Chap. 6.

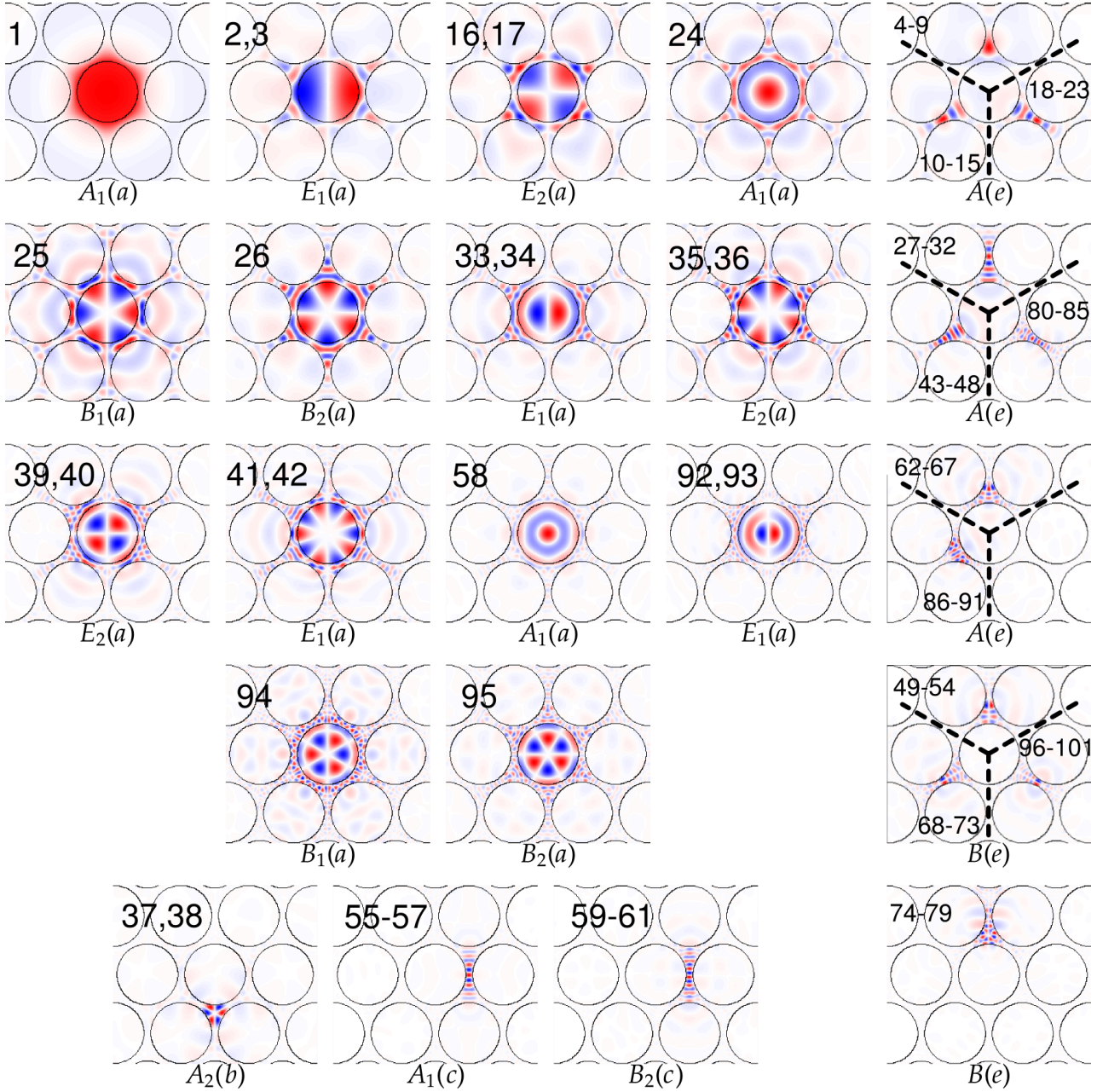


Figure 3.44: WFs created from the parameters of Tab. D.2. This WF set is referred to as WF38-SMV and WF101-SMV for the number of WFs used. When no ambiguities arise, they are abbreviated by WF38 and WF101.

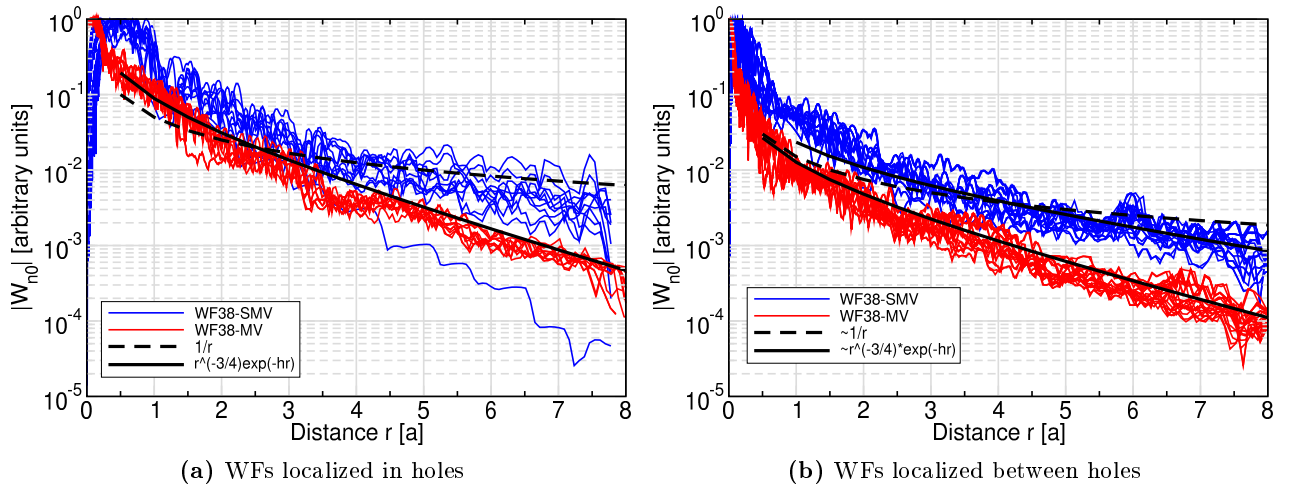


Figure 3.45: Real space decay behavior of WFs 1–38 from Figs. 3.43 (Fully hybridized) and 3.44 (SMV WFs). For distance r from the center $\langle \mathbf{r} \rangle$ of the WF the value $\max_{\mathbf{r}:|\mathbf{r}-\langle \mathbf{r} \rangle|=r} |W_{n0}(\mathbf{r} - \langle \mathbf{r} \rangle)|$ has been plotted (maximal WF value on circles around the localization center). (a) shows the decay of WF localized inside holes (1–12 of Fig. 3.43 and 1,2,3,16,17,24,25,26,33,34,35,36 of Fig. 3.44). (b) shows the decay of the remaining WFs among the first 38.

3.9.3 Symmetrized Souza-Marzari-Vanderbilt Wannier Functions 1–38 (WF38-sym)

Symmetrizing the final WFs from Fig. 3.44 with the symmetrization procedure of Sec. 3.8.3 requires little effort. Therefore, the WFs 1–38 have been symmetrized to yield the set referred to as WF38-sym in the remainder of this work. Some examples of the symmetrized functions are shown in Fig. 3.46.

3.10 Summary

We have given a review of the bottom-up approach to compute maximally localized generalized photonic Wannier functions with the combined Souza-Marzari-Vanderbilt spread minimization. This procedure iteratively constructs a set of unitary transform matrices $U(\mathbf{k})$ by minimizing the combined real space extent of the resulting set of Wannier functions, the so-called spread functional Ω . These minimization procedures require some parameters that have to be provided by a user: the particular sets of Bloch bands building the WFs, a frequency window allowing the exchange of Bloch mode profiles with higher bands, and a set of trial functions, from which initial Wannier functions for the iteration procedure are constructed. These parameters have been chosen by trial and error in previous works.

We applied the site symmetry analysis of Chap. 2 to construct WFs for both model systems of Sec. 1.2.7 and interpreted the resulting WFs in view of their symmetries and the symmetries of the underlying Bloch modes. We have seen that the number of iteration steps needed to obtain the spread minimized WFs and their shape depend on the trial functions used. The strong resemblance between Γ -point Bloch mode profiles and WF profiles was pointed out and optimal unitary transforms according to the anticipated WF irreps were suggested based on the site symmetry analysis. These are the best trial functions in the sense that they give the best initial WFs if WFs are generated from scratch. In particular, the Souza subspace optimization was very sensitive to the choice of trial functions, since the smallest invariant spread Ω_I does not necessarily lead to the smallest overall spread Ω . Thus, determining

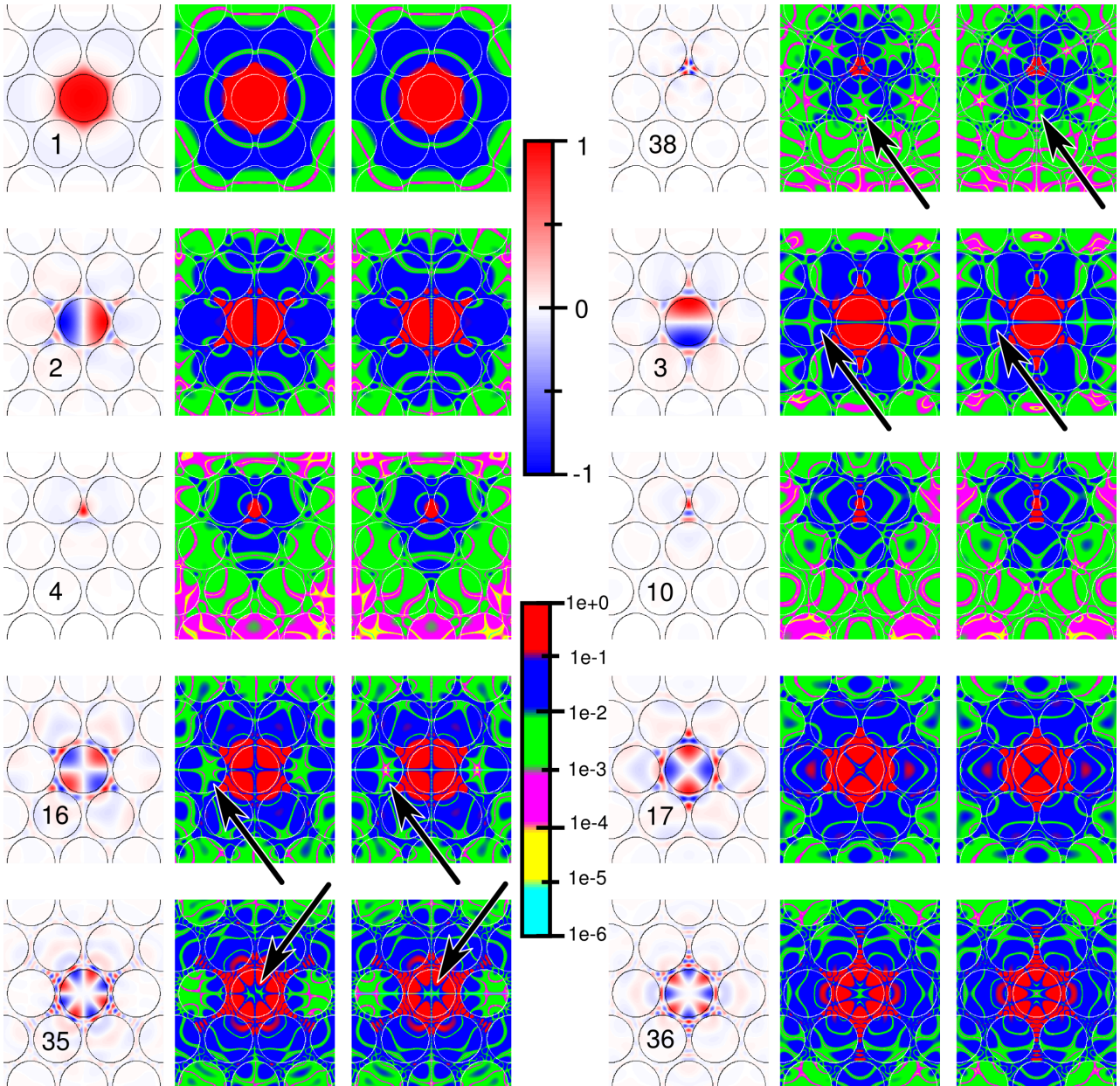


Figure 3.46: *A posteriori* symmetrized WFs from bands 1–38 of Fig. 3.44. They are referred to as WF38-sym. Logarithmic density plots show the profiles before (left) and after the symmetrization (right). Black arrows denote exemplary regions, where the symmetry of the WF profiles improved significantly.

the optimal starting point for the spread minimization is sometimes crucial. Additionally it was shown that the Souza subspace optimization can lead to a $1/|\mathbf{r}|$ decay law of WFs that principally support exponential decay when constructed with the Marzari-Vanderbilt spread minimization for closed sets of bands.

The overlap of Wannier functions with the Bloch modes of the band structure was compared to the overlap of the anticipated trial functions (forming the same irreps as the final WFs) with the Bloch

modes. The similarity was striking and may help to determine good frequency windows for the Souza subspace optimization for future computations.

The site symmetry analysis is only applicable to closed sets of bands. Nevertheless, it does help in the interpretation of the resulting WFs obtained from the Souza subspace optimization for entangled bands. The conjecture that for trivially entangled bands the site symmetry analysis may still be a good guide to the anticipated WFs irreps was stated.

An efficient procedure to easily choose various trial combinations from a few precomputed overlap matrices $A^{(\mathbf{Q})}$ for a spread minimization run was suggested. If the site symmetry analysis does not yield unique sets of possible trial functions, it was suggested to use those combinations that yield initial WFs with the lowest spread. After the spread minimization, deviations of the final WFs from their anticipated irreps can be estimated before actually performing the time consuming assembly procedure from Bloch modes. The sum of the localization centers of the WFs was shown to be a good measure for this task. If twice the sum adds up to a lattice vector, then the resulting WFs are symmetric. Additionally, a procedure for symmetrizing distorted WFs based on projection operators was proposed.

Finally, three sets of maximally localized WFs were presented. These sets are used to reproduce the band structure and compute defect mode frequencies in the following chapters. The results will help to judge if some Wannier function construction parameters should be favored over others.

4 Chapter 4

Wannier Function Expansion

In this chapter, we expand the wave equations into the localized WF basis which yields an effective lattice model for the description of localized defect modes. This procedure transforms the differential operator eigenvalue equations into generalized matrix eigenvalue equations that can be solved by a computer. The diagonalization of these matrices yield frequencies as eigenvalues and mode expansion coefficients in terms of WFs as eigenvectors. The matrices for a particular defect setup can be assembled from a few precomputed matrices describing the pure overlap of WFs, the periodic background of a PC, and individual reference defects. Isotropic as well as anisotropic defects according to the permittivity tensor of Sec. 1.2.4 are incorporated. The Wannier approach allows to compute localized defect cavity modes, supercell waveguide dispersions $\omega(\mathbf{k})$ and on-shell waveguide dispersions $k(\omega)$. Furthermore, transmission/reflection characteristics of functional elements can be computed by determining their scattering matrix, which is briefly summarized.

4.1 Wannier Matrix Elements

We will abbreviate the combined index pair (n, \mathbf{R}) by Greek letters α and β now and denote a WF by $|\alpha\rangle \equiv |n\mathbf{R}\rangle$.

4.1.1 Wave Equations

We will expand the electromagnetic fields in the basis of their respective WFs now, i. e., we set

$$\mathbf{E}(\mathbf{r}) = \sum_{\beta} c_{\beta} \mathbf{W}_{\beta}^{\text{el}}(\mathbf{r}), \quad \mathbf{H}(\mathbf{r}) = \sum_{\beta} c_{\beta} \mathbf{W}_{\beta}^{\text{mag}}(\mathbf{r}). \quad (4.1)$$

The Wannier expansion coefficients $c_{\beta} \in \mathbb{C}$ are the new unknowns and have to be solved for.

Magnetic Field

We insert the expansion (4.1) into the magnetic field wave equation (1.9b) and project on $\langle\alpha|$ from the left:

$$\sum_{\beta} \left[\langle\alpha| \nabla \times \underline{\underline{\eta}} \cdot \nabla \times |\beta\rangle - \frac{\omega^2}{c_0^2} \langle\alpha|\beta\rangle \right] c_{\beta} = 0. \quad (4.2)$$

The first term can be recast as

$$\langle \alpha | \nabla \times \underline{\underline{\eta}} \cdot \nabla \times | \beta \rangle = \int dV \mathbf{W}_\alpha^*(\mathbf{r}) \cdot \nabla \times \left(\underline{\underline{\eta}}(\mathbf{r}) \cdot \nabla \times \mathbf{W}_\beta(\mathbf{r}) \right) \quad (4.3)$$

$$\stackrel{(A.29)}{\equiv} \int dV \left(\nabla \times \mathbf{W}_\alpha(\mathbf{r}) \right)^* \cdot \underline{\underline{\eta}}(\mathbf{r}) \cdot \left(\nabla \times \mathbf{W}_\beta(\mathbf{r}) \right), \quad (4.4)$$

where we performed an integration by parts. The dielectric function can always be written as the sum of the periodic part and the deviations introduced by the defect structures, so we can write

$$\underline{\underline{\eta}}(\mathbf{r}) = \underline{\underline{\eta}}_{\text{per}}(\mathbf{r}) + \Delta \underline{\underline{\eta}}(\mathbf{r}). \quad (4.5)$$

Plugging this into (4.4) yields the following matrix definitions:

3D Vectorial Magnetic Operator Matrices

$$A_{\alpha\beta} := \int dV \mathbf{W}_\alpha^*(\mathbf{r}) \cdot \mathbf{W}_\beta(\mathbf{r}), \quad (4.6a)$$

$$B_{\alpha\beta}[\Delta \underline{\underline{\eta}}] := \int dV \left(\nabla \times \mathbf{W}_\alpha(\mathbf{r}) \right)^* \cdot \Delta \underline{\underline{\eta}}(\mathbf{r}) \cdot \left(\nabla \times \mathbf{W}_\beta(\mathbf{r}) \right), \quad (4.6b)$$

$$C_{\alpha\beta}[\underline{\underline{\eta}}_{\text{per}}] := \int dV \left(\nabla \times \mathbf{W}_\alpha(\mathbf{r}) \right)^* \cdot \underline{\underline{\eta}}_{\text{per}}(\mathbf{r}) \cdot \left(\nabla \times \mathbf{W}_\beta(\mathbf{r}) \right). \quad (4.6c)$$

The matrix A has been included in this list for the sake of completeness, and we further define a function

$$\Lambda^{\text{mag}}(\omega) := \frac{\omega^2}{c_0^2}, \quad (4.7)$$

such that we can write the magnetic field wave equation (4.2) as

$$\sum_{\beta} \left[C_{\alpha\beta} + B_{\alpha\beta} - \Lambda^{\text{mag}}(\omega) A_{\alpha\beta} \right] c_{\beta} = 0. \quad (4.8)$$

This is an infinite generalized matrix eigenvalue equation, whose eigenvalues yield the frequencies ω by (4.7) and whose eigenvectors yield the Wannier expansion coefficients for assembling the actual magnetic fields by (4.1).

Electric Field

The derivation of the electric field matrix eigenvalue equation is analogous to the magnetic field case. Plugging the expansion (4.1) into the electric field wave equation (1.9a) yields

$$\sum_{\beta} \left[\langle \alpha | \nabla \times \nabla \times | \beta \rangle - \frac{\omega^2}{c_0^2} \langle \alpha | \underline{\underline{\epsilon}} | \beta \rangle \right] c_{\beta} = 0. \quad (4.9)$$

The first term can again be written as an integral over just first derivatives as in (4.4), and the second term can be split into two after noting that

$$\underline{\underline{\epsilon}}(\mathbf{r}) = \underline{\underline{\epsilon}}_{\text{per}}(\mathbf{r}) + \Delta \underline{\underline{\epsilon}}(\mathbf{r}). \quad (4.10)$$

This leads to the following matrix definitions for the electric field case:

3D Vectorial Electric Operator Matrices

$$A_{\alpha\beta} := \int dV \left(\nabla \times \mathbf{W}_\alpha(\mathbf{r}) \right)^* \cdot \left(\nabla \times \mathbf{W}_\beta(\mathbf{r}) \right), \quad (4.11a)$$

$$B_{\alpha\beta}[\Delta\underline{\varepsilon}] := \int dV \mathbf{W}_\alpha^*(\mathbf{r}) \cdot \Delta\underline{\varepsilon}(\mathbf{r}) \cdot \mathbf{W}_\beta(\mathbf{r}), \quad (4.11b)$$

$$C_{\alpha\beta}[\underline{\varepsilon}_{\text{per}}] := \int dV \mathbf{W}_\alpha^*(\mathbf{r}) \cdot \underline{\varepsilon}_{\text{per}}(\mathbf{r}) \cdot \mathbf{W}_\beta(\mathbf{r}). \quad (4.11c)$$

Together with the definition

$$\Lambda^{\text{el}}(\omega) := \frac{c_0^2}{\omega^2}, \quad (4.12)$$

we can write (4.9) in terms of the above defined matrices as

$$\sum_{\beta} \left[C_{\alpha\beta} + B_{\alpha\beta} - \Lambda^{\text{el}}(\omega) A_{\alpha\beta} \right] c_{\beta} = 0. \quad (4.13)$$

This corresponds to dividing (4.9) by $-\frac{\omega^2}{c_0^2}$. This matrix equation now has the same form as (4.8) with different matrix definitions. This means that the whole solution process is essentially the same in terms of the operator matrices A , B , and C and the eigenvalues $\Lambda(\omega)$ for the electric and magnetic field.

Operator Matrices for E- and H-Polarization in 2D

In these cases the fields are described by their z -components $E_z(\mathbf{r}_{\parallel})$ and $H_z(\mathbf{r}_{\parallel})$, where the corresponding scalar WFs are assembled from these scalar fields. The curl of such a WF $\mathbf{W}(\mathbf{r}_{\parallel})$ defined in the xy -plane with just a z -component is

$$\mathbf{W}(\mathbf{r}_{\parallel}) = \begin{pmatrix} 0 \\ 0 \\ W(\mathbf{r}_{\parallel}) \end{pmatrix}, \quad \nabla \times \mathbf{W}(\mathbf{r}_{\parallel}) = \begin{pmatrix} \partial_x \\ \partial_y \\ \partial_z \end{pmatrix} \times \begin{pmatrix} 0 \\ 0 \\ W(\mathbf{r}_{\parallel}) \end{pmatrix} = \begin{pmatrix} \partial_y W(\mathbf{r}_{\parallel}) \\ -\partial_x W(\mathbf{r}_{\parallel}) \\ 0 \end{pmatrix}. \quad (4.14)$$

Plugging (4.14) into the vectorial E-field equations (4.11) gives the electric field operator matrices in E-polarization:

2D Electric Operator Matrices (E-polarization)

$$A_{\alpha\beta} = \int d^2r \left(\partial_x W_\alpha(\mathbf{r}_{\parallel}) \right)^* \left(\partial_x W_\beta(\mathbf{r}_{\parallel}) \right) + \left(\partial_y W_\alpha(\mathbf{r}_{\parallel}) \right)^* \left(\partial_y W_\beta(\mathbf{r}_{\parallel}) \right), \quad (4.15a)$$

$$B_{\alpha\beta}[\Delta\varepsilon_{zz}] = \int d^2r W_\alpha^*(\mathbf{r}_{\parallel}) \Delta\varepsilon_{zz}(\mathbf{r}_{\parallel}) W_\beta(\mathbf{r}_{\parallel}), \quad (4.15b)$$

$$C_{\alpha\beta}[\varepsilon_{\text{per},zz}] = \int d^2r W_\alpha^*(\mathbf{r}_{\parallel}) \varepsilon_{\text{per},zz}(\mathbf{r}_{\parallel}) W_\beta(\mathbf{r}_{\parallel}). \quad (4.15c)$$

Again, we see that anisotropic effects cannot be investigated in pure E-polarization, since only the scalar zz -component of the dielectric function enters the equations (1.30a).

In the same fashion, combining (4.14) with the vectorial H-field equations (4.6) gives the magnetic field operator matrices in H-polarization:

2D Magnetic Operator Matrices (H-polarization)

$$A_{\alpha\beta} = \int d^2r W_{\alpha}^*(\mathbf{r}_{\parallel}) W_{\beta}(\mathbf{r}_{\parallel}), \quad (4.16a)$$

$$B_{\alpha\beta}[\underline{\Delta\eta}] = \int d^2r \begin{pmatrix} \partial_y W_{\alpha}^*(\mathbf{r}_{\parallel}) \\ -\partial_x W_{\alpha}^*(\mathbf{r}_{\parallel}) \end{pmatrix} \cdot \underline{\Delta\eta}(\mathbf{r}_{\parallel}) \cdot \begin{pmatrix} \partial_y W_{\beta}(\mathbf{r}_{\parallel}) \\ -\partial_x W_{\beta}(\mathbf{r}_{\parallel}) \end{pmatrix}, \quad (4.16b)$$

$$C_{\alpha\beta}[\underline{\eta}_{\text{per}}] = \int d^2r \begin{pmatrix} \partial_y W_{\alpha}^*(\mathbf{r}_{\parallel}) \\ -\partial_x W_{\alpha}^*(\mathbf{r}_{\parallel}) \end{pmatrix} \cdot \underline{\eta}_{\text{per}}(\mathbf{r}_{\parallel}) \cdot \begin{pmatrix} \partial_y W_{\beta}(\mathbf{r}_{\parallel}) \\ -\partial_x W_{\beta}(\mathbf{r}_{\parallel}) \end{pmatrix}. \quad (4.16c)$$

The tensors used here are lossless (Hermitian) 2×2 tensors:

$$\underline{\eta} = \begin{pmatrix} \eta_{xx} & \eta_{xy} \\ \eta_{xy}^* & \eta_{yy} \end{pmatrix}. \quad (4.17)$$

The scalar variants of the matrix operators are obtained by setting $\eta_{xy} = 0$ and are not written out explicitly here.

4.1.2 Complex Defect Structures in Photonic Crystals

The splittings (4.5) and (4.10) of the dielectric functions into periodic parts and deviations thereof may just seem as a trick to write the matrix equations for the electric and magnetic fields in the same form. However, they actually allow to further decompose defect contributions into smaller, more basic matrices B .

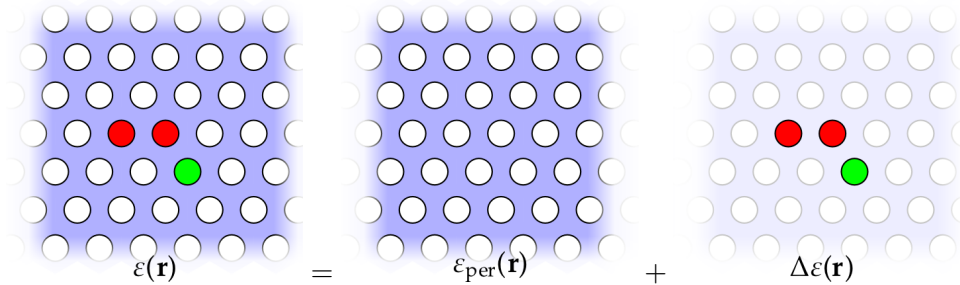


Figure 4.1: Splitting of the dielectric function of a complex defect cluster into periodic and defect parts by (4.5) and (4.10).

We restrict ourselves to cases, where the full deviation $\Delta\varepsilon(\mathbf{r})$ can be written as the sum of various basic contributions $\Delta\varepsilon_m(\mathbf{r})$ associated with a particular home unit cell, but not necessarily constricted to it. These basic contributions can occur multiple times, located at various unit cells \mathbf{R}_m such that the full deviation is given by

$$\Delta\varepsilon(\mathbf{r}) = \sum_m \Delta\varepsilon_m(\mathbf{r} - \mathbf{R}_m). \quad (4.18)$$

When the same basic deviation functions occur shifted at various lattice sites, we can exploit the linearity

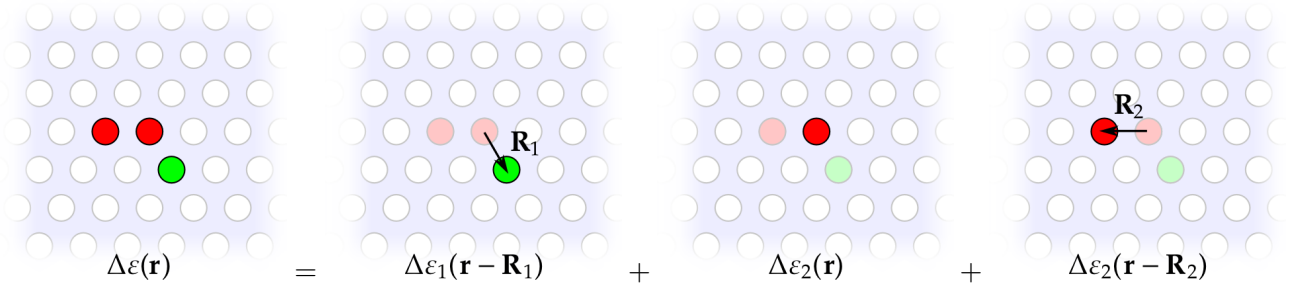


Figure 4.2: The full deviation $\Delta\varepsilon(\mathbf{r})$ is a sum of basic contributions $\Delta\varepsilon_m(\mathbf{r})$ located at different lattice sites \mathbf{R}_m .

of the integral to assemble the full defect operator matrices $B_{n'\mathbf{R}',n\mathbf{R}}^{\text{full}} := B_{n\mathbf{R},n'\mathbf{R}'}[\Delta\varepsilon]$ by shifting around matrices $B_{n\mathbf{R},n'\mathbf{R}'}^{(m)}$ which only depend on the recurring basic defect functions $\Delta\varepsilon_m(\mathbf{r})$:

$$B_{n'\mathbf{R}',n\mathbf{R}}^{\text{full}} = \sum_m B_{n'\mathbf{R}'-\mathbf{R}_m,n\mathbf{R}-\mathbf{R}_m}^{(m)}, \quad (4.19)$$

$$B_{n\mathbf{R},n'\mathbf{R}'}^{(m)} := B_{n'\mathbf{R}',n\mathbf{R}}[\Delta\varepsilon_m]. \quad (4.20)$$

The functional form of $\Delta\varepsilon_m(\mathbf{r})$ can still be rather arbitrary. In practical computations however, some special cases are in the center of interest, allowing to describe a whole class of deviations with just a single or a couple of reference matrices.

Infiltrated Hole, Isotropic Case

For just a single isotropically infiltrated hole, the functional form of $\Delta\varepsilon_m(\mathbf{r})$ is the product of a simple constant $\Delta\varepsilon_m \in \mathbb{R}$ and a form factor $\Theta_{\text{hole}}(\mathbf{r})$ defining the shape of the hole. The scalar inverse permittivity $\Delta\eta_m(\mathbf{r})$ can be described in the same way:

$$\Delta\varepsilon_m(\mathbf{r}) = \Delta\varepsilon_m \Theta_{\text{hole}}(\mathbf{r}), \quad (4.21)$$

$$\Delta\eta_m(\mathbf{r}) = \Delta\eta_m \Theta_{\text{hole}}(\mathbf{r}), \quad (4.22)$$

$$\Theta_{\text{hole}}(\mathbf{r}) = \begin{cases} 1 & \text{for } \mathbf{r} \text{ inside the hole,} \\ 0 & \text{otherwise.} \end{cases} \quad (4.23)$$

By Eqs. (4.5) and (4.10), the choice of these factors is such that the former value ε_{per} of the hole is compensated and a new scalar ε_m for the defect is set, i. e.

$$\Delta\varepsilon_m = \varepsilon_m - \varepsilon_{\text{per}}, \quad (4.24)$$

$$\Delta\eta_m = 1/\varepsilon_m - 1/\varepsilon_{\text{per}}. \quad (4.25)$$

Then the value of the full dielectric function inside the defect hole is given by ε_m or $\eta_m = 1/\varepsilon_m$, respectively.

After defining a reference defect matrix B^{ref} that just depends on the form factor $\Theta_{\text{hole}}(\mathbf{r})$, the full defect matrices B^{full} for a cluster of such isotropically infiltrated holes are due to the linearity of the

integrals given by

$$B_{n'\mathbf{R}',n\mathbf{R}}^{\text{ref}} := B_{n'\mathbf{R}',n\mathbf{R}}[\Theta_{\text{hole}}], \quad (4.26)$$

$$B_{n'\mathbf{R}',n\mathbf{R}}^{\text{full,el}} = \sum_m \Delta\varepsilon_m B_{n'\mathbf{R}'-\mathbf{R}_m,n\mathbf{R}-\mathbf{R}_m}^{\text{ref,el}}, \quad (4.27)$$

$$B_{n'\mathbf{R}',n\mathbf{R}}^{\text{full,mag}} = \sum_m \Delta\eta_m B_{n'\mathbf{R}'-\mathbf{R}_m,n\mathbf{R}-\mathbf{R}_m}^{\text{ref,mag}}. \quad (4.28)$$

However, in real computations one usually chooses an isotropic reference defect with scalar values ε_{ref} not equal to unity. This way, the errors introduced by a particular choice of real space discretizations of the dielectric function are kept as small as possible (see Sec. B.4 for more information on discretization schemes). Once the reference matrix B^{ref} has been computed for a reference defect hole with ε_{ref} , the proper defect operator matrices for a hole infiltrated with ε_m are assembled with a modified scaling factor $\xi_m \in \mathbb{R}$ as

Scaling Factors for Isotropic Defects

$$B_{n'\mathbf{R}',n\mathbf{R}}^{\text{full}} = \sum_m \xi_m B_{n'\mathbf{R}'-\mathbf{R}_m,n\mathbf{R}-\mathbf{R}_m}^{\text{ref}}, \quad (4.29a)$$

$$\xi_m = \begin{cases} \frac{\varepsilon_m - \varepsilon_{\text{per}}}{\varepsilon_{\text{ref}} - \varepsilon_{\text{per}}} & : \text{electric case,} \\ \frac{\varepsilon_{\text{ref}}(\varepsilon_m - \varepsilon_{\text{per}})}{\varepsilon_m(\varepsilon_{\text{ref}} - \varepsilon_{\text{per}})} & : \text{magnetic case.} \end{cases} \quad (4.29b)$$

This procedure is also used when the reference defect has been discretized with the sub-pixel smoothing (SPS) methods of Sec. B.4. That means, we usually choose a non-etched hole as reference, compute the discretized version of $\Delta\eta$ from the discretized periodic parts and defect fields and rescale the resulting matrices with scaling factors for a non-etched hole.

Infiltrated Hole, Birefringent Case

In Sec. 1.2.5 we saw that the H-polarization allows to incorporate in-plane anisotropies defined by three real parameters ε_{ex} , ε_{or} and θ . We will derive the basic defect operator matrices to describe holes that have been infiltrated with such a material, e. g. liquid crystals.

As in the previous section, the deviation $\underline{\underline{\Delta\eta}}(\mathbf{r})$ is the product of a constant tensor $\underline{\underline{\Delta\eta}}$ and the form factor of the hole:

$$\underline{\underline{\Delta\eta}}(\mathbf{r}) = \underline{\underline{\Delta\eta}}\Theta_{\text{hole}}(\mathbf{r}), \quad (4.30)$$

where the constant defect contribution to the dielectric function is given by

$$\underline{\underline{\Delta\eta}} \stackrel{(4.5)}{=} \underline{\underline{\eta}} - \eta_{\text{per}} \cdot \underline{\underline{\mathbf{1}}} \quad (4.31)$$

$$\stackrel{(1.39)}{=} R(\theta) \cdot \underline{\underline{\eta}}_{\text{diag}}^{\text{lc}} \cdot R^T(\theta) - \frac{1}{\varepsilon_{\text{per}}} \cdot \underline{\underline{\mathbf{1}}} \quad (4.32)$$

$$\stackrel{(1.33)}{=} R(\theta) \cdot (\underline{\underline{\varepsilon}}_{\text{diag}}^{\text{lc}})^{-1} \cdot R^T(\theta) - \frac{1}{\varepsilon_{\text{per}}} \cdot \underline{\underline{\mathbf{1}}}. \quad (4.33)$$

Here, we have introduced the unit tensor $\underline{\mathbb{1}}$. We can factor out the rotation matrices by exploiting their orthogonality, i. e., $R \cdot R^T = \underline{\mathbb{1}}$ and $R^T = R^{-1}$, yielding

$$\Delta \underline{\underline{\eta}} = R(\theta) \cdot \left[(\underline{\underline{\varepsilon}}_{\text{diag}}^{\text{lc}})^{-1} - \frac{1}{\varepsilon_{\text{per}}} \cdot \underline{\underline{\mathbb{1}}} \right] \cdot R^T(\theta) \quad (4.34)$$

$$\stackrel{(1.33)}{=} R(\theta) \cdot \begin{pmatrix} 1/\varepsilon_{\text{ex}} - 1/\varepsilon_{\text{per}} & 0 \\ 0 & 1/\varepsilon_{\text{or}} - 1/\varepsilon_{\text{per}} \end{pmatrix} \cdot R^T(\theta) \quad (4.35)$$

$$= \begin{pmatrix} \Delta \eta_{\text{ex}} \cos^2 \theta + \Delta \eta_{\text{or}} \sin^2 \theta & (\Delta \eta_{\text{ex}} - \Delta \eta_{\text{or}}) \sin \theta \cos \theta \\ (\Delta \eta_{\text{ex}} - \Delta \eta_{\text{or}}) \sin \theta \cos \theta & \Delta \eta_{\text{ex}} \sin^2 \theta + \Delta \eta_{\text{or}} \cos^2 \theta \end{pmatrix}. \quad (4.36)$$

Here, we have introduced the deviations of the diagonalized inverse permittivity tensor with diagonal elements

$$\Delta \eta_{\text{ex}} = 1/\varepsilon_{\text{ex}} - 1/\varepsilon_{\text{per}}, \quad \Delta \eta_{\text{or}} = 1/\varepsilon_{\text{or}} - 1/\varepsilon_{\text{per}}. \quad (4.37)$$

When computing the matrix B of (4.16b) for $\Delta \underline{\underline{\eta}}$ of (4.36), one obtains the definitions of three Hermitian defect operator matrices involving only x -derivatives, only y -derivatives or mixed derivatives, respectively. Given a single isotropic reference defect with $\eta_{\text{ref}} = 1/\varepsilon_{\text{ref}}$, these matrices are defined as

2D Birefringent Defect Matrices (H-polarization)

$$B_{\alpha\beta}^{xx,\text{ref}} := \int d^2r \partial_x W_\alpha^*(\mathbf{r}_{||}) \cdot \Delta \eta_{\text{ref}}(\mathbf{r}_{||}) \cdot \partial_x W_\beta(\mathbf{r}_{||}), \quad (4.38a)$$

$$B_{\alpha\beta}^{yy,\text{ref}} := \int d^2r \partial_y W_\alpha^*(\mathbf{r}_{||}) \cdot \Delta \eta_{\text{ref}}(\mathbf{r}_{||}) \cdot \partial_y W_\beta(\mathbf{r}_{||}), \quad (4.38b)$$

$$B_{\alpha\beta}^{\{x,y\},\text{ref}} := \int d^2r \Delta \eta_{\text{ref}}(\mathbf{r}_{||}) \cdot \left[\partial_y W_\alpha^*(\mathbf{r}_{||}) \cdot \partial_x W_\beta(\mathbf{r}_{||}) + \partial_x W_\alpha^*(\mathbf{r}_{||}) \cdot \partial_y W_\beta(\mathbf{r}_{||}) \right]. \quad (4.38c)$$

Once these matrices have been computed, one can assemble the full defect operator matrix B^{full} for a hole infiltrated with a birefringent material with extra-ordinary permittivity ε_{ex} , ordinary permittivity ε_{or} and director angle θ as

2D Birefringent Defect Scaling Factors (H-polarization)

$$B_{\alpha\beta}^{\text{full}} = \xi^{xx} B_{\alpha\beta}^{xx,\text{ref}} + \xi^{yy} B_{\alpha\beta}^{yy,\text{ref}} + \xi^{\{x,y\}} B_{\alpha\beta}^{\{x,y\},\text{ref}}, \quad (4.39a)$$

$$\xi^{xx} = \xi_{\text{ex}} \cos^2 \theta + \xi_{\text{or}} \sin^2 \theta, \quad (4.39b)$$

$$\xi^{yy} = \xi_{\text{ex}} \sin^2 \theta + \xi_{\text{or}} \cos^2 \theta, \quad (4.39c)$$

$$\xi^{\{x,y\}} = (\xi_{\text{ex}} - \xi_{\text{or}}) \sin \theta \cos \theta, \quad (4.39d)$$

$$\xi_{\text{ex/or}} = \frac{\varepsilon_{\text{ref}}(\varepsilon_{\text{ex/or}} - \varepsilon_{\text{per}})}{\varepsilon_{\text{ex/or}}(\varepsilon_{\text{ref}} - \varepsilon_{\text{per}})}. \quad (4.39e)$$

Infiltrated holes at different lattice sites \mathbf{R}_m can be described by shifting these matrix elements to the desired lattice sites as in (4.29a).

Infiltrated Hole, Gyrotropic Case

As in the previous sections, we treat one hole that has been infiltrated with a gyrotropic material. Analogously to (4.30), we have to determine the expression for the constant $\Delta \underline{\underline{\eta}}$ for the infiltrated hole.

Just like for (4.30), we start again with the deviation from the previous isotropic periodic filling:

$$\Delta\underline{\eta} = (\underline{\varepsilon}^{\text{mo}})^{-1} - \frac{1}{\varepsilon_{\text{per}}} \cdot \underline{\mathbb{1}} \quad (4.40)$$

$$= \frac{1}{\varepsilon_{\text{diag}}^2 - g_z^2} \begin{pmatrix} \varepsilon_{\text{diag}} & -ig_z \\ +ig_z & \varepsilon_{\text{diag}} \end{pmatrix} - \frac{1}{\varepsilon_{\text{per}}} \cdot \underline{\mathbb{1}} \quad (4.41)$$

$$= \begin{pmatrix} r - 1/\varepsilon_{\text{per}} & -irg_z/\varepsilon_{\text{diag}} \\ +irg_z/\varepsilon_{\text{diag}} & r - 1/\varepsilon_{\text{per}} \end{pmatrix}, \quad (4.42)$$

with

$$r := \frac{\varepsilon_{\text{diag}}}{\varepsilon_{\text{diag}}^2 - g_z^2}. \quad (4.43)$$

As for (4.39), we evaluate (4.16b) for $\Delta\underline{\eta}$ of (4.42) now and obtain the same Hermitian reference matrices B^{xx} and B^{yy} . Additionally, for the off-diagonal part we obtain the definition for an *anti*-Hermitian matrix $B^{[x,y]}$:

2D Gyrotropic Defect Matrices (H-polarization)

$$B_{\alpha\beta}^{[x,y],\text{ref}} := \int d^2r \Delta\eta_{\text{ref}}(\mathbf{r}_{\parallel}) \cdot \left[\partial_x W_{\alpha}^*(\mathbf{r}_{\parallel}) \cdot \partial_y W_{\beta}(\mathbf{r}_{\parallel}) - \partial_y W_{\alpha}^*(\mathbf{r}_{\parallel}) \cdot \partial_x W_{\beta}(\mathbf{r}_{\parallel}) \right]. \quad (4.44a)$$

The full defect matrices B^{full} are assembled from this matrix and Eqs. (4.38a) and (4.38b) as follows (note the position of the factor $-i$):

2D Magneto-optic Defect Scaling Factors (H-polarization)

$$B_{\alpha\beta}^{\text{full}} = \xi^{\text{diag}} (B_{\alpha\beta}^{xx,\text{ref}} + B_{\alpha\beta}^{yy,\text{ref}}) - i\xi^{\text{off-diag}} B_{\alpha\beta}^{[x,y],\text{ref}}, \quad (4.45a)$$

$$\xi^{\text{diag}} = \frac{\varepsilon_{\text{ref}}}{\varepsilon_{\text{per}} - \varepsilon_{\text{ref}}} \cdot \left(\frac{\varepsilon_{\text{per}}}{\varepsilon_{\text{diag}}^2 - g_z^2} \cdot \varepsilon_{\text{diag}} - 1 \right), \quad (4.45b)$$

$$\xi^{\text{off-diag}} = \frac{\varepsilon_{\text{ref}}}{\varepsilon_{\text{per}} - \varepsilon_{\text{ref}}} \cdot \frac{\varepsilon_{\text{per}}}{\varepsilon_{\text{diag}}^2 - g_z^2} \cdot g_z. \quad (4.45c)$$

Further Defect Types

When separating the periodic and defect parts in the permittivity by (4.10), one is not restricted to the same defect geometries as the unit cells of the PC. Shifted holes or varying radii [72] as in Fig. 1.11 can be modeled as well by (4.29), where the scaling factor is simply chosen as $\xi_m = 1$ such that the full reference defect is used in subsequent computations. Radius defects have been investigated by Hermann [43] and in [72].

In Wannier function based time domain simulations, appropriately adjusted defect matrices can model absorbing boundary conditions [96].

Properties of the Operator Matrices

The operator matrices A , B , C for the electric and magnetic fields describe similar parts of the calculation. The A matrices depend solely on the WFs, the C matrices describe the underlying periodic

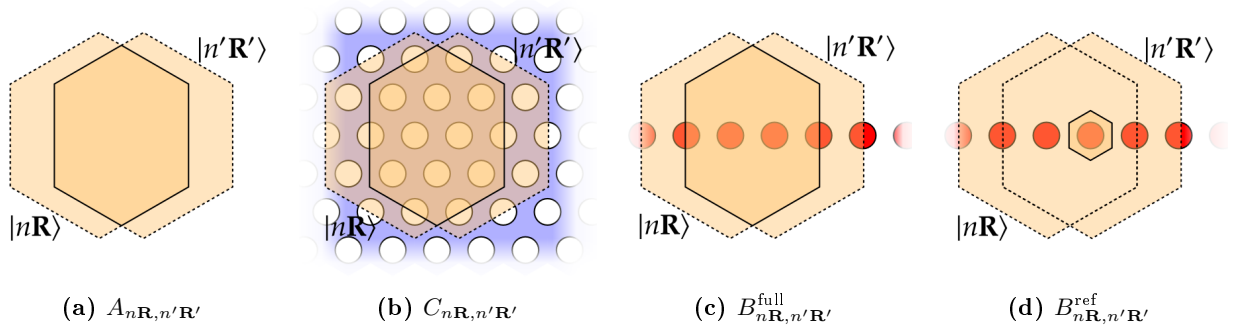


Figure 4.3: Schematic illustration of the integration domains for the respective operator matrix elements (dark orange regions). The numerical WFs have compact support.

PC structure and the B matrices describe the defects (cf. Fig. 4.3). We assume Hermitian dielectric tensors which means we work in lossless dielectric media. Under this premise, the matrices incorporating these tensors become Hermitian as well, as will be shown explicitly for the electric defect matrix B^{el} in Sec. A.3.1. This proof obviously also holds for the A matrices (which feature no dielectric function at all) and the B and C matrices for Hermitian dielectric tensors.

Furthermore, the A and C matrices are invariant under shifts by arbitrary lattice vectors $\boldsymbol{\rho} \in \mathbb{L}_{\text{PC}}$, as is shown for the electric C matrix as an example in Sec. A.3.2. This property holds for the electric and magnetic A and C matrices.

In summary, a matrix $G_{n'\mathbf{R}',n\mathbf{R}}$ in Wannier computations can have these properties:

Translational invariance (A, C): The matrix depends only on the relative distance $\mathbf{R}' - \mathbf{R}$ rather than the absolute values of \mathbf{R}' and \mathbf{R} , i. e.

$$G_{n'\mathbf{R}',n\mathbf{R}} = G_{n'\mathbf{0},n\mathbf{R}-\mathbf{R}'} \quad (4.46)$$

$$= G_{n'\mathbf{R}'-\mathbf{R},n\mathbf{0}}. \quad (4.47)$$

Hermiticity ($A, C, B, B^{xx}, B^{yy}, B^{\{x,y\}}$): The matrix elements obey

$$G_{n'\mathbf{R}',n\mathbf{R}} = G_{n\mathbf{R},n'\mathbf{R}'}^*. \quad (4.48)$$

Anti-Hermiticity ($B^{\{x,y\}}$): The matrix elements obey

$$G_{n'\mathbf{R}',n\mathbf{R}} = -G_{n\mathbf{R},n'\mathbf{R}'}^*. \quad (4.49)$$

Hermiticity and translational invariance (A, C): If the matrix G has both properties, then

$$G_{n'\mathbf{R}',n\mathbf{R}} = G_{n'\mathbf{0},n\mathbf{R}-\mathbf{R}'} \quad (4.50)$$

$$= G_{n'\mathbf{R}'-\mathbf{R},n\mathbf{0}} \quad (4.51)$$

$$= G_{n\mathbf{0},n'\mathbf{R}'-\mathbf{R}}^* \quad (4.52)$$

$$= G_{n\mathbf{R}-\mathbf{R}',n'\mathbf{0}}^*. \quad (4.53)$$

Exploiting these properties can drastically reduce the memory needed to store the matrix elements.

4.2 Truncated Index Domains

So far, all summations were performed over all infinitely many indices $\alpha = (n\mathbf{R})$ in theory. In practise however, only finite sized index domains, i. e., the sets \mathbb{P} containing the allowed or available index elements α , can be used for the following reasons:

- Only a finite number of numerical WF bands n are available.
- The numerical WFs have finite support which limits the sensible choices of \mathbf{R}' and \mathbf{R} , since the matrix entries become 0 for vanishing overlap between WFs as $|\mathbf{R}' - \mathbf{R}|$ exceeds a certain limit.
- Even if many bands n and lattice sites \mathbf{R} are available, one usually wants to restrict the maximal values to save memory and computation time due to the usage of smaller matrices.

Of course, extensive convergence investigations and reference comparison studies have to be conducted in order to be sure to work within sufficient accuracy. For a parameter $R_{\max} \in \mathbb{N}_0$, we define the

R_{\max}	0	1	2	3	4	5	6	7	8	9	10
$\mathbb{L}_{\text{squ,par}}(R_{\max}), \mathbb{L}_{\text{hex,par}}(R_{\max})$	1	9	25	49	81	121	169	225	289	361	441
$\mathbb{L}_{\text{squ,par}}^{\text{shell}}(R_{\max}), \mathbb{L}_{\text{hex,par}}^{\text{shell}}(R_{\max})$	1	8	16	24	32	40	48	56	64	72	80
$\mathbb{L}_{\text{squ}}(R_{\max})$	1	5	13	29	49	81	113	149	197	253	317
$\mathbb{L}_{\text{squ}}^{\text{shell}}(R_{\max})$	1	4	8	16	20	32	32	36	48	56	64
$\mathbb{L}_{\text{hex}}(R_{\max})$	1	7	19	37	61	91	127	187	241	301	367
$\mathbb{L}_{\text{hex}}^{\text{shell}}(R_{\max})$	1	6	12	18	24	30	36	60	54	60	66

Table 4.1: Number of lattice sites for lattice site domains of Fig. 4.4 with parameter R_{\max} .

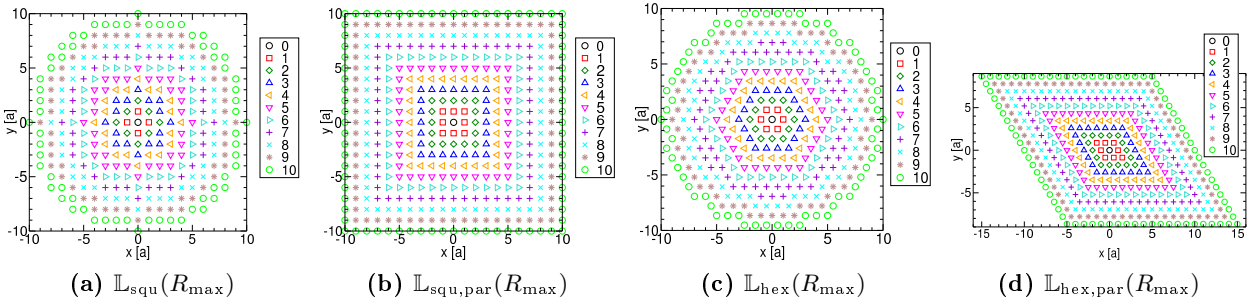


Figure 4.4: Schematic illustrations of lattice site domains for various R_{\max} (shown in legend). The shells of each definition are shown in different colors and symbols shapes. The number of lattice sites of these sets is shown in Tab. 4.1.

following sets of lattice sites:

$\mathbb{L}_{\text{squ}}(R_{\max}), \mathbb{L}_{\text{hex}}(R_{\max})$: All lattice sites within distance $R_{\max}a$ from the origin for the square and triangular lattice, respectively, i. e., $\{\mathbf{R} : |\mathbf{R}| \leq R_{\max}a\}$.

$\mathbb{L}_{\text{squ,par}}(R_{\text{max}}), \mathbb{L}_{\text{hex,par}}(R_{\text{max}})$: All lattice sites within a parallelogram extending $2R_{\text{max}} + 1$ lattice sites in each lattice direction for the square and triangular lattice, respectively, i. e., $\left\{ \sum_i z_i \mathbf{a}_i : z_i \in \{-R_{\text{max}}, -R_{\text{max}} + 1, \dots, R_{\text{max}}\} \right\}$.

$\mathbb{L}_{\text{squ}}^{\text{shell}}(R_{\text{max}}), \mathbb{L}_{\text{hex}}^{\text{shell}}(R_{\text{max}})$: All lattice sites in the difference sets $\mathbb{L}_{\text{squ}}(R_{\text{max}})/\mathbb{L}_{\text{squ}}(R_{\text{max}} - 1)$ (for the triangular lattice analogous).

$\mathbb{L}_{\text{squ,par}}^{\text{shell}}(R_{\text{max}}), \mathbb{L}_{\text{hex,par}}^{\text{shell}}(R_{\text{max}})$: All lattice sites in the difference sets $\mathbb{L}_{\text{squ,par}}(R_{\text{max}})/\mathbb{L}_{\text{squ,par}}(R_{\text{max}} - 1)$ (for the triangular lattice analogous).

The lattice site domains yielded by these definitions are visualized in Fig. 4.4. The number of lattice sites used in each set are shown in Tab. 4.1.

Note that there are two distinct usages for the lattice site domains \mathbb{L} here:

The computational domain \mathbb{L}_{comp} : This domain defines at which lattice sites \mathbf{R} the WFs are located and taken into account for the expansion (4.1). This determines the absolute size of the final matrices that have to be diagonalized for computations, e. g. in (4.54).

The coupling domain $\mathbb{L}_{\text{coupling}}$: This domain determines for which lattice sites \mathbf{R} and $\mathbf{R} - \mathbf{R}'$ the operator matrices (4.6), (4.11), (4.15), and (4.16) are calculated. The coupling domain determines the sparsity of the final matrices that have to be diagonalized, setting elements that are too far away (in terms of lattice sites) to 0. The more localized the WFs are, the better this approximation becomes.

4.3 Cavity Modes

We want to determine the eigenfrequencies ω and the expansion coefficients c_β for defect modes occurring in isolated defect clusters in the PC as in Fig. 4.1. We restrict ourselves to defect configurations that can be described by (4.18) and the corresponding cavity defect operator matrix B^{cav} from (4.19). By Sec. 4.1.1, the wave equation for the magnetic and electric field treatment, as well as for the 2D H-polarized and E-polarized case, can be written as

Eigenmode Computation

$$\sum_{\beta} \left[C_{\alpha\beta} + B_{\alpha\beta}^{\text{cav}} - \Lambda(\omega) A_{\alpha\beta} \right] c_{\beta} = 0. \quad (4.54)$$

This a generalized matrix eigenvalue problem with eigenvalue $\Lambda(\omega)$, from which the corresponding eigenfrequencies ω of the modes can be obtained under consideration of the definitions (4.7) or (4.12) of Λ appropriate for the corresponding electric or magnetic field case. After the Wannier expansion coefficients c_β have been computed, the mode profiles can be obtained by carrying out the sum (4.1).

By truncating the infinite matrices to lattice site domains discussed in Sec. 4.2, one implicitly imposes metallic boundary conditions on the defect modes, meaning that the fields are forced to become 0 at the boundaries of the computational domain (where the WF become 0 as well). This is a sensible approximation when describing defect modes with frequencies in the band gap of the PC where the modes decay exponentially into the PC domain, thus their field strengths decay rapidly to 0 (cf. Fig. 1.13).

4.4 Dispersion Relations $\omega(\mathbf{k})$

We derive the matrix equations for the computation of band structures, supercell calculations and waveguide dispersions $\omega(\mathbf{k})$ for given wave vector \mathbf{k} . The modes are calculated with periodic boundary conditions which enter the equations by construction. For the sake of simplicity, we restrict ourselves to scalar dielectric functions for the derivation, since the resulting matrix equations are independent of the tensorial properties.

We treat dielectric functions which are periodic with respect to a subset $\mathbb{L}_{\text{per}} \subseteq \mathbb{L}_{\text{PC}}$ of lattice vectors \mathbf{S} (Fig. 4.5):

$$\varepsilon(\mathbf{r} + \mathbf{S}) = \varepsilon(\mathbf{r}) \quad \forall \mathbf{S} \in \mathbb{L}_{\text{per}}. \quad (4.55)$$

The lattice vectors \mathbb{L}_{per} define a superlattice in \mathbb{L}_{PC} , with supercells consisting of the relative lattice

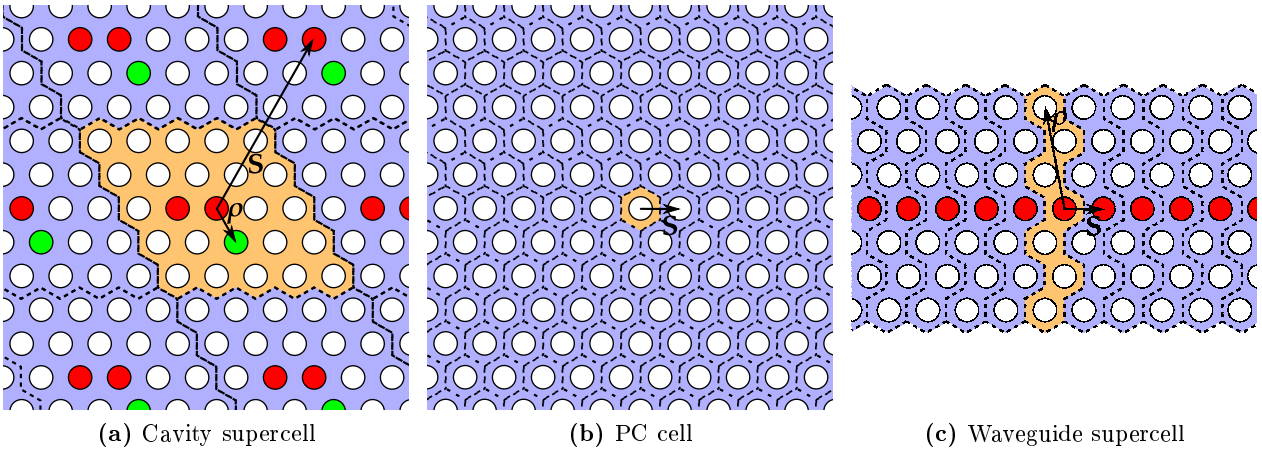


Figure 4.5: Schematic examples for supercells (dashed outlines) used in dispersion relation computations with WFs. Exemplary intra-supercell lattice vectors $\boldsymbol{\rho} \in \mathbb{L}_{\text{sup}}$ (orange) and inter-supercell lattice vectors $\mathbf{S} \in \mathbb{L}_{\text{per}}$ are shown.

sites $\boldsymbol{\rho}$ from a finite subset $\mathbb{L}_{\text{sup}} \subset \mathbb{L}_{\text{PC}}$ such that

$$\mathbb{L}_{\text{PC}} = \mathbb{L}_{\text{per}} \oplus \mathbb{L}_{\text{sup}}. \quad (4.56)$$

That means, any general lattice site $\mathbf{R} \in \mathbb{L}_{\text{PC}}$ of the PC can be written as $\mathbf{R} = \mathbf{S} + \boldsymbol{\rho}$, where $\mathbf{S} \in \mathbb{L}_{\text{per}}$ and $\boldsymbol{\rho} \in \mathbb{L}_{\text{sup}}$ are uniquely determined.

Similar to (4.10), the full dielectric function ε can be split into the part ε_{PC} describing the PC and the deviation $\Delta\varepsilon_{\text{per}}$ within all supercells, giving

$$\varepsilon(\mathbf{r}) = \varepsilon_{\text{PC}}(\mathbf{r}) + \Delta\varepsilon_{\text{per}}(\mathbf{r}), \quad (4.57)$$

where the parts are periodic with respect to the corresponding sets of lattice sites:

$$\varepsilon_{\text{PC}}(\mathbf{r} + \mathbf{R}) = \varepsilon_{\text{PC}}(\mathbf{r}) \quad \forall \mathbf{R} \in \mathbb{L}_{\text{PC}}, \quad (4.58)$$

$$\Delta\varepsilon_{\text{per}}(\mathbf{r} + \mathbf{S}) = \Delta\varepsilon_{\text{per}}(\mathbf{r}) \quad \forall \mathbf{S} \in \mathbb{L}_{\text{per}}. \quad (4.59)$$

The periodic deviation $\Delta\varepsilon_{\text{per}}$ is fully determined by the various local basic defects (4.18), where $\mathbf{R}_m = \mathbf{S} + \boldsymbol{\rho}_m$ according to (4.56), which then yields

$$\Delta\varepsilon_{\text{per}}(\mathbf{r}) = \sum_{\mathbf{S} \in \mathbb{L}_{\text{per}}} \sum_m \Delta\varepsilon_m(\mathbf{r} - \mathbf{S} - \boldsymbol{\rho}_m), \quad \boldsymbol{\rho}_m \in \mathbb{L}_{\text{sup}}. \quad (4.60)$$

By (4.55) and the Bloch theorem (1.19), an electromagnetic eigenmode $\boldsymbol{\psi}_{\mathbf{k}}(\mathbf{r})$ (denoting the electric or magnetic field) of the wave equations with wave vector \mathbf{k} obeys

$$\boldsymbol{\psi}_{\mathbf{k}}(\mathbf{r} + \mathbf{S}) = e^{i\mathbf{k}\mathbf{S}}\boldsymbol{\psi}_{\mathbf{k}}(\mathbf{r}) \quad \forall \mathbf{S} \in \mathbb{L}_{\text{per}}. \quad (4.61)$$

The expansion (4.1) in terms of the electric or magnetic field WFs $\mathbf{W}_{n\mathbf{R}}(\mathbf{r})$ is generally written as

$$\boldsymbol{\psi}_{\mathbf{k}}(\mathbf{r}) = \sum_{n\mathbf{R}} c_{n\mathbf{R}} \mathbf{W}_{n\mathbf{R}}(\mathbf{r}). \quad (4.62)$$

The expansion coefficients $c_{n\mathbf{R}}$ inherit the Bloch phase (4.61) under translations because

$$\boldsymbol{\psi}_{\mathbf{k}}(\mathbf{r} + \mathbf{S}) \stackrel{(4.62)}{=} \sum_{n\mathbf{R}} c_{n\mathbf{R}} \mathbf{W}_{n\mathbf{R}}(\mathbf{r} + \mathbf{S}) \quad (4.63)$$

$$\stackrel{(A.15)}{=} \sum_{n\mathbf{R}} c_{n\mathbf{R}} \mathbf{W}_{n\mathbf{R}-\mathbf{S}}(\mathbf{r}) \quad (4.64)$$

$$= \sum_{n\mathbf{R}} c_{n\mathbf{R}+\mathbf{S}} \mathbf{W}_{n\mathbf{R}}(\mathbf{r}). \quad (\text{sum over all } \mathbf{R} \in \mathbb{L}_{\text{PC}}) \quad (4.65)$$

On the other hand, by (4.61) and (4.62) we have that

$$\boldsymbol{\psi}_{\mathbf{k}}(\mathbf{r} + \mathbf{S}) = \sum_{n\mathbf{R}} e^{i\mathbf{k}\mathbf{S}} c_{n\mathbf{R}} \mathbf{W}_{n\mathbf{R}}(\mathbf{r}). \quad (4.66)$$

Comparing the coefficients of the last two equations above shows that for Bloch-periodic modes the Wannier expansion coefficients obey

$$\boxed{c_{n\mathbf{R}+\mathbf{S}} = e^{i\mathbf{k}\mathbf{S}} c_{n\mathbf{R}}.} \quad (4.67)$$

With this relation and (4.56) we can write the expansion (4.62), where \mathbf{R} runs over \mathbb{L}_{PC} , as

$$\boldsymbol{\psi}_{\mathbf{k}}(\mathbf{r}) \stackrel{(4.67)}{=} \sum_{\mathbf{S} \in \mathbb{L}_{\text{per}}} \sum_{\boldsymbol{\rho} \in \mathbb{L}_{\text{sup}}} \sum_n e^{i\mathbf{k}\mathbf{S}} c_{n\boldsymbol{\rho}} \mathbf{W}_{n\mathbf{S}+\boldsymbol{\rho}}(\mathbf{r}). \quad (4.68)$$

Analogous to Sec. 4.1.1, we write $|n\mathbf{S}+\boldsymbol{\rho}\rangle$ now for the WFs, insert the above expansion into the magnetic field wave equation and project from the left on $\langle n'\mathbf{S}' + \boldsymbol{\rho}' | \cdot$ which gives

$$\begin{aligned} \sum_{\mathbf{S} \in \mathbb{L}_{\text{per}}} \sum_{\boldsymbol{\rho} \in \mathbb{L}_{\text{sup}}} \sum_n \left[\langle n'\mathbf{S}' + \boldsymbol{\rho}' | \nabla \times \boldsymbol{\eta} \cdot \nabla \times |n\mathbf{S} + \boldsymbol{\rho}\rangle \right. \\ \left. - \Lambda^{\text{mag}}(\omega) \langle n'\mathbf{S}' + \boldsymbol{\rho}' | n\mathbf{S} + \boldsymbol{\rho}\rangle \right] e^{i\mathbf{k}\mathbf{S}} c_{n\boldsymbol{\rho}} = 0. \end{aligned} \quad (4.69)$$

Using the definitions from (4.6), this projection is written as the matrix eigenvalue equation with fixed \mathbf{k} and \mathbf{S}'

$$\sum_n \sum_{\boldsymbol{\rho} \in \mathbb{L}_{\text{sup}}} \sum_{\mathbf{S} \in \mathbb{L}_{\text{per}}} e^{i\mathbf{k}\mathbf{S}} \left[C_{n'\mathbf{S}'+\boldsymbol{\rho}',n\mathbf{S}+\boldsymbol{\rho}} + B_{n'\mathbf{S}'+\boldsymbol{\rho}',n\mathbf{S}+\boldsymbol{\rho}} - \Lambda^{\text{mag}}(\omega) A_{n'\mathbf{S}'+\boldsymbol{\rho}',n\mathbf{S}+\boldsymbol{\rho}} \right] c_{n\boldsymbol{\rho}} = 0, \quad (4.70)$$

where the matrix $B = B[\Delta\varepsilon_{\text{per}}]$ models the whole infinitely extended defect distribution (4.60). This means, all these matrices are translationally invariant by shifts $\mathbf{S}' \in \mathbb{L}_{\text{per}}$, so by (4.46) and G standing for any of the above matrices we have

$$G_{n'\mathbf{S}'+\boldsymbol{\rho}',n\mathbf{S}+\boldsymbol{\rho}} = G_{n'\boldsymbol{\rho}',n\mathbf{S}-\mathbf{S}'+\boldsymbol{\rho}}, \quad \text{for } G = A, C, B. \quad (4.71)$$

The summation in (4.70) is performed over all superlattice vectors $\mathbf{S} \in \mathbb{L}_{\text{per}}$. After a shift of the summation vectors \mathbf{S} by the fixed \mathbf{S}' , it is (under consideration of the aforementioned translational invariance) equivalent to

$$\sum_n \sum_{\boldsymbol{\rho} \in \mathbb{L}_{\text{sup}}} \sum_{\mathbf{S} \in \mathbb{L}_{\text{per}}} e^{i\mathbf{k}\mathbf{S}} \left[C_{n'\boldsymbol{\rho}', n\mathbf{S}+\boldsymbol{\rho}} + B_{n'\boldsymbol{\rho}', n\mathbf{S}+\boldsymbol{\rho}} - \Lambda^{\text{mag}}(\omega) A_{n'\boldsymbol{\rho}', n\mathbf{S}+\boldsymbol{\rho}} \right] c_{n\boldsymbol{\rho}} = 0, \quad (4.72)$$

where the additional constant global phase factor $e^{i\mathbf{k}\mathbf{S}'}$ has been absorbed into the complex coefficients $c_{n\boldsymbol{\rho}}$. The matrix B can now be assembled from precalculated matrices $B^{(m)}$ similar to (4.19) from basic defects as

$$B_{n'\boldsymbol{\rho}', n\mathbf{S}+\boldsymbol{\rho}} \stackrel{(4.19)(4.60)}{=} \sum_{\mathbf{S}' \in \mathbb{L}_{\text{per}}} \sum_m B_{n'\boldsymbol{\rho}'-\mathbf{S}'-\boldsymbol{\rho}_m, n\mathbf{S}+\boldsymbol{\rho}-\mathbf{S}'-\boldsymbol{\rho}_m}^{(m)}, \quad \boldsymbol{\rho}_m \in \mathbb{L}_{\text{sup}}. \quad (4.73)$$

Introducing contracted Hermitian matrices \tilde{G} , we can write the final generalized eigenvalue problem as

Supercell calculations in Wannier basis

$$\sum_n \sum_{\boldsymbol{\rho} \in \mathbb{L}_{\text{sup}}} \left[\tilde{C}_{n'\boldsymbol{\rho}', n\boldsymbol{\rho}} + \tilde{B}_{n'\boldsymbol{\rho}', n\boldsymbol{\rho}} - \Lambda(\omega) \tilde{A}_{n'\boldsymbol{\rho}', n\boldsymbol{\rho}} \right] c_{n\boldsymbol{\rho}} = 0. \quad (4.74a)$$

$$\tilde{G}_{n'\boldsymbol{\rho}', n\boldsymbol{\rho}} := \sum_{\mathbf{S} \in \mathbb{L}_{\text{per}}} e^{i\mathbf{k}\mathbf{S}} G_{n'\boldsymbol{\rho}', n\boldsymbol{\rho}+\mathbf{S}}, \quad (4.74b)$$

This form is valid for the electric and magnetic wave equation in 3D and the scalar versions in 2D. For given $\mathbf{k} \in \mathbb{L}_{\text{per}}^*$, the solution of this matrix eigenvalue equation yields $\omega(\mathbf{k})$ from the corresponding eigenvalue $\Lambda(\omega)$ by (4.7) and (4.12) and the Wannier expansion coefficients $c_{n\boldsymbol{\rho}}$ on one supercell for the modes. They can be assembled from WFs by (4.68).

The band structure of the PC can be expressed in the Wannier basis by choosing $B = 0$ (no defects) and $\mathbb{L}_{\text{per}} = \mathbb{L}_{\text{PC}}$. Then one can compute the dispersion relation along the high symmetry lines or on the MP mesh that was used for constructing the WFs which is an important consistency check.

Waveguides are periodic in one dimension, where for the other dimensions the quasi-metallic boundary conditions discussed in Sec. 4.3 are implicitly imposed by using numerically truncated WFs on finite sized supercell domains \mathbb{L}_{sup} .

4.5 On-shell Waveguide Dispersion $k(\omega)$

Starting from the wave equation in terms of WFs for given ω , we will assemble a transfer matrix $\mathcal{T}(\omega)$ which will relate the Wannier expansion coefficients $g_{n\mathbf{R}}$ of the waveguide modes with each other. The eigenvalues of this transfer matrix will then yield the phase factors in (4.61) and its eigenvectors will correspond to the eigenmodes. This technique will yield guided and evanescent waveguide modes alike which are needed for the scattering matrix formalism to work properly.

4.5.1 Wave Equation

The wave equation in its general form (4.54) which is valid for 3D vectorial and 2D scalar electric and magnetic fields, reads

$$\sum_{n\mathbf{R}} \left[C_{n'\mathbf{R}', n\mathbf{R}} + B_{n'\mathbf{R}', n\mathbf{R}} - \Lambda(\omega) A_{n'\mathbf{R}', n\mathbf{R}} \right] g_{n\mathbf{R}} = 0. \quad (4.75)$$

Here, B is given by (4.73) for the particular defect configuration (4.60) within the supercells.

As stated in (4.71), B is periodic with respect to translations by all superlattice vectors $\mathbf{S} \in \mathbb{L}_{\text{per}}$. The matrices A and C are by construction translationally invariant under shifts by *any* lattice vector $\mathbf{R} \in \mathbb{L}_{\text{PC}}$, including \mathbb{L}_{per} . We add up these matrices to the system matrix $M(\omega)$ given by

$$M_{n'\mathbf{R}',n\mathbf{R}}(\omega) := C_{n'\mathbf{R}',n\mathbf{R}} + B_{n'\mathbf{R}',n\mathbf{R}} - \Lambda(\omega)A_{n'\mathbf{R}',n\mathbf{R}}, \quad (4.76)$$

which inherits the translational invariance by $\mathbf{S} \in \mathbb{L}_{\text{per}}$.

The wave equation in terms of WFs then reads

$$\sum_{n\mathbf{R}} M_{n'\mathbf{R}',n\mathbf{R}}(\omega) G_{n\mathbf{R}} = 0, \quad (4.77)$$

$$\text{with } M_{n\mathbf{R}+\mathbf{S},n'\mathbf{R}'+\mathbf{S}} = M_{n'\mathbf{R}',n\mathbf{R}} \quad \forall \mathbf{S} \in \mathbb{L}_{\text{per}}, \quad (4.78)$$

where the frequency ω is a given parameter now. This is no longer an eigenvalue problem, but an infinite system of linear equations. Before we can assemble the transfer matrix, we have to rewrite (4.77) in a more suitable form that takes advantage of the translational invariance (4.78).

In the case of an isolated cavity defect it was convenient to think of the Wannier expansion coefficients attached to a single unit cell of the PC. Here it is more convenient to think of the Wannier expansion coefficients attached to the supercells (we do this in anticipation of (4.95)). We recast (4.77) which is given in terms of unit cells now in terms of a supervector \mathcal{C} of Wannier expansion coefficients. This supervector is a set of vectors of those expansion coefficients, where coefficients belonging to the same supercell placed at $\mathbf{S} \in \mathbb{L}_{\text{per}}$ are grouped together in a vector $\mathcal{C}_{\mathbf{S}}$:

$$\mathcal{C}_{\mathbf{S}} := (c_{n,\mathbf{S}+\boldsymbol{\rho}} : \boldsymbol{\rho} \in \mathbb{L}_{\text{sup}}), \quad (4.79)$$

$$\mathcal{C} := (\mathcal{C}_{\mathbf{S}} : \mathbf{S} \in \mathbb{L}_{\text{per}}) \quad (4.80)$$

This implies a partitioning of the matrix M into smaller submatrices $\mathcal{M}_{\mathbf{S}',\mathbf{S}}$ which couple the coefficients of the supercell at \mathbf{S} to those in the supercell at \mathbf{S}' :

$$\mathcal{M}_{\mathbf{S}',\mathbf{S}} := (M_{n'\boldsymbol{\rho}'+\mathbf{S}',n\boldsymbol{\rho}+\mathbf{S}} : \boldsymbol{\rho}, \boldsymbol{\rho}' \in \mathbb{L}_{\text{sup}}), \quad (4.81)$$

$$\mathcal{M}_{\mathbf{S}'-\mathbf{S}} := \mathcal{M}_{\mathbf{S}'-\mathbf{S},\mathbf{0}} \stackrel{(4.78)}{=} \mathcal{M}_{\mathbf{S}',\mathbf{S}}. \quad (4.82)$$

The last equation stems from the translational invariance property of the system matrix, so (4.77) now reads:

$$\sum_{\mathbf{S} \in \mathbb{L}_{\text{per}}} \mathcal{M}_{\mathbf{S}'-\mathbf{S}}(\omega) \cdot \mathcal{C}_{\mathbf{S}} = 0 \quad \forall \mathbf{S}' \in \mathbb{L}_{\text{per}}. \quad (4.83)$$

The product here is an ordinary matrix-vector product. Eq. (4.83) is in fact a series of infinitely many identical equations: It describes the relation between Wannier expansion coefficients on the supercell at \mathbf{S} with those on the supercell at \mathbf{S}' , and this relation is always the same for the same relative distance $\mathbf{S}' - \mathbf{S}$ between supercells. So we can choose an arbitrary origin supercell (i. e., choose a fixed $\mathbf{S}' = \mathbf{S}'_0$) and solve the resulting matrix equation.

4.5.2 Transfer Matrix For Waveguide Dispersions

So far, the treatment of the wave equation is correct and we just have recast (4.77) into the new form (4.83) which is valid for all cases shown in Fig. 4.5. Now we want to compute $k(\omega)$ for a waveguide as in Fig. 4.5c and specialize (4.83) for that case. Such a waveguide is characterized by a periodic dielectric

function (4.55) with periodicity in only one dimension. The set of lattice vectors \mathbb{L}_{per} defining the superlattice is then explicitly given by

$$\mathbb{L}_{\text{per}} := \{i\mathbf{s}_{\text{wg}} : i \in \mathbb{Z}\} \quad (4.84)$$

for a primitive waveguide translation $\mathbf{s}_{\text{wg}} \in \mathbb{L}_{\text{PC}}$. We allow $|\mathbf{s}_{\text{wg}}| = na$ for $n \in \mathbb{N}$ and the lattice constant a of the underlying 2D PC structure. That way, we are able to describe ordinary W1, W2, etc., waveguides as well as coupled-resonator optical wave guides (CROW), examples of which are shown in Fig. 1.14. However, W x waveguides with some fractional value $x \notin \mathbb{N}$ cannot be treated in this formalism. We also call the supercells in the waveguide problem slices because of their obvious shape.

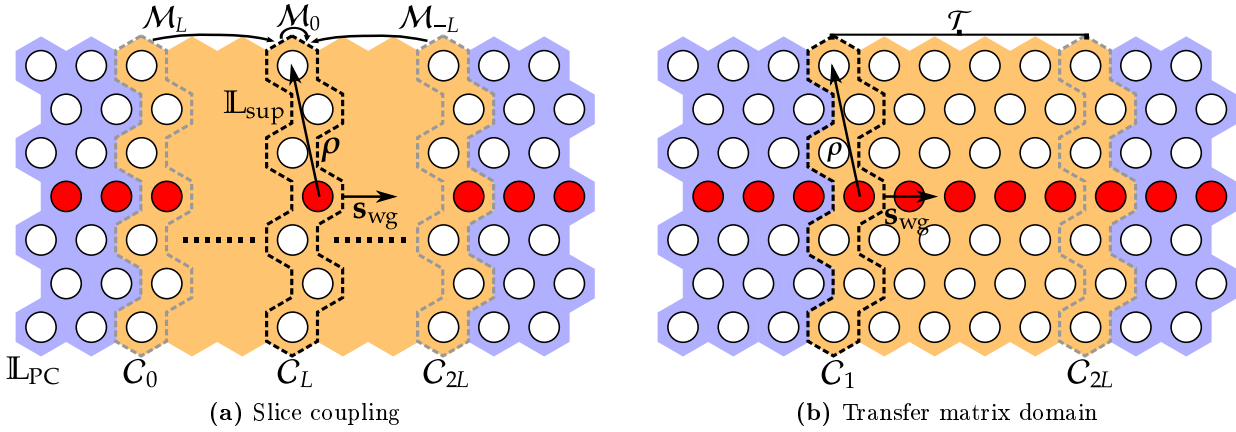


Figure 4.6: Schematic illustrations of waveguide slice domains \mathbb{L}_{sup} (dashed outline) containing one defect site. The periodic repetition of the slices along \mathbf{s}_{wg} spans the whole lattice \mathbb{L}_{PC} of the photonic crystal. The orange regions denote the position of the slice expansion coefficients \mathcal{C}_j . (a) The matrices M_{L-j} couple the expansion coefficients of slice j to the ones at slice L . (b) The domain on which the transfer matrix \mathcal{T} couples $2L$ slice coefficients with each other.

By choosing a particular \mathbf{s}_{wg} , we can label the Wannier expansion coefficients (4.79) on a slice by integers:

$$\mathcal{C}_i := (c_{n,i\mathbf{s}_{\text{wg}}+\boldsymbol{\rho}} : \boldsymbol{\rho} \in \mathbb{L}_{\text{slice}}), \quad (4.85)$$

$$\mathcal{C} := (\mathcal{C}_i : i \in \mathbb{Z}). \quad (4.86)$$

The partitioning (4.81) of the matrix M into smaller submatrices $\mathcal{M}_{i,j}$ which couple the coefficients of slice j to those in slice i , is defined by

$$\mathcal{M}_{i,j} := (M_{n\boldsymbol{\rho}+i\mathbf{s}_{\text{wg}},n'\boldsymbol{\rho}'+j\mathbf{s}_{\text{wg}}} : \boldsymbol{\rho}, \boldsymbol{\rho}' \in \mathbb{L}_{\text{slice}}), \quad (4.87)$$

$$\mathcal{M}_{i-j} := M_{i-j,0} = \mathcal{M}_{i,j}. \quad (4.88)$$

The lattice site domains for the indices i and j for these constructions are shown in Fig. 4.6a.

The wave equation (4.83) for a waveguide in a PC in terms of slices then reads

$$\sum_j \mathcal{M}_{i-j}(\omega) \cdot \mathcal{C}_j = 0 \quad \forall i \in \mathbb{Z}. \quad (4.89)$$

Finally, we have to truncate the infinite problem in order to compute numerical solutions with a computer. This is justified again by the localization properties of the Wannier functions. The matrix entries of \mathcal{M}_{i-j} decay rapidly for increasing coupling distances $|i-j|$, and we treat coupling matrices for distances larger than a long range interaction parameter L to be 0. In practical computations, we usually choose $L \leq 4$. The matrix elements become 0 anyway in the numerical computation because the numerically available Wannier functions exist only on a finite support with finite R_{\max} . This means, only $L \leq R_{\max}$ is sensible in numerical computations, since the results cannot be made better with larger L — there is simply no additional data available. When L is chosen, we have $2L + 1$ non-zero matrices M_{i-j} at our disposal and fix $i = L$. This choice determines the allowed values of $j = 0, \dots, 2L$ and we may formally solve (4.89) for \mathcal{C}_0 , giving

$$\mathcal{C}_0 = -\mathcal{M}_L^{-1} \cdot \sum_{j=1}^{2L} \mathcal{M}_{L-j} \cdot \mathcal{C}_j. \quad (4.90)$$

Here we see that a long range interaction parameter L greater than R_{\max} would lead to M_L containing only zeros (because the slices cannot couple due to the final support of the numerical WFs), thus it could not be inverted. Defining the matrices

$$\mathcal{T}_{1,j} := -\mathcal{M}_L^{-1} \cdot \mathcal{M}_{L-j} \quad \text{for } j = 1, \dots, 2L \quad (4.91)$$

the relation (4.90) between the slice expansion coefficients can be written as

$$\begin{pmatrix} \mathcal{C}_0 \\ \mathcal{C}_1 \\ \vdots \\ \mathcal{C}_{2L-1} \end{pmatrix} = \begin{pmatrix} \mathcal{T}_{1,1} & \mathcal{T}_{1,2} & \dots & \dots & \mathcal{T}_{1,2L} \\ \mathbb{1} & 0 & \dots & \dots & 0 \\ 0 & \ddots & \ddots & & \vdots \\ \vdots & \ddots & \ddots & \ddots & \vdots \\ 0 & \dots & 0 & \mathbb{1} & 0 \end{pmatrix} \cdot \begin{pmatrix} \mathcal{C}_1 \\ \mathcal{C}_2 \\ \vdots \\ \mathcal{C}_{2L-1} \\ \mathcal{C}_{2L} \end{pmatrix}, \quad (4.92)$$

where $\mathbb{1}$ denotes the unit matrix. The lattice site domain for which the transfer matrix \mathcal{T} is defined is shown in Fig. 4.6b.

Finally, we get to exploit the Bloch theorem (4.67) for $\mathbf{S} = \mathbf{s}_{\text{wg}}$ for the Wannier expansion coefficients which transforms this matrix-vector equation into a matrix eigenvalue problem:

$$\mathcal{C}_{i-1} \stackrel{(4.85)}{=} (c_{n, \mathbf{S}_i + \boldsymbol{\rho} - \mathbf{s}_{\text{wg}}}) \quad (4.93)$$

$$\stackrel{(4.67)}{=} e^{-i\mathbf{k}\mathbf{s}_{\text{wg}}} (c_{n, \mathbf{S}_i + \boldsymbol{\rho}}) \quad (4.94)$$

$$\stackrel{(4.85)}{=} e^{-i\mathbf{k}\mathbf{s}_{\text{wg}}} \mathcal{C}_i. \quad (4.95)$$

Adjusting the left hand side of (4.92) by this result yields

$$\mathcal{T} \cdot \mathcal{C} = e^{-i\mathbf{k}\mathbf{s}_{\text{wg}}} \mathcal{C}, \quad (4.96)$$

where we labeled the full transfer matrix from (4.92) as \mathcal{T} and used the numerically truncated supervector $\mathcal{C} = (\mathcal{C}_1, \dots, \mathcal{C}_{2L})$. This transfer matrix \mathcal{T} has eigenvectors $\mathcal{C}^{(\ell)}$ and eigenvalues $\phi^{(\ell)}$, from which the corresponding wavenumbers k in direction of the waveguide ($\mathbf{k}\mathbf{s}_{\text{wg}} = k|\mathbf{s}_{\text{wg}}|$) can be obtained via

$$k^{(\ell)} = \frac{i}{|\mathbf{s}_{\text{wg}}|} \ln(\phi^{(\ell)}). \quad (4.97)$$

The wavenumbers obtained are in general complex numbers, where vanishing imaginary parts belong to the propagating modes of the waveguide and the non-vanishing parts describe the evanescent modes. These evanescent modes are necessary for the scattering matrix formalism to work. The waveguide mode is fully determined by the Wannier coefficients \mathcal{C}_1 , and the other slice coefficients can be obtained by iteratively applying (4.95).

4.5.3 Properties of the System Matrix

The system matrix M from (4.77) is stated in terms of Wannier functions and as long as the dielectric tensors involved are Hermitian (meaning a lossless medium), the system matrix itself is also Hermitian. This reduces the number of different matrices \mathcal{M}_i needed to compute to $L + 1$, as will be shown now.

By the definition (4.87), we have that

$$\mathcal{M}_{i,j} \stackrel{(4.87)}{=} (M_{n\mathbf{s}_i+\boldsymbol{\rho},n'\mathbf{s}_j+\boldsymbol{\rho}'}) \quad (4.98)$$

$$= (M_{n'\mathbf{s}_j+\boldsymbol{\rho}',n\mathbf{s}_i+\boldsymbol{\rho}}^*) \quad (\text{Hermitian system matrix}) \quad (4.99)$$

$$\stackrel{(4.87)}{=} \mathcal{M}_{j,i}^\dagger. \quad (4.100)$$

With (4.88) we obtain

$$\mathcal{M}_{i-j} = \mathcal{M}_{i,j} \quad (4.101)$$

$$= \mathcal{M}_{j,i}^\dagger \quad (4.102)$$

$$= \mathcal{M}_{j-i}^\dagger. \quad (4.103)$$

This means that the matrices \mathcal{M}_1 to \mathcal{M}_L can be deduced from the matrices \mathcal{M}_{-1} to \mathcal{M}_{-L} for Hermitian dielectric functions. Together with the Hermitian \mathcal{M}_0 this makes $L + 1$ different matrices needed to assemble the transfer matrix \mathcal{T} .

4.6 Scattering Matrix Formalism

This is a brief summary of the Wannier based S-matrix (scattering matrix) formalism developed by Hermann [43]. It illustrates the ability of the localized function expansion to compute amplitude transmission and reflection coefficients of individual functional elements and large scale PC circuits assembled from functional elements (see Fig. 4.7). Large in this respect means many lattice constants a . The device of interest is connected to waveguides, where incoming guided modes of one waveguide enter the device region \mathbb{L}_{dev} on one side and get scattered by the device. This excites a number of outgoing guided modes in all attached waveguides. The amplitudes of these waveguide modes are denoted by a_ℓ for incoming modes and b_ℓ for outgoing modes. The natural index ℓ consecutively labels all possible waveguide modes in all waveguides. The effect of the device can then be described by its S-matrix $S(\omega)$ which relates the amplitudes of incoming and outgoing guided modes in the waveguides via

$$b_\ell = \sum_{\ell'} S_{\ell\ell'}(\omega) a_{\ell'}. \quad (4.104)$$

The elements of $S(\omega)$ can be computed by solving the wave equation in the form of (4.77) as a system of linear equations. However, the solutions are subject to boundary conditions that require the fields in the waveguide to have a special form. The incoming amplitude a_ℓ of one single guided mode in a

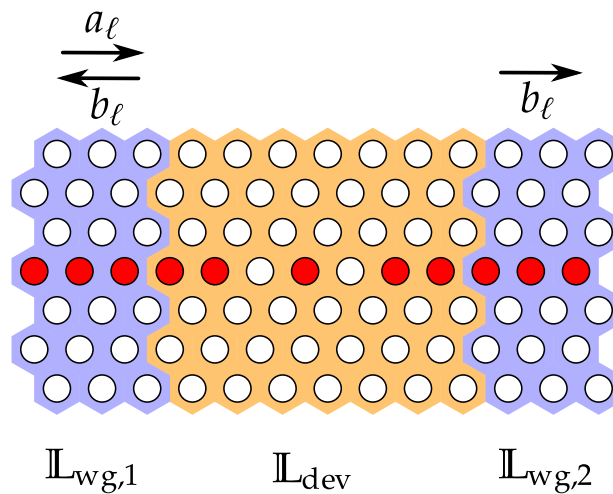


Figure 4.7: Schematic illustration of the lattice site domains for a photonic device, \mathbb{L}_{dev} , attached to waveguides $\mathbb{L}_{\text{wg},i}$. The amplitudes of incoming (a_{ℓ}) and outgoing (b_{ℓ}) waveguide modes are also shown.

dedicated waveguide is set to 1 and all other incoming amplitudes to 0. The solution of the system of linear equations of (4.77) is then expressed in terms of all possible outgoing waveguide modes which yields the amplitudes b_{ℓ} . From these amplitudes, the S-matrix can be constructed. The guided and evanescent waveguide modes obtained from a previous on-shell computation according to Sec. 4.5.2 have to be used for this expansion. Finally, only the S-matrix elements relating guided modes are retained, yielding very small reduced S-matrices.

The S-matrix of a large scale circuit assembled from a number of devices connected by waveguides can then be expressed as the product of the reduced S-matrices for each constituent (waveguides are also expressed in terms of an S-matrix). This approximation of using only the reduced S-matrices was justified and shown to give correct results in [43].

Thus, the transmission and reflection coefficients of a large PC circuit can be obtained by simple matrix-matrix products of small S-matrices.

4.7 Summary

We expressed the eigenmodes of the wave equations in terms of Wannier functions, thus rewriting the differential operator eigenproblems as generalized matrix eigenvalue problems. The matrices for a particular defect setup can be assembled from a few precomputed matrices describing the pure overlap of WFs, the periodic part of the underlying PC, and a single reference defect. For isotropic reference defects, a single Hermitian reference defect matrix is needed which can be computed from scalar or tensorial discretization schemes for the reference permittivity. This reference matrix is used to assemble the final defect matrices describing complex clusters of defects with varying strength. For the anisotropic defects of Secs. 1.2.5 and 1.2.6, Hermitian and antihermitian reference matrices describing pure x -derivatives, pure y -derivatives, and mixed derivatives of the WFs are needed. These reference matrices have to be

computed using a scalar permittivity discretization. Therefore, the numerical accuracy of the scalar discretization has been investigated carefully and compared to the tensorial discretization scheme in the following chapters.

Exploiting the translational invariance and Hermiticity of the operator matrices reduces computational time, storage space and memory consumption considerably. Definitions for various sets of lattice sites were given that define the allowed positions of the basis functions in computations. The influence of these lattice sites on the accuracy of band structure and defect computations is examined in subsequent chapters.

The matrix equations for the computation of localized defect cavity modes, supercell waveguide dispersions and on-shell waveguide dispersions were derived. In this matrix form, the wave equation can be solved numerically by a computer, employing standard matrix diagonalization routines. The supercell approach diagonalizes a small matrix and computes the real-valued frequencies ω of guided modes for a given wave vector \mathbf{k} . The on-shell approach diagonalizes a large transfer matrix and yields all complex-valued components k of the wave vector \mathbf{k} along the given waveguide direction $\hat{\mathbf{s}}_{\text{wg}}$ for a given frequency ω . Real-valued wave numbers k correspond to guided modes, while non-vanishing imaginary parts of k describe evanescent modes in the waveguide. In transmission calculations of functional elements, a large system of linear equations has to be solved. The corresponding matrices are assembled from the operator matrices. The eigenmodes of the setup are computed under the constraints of one incoming guided mode that is scattered by the functional element into outgoing guided and evanescent modes. This yields amplitude transmission and reflection coefficients as solutions of the system of linear equations. These complex coefficients describe amplitude and phase of the outgoing waves and constitute the scattering matrix of the device. Finally, transmission coefficients of large scale photonic circuits can be computed from assembling the full circuit scattering matrix. This matrix is given by products of the small scattering matrices of the individual functional elements in the circuit.

5

Chapter 5

Wannier Function Parameters

In this chapter, we are going to investigate which numerical parameters we have to choose in order to reproduce the band structure with WFs of the PC from which they were constructed. This is an important consistency check and allows to estimate the accuracy of the defect mode frequencies which we can expect from WF computations.

Furthermore, localization properties of WFs and sparsity of operator matrices are investigated depending on different sets of WFs. These sets differ in the spread minimization algorithm used (combined Souza-Marzari-Vanderbilt or Marzari-Vanderbilt only). The artificially a posteriori symmetrized WFs have been considered as well.

5.1 Choice of Resolutions

In the discretization of all quantities, we have several types of resolutions to handle. There is the real space resolution $N_{\text{res},i}$ (cf. App. B) for Bloch modes and WFs, affecting the accuracy of derivatives and operator matrix integrals. We also have to specify the MP mesh resolution $N_{\mathbf{k}\text{-res},i}$, which affects the approximation quality of the infinitely extended WFs by their discretized periodic versions with finite support.

5.1.1 Wannier Functions

The lowest five WFs of Figs. 3.31a and 3.31b are investigated in this section because they can be generated consistently for various real space and MP mesh resolutions. They are shown in Fig. 5.1a.

Fig. 5.1b shows numerical noise of the order of 10^{-6} (maximal field values are normalized to 1) in the directions \mathbf{a}_1 and \mathbf{a}_2 , but not $\mathbf{a}_1 + \mathbf{a}_2$, as could be expected from the triangular symmetry. It is not yet clear, whether this asymmetry is due to the choice of the MP mesh (Fig. B.7b) which is parallelogram shaped and may violate the triangular symmetry.

5.1.2 Real Space Decay Behavior of Wannier Functions

The decay behavior along the cut direction of Fig. 5.1 with varying MP mesh resolution $N_{\mathbf{k}\text{-res},i}$ is shown in Fig. 5.2. One can clearly see the exponential decay and that the mode profiles are converged for $N_{\mathbf{k}\text{-res},i} = 21$ in the relevant region of 9 lattice sites around the origin. Further away from the origin, there is numerical noise of the order of 10^{-7} of the maximal WF value. The noise is not reduced when increasing the MP mesh resolution any further. Based on that evidence, we may not expect any significant improvements on other quantities computed from these WFs for higher MP mesh resolutions.

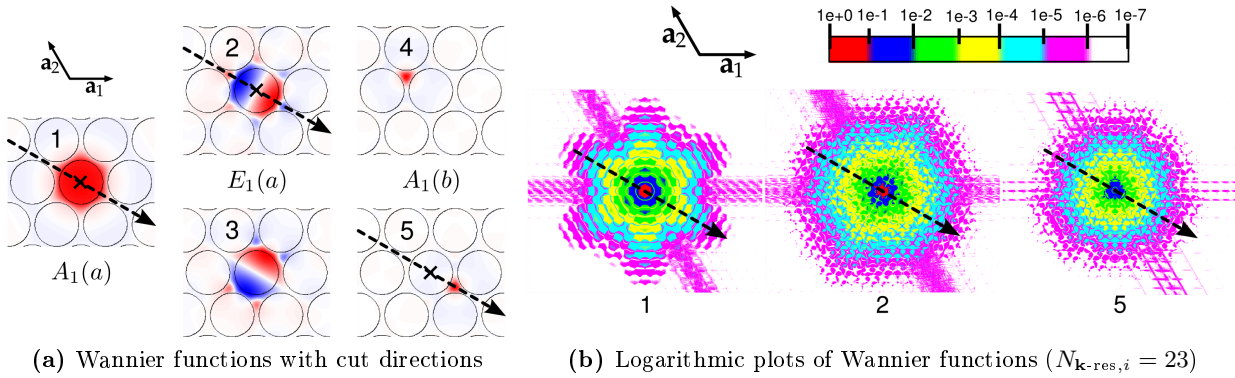


Figure 5.1: The WFs of Figs. 3.31a and 3.31b with cut directions (dashed arrows) for profile plots. The origin is denoted by a black X.

5.1.3 Convergence of Operator Matrix Elements

From the WFs of Fig. 5.1 the operator matrices (4.16)

$$A_{n'0,n\Delta\mathbf{R}}, \quad C_{n'0,n\Delta\mathbf{R}}, \quad B_{n'\mathbf{R}',n\mathbf{R}} \quad (5.1)$$

for the PCs and a non-etched hole have been computed for various MP mesh resolutions $N_{\mathbf{k}\text{-res},i} = 3, 5, \dots, 41$ and a fixed real space resolution of $N_{\text{res},i} = 96$ if not stated otherwise.

In Fig. 5.3a, the error of the discretized orthogonality relation is plotted. It shows the maximal off-diagonal elements

$$\max_{\alpha,\beta} |A_{\alpha\beta} - \delta_{\alpha\beta}| \quad (5.2)$$

of the pure overlap matrices (4.16a) for various MP mesh resolutions $N_{\mathbf{k}\text{-res},i}$, with the Kronecker delta $\delta_{\alpha\beta}$. In theory, (5.2) should be zero. The plot reveals that the orthogonality of the WFs does not improve for $N_{\mathbf{k}\text{-res},i} > 25$ any more.

Fig. 5.3b shows the maximum-norm convergence (A.43) of the C -matrix. For $N_{\mathbf{k}\text{-res},i} > 31$, no improvement is observed and the matrix elements can be considered converged. The same is true for the maximum-norm convergence of the B -matrix in Fig. 5.3c.

5.1.4 Decay and Sparsity of Operator Matrix Elements

The sparsity of the matrices (5.1) is shown in Figs. 5.4a and 5.4b. The sparsity does not change for MP mesh resolutions $N_{\mathbf{k}\text{-res},i} > 11$.

Figs. 5.4c and 5.4d show the decay of the matrix elements. The elements decay exponentially with increasing separation distance $\mathbf{R} - \mathbf{R}'$ between the WFs.

5.1.5 Band Structure Accuracy

Fig. 5.5 shows the errors in the reconstructed band structures after (4.74). In Fig. 5.5a, the band structure frequencies $\omega_{n\mathbf{k}}$ have been computed for the very same \mathbf{k} -points on the MP mesh that were used to construct the WFs. This measures the accuracy of the numerical WFs and the discretized Fourier lattice transform. Two discretization methods for the permittivity distribution and derivatives of WFs are compared as well:

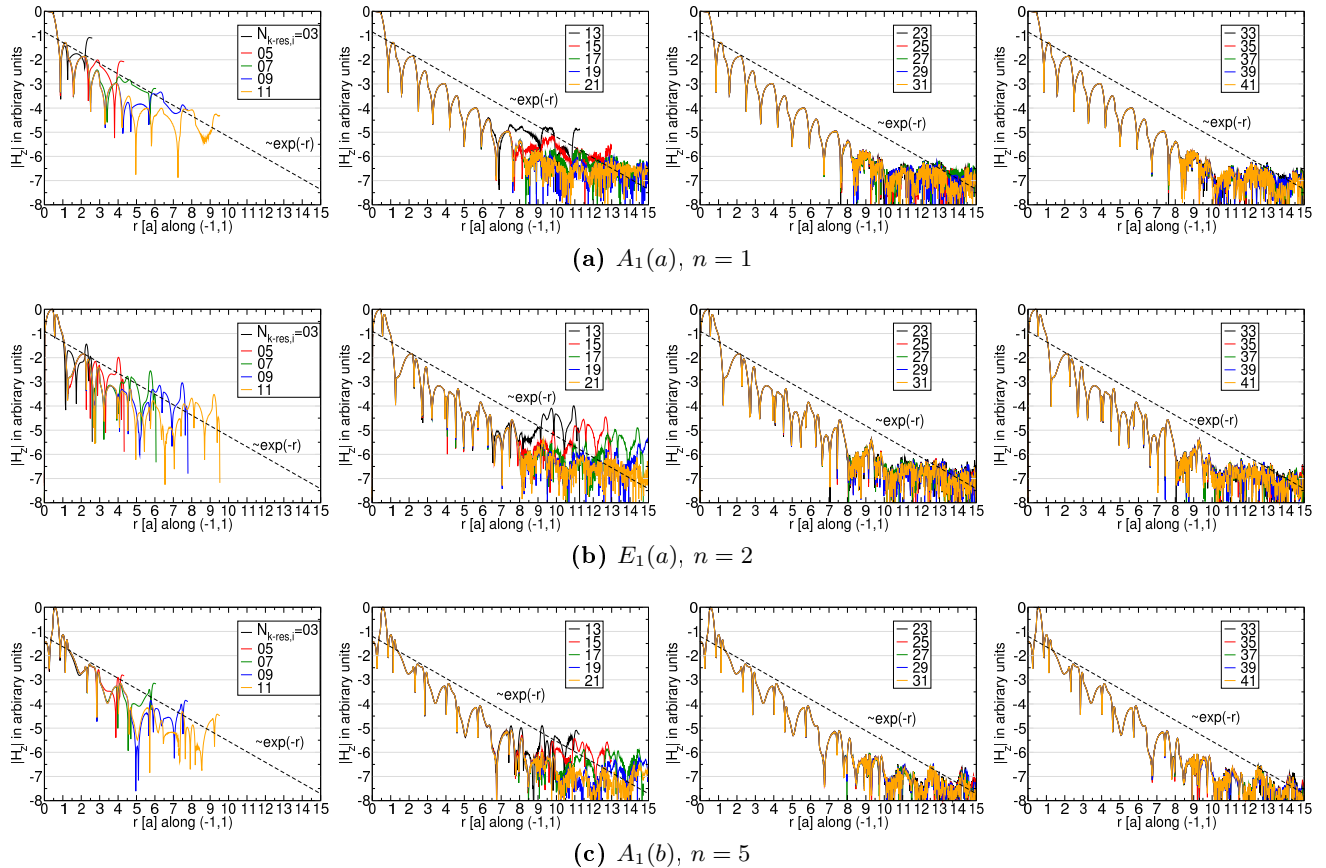


Figure 5.2: Logarithmic plots (in powers of 10) of WF real space decay behavior along the cut directions of Fig. 5.1 for various MP mesh resolutions $N_{\mathbf{k}\text{-res},i}$. The WF profiles can be considered fully converged with the choice of $N_{\mathbf{k}\text{-res},i} = 21$. In a distance of 9 cells from the origin, the WF profiles do not decay further, but show numerical noise of the order of 10^{-7} .

FFT-tensor: The tensor SPS (B.23) with discretized spectral derivatives (Sec. B.3.2).

FDS-scalar: The scalar SPS (B.21) with 4th-order finite difference stencils (Fig. B.3b).

Though the FFT-tensor version is more accurate, the FDS-scalar discretization method produces a mean relative error below 0.1 %, proving that this method is capable of computing the proper band structure. Furthermore, all errors do not improve any further for $N_{\mathbf{k}\text{-res},i} > 9$.

Fig. 5.5b shows the errors of the band structure $\omega_{n\mathbf{k}}$ computed for \mathbf{k} -points on a MP mesh with highest resolution of $N_{\mathbf{k}\text{-res},i} = 41$. This demonstrates the ability of the WFs to interpolate the band structure for \mathbf{k} -points that were not included in the numerical evaluation of (3.12). The mean errors do not improve beyond $N_{\mathbf{k}\text{-res},i} > 13$, while the maximal errors do not improve any further for $N_{\mathbf{k}\text{-res},i} > 17$. If the WFs should be used for high accuracy interpolation of the band structure,¹ the latter MP mesh resolution combined with the FFT-tensor discretization should be used. On the other hand, the mean FFT-tensor and FDS-scalar results do not differ much. Thus, the FDS-scalar discretization can be considered valid.

¹The photonic WFs are used for that task in [97].

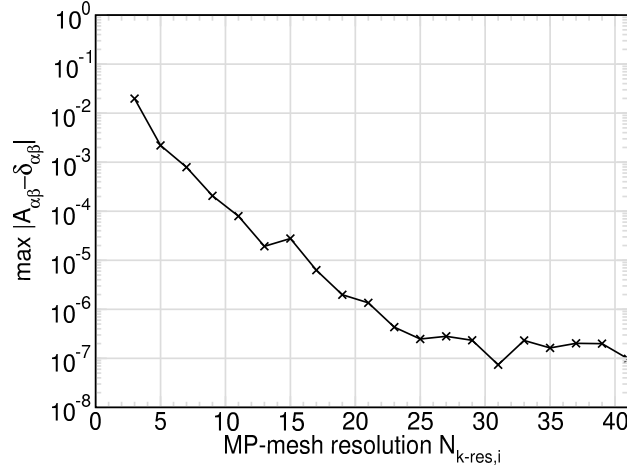
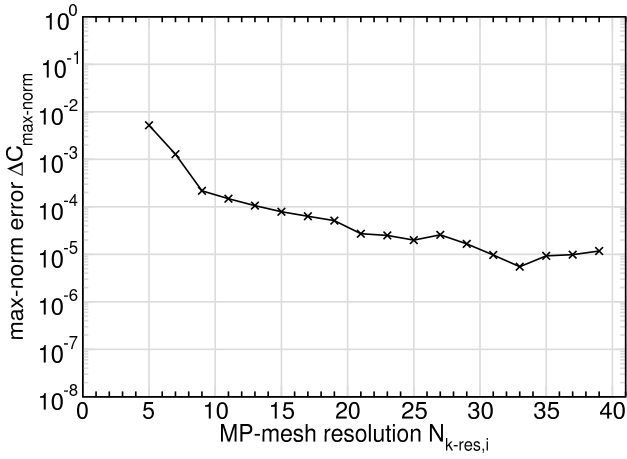
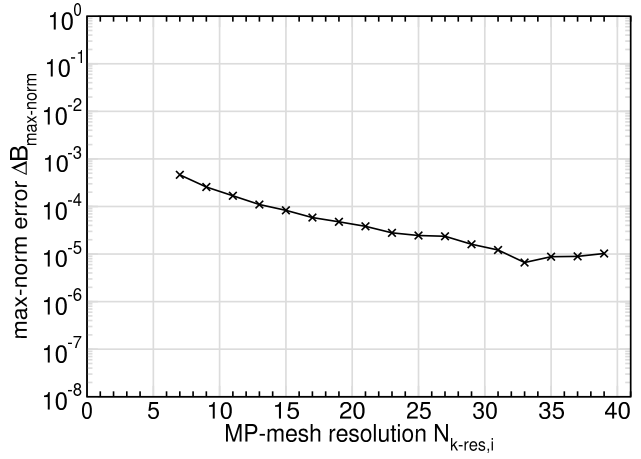
(a) Orthogonality of WFs, $\Delta \mathbf{R} \in \mathbb{L}_{\text{hex}}(\frac{N_{k-res,i}-1}{2})$ (b) Maximum-norm error of C -matrix, $\Delta \mathbf{R} \in \mathbb{L}_{\text{hex}}(3)$ (c) Maximum-norm error of B -matrix, $\mathbf{R}', \mathbf{R} \in \mathbb{L}_{\text{hex}}(3)$

Figure 5.3: Convergence of operator matrix elements with increasing MP mesh resolutions $N_{\mathbf{k}\text{-res},i}$ obtained from the WFs of Fig. 5.1 with real space resolution $N_{\text{res},i} = 96$. For explanations, see text.

Finally, Fig. 5.6 shows the maximal and mean errors in the band structures for fixed MP mesh resolution $N_{\mathbf{k}\text{-res},i} = 5$ (for both the construction of WFs and the reconstruction of the band structure) but varying real space resolution $N_{\text{res},i}$ for the WFs. The MPB band structures computed with the same spatial resolution were used as reference. The FDS-scalar and FFT-tensor discretizations yield band structures with similar deviations from the reference frequencies. Moreover, the error decreases only linearly with increasing resolution $N_{\text{res},i}$ for both discretization methods. Thus, there is no difference in the accuracy of the WF computations regardless of the discretization schemes used to numerically evaluate the operator matrix elements. This justifies the use of the FDS-scalar methods for subsequent defect computations.

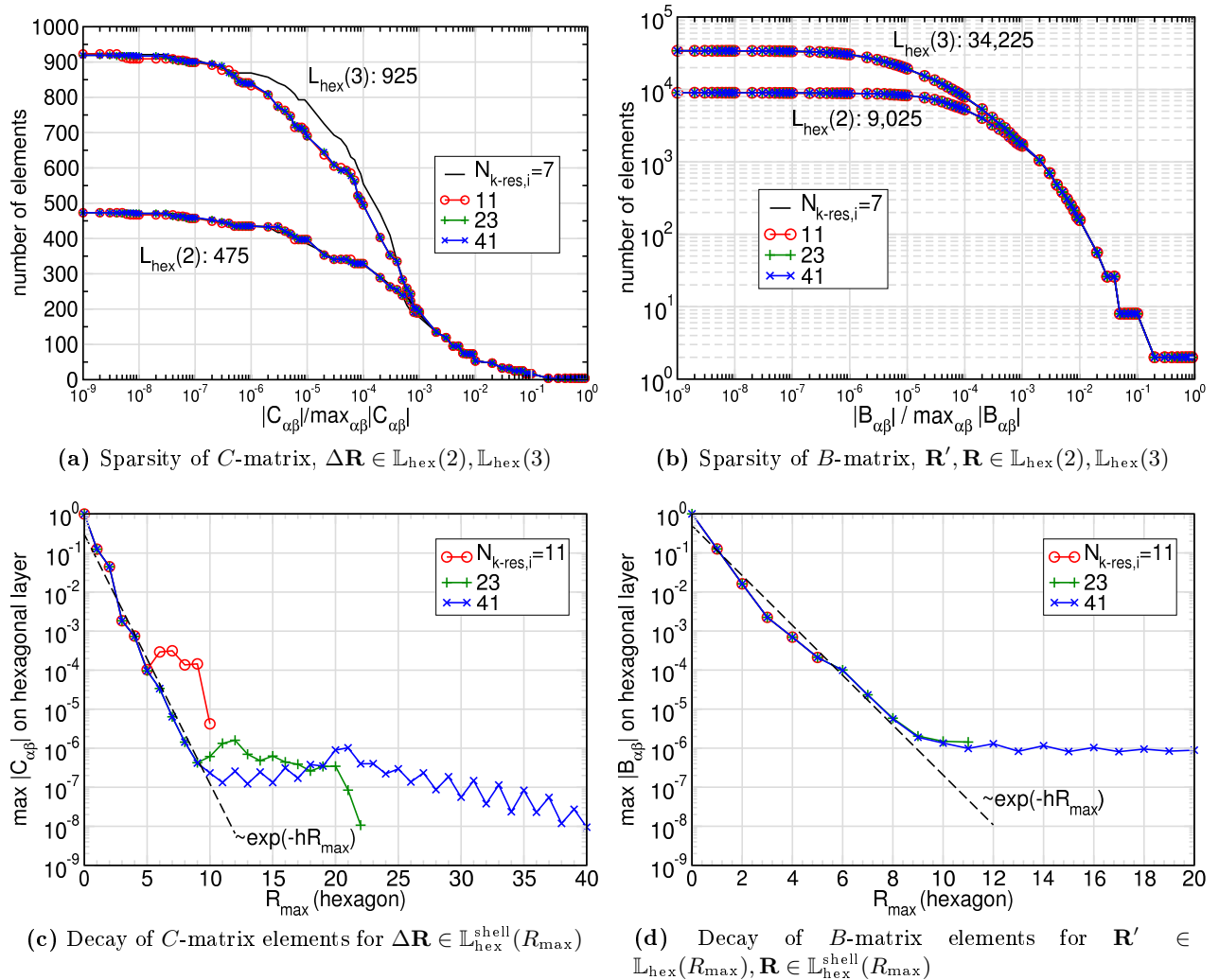


Figure 5.4: Sparsity and decay behavior of operator matrix elements. (a) and (b) show the number of matrix elements (ordinate) with absolute values greater than a threshold defined by a fraction of the maximal matrix element (abscissa). These elements were counted on two lattice site domains. The number of elements stored in each matrix of (5.1) is shown after the colon behind the respective lattice domain. As an example, there are approximately 200 C -matrix elements and 1,500 B -matrix elements greater than 10^{-3} of the respective maximal matrix element. (c) and (d) show the maximal ratio of matrix elements on a shell of lattice sites (cf. Fig. 4.4) to the maximal matrix element at all. The eyeball fit shows exponential decay with parameter $h = 0.68$.

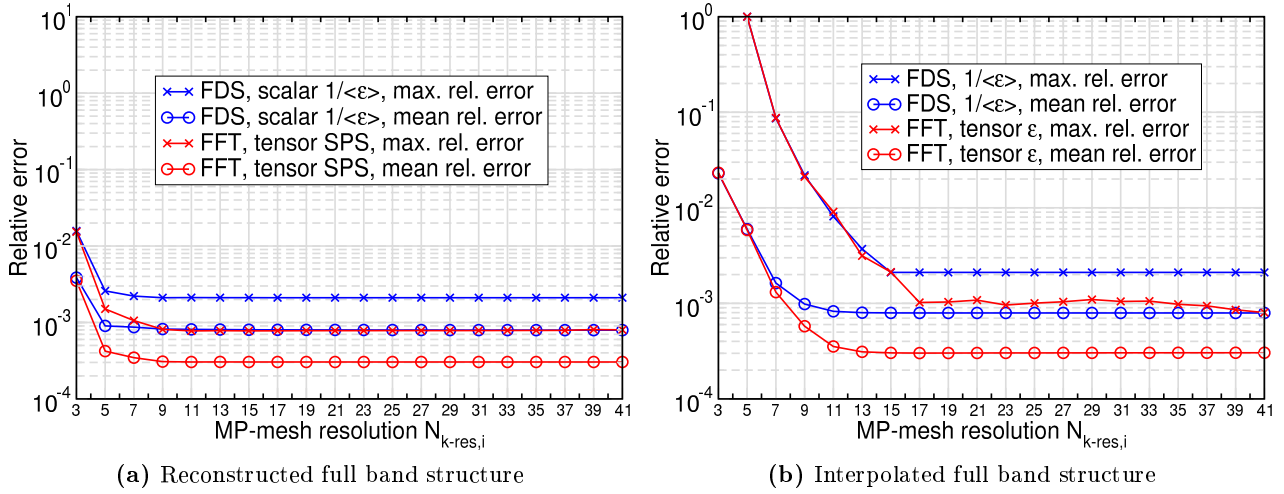


Figure 5.5: Relative errors in band structure frequencies for the WFs of Fig. 5.1 for various MP mesh resolutions and fixed real space resolution $N_{res,i} = 96$. (a) shows the mean and maximal relative error for band structures computed on a MP mesh of the same resolution as the WFs. In (b), the band structure was always computed on a MP mesh of resolution 41.

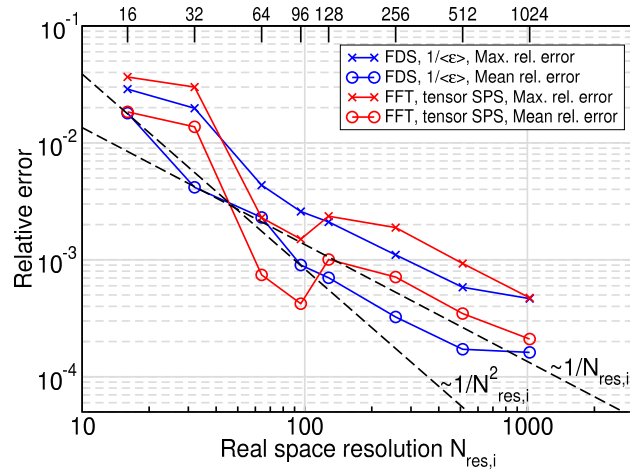


Figure 5.6: Accuracy of reproduced band structure frequencies obtained from the first five WFs on a MP mesh with fixed resolution $N_{k-res,i} = 5$ with increasing real space resolution $N_{res,i}$.

5.2 Operator Matrices of Final Wannier Functions

Based on the convergence investigations of the previous section, a real space resolution of $N_{\mathbf{k}\text{-res},i} = 96$ and a MP mesh resolution of $N_{\mathbf{k}\text{-res},i} = 11$ was chosen as a good compromise for the construction of the WFs of Fig. 3.44 (referred to as WF101-SMV and WF38-SMV² from here on) and Fig. 3.43 (referred to as WF38-MV³) as well as the symmetrized versions of Fig. 3.46 (referred to as WF38-sym). The operator matrices have been computed for the PC and a single non-etched hole as defect.

It is not a priori clear, whether the asymmetric WF38-MV WFs are better or worse suited for subsequent computations than the nicely looking WF38-SMV. The hybridized WF38-MV versions were computed with the pure Marzari-Vanderbilt spread minimization for a large closed set of bands. By this construction, they needed no further parameters from the user, thus they were much faster found and assembled than the WF38-SMV. It is therefore natural to ask if there is any benefit from spending the time to find the more symmetric versions.

First of all, the Wannier functions should be able to reproduce the band structure from the discretized matrix operator elements. Additionally, some statistics of the operator matrices are also given in order to find out if the better localization properties of the hybridized WF38-MV functions (as seen in Fig. 3.45) yield any benefits. In Sec. 6, their ability to model defect modes is investigated.

5.2.1 Statistics of Operator Matrices

The orthogonality of the WF sets is shown in Fig. 5.7a. The WF38-MV are more localized and therefore the pure overlaps are smaller than for the other sets of WFs, but the plot has the same principal shape as for the less localized WF38/101-SMV versions. Furthermore, the principal shape of the plots is also the same for both the 38 and 101 WFs, which must be a property of the MP mesh resolution then.

Fig. 5.7b shows the decay of the C -matrix elements (normalized to the maximum element) for increasing separation distance between the WFs, where the better localization of the WF38-MV is barely visible. The decay of the defect B -matrix elements (normalized to the maximum matrix element) is the same for all sets.

Figs. 5.7d and 5.7e show the sparsity of the C - and B -matrices, respectively. The better localization of the WF38-MV does not improve the sparsity of the B -matrix drastically compared to the WF38-SMV. The influence of the sparsity on defect computations is investigated in Chap. 7.

Based on the data presented here, no substantial advantage of the better localized WF38-MV WFs over the WF38-SMV has been observed.

²They were constructed with the full Souza-Marzari-Vanderbilt algorithm.

³These were constructed from the pure Marzari-Vanderbilt spread minimization.

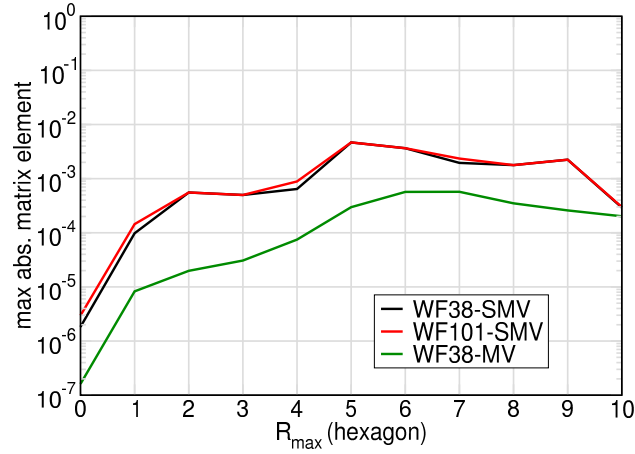
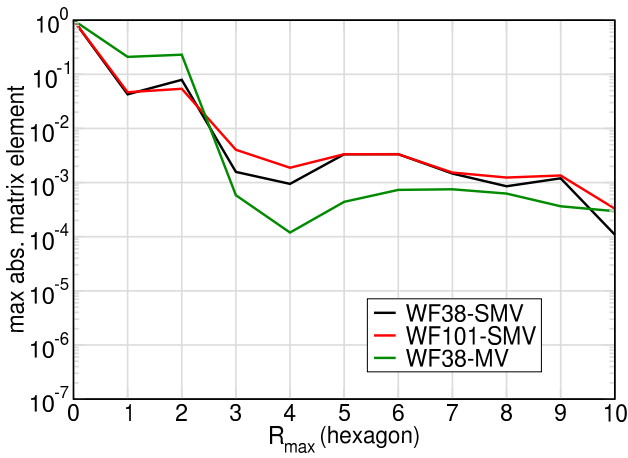
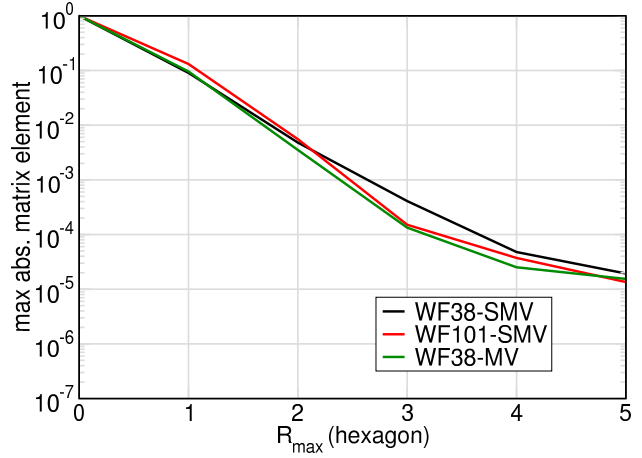
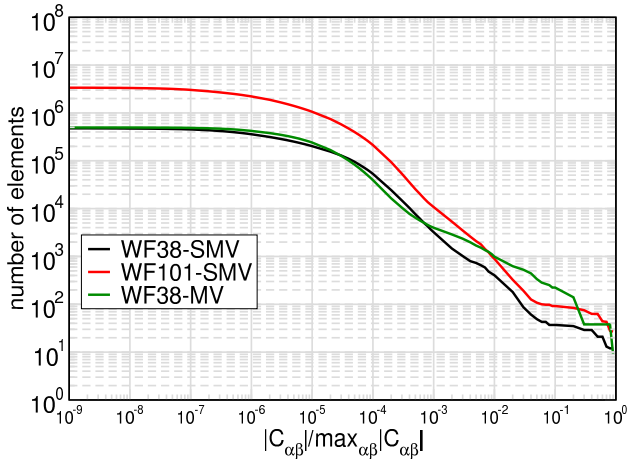
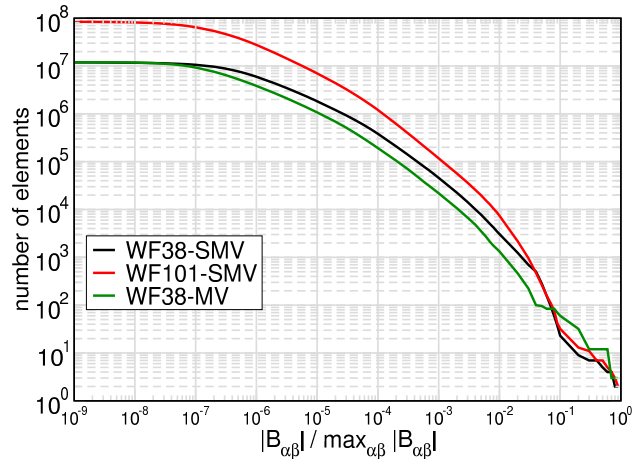

 (a) Orthogonality for $\Delta \mathbf{R} \in \mathbb{L}_{\text{hex}}^{\text{shell}}(R_{\text{max}})$

 (b) Decay of C -matrix elements for $\Delta \mathbf{R} \in \mathbb{L}_{\text{hex}}^{\text{shell}}(R_{\text{max}})$

 (c) Decay of B -matrix elements for $\mathbf{R}' \in \mathbb{L}_{\text{hex}}(R_{\text{max}}), \mathbf{R} \in \mathbb{L}_{\text{hex}}^{\text{shell}}(R_{\text{max}})$

 (d) Sparsity of C -matrix, $\Delta \mathbf{R} \in \mathbb{L}_{\text{hex}}(5)$

 (e) Sparsity of B -matrix, $\mathbf{R}', \mathbf{R} \in \mathbb{L}_{\text{hex}}(5)$

Figure 5.7: Operator matrix statistics for the WFs of Fig. 3.44 (WF38-SMV and WF101-SMV) and the hybridized WFs of Fig. 3.43 (WF38-MV). The plots are analogous to Figs. 5.3 and 5.4.

5.2.2 Band Structure Reconstruction

We are going to investigate the ability of the various sets of WFs to model the band structure which is an important consistency check. The two discretization schemes FFT-tensor and FDS-scalar are also compared again: for the reconstruction of band structures on the MP mesh of $N_{\mathbf{k}\text{-res},i} = 11$ and on 50 discretization points along the path of high symmetry lines $\overline{\Gamma MK\Gamma}$. The maximal and mean errors obtained are shown in Fig. 5.8.

The FFT-tensor discretization yields smaller mean errors for the WF38-SMV and WF38-MV sets, where the latter one produced the smallest errors of all sets investigated. However, they interpolate the band structure (on the high symmetry lines) just as good as the WF38-SMV. However, all sets of WFs and discretization methods give reasonable mean errors around 0.5% or below, meaning in particular that no information was lost in the symmetrization process for the WF38-sym. As an example, the reconstructed band structure along the high symmetry lines for WF38-MV is shown in Fig. 5.8a. So far, neither a particular WF set nor a discretization method has to be discarded based on that evidence.

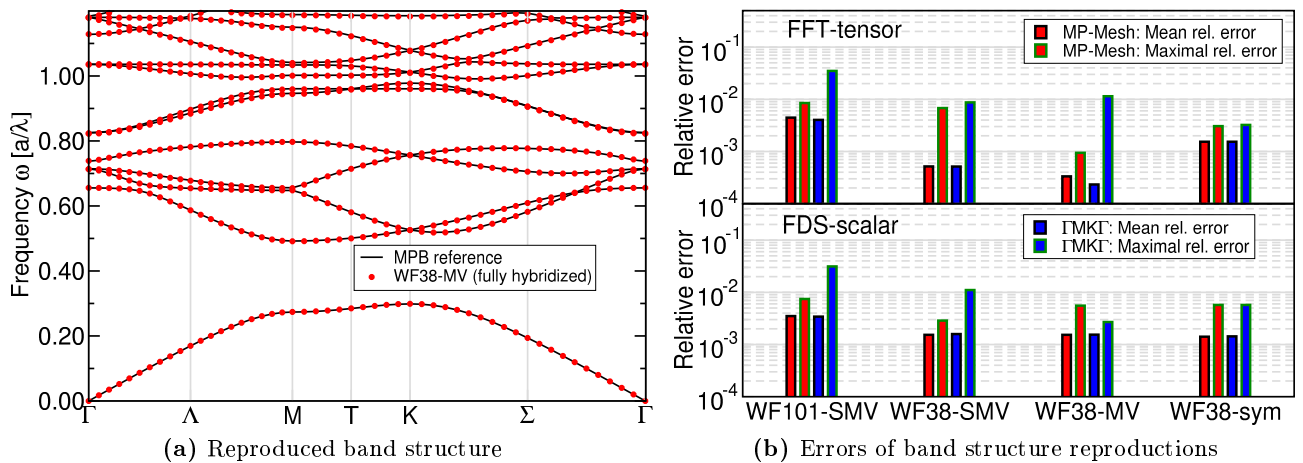


Figure 5.8: (a) *Reproduced band structure based on (4.74) for the set WF38-MV of Fig. 3.43.* (b) *Accuracies of reproduced band structures on a MP mesh ($N_{\mathbf{k}\text{-res},i} = 11$) and the high symmetry lines $\overline{\Gamma MK\Gamma}$ of the PC for various sets of WFs and discretization methods.*

5.3 Summary

We investigated the influence of the numerical parameters that have to be specified in the creation of the discretized WFs. These are the real space resolution $N_{\text{res},i}$ of the fields and the MP mesh resolution $N_{\mathbf{k}\text{-res},i}$ used in the discretization of the reciprocal space integral for generating the WFs from the Bloch modes. Only the first five bands generated by the MV spread minimization for closed groups have been considered here. The WF profiles were found not to change any more for MP mesh resolutions $N_{\mathbf{k}\text{-res},i} > 21$. The exponential decay of the discretized WF profiles was observed. The sparsity of the operator matrices was unaffected for choices of $N_{\mathbf{k}\text{-res},i} > 11$, as well as the mean error of reproduced and interpolated band structures. Both the FFT-tensor and FDS-scalar discretization methods yielded small mean errors below 0.1% in the band structure computations for $N_{\mathbf{k}\text{-res}} = 11$ and a real space resolution of $N_{\text{res},i} = 96$. These resolutions were therefore picked for the remainder of this thesis.

For these resolution choices, several sets of WFs with different construction parameters for the spread minimization algorithms have been generated: 38 WFs with the combined Souza-Marzari-Vanderbilt minimization, the a posteriori symmetrized variants of the same 38 WFs, 38 WFs generated from a closed set with the pure Marzari-Vanderbilt minimization and 101 WFs with the SMV minimization. All of these sets were able to reproduce their respective band structures with reasonable mean accuracy. The set WF38-MV yielded particularly small mean errors of 0.03% for the reproduced band structure, but also a quite large maximal error (1%) in the interpolated band structure, both in combination with the FFT-tensor discretization. Overall, the FDS-scalar discretization scheme did not perform significantly worse (the maximal error in the latter case was actually better with 0.2%), which justifies its usage for subsequent defect computations.

Based on the evidence presented in this chapter, the WF38-MV performed better in the reproduction of the band structure than the WF38-SMV versions. This is an astonishing result, since the WF38-MV set of functions was also much easier and faster obtained than the SMV versions, where the frequency windows for the Souza subspace optimization had to be tediously determined by trial and error.

The structure of the operator matrices (regarding sparsity and decay of the matrix elements) was similar for all of the examined sets, though the WF38-MV decay faster than the SMV versions, as Sec. 3.9 showed.

Parameter	Value
$N_{\text{res}, i}$	96
$N_{\mathbf{k}\text{-res}, i}$	11
Discretization	FDS-scalar
SMV parameters	—

Table 5.1: *WFs construction parameters used for the remainder of this thesis. These yielded mean errors of the reproduced band structure frequencies between 0.1% and 0.3%. SMV parameters denotes the band set and frequency window choices for the construction of WFs by the combined Souza-Marzari-Vanderbilt spread minimization. The results of this chapter did not favor a particular choice.*

Finally, the choice of parameters in Tab. 5.1 is justified on the basis of the correct band structure reproduction. The results of this chapter do not favor a particular choice of SMV construction parameters (band set choices and frequency windows).

6

Chapter 6

Auxiliary Basis Functions

So far, localization and symmetry properties of WFs were discussed. Now we will investigate the ability of WFs to model localized defect modes in PC defect structures. This chapter starts with a review of the continuity conditions of the electric and magnetic fields across dielectric boundaries. We are going to review early results for E-polarized light, where the WFs performed as efficiently as was anticipated. For H-polarized fields, however, we are going to show that the magnetic field WFs are incapable of modeling the correct continuity conditions for defect modes, seriously limiting the accuracy of the defect mode frequencies.

We try to ameliorate this drawback by incorporating auxiliary basis functions into the expansion basis that retain the localization of the pure Wannier basis and can be used within the Wannier framework of Chap. 4. The idea of choosing basis functions that are adapted to the problem one wants to solve is found in various parts of computational physics such as quantum chemistry [98].

Three suggestions for auxiliary basis sets are given and their ability to produce more accurate results than the proper WFs alone is investigated. This chapter closes with extensive convergence studies for simple and complex defect structures involving isotropic and anisotropic materials introduced in Secs. 1.2.5 and 1.2.6.

The error plots present the individual errors of each defect mode and the maximal errors over all defect modes for each defect strength. Multiple sets of auxiliary basis functions are shown in each error plot. For clarity, these plots have been shifted a bit to the right but present data only for integer values of defect permittivities. The numerical parameters for reference modes computed with MPB are documented in App. C.

In this work, only permittivity defects made from infiltrated holes are treated. Radius defects and auxiliary functions have been investigated in a previous thesis by Hermann [43].

6.1 Boundary Conditions

We chose the H-field WFs to describe defect states in PCs, because they share many properties of the defect states we are interested in. In particular, they have the following nice properties:

- The divergence condition $\nabla \cdot \mathbf{H} = 0$ is always satisfied for any solution obtained with WFs since each WF has vanishing divergence and so does any linear combination of WFs. In 1D and 2D, this property is always trivially fulfilled.
- The WFs are a complete orthonormal set, thus forming a basis in the function space of solutions of the wave equation.

- The WFs can be chosen to be highly localized. Thus defect computations can be treated in terms of sparse matrices.
- The WFs resemble the lattice symmetry just as the defect states do.

These are the properties, on which the numerical efficiency of the WF method relies. Though this numerical efficiency has been shown in the 2D E-polarized polarized case [31, 99] and is reviewed here in Sec. 6.1.1, where very few electric field WFs have been used for converged defect mode and waveguide dispersion computations, they have the following shortcomings:

- For the 2D H-polarized case (i. e., magnetic field WFs) and the general 3D case (E field and H field formulation), they cannot model the correct boundary conditions for the electric and magnetic fields at dielectric boundaries.
- In order to describe all defect modes properly, the necessary symmetries have to be present in the WF basis used.

The latter problem is obvious: e. g. if there is no WF with dipole symmetry in a given basis set, it is hard (if not even impossible) to describe the field of a defect dipole by a linear combination of the given basis functions. This problem can be solved by generating more WFs with the bottom-up approach [35], until WFs with the desired symmetries and field distributions are found.

The former problem is of more fundamental nature and we are going to state it analytically now, following the analysis of [39].

E-Field Formulation

By (1.9a), the solutions $\mathbf{E}(\mathbf{r})$ of the electric field wave equation have to obey

$$\nabla \cdot [\varepsilon(\mathbf{r})\mathbf{E}(\mathbf{r})] \stackrel{!}{=} 0. \quad (6.1)$$

This is a problem for the 3D vectorial electric field WFs which are constructed from Bloch modes obeying (6.1) for the unperturbed PC, and so do the WFs. The electric field WFs and any linear combinations of these then obey

$$\nabla \cdot [\varepsilon_{\text{PC}}(\mathbf{r})\mathbf{W}^{\text{el}}(\mathbf{r})] = 0, \quad (6.2)$$

whereas the proper solutions for the electric fields of the defect modes fulfill (6.1) with $\varepsilon(\mathbf{r}) = \varepsilon_{\text{PC}}(\mathbf{r}) + \Delta\varepsilon(\mathbf{r})$ instead of ε_{PC} . Thus, the vectorial electric field WFs \mathbf{W}^{el} are not able to reproduce the correct divergence conditions for defect modes in the presence of a defect.

In the 2D TM polarized case, we have $\mathbf{E}(\mathbf{r}) \equiv E_z(\mathbf{r}_{\parallel})\hat{\mathbf{z}}$, so (6.1) simplifies to

$$\partial_z [\varepsilon(\mathbf{r}_{\parallel})E_z(\mathbf{r}_{\parallel})] \stackrel{!}{=} 0. \quad (6.3)$$

This equation is trivially fulfilled in 2D TM polarization, since the prerequisites for this polarization case implied $\partial_z \varepsilon(\mathbf{r}_{\parallel}) = 0$ and $\partial_z E_z(\mathbf{r}_{\parallel}) = 0$ by Sec. 1.2.4.

The E-field WFs $W^{\text{el}}(\mathbf{r}_{\parallel})$ in TM polarization are constructed from the Bloch modes of the unperturbed PC, i. e., for $\varepsilon(\mathbf{r}_{\parallel}) = \varepsilon_{\text{PC}}(\mathbf{r}_{\parallel})$. By the same argument as above, for scalar $\varepsilon(\mathbf{r}_{\parallel})$ containing also defects, we have that

$$\partial_z [\varepsilon(\mathbf{r}_{\parallel})W^{\text{el}}(\mathbf{r}_{\parallel})] = 0 \quad (6.4)$$

always holds, regardless of the actual defect structure contained in $\varepsilon(\mathbf{r}_{\parallel})$ (as long as it still allows to separate the problem into two independent scalar TE and TM wave equations). Thus any linear combination of WFs also satisfies (6.3). An exemplary test system demonstrating the efficiency of 2D TM WFs is discussed in Sec. 6.1.1.

H-Field Formulation

For the H-field WFs $W^{\text{mag}}(\mathbf{r}_i)$, this problem is already apparent in the 2D case. Though the divergence condition (1.9b) is always fulfilled, the derivatives of the WFs cannot model the proper continuity conditions. As discussed in [39], for any H-field solution of the magnetic field wave equation the following expression is continuous across dielectric boundaries, where $\eta(\mathbf{r})$ changes values discontinuously:

$$\hat{\mathbf{n}}(\mathbf{r}) \times \left[\eta(\mathbf{r}) \nabla \times \mathbf{W}^{\text{mag}}(\mathbf{r}) \right]. \quad (6.5)$$

Here, $\hat{\mathbf{n}}(\mathbf{r})$ is the normal vector of the dielectric interface¹ (see also Fig. B.5a). In 3D, the Bloch modes and, hence, also the magnetic field WFs satisfy equation (6.5) for the periodic PC, i. e., for $\eta(\mathbf{r}) = \eta_{\text{PC}}(\mathbf{r})$, whereas the defect states fulfill (6.5) for the full defect configuration, i. e., for $\eta(\mathbf{r}) = \eta_{\text{PC}}(\mathbf{r}) + \Delta\eta(\mathbf{r})$. Since any finite linear combination of the magnetic field WFs also inherits their continuity properties, they are incapable of modelling the correct boundary conditions of defect states.

In the 2D TE polarized case, we have $\mathbf{H}(\mathbf{r}) \equiv H_z(\mathbf{r}_i)\hat{\mathbf{z}}$, hence (6.5) simplifies to the continuity of the following expression for any solution of the TE wave equation:

$$\eta(\mathbf{r}_i) \left(\hat{\mathbf{n}}_i(\mathbf{r}_i) \cdot \nabla_i \right) H_z(\mathbf{r}_i). \quad (6.6)$$

Here, $\hat{\mathbf{n}}_i \cdot \nabla_i$ is the derivative in the direction of $\hat{\mathbf{n}}_i$. As argued above, any finite linear combination of WFs inherits their continuity properties (6.6) for $\eta(\mathbf{r}_i) = \eta_{\text{PC}}(\mathbf{r}_i)$, whereas defect states obey (6.6) for $\eta(\mathbf{r}_i) = \eta_{\text{PC}}(\mathbf{r}_i) + \Delta\eta(\mathbf{r}_i)$. This is one of the reasons, why the convergence of the WF solutions gets worse with increased defect strength, as can be seen clearly in Fig. 6.5.

6.1.1 2D TM Modes

We review the convergence of WFs-based defect mode computations for E-polarized light. The PC under consideration consists of a square lattice of silicon rods in air. The parameters for the computation of the Bloch modes is shown in Tab. D.3a, the band structure is depicted in Fig. 6.2. This system features a relatively large band gap from $\omega = 0.289 \frac{2\pi c_0}{a}$ to $\omega = 0.441 \frac{2\pi c_0}{a}$.

From these Bloch modes, a total of 23 WFs has been generated with the Souza-Marzari spread generation process discussed in Chap. 3 with the parameter choices of Tab. D.3b. The operator matrix elements (4.11) have been computed from these WFs with the parameters from Tab. D.3c. The cavity defect modes have been obtained from these operator matrices by assembling and diagonalizing the eigenvalue problem (4.54) under consideration of (4.29). Finally, the reference solutions have been obtained by a supercell computation with MPB and the parameter choices of Tab. D.3d. These numerical parameter choices have been taken from appendix App. C, where an accuracy below 0.1% has been achieved for the reference modes.

Figs. 6.3a and 6.3b show that the WFs are able to compute the defect mode frequencies of a single defect rod with permittivities ε_A in the huge range [1, 80] to accuracies below 0.5%. Not all 23 WFs available are needed for this accuracy. The monopole and dipole modes for $\varepsilon_A < 50$, e. g., can be described within the same accuracy with only the first 6 WFs [31]. This result drastically demonstrated the high efficiency of the WF-method and sparked hope to describe H-polarized modes and 3D problems equally well.

Fig. 6.4 further illustrates the reasons for the ability of the WF to describe the defect modes properly. The WFs and defect modes already have very similar mode profiles and the same exponential decay

¹Only the direction is important, but not whether $\hat{\mathbf{n}}$ is pointing inward or outward, since this is irrelevant for the continuity condition.

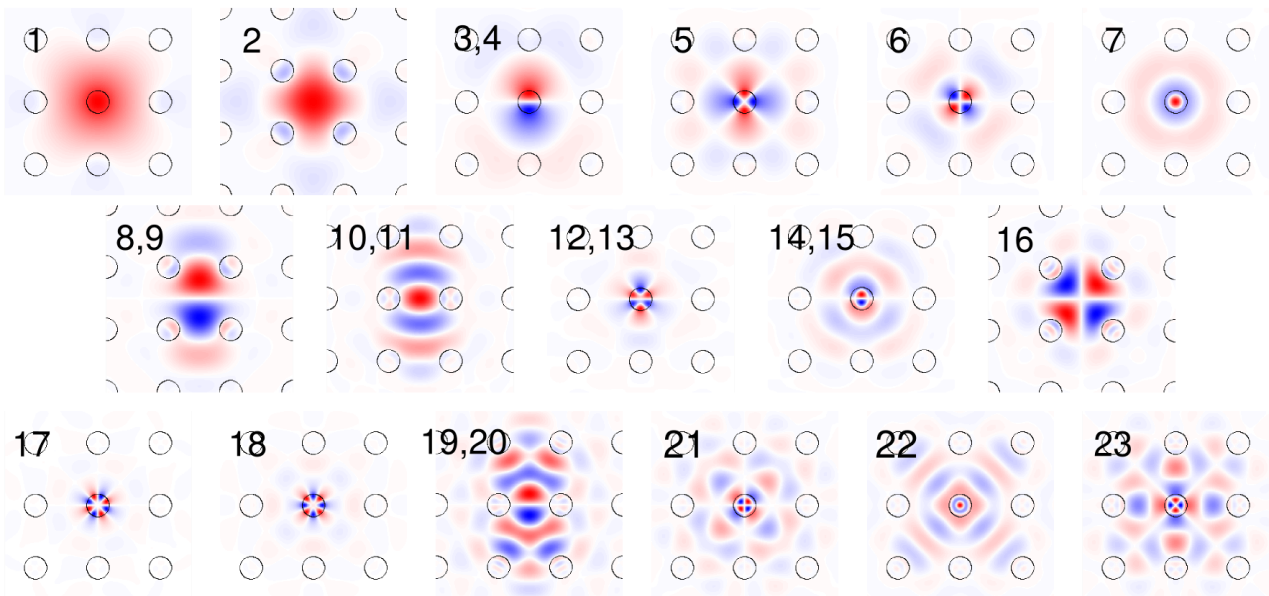


Figure 6.1: 2D TM WFs obtained with the parameters of Tab. D.3. Note the various localization centers of the WFs.

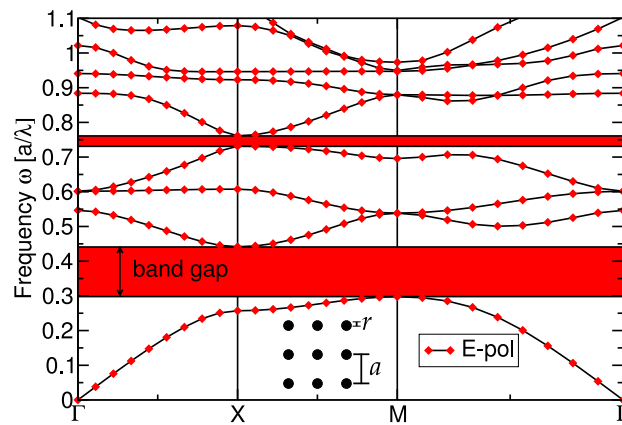


Figure 6.2: TM band structure of the square lattice silicon rod system.

behavior discussed in Sec. 1.2.10. The mode profiles computed by WFs and MPB practically coincide (Fig. 6.4b). Most of all, one can clearly see that the TM WFs and MPB reference modes are smooth (continuously differentiable) across all dielectric boundaries.

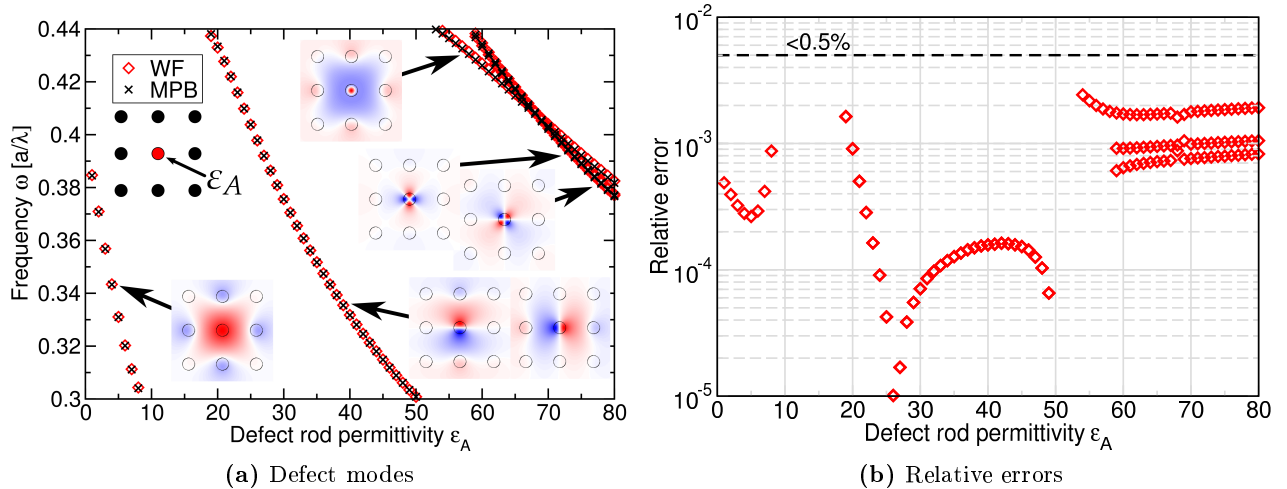


Figure 6.3: (a) Defect mode frequencies in the band gap for a single defect rod with varying permittivity ϵ_A . The results obtained with the WFs from Fig. 6.1 are compared to the reference solutions obtained with MPB. (a) The relative errors of WF results compared to the reference solutions. The agreement between both methods is better than 0.5% over a wide range of defect strengths ϵ_A .

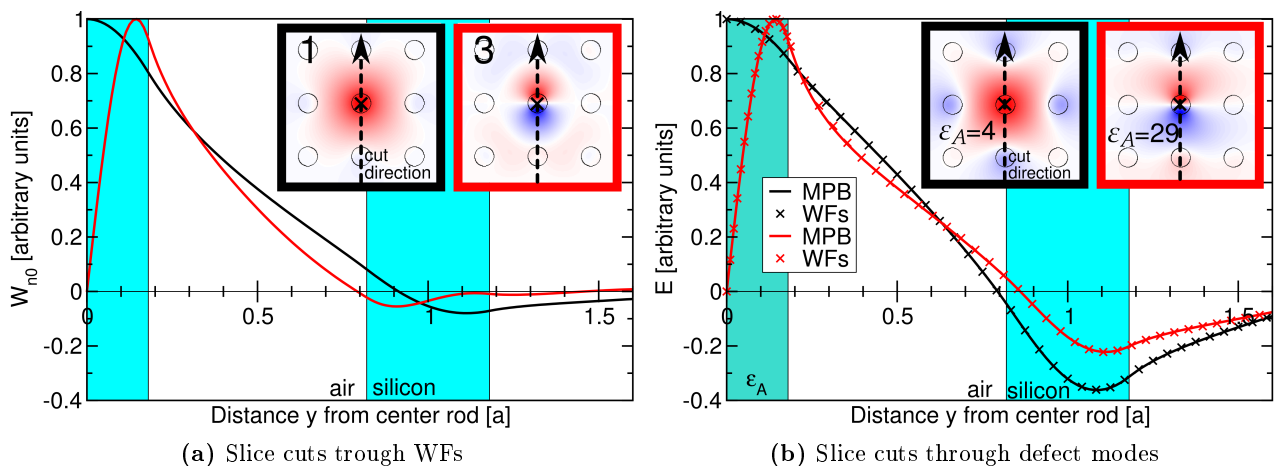


Figure 6.4: Slice cuts along the y -direction through (a) WFs and (b) defect mode profiles. The TM WFs and defect modes are already quite similar and they are both continuously differentiable across each dielectric boundary. In (b), defect mode profiles obtained with the WF approach by (4.1) are compared to MPB results. Differences cannot be made out by eye.

6.1.2 2D TE Modes

This system is of great technical importance as discussed in Chap. 1. It consists of a triangular lattice of cylindrical air holes in silicon with radii $r = 0.45a$ (see Figs. 1.9b and 1.8c). The Bloch mode construction parameters are shown in Tab. D.2a. The WFs made thereof are depicted in Fig. 3.44, where the parameters from Tab. D.1 have been used.

For historical reasons, the results for 38 WFs are shown here, since only these were available from the previous work of Schillinger [35] when this thesis started. In the course of this work, up to 101 WFs were constructed. Their effect on the defect mode convergence is discussed in the subsequent sections of this chapter.

The operator matrices of Sec. 4.1 were computed with the parameters from Tab. D.2b. All reference modes, with which the WF results are compared, have been computed with MPB with the parameters of Tab. D.2c. By App. C, these parameters are known to yield converged reference frequencies.

The continuity of expression (6.6) and its consequences are visualized in Fig. 6.5. Fig. 6.5a shows the WFs which obey the same boundary conditions as the Bloch modes for the perfectly periodic ε_{PC} . The steep slopes in the high index regions (silicon) and slight slopes in the low index regions (air) are clearly visible. Figs. 6.5b and 6.5c show that the kinks of the WFs are still present in the WF solutions, but not the reference solutions. Additionally, Fig. 6.5c shows the importance of the proper WF profiles. In the regions between the holes, the WF approximation lacks contributions from WFs centered at Wyckoff positions c and e .² Fig. 3.44 reveals that these WFs occur mostly after the first 38 WFs. Thus one needs more basis functions that

- model the correct boundary conditions at dielectric interfaces, and
- contribute to the defect mode profiles at the right positions in the PC.

In the following sections, several sets of additional basis functions are introduced and their ability to correct flaws are quantitatively and qualitatively investigated.

²The rigorous proof for this hypothesis is given in Sec. 7.1.3 and can also be seen in Fig. 6.11b.

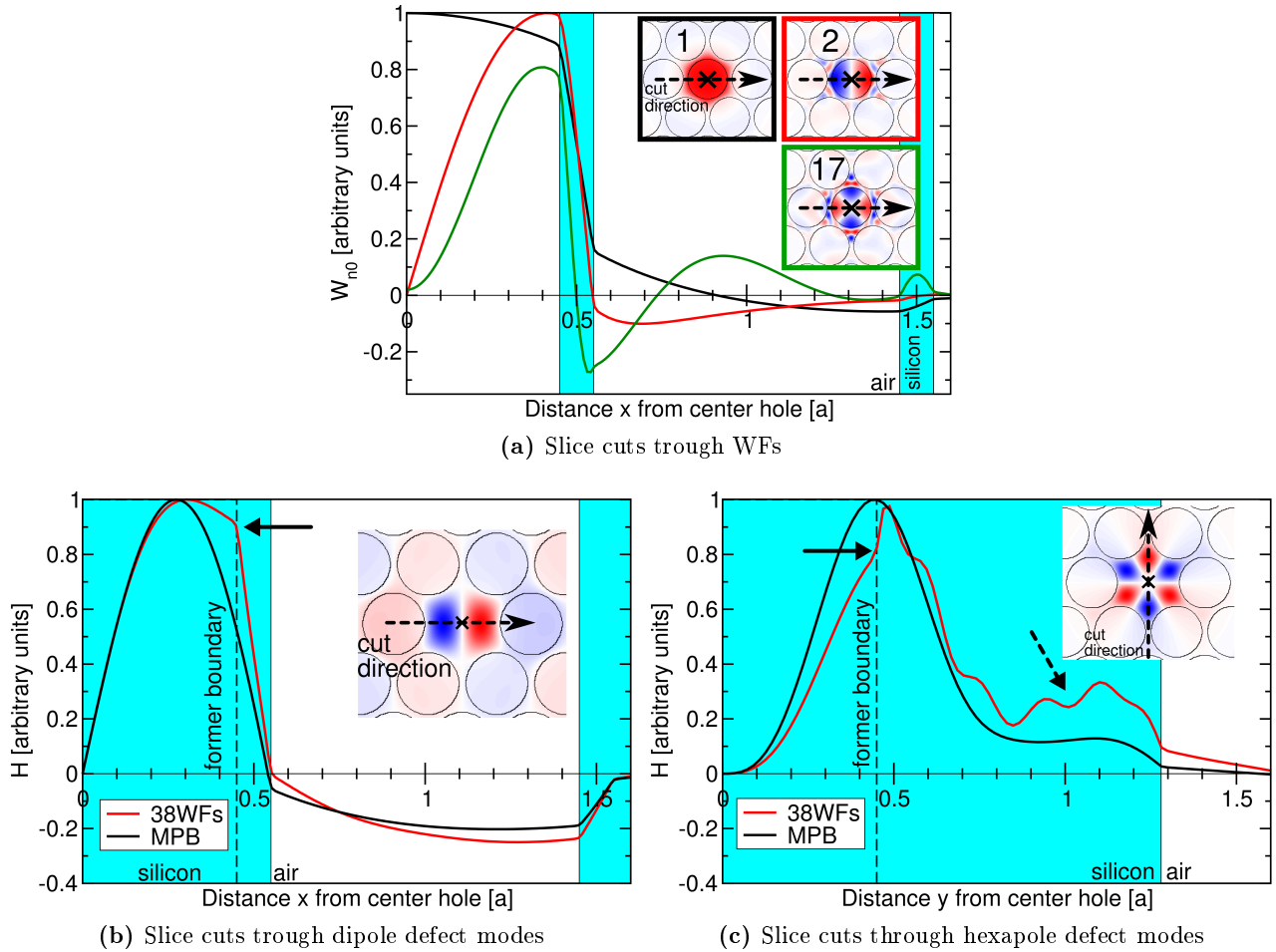


Figure 6.5: *Slice cuts along the x -direction and y -direction of TE WFs and defect modes obtained from them. In (a), one can clearly see the different slopes of the WFs in the low index (air) and high index (silicon) region which is expressed in the continuity of the expression (6.6). The arrows in (b) and (c) denote the kink in the defect mode profiles obtained from the first 38 WFs of Fig. 3.44 which is not present in the reference solutions. In (c) one can also see that profile contributions from WFs centered at Wyckoff positions c and e are missing to describe this reference defect mode properly (dashed arrow).*

6.2 Sets of Auxiliary Basis Functions

Takeda et al. [39] suggested modifications to the WFs for each new defect distribution $\Delta\varepsilon$ to ameliorate for the drawbacks identified in Sec. 6.1.2. In their approach, a plane wave base supercell problem has to be solved for each new field $\Delta\varepsilon$ in order to determine the necessary (and rather complicated) modification.

For the 2D TE case, we propose to incorporate (in the best case just a few) additional basis functions into the WF basis, that have the following properties:

- They should be easily integrated into the WF formalism, i. e., yield several functions n at different lattice sites \mathbf{R} with the same translational properties (A.15) as the WFs.
- They should share the convenient properties of WFs, i. e., they should be highly localized, respect the lattice symmetry, and be divergenceless.
- They should fix the problems of the WFs, i. e., introduce the proper boundary conditions at dielectric interfaces for defects and contribute field values where they are needed in the defect modes.
- They must not introduce any spurious modes which are numerical solutions that do not correspond to real physical solutions of Maxwell's Equations.

We will investigate various possible choices of such additional basis functions in the following and quantify their ability to describe defect mode profiles and waveguide dispersions.

6.2.1 More Wannier Functions

As alluded to earlier, in the beginning of this thesis only WFs constructed from the first 38 bands of the PC were available. In the course of this work, up to 101 WFs from Fig. 3.44 have been constructed. We will refer to these WFs as proper Wannier functions to distinguish them from the WFs of the inverse system introduced below. We will see in Sec. 6.3.1 that they improve the accuracy of the pure WF defect mode calculations a bit, but the continuity problem still persists. However, these many functions are still needed in addition to the auxiliary basis functions introduced below, as we will see in the following sections.

On the other hand, it is not practical to keep generating more and more higher-band WFs since the efficiency of the WF expansion relies on the usage of few basis functions. That is why it is desirable to use additional auxiliary basis functions, whose construction is based on different methods.

6.2.2 Supercell Defect Modes

The defect modes for a single non-etched hole (cf. Fig. 1.12) are localized, model the proper boundary conditions for the 'worst case' of a non-etched hole (strong deviation from periodicity), respect the lattice symmetry, and are divergenceless. Though they are not orthogonal when shifted to different lattice sites, their overlap is still small. Furthermore, they can be systematically computed by a supercell approach. The basic idea is to use just $n = 6$ of these functions at lattice sites \mathbf{R} with an infiltrated hole to interpolate the boundary conditions for all intermediary defect strengths from no defect to non-etched hole.

The advantage of using supercell defect modes lies in the fact that this approach could easily be ported to 3D computations, as long as supercell computations are feasible.

6.2.3 Fourier-Bessel Functions

As briefly mentioned in Jackson [45], Fourier-Bessel functions (FBF) are well suited for expansions of functions that vanish on the surface of a circle. Since WFs obey the correct PC boundary conditions *outside* any defect region, one can think of the defect mode H-field that is missing in the pure WF solution as a small perturbation that vanishes on the surface of the defect holes. Thus the FBFs are just needed in the defect region to correct the pure WF defect mode solution. This is only possible, when we restrict ourselves to cylindrical defects of the same radius as the PC holes, namely infiltrated holes.

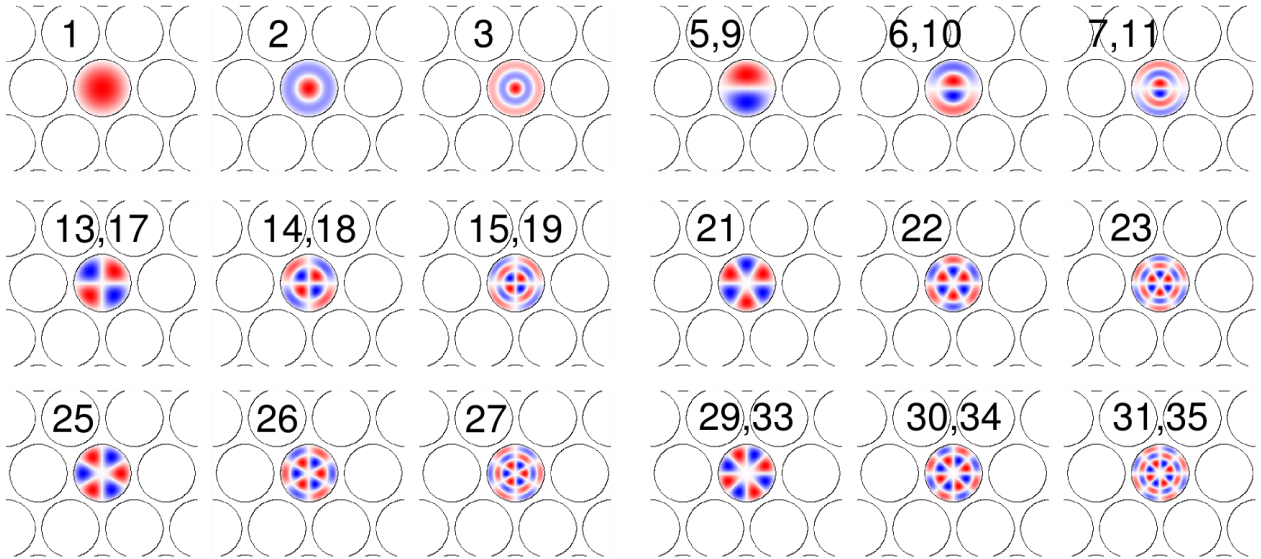


Figure 6.6: *Fourier-Bessel functions obtained by (6.7). The label n is shown in the plots for discrimination, but the numbering is rather arbitrary.*

The FBFs $W'_{n\mathbf{R}}$ depicted in Figs. 6.6 and 6.7 are defined in 2D polar coordinates (ρ, ϕ) centered around the hole at \mathbf{R} , i. e., $\rho = |\mathbf{r}_\parallel - \mathbf{R}|$:

$$W'_{n\mathbf{R}} := J_m(x_{m,\nu}\rho/r) \times \begin{cases} \sin(k\phi) \\ \cos(k\phi) \end{cases}, \quad \rho \in [0, r]. \quad (6.7)$$

Here, J_m is the Bessel function of the first kind with $m \in \mathbb{N}_0$, $x_{m,\nu}$ the ν th zero thereof, r the radius of the PC holes, and $k \in \mathbb{N}_0$. The index $n \in \mathbb{N}$ labels the various combinations of m , ν , k and whether sin or cos are used for the angular modulation: i. e., $n \equiv (m, \nu, k, \sin / \cos)$. In practise, these functions are normalized in the L_2 -norm by the numerical normalization routines. The incorporation of the zeroes $x_{m,\nu}$ ensures that these functions indeed take on the value 0 for $\rho = r$, i. e. on the surface of the defect hole.

The choice of these functions was guided by the defect geometry of infiltrated cylindrical holes with fixed radius r , so it is not directly applicable to other geometries. Furthermore, in 2D calculations all functions are intrinsically divergence-free and it is not straightforward to generalize this function system to divergenceless vectorial for 3D computations.

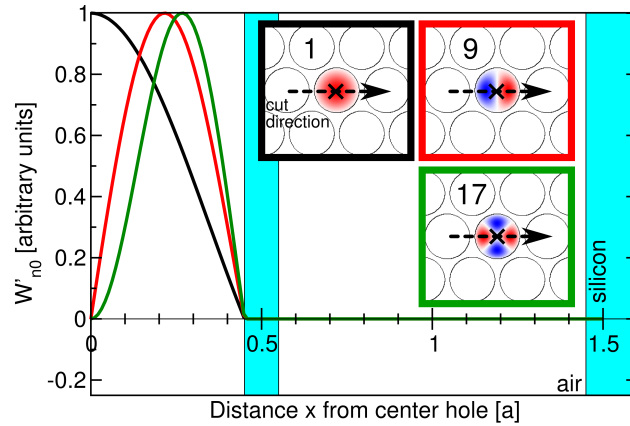


Figure 6.7: Slice cuts through the FBFs of Fig. 6.6. Note that the support of these functions is restricted to a single hole.

6.2.4 Inverse System Wannier Functions

In order to correct the boundary conditions of the WFs one could introduce functions with opposite ratios of slopes across the hole-background boundaries. This is most easily accomplished when computing WFs for the opposite distribution of dielectric media in the PC, i. e., to switch the permittivities of holes and background.

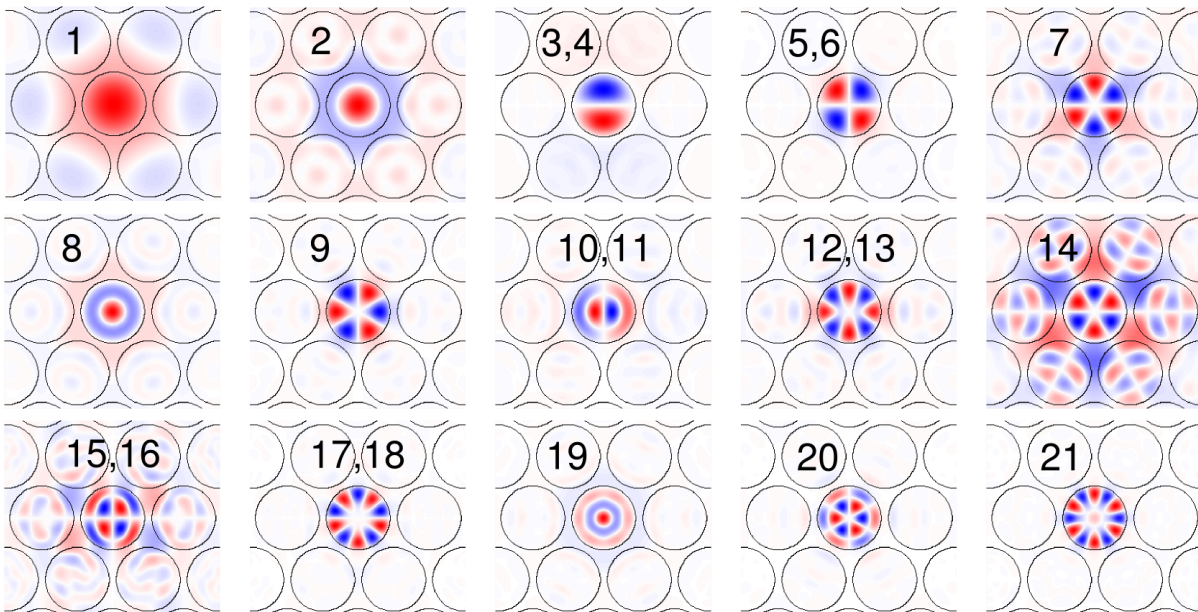


Figure 6.8: The inverse system Wannier functions (IWF) for the triangular silicon rods in air system. Note the similarity of the profiles to the FBFs of Fig. 6.6. Some IWFs are quite extended which stems from ignoring their natural symmetry and enforcing Wyckoff position a as the localization center (1,2,14,15,16).

The WFs constructed for this inverse silicon rods in air system (with the otherwise same parameters

as the air holes in silicon system) are the inverse system Wannier functions (IWF). These functions were created before the influence of symmetry and centers on localization (Chap. 3) were fully understood by the author. This is why only the initial IWFs from rod centered—i. e., Wyckoff position a —trials of Γ -point Bloch modes have been constructed here, meaning that no spread minimization was carried out.

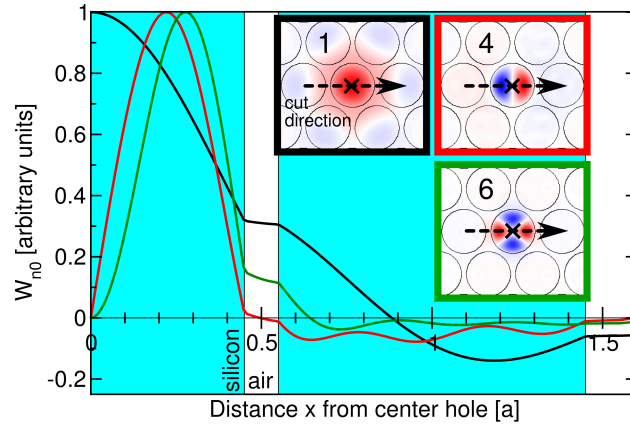


Figure 6.9: *Slice cuts through the IWFs of Fig. 6.1. These functions have steep slopes in those areas, where the WFs of Fig. 6.5a have flat slopes and vice versa.*

Fig. 6.8 shows the lowest few IWFs constructed in this fashion, where a total of 66 IWFs have been used as auxiliary basis functions. Some of these functions are not optimally localized, since their natural symmetry has been ignored and the localization center was forced to be Wyckoff position a (center of a rod/hole). Fig. 6.9 reveals that the slopes of the IWFs show the opposite behavior than that of the WFs of Fig. 6.5a.

This approach could easily be extended to 3D PCs since the IWFs are also divergence-free and can be systematically constructed after a symmetry analysis of the resulting PC. However, they describe a totally different band structure which may introduce spurious modes to the defect mode calculations. A careful analysis has to be performed, in order to rule out the possibilities of false, unphysical solutions to the wave equations.

6.3 Cavity Defect Modes Convergence

Now we will investigate the performance of the auxiliary basis functions introduced in the previous section for cavity mode computations after (4.54).

Defect Setup Notation: We investigate localized cavity defects and waveguides consisting of point-like defects (Fig. 1.11) in our model system. We consider single air pores that are infiltrated with various materials having different relative permittivities and are therefore described by a variety of dielectric functions: isotropic materials are described by a scalar permittivity, birefringent materials (e. g., liquid crystals) have a real symmetric tensorial epsilon tensor and magneto-optic materials are described by a complex Hermitian tensor.

Letter	Meaning
i	Infiltration with isotropic material
b	Infiltration with birefringent material
m	Infiltration with magneto-optic material

Table 6.1: Nomenclature definitions of types of point defects.

In order to describe which pores are substituted by which kind of defect, we introduce the following nomenclature to distinguish the various cavity defect setups. The position of the pores is denoted by the capital Latin letters A–G defined in Fig. 6.10 and Tab. 6.2, the type of defect by a lowercase Latin letter summarized in Tab. 6.1.

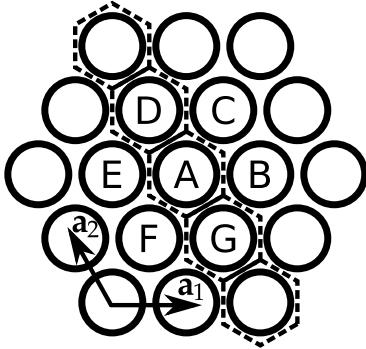


Figure 6.10: Nomenclature definitions of relative point defect positions for cavities and waveguide slices.

Letter	Relative position
A	$\mathbf{R}_A = (0, 0)$
B	$\mathbf{R}_B = (1, 0)$
C	$\mathbf{R}_C = (1, 1)$
D	$\mathbf{R}_D = (0, 1)$
E	$\mathbf{R}_E = (-1, 0)$
F	$\mathbf{R}_F = (-1, -1)$
G	$\mathbf{R}_G = (0, -1)$

Table 6.2: The relative point defect positions in lattice coordinates.

A cavity defect can thus be described by the positions of a particular point defect type followed by the type identifier, e. g. ABEi refers to isotropically infiltrated holes forming a line along the \mathbf{a}_1 direction, where no information about the particular value of relative defect permittivities ε_A , ε_B or ε_E is explicitly given (cf. Fig. 6.20c).

Basis Function Set Notation: The legends of the plots denote the sets of basis functions that have been used as well as the discretization methods for the permittivity distribution. They include information on

- the number of proper WFs,
- whether and which set of auxiliary basis functions (ABF) has been used,
- on which lattice sites of the computational domain these functions were included,
- whether the ABF were orthogonalized with respect to the proper WFs,
- the permittivity and derivative discretization used.

The influence of all these parameters on the defect mode frequency errors is documented in this chapter. Therefore, the legends use the following notation to denote which combination of parameters has been used in a particular computation:

[WF set]-[domain size]-[ABF set]-[domain size]-[orthogonalized?]-[discretization]

The WFs sets used are

WF38, WF101, WF38-SMV, WF101-SMV: the WFs of Fig. 3.44 obtained by the bottom-up approach with the combined SMV spread minimization,

WF38-MV: the WFs of Fig. 3.43,

WF38-sym: the a posteriori symmetrized WFs of Fig. 3.46.

In order to distinguish these WFs from the IWF they are called proper WF in the following.

The auxiliary basis functions (ABF) sets used are

SMD6: the MPB supercell defect modes for a non-etched hole,

FBF36: the Fourier-Bessel functions with compact support,

IWF66: the initial Wannier functions of irreps for Wyckoff position a for the inverse system, i. e., silicon rods in air.

These are usually used only at defect sites and are orthogonalized with respect to the proper WFs. For comparison, results for non-orthogonal ABFs and ABFs used at all lattice sites are sometimes shown.

The discretization methods used are

FFT-tensor: the spectral derivative discretization of Sec. B.3.2 and the tensor sub-pixel smoothing for the permittivity of (B.23),

FDS-scalar: the finite-difference derivative discretization of Sec. B.3.1 and the scalar sub-pixel smoothing from (B.20).

These discretization methods have to be compared because the reference modes of MPB are obtained by the FFT-tensor discretization, for which quadratic convergence with the real space resolution was proven [41, 57, 100]. We have to make sure that no additional errors are introduced when using a different discretization scheme.

The domain sizes denote the R_{\max} parameter of the ‘basic’ symmetric lattice site domains $\mathbb{L}_{\text{hex}}(R_{\max})$ (cf. Sec. 4.2) for cavity computations and slice domains $\mathbb{L}_{\text{slice}}(R_{\max})$ for waveguide computations. For defect clusters, these basic domains are shifted to each defect site, generating the whole computational domain \mathbb{L}_{comp} for the defect cluster computation. The construction of the full computational domain \mathbb{L}_{comp} for proper WFs and ABF used in this scheme is explained in more detail in Sec. 7.1.1.

Examples: WF38-sym-R4d-FFT-tensor denotes the a posteriori symmetrized 38 proper WFs on a computational domain $\mathbb{L}_{\text{comp}} = \mathbb{L}_{\text{hex}}(4)$, where the operator matrix elements have been evaluated with the FFT-tensor discretization schemes. WF101-R4d-DM6-R0d-noortho-FDS-scalar denotes the 101 proper WFs on the same computational domain with additionally taking the 6 MPB defect modes into account at the defect sites ($\mathbb{L}_{\text{hex}}(0)$ contains only the origin site). These auxiliary functions are not orthogonalized.

6.3.1 Cavity Setup Ai

We investigate the accuracy of defect modes for a single isotropically infiltrated hole with permittivity ϵ_A .

Wannier Functions Only

We use 38 and 101 WFs (Fig. 3.44, constructed with parameters from Tab. D.2) and compare results obtained for different combinations of discretizations for derivatives and permittivity distributions introduced in App. B. This is necessary because the reference frequencies are obtained by MPB supercell computations which employs spectral derivatives (Sec. B.3.2) and the tensorial discretization scheme (B.23) for isotropic permittivities and the scheme (B.26) for anisotropic permittivities. Therefore, we have to make sure no additional errors due to the discretization methods used are introduced.

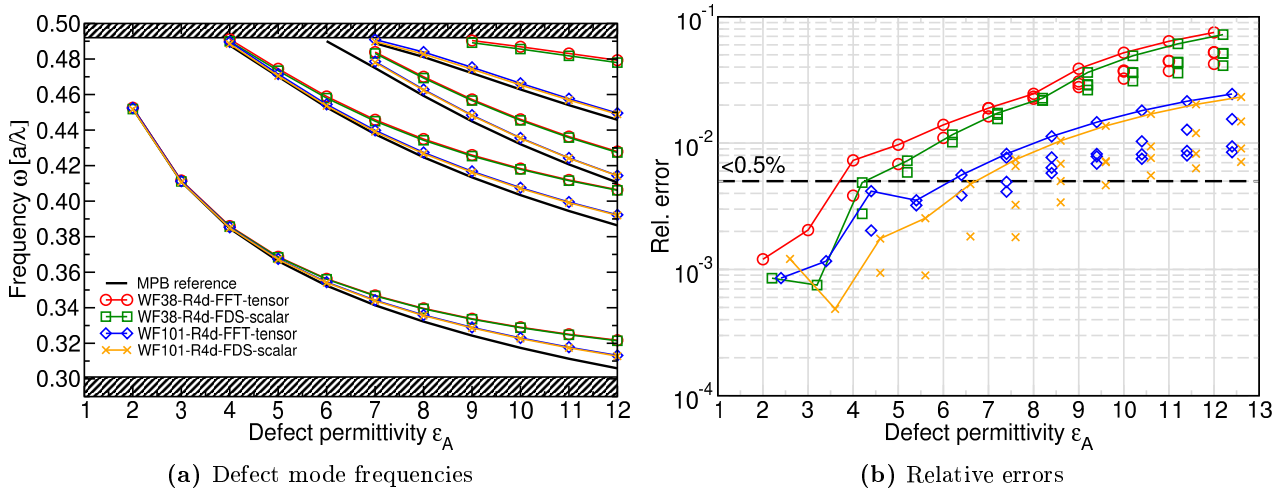


Figure 6.11: Defect mode frequencies and relative errors compared to MPB reference modes computed with the parameters from App. C.

In the Wannier framework we are free to choose between finite-difference stencils or spectral derivatives for the discretization of derivatives. For the treatment of isotropic defects, the same effective tensor discretization as in MPB calculation can be used. However, for the treatment of anisotropic defects by Eqs. (4.38) and (4.44), only scalar permittivity distributions can be used, since one cannot separate the contributions of the various derivatives then. So it is favorable to use a scalar discretization scheme for the Wannier defect computations.

We have to submit the computations to a careful examination in order to attribute deviations from the reference frequencies by MPB to either different discretizations or deficiencies in the (auxiliary) basis functions used.

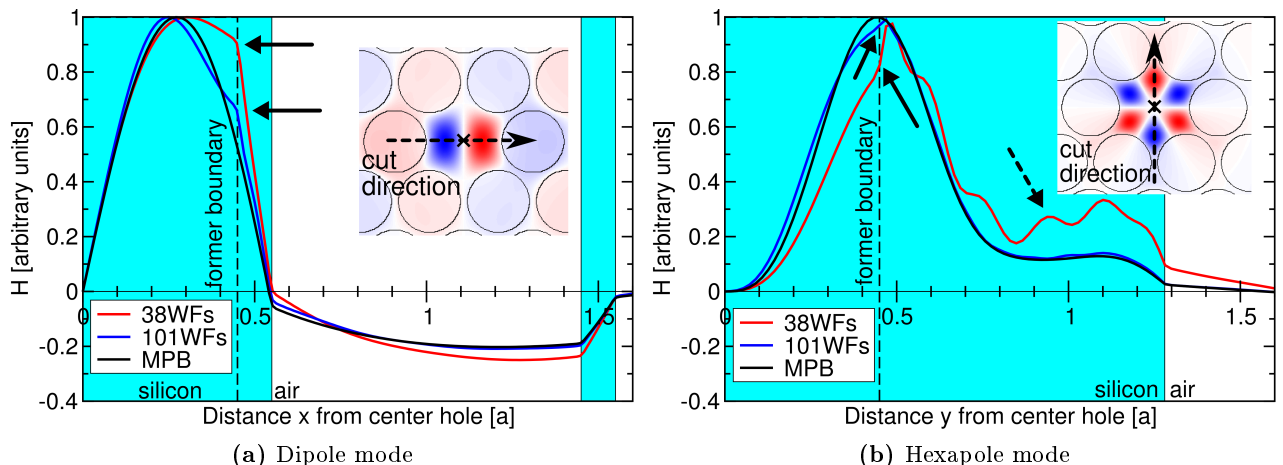


Figure 6.12: Defect mode profiles for $\epsilon_A = 12$ (non-etched hole). The kinks in the proper WF solutions are still visible (straight black arrows). In (b), the use of more WFs (centered at Wyckoff positions c and e) flattened out the oscillations (dashed arrow).

Fig. 6.11 shows the defect mode frequencies for these sets of operator matrices: The error plots in Fig. 6.11b reveal two things. First, the use of a scalar permittivity discretization with finite-difference stencils performs slightly better, so we may use this approach for both isotropic and anisotropic defect computations. Second, 38 proper WFs are sufficient to describe defect strengths up to $\epsilon_A = 5$ with an accuracy below 0.8%, and 101 WFs extend the defect range for this accuracy to $\epsilon_A = 7$. In particular, the upper defect mode frequencies (monopole and hexapole of Fig. 1.12) improve drastically. However, for the most extreme case of a non-etched hole ($\epsilon_A = 12$), the errors still range from 0.7% to 2.2%. The reasons for this behavior can be seen from the defect mode profiles in Fig. 6.12 obtained via (4.1). The straight black arrows denote the kink in the WF solutions for a non-etched hole. That kink is absent in the smooth reference solutions. The use of more WF relieves the error a bit, but this feature of the WF solution does not vanish entirely. Fig. 6.11b shows the relevance of the higher WF bands after the first 38 bands. The WFs centered at Wyckoff positions c and e flatten out the oscillations outside the defect area, denoted by the dashed black arrow.

In Sec. 3.9 we have introduced several different sets of 38 WFs which reproduced the band structures of the PC equally well. However, while this is an important consistency check, it does not imply that these WFs are also suited well to describe defect states in the PC. Therefore, defect mode frequencies obtained by these sets are shown in Fig. 6.13.

We see that the symmetrized WFs from Fig. 3.46 yield the same defect mode frequencies as the unprocessed WFs of Fig. 3.44. The highly localized hybridized versions of Fig. 3.43 as well yield the same defect mode frequencies, but also lots of spurious modes which renders them useless. This may be due to the high degree of localization of the $A(f)$ WFs of Fig. 3.43 which cannot be resolved properly by the spatial resolution $N_{\text{res},i}$ chosen and may introduce errors in the discretized derivatives. Another possible source of errors could consist in the incomplete irreps that lack some basis functions for these irreps. Thus, the source of the spurious modes is not fully clear, yet.

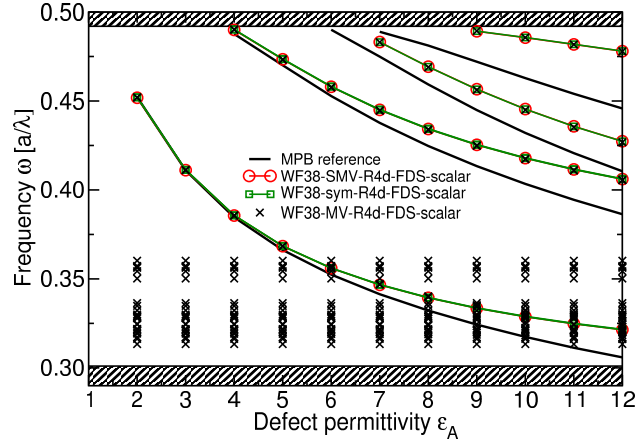


Figure 6.13: Defect mode frequencies for alternate sets of the first 38 proper WFs from Sec. 3.9. The symmetrized WFs of Fig. 3.46 yield the very same frequencies as the unprocessed ones of Fig. 3.44, as do the hybridized ones from Fig. 3.43. However, the latter set also introduces lots of spurious modes.

Bessel-Fourier Functions

The 36 FBF from Fig. 6.6 were added to 38 WFs and 101 WFs, respectively. Fig. 6.14a shows the defect mode frequencies obtained. The additional basis functions were used on the whole computational domain and only at the defect site for comparison. The FBF are not orthogonalized in this example.

The use of spectral derivatives introduced spurious modes, probably due to the inability of the Fourier transform to treat the sharp kinks of the FBFs on the hole surface properly (cf. Fig. B.4). On the other hand, finite-difference stencils and scalar SPS featured very well.

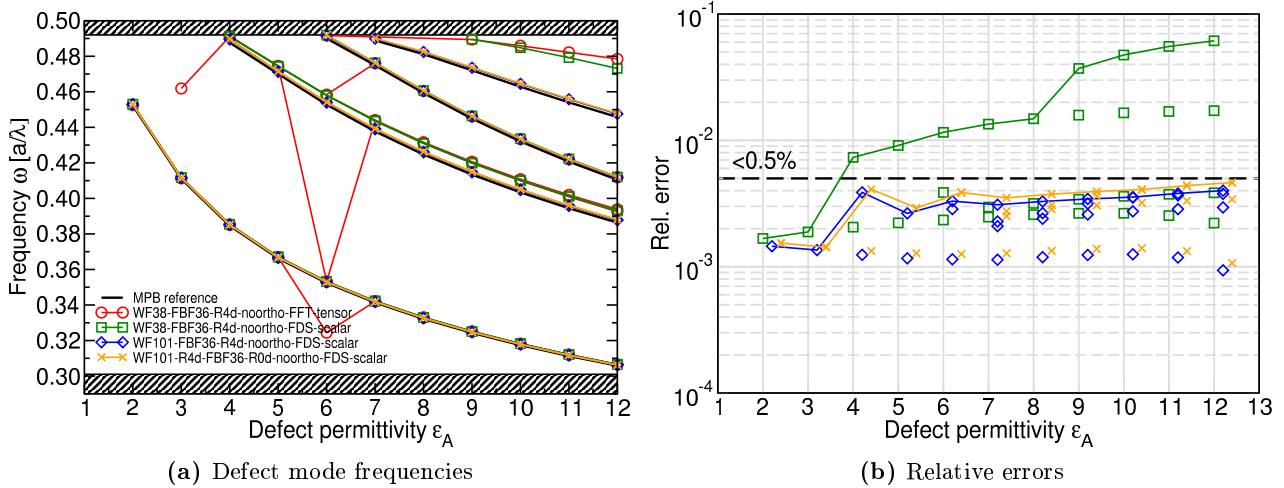


Figure 6.14: Defect mode frequencies and relative errors compared to MPB reference modes computed with the parameters from App. C.

For 38 proper WFs adding the FBFs increased the accuracy of the dipole and monopole modes, but the quadrupole modes got only slightly better and the hexapole modes are practically unchanged compared

to Fig. 6.11.

When adding the FBFs to 101 WFs, we achieved accuracies below 0.5% for all modes over the whole defect range $\varepsilon_A = 2 \dots 12$. Spurious modes were not found when using the auxiliary basis functions on the full domain. It is sufficient, to only include the FBFs at the defect site to obtain this accuracy. Note that this increases the total number of basis functions needed only slightly.

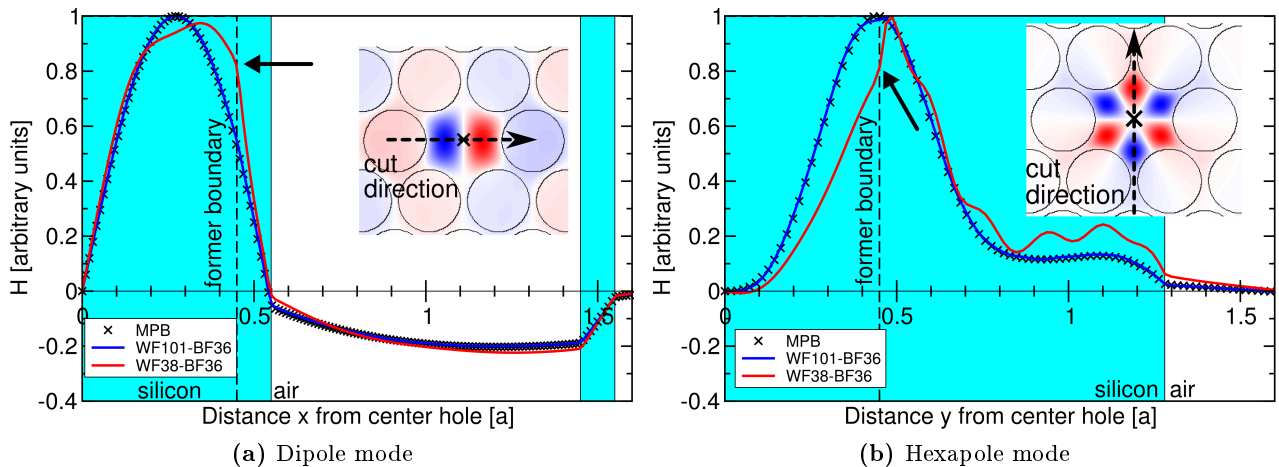


Figure 6.15: Defect mode profiles for $\varepsilon_A = 12$ (non-etched hole). Black arrows denote the kinks in the solutions for 38 WFs and 36 FBFs. These kinks are absent when using 101 WFs together with 36 FBFs.

The profile cuts of Fig. 6.15 show, how the FBF reduce the kinks of the pure WFs solutions to an amount that is barely visible in the plots. The mode profiles obtained lie practically on the reference profiles by MPB, proving the necessity to introduce the proper boundary conditions into the basis functions used to improve the overall accuracy.

Supercell Defect Modes

The 6 supercell defect modes computed by MPB for a non-etched hole from Fig. 1.12 have been added to 38 WFs and 101 WFs, respectively. The defect mode frequencies obtained by the Wannier approach are shown in Fig. 6.16. The auxiliary functions were orthogonalized by a Gram-Schmidt procedure with respect to all proper WFs. For 38 WFs this was not necessary, but in conjunction with 101 WFs a plethora of spurious modes were found with the non-orthogonalized auxiliary functions. After the orthogonalization procedure, these spurious modes were absent.

The periodic Gram-Schmidt orthogonalization procedure applied is shown schematically in Fig. 6.17. The WFs are given on a parallelepiped shaped support, on the edges of which the function values drop sharply to 0. A naive approach introduced numerical artifacts on the fields which in turn led to significant errors when computing derivatives. Therefore, a periodic orthogonalization scheme has been used as follows. The normalized WFs and the normalized auxiliary functions to orthogonalize had to be extended periodically in all directions. The scalar product for the Gram-Schmidt procedure was computed between the single WF and the periodically extended auxiliary function. Afterwards the periodically extended WF was subtracted from the auxiliary function. Finally, a single auxiliary function was cropped from the periodically extended version. The resulting orthogonalized auxiliary function showed no artifacts any more.

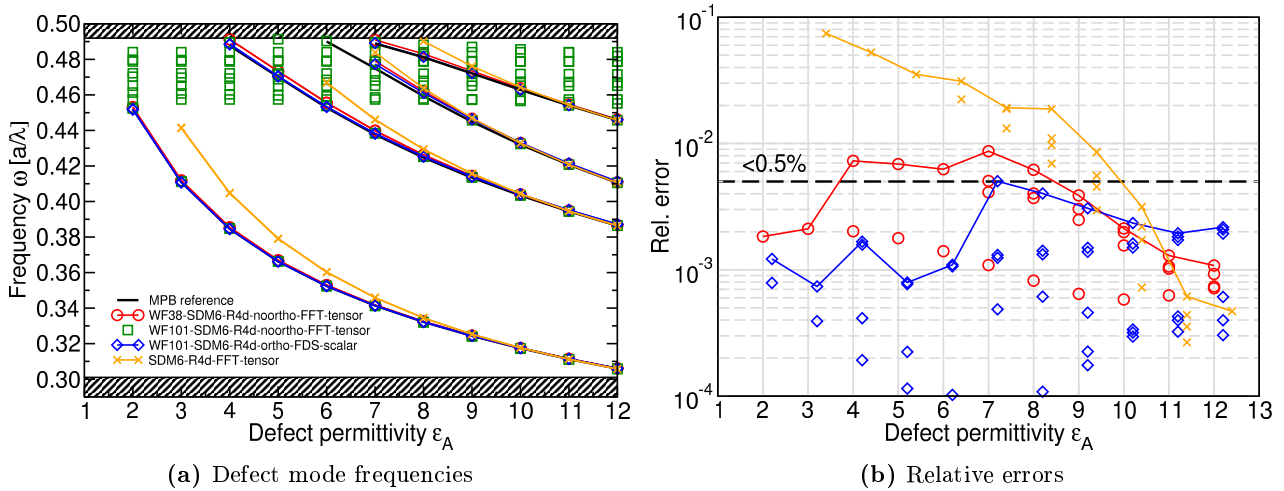


Figure 6.16: Defect mode frequencies and relative errors compared to MPB reference modes computed with the parameters from App. C.

From the error plot Fig. 6.16b we see that the use of finite-difference stencils and a scalar permittivity discretization yields errors below 0.5% for 101 WFs over a wide range of defect strengths. For the case of 38 WFs, errors below 0.9% could be achieved. Note that these are considerably less basis functions which speeds up the computations dramatically.

For comparison, the performance of the non-orthogonalized auxiliary functions alone (without any proper WFs) is also shown. They are insufficient to describe a wider range of defect strengths, proving that the proper WFs are indeed necessary.

These results were unaltered when using the auxiliary functions only at the defect site (error plots are not shown). In that case, the total number of basis functions used (compared to 38 WFs and 101 WFs) increased insignificantly.

Inverse System Wannier Functions

Fig. 6.18 shows the defect mode frequencies for using 66 IWF as auxiliary basis functions in addition to 101 proper WFs. The IWFs were orthogonalized by the periodic Gram-Schmidt procedure shown in Fig. 6.17.

The plots show results obtained by taking the auxiliary functions into account only at the defect site \mathbf{R}_A as well as on the full computational domain.

Taking the auxiliary functions into account on the full computational domain gave defect mode frequencies with an accuracy better than 0.5% for all defect strengths from 2 to 12. The particular choice of derivative and permittivity discretizations had no effect on the frequencies obtained. No spurious modes occurred; on the contrary, all of the 8 defect modes for $\epsilon_A = 12$ were found (Fig. 6.18a) in that case, including the higher order dipoles modes near the upper band edge. However, using 167 bands on 61 lattice sites equals 10187 basis functions in total which is an unfeasible number for subsequent, more complex computations.

The results for including the auxiliary functions just at the defect site show that in conjunction with 101 proper WFs all defect mode frequencies obtained have an accuracy better than 0.8% for all defect strengths from 2 to 12. Only the lower 6 defect modes were found to lie in the band gap for $\epsilon_A = 12$.

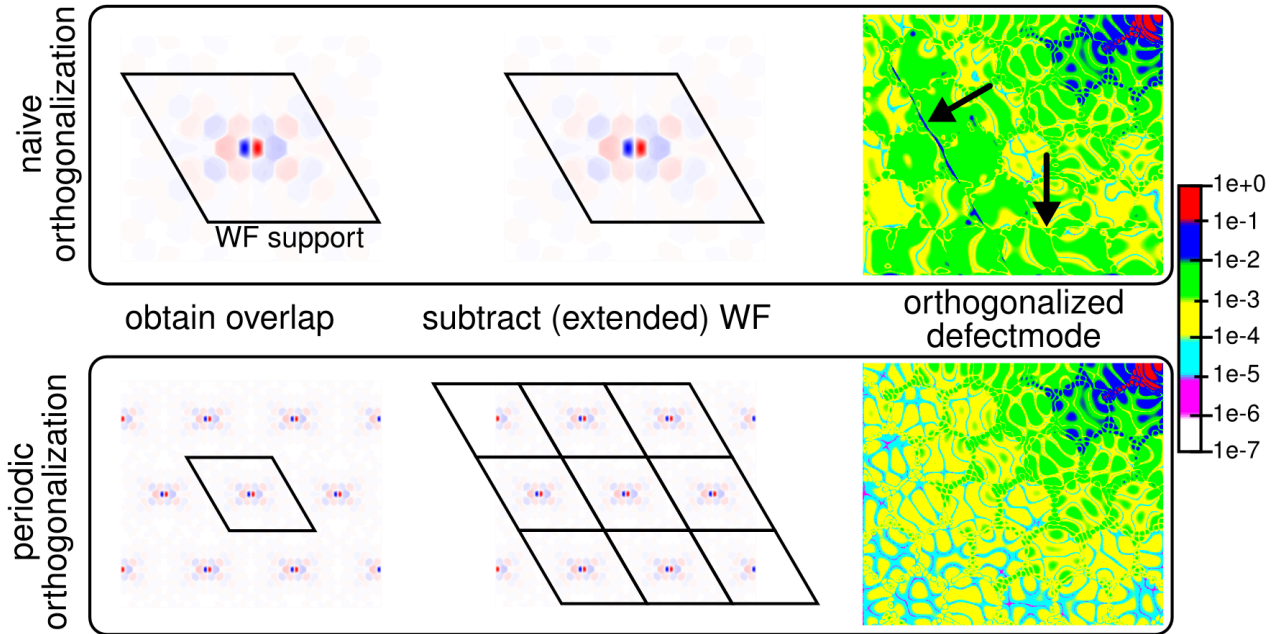


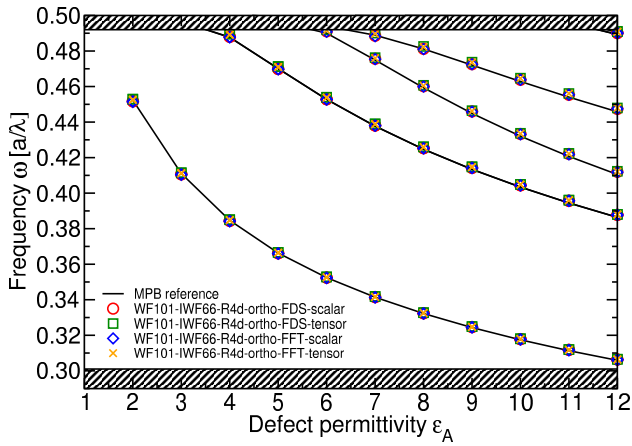
Figure 6.17: *Periodic and non-periodic Gram-Schmidt orthogonalization. The WFs are given on a parallelogram shaped support domain. Black arrows denote artifacts from the parallelogram edges that introduce errors in the numerical derivatives as explained in Fig. B.4. These artifacts are absent in the periodic orthogonalization scheme.*

However, the higher order dipole modes lie very close at the band edge and it is quite hard to obtain the frequencies to an accuracy such that the numerical frequencies lie in the band gap as well. One should bear in mind that including the 66 auxiliary functions on the full domain increases the computational effort tremendously compared to only including them on the defect site which corresponds to 6227 basis functions in total.

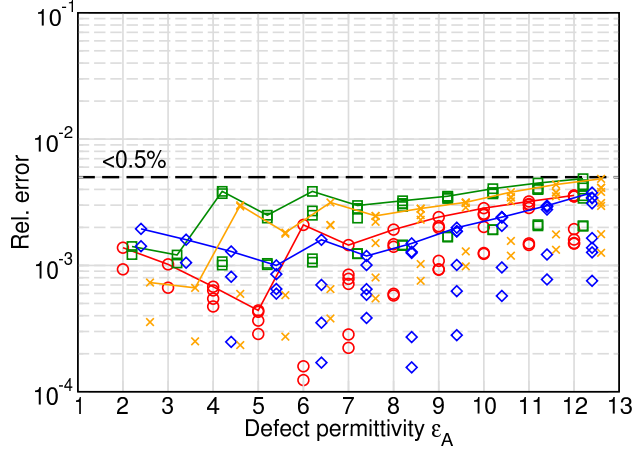
6.4 Comparison of all Auxiliary Basis Functions

We have seen that each set of auxiliary basis functions introduced is capable to increase the accuracy of defect mode frequencies for a non-etched hole significantly compared to just using 101 proper WFs. Here, we compare the relative errors to the reference frequencies of the sets of auxiliary functions with each other.

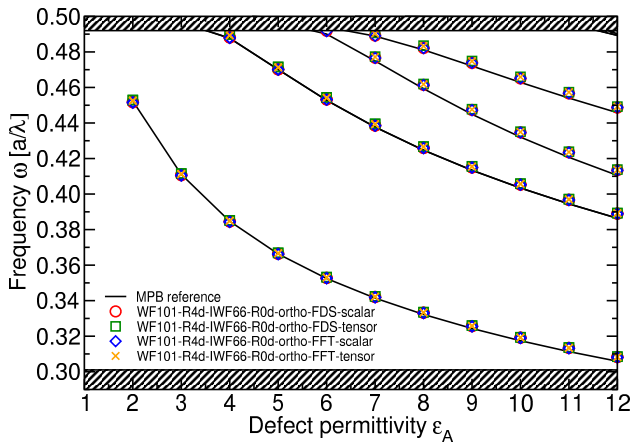
All ABFs used decreased the errors for the high-index defects significantly, where the FBFs showed the best performance with the least error over all defect strengths investigated. All ABF sets yielded maximal errors below 0.8% and increased the total number of basis functions only insignificantly. In particular, the 38 WFs with 6 defect modes used very few basis functions to obtain errors below 1%. However, this basis set was highly adapted to the single-pore setup Ai. In order to be relevant for practical computations, complex defect clusters consisting of more than one defect site and waveguide dispersions have to be modeled equally well. This is investigated in the following sections.



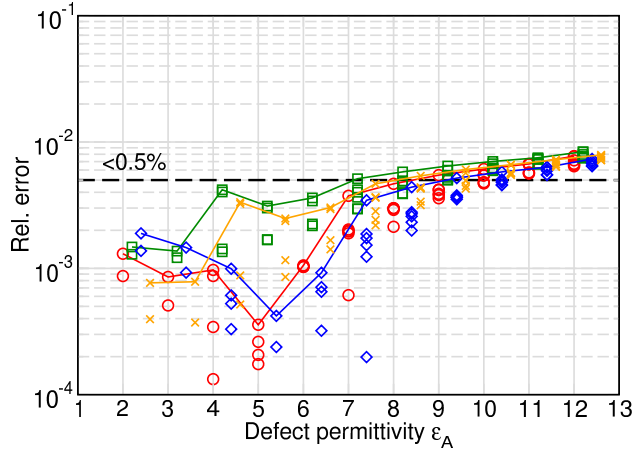
(a) Defect mode frequencies for IWFs used on full domain



(b) Rel. errors of (a)



(c) Defect mode frequencies for IWFs used on defect site only



(d) Rel. errors of (c)

Figure 6.18: Defect mode frequencies and relative errors compared to MPB reference modes computed with the parameters from App. C. Note that in (a) all 8 modes for $\epsilon_A = 12$ are found.

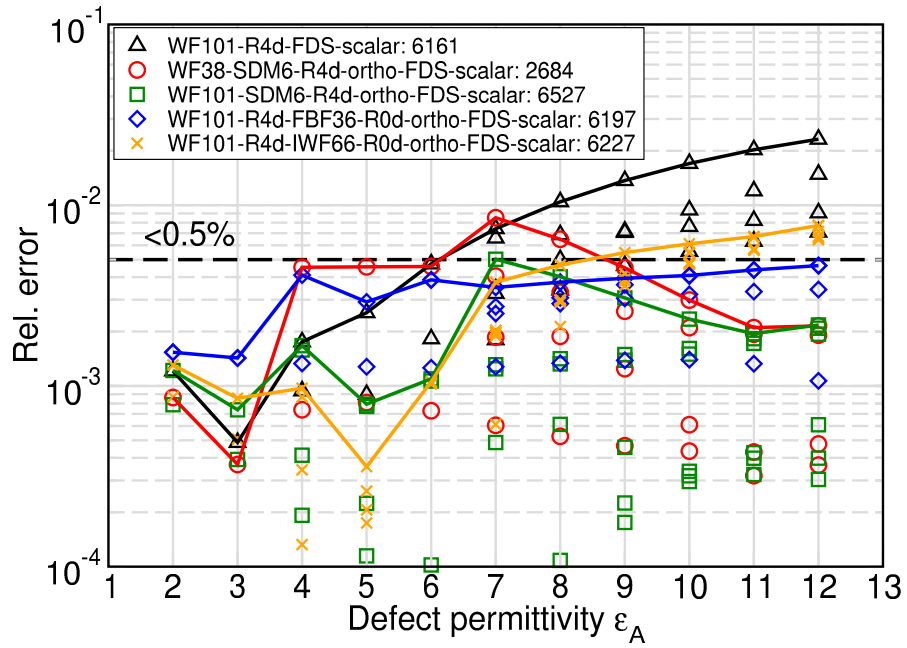


Figure 6.19: Relative errors of A_i cavity modes for all auxiliary functions introduced in this section. The 101 proper WFs were used on $\mathbb{L}_{\text{hex}}(4)$, the ABFs were only used at the defect site. The legend also displays the total number of basis functions and expansion coefficients N_{ec} used.

6.5 Complex Isotropic Defect Clusters

Modeling a single infiltrated hole properly is only the first step. Real functional elements in PC circuits consist of whole clusters of infiltrated holes.³ Therefore, we have to quantify the ability of those auxiliary functions that featured well so far to describe defect modes of defect clusters. We treat isotropically infiltrated holes here, the anisotropic defects are investigated in subsequent sections. A summary of the errors for the various defect setups from Fig. 6.20 is given in Tab. 6.3. The nomenclature is explained in Fig. 6.10 and Tab. 6.2. The full study can be found in Sec. E.1.

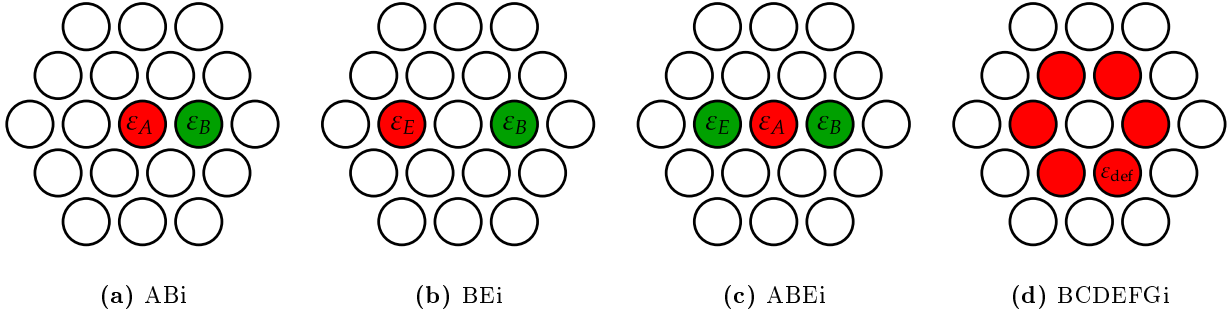


Figure 6.20: Cavity setups investigated in this section. Green defect strengths are set to 12, while the red defect strengths run from 1 to 12.

The results of Tab. 6.3 show that the FBFs perform best of all chosen sets of auxiliary basis functions. Mean and maximal errors were below 1% for the defect clusters investigated.

The supercell defect modes (SDM) only have a slight advantage when describing a single infiltrated hole (for which they were specifically designed) and infiltrated holes that are separated by at least one air hole. The latter case can be understood by the weak coupling of separated defect holes. The resulting defect modes can then be described well by a superposition of auxiliary defect modes for isolated defects.

The IWFs perform not as good the two sets mentioned above, but they also do not yield frequencies that are utterly wrong. This result sparks hope to be transferred to 3D computations if auxiliary defect modes are not sufficient and an educated guess based on the defect geometry (as the FBFs were) is not available.

³And maybe other point-like defects which are not investigated here.

Basis set	N	N^2	mean error	max error
WF38-DM6-R4d-ortho-FDS-scalar	2684	7.2×10^6	2.2×10^{-3}	8.5×10^{-3}
WF101-DM6-R4d-ortho-FDS-scalar	6527	4.2×10^7	1.0×10^{-3}	5.0×10^{-3}
WF101-R4d-BF36-R0d-ortho-FDS-scalar	6197	3.8×10^7	2.8×10^{-3}	4.7×10^{-3}
WF101-R4d-IWF66-R0d-ortho-FDS-scalar	6227	3.8×10^7	4.3×10^{-3}	7.9×10^{-3}

(a) Setup Ai with $\varepsilon_A = 2, \dots, 12$.

Basis set	N	N^2	mean error	max error
WF38-DM6-R4d-ortho-FDS-scalar	3080	9.5×10^6	5.4×10^{-3}	2.1×10^{-2}
WF101-DM6-R4d-ortho-FDS-scalar	7490	5.6×10^7	2.4×10^{-3}	7.4×10^{-3}
WF101-R4d-BF36-R0d-ortho-FDS-scalar	7142	5.1×10^7	2.2×10^{-3}	7.3×10^{-3}
WF101-R4d-IWF66-R0d-ortho-FDS-scalar	7202	5.2×10^7	5.6×10^{-3}	1.0×10^{-2}

(b) Setup ABi with $\varepsilon_B = 12, \varepsilon_A = 2, \dots, 12$.

Basis set	N	N^2	mean error	max error
WF38-SDM6-R4d-ortho-FDS-scalar	3476	1.2×10^7	1.7×10^{-3}	1.1×10^{-2}
WF101-SDM6-R4d-ortho-FDS-scalar	8453	7.1×10^7	1.1×10^{-3}	5.6×10^{-3}
WF101-R4d-FBF36-R0d-ortho-FDS-scalar	8087	6.5×10^7	1.7×10^{-3}	3.4×10^{-3}
WF101-R4d-IWF66-R0d-ortho-FDS-scalar	8177	6.6×10^7	4.9×10^{-3}	7.8×10^{-3}

(c) Setup BEi with $\varepsilon_B = 12, \varepsilon_E = 2, \dots, 12$.

Basis set	N	N^2	mean error	max error
WF38-SDM6-R4d-ortho-FDS-scalar	3476	1.2×10^7	7.1×10^{-3}	2.7×10^{-2}
WF101-SDM6-R4d-ortho-FDS-scalar	8453	7.1×10^7	3.2×10^{-3}	9.8×10^{-3}
WF101-R4d-FBF36-R0d-ortho-FDS-scalar	8087	6.5×10^7	2.6×10^{-3}	7.9×10^{-3}
WF101-R4d-IWF66-R0d-ortho-FDS-scalar	8177	6.6×10^7	6.2×10^{-3}	1.0×10^{-2}

(d) Setup ABEi with $\varepsilon_B = 12, \varepsilon_E = 12, \varepsilon_A = 2, \dots, 12$.

Basis set	N	N^2	mean error	max error
WF38-SDM6-R4d-ortho-FDS-scalar	4004	1.6×10^7	7.9×10^{-3}	3.5×10^{-2}
WF101-SDM6-R4d-ortho-FDS-scalar	9737	9.5×10^7	3.1×10^{-3}	9.1×10^{-3}
WF101-R4d-FBF36-R0d-ortho-FDS-scalar	9407	8.8×10^7	1.9×10^{-3}	6.8×10^{-3}
WF101-R4d-IWF66-R0d-ortho-FDS-scalar	9587	9.1×10^7	3.5×10^{-3}	1.3×10^{-2}

(e) Setup BCDEFGi with $\varepsilon_{\text{def}} = 2, \dots, 12$.**Table 6.3:** Errors and matrix sizes for various sets of auxiliary basis functions. Best values are highlighted green, second best values are highlighted orange. Largest errors are highlighted in red.

6.6 Anisotropic Defects

Here we will investigate the ability of WFs combined with auxiliary functions to describe the defect modes of a single hole infiltrated with birefringent and magneto-optical materials, respectively. The operator matrices (4.38) and (4.44) needed for the Wannier approach are computed by using finite-difference stencils (Sec. B.3.1) and a scalar permittivity discretization (B.6a). However, the reference modes obtained by MPB are computed by utilizing spectral derivatives (Sec. B.3.2) and a tensorial permittivity discretization for anisotropic permittivity distributions (B.6b). So we cannot simply conclude from the isotropic results of the previous sections that anisotropic defects are modeled equally well by the auxiliary functions. In order to demonstrate the performance of the auxiliary functions with as few

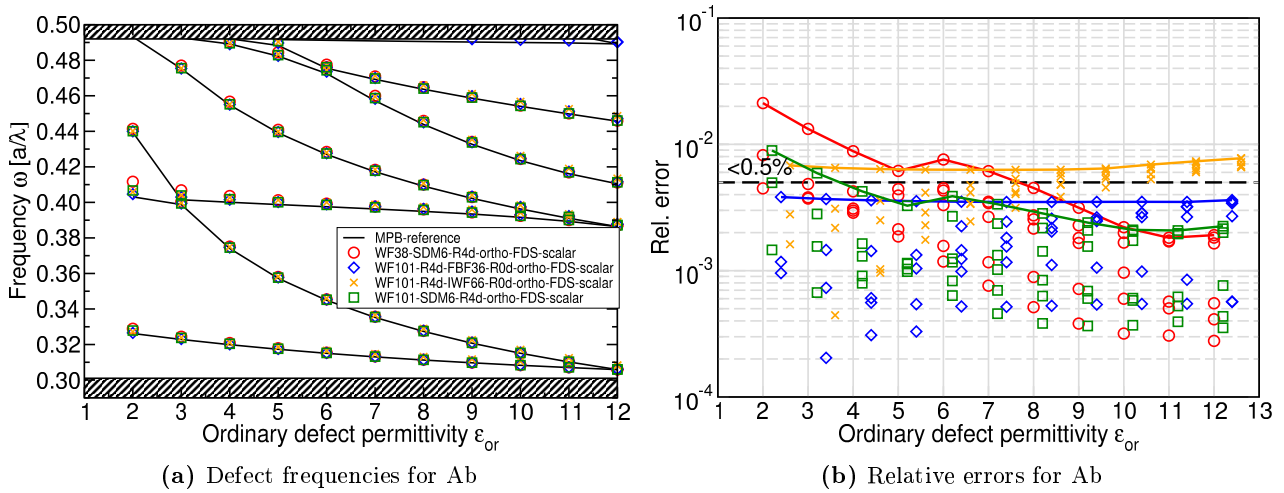


Figure 6.21: Defect setup *Ab* with fixed extra-ordinary permittivity $\varepsilon_{\text{ex}} = 12$ and director angle $\theta = 30^\circ$. The ordinary permittivity runs from $\varepsilon_{\text{or}} = 2$ to $\varepsilon_{\text{or}} = 12$.

plots and different systems as possible, extreme values for the permittivities have been chosen that do not occur in natural materials. However, this impressively demonstrates the applicability of the Wannier approach combined with auxiliary functions over a broad range of computational parameters.

Fig. 6.21 shows a single hole infiltrated with a liquid crystal with extra-ordinary permittivity $\varepsilon_{\text{ex}} = 12$ and fixed director angle $\theta = 30^\circ$. The ordinary permittivity ε_{or} runs from 2 to 12. As the error plot Fig. 6.21 shows, the FBFs frequencies have errors below 0.4% and perform best of the auxiliary function sets. The IWFs are still able to describe the defect mode frequencies within 0.8% accuracy. The SDM with 38 proper WFs yield errors below 0.5% only for the high index region $\varepsilon_{\text{or}} \geq 8$ and up to 2% error for the low index region $\varepsilon_{\text{or}} \sim 2$. The performance of the SDM with 101 proper WFs is much better, with maximal errors below 1% for all values of ε_{or} in the given range.

Fig. 6.22 shows defect mode frequencies for a single hole infiltrated with a magneto-optical material with $\varepsilon_{\text{diag}} = 12$. The off-diagonal component g_z runs from $10^{-3} \times \varepsilon_{\text{diag}}$ to $10^0 \times \varepsilon_{\text{diag}}$. The error plot Fig. 6.22 reveals, that the FBFs are able to describe the frequencies with errors below 0.4% over the physically sensible region for g_z (i. e., $g_z \ll \varepsilon_{\text{diag}}$) and 0.7% over the remaining parameter region.

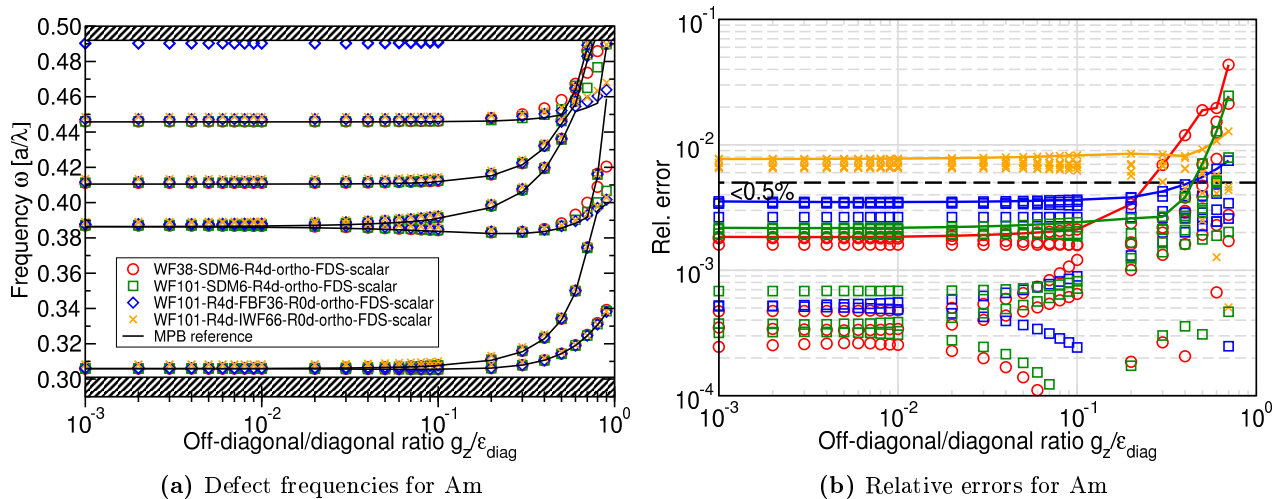


Figure 6.22: Defect setup Am with fixed diagonal permittivity $\varepsilon_{\text{diag}} = 12$. The ratio $g_z/\varepsilon_{\text{diag}}$ runs from 10^{-3} to 1.

6.7 Isotropic Waveguide Dispersion, W1-1

Here we investigate the ability of the auxiliary functions to describe waveguide dispersions by the supercell approach (4.74) and the on-shell technique (Sec. 4.5.2). We look at a W1-1 waveguide formed by a non-etched hole (Fig. 1.14b), the more complex waveguide designs of Fig. 1.14 including also anisotropic defects are treated in subsequent sections. Furthermore, we compare the supercell results with the on-shell computations. Only a small portion of computations is shown here for brevity; the full series of computations is found in Sec. E.2.

Fig. 6.23 shows the supercell results for pure WFs only and for WFs combined with auxiliary functions. While the pure WFs are only able to model the principal characteristics of the dispersion, the FBFs (together with 101 WFs) describe most branches with frequency accuracies below 1.0%. The error plot Fig. 6.23d reveals that the accuracy of the dispersion frequencies increases tremendously when adding the ABFs. In particular, the use of the FBFs yields the most accurate dispersion, with maximal frequency errors between 0.5% and 1.0%. Only this set of ABFs has been considered for the comparison with the on-shell waveguide dispersion. It is shown in Fig. 6.24a for two choices of the long range parameter L . The size of the transfer matrix in (4.92) grows fast with L , as does the time needed to diagonalize that matrix. The on-shell dispersion is now given as $k(\omega)$, whereas the MPB reference dispersion is given as $\omega(k)$. Computing the errors is not straightforward then and the yellow envelopes around the reference dispersion are used here to estimate the errors. This envelope denotes the region of $\pm 1\%$ deviation from the reference dispersion. For $L = 3$, many branches of the dispersion are modeled within 1% accuracy, and the overall agreement is very good. Only the branches near the upper band edge have larger errors. However, for technical applications, the mono-modal branch is preferred which is described better than 1% already. Increasing the long range interaction to $L = 5$ increases the overall accuracy only slightly.

Summarizing, the low errors from the supercell calculations are also found in the on-shell approach. More extensive convergence investigations are found in Chap. 7.

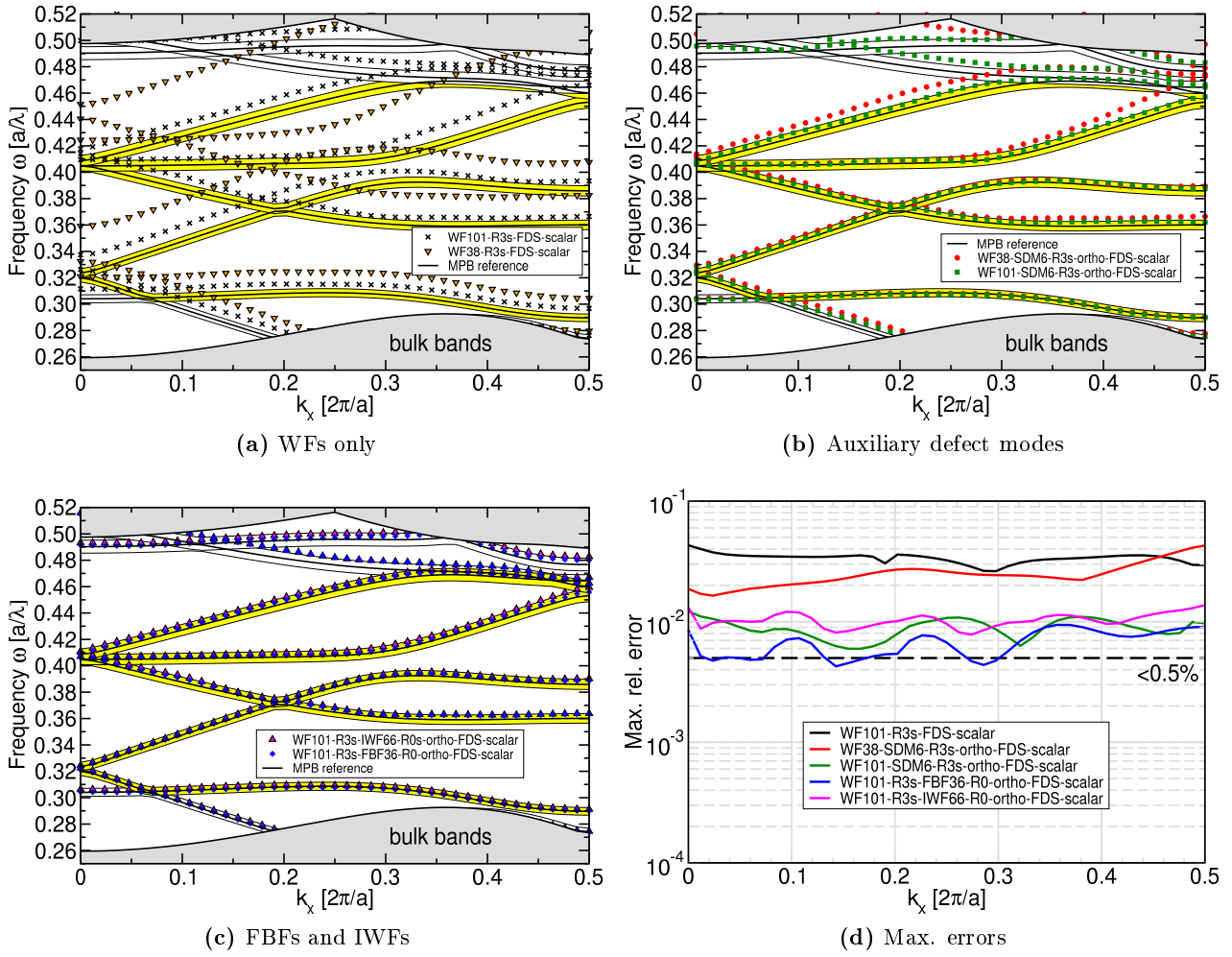
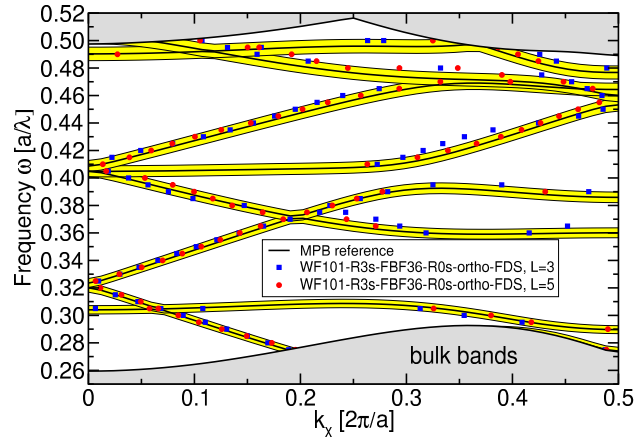


Figure 6.23: Supercell $W1-1$ waveguide dispersions after Eq. (4.74) made from one row of infiltrated holes with ϵ_A (Fig. 1.14b). Yellow/white shaded envelopes denote $\pm 1\%$ errors around reference frequencies. Only branches with yellow error region have been taken into account for computing relative errors in (d). Note that many branches are described much better than the maximal error (cf. Fig. 7.7). The use of auxiliary functions increased the accuracy tremendously.

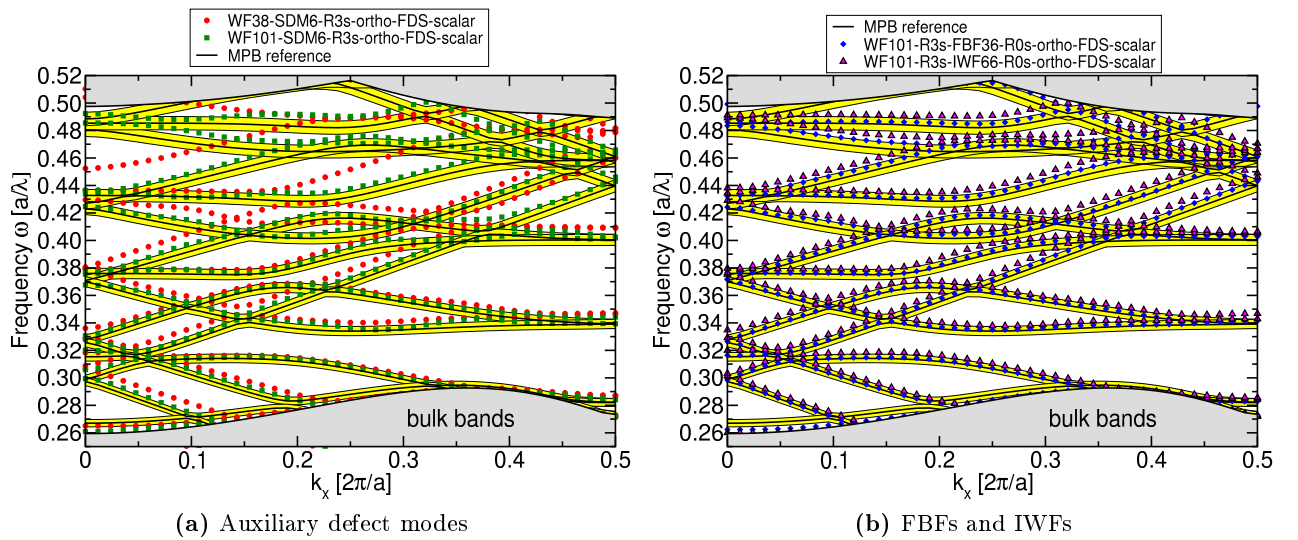
6.8 Complex Isotropic Waveguides

Here, the $W1-2$ (Fig. 1.14c) and $W2-1$ (Fig. 1.14d) waveguides made of non-etched holes are explored. For the $W2-1$ it was necessary to orthogonalize also the FBFs by the periodic Gram-Schmidt procedure shown in Fig. 1.14d. Only then were the computations stable. The results are shown in Fig. 6.26. The accuracy of the FBFs auxiliary functions is still below 1.0% for most of the branches. The other sets yield larger errors, but reproduce the essential shape of all the branches very well.



(a) On-shell dispersion

Figure 6.24: (a) On-shell dispersion of a $W1-1$ waveguide made from non-etched holes for 101 WFs and 36 FBFs and different long range interaction parameters L . For $L = 3$, many branches of the dispersion are modeled with an accuracy better than 1.0%. Using $L = 5$ increases the accuracy, but also the computational effort.



(a) Auxiliary defect modes

(b) FBFs and IWFs

Figure 6.25: Supercell waveguide dispersions for a $W2-1$ made from non-etched holes (Fig. 1.14d). For legend explanation, see caption of Fig. 6.23.

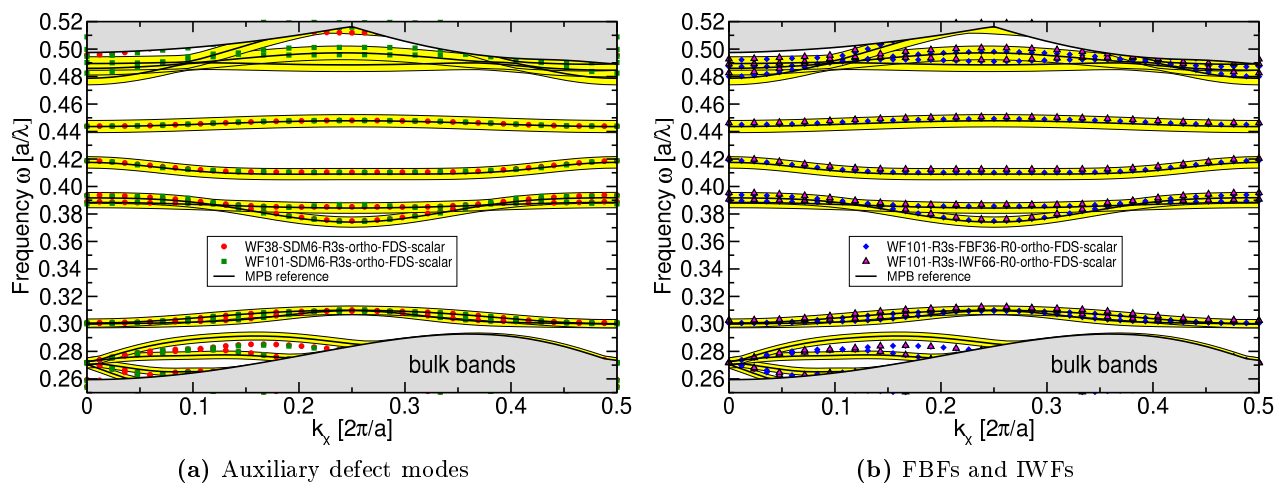


Figure 6.26: Supercell waveguide dispersions for a $W1-2$ made from non-etched holes (Fig. 1.14c). For legend explanation, see caption of Fig. 6.23.

6.9 Anisotropic Waveguides

Finally, the ability of the auxiliary functions to describe W1-1 waveguides infiltrated with anisotropic materials is investigated. Only the FBF have been considered for brevity here, because they featured best of all the sets investigated so far.

Fig. 6.27 shows a W1-1 infiltrated with a magneto-optic material with the extreme unphysical parameters $\varepsilon_{\text{diag}} = 12$ and $g_z = 6$.

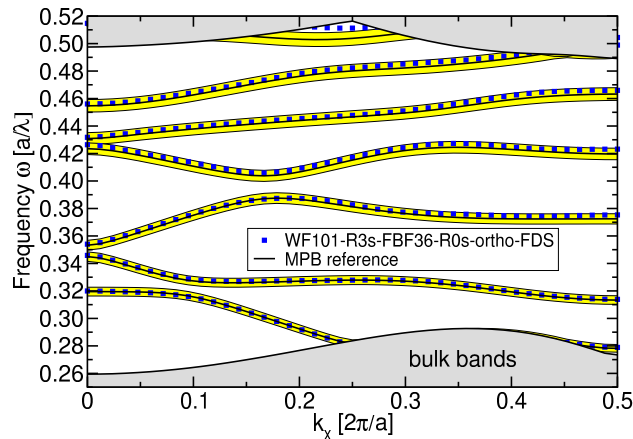


Figure 6.27: Waveguide dispersions for W1-1, Am , $\varepsilon_{\text{diag}} = 12$, $g_z = 6$ (Fig. 1.14a).

Fig. 6.28 features a W1-1 made of holes infiltrated with a birefringent material with parameters $\varepsilon_{\text{ex}} = 12$ and $\varepsilon_{\text{or}} = 2$. The director angle θ was set to 0° , 30° , 60° and 90° successively in the plots. This demonstrates the ability of the auxiliary functions, to model tunable waveguide dispersions properly. The errors in most of the branches are again below 1.0%. The dispersions are in excellent agreement with the MPB reference, featuring accuracies much better than 1% for most of the branches.

6.10 Summary

We reviewed the continuity conditions of the electric and magnetic fields in E-polarization and H-polarization across dielectric boundaries in 2D systems, respectively. E-polarized fields are continuously differentiable whereas the derivatives of H-polarized fields are discontinuous which is visible as kinks in the field profiles. The accuracy of Wannier based defect mode computations in the TM square lattice of cylindrical silicon rods in air was reviewed, where the method works very efficiently. A few WFs are sufficient to describe the localized defect modes of a single defect rod with permittivities ranging over values from 1 to 80 with accuracies below 0.5%. Two reasons were identified for this behavior. Firstly, the WF profiles strongly resembled the defect mode profiles already. Secondly, both the defect modes and the WFs were continuously differentiable across dielectric boundaries between silicon and air, and in particular between the defect rod and air.

For the TE triangular lattice of cylindrical air holes in silicon, it was shown that the kinks in the magnetic fields are responsible for the poor convergence of defect mode frequencies. This was demonstrated on various slice cuts through WFs and defect modes. These cuts also revealed how increasing the number of WFs helps in modelling the correct defect modes. WFs with localization centers between air holes are equally important as those localized in the center of air holes. This qualitative observation is quantified in Chap. 7.

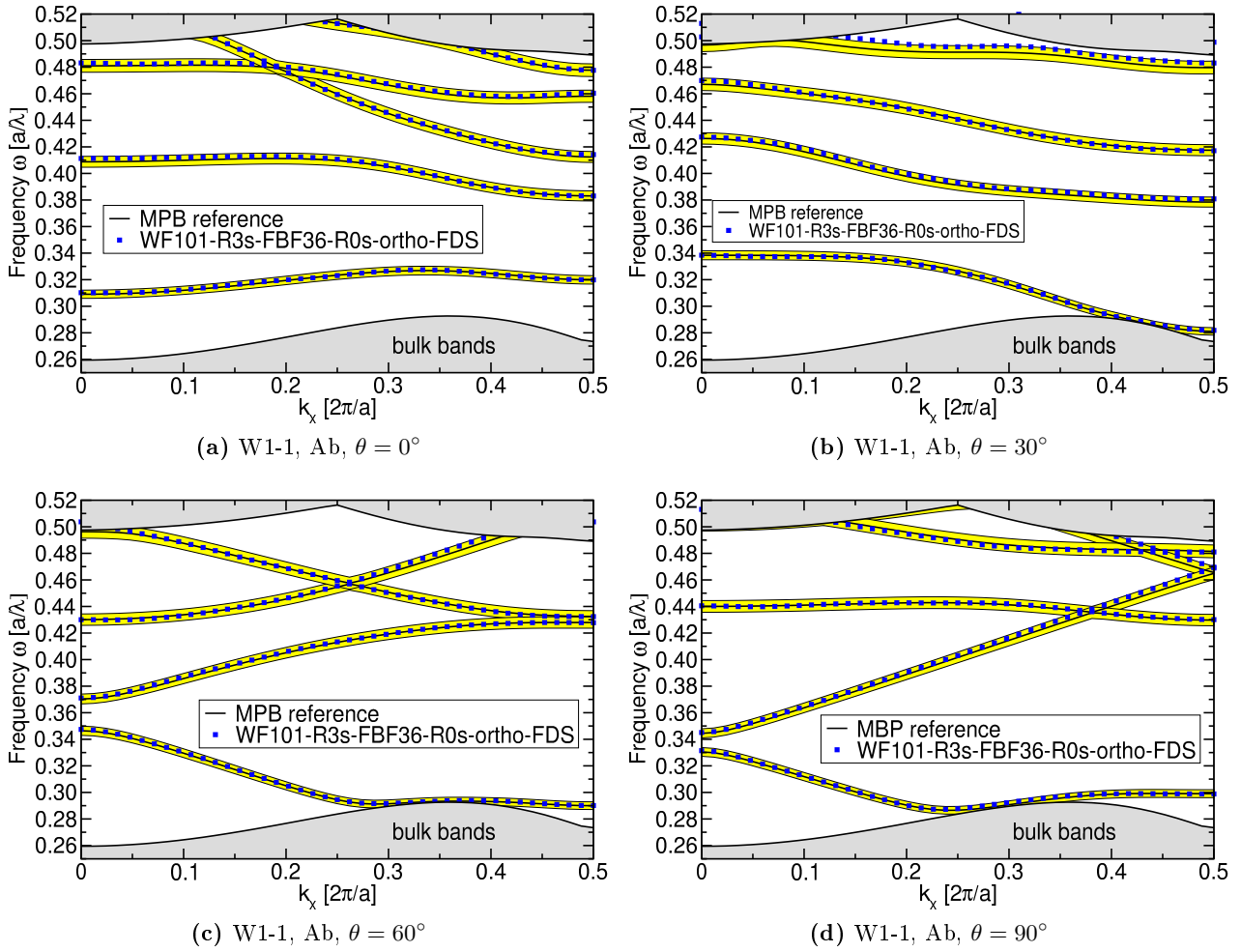


Figure 6.28: Waveguide dispersions for W1-1, Ab with $\epsilon_{\text{ex}} = 12$ and $\epsilon_{\text{or}} = 2$ for various director angles θ .

Based on these observations, three sets of additional basis functions to augment the WF basis were suggested that should help the WFs to model the correct continuity conditions of defect modes. Among these suggestions were the Fourier-Bessel functions, which were obtained from a closed expression and an educated guess based on the fixed geometry of the defect class of infiltrated holes. The supercell defect modes were obtained from an MPB supercell calculation of a non-etched hole which was the case with largest errors for the pure WFs. These auxiliary functions model the continuity of non-etched hole defect modes perfectly. The idea of this set of ABFs was that they should be able to interpolate the defect modes for medium index defects in conjunction with the WFs. Finally, inverse system Wannier functions for the triangular lattice of silicon rods in air were proposed. Their kinks have the opposite direction of those of the proper WFs. All of these ABF had to be orthonormalized by the Gram-Schmidt procedure in order to suppress spurious modes in the calculations. A periodic orthonormalization procedure was described that reduces artifacts in the basis field profiles to reduce errors of the discretized derivatives.

All of the ABF sets in conjunction with 101 proper WFs reduced the errors to the order of or below 1% for the cavity computations. This is a drastic improvement compared to using only the proper

WFs. Isotropically as well as anisotropically infiltrated holes were described sufficiently well with the FDS-scalar discretization scheme. It yielded the same errors as the FFT-tensor scheme which justifies the usage of the scalar discretization for both the description of isotropic as well as anisotropic defects.

The FBFs yielded the least errors of all sets, in the cavity as well as in the waveguide dispersion computations. However, the FBFs were particularly adapted to the 2D cylindrical hole geometry, where the scalar basis functions are always divergence-free. Thus, this ansatz cannot be applied to general 3D PC systems in a straightforward fashion. The other two sets investigated, however, can be generated in the same fashion for any geometry in 3D PC as vectorial fields. They are always divergence-free by construction.

Additionally, the A_i defect mode frequencies obtained from the three sets of proper WFs introduced in Sec. 3.9 were compared. The symmetrized variants WF38-sym yield the same frequencies as the unprocessed WF38-SMV versions. The WF38-MV versions also yielded the same frequencies, but with a large number of additional spurious modes. The reason for this behavior is not yet clear. However if the spurious modes can be suppressed in the future, this set of WFs is preferable over the WF38-SMV set because the construction of the latter took some weeks, in order to find the proper parameters for the SMV spread minimizations in the bottom-up approach. The symmetrization of the WF38-SMV set to yield the WF38-sym set did not introduce new errors. Exploiting the perfect symmetry of the resulting matrix elements could help in accelerating some computations in the future, e. g., the determination of scattering matrices according to Sec. 4.6.

Summarizing, the accuracy of the pure Wannier based computations has been improved drastically by the use of auxiliary basis functions. At the same time, the total number of basis functions used increased only marginally, since it was sufficient to incorporate the ABFs only at the few defect sites. This allows to treat defect structures containing non-etched holes now in the localized basis expansion which was not possible with using only the proper WFs before.

7

Defect Mode Convergence

So far we have shown that the ABFs are in principle able to describe defect clusters of non-etched holes in the triangular model system. Here we will investigate which of the basis functions at which lattice sites in the computational domain are needed to obtain a particular accuracy. Reducing the total number of basis functions reduces the total number of expansion coefficients $c_{n\mathbf{R}}$ to describe defect modes and thus leads to smaller matrices and faster computations. Furthermore, the V-parameter, measuring the significance of the Wannier function bands for a particular defect mode [31], is reviewed and its definition is adjusted for degenerate WFs.

7.1 Cavity Defect Clusters

We investigate the cavity defect setups Ai and BCDEFGi. When N_{WF} WFs are used at all N_{cd} lattice sites of the computational domain, then

$$N_{\text{ec}} := N_{\text{WF}} N_{\text{cd}} \quad (7.1)$$

expansion coefficients have to be computed from matrices with $N_{\text{ec}}^2 = N_{\text{WF}}^2 N_{\text{cd}}^2$ complex entries. Thus, by Tab. 4.1 one can save large amounts of memory in computation when using smaller computational domains and less proper WFs.

We will use the 101 proper WFs at all lattice sites of the computational domain \mathbb{L}_{comp} and the ABFs only at sites containing defects. Therefore, the ABFs do not contribute many coefficients and the order of magnitude of N_{ec} is defined in good approximation by the 101 proper WFs on the N_{cd} lattice sites.

7.1.1 Computational Domain Size

The parameter $R_{\text{max}} \in \mathbb{N}$ is used to define a symmetric domain $\mathbb{L}_{\text{hex}}(R_{\text{max}})$ around the origin $\mathbf{R} = (0, 0)$ that is shifted to each defect site \mathbf{R}_m building up the full computational domain as

$$\mathbb{L}_{\text{comp}} := \bigcup_m \left(\mathbb{L}_{\text{hex}}(R_{\text{max}}) + \mathbf{R}_m \right), \quad (7.2)$$

where the sum of a set and a lattice site is defined in the usual way as

$$\mathbb{L}_{\text{hex}}(R_{\text{max}}) + \mathbf{R}_m := \{ \mathbf{R} + \mathbf{R}_m : \mathbf{R} \in \mathbb{L}_{\text{hex}}(R_{\text{max}}) \}. \quad (7.3)$$

Examples for the cavity setups Ai and BCDEFGi are shown in Fig. 7.1a.

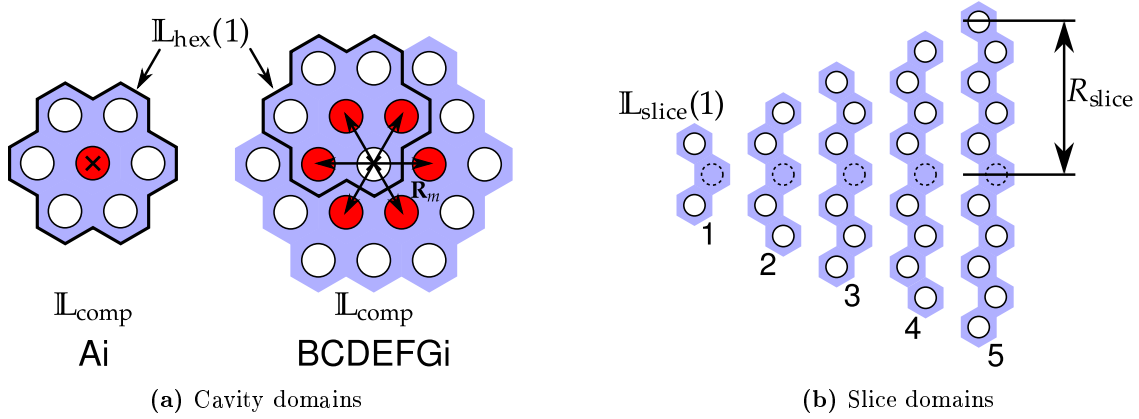


Figure 7.1: Example for computational lattice site domains \mathbb{L}_{comp} . (a) The assembly of computational domains \mathbb{L}_{comp} after (7.2). The origin is denoted by a cross, the defect sites are located at the \mathbf{R}_m . (b) Waveguide slice domains $\mathbb{L}_{\text{slice}}(R_{\text{slice}})$ for various parameters R_{slice} .

For waveguide dispersions, the number of cladding cells $R_{\text{slice}} \in \mathbb{N}$ in a waveguide slice is used to define slice domain $\mathbb{L}_{\text{slice}}$. This computational domain is given by R_{slice} lattice sites above and below the center site at the origin $(0,0)$. Such a lattice site domain is denoted by $\mathbb{L}_{\text{slice}}(R_{\text{slice}})$ and contains $2R_{\text{slice}} + 1$ lattice sites. Examples are shown in Fig. 7.1b.

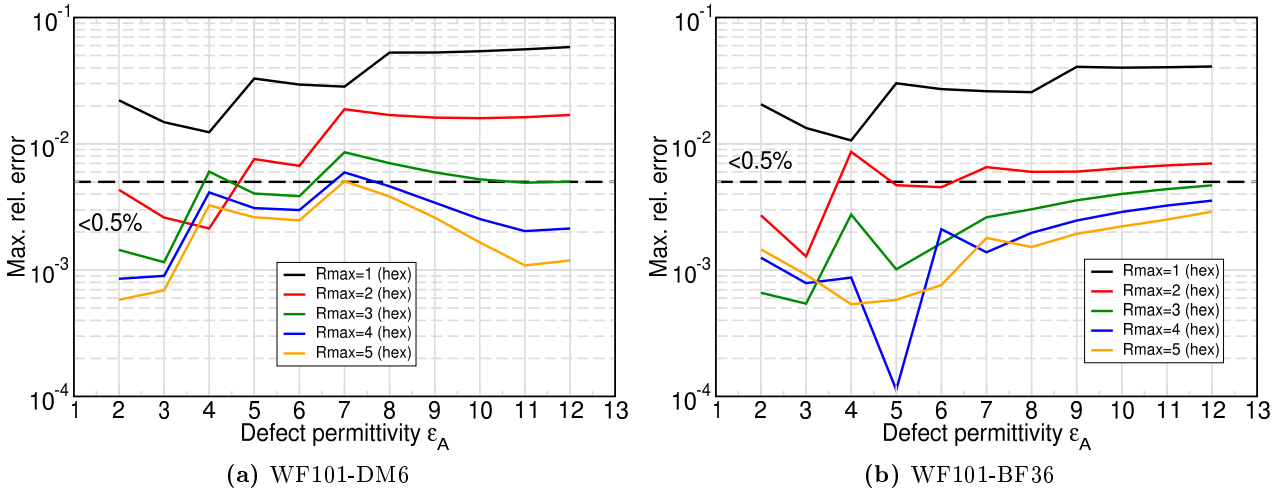


Figure 7.2: Maximal relative errors for a non-etched hole compared to MPB reference values for using different R_{max} in (7.2).

For the setup Ai, the errors obtained for various defect strengths and increasing R_{max} are shown in Fig. 7.2. For the set WF101-DM6, the largest errors are found for $\varepsilon_{\text{def}} = 7.0$, whereas for WF101-BF36 the largest errors are obtained for a non-etched hole with $\varepsilon_{\text{def}} = 12.0$. Therefore, in Fig. 7.3a these setups have been investigated for the respective ABF. Fig. 7.3 shows again that the WF101-FBF36 gives the least errors which do not decrease significantly for $R_{\text{max}} > 3$. Thus, $R_{\text{max}} = 3$ is sufficient for this set to obtain errors of about 1% and less.

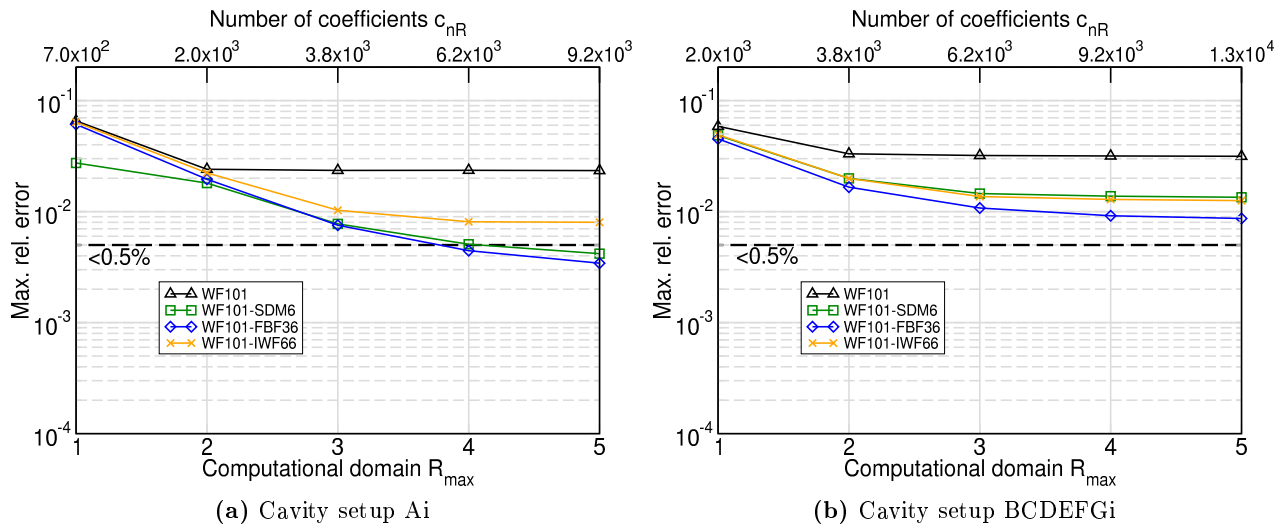


Figure 7.3: Maximal relative errors for increasing parameter R_{\max} of the computational domain $\mathcal{L}_{\text{hex}}(R_{\max})$ around each defect hole compared to MPB reference values. The total number of expansion coefficients $c_{n\mathbf{R}}$ used is shown as well for each R_{\max} . (a) shows the maximal errors over all defect modes and defect strengths ε_{def} ranging over values from 2 to 12. (b) shows the maximal errors over all 36 defect modes for the ring of 6 non-etched holes of Fig. 6.20d (with $\varepsilon_{\text{def}} = 12.0$ for all ABF sets, since that setup yields the maximal errors).

7.1.2 Sparsity

One could skip time consuming test computations if there was a criterion that told the user from the matrices themselves, whether the basis functions are relevant or not. Judging from the sparsity of the defect matrices for a non-etched hole (Fig. 5.7e), one could save a lot of memory and also accelerate computations at the same time when taking only matrix elements larger than some threshold into account. However, in the current state of the code used to compute the defect mode frequencies, it is not possible to exploit this kind of sparsity. If a matrix element for an index $(n\mathbf{R})$ is larger than the chosen threshold, any matrix elements with index pairs $(n'\mathbf{R}', n\mathbf{R})$ have to be included as well.

The resulting errors in defect mode frequencies compared to the case when all available basis functions were used, are shown in Fig. 7.4. The number of basis functions (which is the number N_{ec} of expansion coefficients) is shown in the plot as well.

Compared to Fig. 7.3a, where the computational domain around each defect was enlarged, the ratio between maximal error and number of coefficients used is worse. Thus, it is better to judge the relevance of a basis function by its distance from the defect rather than its contribution to the defect matrix B . However, since there are many norms to classify the 'largeness' of matrix entries, other techniques more suitable for diagonalization could yield better estimates for the contribution to the final eigenvalues.

7.1.3 Relevant Basis Functions

In order to judge the relevance of a particular band n of orthonormal WFs to model a given defect mode, one can introduce the band contribution parameter V_n as the square sum of expansion coefficients $c_{n\mathbf{R}}$

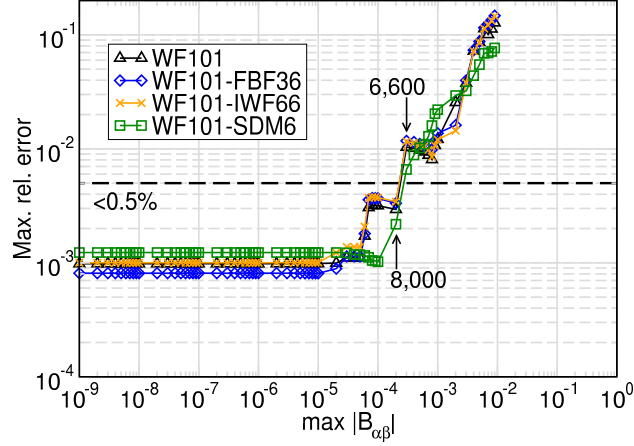


Figure 7.4: Maximal relative errors of A_i defect mode frequencies when taking matrix elements above a certain threshold into account. The threshold is normalized to the maximal matrix element in the defect matrix. Arrows denote the number N_{ec} of expansion coefficients that were used.

from (4.1),

$$V_n := \sum_{\mathbf{R}} |c_{n\mathbf{R}}|^2. \quad (7.4)$$

We will now demonstrate the significance of this quantity. We employ the notation (1.54) for a given eigenmode $|\psi\rangle$ of the wave equation which is expanded into electric or magnetic field WFs as in (4.1):

$$|\psi\rangle = \sum_{n\mathbf{R}} c_{n\mathbf{R}} |n\mathbf{R}\rangle. \quad (7.5)$$

Then the squared norm with respect to the scalar product is given by

$$\langle\langle \psi | \psi \rangle\rangle = \sum_{n\mathbf{R}} \sum_{n'\mathbf{R}'} c_{n\mathbf{R}}^* c_{n'\mathbf{R}'} \langle\langle n\mathbf{R} | n'\mathbf{R}' \rangle\rangle \quad (7.6)$$

$$\stackrel{(1.54)}{=} \sum_n \underbrace{\sum_{\mathbf{R}} |c_{n\mathbf{R}}|^2}_{=V_n} \quad (7.7)$$

$$\stackrel{(7.4)}{=} \sum_n V_n. \quad (7.8)$$

Thus, the quantity V_n determines how much the WF band n contributes to a given defect mode. Note that this parameter defined by (7.4) only makes sense for orthonormalized basis functions.

In the case of degenerate basis functions (e.g., WF bands $n = 4, \dots, 9$ in Fig. 3.44), the combined contribution V_n^{deg} for the whole set of degenerate functions is more relevant and defined as follows. Let $\mathbb{D}_n^{\text{deg}}$ be the set of all band indices n' for a set of ν -fold degenerate sets of WFs, i.e.

$$\mathbb{D}_n^{\text{deg}} := \{n, n+1, \dots, n+\nu\}. \quad (7.9)$$

Then we define the combined contribution of the degenerate set of WFs as

$$V_n^{\text{deg}} := \sum_{n' \in \mathbb{D}_n^{\text{deg}}} V_{n'}. \quad (7.10)$$

This takes the contribution of whole sets of WFs with equal shapes into account.

101 WFs

The plots in Fig. 7.5 show the significance of the combined contribution V_n^{deg} for the defect mode frequencies that are obtained when the corresponding bands are *not* used in the Wannier expansion. Therefore, for each band label n denoting the first WFs in the degenerate set, the relative frequency change

$$\Delta\omega_{\text{rel},n} := \frac{\omega_n - \omega_{\text{ref}}}{\omega_{\text{ref}}} \quad (7.11)$$

has been plotted, where the reference frequency ω_{ref} is the one obtained by using all available basis functions and ω_n is the frequency obtained by *omitting* the (possibly degenerate) bands with indexes in $\mathbb{D}_n^{\text{deg}}$.

From Fig. 7.5e we can deduce by an eyeball fit that the relative frequency change

$$\Delta\omega_{\text{rel},n} \approx 2 \left(V_n^{\text{deg}} \right)^{\frac{1}{\sqrt{2}}} \quad (7.12)$$

is a good estimate for the influence of a degenerate band set n on the accuracy of the defect mode frequencies. This fit allows to estimate the frequency change when omitting WFs with certain contributions. As an example, in order to obtain the same frequencies within 0.1 % accuracy, one could ignore all band sets n with an influence parameter V_n^{deg} less than

$$\left(\frac{1}{2} \cdot 10^{-3} \right)^{\sqrt{2}} = 2.1 \times 10^{-5}. \quad (7.13)$$

However, only the WF with $n = 94$ of Fig. 3.44 is below that threshold for each of the six defect modes of a non-etched hole. If one is interested only in a particular defect mode for some application, however, an analysis of the influence parameter immediately gives an estimate of the WFs that have to be included in a computation for a desired accuracy.

101 WFs, 36 FBFs

When using any auxiliary basis functions, are we allowed to omit some of the proper WFs and still get sufficiently accurate results? To answer this question, we must not use the orthogonalized auxiliary functions because in this case the WFs and the auxiliary functions would contribute mutually exclusive information to the defect modes. Then we may not use the degenerate contribution parameter (7.10) which was introduced for orthonormal functions only. We have to resort to the maximal frequency change (7.11) to judge the importance of the basis functions. In Fig. 7.6, the non-etched hole defect mode frequencies are investigated, where the maximal frequency error (compared to using all basis functions) over all defect modes is shown.

Choosing the relative threshold 10^{-3} , we could easily omit the proper WFs 41,42,58,80-85,92,93,94,96-101, and some of the FBFs. Since we used the auxiliary functions at defect sites only anyway, the saving in memory when omitting the 18 WF bands is much more beneficial. This reduces the total number of expansion coefficients by almost 20 %. However, these results are obtained from one single test system only. When looking at more complex defect clusters, the WFs that contribute little to the non-etched hole results may become more important then.

Such investigations can also be carried out in principle for the 66 IWFs, which has been omitted here. When using the 6 SDMs, omitting any of these would make no sense, since they were particularly chosen to model the respective defect modes in the Wannier approach with high accuracy.

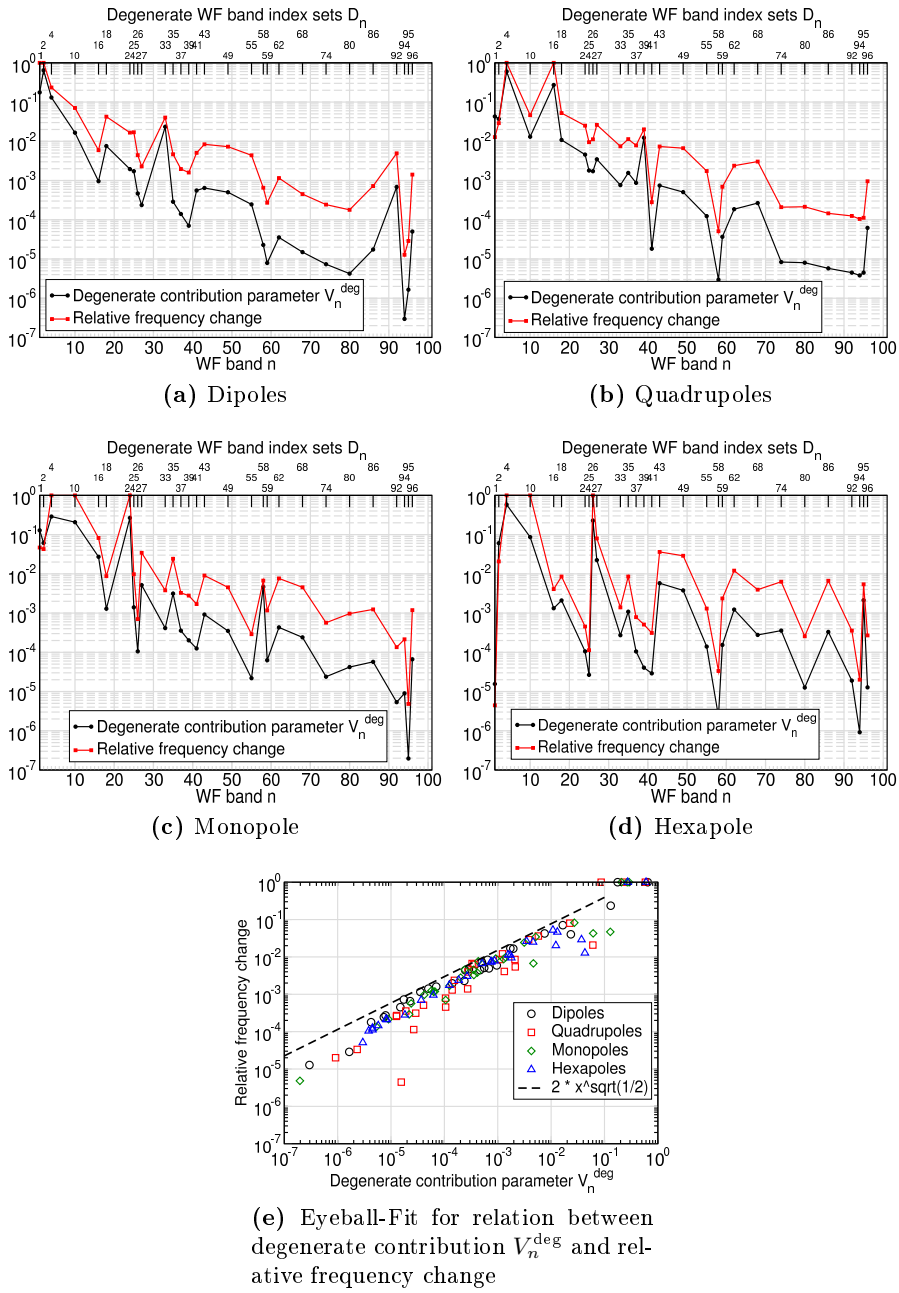


Figure 7.5: (a)–(d) Degenerate contribution parameter V_n^{deg} and relative frequency changes after (7.11) for the defect modes of a non-etched hole computed by 101 WFs. (e) Estimate of the relation between the two parameters. Frequency changes have been set to 1 if no frequency within the band gap was obtained.

7.2 Waveguide Dispersions

The accuracy of waveguide dispersions for both the supercell and the on-shell approach are discussed here. It depends on the parameters R_{slice} and the long range interaction parameter L .

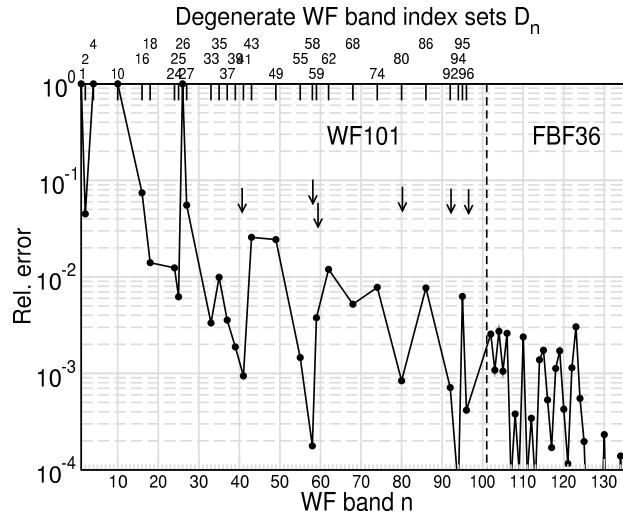


Figure 7.6: Maximal frequency change for the defect modes of the non-etched hole when omitting some of non-orthogonalized basis functions of the set WF101-BF36. If a particular defect mode was not found in the band gap, the relative error was set to 1. Proper WFs with contributions less than 10^{-3} are denoted by arrows. The 101 proper WFs were used on a computational domain $\mathbb{L}_{\text{hex}}(4)$, the 36 BBFs only at the defect site.

7.2.1 Supercell Computations

The case that is hardest to describe by WFs is a waveguide made of non-etched holes. Only the set WF101-BF36 has been used here because Sec. 6.7 shows that this set yields the most accurate results. Fig. 7.7 shows the errors of the dispersion frequencies in the supercell approach for a W1-1 waveguide made from a row of non-etched holes for various choices of R_{slice} of the slice domain (cf. Fig. 7.1b). As for the cavity setups Ai and BCDEFGi, a parameter $R_{\text{slice}} = 3$ is sufficient and larger values do not decrease the errors significantly. In particular, the monomode branch between $\omega = 0.325 \frac{2\pi c_0}{a}$ and $\omega = 0.355 \frac{2\pi c_0}{a}$ is described better than 0.5% even with $R_{\text{slice}} = 2$. This branch is interesting for monomode photonic devices in possible applications.

7.2.2 On-Shell Computations

As the previous Sec. 7.2.1 shows, $R_{\text{slice}} = 3$ yields sufficiently converged dispersion results. Again, only the set WF101-BF36 is investigated here. The on-shell computations feature a long range interaction parameter L determining the size of the transfer matrix (4.92) which has to be diagonalized. Only the monomode branch has been investigated in detail because the computation time increases drastically for $L = 5$. As Fig. 7.8b shows, the dispersion for on-shell computations of the monomode branch can be described with frequency accuracies below 0.5% with $L = 3$. Larger values for L improve the accuracy slightly, but the computation time and memory consumption increases drastically.

7.3 Summary

The influence of various numerical parameters on the accuracy of the Wannier approach with ABFs has been investigated. This comprised the size of the computational domain, the basis functions which are actually needed, and for on-shell waveguide dispersions, the long range interaction parameter L .

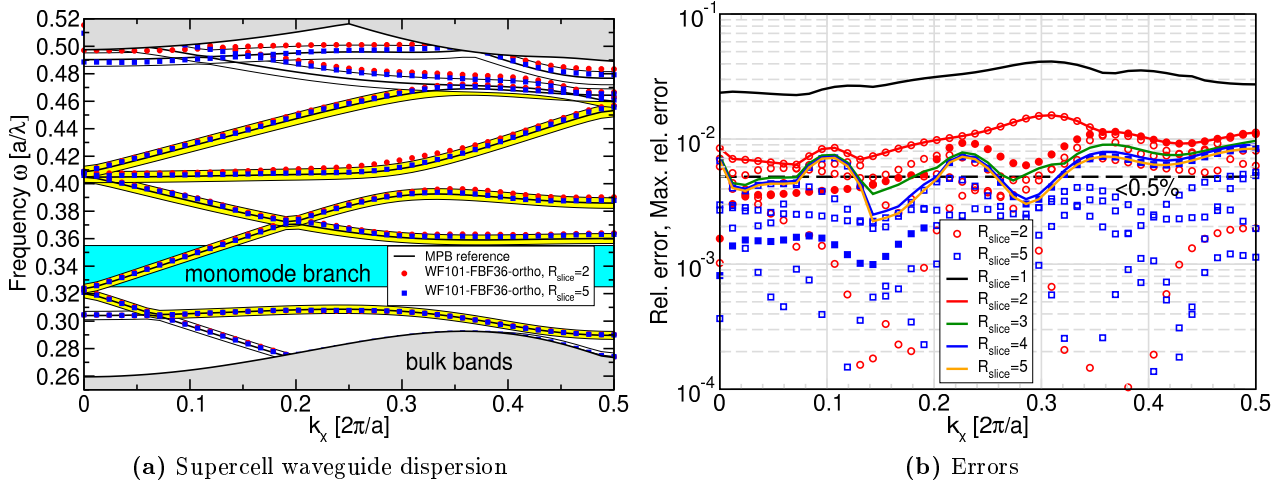


Figure 7.7: (a) Supercell waveguide dispersions by (4.74) for a non-etched W1-1 (A_i , $\varepsilon_{\text{def}} = 12$, Fig. 1.14b) for 101 WFs and 36 orthogonalized FBFs. The slice extent R_{slice} ranges from 1 to 5. Only the branches in the yellow regions have been used for computing the errors. (b) Maximal errors in waveguide dispersion compared to the MPB reference dispersion. For $R_{\text{slice}} = 2$ and 5, the individual errors of each branch are also shown. The filled symbols show the errors for the monomode branch between $\omega = 0.325 \frac{2\pi c_0}{a}$ and $\omega = 0.355 \frac{2\pi c_0}{a}$.

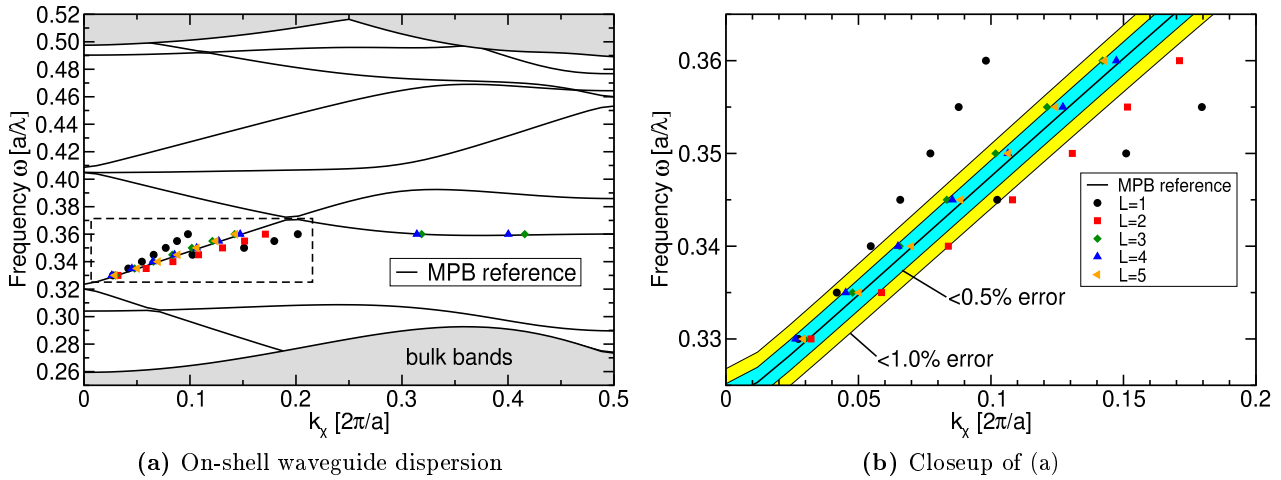


Figure 7.8: (a) On-shell waveguide dispersions after Sec. 4.5.2 for 101 WFs with 36 FBFs for various values of the long range interaction (LRI) parameter L . R_{slice} was set to 3. (b) Closeup of the mono-mode branch of (a). For $L \geq 3$ the on-shell dispersion is within 0.5% accuracy compared to the MPB reference dispersion.

For cavity defect modes, the degenerate contribution parameter was introduced that allows to estimate the contribution of a particular basis function to the eigenmode frequency. It can be computed from the expansion coefficients of a defect mode in terms of the localized basis functions and is only applicable for orthonormalized bases. For the non-orthonormalized set WF101-BF36, it was shown that about 20% of basis functions can be omitted without diminishing the accuracy of the A_i defect modes severely. This

result cannot easily be transferred to complex defect clusters, since the omitted basis functions may become important then to model the more complex defect mode profiles properly. Their contribution would have to be evaluated anew for each defect configuration. However, if a series of computations is restricted to a certain frequency range (as is often the case for transmission computations [40]), some basis functions may indeed be omitted without affecting the overall accuracy much. The techniques to judge the basis function contribution may help then.

Omission of basis functions to reduce matrix sizes based on the sparsity of defect matrices yielded no conclusive results.

Parameter	Value
R_{\max} (cavities)	3
R_{slice} (waveguides)	3
L (on-shell dispersion)	3

Table 7.1: *Numerical parameters for the Wannier approach that yield frequency errors of 1% or below.*

Finally, the numerical parameters of Tab. 7.1 have been shown to yield sufficiently converged results with maximal frequency errors of 1% or below.

8

Symmetric Wannier Functions

In this brief chapter, the effect of using the symmetrized WF set WF38-sym from Fig. 3.46 is documented. One would expect perfectly degenerate frequencies for respective defect modes, as well as identical solutions for waveguides pointing in different directions. However, the systems investigated show no systematic improvements in this respect whatsoever. This behavior is not yet clear and may indicate a minor bug in the implementation of the matrix computations of Chap. 4 that does not affect the overall performance, as the good agreement of the defect mode frequencies in previous chapters showed.

8.1 Degeneracy of Cavity Defect Modes

The cavity setup Ai in the triangular model system supports two doubly-degenerate dipole modes of symmetry $E_1(a)$ and two doubly-degenerate quadrupole modes of symmetry $E_2(a)$, as seen in Fig. 1.12. The resulting defect mode frequencies obtained with the basis sets WF38-SMV and WF38-sym are shown in Fig. 6.13. However, the degeneracy of the frequencies is not visible in those plots. Therefore, analogous to (C.3), the frequency asymmetry

$$\Delta\omega_{as} := \frac{\omega_{\max} - \omega_{\min}}{\omega_{\max} + \omega_{\min}} \quad (8.1)$$

for the two sets of basis functions is calculated and shown in Fig. 8.1. The lower this value, the better the degeneracy of the defect mode frequencies, where $\Delta\omega_{as} = 0$ denotes identical frequencies. As the plot reveals, the use of the symmetrized set WF38-sym does not improve the degeneracy of the frequencies. On the contrary, for some defect strengths ε_A , the asymmetry is even larger than for the unprocessed set WF38-SMV. The sources for this behavior are not yet clear.

8.2 Symmetry of Waveguide Modes

Here, the degeneracy of frequencies and wave numbers of waveguide modes from the supercell and on-shell method are investigated. The waveguide slice definitions used are shown in Fig. 8.2. In theory, the very same frequencies and wavenumbers should be obtained regardless of the orientation of the waveguide slices. The dispersion relation obtained for a W1-1 waveguide made of infiltrated pores of $\varepsilon_{\text{def}} = 2.89$ are shown in Fig. 8.3 for the sets WF38-sym and WF38-SMV. Results for all orientations of Fig. 8.3 are shown simultaneously. These plots show, that no additional errors due to the symmetrization procedure for the WF38-sym set have been introduced. Both sets of basis functions yield the same dispersion relations. The asymmetries of frequencies for the supercell method (8.1) are shown in Fig. 8.4a.

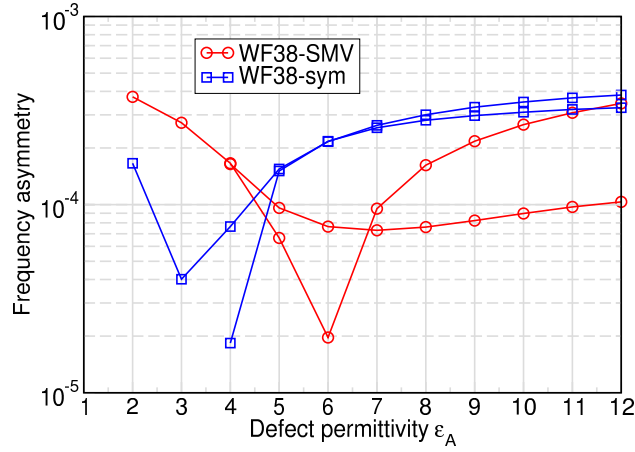


Figure 8.1: Asymmetries of frequencies for the degenerate dipole and quadrupole defect modes of the A_i cavity setup from Fig. 6.13.

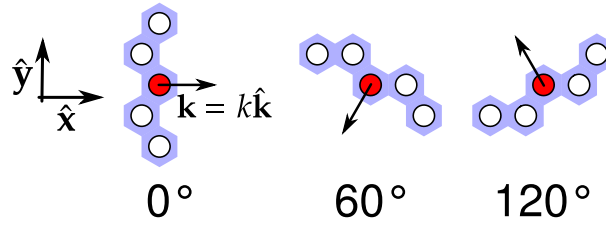


Figure 8.2: Computational domain L_{comp} for waveguide slices oriented along various directions.

The asymmetries in the wave numbers k for the guided modes of the on-shell method are shown in Fig. 8.4b. In the supercell method, the asymmetries for both sets of basis functions are practically identical. The wave number asymmetry of the WF38-sym set from the on-shell approach is lower for some frequencies, but also higher for some other frequencies compared to the unprocessed set WF38-SMV. A systematic improvement is not visible.

8.3 Summary

The potential benefits of using highly symmetric WFs was investigated. Therefore, the asymmetry of degenerate defect mode frequencies and wave numbers for identical rotated waveguides was investigated. No substantial or systematic improvements were found. However, for a full analysis, one should also investigate the symmetry of scattering matrices in further transmission computations. This has not been done in this thesis and remains as an outlook for further investigations.

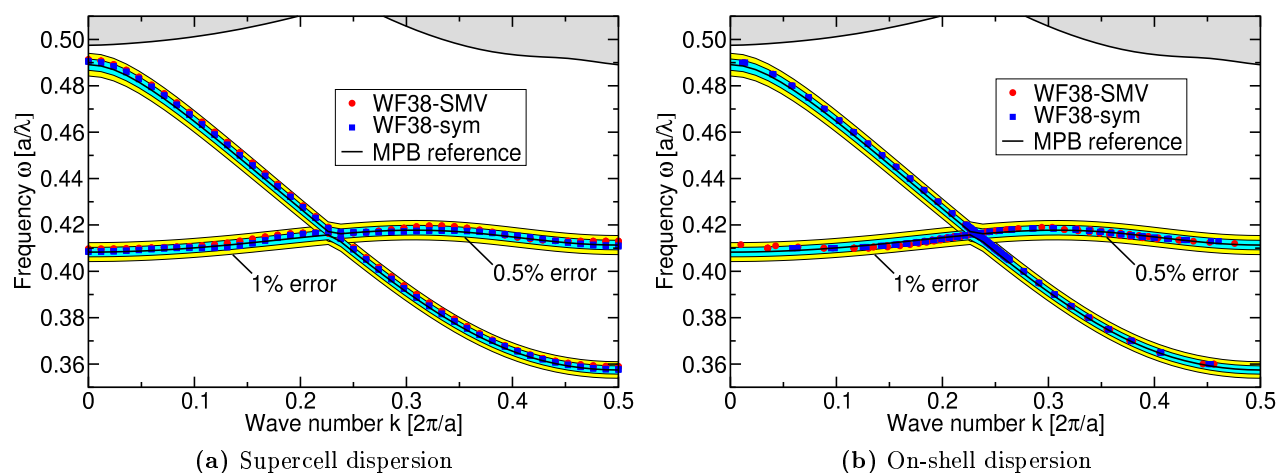


Figure 8.3: Waveguide dispersions of a W1-1 made from isotropically infiltrated holes with $\epsilon_{\text{def}} = 2.89$. The plots show results for all orientations of Fig. 8.2.

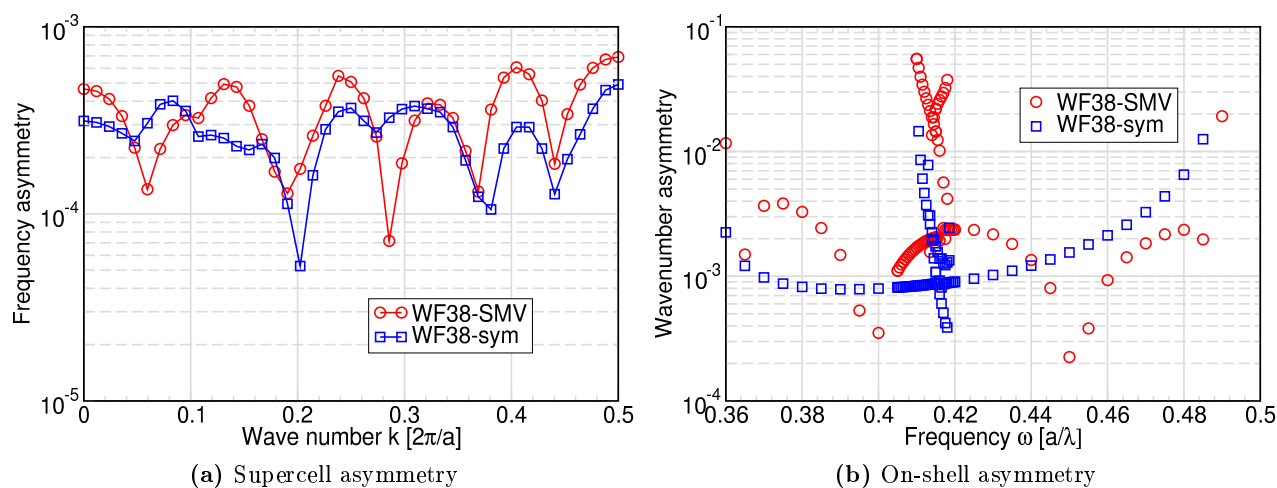


Figure 8.4: Asymmetries of (a) frequency ω and (b) wavenumbers k along the waveguide directions of 0° , 60° and 120° .

9

Chapter 9

Summary and Outlook

Photonic crystal based integrated optical circuitry may constitute a key technology to revolutionize optical signal processing. The analysis and optimization of functional elements in such systems requires fast and efficient numerical methods. In the present thesis, the lattice model obtained by an expansion of the wave equations into a localized basis comprising photonic Wannier functions was investigated for this task. Therefore, an existing Wannier function construction algorithm was reviewed and improved based on group theoretical considerations. Additionally, convergence problems in this method were thoroughly analyzed and the augmentation of the pure Wannier basis by auxiliary basis functions was shown to enhance the accuracy of numerical computations drastically. This enables the accurate treatment of high-index defect structures that were previously inaccessible by the pure Wannier approach.

9.1 Summary

Photonic crystals are periodic arrangements of dielectric materials exhibiting a band structure for light. Carefully chosen fabrication parameters can give rise to frequency ranges, where light propagation is prohibited regardless of direction, the so-called complete photonic band gaps. Purposely designed defects, breaking the translational invariance, introduce localized light modes with frequencies in the band gap. In order to compute such localized eigenmodes numerically, an expansion of the wave equations into a set of suitable basis functions can be used. Such a method is expected to be very efficient if as many properties of the desired defect states as possible are already present in the expansion basis. For magnetic field defect states in three-dimensional photonic crystals (PC), these properties are the high degree of mode localization, the vanishing divergence of the fields, and symmetries dictated by the underlying crystal structure. Photonic Wannier functions (WF) were recognized to have all these desired properties and were used as an expansion basis in this scheme in previous works.

Two-dimensional PCs allow the separation of the vectorial equations into two independent scalar equations, where defect modes and basis functions are inherently divergence-free. In the transverse magnetic (TM) case, the expansion into a basis of pure electric field WFs proved to be as efficient as anticipated, and very few basis functions yield defect modes with high accuracies. In the transverse electric (TE) case, however, the magnetic field WFs fail to model an additional aspect of defect modes, namely the continuity conditions of magnetic fields across dielectric boundaries. The more the defect permittivity deviates from the former permittivity of the periodic PC, the larger the errors become.

In this thesis, the augmentation of the pure Wannier basis by auxiliary basis functions (ABF) was proposed to reduce errors. These ABFs were chosen in view of their ability to model the correct continuity conditions of magnetic field defect modes in two-dimensional PC in TE polarization. Three sets of ABFs

were proposed, the Fourier-Bessel functions (FBF), the inverse system Wannier functions (IWF), and supercell defect modes (SDM) from a plane-wave based computation with the MIT photonic bands (MPB) software. To distinguish the IWFs from the WFs, the latter were referred to as proper WFs, because they are able to describe the band structure of the host PC perfectly. All of these ABFs reduced the errors in localized cavity defect mode, supercell waveguide dispersion and on-shell waveguide dispersion computations drastically compared to using only the basis of proper WFs. Maximal errors of 1% for a wide range of isotropic and anisotropic defect strengths were achieved, both for simple and complex defect designs. Hereby, the total number of basis functions needed increases only marginally, since the ABF only have to be incorporated at the defect sites. The FBFs performed best in this respect and should be used in subsequent Wannier based scattering matrix computations for high-index defect structures. However, they are an educated guess depending on the cylindrical geometry and are only applicable in two-dimensional PCs. The SDMs and IWFs, on the other hand, can also be used in general two- and three-dimensional computations, meeting all of the requirements for magnetic fields stated above. These findings were accompanied by extensive investigations about the influence of various numerical parameters on the accuracy of the localized basis expansion. These are intended as a reference for future computations.

In order to reach satisfactory accuracies, more WFs than provided by previous works had to be generated. For the computation of these functions, the bottom-up approach after Schillinger [35] was used. This is an implementation of the Souza-Marzari-Vanderbilt algorithm, that constructs maximally localized WFs by minimizing their real space spread in an iteration procedure. This method requires a couple of parameters from the user: the band sets of Bloch modes to construct generalized WFs from, the trial functions acting as initial WFs for the spread minimization process, and a frequency window that allows the exchange of Bloch mode profiles with higher bands. The choice of these parameters was based mostly on trial-and-error in the past, with only a few rules of thumb available. This made the WF construction a tedious and time consuming process. Therefore, an in-depth investigation of the influence of these parameters on the final WFs has been conducted in this thesis. It is intended as a reference for future computations. The importance of the proper choice of trial functions was pointed out. These provide the initial WFs, which are the starting point for the iteration procedure. Suboptimal choices can lead to more iteration steps and strongly distorted final WFs, that are not optimally localized. Based on a thorough group theoretical analysis, a connection between Bloch mode symmetries and WF symmetries and localization was established. This site symmetry analysis culminated in the Tabs. 2.1 and 2.2, completing the set of selection rules stated by Schillinger [35] based on empirical evidence. These tables determine the symmetries and localization centers of the maximally localized WFs from the symmetries of the Bloch modes. This helps to determine optimal trial functions with the anticipated properties of the WFs. The trial functions suggested in this work consist of Γ -point Bloch modes that are cropped on a Wigner-Seitz cell, centered around the anticipated localization center of the WFs. Furthermore, these trials are unitarily transformed to be basis functions for the anticipated site symmetry irreps of the WFs. The improvements of these group theory based choices were documented by many examples. Also, the efficient incorporation of these rules based on a few precomputed matrices (instead of time consuming scalar products between fields) was proposed. Additionally, a method to estimate good frequency windows by investigating the scalar products between trial functions and Bloch modes was suggested. Finally, this provided much insight in the WF construction process and will help to drastically reduce the time to obtain WFs in the future.

The Wannier basis for the localized basis expansion is not uniquely determined. Different choices in construction parameters yield different sets of WFs. Therefore, three sets of WFs have been investigated considering their ability to model the PC band structure and defect modes. The WF38-SMV were WFs generated by the combined Souza-Marzari-Vanderbilt (SMV) procedure. They all formed the

anticipated irreps according to the site symmetry analysis. The WF38-MV set was constructed from the pure Marzari-Vanderbilt (MV) for a single closed set of Bloch bands and much faster constructed than the WF38-SMV versions.¹ Finally, the WF38-sym set was obtained by applying a symmetrization procedure to the WF38-SMV set to yield perfectly symmetric WFs. Though all of these sets were highly localized, only the WF38-MV set showed the anticipated decay behavior of $|\mathbf{r}|^{-3/4} \exp(-h|\mathbf{r}|)$, whereas the other two sets decayed like $1/|\mathbf{r}|$. They all reproduced the band structure as expected. However, the WF38-MV set yielded many spurious modes in defect computations, justifying the time consuming construction process to obtain the WF38-SMV set. The symmetrized variants WF38-sym provided no substantial improvements, but the symmetrization process also introduced no additional errors. However, based on the evidence in this work, no advantages of using a highly symmetrized basis are apparent yet.

9.2 Outlook

The benefits of using highly symmetric basis functions in future scattering matrix computations remains to be seen. However, exploiting the perfect symmetry may allow optimizations and reduction of computational time. Nevertheless, the foundations for obtaining a highly symmetric basis set are documented in this work.

The site symmetry analysis as presented in Chap. 2 is directly applicable to the generation of vectorial photonic WFs in PC slabs for TE and TM polarization, as long as the underlying plane groups are symmorphic. Only the case of symmorphic plane groups has been covered in the present thesis. Three-dimensional PC studies today focus mainly on the woodpile structure, whose space group is non-symmorphic. In that case, the site symmetry analysis is more complicated but nevertheless possible and valid.

The sets of ABFs reduced computational errors but did not increase the computational effort. However, the small errors also depend on the usage of 101 WFs, which is considerably more than the 6 WFs that were sufficient in TM computations of [32]. By using the methods of Sec. 7, it may be possible to reduce the number of basis functions if one is restricted to a small frequency range. Photonic circuits including non-etched holes can nevertheless now be treated with reasonable accuracy. This is of great importance, since this class of defects is in wide use in experiments at the moment.

¹The WF38-SMV WFs were one of the major results of the dissertation [35].

A

Appendix A

Definitions and Proofs

This appendix features calculations proving some statements or defining additional quantities for reference.

A.1 Fourier Transforms

We summarize the mathematical properties of Fourier transforms as far as they are needed in this thesis. We employ the infinite as well as the cyclic model of crystals with N_i cells per lattice direction \mathbf{a}_i . In the finite case, the set of lattice vectors \mathbb{L}_{per} contains $N = \prod_i^d N_i$ lattice sites in direct space and the corresponding Brillouin zone (BZ) $\mathbb{L}_{\text{per}}^*$ contains N \mathbf{k} -vectors. This compilation of identities is taken from Ashcroft and Mermin [56].

A.1.1 Lattice Periodic Functions in Direct Space

Let f be a lattice periodic function in direct space, i. e.

$$f(\mathbf{r} + \mathbf{R}) = f(\mathbf{r}) \quad \forall \mathbf{R} \in \mathbb{L}_{\text{per}}. \quad (\text{A.1})$$

Then f can be expanded into plane waves for reciprocal lattice vectors $\mathbf{K} \in \mathbb{L}_{\text{per}}^*$ as

$$\tilde{f}_{\mathbf{K}} := \frac{1}{V_{\text{PUC}}} \int_{\text{PUC}} d^d r e^{-i\mathbf{K}\mathbf{r}} f(\mathbf{r}), \quad (\text{A.2})$$

$$\Rightarrow f(\mathbf{r}) = \sum_{\mathbf{K} \in \mathbb{L}_{\text{per}}^*} \tilde{f}_{\mathbf{K}} e^{i\mathbf{K}\mathbf{r}}. \quad (\text{A.3})$$

Note that the integration is performed over the primitive unit cell of the lattice \mathbb{L}_{per} which may be a supercell of the photonic crystal unit cells \mathbb{L}_{PC} . If only finitely many \mathbf{K} are available, the remaining coefficients $\tilde{f}_{\mathbf{K}}$ are implicitly taken to be 0 and the resulting $f(\mathbf{r})$ in (A.3) is an approximation to the full one in (A.2).

A.1.2 Lattice Periodic Functions in Reciprocal Space

This is the same relation as in the previous section, now written for lattice periodic functions ϕ in reciprocal space of the PC, i. e.

$$\phi(\mathbf{k} + \mathbf{K}) = \phi(\mathbf{k}) \quad \forall \mathbf{K} \in \mathbb{L}_{\text{PC}}^* \quad (\text{A.4})$$

Then ϕ can be expanded into plane waves for direct lattice vectors $\mathbf{R} \in \mathbb{L}_{\text{PC}}$ as

$$\tilde{\phi}_{\mathbf{R}} := \frac{1}{V_{\text{BZ}}} \int_{\text{BZ}} d^d k e^{-i\mathbf{k}\mathbf{R}} \phi(\mathbf{k}), \quad (\text{A.5})$$

$$\Rightarrow \phi(\mathbf{k}) = \sum_{\mathbf{R} \in \mathbb{L}_{\text{PC}}} \tilde{\phi}_{\mathbf{R}} e^{i\mathbf{k}\mathbf{R}}. \quad (\text{A.6})$$

If $\phi(\mathbf{k})$ is only given for N discrete wave vectors in the BZ of a finite cyclic PC, then by (B.11) we have to substitute¹

$$\frac{1}{V_{\text{BZ}}} \int_{\text{BZ}} \mapsto \frac{1}{N} \sum_{\mathbf{k}}, \quad (\text{A.7})$$

such that (A.5) changes to

$$\tilde{\phi}_{\mathbf{R}} := \frac{1}{N} \sum_{\mathbf{k} \in \text{BZ}} e^{-i\mathbf{k}\mathbf{R}} \phi(\mathbf{k}), \quad (\text{A.8})$$

and the sum in (A.6) runs over the N direct lattice vectors \mathbf{R} of the main region \mathbb{L}_{main} of the cyclic crystal.

A.1.3 Fourier Sum Identities

In the cyclic crystal with a total of N direct lattice vectors $\mathbf{R} \in \mathbb{L}_{\text{main}}$ and a total of N allowed wave vectors \mathbf{k} of (2.33) in the corresponding discrete BZ, we have the identities

$$\sum_{\mathbf{R} \in \mathbb{L}_{\text{main}}} e^{i\mathbf{k}\mathbf{R}} = N\delta_{\mathbf{k},\mathbf{0}}, \quad (\text{A.9})$$

$$\sum_{\mathbf{k} \in \text{BZ}} e^{i\mathbf{k}\mathbf{R}} = N\delta_{\mathbf{R},\mathbf{0}}. \quad (\text{A.10})$$

In the continuous case, the lattice site sum extends over the infinitely many sites of \mathbb{L}_{PC} , and the \mathbf{k} -points in the corresponding BZ are a dense set. Then we can apply (A.7), making the sum (A.10) an integral

$$\frac{1}{V_{\text{BZ}}} \int_{\text{BZ}} d^d k e^{i\mathbf{k}(\mathbf{R}'-\mathbf{R})} = \delta_{\mathbf{R}'\mathbf{R}}. \quad (\text{A.11})$$

A.2 Wannier Function Properties

Some properties of WFs are summarized here.

¹This is basically an application of (B.11).

A.2.1 Translational Properties

This is a proof of (3.4). The action of a shift by a lattice vector \mathbf{R}' is given by

$$\hat{D}(\{E|\mathbf{R}'\})\mathbf{W}_{n,\mathbf{R}}(\mathbf{r}) = \frac{1}{V_{\text{BZ}}} \int_{\text{BZ}} d^d k e^{-i\mathbf{k}\mathbf{R}} \hat{D}(\{E|\mathbf{R}'\})\tilde{\psi}_{n\mathbf{k}}(\mathbf{r}) \quad (\text{by (3.1) and (2.10)}) \quad (\text{A.12})$$

$$= \frac{1}{V_{\text{BZ}}} \int_{\text{BZ}} d^d k e^{-i\mathbf{k}\mathbf{R}} \tilde{\psi}_{n\mathbf{k}}(\mathbf{r} - \mathbf{R}') \quad (\text{by (2.10)}) \quad (\text{A.13})$$

$$= \frac{1}{V_{\text{BZ}}} \int_{\text{BZ}} d^d k e^{-i\mathbf{k}(\mathbf{R}+\mathbf{R}')} \tilde{\psi}_{n\mathbf{k}}(\mathbf{r}) \quad (\text{by (1.19)}) \quad (\text{A.14})$$

$$= \mathbf{W}_{n,\mathbf{R}+\mathbf{R}'}(\mathbf{r}). \quad (\text{A.15})$$

Therefore, it is sufficient to just compute $\mathbf{W}_{n,\mathbf{0}}(\mathbf{r})$, because the WFs associated with lattice site $\mathbf{R} \in \mathbb{L}_{\text{PC}}$ is obtained via

$$\mathbf{W}_{n,\mathbf{R}}(\mathbf{r}) = \mathbf{W}_{n,\mathbf{0}}(\mathbf{r} - \mathbf{R}). \quad (\text{A.16})$$

A.2.2 Orthonormality

The generalized Bloch modes $\tilde{\psi}$ are orthonormal, since they are obtained as unitary transforms from the orthonormalized proper Bloch modes. We write down the corresponding proof for the electric field case. For the magnetic field, the proof is analogous but does not feature the permittivity $\underline{\underline{\epsilon}}_{\text{PC}}$:

$$\langle\langle \mathbf{W}_{n'\mathbf{R}'} | \mathbf{W}_{n\mathbf{R}} \rangle\rangle = \int d^d r \mathbf{W}_{n'\mathbf{R}'}^* \cdot \underline{\underline{\epsilon}}_{\text{PC}} \cdot \mathbf{W}_{n\mathbf{R}} \quad (\text{by (1.54)}) \quad (\text{A.17})$$

$$= \frac{1}{V_{\text{BZ}}^2} \int_{\text{BZ}} d^d k' \int_{\text{BZ}} d^d k e^{i\mathbf{k}'\mathbf{R}'} e^{-i\mathbf{k}\mathbf{R}} \int d^d r \tilde{\psi}_{n'\mathbf{k}'}^* \cdot \underline{\underline{\epsilon}}_{\text{PC}} \cdot \tilde{\psi}_{n\mathbf{k}} \quad (\text{by (3.1)}) \quad (\text{A.18})$$

$$= \frac{1}{V_{\text{BZ}}^2} \delta_{n'n} \int_{\text{BZ}} d^d k' \int_{\text{BZ}} d^d k e^{i\mathbf{k}'\mathbf{R}'} e^{-i\mathbf{k}\mathbf{R}} \delta^{(d)}(\mathbf{k}' - \mathbf{k}) \quad (\text{by (1.56)}) \quad (\text{A.19})$$

$$= \frac{1}{V_{\text{BZ}}^2} \delta_{n'n} \int_{\text{BZ}} d^d k' e^{i\mathbf{k}'(\mathbf{R}' - \mathbf{R})} \quad (d^d k) \quad (\text{A.20})$$

$$= \frac{1}{V_{\text{BZ}}} \delta_{n'n} \delta_{\mathbf{R}'\mathbf{R}}. \quad (\text{by (A.11)}) \quad (\text{A.21})$$

By the definition (3.1), the WFs are not normalized, but they can be normalized after construction by the Marzari-Vanderbilt algorithm. This corresponds to the alternative definition

$$|W_{n\mathbf{R}}\rangle := \frac{1}{\sqrt{V_{\text{BZ}}}} \int_{\text{BZ}} d^d k e^{-i\mathbf{k}\mathbf{R}} |\tilde{\psi}_{n\mathbf{k}}\rangle, \quad (\text{A.22})$$

where the generalized Bloch modes are obtained back again via (A.6) from

$$|\tilde{\psi}_{n\mathbf{k}}\rangle = \frac{1}{\sqrt{V_{\text{BZ}}}} \sum_{\mathbf{R}} e^{i\mathbf{k}\mathbf{R}} |W_{n\mathbf{R}}\rangle. \quad (\text{A.23})$$

A.2.3 Integration by Parts

Let the vectorial functions $\mathbf{a}(\mathbf{r})$ and $\mathbf{b}(\mathbf{r})$ decay sufficiently fast to 0 for $|\mathbf{r}| \rightarrow \infty$ as the Wannier functions do. We employ the Levi-Civita symbol ϵ_{ijk} and get

$$\int dV \mathbf{a} \cdot (\nabla \times \mathbf{b}) = \sum_{ijk} \int dV \epsilon_{ijk} a_i (\partial_j b_k) \quad (\text{def. of curl}) \quad (\text{A.24})$$

$$= - \sum_{ijk} \int dV \epsilon_{ijk} (\partial_j a_i) b_k \quad (\text{int. by parts}) \quad (\text{A.25})$$

$$= \sum_{ijk} \int dV \epsilon_{kji} b_k (\partial_j a_i) \quad (\text{total antisymmetry}) \quad (\text{A.26})$$

$$= \sum_{ijk} \int dV \epsilon_{ijk} b_i (\partial_j a_k) \quad (\text{index switch: } i \leftrightarrow k) \quad (\text{A.27})$$

$$= \int dV \mathbf{b} \cdot (\nabla \times \mathbf{a}) \quad (\text{by (A.24)}) \quad (\text{A.28})$$

$$= \int dV (\nabla \times \mathbf{a}) \cdot \mathbf{b}. \quad (\text{A.29})$$

The boundary values of the integration by parts vanish due to the localization properties of the functions \mathbf{a} and \mathbf{b} .

A.3 Operator Matrix Properties

Some properties from Sec. 4.1.2 of the operator matrices (4.6), (4.11), (4.15), and (4.16) are proven here.

A.3.1 Hermiticity

The Hermiticity of the defect matrices for Hermitian permittivity tensors is shown here for one example. This proof also applies to the pure overlap matrices.

$$B_{n'\mathbf{R}',n\mathbf{R}}^{\text{el}} \stackrel{(4.11\text{b})}{=} \int dV \mathbf{W}_{n'\mathbf{R}'}^*(\mathbf{r}) \cdot \Delta_{\underline{\underline{\epsilon}}}(\mathbf{r}) \cdot \mathbf{W}_{n\mathbf{R}}(\mathbf{r}) \quad (\text{A.30})$$

$$= \int dV \left(\mathbf{W}_{n'\mathbf{R}'}(\mathbf{r}) \cdot \Delta_{\underline{\underline{\epsilon}}}^*(\mathbf{r}) \cdot \mathbf{W}_{n\mathbf{R}}^*(\mathbf{r}) \right)^* \quad (\text{complex conjugation}) \quad (\text{A.31})$$

$$= \int dV \left(\mathbf{W}_{n\mathbf{R}}^*(\mathbf{r}) \cdot \Delta_{\underline{\underline{\epsilon}}}(\mathbf{r}) \cdot \mathbf{W}_{n'\mathbf{R}'}(\mathbf{r}) \right)^* \quad (\text{Hermitian tensor}) \quad (\text{A.32})$$

$$= B_{n\mathbf{R},n'\mathbf{R}'}^{\text{el}*} \quad (\text{by (A.30)}) \quad (\text{A.33})$$

A.3.2 Translational Invariance

The translational properties of the A - and C -matrix are proven here.

$$C_{n'\mathbf{R}'+\boldsymbol{\rho},n\mathbf{R}+\boldsymbol{\rho}}^{\text{el}} \stackrel{(4.11c)}{=} \int dV \mathbf{W}_{n'\mathbf{R}'+\boldsymbol{\rho}}^*(\mathbf{r}) \cdot \underline{\underline{\epsilon}}_{\text{per}}(\mathbf{r}) \cdot \mathbf{W}_{n\mathbf{R}+\boldsymbol{\rho}}(\mathbf{r}) \quad (\text{A.34})$$

$$\stackrel{(A.15)}{=} \int dV \mathbf{W}_{n'\mathbf{R}'}^*(\mathbf{r} - \boldsymbol{\rho}) \cdot \underline{\underline{\epsilon}}_{\text{per}}(\mathbf{r}) \cdot \mathbf{W}_{n\mathbf{R}}(\mathbf{r} - \boldsymbol{\rho}) \quad (\text{A.35})$$

$$= \int dV \mathbf{W}_{n'\mathbf{R}'}^*(\mathbf{r}) \cdot \underline{\underline{\epsilon}}_{\text{per}}(\mathbf{r} + \boldsymbol{\rho}) \cdot \mathbf{W}_{n\mathbf{R}}(\mathbf{r}) \quad (\text{int. over all space}) \quad (\text{A.36})$$

$$= \int dV \mathbf{W}_{n'\mathbf{R}'}^*(\mathbf{r}) \cdot \underline{\underline{\epsilon}}_{\text{per}}(\mathbf{r}) \cdot \mathbf{W}_{n\mathbf{R}}(\mathbf{r}) \quad (\text{per. dielectric}) \quad (\text{A.37})$$

$$= C_{n'\mathbf{R}',n\mathbf{R}}^{\text{el}}. \quad (\text{A.38})$$

A.4 Relative Errors

Numerical results can usually be made more accurate by increasing one or more parameters, e. g. resolutions and supercell sizes for band structure and supercell calculations. In order to measure the accuracy of the relevant quantities obtained in such computations (mostly eigenfrequencies), one would have to compare the numerically obtained quantities with analytically exact reference values. Unfortunately such exact reference values are mostly not available, even for the simplest physical setups possible. In such a case one can at least compare the numerical results with each other, when computing numerical solutions with the largest parameters that are computationally accessible which is supposed to yield the most accurate approximation to the real solution of the analytical problem.

A.4.1 Relative Errors

The relative error $\Delta f_{\text{rel}}(p)$ of a quantity $f(p)$ depending on a parameter p is defined as

$$\Delta f_{\text{rel}}(p) := \frac{|f(p) - f_{\text{ref}}|}{|f_{\text{ref}}|}. \quad (\text{A.39})$$

When lacking an analytical reference solution, we usually use the value $f(p_{\text{max}})$ obtained for the maximally possible parameter p as reference f_{ref} .

If we have a whole sequence of the quantities $f_n(p)$ with reference values $f_{\text{ref},n}$ depending on an additional parameter n , we also get a sequence of relative errors $\Delta f_{\text{rel},n}$. In order to quantify the quality of the whole computation we can define the maximal relative error

$$\Delta f_{\text{maxrel}}(p) := \max_n \Delta f_{\text{rel},n}(p), \quad (\text{A.40})$$

and the (arithmetic) mean relative error²

$$\Delta f_{\text{meanrel}}(p) := \frac{1}{N} \sum_{n=1}^N \Delta f_{\text{rel},n}(p). \quad (\text{A.41})$$

Here, N is the number of reference values $f_{\text{ref},n}$.

²Also known as mean percentage error in statistics.

A.4.2 Comparing Matrices

When comparing the elements $M_{ij}(p)$ of matrices $M(p)$ that depend on a parameter p , the relative error of each individual matrix element is usually not a good measure for convergence. For if some of the reference matrix elements $M_{ij,\text{ref}}$ are near 0 (numerically modeling true values of 0), the individual relative errors

$$\Delta M_{\text{rel},ij}(p) = \frac{|M_{ij}(p) - M_{ij,\text{ref}}|}{|M_{ij,\text{ref}}|} \quad (\text{A.42})$$

can become large and bias the mean or maximal values computed thereof.

In such a case it is better to compare the maximum-norms (also called ∞ -norms) of the matrices, i. e.

$$\Delta M_{\text{max-norm}}(p) := \frac{\|M(p) - M_{\text{ref}}\|_{\infty}}{\|M_{\text{ref}}\|_{\infty}} \quad (\text{A.43})$$

$$= \frac{\max_{ij} |M_{ij}(p) - M_{ij,\text{ref}}|}{\max_{ij} |M_{ij,\text{ref}}|}. \quad (\text{A.44})$$

Such an error can be used to compare different computational schemes with each other. It is employed in this thesis when quantifying the convergence of operator matrix elements.

A.4.3 Orders Of Convergence

In computational schemes where the quantities f computed depend on the resolution of a discretization of some region of space (e. g., eigenfrequencies computed by MPB), one can also quantify the rate of convergence when increasing the resolution. In that case, the parameter p is the spacing distance $1/N_{\text{res}}$ between the discretized points in space. The relative errors $\Delta f_{\text{rel}}(p)$ often decrease like a power p^t , with t being the order of convergence. Then we say that the relative error is of order t and write $\Delta f_{\text{rel}}(p) \sim \mathcal{O}(p^t)$. This order can be visualized in double logarithmic plots as the slope of linear functions. In the case $p = 1$, we speak of linear convergence, for $p = 2$ we have quadratic convergence.

A.5 Scalar Product for Electrical Fields

We will show that the electric field wave equation (1.9a) in the standard eigenvalue form

$$\underline{\underline{\epsilon}}^{-1} \cdot \nabla \times (\nabla \times \mathbf{E}) - \frac{\omega^2}{c_0^2} \cdot \mathbf{E} = 0 \quad (\text{A.45})$$

features a Hermitian differential operator

$$\hat{H}^{\text{el}} := \underline{\underline{\epsilon}}^{-1} \cdot \nabla \times (\nabla \times \cdot), \quad (\text{A.46})$$

where application of the curls is intended from the right to left. Given two electric fields \mathbf{E} and \mathbf{E}' , this operator \hat{H}^{el} is Hermitian with respect to the scalar product $\langle\langle \cdot | \cdot \rangle\rangle$ of Eq. (1.54):³

$$\langle\langle \mathbf{E} | \hat{H}^{\text{el}} \mathbf{E}' \rangle\rangle = \int dV \mathbf{E}^* \underbrace{\underline{\underline{\epsilon}}^{-1}}_{=1} \cdot \nabla \times (\nabla \times \mathbf{E}') \quad (\text{by (1.54)}) \quad (\text{A.47})$$

$$= \int dV (\nabla \times \mathbf{E}^*) \cdot (\nabla \times \mathbf{E}') \quad (\text{by (A.29)}) \quad (\text{A.48})$$

$$= \int dV \nabla \times (\nabla \times \mathbf{E}^*) \cdot \underbrace{\underline{\underline{\epsilon}}^{-1} \underline{\underline{\epsilon}}}_{=1} \cdot \mathbf{E}' \quad (\text{by (A.29)}) \quad (\text{A.49})$$

$$= \int dV [(\underline{\underline{\epsilon}}^{-1})^T \cdot \nabla \times (\nabla \times \mathbf{E}^*)] \cdot \underline{\underline{\epsilon}} \cdot \mathbf{E}' \quad (\text{A.50})$$

$$= \int dV \left[\underbrace{(\underline{\underline{\epsilon}}^{-1})^T}_{\underline{\underline{\epsilon}}^{-1}} \cdot \nabla \times (\nabla \times \mathbf{E}) \right]^* \cdot \underline{\underline{\epsilon}} \cdot \mathbf{E}' \quad (\text{A.51})$$

$$= \int dV \left[\underline{\underline{\epsilon}}^{-1} \cdot \nabla \times (\nabla \times \mathbf{E}) \right]^* \cdot \underline{\underline{\epsilon}} \cdot \mathbf{E}' \quad (\text{Hermitian } \underline{\underline{\epsilon}}^{-1}) \quad (\text{A.52})$$

$$= \int dV \left[\hat{H}^{\text{el}} \mathbf{E} \right]^* \cdot \underline{\underline{\epsilon}} \cdot \mathbf{E}' \quad (\text{A.53})$$

$$= \langle\langle \hat{H}^{\text{el}} \mathbf{E} | \mathbf{E}' \rangle\rangle. \quad (\text{A.54})$$

Boundary terms from an integration by parts vanish due to periodicity (for Bloch waves) or localization (defect modes). Thus, \hat{H}^{el} is Hermitian with respect to the scalar product $\langle\langle \cdot | \cdot \rangle\rangle$ and the electric field eigenmodes can be chosen orthonormalized for that particular scalar product.

³Thanks to Martin Köhl, who pointed this proof out to me.

B Appendix B

Discretizations

A computer can only operate on discrete values in memory, therefore all mathematical objects and actions defined continuously have to be represented in a discrete way. The particular method to obtain this discrete representation is called the discretization scheme or discretization for short. However, the term discretization is also used for the set of discretized values.

B.1 Fields

Functions $f : \mathbb{R}^d \mapsto \mathbb{C}^d$ such as scalar/vectorial electric/magnetic fields (Bloch modes and Wannier functions), scalar or tensor dielectric functions, can be represented in a nodal fashion. This means, a finite domain of the real space \mathbb{R}^d is represented by a uniform mesh (or grid) of points $\mathbf{r}_{\mathbf{z}}$, the nodes of the mesh

$$\mathbf{r}_{\mathbf{z}} := \sum_{i=1}^d z_i \frac{\mathbf{a}_i}{N_{\text{res},i}}, \quad z_i \in \left\{ -\frac{N_{\text{nodes},i}}{2}, -\frac{N_{\text{nodes},i}}{2} + 1, \dots, 0, \dots, \frac{N_{\text{nodes},i}}{2} - 1 \right\}. \quad (\text{B.1})$$

The \mathbf{a}_i are the primitive lattice translations and z_i are integers with the total number of nodes $N_{\text{nodes},i}$ per lattice direction. At these nodes, the continuous fields are represented by their values $f_{\mathbf{z}} := f(\mathbf{r}_{\mathbf{z}})$. In this work, we only deal with fields defined on unit cells or supercells of periodic structures. Therefore, the resolution $N_{\text{res},i}$ always denotes the number of nodes per lattice direction i in one unit cell, while $N_{\text{cells},i}$ defines the number of unit cells per lattice direction i in the supercell. The total number $N_{\text{nodes},i}$ of nodes per direction of the field representation is then given by the product

$$N_{\text{nodes},i} = N_{\text{cells},i} N_{\text{res},i}. \quad (\text{B.2})$$

The total number N_{cells} of unit cells and number of nodes N_{nodes} in the supercell is correspondingly given by

$$N_{\text{cells}} = \prod_i N_{\text{cells},i}, \quad N_{\text{nodes}} = \prod_i N_{\text{nodes},i}. \quad (\text{B.3})$$

In a *modal* representation, instead of field values $f_{\mathbf{z}}$ one stores a set of expansion coefficients c_i with respect to a given set of basis functions ϕ_i such that

$$f(\mathbf{r}) := \sum_i c_i \phi_i(\mathbf{r}). \quad (\text{B.4})$$

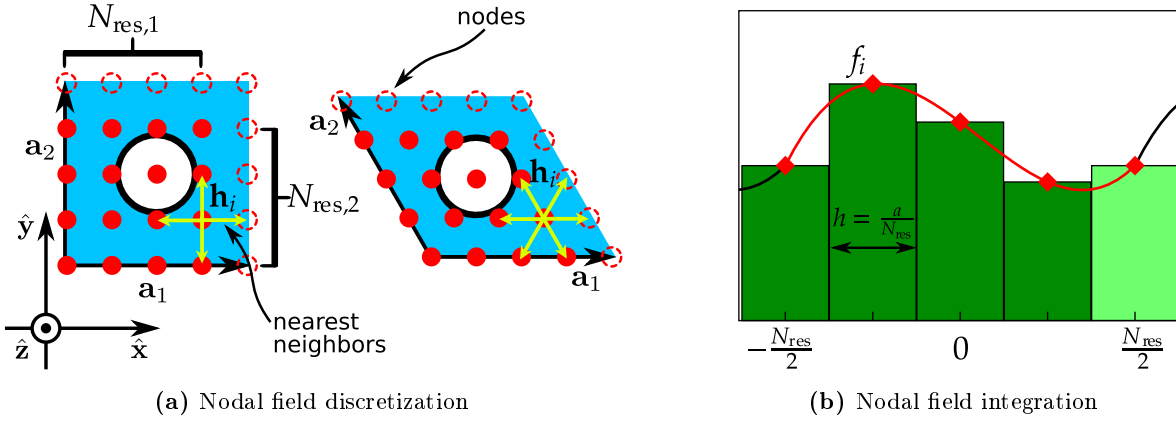


Figure B.1: Discretization schemes for fields and field integration. (a) Definition of real space resolution $N_{\text{res},i}$, nodal discretization $\mathbf{r}_{\mathbf{z}}$ and neighbors \mathbf{h}_j for the lattices defined by (B.5) and (B.6). (b) Discretized integration over one unit cell in one dimension for a periodic function f , discretized by its values $f_i = f(\mathbf{r}_i)$. The area under the function is approximated by $\sum_i f_i h = \sum_i f_i a / N_{\text{res}}$. The node $f_{N_{\text{res}}/2}$ is not taken into account hereby, since it would be counted twice.

Examples for such basis functions ϕ_i are Wannier functions or plane waves, where for the latter the c_i are the Fourier coefficients of the field f . Technically, the nodal representation can be considered to be a modal representation with a basis of localized step functions.

For a given discretized position node $\mathbf{r}_{\mathbf{z}}$ one can define a set of vectors \mathbf{h}_j that point to the neighboring nodes, where it is convenient to start the numbering with $\mathbf{h}_0 = 0$.

There are various possible choices for primitive lattice translations, in this work the following are exclusively used (with lattice constant a):

2D Square Lattice PLTs

$$\begin{aligned} \mathbf{a}_1 &= a\hat{\mathbf{x}}, \\ \mathbf{a}_2 &= a\hat{\mathbf{y}}, \end{aligned} \quad (\text{B.5})$$

2D Triangular Lattice PLTs

$$\begin{aligned} \mathbf{a}_1 &= a\hat{\mathbf{x}}, \\ \mathbf{a}_2 &= a\left(-\frac{1}{2}\hat{\mathbf{x}} + \frac{\sqrt{3}}{2}\hat{\mathbf{y}}\right). \end{aligned} \quad (\text{B.6})$$

Examples for the nodal discretization and the neighbors \mathbf{h}_j are shown in Fig. B.1a.

B.2 Integration

Given a nodal discretization $f_{\mathbf{z}}$ which can be regarded as a step function approximation to $f(\mathbf{r})$, a common approximation of the integral over f is the integral of a step function with piecewise constant values $f_{\mathbf{z}}$, defined as

$$\int d^d r f(\mathbf{r}) \approx \sum_{\mathbf{z}} f_{\mathbf{z}} \text{vol}_d \{\mathbf{a}_i / N_{\text{res},i}\}. \quad (\text{B.7})$$

Here, $\text{vol}\{\mathbf{a}_i/N_{\text{res},i}\}$ is the volume of a cuboid spanned by the vectors $\mathbf{a}_i/N_{\text{res},i}$, in various dimensions given by

$$\text{vol}_1\{\mathbf{a}_1/N_{\text{res},1}\} = \frac{1}{N_{\text{res},1}}|\mathbf{a}_1|, \quad (\text{B.8})$$

$$\text{vol}_2\{\mathbf{a}_1/N_{\text{res},1}, \mathbf{a}_2/N_{\text{res},2}\} = \frac{1}{N_{\text{res},1}N_{\text{res},2}}|\mathbf{a}_1 \times \mathbf{a}_2|, \quad (\text{B.9})$$

$$\text{vol}_3\{\mathbf{a}_1/N_{\text{res},1}, \mathbf{a}_2/N_{\text{res},2}, \mathbf{a}_3/N_{\text{res},3}\} = \frac{1}{N_{\text{res},1}N_{\text{res},2}N_{\text{res},3}}|\mathbf{a}_1 \cdot (\mathbf{a}_2 \times \mathbf{a}_3)|. \quad (\text{B.10})$$

With $N_{\text{res}} = \prod_i N_{\text{res},i}$ these volumes are equal to $V_{\text{WSC}}/N_{\text{res}}$ in each respective dimension such that (B.7) can be written as

$$\boxed{\frac{1}{V_{\text{WSC}}} \int dV f(\mathbf{r}) \approx \frac{1}{N_{\text{res}}} \sum_{\mathbf{z}} f_{\mathbf{z}}} \quad (\text{B.11})$$

Note that the integration domain is *not* restricted to a single unit cell here and that N_{res} is the total number of nodes within the Wigner-Seitz cell (WSC). If any other supercell volume V_{cell} is used as a prefactor, then the total number of nodes N_{nodes} in that cell has to be used, regardless of the actual integration domain (which only affects the subset of \mathbf{z} to sum over):

$$\boxed{\frac{1}{V_{\text{cell}}} \int dV f(\mathbf{r}) \approx \frac{1}{N_{\text{nodes}}} \sum_{\mathbf{z}} f_{\mathbf{z}}} \quad (\text{B.12})$$

This form of the integration approximation is well known and widely used in solid state physics. Its advantage lies in the fast evaluation scheme for scalar products of the type $\langle f_1, f_2 \rangle$, for which any implementation of the fast BLAS libraries can be used in practice. For reciprocal space integration V_{WSC} has to be substituted by the volume V_{BZ} of the BZ.

B.3 Derivatives

There are two types of discretization schemes for derivatives used and compared in this work.

B.3.1 Finite Differences

In this method, the continuous limits in the definition of the derivative are approximated by finite differences. In the most simple one-dimensional case by forward differences

$$\frac{d}{dx}f(x) := \lim_{h \rightarrow 0} \frac{1}{h} \left(f(x+h) - f(x) \right) \approx \frac{1}{h} \left(f(x+h) - f(x) \right) \text{ for small } h. \quad (\text{B.13})$$

This discretization yields the exact derivatives up to first order in h and is quite a crude approximation. It can be made more accurate as follows. For meshes on arbitrary lattices and arbitrary dimensions d , the finite difference stencils of order $p \in \mathbb{N}$ are given by weights $\mathbf{w}_j \in \mathbb{R}^d$ for the neighbors \mathbf{h}_j such that the Cartesian gradient ∇ is approximated by

$$\boxed{\nabla f(\mathbf{r}_{\mathbf{z}}) = \sum_j \mathbf{w}_j f(\mathbf{r}_{\mathbf{z}} + \mathbf{h}_j) + \mathcal{O}(h^p)}. \quad (\text{B.14})$$

The \mathbf{h}_j are given by the lattice and the weights \mathbf{w}_j are determined by a Taylor series expansion up to order p :

$$f(\mathbf{r}_z + \mathbf{h}_j) = f(\mathbf{r}_z) + \sum_{n=1}^p \frac{1}{n!} (\mathbf{h}_j \nabla)^n f(\mathbf{r}_z) + \mathcal{O}(h^{p+1}). \quad (\text{B.15})$$

For a given set of \mathbf{h}_j , this is a system of linear equations for the partial derivatives $\partial_x f, \partial_y f, \partial_z f, \partial_x \partial_y f, \dots$, at a given node $\mathbf{r} = \mathbf{r}_z$. Solving for the desired derivatives, one obtains the weights \mathbf{w}_j for (B.14). Increasing the number of neighbors \mathbf{h}_j (nearest neighbors, next-to-nearest neighbors, etc.) increases the possible orders p one can obtain and thus makes the approximation better. The weight factors for the lattices defined by (B.5) and (B.6) are shown in Figs. B.2 and B.3.

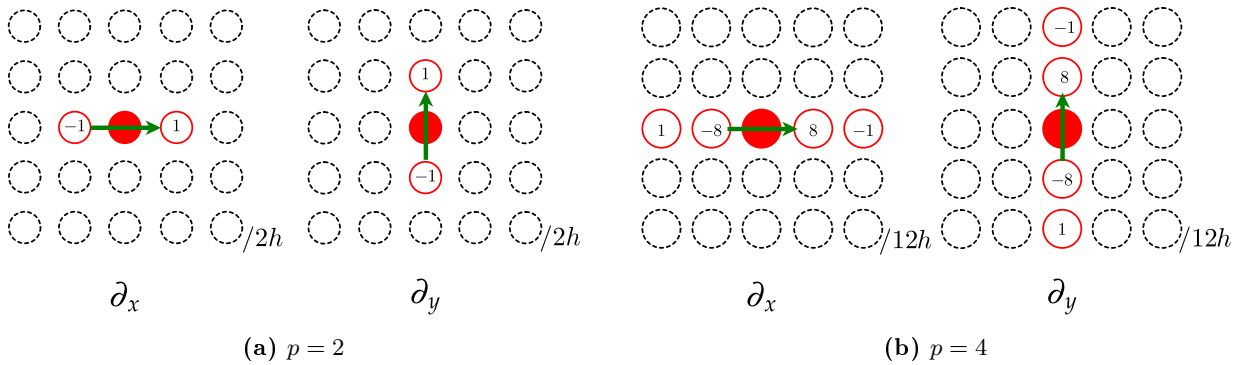


Figure B.2: Finite difference stencils for a uniform mesh in the 2D square lattice. The distance between nearest neighbors for each direction is $h = |\mathbf{h}_j|$. As an example, in (a) the weights \mathbf{w}_j have values $(\pm \frac{1}{2h}, 0)$ for ∂_x and $(0, \pm \frac{1}{2h})$ for ∂_y .

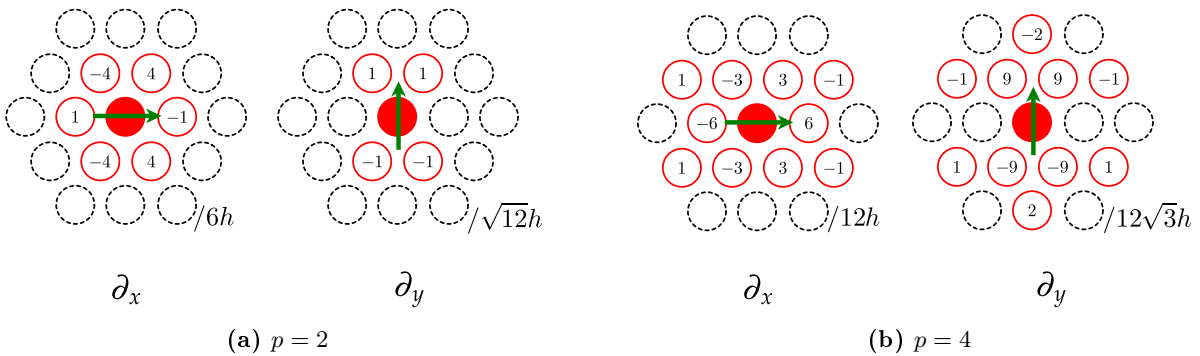


Figure B.3: Finite difference stencils for a uniform mesh in the 2D triangular lattice. See also the caption of Fig. B.2.

B.3.2 Spectral Derivatives

This discretization is based on a discrete Fourier transform of the nodal field discretization and can be implemented using the fast routines of the FFTW library.

By (A.3), the derivatives of lattice periodic scalar functions $f(\mathbf{r})$ and vectorial functions $\mathbf{f}(\mathbf{r})$ can be expressed by their Fourier coefficients $\tilde{f}_{\mathbf{K}}$ and $\tilde{\mathbf{f}}_{\mathbf{K}}$ as

$$\nabla f(\mathbf{r}) = \sum_{\mathbf{K} \in \mathbb{L}_{\text{PC}}^*} i\mathbf{K} \tilde{f}_{\mathbf{K}} e^{i\mathbf{K}\mathbf{r}}, \quad \nabla \times \mathbf{f}(\mathbf{r}) = \sum_{\mathbf{K} \in \mathbb{L}_{\text{PC}}^*} i\mathbf{K} \times \tilde{\mathbf{f}}_{\mathbf{K}} e^{i\mathbf{K}\mathbf{r}}. \quad (\text{B.16})$$

For nodal discretizations $f_{\mathbf{z}}$ and $\mathbf{f}_{\mathbf{z}}$ of the fields, there is only a finite set of allowed reciprocal lattice vectors $\mathbf{K}_{\mathbf{w}} = \sum_i w_i \mathbf{b}_i$. Furthermore, the integrals (A.2) have to be evaluated by the scheme (B.12), leading to the discretized Fourier coefficients

$$\tilde{f}_{\mathbf{w}} := \tilde{f}_{\mathbf{K}_{\mathbf{w}}} \approx \frac{1}{N_{\text{nodes}}} \sum_{\mathbf{z}} e^{-i\mathbf{K}_{\mathbf{w}}\mathbf{r}_{\mathbf{z}}} f_{\mathbf{z}}, \quad (\text{B.17})$$

where by the definition of (B.1) for $\mathbf{r}_{\mathbf{z}}$ and $\mathbf{K}_{\mathbf{w}}$ the exponential is equal to

$$\exp(-i\mathbf{K}_{\mathbf{w}}\mathbf{r}_{\mathbf{z}}) = \exp\left(-2\pi i \sum_i \frac{w_i z_i}{N_{\text{res},i}}\right). \quad (\text{B.18})$$

B.3.3 Problems of Discretized Derivatives

The discretizations introduced converge to the exact derivatives only for continuously differentiable functions. If the functions have kinks (as the magnetic field eigenmodes do), then the approximation becomes worse in the vicinity of these kinks. An example for these errors is shown in Fig. B.4.

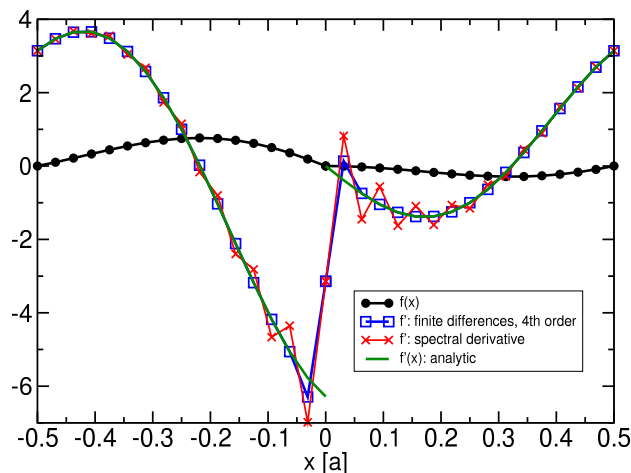


Figure B.4: Example of derivative discretization schemes for a function f that is not continuously differentiable at $x = 0$.

B.4 Dielectric Function

The discontinuous permittivity (1.44) leads to kinks in the magnetic field which by Fig. B.4 poses problems for the discretized derivatives. It is known that the discontinuities in the permittivity worsen the

convergence of numerical methods to solve the wave equations [57, 100, 101]. Therefore, various schemes to discretize this permittivity have been suggested in the literature for computational electrodynamics to improve convergence. They are shown in Fig. B.5a.

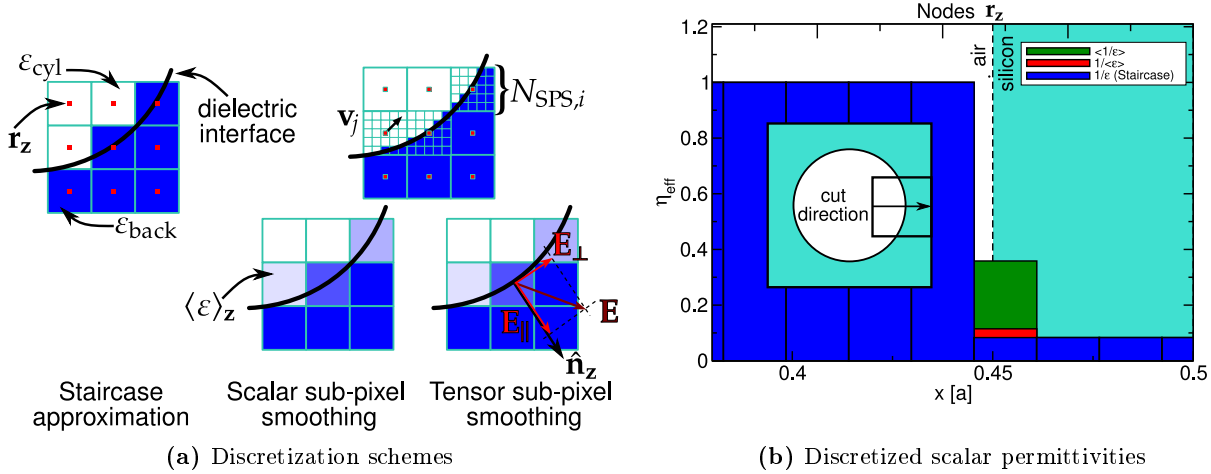


Figure B.5: (a) Examples for the various permittivity discretization schemes. (b) Effective discretized values for the inverse permittivity η at dielectric interfaces for the scalar permittivity discretizations.

The most simple nodal discretization $\varepsilon_{\mathbf{z}}$ that neglects any further treatment of this problem, is the stair-case approximation. Here the nodes are just assigned the values of the step function at the positions $\mathbf{r}_{\mathbf{z}}$:

Staircase Approximation

$$\varepsilon_{\mathbf{z}} := \varepsilon(\mathbf{r}_{\mathbf{z}}). \quad (\text{B.19})$$

This discretization leads to linear convergence of the frequencies with increasing real space resolution $N_{\text{res},i}$ (cf. Fig. C.3).

The scalar sub-pixel smoothing assigns $\varepsilon_{\mathbf{z}}$ averaged function values $\langle \varepsilon \rangle_{\mathbf{z}}$ that are averaged over the nodes of a smaller mesh of resolution $N_{\text{SPS},i}$ with $N_{\text{SPS}} = \prod_i N_{\text{SPS},i}$:

Scalar Sub-pixel Smoothing (Permittivity)

$$\varepsilon_{\mathbf{z}} := \langle \varepsilon \rangle_{\mathbf{z}} = \frac{1}{N_{\text{SPS}}} \sum_j \varepsilon(\mathbf{r}_{\mathbf{z}} + \mathbf{v}_j). \quad (\text{B.20})$$

This method is known to improve convergence for E-polarization but slow down convergence for H-polarization [57].

Obviously, (B.19) yields values different from (B.20) only in the vicinity of dielectric boundaries. However, in most numerical schemes the inverse permittivity function $\eta(\mathbf{r}) = 1/\varepsilon(\mathbf{r})$ is needed which

can be discretized in the same fashion

Scalar Sub-pixel Smoothing (Inverse Permittivity)

$$\eta_{\mathbf{z}} := \langle 1/\varepsilon \rangle_{\mathbf{z}} = \frac{1}{N_{\text{SPS}}} \sum_j \frac{1}{\varepsilon(\mathbf{r}_{\mathbf{z}} + \mathbf{v}_j)} \quad (\text{B.21})$$

$$\iff \varepsilon_{\mathbf{z}} = \frac{1}{\langle 1/\varepsilon \rangle_{\mathbf{z}}} \neq \langle \varepsilon \rangle_{\mathbf{z}}. \quad (\text{B.22})$$

At the dielectric boundaries, this yields different values for ε than (B.20). Opposite to (B.20), this scheme improves convergence for H-polarization and slows down convergence for E-polarization [57].

As described in [41, 57, 100], a sensible discretization for obtaining second order convergence for both polarizations and general vectorial computations is the use of an effective tensor permittivity, that combines the scalar sub-pixel smoothing (SPS) for ε and η by using tensorial values defined by

Tensorial Sub-pixel Smoothing (Isotropic)

$$\underline{\underline{\eta}}_{\mathbf{z}} := \langle 1/\varepsilon \rangle_{\mathbf{z}} \underline{\underline{P}}(\hat{\mathbf{n}}_{\mathbf{z}}) + \frac{1}{\langle \varepsilon \rangle_{\mathbf{z}}} (\underline{\underline{\mathbf{1}}} - \underline{\underline{P}}(\hat{\mathbf{n}}_{\mathbf{z}})) \quad (\text{B.23})$$

Here,

$$\underline{\underline{P}}(\hat{\mathbf{n}}) := \hat{\mathbf{n}} \otimes \hat{\mathbf{n}} \quad (\text{B.24})$$

$$\iff$$

$$P_{ij} = n_i n_j \quad (\text{B.25})$$

is a projection matrix that projects the electric field vector $\mathbf{E}(\mathbf{r}) \in \mathbb{C}^d$ on the surface normal $\hat{\mathbf{n}}(\mathbf{r})$ of the boundary between two dielectrics, creating $\mathbf{E}_{\parallel}(\mathbf{r}) = \underline{\underline{P}} \cdot \mathbf{E}(\mathbf{r})$. The tangential component $\mathbf{E}_{\perp}(\mathbf{r}) = (\underline{\underline{\mathbf{1}}} - \underline{\underline{P}}) \cdot \mathbf{E}(\mathbf{r})$ is orthogonal to $\hat{\mathbf{n}}$. In practice, an averaged normal vector $\hat{\mathbf{n}}_{\mathbf{z}}$ associated with the discretized position $\mathbf{r}_{\mathbf{z}}$ is used, since $\mathbf{r}_{\mathbf{z}}$ itself does in general not coincide with the boundary. The second order convergence of frequencies using this discretization scheme is also demonstrated in Fig. C.3.

For the sake of completeness it should also be mentioned that in [41] a tensorial SPS scheme was suggested that also deals with the description of anisotropic materials. With $\{\cdot, \cdot\}$ being the anticommutator, they use

Tensorial Sub-pixel Smoothing (Anisotropic)

$$\underline{\underline{\eta}}_{\mathbf{z}} := \frac{1}{2} \left[\left\{ \langle \underline{\underline{\varepsilon}}^{-1} \rangle_{\mathbf{z}}, \underline{\underline{P}}(\hat{\mathbf{n}}_{\mathbf{z}}) \right\} + \left\{ (\langle \underline{\underline{\varepsilon}} \rangle_{\mathbf{z}})^{-1}, (\underline{\underline{\mathbf{1}}} - \underline{\underline{P}}(\hat{\mathbf{n}}_{\mathbf{z}})) \right\} \right]. \quad (\text{B.26})$$

This is the discretization scheme that MPB uses to obtain the reference solutions for this work. For isotropic media, it reduces to (B.23).

In Fig. B.6, examples for the various discretization schemes are shown for a 2D permittivity.

B.5 Brillouin Zone

The primitive lattice translations \mathbf{b}_i for the reciprocal lattice $\mathbb{L}_{\text{per}}^*$ of a real space lattice \mathbb{L}_{per} are determined via (1.14) by our choice of real space primitive lattice translation (PLT) (B.27) and (B.28) as

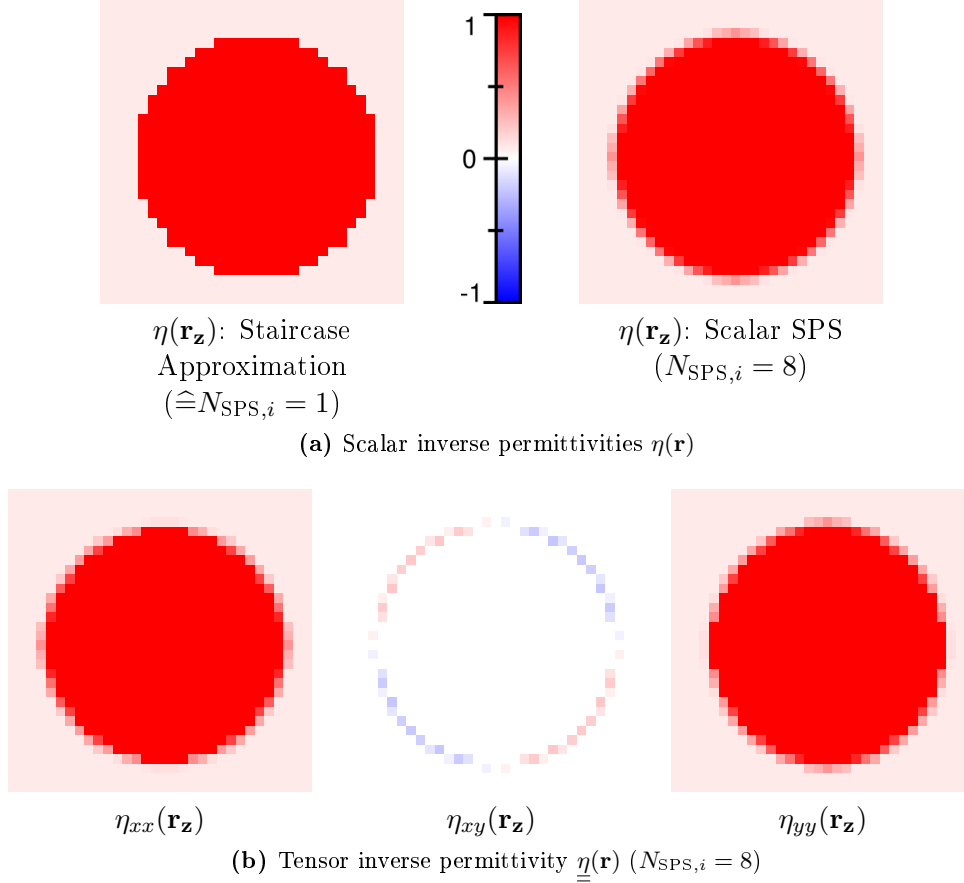


Figure B.6: Examples for the discretized dielectric functions $\eta_{\mathbf{z}}$ and $\underline{\underline{\eta}}_{\mathbf{z}}$ on a unit cell in the square lattice of cylindrical air holes in silicon. (a) show the discretizations (B.19) and (B.20). (b) shows the entries of $\underline{\underline{\eta}}_{\mathbf{z}}$ by the discretization (B.23).

2D Square Lattice

$$\mathbf{b}_1 = \frac{2\pi}{a} \hat{\mathbf{x}},$$

$$\mathbf{b}_2 = \frac{2\pi}{a} \hat{\mathbf{y}},$$

(B.27)

2D Triangular Lattice

$$\mathbf{b}_1 = \frac{2\pi}{a} \left(\hat{\mathbf{x}} + \frac{\sqrt{3}}{3} \hat{\mathbf{y}} \right),$$

$$\mathbf{b}_2 = \frac{2\pi}{a} \left(\frac{2\sqrt{3}}{3} \hat{\mathbf{y}} \right).$$

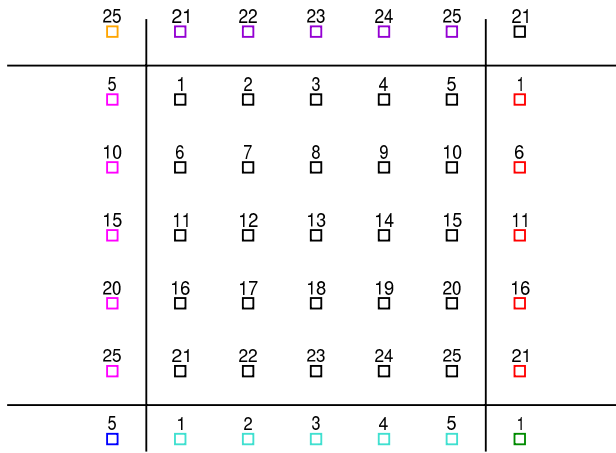
(B.28)

The Bloch modes $\psi_{n\mathbf{k}}$ are periodic in the parameter \mathbf{k} , like (A.4). For brevity we call such functions \mathbf{K} -periodic. For discretizations (3.12) of \mathbf{k} -space integrations (3.1) of such \mathbf{K} -periodic functions, the Monkhorst-Pack mesh [92] is known to be a better choice for a BZ discretization than the mesh introduced in (2.33). The Monkhorst-Pack (MP) mesh defines a discrete set of BZ wave vectors $\mathbf{k}_{\mathbf{p}}$ for resolutions $N_{\mathbf{k}\text{-res},i}$ as

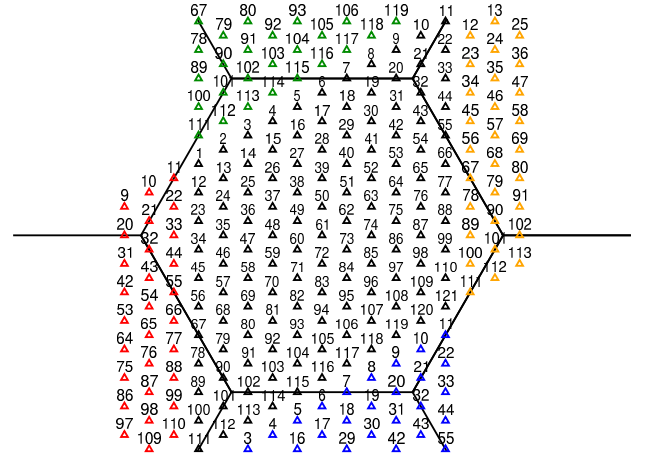
$$\mathbf{k}_{\mathbf{p}} := \sum_i \kappa_i(p_i) \mathbf{b}_i, \quad (\text{B.29})$$

$$\kappa_i(p_i) := \frac{1}{2N_{\mathbf{k}\text{-res},i}} (2p_i - N_{\mathbf{k}\text{-res},i} - 1), \quad \text{for } p_i = 1, 2, \dots, N_{\mathbf{k}\text{-res},i}. \quad (\text{B.30})$$

We choose odd values for $N_{\mathbf{k}\text{-res},i}$ such that the Γ point $\mathbf{k}_{\mathbf{p}} = 0$ is included in the MP mesh.



(a) 2D Square lattice, $N_{\mathbf{k}\text{-res},i} = 5$



(b) 2D triangular lattice, $N_{\mathbf{k}\text{-res},i} = 11$

Figure B.7: *Monkhorst-Pack meshes discretizing the primitive unit cell of 2D reciprocal lattices. The nodes $\mathbf{k}_{\mathbf{p}}$ are consecutively numbered, where the Γ -point $\mathbf{k}_{\mathbf{p}} = 0$ has the number $(1 + \prod_i N_{\mathbf{k}\text{-res},i})/2$ for odd values of $N_{\mathbf{k}\text{-res},i}$.*

C

Reference Modes

The WF defect mode calculations in this work are all compared to the reference solutions by MPB which is a freely available implementation of the supercell method [102]. The SPS discretization for the effective dielectric tensor by (B.23) has been used for these computations. In the following, the accuracy and dependence on numerical parameters of these reference solutions is documented. Furthermore, the convergence order of frequencies depending on the permittivity discretizations of Sec. B.4 is presented.

C.1 Numerical Parameters

This is a brief summary of the numerical parameters in supercell calculations that affect the accuracy of the defect mode frequencies obtained.

C.1.1 Tolerance

MPB features the parameter `tolerance` that defines a termination condition for its iteration procedure. Therefore, the choice of this parameter affects the accuracy of the final eigenmode frequencies.

C.1.2 Sub-Pixel Smoothing Mesh Size $N_{\text{SPS},i}$

MPB uses the tensorial SPS (B.26) for anisotropic dielectrics that reduces to the tensorial SPS (B.23) in the isotropic case. The actual values $\langle \epsilon \rangle_{\mathbf{z}}$ of the discretized permittivity depend on the chosen resolution $N_{\text{SPS},i}$ of the sub-pixel mesh in Fig. B.5a. This is the parameter `mesh-size` in MPB control files. It is not a priori clear, how the choice of this parameter affects the frequencies of eigenmodes.

C.1.3 Real Space Resolution $N_{\text{res},i}$

As explained in Sec. B.3, the quality of numerical derivatives and thus defect mode frequencies becomes better with higher resolutions. By increasing the real space resolution $N_{\text{res},i}$, the frequencies obtained by MPB will approach their final values for $N_{\text{res},i} = \infty$. Since the exact defect mode frequencies for the test system are not known, we compare the frequencies to the best approximation we can achieve that is the results for the maximal resolutions available.

C.1.4 Supercell Size $N_{\text{cells},i}$

In supercell calculations with periodic boundary conditions, the computational domains are taken to be periodically extended in all lattice directions for cavity defect modes and waveguide dispersions

(Fig. C.1). Therefore, a wave vector \mathbf{k} from the corresponding BZ has to be provided, for which the defect modes are calculated. The exact cavity defect modes should be independent of \mathbf{k} since they are non-propagating modes. However, the numerical results differ with \mathbf{k} for small supercells, since they are affected by the influence of the neighboring supercells. Therefore, one has to make sure that the supercell size is chosen sufficiently large such that the numerical solutions become effectively independent of the chosen \mathbf{k} -vector.

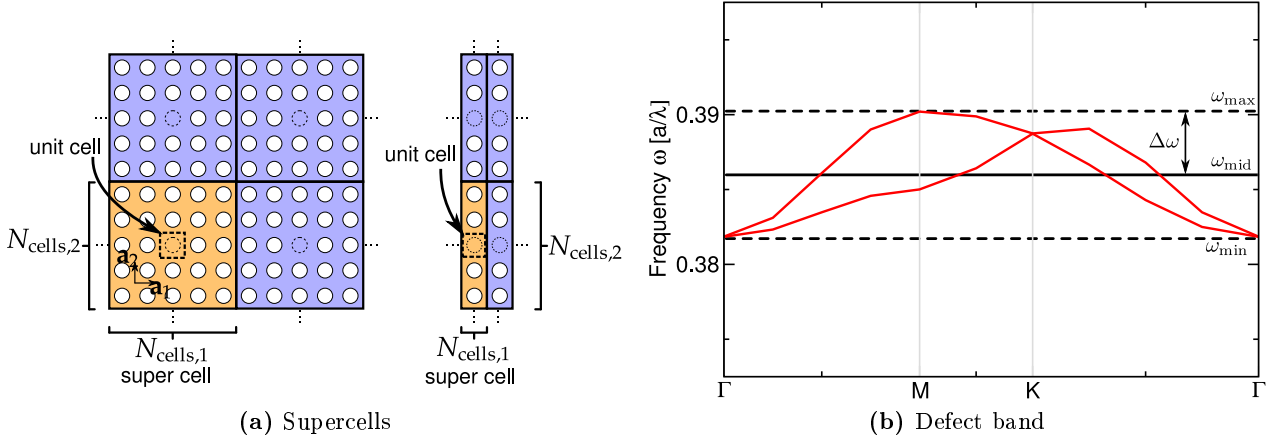


Figure C.1: (a) Computational domains (orange) and number of unit cells per supercell direction $N_{\text{cells},i}$. Supercells used for cavity defect modes (left) and waveguide dispersions (right) are shown. In the supercell method, the computational domains are implicitly taken to be periodic in each lattice direction. One unit cell is discretized as described in Fig. B.1a. (b) The definitions for the maximal and minimal frequencies ω_{max} and ω_{min} , the middle frequency ω_{mid} and the frequency splitting $\Delta\omega$ for a defect band obtained from a supercell calculation for varying \mathbf{k} .

In defect cavity mode computations, whole defect bands are obtained for varying \mathbf{k} with upper frequencies ω_{max} and lower frequencies ω_{min} . If these bands become straight lines, the results can be considered converged. One measure for convergence then is the splitting ratio $\Delta\omega_{\text{sr}}$ (similar to the gap-to-midgap ratio for band gaps), i. e., the ratio between the difference $\Delta\omega$ and the mean value ω_{mid} of the obtained extremal frequencies (see Fig. C.1b):

$$\omega_{\text{mid}} := \frac{1}{2}(\omega_{\text{max}} + \omega_{\text{min}}), \quad (\text{C.1})$$

$$\Delta\omega := \frac{1}{2}(\omega_{\text{max}} - \omega_{\text{min}}), \quad (\text{C.2})$$

$$\Delta\omega_{\text{sr}} := \frac{\Delta\omega}{\omega_{\text{mid}}} = \frac{\omega_{\text{max}} - \omega_{\text{min}}}{\omega_{\text{max}} + \omega_{\text{min}}}. \quad (\text{C.3})$$

When $\Delta\omega_{\text{sr}}(N_{\text{cells},i})$ becomes small, the frequency can be considered independent of \mathbf{k} .

C.2 Reference Frequencies and Parameters

C.2.1 Band Structure in Triangular Model System

First, we look at the sub-pixel mesh resolution $N_{\text{SPS},i}$. Therefore, the maximal relative error in the discretized scalar permittivities $\varepsilon_{\mathbf{z}}$ after (B.20) is plotted in Fig. C.2a, i. e.

$$\text{maximal relative error} := \max_{\mathbf{z}} \frac{|\langle \varepsilon \rangle_{\mathbf{z}}(N_{\text{SPS},i}) - \langle \varepsilon \rangle_{\mathbf{z}}(N_{\text{SPS},\text{max}})|}{|\langle \varepsilon \rangle_{\mathbf{z}}(N_{\text{SPS},\text{max}})|}. \quad (\text{C.4})$$

The plot suggests that there are quite large errors in the actual discretized values $\langle \varepsilon \rangle_{\mathbf{z}}$, depending on the choice of $N_{\text{SPS},i}$. However, Fig. C.3 shows that the actual value of $N_{\text{SPS},i}$ does not affect the eigenmode frequencies, as long as it is not set to 1.

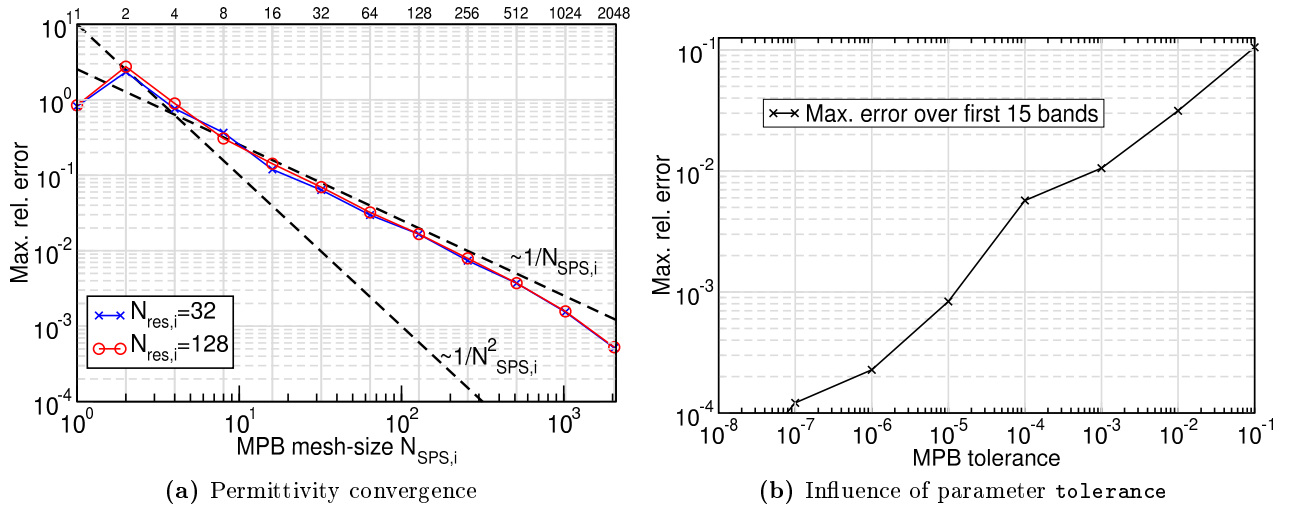


Figure C.2: (a) The maximal relative error (C.4) in the discretized scalar permittivities $\varepsilon_{\mathbf{z}}$ according to (B.20) of one unit cell of the triangular model system, depending on the chosen sub-pixel mesh resolution $N_{\text{SPS},i}$. Two real space resolutions have been investigated. (b) Maximal relative error of the first 15 Bloch bands in the triangular model system for various values of the MPB parameter tolerance ($N_{\text{SPS},i} = 8$ and $N_{\text{res},i} = 64$). For values $\leq 10^{-8}$, the relative error was exactly 0 (MPB frequencies are output with 6 decimal digits). Reference frequencies were those obtained for minimal tolerance of 10^{-14} .

In Fig. C.3a, the absolute Bloch mode frequencies for bands 2–9 are shown for increasing real space resolution $N_{\text{res},i}$. The plot proves that the final eigenmode frequencies for largest real space resolutions $N_{\text{res},i}$ do not change when the sub-pixel smoothing is activated. The accuracy of the frequencies for lower resolutions, however, is improved drastically, as Fig. C.3b shows. With activated SPS the frequencies converge quadratically instead of linearly with deactivated SPS. There is practically no difference between using a mesh resolution $N_{\text{SPS},i} = 8$ or $N_{\text{SPS},i} = 128$. Thus we can conclude that the actual value is not important and $N_{\text{SPS},i} = 8$ yields converged results that cannot be improved further by adjusting this parameter.

The influence of the MPB parameter tolerance is shown in Fig. C.2b, where the maximal relative error of the first 15 Bloch bands in the triangular model system is shown. A tolerance value of 10^{-7} is sufficient for converged results, as the MPB user’s guide also suggests [102].

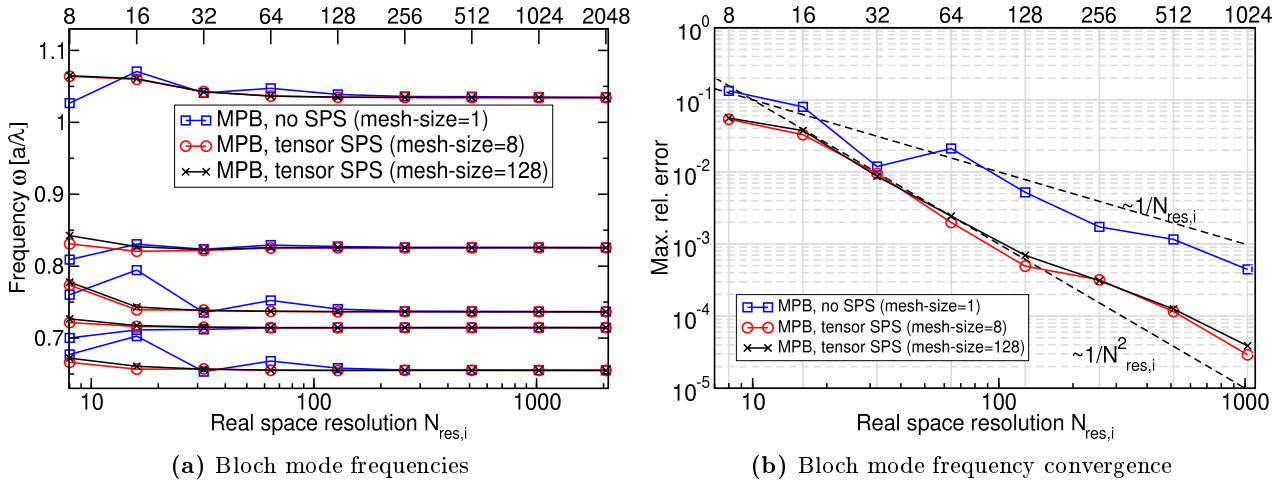


Figure C.3: Frequencies and convergence of frequencies for the first 9 bands of the triangular model system for various values of the sub-pixel mesh resolution $N_{SPS,i}$. Reference values for the convergence plot were the frequencies obtained for maximal real space resolution $N_{res,i} = 2048$.

Finally, the parameter choices $N_{SPS,i} = 8$, $N_{res,i} = 128$ and a tolerance of 10^{-7} are sufficient to compute band structure frequencies below an accuracy of 0.1 %.

For the sake of completeness the lower and upper edges of the first band gap in the triangular model system are given in Tab. C.1. These are reference values that should also be reproduced by WF computations.

$N_{res,i}$	l. edge	u. edge	error in l. edge	error in u. edge
8	0.31181	0.47673	4.5×10^{-2}	3.2×10^{-2}
16	0.30090	0.48781	8.5×10^{-3}	9.3×10^{-3}
32	0.29929	0.49128	3.1×10^{-3}	2.2×10^{-3}
64	0.29884	0.49193	1.6×10^{-3}	9.3×10^{-4}
128	0.29851	0.49212	5.1×10^{-4}	5.4×10^{-4}
256	0.29843	0.49230	2.5×10^{-4}	1.7×10^{-4}
512	0.29838	0.49236	6.1×10^{-5}	5.6×10^{-5}
1024	0.29836	0.49238	—	—

Table C.1: Lower (l.) and upper (u.) band edges obtained by MPB for various real space resolutions $N_{res,i}$ and errors compared to the computation with largest real space resolution. $N_{SPS,i} = 8$ and a tolerance of 10^{-7} were used in the computations.

C.2.2 Non-Etched Hole in Triangular Model System

The cavity setup Ai for $\varepsilon_{\text{def}} = 12$ is computed with MPB. The SPS resolution $N_{\text{SPS},i} = 8$ and a tolerance parameter of 10^{-7} according to Sec. C.2.1 is used here. The frequencies for the lowest six defect modes from Fig. 1.12 for a computation with $N_{\text{cells},i} = 7$ are shown in Fig. C.4a. The SPS yields a convergence order between 1 and 2, as can be seen from Fig. C.4b. Each frequency error is below 0.1% for real space resolutions $N_{\text{res},i} = 64$. For the sake of completeness, the defect mode frequencies obtained for the various real space resolutions are documented in Tab. C.2.

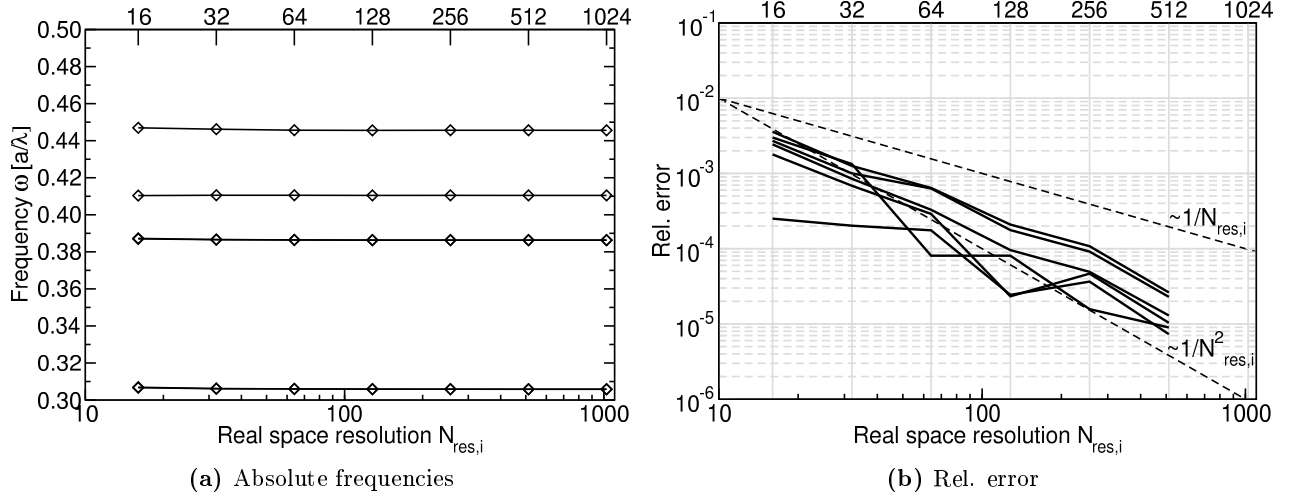


Figure C.4: (a) Absolute frequencies ω obtained by MPB for a 7×7 supercell calculation. (b) Relative error $\Delta\omega/\omega_{\text{ref}}$ with increasing resolution, where the frequency obtained for $N_{\text{res}} = 1024$ is taken as the reference frequency ω_{ref} .

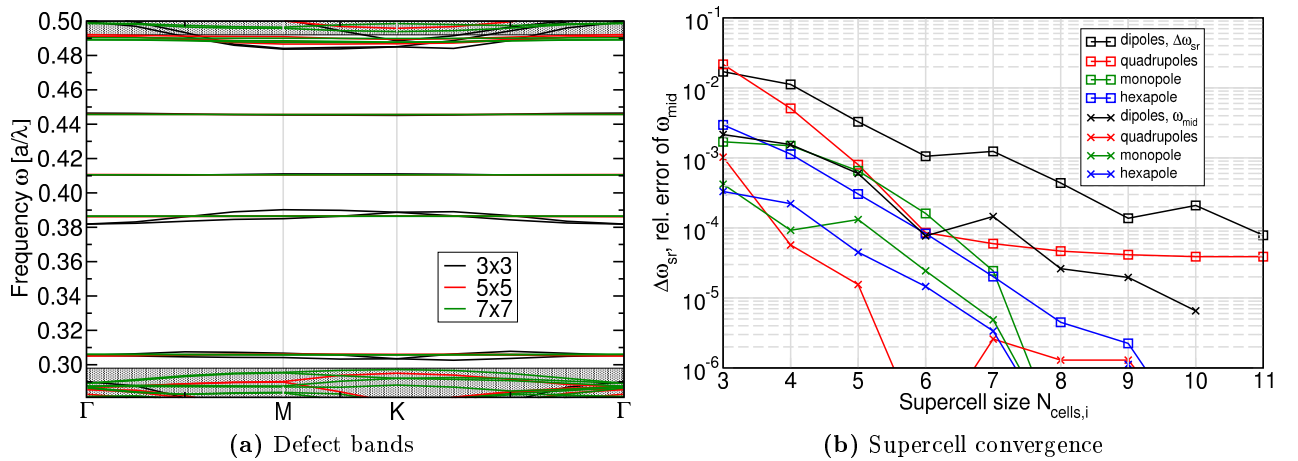


Figure C.5: (a) The defect mode frequencies obtained by MPB for various supercell sizes and variations at different \mathbf{k} -points ($N_{\text{res},i} = 64$, $N_{\text{SPS},i} = 8$). (b) Convergence of mean frequencies ω_{mid} as compared to 11 cells (squares) and frequency splitting ratios $\Delta\omega_{\text{sr}}$ (crosses) for the six lowest defect modes with increasing supercell sizes.

N_{res}	dipoles		quadrupoles	
	ω	$\Delta\omega/\omega_{\text{ref}}$	ω	$\Delta\omega/\omega_{\text{ref}}$
16	0.306648	2.7×10^{-3}	0.387243	2.4×10^{-3}
32	0.306127	1.0×10^{-3}	0.386631	8.5×10^{-4}
64	0.306013	6.3×10^{-4}	0.386430	3.2×10^{-4}
128	0.305874	1.7×10^{-4}	0.386340	9.5×10^{-5}
256	0.305848	9.1×10^{-5}	0.386322	4.9×10^{-5}
512	0.305827	2.3×10^{-5}	0.386308	1.3×10^{-5}
1024	$\omega_{\text{ref}} = 0.305820$	n.a.	$\omega_{\text{ref}} = 0.386303$	n.a.
N_{res}	monopole		hexapole	
	ω	$\Delta\omega/\omega_{\text{ref}}$	ω	$\Delta\omega/\omega_{\text{ref}}$
16	0.410358	2.5×10^{-4}	0.446950	3.0×10^{-3}
32	0.410544	2.0×10^{-4}	0.446206	1.3×10^{-4}
64	0.410533	1.7×10^{-4}	0.445648	8.1×10^{-5}
128	0.410471	2.4×10^{-5}	0.445576	8.1×10^{-5}
256	0.410476	3.7×10^{-5}	0.445619	1.6×10^{-5}
512	0.410464	7.3×10^{-5}	0.445616	9.0×10^{-6}
1024	$\omega_{\text{ref}} = 0.410461$	n.a.	$\omega_{\text{ref}} = 0.445612$	n.a.

Table C.2: MPB defect mode frequencies ω and relative error from ω_{ref} for the non-etched hole in a 7×7 supercell and activated sub-pixel smoothing after (B.23) ('n.a.' means 'not available').

The influence of the supercell size on the frequencies is shown in Fig. C.5. For $N_{\text{cells},i} = 6$ unit cells per lattice direction, the maximal error over all six defect mode frequencies is $\leq 0.1\%$.

Finally, in order to compute reference solutions with accuracy of at least 0.1% for the non-etched hole with MPB, the parameters of Tab. C.3a were used. The parameters were chosen slightly larger than necessary. The corresponding frequencies are shown in Tab. C.3b.

Parameter	value	mode	frequency ω
tolerance	10^{-7}	dipoles	0.305(8)
$N_{\text{res},i}$	96	quadrupoles	0.386(4)
$N_{\text{SPS},i}$	8	monopole	0.410(5)
$N_{\text{cells},i}$	7	hexapole	0.445(6)
(a) Non-etched hole reference parameters		(b) Non-etched hole reference frequencies	

Table C.3: (a) MPB parameters for obtaining the non-etched hole reference frequencies with accuracies below 0.1% . (b) Defect mode frequencies obtained with MPB for a non-etched hole for the numerical parameters of (a). The last digit in parentheses is uncertain.

C.2.3 Ring of Six Non-Etched Holes in Triangular Model System

The convergence of the 36 defect modes in the BCDEFGi cavity setup of Fig. 6.20d for $\varepsilon_{\text{def}} = 12$ is investigated in Fig. C.6.

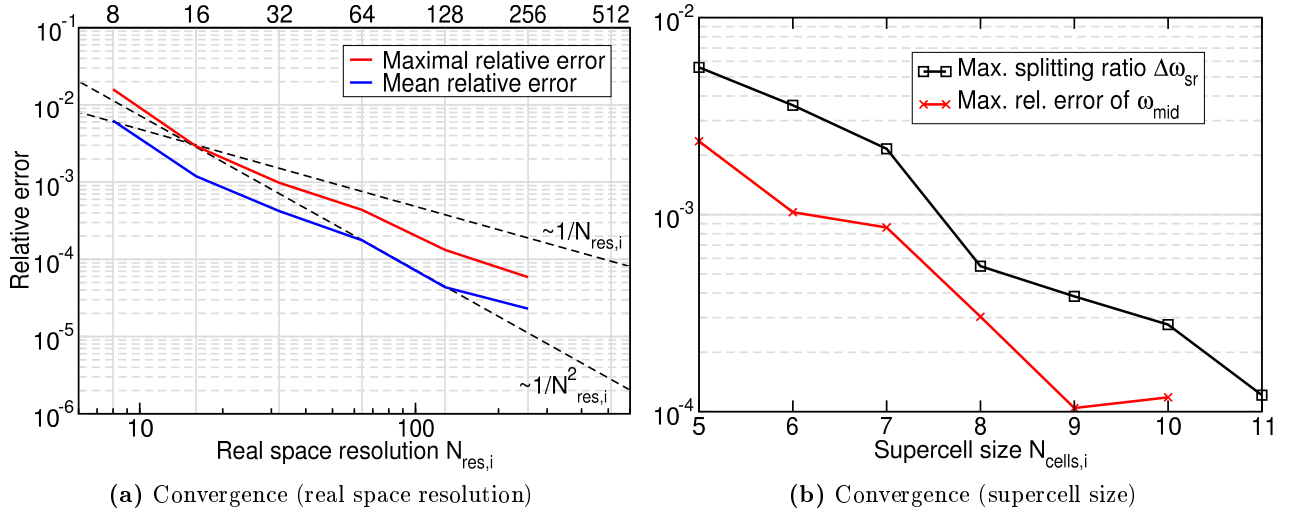


Figure C.6: Defect mode frequency convergence with supercell size and real space resolution. The SPS mesh resolution parameter $N_{\text{SPS},i} = 8$ is used. In (a), the maximal and mean relative errors of the 36 modes are shown, where the reference frequencies used were the ones obtained with the highest real space resolution of $N_{\text{res},i} = 512$. The cell size for these computations were $N_{\text{cells},i} = 7$. In (b), a real space resolution of $N_{\text{res},i} = 32$ was used.

For accuracies below 0.1%, the parameters $N_{\text{cells},i} = 8$ and $N_{\text{res},i} = 32$ have to be used, corresponding to 65,000 degrees of freedom per mode in total (total number of discretization points). For accuracies comparable to 101 WFs with 36 FBFs (0.68% after Tab. 6.3e), $N_{\text{cells},i} = 5$ and $N_{\text{res},i} = 16$ is sufficient which means 6,400 degrees of freedom.

C.2.4 W1-1 Waveguide of Non-Etched Holes in Triangular Model System

According to Figs. C.4b and C.6a, a real space resolution of $N_{\text{res},i} = 64$ is sufficient for accuracies below 0.1% which is used for the computations here. The accuracy of the waveguide frequencies with increasing number of unit cells N_{cells} per waveguide slice (cf. Fig. 7.1b) is shown in Fig. C.7. For accuracies below 0.1%, one has to use $N_{\text{cells}} = 10$.

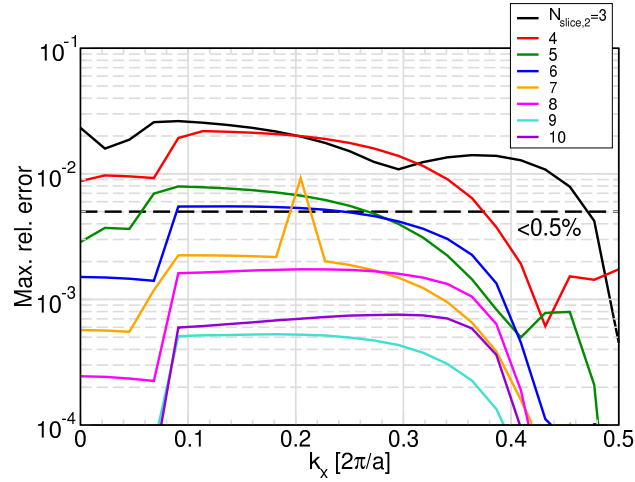


Figure C.7: Convergence of dispersion branches for real space resolution $N_{\text{res},i} = 64$. Reference frequencies were those obtained for 11 cells.

Finally, the reference values for waveguide dispersions have been computed with MPB with $N_{\text{res},i} = 64$ and $R_{\text{slice}} = 5$ cladding cells around the defects in the waveguide domain, resulting in $N_{\text{cells}} = 11$ unit cells for a W1-1 (cf. Fig. 7.1b).

D Appendix D

Numerical Parameters

This appendix features a series of tables containing numerical parameters for various computations in this thesis. The captions refer to the figures and results obtained with the parameters.

Parameter	Value
Lattice	Triangular
r	$0.45a$
ϵ_{cyl}	$\epsilon_{\text{air}} = 1$
ϵ_{back}	$\epsilon_{\text{Si}} = 12$
Polarization	TE
Method	MPB
Permittivity discretization	tensor SPS
tolerance	10^{-9}
$N_{\text{SPS},i}$	8
$N_{\text{res},i}$	96
$N_{\mathbf{k}\text{-res},i}$	11
N_{WF}	101

(a) Bloch mode construction parameters

First band	Last band	ω_{inner}	ω_{outer}
1	1	0	0
2	9	0.88	1.12
10	17	1.3	1.49
18	26	1.6	1.75
27	38	0	0
39	57	0	2.5
58	73	0	2.93
74	101	0	3.32

(b) WF generation parameters

Table D.1: Numerical parameters and methods used for creating the WFs of Fig. 3.44. For $\omega_{\text{inner}} = \omega_{\text{outer}} = 0$, only the Marzari-Vanderbilt spread minimization for closed sets of bands was carried out.

Parameter	Value
Lattice	Triangular, (B.6)
r	0.45a
ϵ_{cyl}	$\epsilon_{\text{air}} = 1$
ϵ_{back}	$\epsilon_{\text{Si}} = 12$
Polarization	TE
Method	MPB, [41]
Permittivity discretization	tensor SPS, (B.23)
$N_{\text{res},i}$	96
$N_{\mathbf{k}\text{-res},i}$	11
N_{WF}	101

(a) Bloch mode construction parameters

Parameter	Value
Permittivity discretization	tensor SPS (B.23), scalar SPS (B.20)
reference defect	missing hole $\epsilon_{\text{ref}} = 12$
R_{max} (coupling and domain)	5
Derivative discretization	FDS (Sec. B.3.1), SD (Sec. B.3.2)

(b) Operator matrix parameters

Parameter	Value
Permittivity discretization	tensor SPS, (B.23)
$N_{\text{res},i}$	96
\mathbf{k}	$(0, 0) \hat{=} \Gamma\text{-point}$
$N_{\text{cells},i}$	7
Tolerance	10^{-9}

(c) MPB supercell reference modes

Table D.2: Numerical parameters and methods used to obtain the TE WFs results of Sec. 6.1.2. The corresponding WFs are depicted in Fig. 3.44. WF generation parameters are shown in Tab. D.1.

Parameter	Value
Lattice	Square, (B.5)
r	0.18a
ε_{cyl}	$\varepsilon_{\text{Si}} = 12$
$\varepsilon_{\text{back}}$	$\varepsilon_{\text{air}} = 1$
Polarization	TM
Method	plane wave expansion (PWE), [103]
Permittivity discretization	Ho-Chan-Soukoulis (HCS), [18]
$N_{\mathbf{K}}$	1,600
$N_{\mathbf{k}\text{-res},i}$	11
N_{WF}	23

(a) Bloch mode construction parameters

First band	Last band	ω_{inner}	ω_{outer}
1	1	0	0
2	4	0	0
5	9	0.947	1.365
10	16	1.39	1.75
17	23	1.75	2.10

(b) WF generation parameters

Parameter	Value
Permittivity discretization	scalar SPS
reference defect	missing rod $\varepsilon_{\text{ref}} = 1$
R_{max} (coupling and domain)	5
Derivative discretization	finite difference stencil (FDS), 4th order

(c) Operator matrix parameters

Parameter	Value
Permittivity discretization	tensor SPS
$N_{\text{res},i}$	96
\mathbf{k}	$(0, 0) \hat{=} \Gamma\text{-point}$
$N_{\text{cells},i}$	7
Tolerance	10^{-9}

(d) MPB supercell reference modes

Table D.3: Numerical parameters and methods used to obtain the TM WFs results of Sec. 6.1.1. The corresponding WFs are depicted in Fig. 6.1.

E

Appendix E

Auxiliary Basis Functions

This appendix lists further cavity cluster and waveguide computations with the ABF sets introduced in Chap. 6. All ABFs have been orthogonalized with respect to proper WFs used in the sets. Proper WFs were used on a computational domain according to (7.2) with $R_{\max} = 4$, whereas auxiliary functions have only been used at the defect sites. This is denoted in the plot legends as “R4d” and “R0d”, respectively. The FDS-scalar discretization scheme was used and is also denoted also in the legends (cf. Sec. 5.1.5).

E.1 Comparison of Various Auxiliary Basis Function Sets

The defect modes of the defect cluster setups of Fig. 6.20 for the sets of auxiliary basis functions investigated in Sec. 6.5 are gathered beginning on page 212.

E.2 Waveguides W1-1

This is a collection of W1-1 waveguide dispersions computed with proper WFs only and the WF101-FBF36 set, respectively. It shows the accuracies, with which the different branches of the dispersion can be modeled by the proper WFs only. The collection starts on page 214.

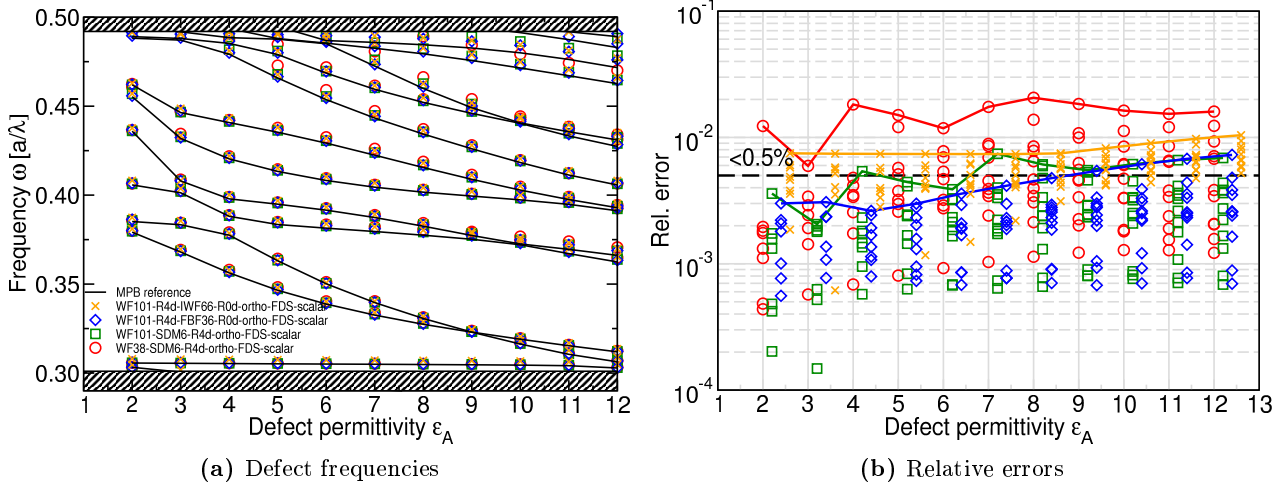


Figure E.1: Cavity setup ABi (Fig. 6.20a) for $\epsilon_B = 12$.

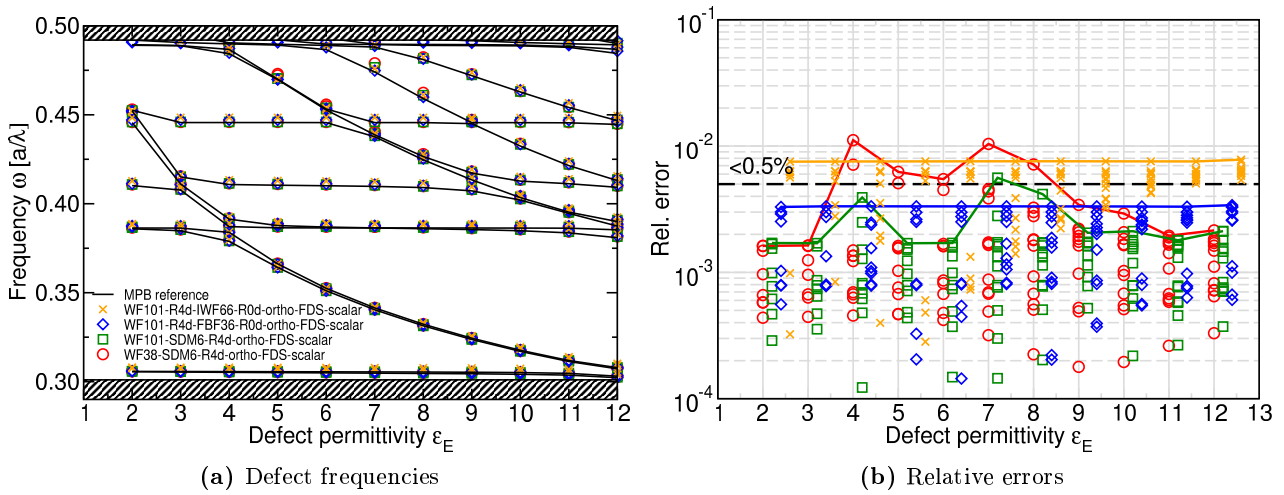


Figure E.2: Cavity setup BEi (Fig. 6.20b) for $\epsilon_B = 12$.

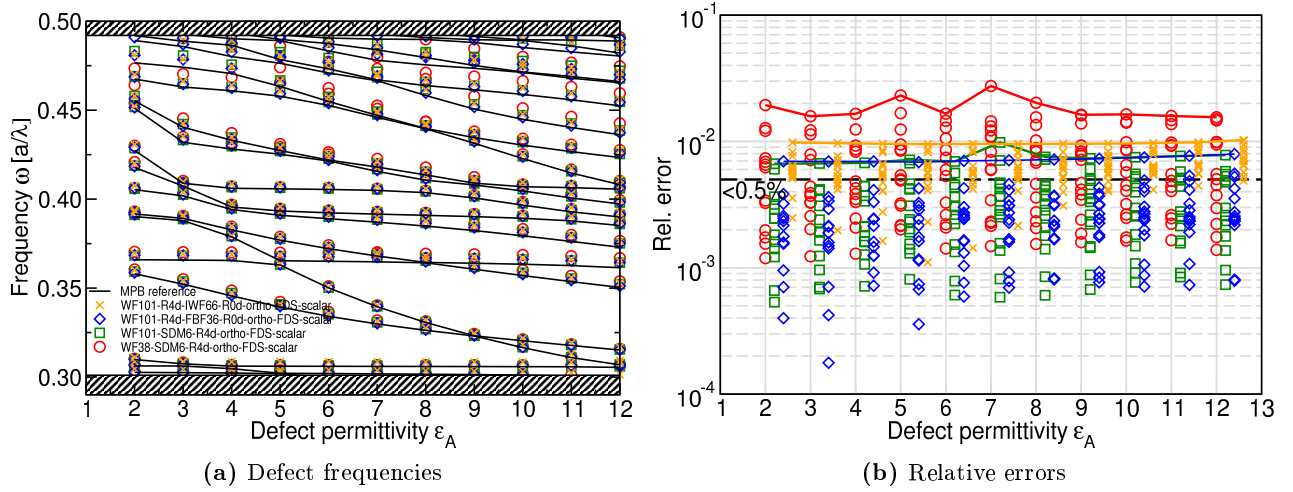


Figure E.3: Cavity setup *ABEi* (Fig. 6.20c) for $\epsilon_B = 12$ and $\epsilon_E = 12$.

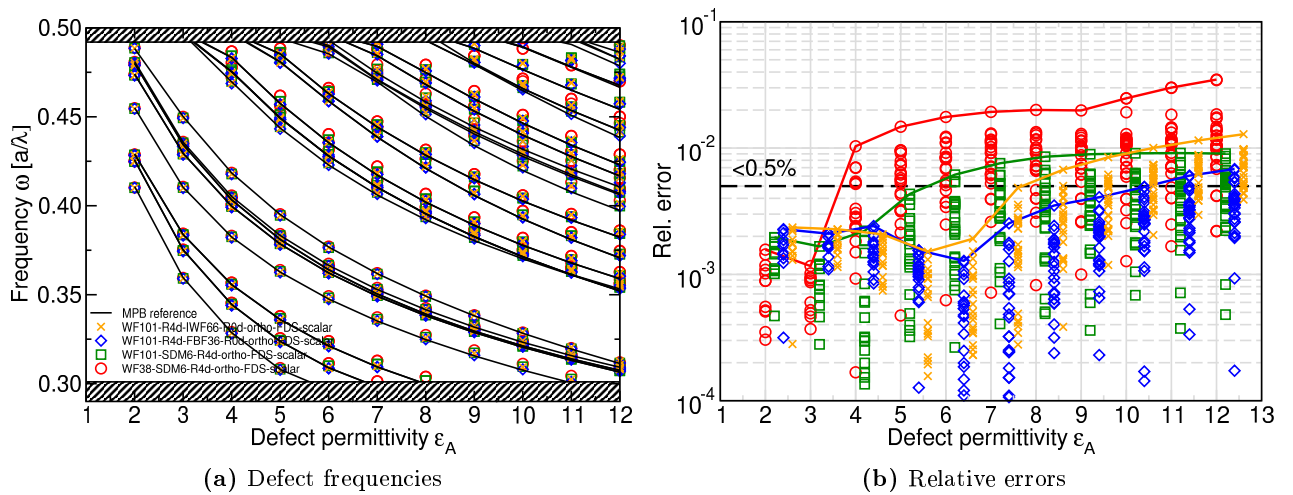


Figure E.4: Cavity setup *BCDEFGi* (Fig. 6.20d).

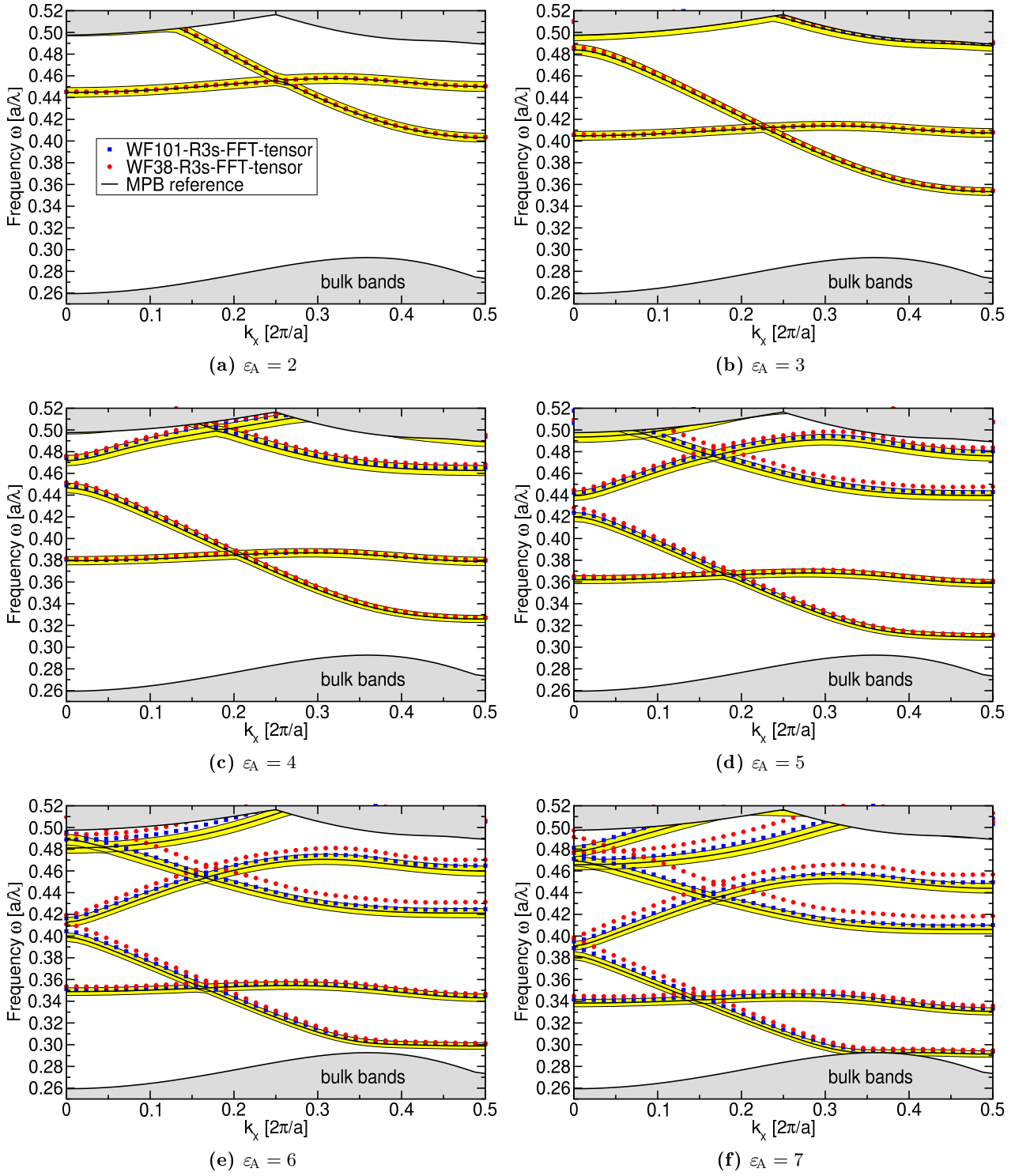


Figure E.5: *W1-1* waveguide dispersions made from one row of infiltrated holes with ε_A . Results are obtained by the WFs supercell approach (4.74). Yellow regions denote $\pm 1\%$ errors around reference frequencies.

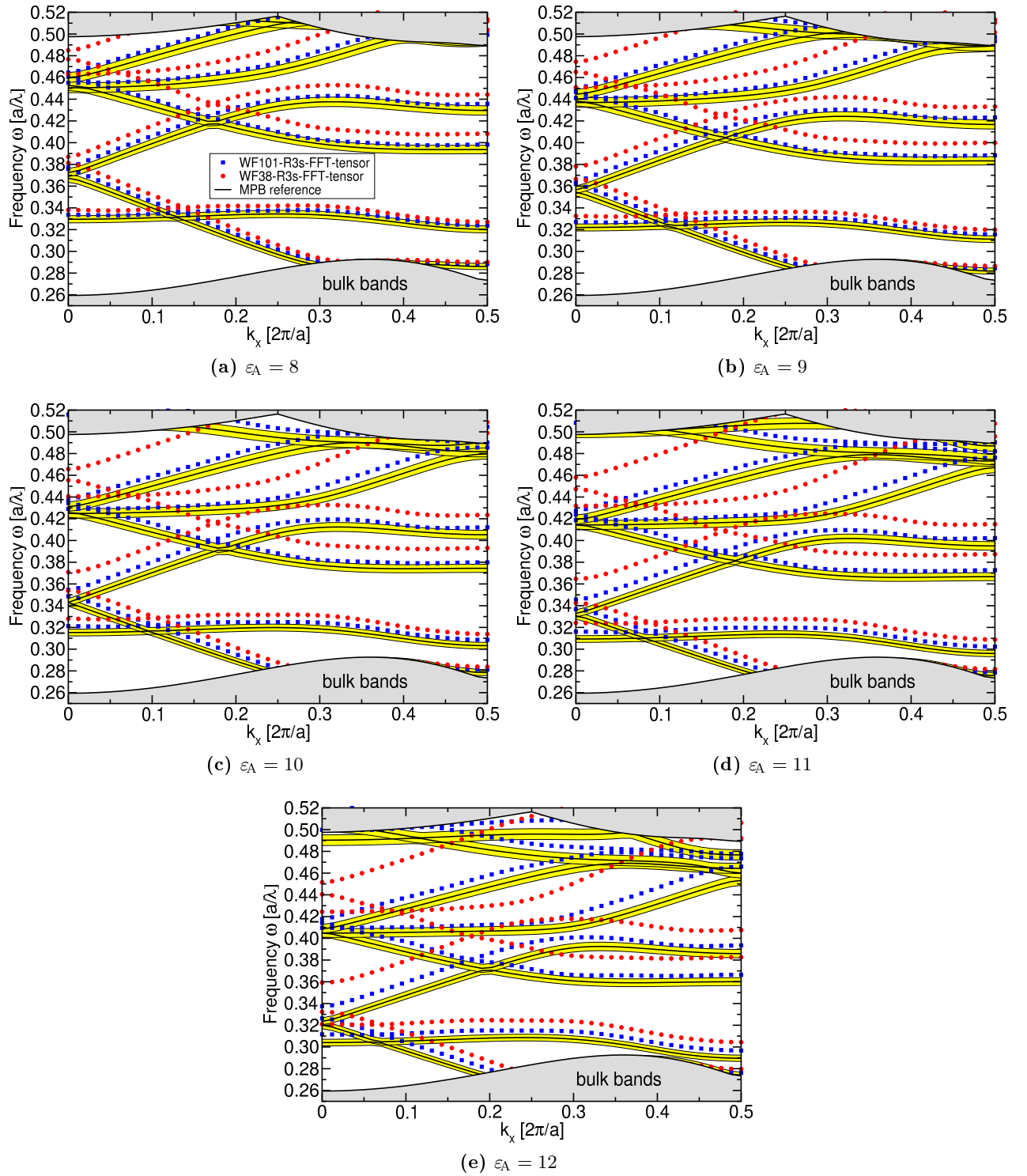


Figure E.6: *W1-1* waveguide dispersions made from one row of infiltrated holes with ϵ_A . Results are obtained by the WFs supercell approach (4.74). Yellow regions denote $\pm 1\%$ errors around reference frequencies.

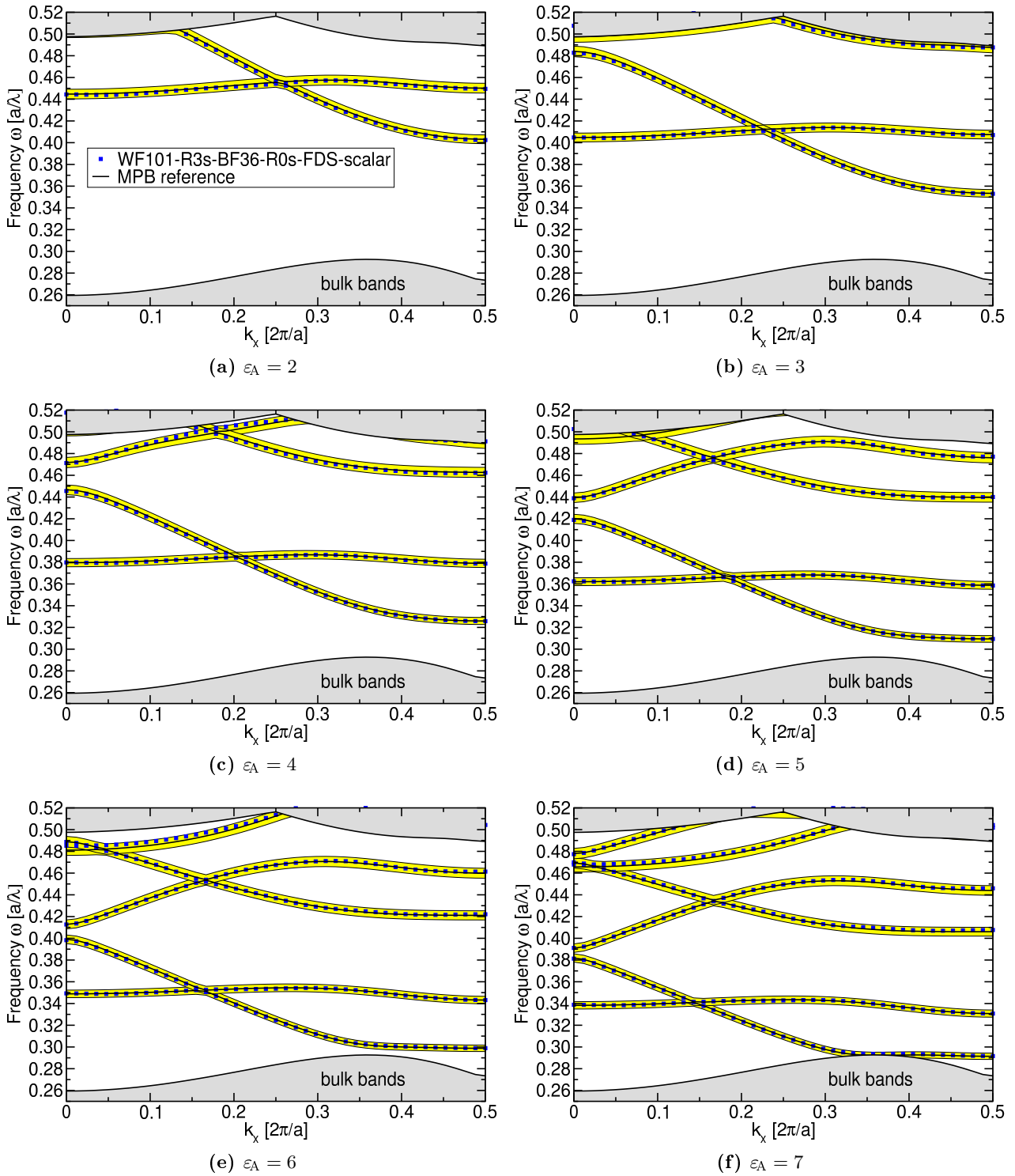


Figure E.7: *W1-1* waveguide dispersions made from one row of infiltrated holes with ϵ_A . Results are obtained by the WFs supercell approach (4.74). Yellow regions denote $\pm 1\%$ errors around reference frequencies.

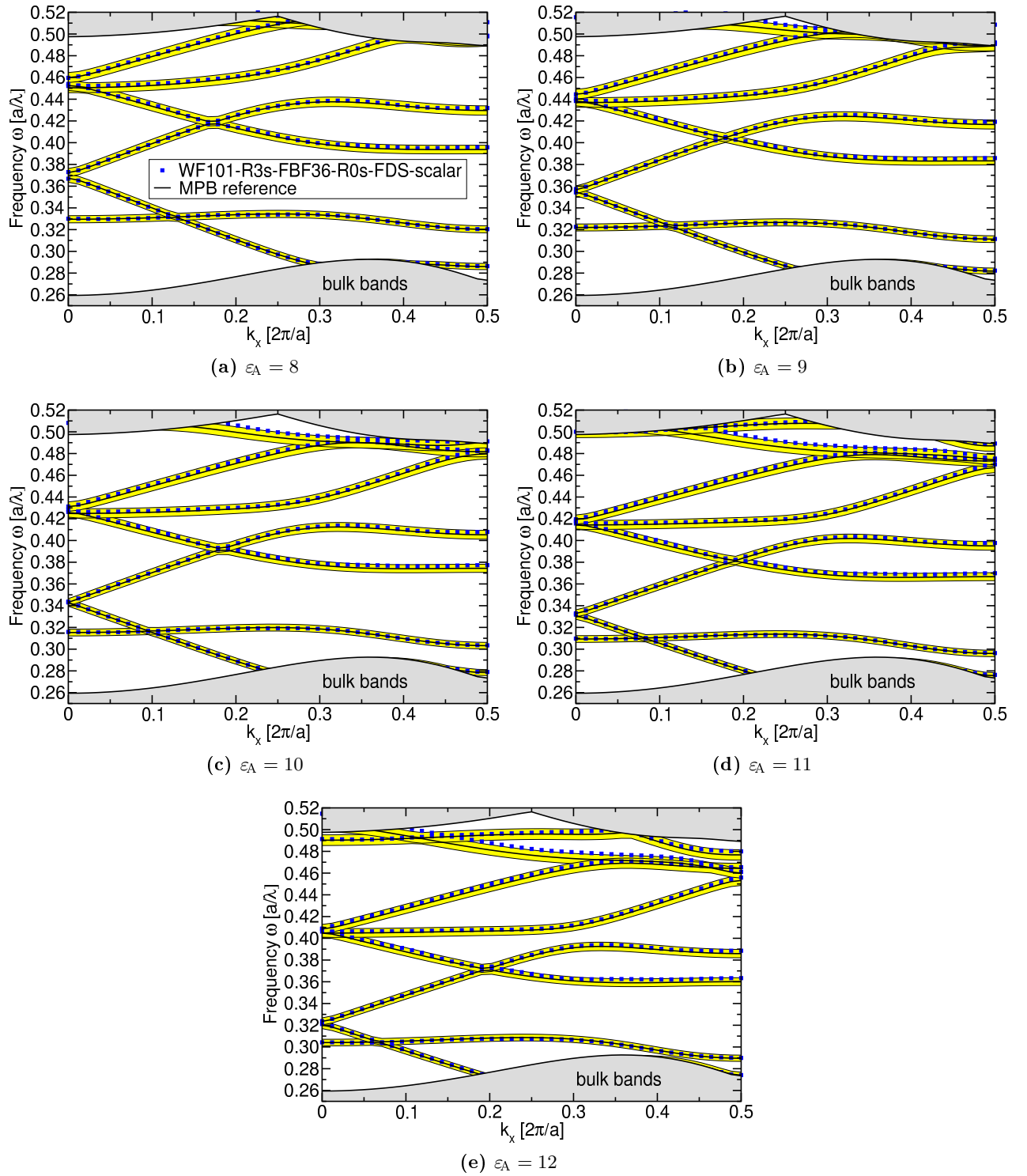


Figure E.8: *W1-1* waveguide dispersions made from one row of infiltrated holes with ϵ_A . Results are obtained by the WFs supercell approach (4.74). Yellow regions denote $\pm 1\%$ errors around reference frequencies.

F

Appendix F

Group Representation Theory

This is a collection of proofs and tables regarding the representation theory and crystallographic notation.

F.1 Index Ordering of (2.21)

The order of the subscript indices ensures the consistency of the definition for products g_2g_1 of plane group elements as in (2.5) such that first transforming by g_1 and then by g_2 leads to

$$\hat{D}(g_2)\hat{D}(g_1)f_j = \hat{D}(g_2)\left(\sum_{i'} f_{i'} D_{i'j}(g_1)\right) \quad (\text{by (2.21)}) \quad (\text{F.1})$$

$$= \sum_{i'} \hat{D}(g_2)f_{i'} D_{i'j}(g_1) \quad (\hat{D} \text{ is linear operator}) \quad (\text{F.2})$$

$$= \sum_{i'} \sum_i f_i D_{ii'}(g_2) D_{i'j}(g_1) \quad (\text{by (2.21)}) \quad (\text{F.3})$$

$$= \sum_i f_i \underbrace{\left(\sum_{i'} D_{ii'}(g_2) D_{i'j}(g_1)\right)}_{=D(g_2) \cdot D(g_1)} \quad (\text{reorder summation}) \quad (\text{F.4})$$

$$= \sum_i f_i D_{ij}(g_2g_1) \quad (\text{F.5})$$

$$= \hat{D}(g_2g_1)f_j \quad (\text{by (F.1)}) \quad (\text{F.6})$$

Hence, the mapping from the group G to the group of rep matrices $D(g)$ is a group homomorphism (2.1) with respect to the standard matrix-matrix product:

$$D(g_2g_1) = D(g_2) \cdot D(g_1). \quad (\text{F.7})$$

The coordinates \mathbf{c} with $c_i \in \mathbb{C}$ in the function space spanned by the f_i are transformed by the matrices

$D(g)$ in the usual way, i. e., for $f = \sum_i c_i \cdot f_i$ we have

$$f' = \hat{D}(g)f \tag{F.8}$$

$$= \sum_j c_j \cdot \hat{D}(g)f_j \tag{by (2.21)} \tag{F.9}$$

$$= \sum_i f_i \left(\underbrace{\sum_j D_{ij}(g)c_j}_{=:c'_i} \right) \tag{reorder summation}. \tag{F.10}$$

which is compactly written as a matrix vector product

$$\mathbf{c}' = D(g) \cdot \mathbf{c}. \tag{F.11}$$

F.2 Cell Diagram Notation

Elements	Meaning
	a center of rotation of order two ($\frac{2\pi}{2} \equiv 180^\circ$)
	a center of rotation of order three ($\frac{2\pi}{3} \equiv 120^\circ$)
	a center of rotation of order four ($\frac{2\pi}{4} \equiv 90^\circ$)
	a center of rotation of order six ($\frac{2\pi}{6} \equiv 60^\circ$)
	an axis of reflection
	an axis of glide reflection

Table F.1: *Symmetry items in cell structure diagrams.*

F.3 Square Lattice: P4mm (C_{4v})

This is the plane group P4mm (99, international notation) which consists of translations along the primitive lattice translations (B.5) and the orthogonal transforms of the point group C_{4v} (Schönflies notation, see Fig. F.1b).

Unfortunately, the physicist's choice of coordinates (B.5) (denoted here by primitive lattice translations $\mathbf{a}_1, \mathbf{a}_2$, PLT) and the crystallographer's choice (used in the International Tables of Crystallography, ITA)

$$\mathbf{a} = -a\hat{\mathbf{y}}, \quad \mathbf{b} = a\hat{\mathbf{x}}, \tag{F.12}$$

does not coincide. The methods for transforming coordinates will be explained here. We need transformation matrices

$$M_{\text{ITA} \leftarrow \text{PLT}} := \begin{pmatrix} 0 & -1 \\ 1 & 0 \end{pmatrix}, \quad M_{\text{PLT} \leftarrow \text{ITA}} := M_{\text{ITA} \leftarrow \text{PLT}}^{-1} = \begin{pmatrix} 0 & 1 \\ -1 & 0 \end{pmatrix}, \tag{F.13}$$

From the Wyckoff positions $(x, y)_{\text{ITA}}$ in ITA coordinates, we can compute the corresponding coordinates in PLT as

$$M_{\text{PLT} \leftarrow \text{ITA}} \cdot \begin{pmatrix} x \\ y \end{pmatrix}_{\text{ITA}} = \begin{pmatrix} -y \\ x \end{pmatrix}_{\text{PLT}}, \quad (\text{F.14})$$

meaning that $x\mathbf{a} + y\mathbf{b} = -y\mathbf{a}_1 + x\mathbf{a}_2$. The notation for the symmetry operations from PLT to ITA is converted, e. g. via

$$M_{\text{ITA} \leftarrow \text{PLT}} \cdot R(\sigma_x) \cdot M_{\text{PLT} \leftarrow \text{ITA}} \cdot \begin{pmatrix} x \\ y \end{pmatrix}_{\text{ITA}} = \begin{pmatrix} x \\ -y \end{pmatrix}_{\text{ITA}} \equiv x, -y. \quad (\text{F.15})$$

Note that any equivalent Wyckoff position (shifted by any lattice vector) has the same site symmetry group and, therefore, the same irreps. These matrices have been used to construct Tab. F.2 and Tab. F.4.

The reciprocal lattice vectors \mathbf{b}_i in PLT and $\mathbf{a}^*, \mathbf{b}^*$ in ITA coordinates are defined via

$$\mathbf{b}_i \propto \mathbf{a}_j \times \mathbf{a}_k, \quad (\text{F.16a})$$

$$\mathbf{a}^* = \mathbf{b} \times \mathbf{c}, \quad (\text{F.16b})$$

$$\mathbf{b}^* = \mathbf{c} \times \mathbf{a}, \quad (\text{F.16c})$$

where we set implicitly $\mathbf{c} = \mathbf{a}_3 = a\hat{z}$. Since the directions of the primitive lattice translations in direct and reciprocal coincide for both the PLT and ITA bases, one can use the same conversion matrices (F.13) also for conversion of reciprocal lattice coordinates. This has been used to construct Tab. F.6.

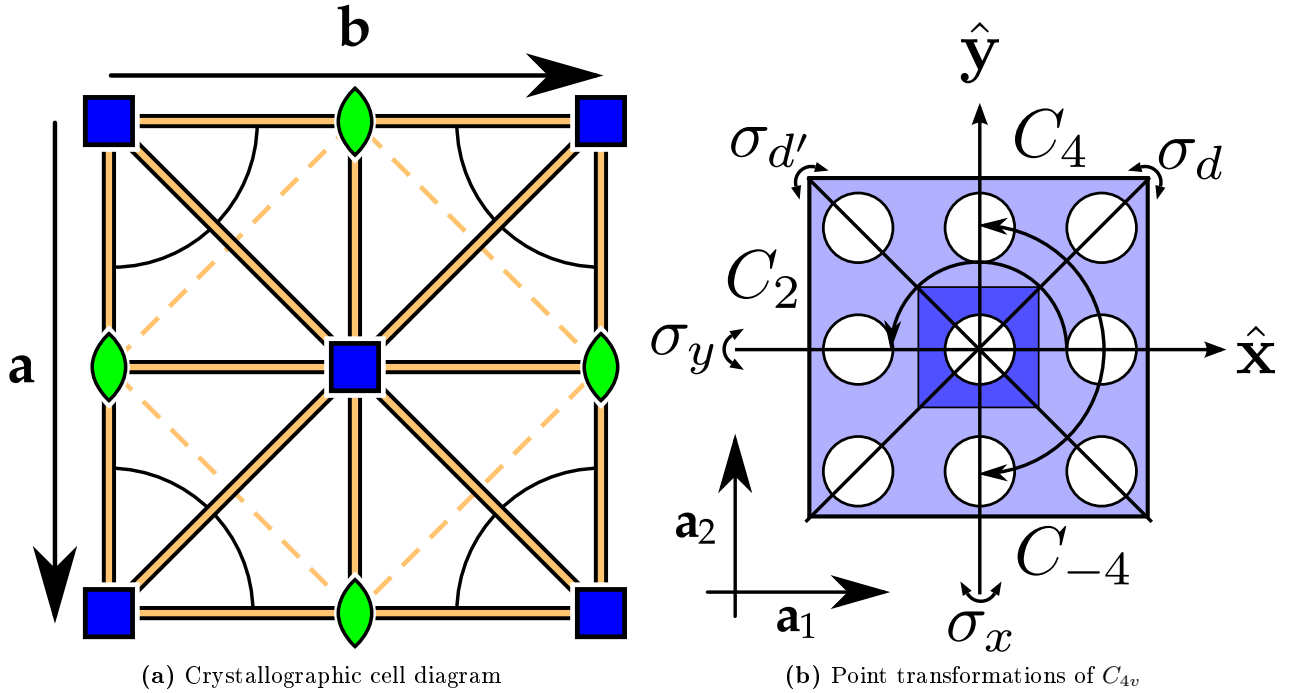


Figure F.1: (a) Crystallographic cell diagram of the $P4mm$ space group with ITA coordinate vectors. The hole is located in the corners of the cell. (b) Point transforms of C_{4v} with origin in the center of a hole with PLT coordinates.

Class	Symbol	ITA	Meaning
E	E	x, y	Identity
C_2	C_2	$-x, -y$	Rotation of $\frac{2\pi}{2} \equiv 180^\circ$
$2C_4$	C_4	$-y, x$	Rotation of $\frac{2\pi}{4} \equiv 90^\circ$
$2C_4$	C_{-4}	$y, -x$	Rotation of $\frac{2\pi}{-4} \equiv -90^\circ$
$2\sigma_v$	σ_x	$x, -y$	Reflection with normal $\hat{\mathbf{y}}$
$2\sigma_v$	σ_y	$-x, y$	Reflection with normal $\hat{\mathbf{x}}$
$2\sigma_d$	σ_d	$-y, -x$	Reflection with normal $\frac{1}{\sqrt{2}}(\hat{\mathbf{x}} + \hat{\mathbf{y}})$
$2\sigma_d$	$\sigma_{d'}$	y, x	Reflection with normal $\frac{1}{\sqrt{2}}(-\hat{\mathbf{x}} + \hat{\mathbf{y}})$
σ	σ		One of $\sigma_x, \sigma_y, \sigma_d, \sigma_{d'}$. Depends on the particular realization.

Table F.2: List of symmetry operations of the point group C_{4v} . The number before the class denotes the number of representatives in that class. ITA means notation by [85].

C_{4v}	E	C_2	$2C_4$	$2\sigma_v$	$2\sigma_d$	C_{2v}	E	C_2	σ_y	σ_x	C_{1h}	E	σ	C_1	E
A_1	1	1	1	1	1	A_1	1	1	1	1	A	1	1	A	1
A_2	1	1	1	-1	-1	A_2	1	1	-1	-1	B	1	-1	A	1
B_1	1	1	-1	1	-1	B_1	1	-1	1	-1					
B_2	1	1	-1	-1	1	B_2	1	-1	-1	1					
E	2	-2	0	0	0										

Table F.3: Character tables for the conjugacy classes and irreducible representations of the point group C_{4v} and its subgroups. The elements are defined by Tab. F.2 and Fig. F.1b. The geometric transform associated with σ depends on the actual realization of the abstract group C_{1h} .

The interpretation of the SITESYM output requires great care, since the notation is not identical to the one used in this work. First of all, $m_x = \sigma_y$ and $m_y = \sigma_x$ for the C_{2v} (2mm) site symmetry character table for Wyckoff position c_1 of Tab. F.4.¹ This leads to B_2 (SITESYM) being B_1 (this work) and vice versa for the site symmetry irreps of C_{2v} . The space group irreps for SITESYM are induced by the little co-group irreps of the respective \mathbf{k} -point coordinates (Tab. F.6) used. They are labeled by SITESYM with an arbitrary chosen label A as *A1, *A2, etc., where the corresponding irrep in our notation can be deciphered with the use of the symmetry operations Tab. F.2 and the characters Tab. F.3. The ambiguous relations have been compiled in Tab. F.5, all others are straightforward. With the help of this “dictionary”, Tab. 2.1 was assembled.

¹This is because Schönflies and Hermann-Mauguin notation are mixed here and defined differently.

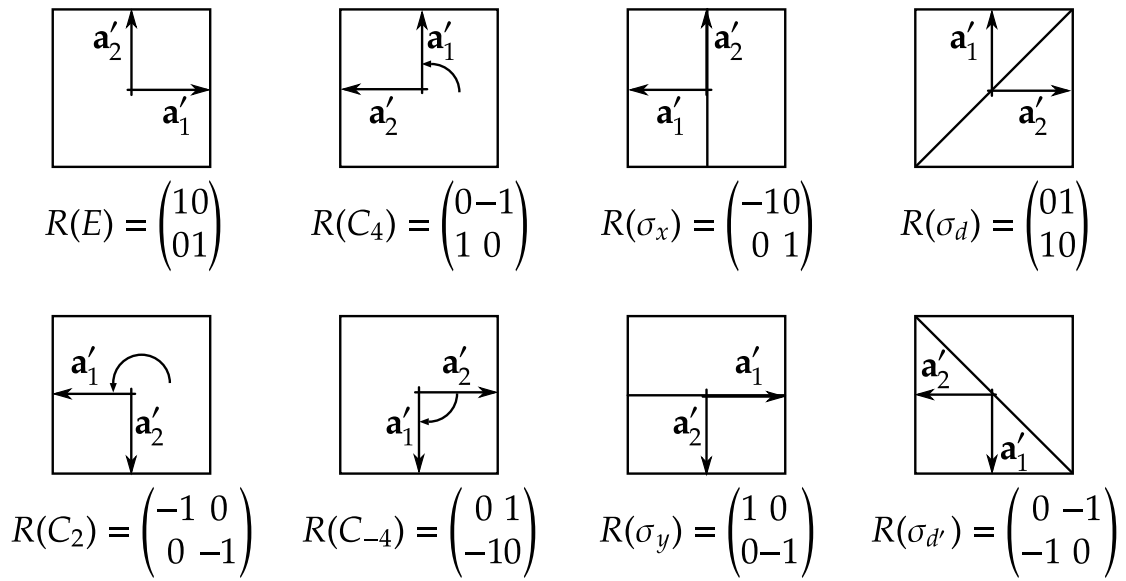


Figure F.2: The orthogonal transformation matrices for C_{4v} in the basis of the primitive lattice translations \mathbf{a}_i .

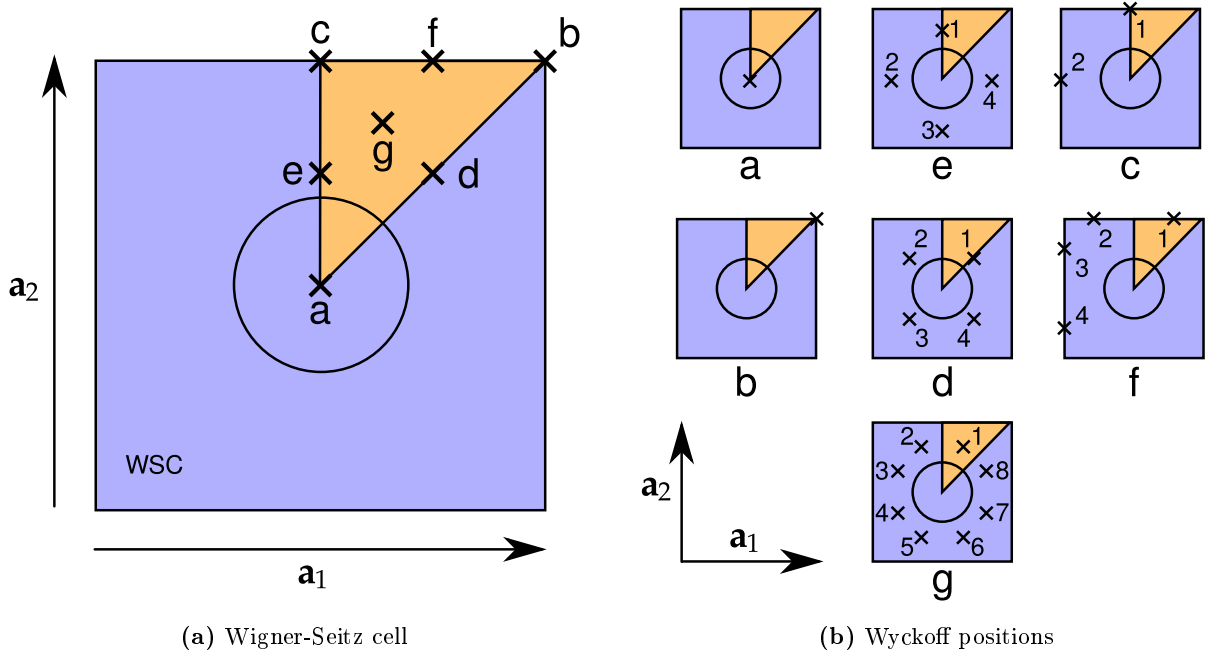


Figure F.3: The Wigner-Seitz cell of the square lattice and its Wyckoff positions. The labeling with roman letters is standardized, the numbering is arbitrary. A particular position can be denoted by letter and number, e. g. d2 for the upper left Wyckoff position d. Note that the Wyckoff positions are actually points as well as whole lines with the same site symmetry group. Site symmetry groups of the same roman letter but different number are isomorphic by (2.44).

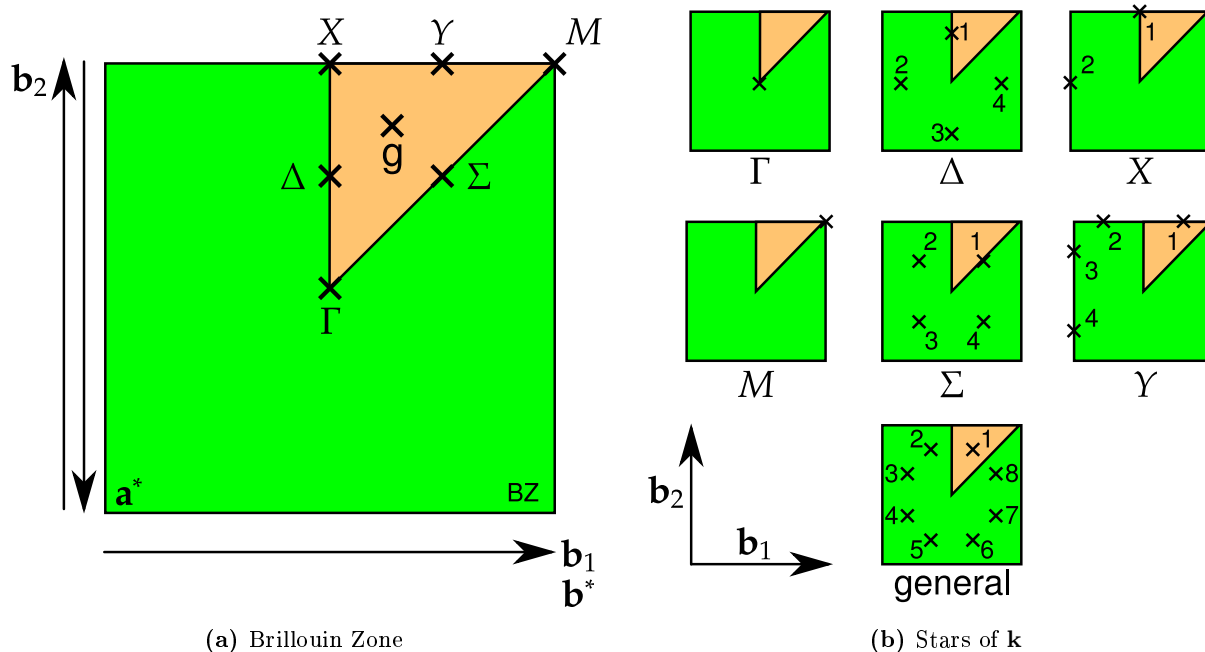


Figure F.4: The BZ and irreducible wedge of the Brillouin zone (IBZ) together with the possible stars of vectors $\mathbf{k} \in \text{IBZ}$. The numbers denote different wave vectors in the stars. Equivalent positions differ by a reciprocal lattice translation and have not been plotted.

Wyckoff letter	label ITA	ITA	PLT	label PLT	$G_{0\mathbf{q}} \cong$
1a	a_1	0, 0	0, 0	$a_1 \leftarrow$	C_{4v}
1b	b_1	1/2, 1/2	1/2, 1/2	$b_1 \leftarrow$	C_{4v}
2c	c_1	1/2, 0	0, 1/2	$c_1 \leftarrow$	C_{2v}
	c_2	0, 1/2	-1/2, 0	c_2	
4d	d_1	x, x	$x, -x$	d_4	$C_{1h}, \sigma = \sigma_d$
	d_2	$-x, -x$	$-x, x$	d_2	
	d_3	$-x, x$	x, x	$d_1 \leftarrow$	
	d_4	$x, -x$	$-x, -x$	d_3	
4e	e_1	$x, 0$	$0, -x$	e_3	$C_{1h}, \sigma = \sigma_x$
	e_2	$-x, 0$	$0, x$	$e_1 \leftarrow$	
	e_3	$0, x$	$x, 0$	e_4	
	e_4	$0, -x$	$-x, 0$	e_2	
4f	f_1	$x, 1/2$	$-1/2, -x$	f_4	$C_{1h}, \sigma = \sigma_y$
	f_2	$-x, 1/2$	$-1/2, x$	f_3	
	f_3	$1/2, x$	$x, 1/2$	$f_1 \leftarrow$	
	f_4	$1/2, -x$	$-x, 1/2$	f_2	
8g	g	x, y	—		

Table F.4: Wyckoff positions in ITA and PLT coordinates and labeling. The arrows \leftarrow denote the particular positions whose site symmetry group irreps were used to label the Wannier function symmetries of Figs. F.8 and F.9.

this work (C_{2v} , Tab. F.3)	A_1	A_2	B_2	B_1
SITESYM (2mm)	A_1	A_2	B_1	B_2

(a) Notation for C_{2v} (2mm) irreps

little co-group irrep (C_{4v} , Tab. F.3)	A_1	B_1	B_2	A_2	E
induces in SITESYM	*GM1	*GM2	*GM3	*GM4	*GM5

(b) Notation for Γ -point and M -point irreps of space group

little co-group irrep (C_{2v} , Tab. F.3)	A_1	A_2	B_1	B_2
induces in SITESYM	*X1	*X2	*X3	*X4

(c) Notation for X -point irreps of space group

Table F.5: Relations between SITESYM notation and the notation used in this work. For explanation, see text.

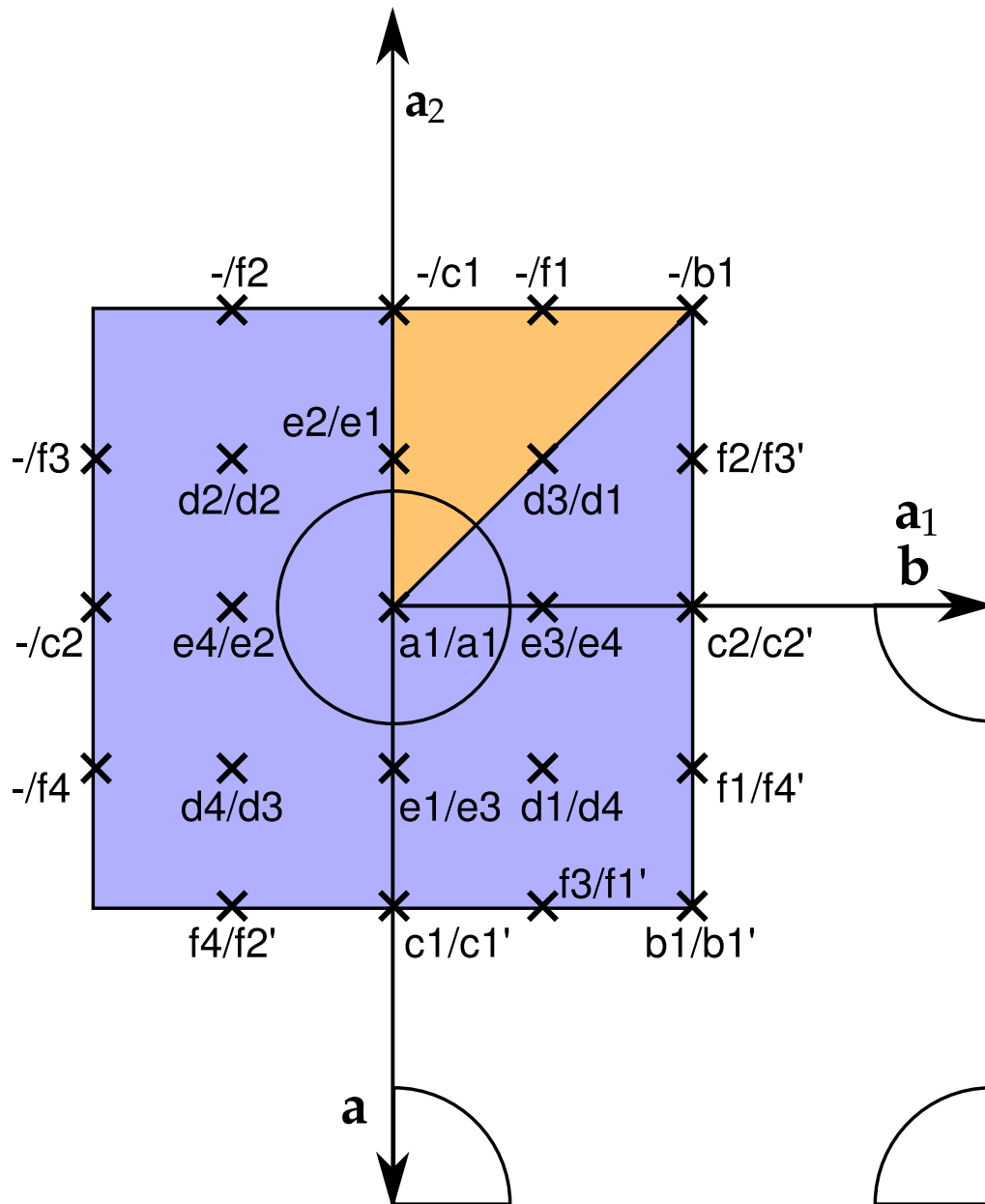


Figure F.5: Nomenclature and numbering scheme for ITA (first) and PLT (second) coordinates. Primed labels are the Wyckoff positions of Fig. F.3b shifted by a lattice translation.

Letter	ITA	PLT	\mathbf{k}_{HS}	$G_{0\mathbf{k}_{\text{HS}}}$
Γ	0,0	0,0	Γ, M	C_{4v}
X	-1/2,0	0,1/2	X	$C_{2v}, \sigma_x = \sigma_x, \sigma_y = \sigma_y$
M	-1/2,1/2	1/2,1/2	Δ	$C_{1h}, \sigma = \sigma_x$
			Y	$C_{1h}, \sigma = \sigma_y$
			Σ	$C_{1h}, \sigma = \sigma_d$

Table F.6: High symmetry points in the BZ in PLT and ITA reciprocal lattice vectors. The little co-groups $G_{0\mathbf{k}_{\text{HS}}}$ for the particular choices of high symmetry point coordinates are given as well. Equations denote the connection between classes of Tab. F.3 (left hand sides) and transforms of Fig. F.1 (right hand sides) that have been used to construct Tab. 2.1. Example: At Σ , class σ of C_{1h} has the meaning σ_d to identify the irreps of the Bloch modes (cf. Figs. F.6 and F.7).

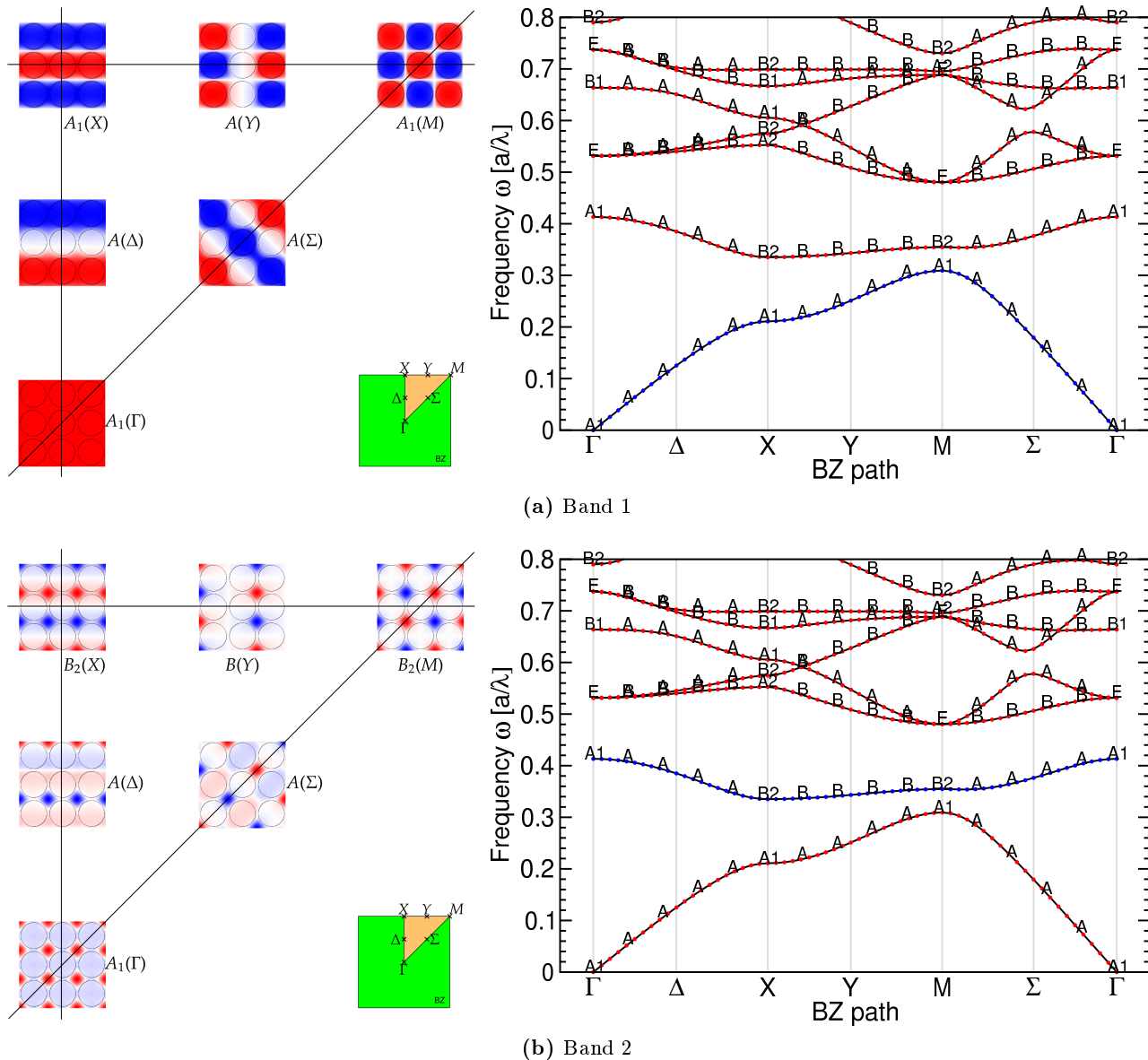
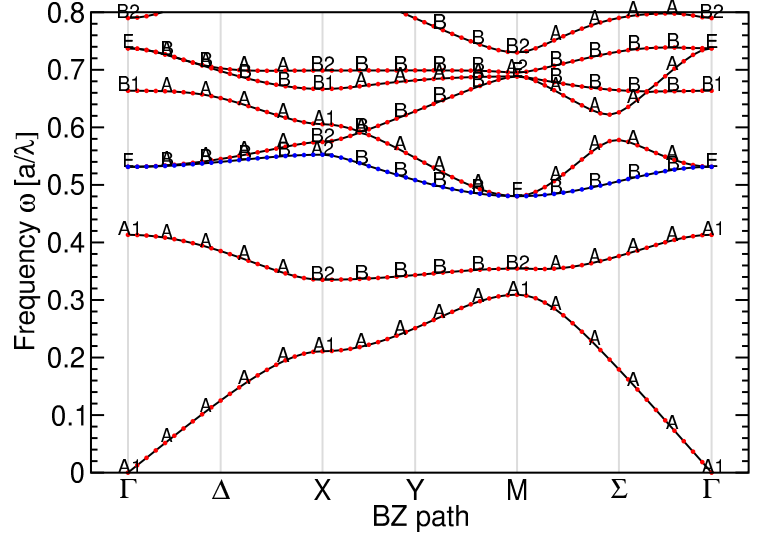
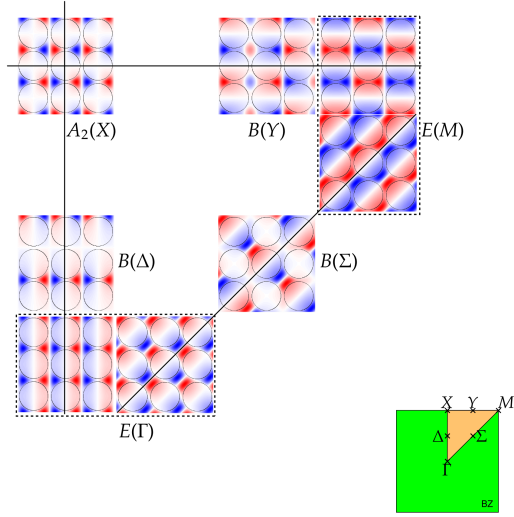


Figure F.6: Plots and little co-group irreps $D^{(k\alpha)}$ of Bloch modes (real parts) in the square lattice model system.



(a) Band 3

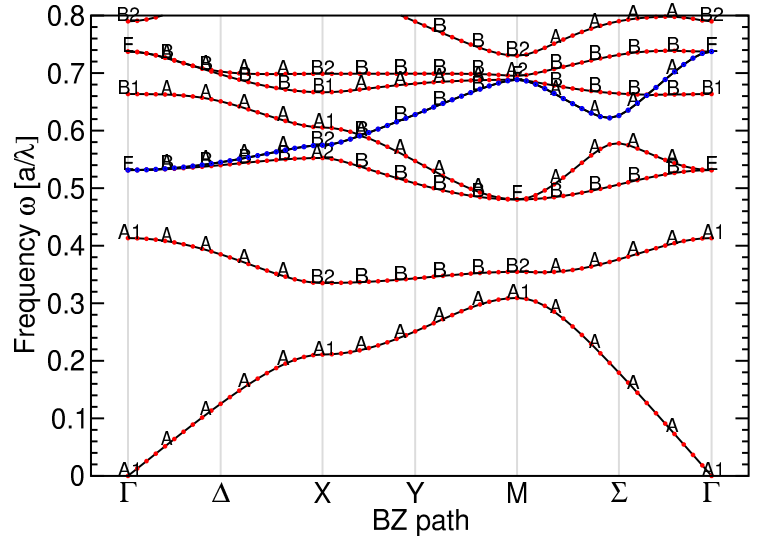
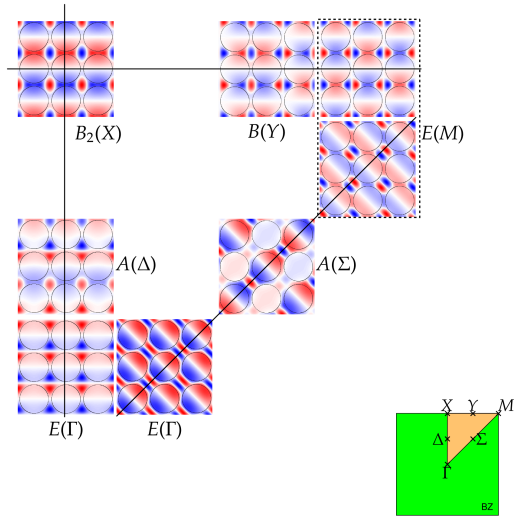

 (b) Band 4 (starting with the 4th frequency ordered Bloch mode at Γ)

Figure F.7: Plots and little co-group irreps $D^{(\mathbf{k}\alpha)}$ of Bloch modes (real parts) in the square lattice model system. Note that starting in Γ and following the Bloch modes continuously along ΓX in band 4 may not lead to the same Bloch modes at the Γ -point.

F.3.1 Possible Site Symmetry Group Representations $D^{(\mathbf{q}\beta)}$

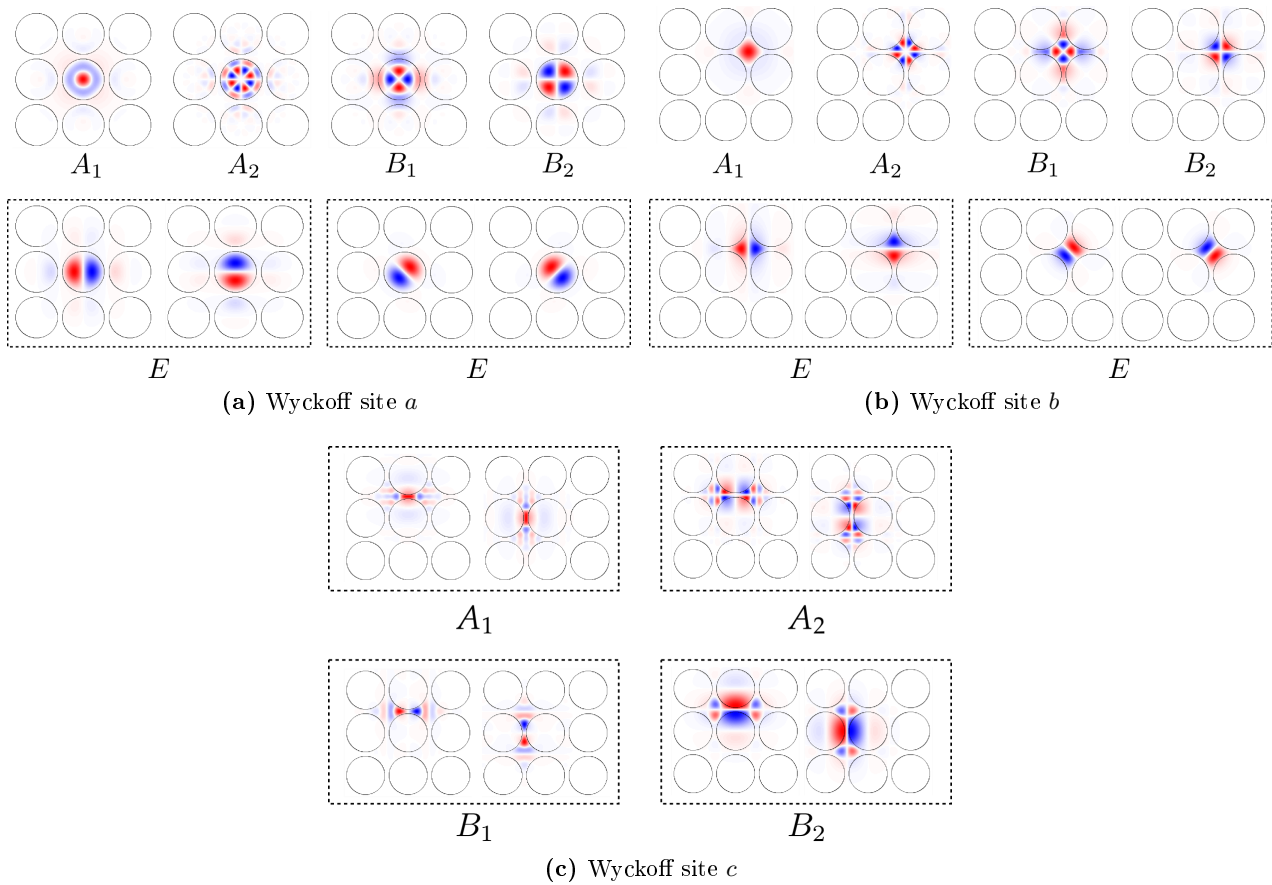


Figure F.8: Examples for the possible Wannier function symmetries based on the irreps $D^{(\mathbf{q}\beta)}$ of the site symmetry groups $G_{\mathbf{q}}$ for the Wyckoff sets in one WSC from Fig. F.3b. The degenerate E reps have been plotted in two orientations for illustrative reasons, i. e., they show two equivalent reps. Basis functions belonging to the same degenerate rep are framed by a dashed box. The centers of the functions have been chosen to coincide with the convention from Fig. F.3b. The functions at position \mathbf{q}_1 have been used to label the irrep and induce the other functions of the basis set. As an example if c'_2 had been used instead of c_1 to label the irreps, the labels $B_1(c)$ and $B_2(c)$ were interchanged. To avoid this confusion, the extensive definitions of this appendix were necessary.

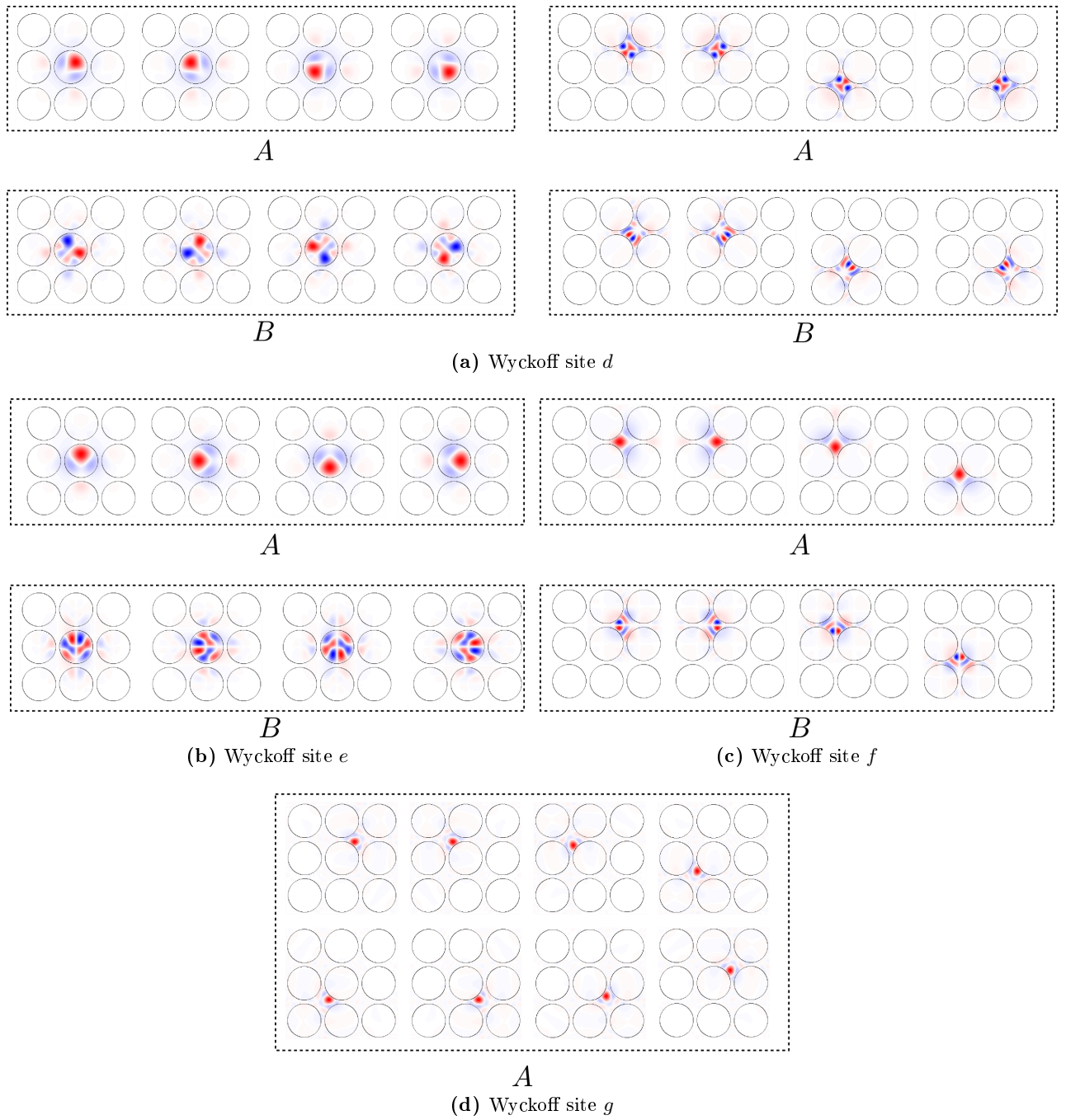


Figure F.9: See caption of Fig. F.8 for explanation. For Wyckoff site d , two separate sets of basis functions have been shown. They are not related by a unitary transform.

F.4 Triangular Lattice: P6mm (C_{6v})

This is the space group P6mm (183, international notation) which consists of translations along the primitive lattice translations (B.6) and the orthogonal transforms of the point group C_{6v} (see Fig. F.10b).

Analogously to Sec. F.3, we need transformation matrices between the PLT coordinates \mathbf{a}_i (B.6) and the ITA coordinates

$$\mathbf{a} = -\frac{1}{2}\hat{\mathbf{x}} - \frac{\sqrt{3}}{2}\hat{\mathbf{y}}, \quad \mathbf{b} = a\hat{\mathbf{x}}, \quad (\text{F.17})$$

By (F.16), this leads to the reciprocal primitive lattice translations in ITA coordinates,

$$\mathbf{a}^* = -\hat{\mathbf{y}}, \quad \mathbf{b}^* = \frac{\sqrt{3}}{2}\hat{\mathbf{x}} - \frac{1}{2}\hat{\mathbf{y}}, \quad (\text{F.18})$$

The direct space coordinates are transformed via

$$M_{\text{ITA} \leftarrow \text{PLT}} := \begin{pmatrix} 0 & -1 \\ 1 & -1 \end{pmatrix}, \quad M_{\text{PLT} \leftarrow \text{ITA}} := M_{\text{ITA} \leftarrow \text{PLT}}^{-1} = \begin{pmatrix} -1 & 1 \\ -1 & 0 \end{pmatrix}, \quad (\text{F.19})$$

and the reciprocal space coordinates are transformed via

$$M_{\text{ITA} \leftarrow \text{PLT}} := \begin{pmatrix} -1 & -1 \\ 1 & 0 \end{pmatrix}, \quad M_{\text{PLT} \leftarrow \text{ITA}} := M_{\text{ITA} \leftarrow \text{PLT}}^{-1} = \begin{pmatrix} 0 & 1 \\ -1 & -1 \end{pmatrix}. \quad (\text{F.20})$$

These matrices have been used to construct Tabs. F.7, F.10 and F.11.

Class	Symbol	ITA	Meaning
E	E	x, y	Identity
C_2	C_2	$-x, -y$	Rotation of $\frac{2\pi}{2} \equiv 180^\circ$
$2C_3$	C_3	$-y, x - y$	Rotation of $\frac{2\pi}{3} \equiv 120^\circ$
$2C_3$	C_{-3}	$-x + y, -x$	Rotation of $\frac{2\pi}{3} \equiv -120^\circ$
$2C_6$	C_6	$x - y, x$	Rotation of $\frac{2\pi}{6} \equiv 60^\circ$
$2C_6$	C_{-6}	$y, -x + y$	Rotation of $\frac{2\pi}{6} \equiv -60^\circ$
$3\sigma_x$	σ_x	$x, x - y$	Reflection with normal \mathbf{a}_1
$3\sigma_x$	$\sigma_{x'}$	$-y, -x$	Reflection with normal \mathbf{a}_2
$3\sigma_x$	$\sigma_{x''}$	$-x + y, y$	Reflection with normal $\mathbf{a}_1 + \mathbf{a}_2$
$3\sigma_y$	σ_y	$-x, -x + y$	Reflection with normal $\mathbf{a}_1 + 2\mathbf{a}_2$
$3\sigma_y$	$\sigma_{y'}$	y, x	Reflection with normal $2\mathbf{a}_1 + \mathbf{a}_2$
$3\sigma_y$	$\sigma_{y''}$	$x - y, -y$	Reflection with normal $-\mathbf{a}_1 + \mathbf{a}_2$
σ			One of $\sigma_x, \sigma_{x'}, \sigma_{x''}, \sigma_y, \sigma_{y'}, \sigma_{y''}$. Depends on the particular realization.

Table F.7: List of symmetry operations of the group C_{6v} and its subgroups. The number before the class denotes the number of representatives in that class.

The interpretation of the SITESYM output has to be interpreted correctly as in the square lattice case. The differences in notation between the SITESYM output and the notation used in this work is listed in Tab. F.9.

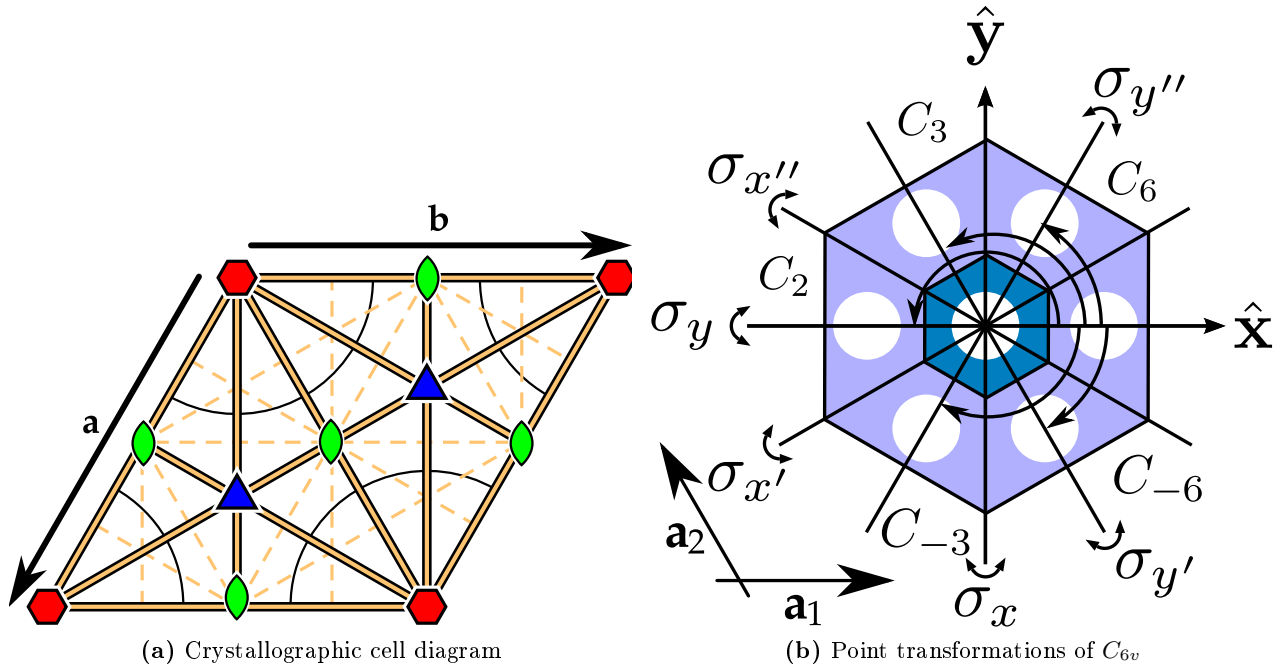


Figure F.10: (a) Crystallographic cell diagram of the $P6mm$ space group with ITA coordinate vectors. The hole is located in the corners of the cell. (b) Point transforms of C_{6v} with origin in the center of a hole with PLT coordinates.

C_{6v}	E	$2C_6$	$2C_3$	C_2	$3\sigma_y$	$3\sigma_x$
A_1	1	1	1	1	1	1
A_2	1	1	1	1	-1	-1
B_1	1	-1	1	-1	1	-1
B_2	1	-1	1	-1	-1	1
E_1	2	1	-1	-2	0	0
E_2	2	-1	-1	2	0	0

C_{2v}	E	C_2	σ_y	σ_x
A_1	1	1	1	1
A_2	1	1	-1	-1
B_1	1	-1	1	-1
B_2	1	-1	-1	1

C_{3v}	E	$2C_3$	3σ
A_1	1	1	1
A_2	1	1	-1
E	2	-1	0

C_{1h}	E	σ
A	1	1
B	1	-1

C_1	E
A	1

Table F.8: Character tables for the conjugacy classes and irreducible representations of the point group C_{6v} and its subgroups. The elements are defined by Tab. F.2 and Fig. F.1b. The geometric transform associated with σ depends on the actual realization of the abstract group C_{1h} .

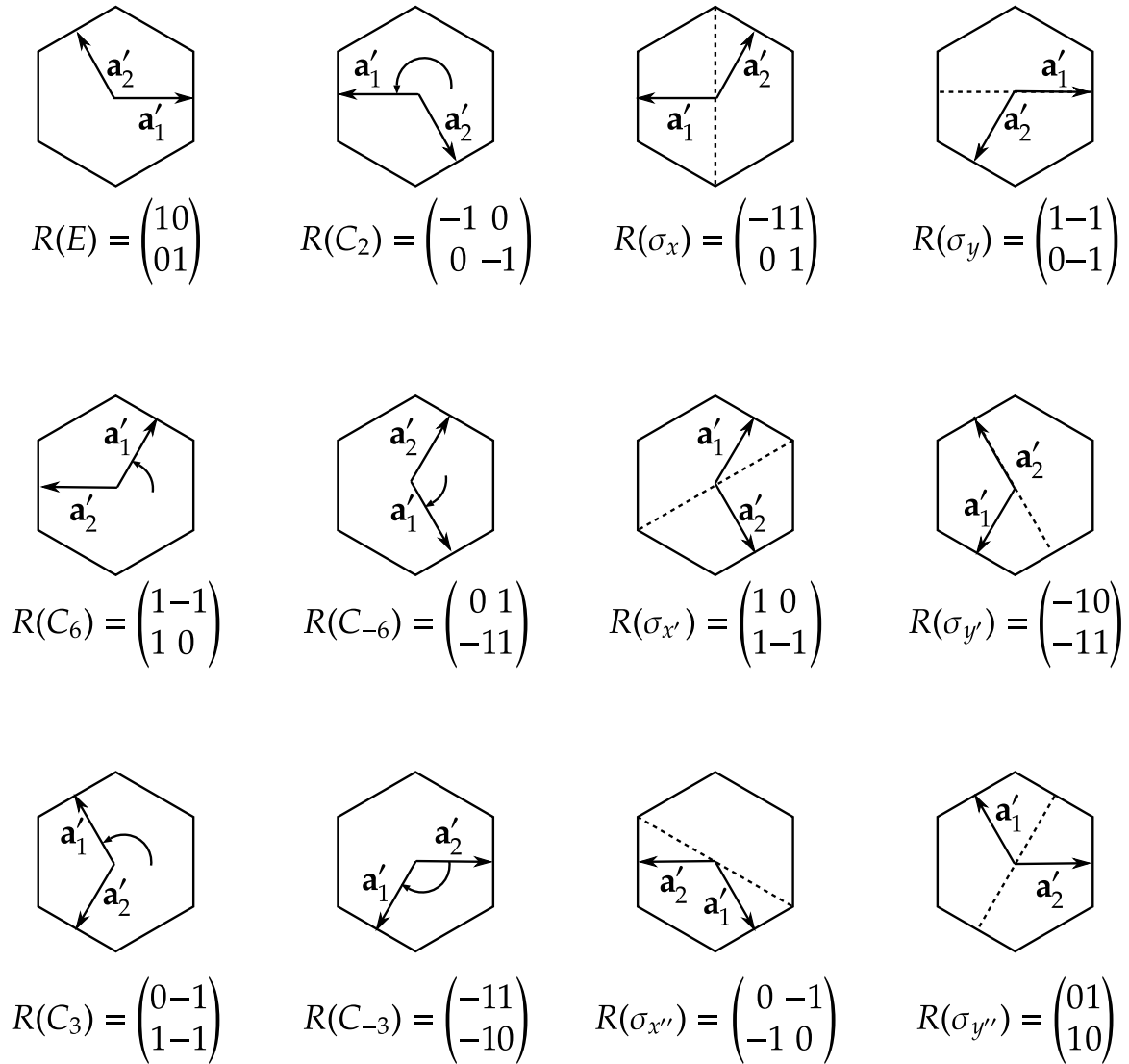


Figure F.11: The orthogonal transformation matrices for C_{6v} in the basis of the primitive lattice translations \mathbf{a}_i .

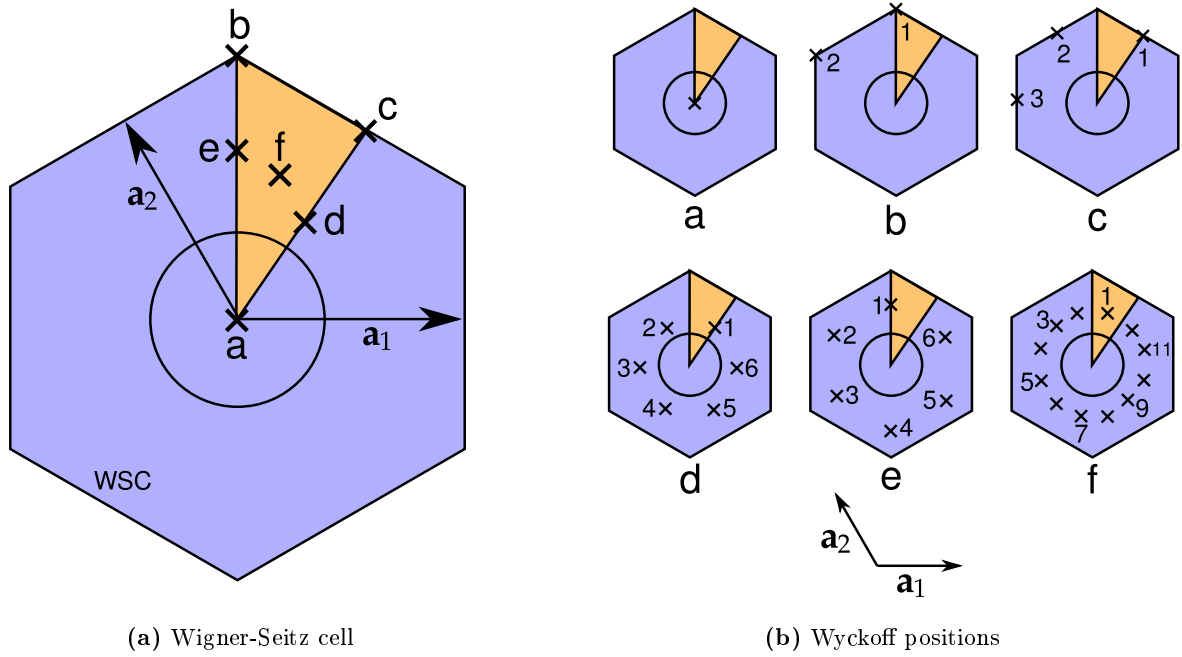


Figure F.12: The Wigner-Seitz cell of the triangular lattice and its Wyckoff positions. See also caption of Fig. F.3.

this work (C_{2v} , Tab. F.8)	A_1	A_2	B_2	B_1
SITESYM (2mm)	A_1	A_2	B_1	B_2

(a) Notation for C_{2v} (2mm) irreps

little co-group irrep (C_{6v} , Tab. F.3)	A_1	A_2	B_2	B_1	E_2	E_1
induces in SITESYM	*GM1	*GM2	*GM3	*GM4	*GM5	*GM6

(b) Notation for Γ -point irreps of space group

little co-group irrep (C_{2v} , Tab. F.8)	A_1	A_2	B_1	B_2
induces in SITESYM	*M1	*M2	*M3	*M4

(c) Notation for M -point irreps of space group

little co-group irrep (C_{3v} , Tab. F.8)	A_1	A_2	E
induces in SITESYM	*K1	*K2	*K3

(d) Notation for K -point irreps of space group

Table F.9: Relations between SITESYM notation and the notation used in this work. For explanation, see text.

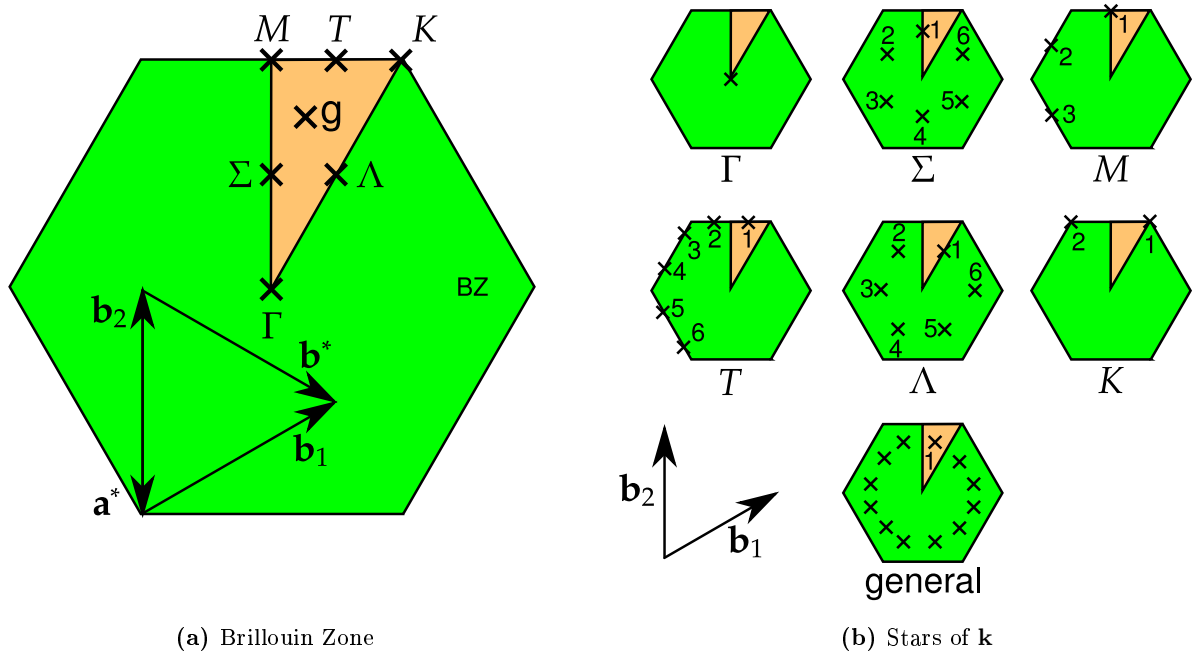


Figure F.13: The BZ and irreducible wedge of the Brillouin zone (IBZ) together with the possible stars of vectors $\mathbf{k} \in \text{IBZ}$. The numbers denote different wave vectors in the stars. Equivalent positions differ by a reciprocal lattice translation and have not been plotted.

Wyckoff letter	label ITA	ITA	PLT	label PLT	$G_{0\mathbf{q}} \cong$
1a	a_1	0, 0	0, 0	$a_1 \leftarrow$	C_{6v}
2b	b_1	1/3, 2/3	1/3, -1/3	$b_1 \leftarrow$	$C_{3v}, 3\sigma = 3\sigma_x$
	b_2	2/3, 1/3	-1/3, -2/3	b_2	
3c	c_1	1/2, 0	-1/2, -1/2	c_1	C_{2v}
	c_2	0, 1/2	1/2, 0	$c_3 \leftarrow$	
	c_3	1/2, 1/2	0, -1/2	c_2	
6d	d_1	$x, 0$	$-x, -x$	d_4	$C_{1h}, \sigma = \sigma_y$
	d_2	$0, x$	$x, 0$	$d_6 \leftarrow$	
	d_3	$-x, -x$	$0, x$	d_2	
	d_4	$-x, 0$	x, x	d_1	
	d_5	$0, -x$	$-x, 0$	d_3	
	d_6	x, x	$0, -x$	d_5	
6e	e_1	$x, -x$	$-2x, -x$	e_3	$C_{1h}, \sigma = \sigma_x$
	e_2	$x, 2x$	$x, -x$	e_5	
	e_3	$-2x, -x$	$x, 2x$	$e_1 \leftarrow$	
	e_4	$-x, x$	$2x, x$	e_6	
	e_5	$-x, -2x$	$-x, x$	e_2	
	e_6	$2x, x$	$-x, -2x$	e_4	
12f	f	x, y	—		

Table F.10: Wyckoff positions in ITA and PLT coordinates and labeling. The arrows \leftarrow denote the particular positions whose site symmetry group irreps were used to label the Wannier function symmetries of Figs. F.15, F.16, and F.17.

Letter	ITA	PLT	\mathbf{k}_{HS}	$G_{0\mathbf{k}_{\text{HS}}}$
Γ	0, 0	0, 0	Γ	C_{6v}
M	-1/2, 0	0, 1/2	M	$C_{2v}, \sigma_x = \sigma_x, \sigma_y = \sigma_y$
K	-2/3, 1/3	1/3, 1/3	K	$C_{3v}, 3\sigma = 3\sigma_y$
			Σ	$C_{1h}, \sigma = \sigma_x$
			T	$C_{1h}, \sigma = \sigma_y$
			Λ	$C_{1h}, \sigma = \sigma_{y''}$

Table F.11: High symmetry points in the BZ in PLT and ITA reciprocal lattice vectors. The little co-groups $G_{0\mathbf{k}_{\text{HS}}}$ for the particular choices of high symmetry point coordinates are given as well. See also caption of Tab. F.11.

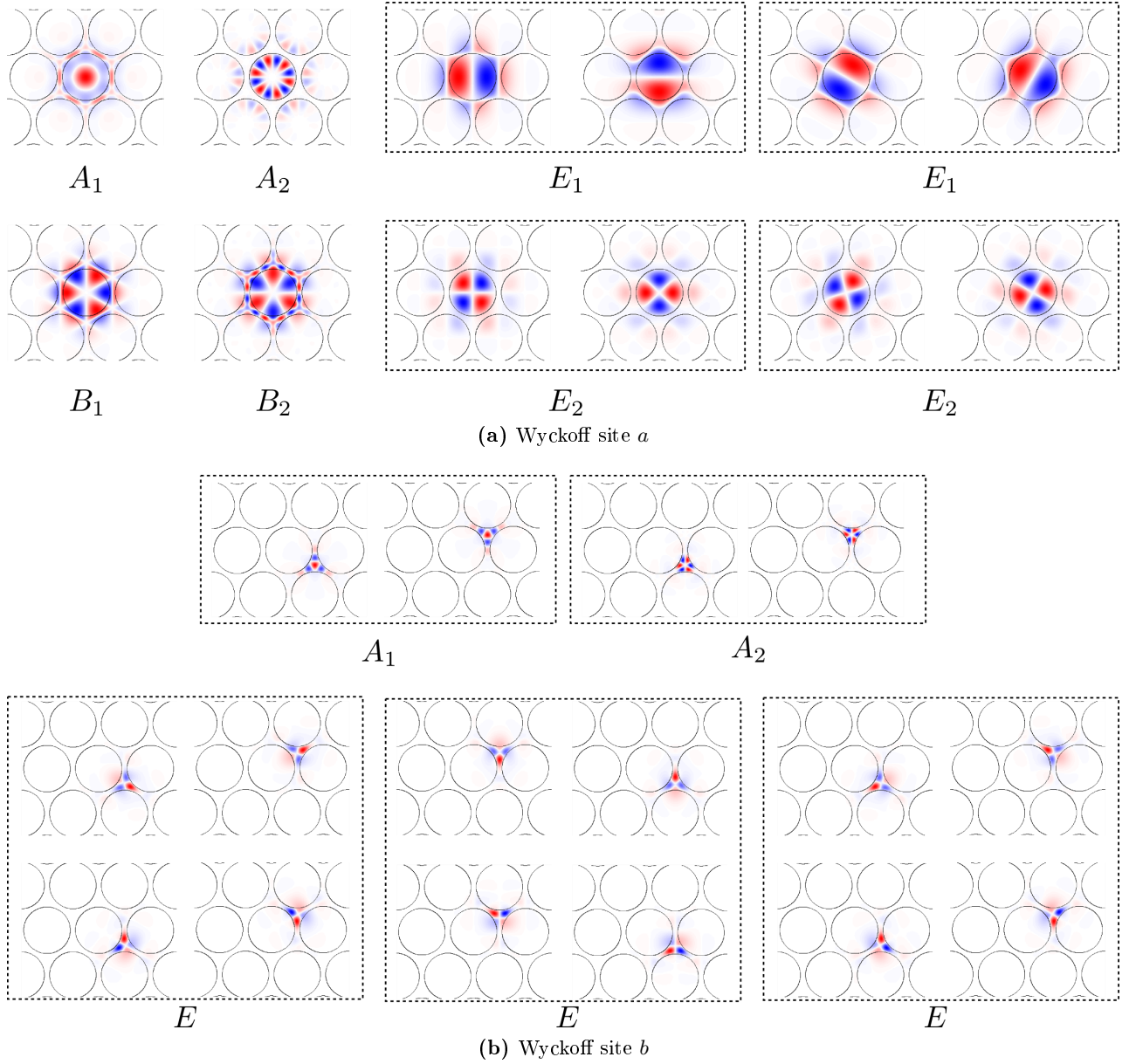
F.4.1 Possible Site Symmetry Group Representations $D^{(\mathbf{q}\beta)}$


Figure F.15: Examples for the possible Wannier function symmetries based on the irreps $D^{(\mathbf{q}\beta)}$ of the site symmetry groups $G_{\mathbf{q}}$ for the Wyckoff sets in one WSC from Fig. F.12b. The degenerate E reps have been plotted in two (three) orientations for illustrative reasons, i. e., they show two (three) equivalent reps. Basis functions belonging to the same degenerate rep are framed by a dashed box. The centers of the functions have been chosen to coincide with the convention from Fig. F.3b.

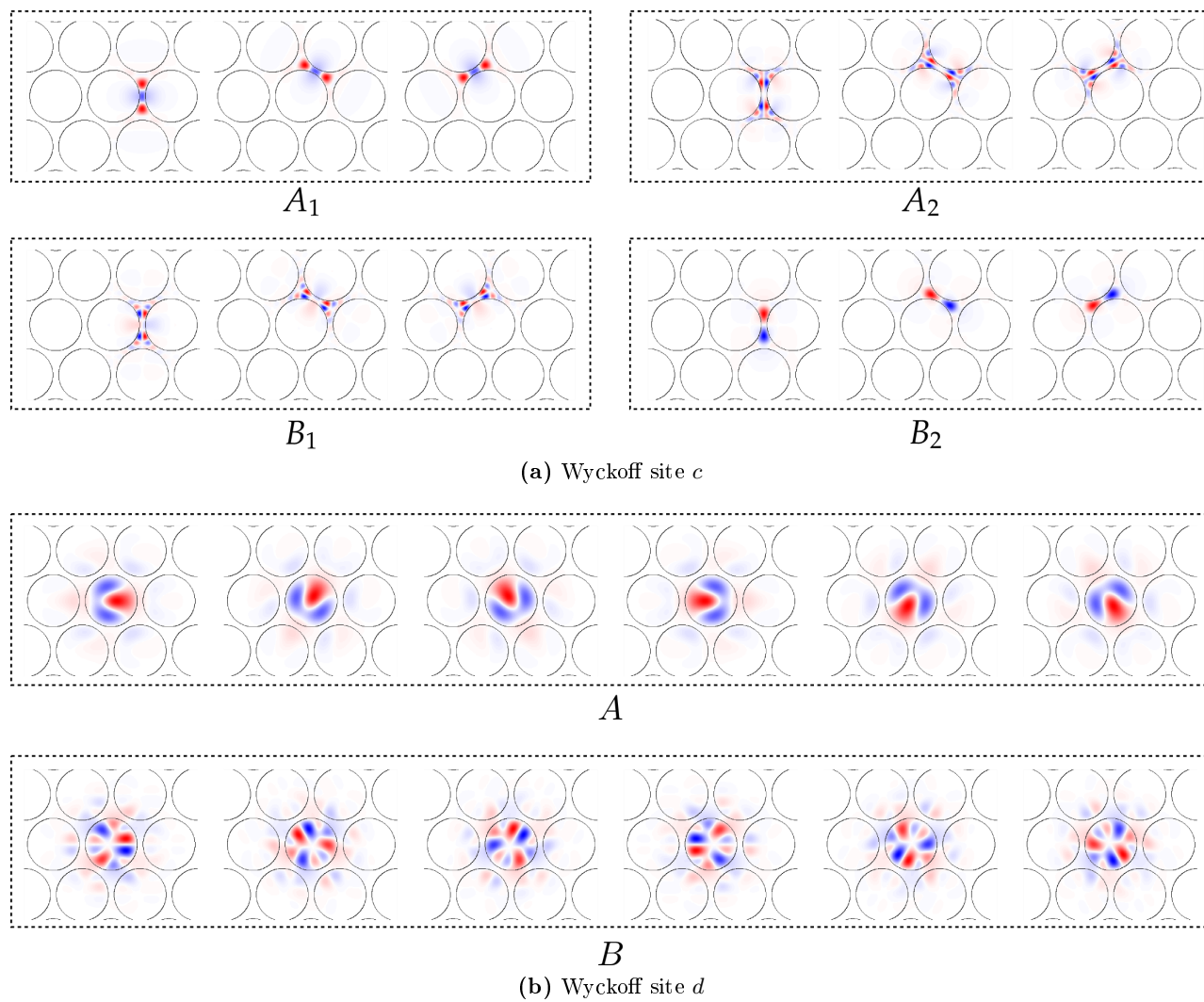


Figure F.16: See caption of Fig. F.15.

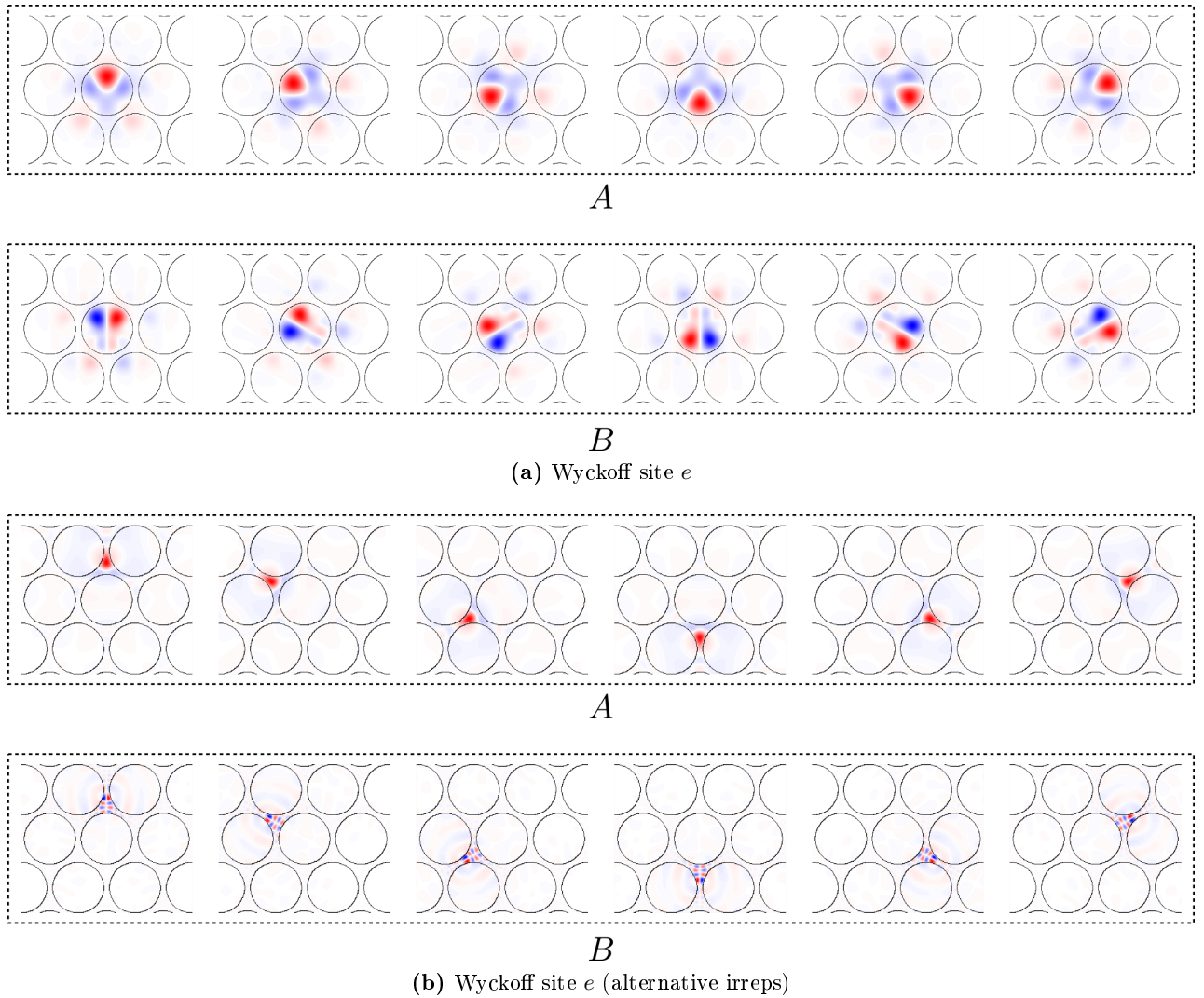
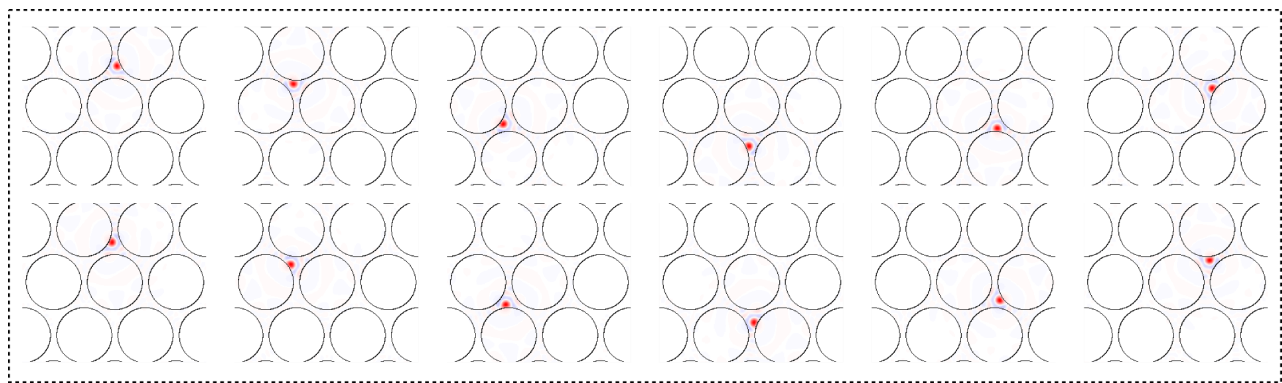


Figure F.17: Here, two different sets of basis functions for the same representations are shown. See also caption of Fig. F.15.



general
(a) Wyckoff site f

Figure F.18: See caption of Fig. F.15.

List of Acronyms

- ABF** auxiliary basis function, 143, 149, 155, 159–161, 163, 164, 169, 177, 179, 211
- BZ** Brillouin zone, 5, 6, 20, 37, 42–44, 50, 52, 54, 55, 58, 64, 70, 181, 182, 191, 196, 199, 221, 222, 232
- CG** conjugate gradient, 53, 66
- CROW** coupled-resonator optical wave guide, 115
- FBF** Fourier-Bessel function, 138, 139, 145–147, 149, 152, 154, 155, 159, 161, 167–169, 177, 205
- FDS** finite difference stencil, 207
- HCS** Ho-Chan-Soukoulis, 207
- IBZ** irreducible wedge of the Brillouin zone, 5, 37, 93, 221, 232
- IWF** inverse system Wannier function, 139–141, 143, 148, 152, 154, 167, 177
- LC** liquid crystal, 10, 11, 20
- MP** Monkhorst-Pack, 52, 54, 58, 65, 69, 82–84, 114, 121–123, 127, 129, 196
- MPB** MIT photonic bands, xii, 16, 87, 123, 131, 133, 136, 143, 144, 147, 154, 155, 159, 163, 164, 168, 177, 195, 199, 201–204, 206, 207
- MV** Marzari-Vanderbilt, 82–84, 86, 87, 94, 129, 178
- 1D** one dimensional, 21
- PBG** photonic band gap, vii, viii
- PC** photonic crystal, vii–xi, 4, 5, 7–9, 11, 13–17, 21, 25, 28, 33, 36, 41, 44, 49, 84, 93–95, 101, 108, 111, 112, 114–116, 118, 119, 121, 122, 127, 129, 131–133, 136, 138, 139, 141, 145, 152, 161, 177–179, 181, 182
- PLT** primitive lattice translation, 44, 195
- PWE** plane wave expansion, 207
- SDM** supercell defect mode, 152, 154, 167, 177
- SI** International System, 1, 7
- SMV** Souza-Marzari-Vanderbilt, 57, 74, 86, 95, 129, 130, 143, 161, 178
- SPS** sub-pixel smoothing, 106, 122, 123, 146, 195, 199, 201, 203, 204, 207

- TE** transverse electric, viii, x, xi, 9, 11, 13, 14, 16, 17, 25, 50, 58, 69, 132, 133, 136, 138, 159, 177, 179, 207
- 3D** three dimensional, 21, 22, 44, 114, 138, 139, 141, 152, 161
- TM** transverse magnetic, viii, x, xi, 9, 13, 25, 132, 133, 159, 177, 179, 207
- 2D** two dimensional, 5, 7–9, 13–15, 21, 22, 93, 111, 114, 115, 138, 139, 159, 161
- WF** Wannier function, ix–xii, 20–22, 36, 40–43, 47–50, 52–54, 56–58, 63, 64, 66–70, 73, 74, 79, 80, 82–84, 86, 87, 91–99, 101, 103, 108, 110–115, 117, 119, 121–123, 127, 129–133, 136, 138–149, 154, 155, 159–161, 163, 165–169, 173, 174, 177–179, 182, 183, 199, 202, 205, 207, 211, 214
- WSC** Wigner-Seitz cell, 5, 14, 21, 36, 44, 54, 58, 66, 73, 74, 91–93, 191, 230, 239

Bibliography

- [1] J. Clerk Maxwell. A dynamical theory of the electromagnetic field. *Philosophical Transactions of the Royal Society of London*, 155:pp. 459–512, 1865. ISSN 02610523. URL <http://www.jstor.org/stable/108892>.
(Cited on page vii.)
- [2] A. Einstein. Über einen die Erzeugung und Verwandlung des Lichtes betreffenden heuristischen Gesichtspunkt. *Ann. Phys.*, 322(6):pp. 132–148, 1905. URL <http://dx.doi.org/10.1002/andp.19053220607>.
(Cited on page vii.)
- [3] Sajeev John. Strong localization of photons in certain disordered dielectric superlattices. *Phys. Rev. Lett.*, 58(23):2486–2489, Jun 1987. doi: 10.1103/PhysRevLett.58.2486. URL <http://link.aps.org/doi/10.1103/PhysRevLett.58.2486>.
(Cited on page vii.)
- [4] Eli Yablonovitch. Inhibited spontaneous emission in solid-state physics and electronics. *Phys. Rev. Lett.*, 58(20):2059–2062, May 1987. doi: 10.1103/PhysRevLett.58.2059. URL <http://link.aps.org/doi/10.1103/PhysRevLett.58.2059>.
(Cited on page vii.)
- [5] V. A. Tolmachev, T. S. Perova, E. V. Astrova, B. Z. Volchek, and J. K. Vij. Vertically etched silicon as 1d photonic crystal. *phys. stat. sol. (a)*, 197(2):544–548, 2003. doi: 10.1002/pssa.200306561. URL <http://dx.doi.org/10.1002/pssa.200306561>.
(Cited on page vii.)
- [6] Sharee McNab, Nikolaj Moll, and Yurii Vlasov. Ultra-low loss photonic integrated circuit with membrane-type photonic crystal waveguides. *Opt. Express*, 11(22):2927–2939, Nov 2003. doi: 10.1364/OE.11.002927. URL <http://www.opticsexpress.org/abstract.cfm?URI=oe-11-22-2927>.
(Cited on page vii.)
- [7] Markus Deubel, Georg von Freymann, Martin Wegener, Suresh Pereira, Kurt Busch, and Costas M. Soukoulis. Direct laser writing of three-dimensional photonic-crystal templates for telecommunications. *Nat. Mater.*, 3:444–447, 2004. doi: 10.1038/nmat1155. URL <http://dx.doi.org/10.1038/nmat1155>.
(Cited on page vii.)
- [8] Harry J. R. Dutton. *Understanding optical communications*. The ITSO networking series. Prentice Hall PTR, Upper Saddle River, NJ, 1998. ISBN 0-13-020141-3. URL http://www.ubka.uni-karlsruhe.de/hylib-bin/suche.cgi?opacdb=UBKA_OPAC&nd=8211453&session=1377180909. Includes index.
(Cited on page viii.)

- [9] Alcatel-lucent bell labs announces new optical transmission record and breaks 100 petabit per second kilometer barrier, sep 2009. URL <http://www.alcatel-lucent.com/>.
(Cited on page viii.)
- [10] Toshihiko Baba. Photonic crystals: Remember the light. *Nat. Photon.*, 1(1):11–12, 2007. URL <http://dx.doi.org/10.1038/nphoton.2006.58>.
(Cited on page viii.)
- [11] P. W. Nolte, D. Pergande, S. L. Schweizer, M. Geuss, R. Salzer, B. T. Makowski, M. Steinhart, P. Mack, D. Hermann, K. Busch, C. Weder, and R. B. Wehrspohn. Local infiltration of individual pores with dyes in 2d macroporous silicon photonic crystals. *Adv. Mater.*, 2010. doi: 10.1002/adma.201001718. URL <http://dx.doi.org/10.1002/adma.201001718>.
(Cited on pages ix and 16.)
- [12] P. Nolte, D. Pergande, S.L. Schweizer, R.B. Wehrspohn, M. Geussy, M. Steinhart, and R. Salzer. Local infiltration of individual pores with dyes in 2d macroporous silicon photonic crystals. pages 234–236, sep. 2008. doi: 10.1109/GROUP4.2008.4638156. URL http://ieeexplore.ieee.org/xpls/abs_all.jsp?arnumber=4638156.
(Not cited.)
- [13] Francesca Intonti, Silvia Vignolini, Volker Türec, Marcello Colocci, Paolo Bettotti, Lorenzo Pavesi, Stefan L. Schweizer, Ralf Wehrspohn, and Diederik Wiersma. Rewritable photonic circuits. *Applied Physics Letters*, 89(21):211117, 2006. doi: 10.1063/1.2392720. URL <http://link.aip.org/link/?APL/89/211117/1>.
(Cited on pages ix and 16.)
- [14] Sergei F. Mingaleev, Matthias Schillinger, Daniel Hermann, and Kurt Busch. Tunable photonic crystal circuits: concepts and designs based on single-pore infiltration. *Opt. Lett.*, 29(24):2858–2860, Dec 2004. doi: 10.1364/OL.29.002858. URL <http://ol.osa.org/abstract.cfm?URI=ol-29-24-2858>.
(Cited on pages ix and 20.)
- [15] K. Busch, G. von Freymann, S. Linden, S.F. Mingaleev, L. Tkeshelashvili, and M. Wegener. Periodic nanostructures for photonics. *Physics Reports*, 444(3-6):101 – 202, 2007. ISSN 0370-1573. doi: DOI:10.1016/j.physrep.2007.02.011. URL <http://www.sciencedirect.com/science/article/B6TVP-4N66R3V-1/2/74ce90699cd185d5fb309738ea953a37>.
(Cited on page ix.)
- [16] Susan C. Taflove, Allen ; Hagness. *Computational electrodynamics : the finite-difference time-domain method*. Artech House antennas and propagation library. Artech House, Boston [u.a.], 3. ed. edition, 2005. ISBN 1-58053-832-0 ; 978-1-58053-832-9. URL http://www.ubka.uni-karlsruhe.de/hylib-bin/suche.cgi?opacdb=UBKA_OPAC&nd=12163134&session=838318130. Includes bibliographical references and index. - Previous ed.: 2000; cased. - : £85.00 : CIP entry (May).
(Cited on page ix.)
- [17] Steven Johnson and John Joannopoulos. Block-iterative frequency-domain methods for maxwell's equations in a planewave basis. *Opt. Express*, 8(3):173–190, Jan 2001. doi: 10.1364/OE.8.000173. URL <http://www.opticsexpress.org/abstract.cfm?URI=oe-8-3-173>.
(Cited on page ix.)

- [18] K. M. Ho, C. T. Chan, and C. M. Soukoulis. Existence of a photonic gap in periodic dielectric structures. *Phys. Rev. Lett.*, 65(25):3152–3155, Dec 1990. doi: 10.1103/PhysRevLett.65.3152. URL <http://link.aps.org/doi/10.1103/PhysRevLett.65.3152>.
(Cited on pages ix and 209.)
- [19] Esteban Moreno, Daniel Erni, and Christian Hafner. Modeling of discontinuities in photonic crystal waveguides with the multiple multipole method. *Phys. Rev. E*, 66(3):036618, Sep 2002. doi: 10.1103/PhysRevE.66.036618. URL <http://link.aps.org/doi/10.1103/PhysRevE.66.036618>.
(Cited on page ix.)
- [20] Kazuo Ohtaka and Yukito Tanabe. Photonic band using vector spherical waves. i. various properties of bloch electric fields and heavy photons. *Journal of the Physical Society of Japan*, 65(7):2265–2275, 1996. doi: 10.1143/JPSJ.65.2265. URL <http://jpsj.ipap.jp/link?JPSJ/65/2265/>.
(Cited on page ix.)
- [21] Jian-Ming Jin. *The finite element method in electromagnetics*. Wiley, New York [u.a.], 2. ed. edition, 2002. ISBN 0-471-43818-9. URL <http://swbplus.bsz-bw.de/bsz108076067cov.htm>. Includes bibliographical references and index. - Previous ed.: 1993. - A Wiley-Interscience publication.; : No price.
(Cited on pages ix and 22.)
- [22] Clive A. J. Fletcher. *Computational Galerkin methods*. Springer series in computational physics. Springer, New York [u.a.], 1984. ISBN 3-540-12633-3 ; 0-387-12633-3. URL http://www.ubka.uni-karlsruhe.de/hylib-bin/suche.cgi?opacdb=UBKA_OPAC&nd=923178&session=346166926.
(Cited on page ix.)
- [23] Jens Niegemann. *Higher-Order Methods for Solving Maxwells Equations in the Time-Domain*. PhD thesis, University of Karlsruhe, 2009. URL <http://digbib.ubka.uni-karlsruhe.de/volltexte/1000011812>.
(Cited on page ix.)
- [24] D. Mogilevtsev, T.A. Birks, and P.S.J. Russell. Localized function method for modeling defect modes in 2-d photonic crystals. *Lightwave Technology, Journal of*, 17(11):2078 –2081, November 1999. ISSN 0733-8724. doi: 10.1109/50.802997. URL <http://dx.doi.org/10.1109/50.802997>.
(Cited on page x.)
- [25] Tanya M. Monro, D. J. Richardson, N. G. R. Broderick, and P. J. Bennett. Holey optical fibers: An efficient modal model. *J. Lightwave Technol.*, 17(6):1093, Jun 1999. URL <http://jlt.osa.org/abstract.cfm?URI=JLT-17-6-1093>.
(Cited on page x.)
- [26] Gregory H. Wannier. The structure of electronic excitation levels in insulating crystals. *Phys. Rev.*, 52(3):191–197, Aug 1937. doi: 10.1103/PhysRev.52.191. URL http://prola.aps.org/abstract/PR/v52/i3/p191_1.
(Cited on pages x, 20, and 47.)
- [27] Lixin He and David Vanderbilt. Exponential decay properties of wannier functions and related quantities. *Phys. Rev. Lett.*, 86(23):5341–5344, Jun 2001. doi: 10.1103/PhysRevLett.86.5341. URL

<http://link.aps.org/doi/10.1103/PhysRevLett.86.5341>.

(Cited on pages x, 21, and 82.)

- [28] K. M. Leung. Defect modes in photonic band structures: a green's function approach using vector wannier functions. *J. Opt. Soc. Am. B*, 10(2):303–306, 1993. URL <http://josab.osa.org/abstract.cfm?URI=josab-10-2-303>.
(Cited on pages x and 21.)
- [29] Nicola Marzari and David Vanderbilt. Maximally localized generalized wannier functions for composite energy bands. *Phys. Rev. B*, 56(20):12847–12865, Nov 1997. doi: 10.1103/PhysRevB.56.12847. URL <http://link.aps.org/doi/10.1103/PhysRevB.56.12847>.
(Cited on pages x, 22, 47, 48, 52, and 53.)
- [30] Ivo Souza, Nicola Marzari, and David Vanderbilt. Maximally localized wannier functions for entangled energy bands. *Phys. Rev. B*, 65(3):035109, Dec 2001. doi: 10.1103/PhysRevB.65.035109. URL <http://link.aps.org/doi/10.1103/PhysRevB.65.035109>.
(Cited on pages x, 22, and 47.)
- [31] Kurt Busch, Sergei F Mingaleev, Antonio Garcia-Martin, Matthias Schillinger, and Daniel Hermann. The wannier function approach to photonic crystal circuits. *Journal of Physics: Condensed Matter*, 15(30):R1233, 2003. URL <http://stacks.iop.org/0953-8984/15/i=30/a=201>.
(Cited on pages x, 132, 133, and 163.)
- [32] K. Busch, M. Frank, A. Garcia-Martin, D. Hermann, S. F. Mingaleev, M. Schillinger, and L. Tkeshelashvili. A solid state theoretical approach to the optical properties of photonic crystals. *physica status solidi (a)*, 197(3):637–647, 6 2003. URL <http://dx.doi.org/10.1002/pssa.200303111>.
(Cited on pages x, 21, and 179.)
- [33] D. M. Whittaker and M. P. Croucher. Maximally localized wannier functions for photonic lattices. *Physical Review B (Condensed Matter and Materials Physics)*, 67(8):085204, 2003. URL <http://link.aps.org/abstract/PRB/v67/e085204>.
(Not cited.)
- [34] P. Sotirelis and J. D. Albrecht. Numerical simulation of photonic crystal defect modes using unstructured grids and wannier functions. *Phys. Rev. B*, 76(7):075123, Aug 2007. doi: 10.1103/PhysRevB.76.075123. URL <http://prb.aps.org/abstract/PRB/v76/i7/e075123>.
(Cited on page x.)
- [35] Matthias Schillinger. *Maximally localized photonic Wannier functions for the highly efficient description of integrated Photonic Crystal circuits*. PhD thesis, University of Karlsruhe, 2006. URL <http://digbib.ubka.uni-karlsruhe.de/volltexte/1000007183>.
(Cited on pages x, 22, 47, 48, 53, 54, 94, 132, 136, 178, and 179.)
- [36] Jacques Des Cloizeaux. Orthogonal orbitals and generalized wannier functions. *Phys. Rev.*, 129(2):554–566, Jan 1963. doi: 10.1103/PhysRev.129.554. URL http://prola.aps.org/abstract/PR/v129/i2/p554_1.
(Cited on pages x, 22, 39, 42, and 43.)

- [37] E. Krüger. Symmetrische verallgemeinerte Wannierfunktionen. *phys. stat. sol. (b)*, 52:215, 1972. URL <http://www3.interscience.wiley.com/journal/112583201/abstract>. (Cited on pages x, 22, 36, 37, 38, 42, 58, 64, and 93.)
- [38] E. Krüger. Symmetrische verallgemeinerte Wannierfunktionen. *phys. stat. sol. (b)*, 52:519, 1972. URL <http://www3.interscience.wiley.com/journal/112580408/abstract>. (Cited on pages x, 22, 37, 42, 64, and 93.)
- [39] Hiroyuki Takeda, Alongkarn Chutinan, and Sajeew John. Localized light orbitals: Basis states for three-dimensional photonic crystal microscale circuits. *Physical Review B (Condensed Matter and Materials Physics)*, 74(19):195116, 2006. URL <http://link.aps.org/abstract/PRB/v74/e195116>. (Cited on pages x, xi, 132, 133, and 138.)
- [40] Daniel Hermann, Matthias Schillinger, Sergei F. Mingaleev, and Kurt Busch. Wannier-function based scattering-matrix formalism for photonic crystal circuitry. *J. Opt. Soc. Am. B*, 25(2):202–209, Feb 2008. doi: 10.1364/JOSAB.25.000202. URL <http://josab.osa.org/abstract.cfm?URI=josab-25-2-202>. (Cited on pages xi, 20, and 171.)
- [41] Steven G. Johnson and J. D. Joannopoulos. Block-iterative frequency-domain methods for maxwell's equations in a planewave basis. *Opt. Express*, 8(3):173–190, 2001. URL <http://www.opticsexpress.org/abstract.cfm?URI=OPEX-8-3-173>. (Cited on pages xi, 143, 195, and 208.)
- [42] Ardavan Farjadpour, David Roundy, Alejandro Rodriguez, Mihai Ibanescu, Peter Bermel, J. D. Joannopoulos, Steven G. Johnson, and Geoffrey Burr. Improving accuracy by subpixel smoothing in FDTD. *Optics Letters*, 31:2972–2974, October 2006. URL <http://www.opticsinfobase.org/abstract.cfm?URI=ol-31-20-2972>. (Cited on page xi.)
- [43] Daniel Hermann. *Wannier-Function based Scattering-Matrix Formalism for Photonic Crystal Circuitry*. PhD thesis, University of Karlsruhe, 2008. URL <http://digbib.ubka.uni-karlsruhe.de/volltexte/1000009666>. (Cited on pages xii, 94, 108, 118, 119, and 131.)
- [44] David J. Griffiths. *Introduction to electrodynamics*. Prentice Hall, Upper Saddle River, NJ [u.a.], 3. ed. edition, 1999. ISBN 0-13-805326-X. URL http://www.ubka.uni-karlsruhe.de/hylib-bin/suche.cgi?opacdb=UBKA_OPAC&nd=7525831. Includes bibliographical references and index. - Previous ed.: 1989. (Cited on pages 1 and 2.)
- [45] John David Jackson. *Classical electrodynamics*. Wiley, New York, 3. ed. edition, 1999. ISBN 978-0-471-30932-1 ; 0-471-30932-X. URL http://www.ubka.uni-karlsruhe.de/hylib-bin/suche.cgi?opacdb=UBKA_OPAC&nd=7281656. (Cited on pages 1, 2, 3, and 139.)
- [46] Hartmann Römer. *Theoretical optics : an introduction*. Wiley-VCH, Weinheim, 2., rev. and enlarged ed. edition, 2009. ISBN 978-3-527-40776-7. URL http://www.ubka.uni-karlsruhe.de/hylib-bin/suche.cgi?opacdb=UBKA_OPAC&nd=283302313. (Cited on pages 1, 2, and 12.)

- [47] John D. Joannopoulos, Steven G. Johnson, Joshua N. Winn, and Robert D. Meade. *Photonic Crystals: Molding the Flow of Light (Second Edition)*. Princeton University Press, 2 edition, February 2008. ISBN 0691124566. URL <http://ab-initio.mit.edu/book/>.
(Cited on pages 1, 6, 7, and 25.)
- [48] Kazuaki Sakoda. *Optical properties of photonic crystals*. Springer series in optical sciences ; 80. Springer, Berlin, 2001. ISBN 3-540-41199-2. URL http://www.ubka.uni-karlsruhe.de/hylib-bin/suche.cgi?opacdb=UBKA_OPAC&nd=9049639.
(Cited on pages 1 and 25.)
- [49] Kuon [Hrsg.] Inoue, editor. *Photonic crystals : physics, fabrication and applications*. Springer series in optical sciences ; 94. Springer, Berlin, 2004. ISBN 3-540-20559-4. URL http://www.ubka.uni-karlsruhe.de/hylib-bin/suche.cgi?opacdb=UBKA_OPAC&nd=11123656&fbt=7855379-10979714. Includes bibliographical references and index; : £77.00 : CIP entry (Feb.).
(Cited on pages 1 and 16.)
- [50] VG Veselago. Electrodynamics of substances with simultaneously negative values of σ and μ . *Sov. Phys. USPEKHI*, 10(4):509–&, 1968. URL http://www.turpion.org/php/full/infoFT.phtml?journal_id=pu&paper_id=3699.
(Cited on page 3.)
- [51] D. R. Smith, J. B. Pendry, and M. C. K. Wiltshire. Metamaterials and negative refractive index. *Science*, 305(5685):788–792, 2004. doi: 10.1126/science.1096796. URL <http://www.sciencemag.org/cgi/content/abstract/305/5685/788>.
(Cited on page 3.)
- [52] J. B. Pendry. Negative refraction makes a perfect lens. *Phys. Rev. Lett.*, 85(18):3966–3969, Oct 2000. doi: 10.1103/PhysRevLett.85.3966. URL <http://link.aps.org/doi/10.1103/PhysRevLett.85.3966>.
(Cited on page 3.)
- [53] T. Ochiai, U. Leonhardt, and J. C. Nacher. A novel design of dielectric perfect invisibility devices. *J. Math. Phys.*, 49(3):032903, 2008. doi: 10.1063/1.2889717. URL <http://link.aip.org/link/?JMP/49/032903/1>.
(Cited on page 3.)
- [54] Tolga Ergin, Nicolas Stenger, Patrice Brenner, John B. Pendry, and Martin Wegener. Three-Dimensional Invisibility Cloak at Optical Wavelengths. *Science*, 328(5976):337–339, 2010. doi: 10.1126/science.1186351. URL <http://www.sciencemag.org/cgi/content/abstract/328/5976/337>.
(Cited on page 3.)
- [55] Malvin C. Saleh, Bahaa E. ; Teich. *Fundamentals of Photonics*. Wiley series in pure and applied optics. Wiley, Hoboken, N.J., 2. ed. edition, 2007. ISBN 978-0-471-35832-9. URL http://www.ubka.uni-karlsruhe.de/hylib-bin/suche.cgi?opacdb=UBKA_OPAC&nd=253454905.
(Cited on page 4.)
- [56] Neil W. Ashcroft and N. David Mermin. *Solid state physics*. Saunders College, Orlando, Fla., college ed., [repr.] edition, 2000. ISBN 0-03-083993-9. URL <http://www.ubka.uni-karlsruhe>.

- de/hylib-bin/suche.cgi?opacdb=UBKA_OPAC&nd=8905178.
(Cited on pages 6 and 181.)
- [57] R. D. Meade, A. M. Rappe, K. D. Brommer, J. D. Joannopoulos, and O. L. Alerhand. Accurate theoretical analysis of photonic band-gap materials. *Phys. Rev. B*, 48(11):8434–8437, Sep 1993. doi: 10.1103/PhysRevB.48.8434. URL http://prb.aps.org/abstract/PRE/v48/i11/p8434_1.
(Cited on pages 9, 143, 194, and 195.)
- [58] S. Kralj and S. Žumer. Saddle-splay elasticity of nematic structures confined to a cylindrical capillary. *Phys. Rev. E*, 51(1):366–379, Jan 1995. doi: 10.1103/PhysRevE.51.366. URL <http://link.aps.org/doi/10.1103/PhysRevE.51.366>.
(Cited on page 11.)
- [59] Kurt Busch and Sajeev John. Liquid-crystal photonic-band-gap materials: The tunable electromagnetic vacuum. *Phys. Rev. Lett.*, 83(5):967–970, Aug 1999. doi: 10.1103/PhysRevLett.83.967. URL <http://link.aps.org/doi/10.1103/PhysRevLett.83.967>.
(Cited on page 12.)
- [60] S. W. Leonard, J. P. Mondia, H. M. van Driel, O. Toader, S. John, K. Busch, A. Birner, U. Gösele, and V. Lehmann. Tunable two-dimensional photonic crystals using liquid crystal infiltration. *Phys. Rev. B*, 61(4):R2389–R2392, Jan 2000. doi: 10.1103/PhysRevB.61.R2389. URL <http://link.aps.org/doi/10.1103/PhysRevB.61.R2389>.
(Cited on page 12.)
- [61] H. Takeda and K. Yoshino. Tunable light propagation in Y-shaped waveguides in two-dimensional photonic crystals composed of semiconductors depending on temperature. *Optics Communications*, 219:177–182, April 2003.
(Cited on page 12.)
- [62] R J Potton. Reciprocity in optics. *Rep. Prog. Phys.*, 67(5):717–754, 2004. URL <http://stacks.iop.org/0034-4885/67/717>.
(Cited on page 12.)
- [63] C. Kölper. Guided mode based wannier function for photonic crystal slab circuitry. Master’s thesis, Universität Karlsruhe, nov 2008.
(Cited on page 12.)
- [64] Feng Wen, Sylvain David, Xavier Checoury, Moustafa El Kurdi, and Philippe Boucaud. Two-dimensional photonic crystals with large complete photonic band gaps in both te and tm polarizations. *Opt. Express*, 16(16):12278–12289, 2008. URL <http://www.opticsexpress.org/abstract.cfm?URI=oe-16-16-12278>.
(Cited on page 13.)
- [65] Lars H. Frandsen, Andrei V. Lavrinenko, Jacob Fage-Pedersen, and Peter I. Borel. Photonic crystal waveguides with semi-slow light and tailored dispersion properties. *Opt. Express*, 14(20):9444–9450, 2006. URL <http://www.opticsexpress.org/abstract.cfm?URI=oe-14-20-9444>.
(Cited on page 16.)
- [66] N. Moll and G.-L. Bona. Bend design for the low-group-velocity mode in photonic crystal-slab waveguides. *Applied Physics Letters*, 85(19):4322–4324, nov 2004. ISSN 0003-6951. doi: 10.1063/

- 1.1818340. URL http://ieeexplore.ieee.org/xpl/freeabs_all.jsp?arnumber=4874753.
(Cited on page 16.)
- [67] Yoshihiro Akahane, Takashi Asano, Bong-Shik Song, and Susumu Noda. Fine-tuned high-q photonic-crystal nanocavity. *Opt. Express*, 13(4):1202–1214, 2005. URL <http://www.opticsexpress.org/abstract.cfm?URI=oe-13-4-1202>.
(Cited on page 16.)
- [68] Susumu Noda. Recent progresses and future prospects of two- and three-dimensional photonic crystals. *J. Lightwave Technol.*, 24(12):4554–4567, 2006. URL <http://jlt.osa.org/abstract.cfm?URI=JLT-24-12-4554>.
(Cited on page 16.)
- [69] C. Grillet, C. Monat, C.L. Smith, M.W. Lee, S. Tomljenovic-Hanic, C. Karnutsch, and B.J. Eggleton. Reconfigurable photonic crystal circuits. *Laser & Photonics Reviews*, 4(2):192–204, 2010. doi: 10.1002/lpor.200810072. URL <http://dx.doi.org/10.1002/lpor.200810072>.
(Cited on page 16.)
- [70] Pascale El-Kallassi, Sandor Balog, Romuald Houdré, Laurent Balet, Lianhe Li, Marco Francardi, Annamaria Gerardino, Andrea Fiore, Rolando Ferrini, and Libero Zuppiroli. Local infiltration of planar photonic crystals with uv-curable polymers. *J. Opt. Soc. Am. B*, 25(10):1562–1567, Oct 2008. doi: 10.1364/JOSAB.25.001562. URL <http://josab.osa.org/abstract.cfm?URI=josab-25-10-1562>.
(Cited on page 16.)
- [71] T. Yoshie, A. Scherer, J. Hendrickson, G. Khitrova, H. M. Gibbs, G. Rupper, C. Ell, O. B. Shchekin, and D. G. Deppe. Vacuum Rabi splitting with a single quantum dot in a photonic crystal nanocavity. *Nature*, 432(7014):200–203, November 2004. ISSN 0028-0836. doi: 10.1038/nature03119. URL <http://dx.doi.org/10.1038/nature03119>.
(Cited on page 16.)
- [72] Y. Jiao, S. F. Mingaleev, M. Schillinger, D. A. B. Miller, S. Fan, and K. Busch. Wannier basis design and optimization of a photonic crystal waveguide crossing. *IEEE Photonics Technology Letters*, 17(9):1875, 9 2005. doi: 10.1109/LPT.2005.852326. URL http://ieeexplore.ieee.org/xpls/abs_all.jsp?arnumber=1498888.
(Cited on pages 20 and 108.)
- [73] J.P. Albert, C. Jouanin, D. Cassagne, and D. Monge. Photonic crystal modelling using a tight-binding wannier function method. *Optical and Quantum Electronics*, 34:251–263, 2002. ISSN 0306-8919. URL <http://dx.doi.org/10.1023/A:1013393918768>. 10.1023/A:1013393918768.
(Cited on page 21.)
- [74] W. Kohn. Analytic properties of bloch waves and wannier functions. *Phys. Rev.*, 115(4):809–821, Aug 1959. doi: 10.1103/PhysRev.115.809. URL http://prola.aps.org/abstract/PR/v115/i4/p809_1.
(Cited on pages 21 and 82.)
- [75] C S Feng, L M Mei, L Z Cai, X L Yang, S S Wei, and P Li. A plane-wave-based approach for complex photonic band structure and its applications to semi-infinite and finite system. *Journal of Physics D: Applied Physics*, 39(20):4316, 2006. URL <http://stacks.iop.org/0022-3727/39/>

- i=20/a=005.
(Cited on page 21.)
- [76] C. Schuler. Thermal emission of photonic crystals. Master's thesis, Karlsruhe Institute of Technology (KIT), sep 2009.
(Cited on page 21.)
- [77] Maria C Romano, Denis R Nacbar, and A Bruno-Alfonso. Wannier functions of a one-dimensional photonic crystal with inversion symmetry. *Journal of Physics B: Atomic, Molecular and Optical Physics*, 43(21):215403, 2010. URL <http://stacks.iop.org/0953-4075/43/i=21/a=215403>.
(Cited on page 22.)
- [78] A. Graham. Time domain simulations of non-linear photonic crystals using wannier functions. Master's thesis, Karlsruhe Institute of Technology (KIT), sep 2010.
(Cited on page 22.)
- [79] C. Wolff. *Title to be announced*. PhD thesis, Karlsruhe Institute of Technology (KIT).
(Cited on pages 22, 47, and 53.)
- [80] John F. Cornwell. *Group Theory in Physics*. Techniques of physics ; ... Acad. Press, London [u.a.], 19XX. URL http://www.ubka.uni-karlsruhe.de/hylib-bin/suche.cgi?opacdb=UBKA_OPAC&nd=955780.
(Cited on pages 25 and 30.)
- [81] Melvin Lax. *Symmetry Principles in Solid State and Molecular Physics*. A Wiley-Interscience publication. Wiley, New York, c 1974. ISBN 0-471-51903-0 ; 0-471-51904-9. URL http://www.ubka.uni-karlsruhe.de/hylib-bin/suche.cgi?opacdb=UBKA_OPAC&nd=1101372. Literaturangaben.
(Cited on page 25.)
- [82] Mildred S. Dresselhaus, Gene Dresselhaus, and Ado Jorio. *Group Theory : Application to the Physics of Condensed Matter*. Springer, Berlin, 2008. ISBN 3-540-32897-1 ; 978-3-540-32897-1. URL http://www.ubka.uni-karlsruhe.de/hylib-bin/suche.cgi?opacdb=UBKA_OPAC&nd=267535481. Erscheint: Juni 2006; Erscheinungstermin verschoben auf Dezember 2007.
(Cited on pages 25 and 33.)
- [83] Vjačeslav P. Evarestov, Robert A. ; Smirnov. *Site Symmetry in Crystals : Theory and Applications*. Springer series in solid state sciences ; 108. Springer, Berlin, 1993. ISBN 3-540-56052-1 ; 0-387-56052-1. URL http://www.ubka.uni-karlsruhe.de/hylib-bin/suche.cgi?opacdb=UBKA_OPAC&nd=3448590.
(Cited on pages 25, 29, 36, 37, 38, and 39.)
- [84] Walter Borchardt-Ott. *Kristallographie*. Springer-Lehrbuch. Springer, Berlin, 7., überarb. und erw. aufl. edition, 2009. ISBN 978-3-540-78270-4. URL http://www.ubka.uni-karlsruhe.de/hylib-bin/suche.cgi?opacdb=UBKA_OPAC&nd=285145150.
(Cited on page 25.)
- [85] International tables for crystallography, 19XX. URL http://www.ubka.uni-karlsruhe.de/hylib-bin/suche.cgi?opacdb=UBKA_OPAC&nd=958128. Teilw. ersch. in Kluwer-Verl., teilw. in Springer-Verl.
(Cited on pages 25 and 222.)

- [86] Jacques Des Cloizeaux. Energy bands and projection operators in a crystal: Analytic and asymptotic properties. *Phys. Rev.*, 135(3A):A685–A697, Aug 1964. doi: 10.1103/PhysRev.135.A685. URL http://prola.aps.org/abstract/PR/v135/i3A/pA685_1.
(Cited on page 42.)
- [87] Jacques Des Cloizeaux. Analytical properties of n -dimensional energy bands and wannier functions. *Phys. Rev.*, 135(3A):A698–A707, Aug 1964. doi: 10.1103/PhysRev.135.A698. URL http://prola.aps.org/forward/PR/v135/i3A/pA698_1.
(Cited on pages 42 and 54.)
- [88] Bilbao crystallographic server. <http://www.cryst.ehu.es/>.
(Cited on page 43.)
- [89] Mois Ilia Aroyo, Juan Manuel Perez-Mato, Cesar Capillas, Eli Kroumova, Svetoslav Ivantchev, Gotzon Madariaga, Asen Kirov, and Hans Wondratschek. Bilbao crystallographic server: I. databases and crystallographic computing programs. *Zeitschrift für Kristallographie*, 221(1):15–27, 2006. doi: 10.1524/zkri.2006.221.1.15. URL <http://www.oldenbourg-link.com/doi/abs/10.1524/zkri.2006.221.1.15>.
(Cited on page 43.)
- [90] M. I. Aroyo, A. Kirov, C. Capillas, J. M. Perez-Mato, and H. Wondratschek. Bilbao crystallographic server ii: Representations of crystallographic point groups and space groups. *Acta Cryst. A*, A62:115–128, 2006. doi: doi:10.1107/S0108767305040286. URL <http://scripts.iucr.org/cgi-bin/paper?S0108767305040286>.
(Cited on page 43.)
- [91] Susumu Noda, Katsuhiko Tomoda, Noritsugu Yamamoto, and Alongkarn Chutinan. Full Three-Dimensional Photonic Bandgap Crystals at Near-Infrared Wavelengths. *Science*, 289(5479):604–606, 2000. doi: 10.1126/science.289.5479.604. URL <http://www.sciencemag.org/content/289/5479/604.abstract>.
(Cited on page 44.)
- [92] Hendrik J. Monkhorst and James D. Pack. Special points for brillouin-zone integrations. *Phys. Rev. B*, 13(12):5188–5192, Jun 1976. doi: 10.1103/PhysRevB.13.5188. URL http://prb.aps.org/abstract/PRB/v13/i12/p5188_1.
(Cited on pages 52 and 196.)
- [93] B. C. Carlson and Joseph M. Keller. Orthogonalization procedures and the localization of wannier functions. *Phys. Rev.*, 105(1):102–103, Jan 1957. doi: 10.1103/PhysRev.105.102. URL http://prola.aps.org/pdf/PR/v105/i1/p102_1.
(Cited on page 54.)
- [94] Peter Kuchment. Tight frames of exponentially decaying wannier functions. *Journal of Physics A: Mathematical and Theoretical*, 42(2):025203, 2009. URL <http://stacks.iop.org/1751-8121/42/i=2/a=025203>.
(Cited on page 86.)
- [95] Christian Brouder, Gianluca Panati, Matteo Calandra, Christophe Mourougane, and Nicola Marzari. Exponential localization of wannier functions in insulators. *Phys. Rev. Lett.*, 98(4):046402, Jan 2007. doi: 10.1103/PhysRevLett.98.046402. URL <http://link.aps.org/doi/10.1103/PhysRevLett.98.046402>.

- 1103/PhysRevLett.98.046402.
(Cited on page 86.)
- [96] C. Blum. Time-domain method for the solution of Maxwell's equations in periodic media using Wannier functions. Master's thesis, Karlsruhe Institute of Technology (KIT), jan 2010.
(Cited on page 108.)
- [97] M. Köhl. Ungeordnete Photonische Kristalle: Eine Untersuchung basierend auf Green'schen Funktionen und der Wannierbasis. Master's thesis, Karlsruhe Institute of Technology (KIT), dec 2010.
(Cited on page 123.)
- [98] Ernest R. Davidson and David Feller. Basis set selection for molecular calculations. *Chemical Reviews*, 86(4):681–696, 1986. doi: 10.1021/cr00074a002. URL <http://pubs.acs.org/doi/abs/10.1021/cr00074a002>.
(Cited on page 131.)
- [99] M. Schillinger, S. F. Mingaleev, D. Hermann, and K. Busch. Highly localized wannier functions for the efficient modeling of photonic crystal circuits. In Ali Adibi, Shawn-Yu Lin, and Axel Scherer, editors, *Proceedings of SPIE: Volume 5733 – Photonic Crystal Materials and Devices III*, pages 324–335. SPIE, 2005. URL http://mingaleev.scilib.org/papers/pdf/SPIE_2005_5733_00324.pdf.
(Cited on page 132.)
- [100] R. D. Meade, A. M. Rappe, K. D. Brommer, J. D. Joannopoulos, and O. L. Alherhand. Erratum: Accurate theoretical analysis of photonic band-gap materials [phys. rev. b 48, 8434 (1993)]. *Phys. Rev. B*, 55(23):15942, Jun 1997. doi: 10.1103/PhysRevB.55.15942. URL http://prb.aps.org/abstract/PRB/v55/i23/p15942_1.
(Cited on pages 143, 194, and 195.)
- [101] A. Farjadpour, David Roundy, Alejandro Rodriguez, M. Ibanescu, Peter Bermel, J. D. Joannopoulos, Steven G. Johnson, and G. W. Burr. Improving accuracy by subpixel smoothing in the finite-difference time domain. *Opt. Lett.*, 31(20):2972–2974, Oct 2006. doi: 10.1364/OL.31.002972. URL <http://ol.osa.org/abstract.cfm?URI=ol-31-20-2972>.
(Cited on page 194.)
- [102] Steven G. Johnson, J. D. Joannopoulos, and Marin Soljačić. Nanostructures and computation wiki at mit. URL http://ab-initio.mit.edu/wiki/index.php/Main_Page.
(Cited on pages 199 and 201.)
- [103] M. Plihal and A. A. Maradudin. Photonic band structure of two-dimensional systems: The triangular lattice. *Phys. Rev. B*, 44(16):8565–8571, Oct 1991. doi: 10.1103/PhysRevB.44.8565. URL http://prb.aps.org/abstract/PRB/v44/i16/p8565_1.
(Cited on page 209.)

